ransactions
f the ASME

EDITORIAL STAFF
Editor, J. J. JAKLITSCH, JR.
Production Editor,
STELLA ROBINSON
Editorial Production Asst.
BETH DARCHI
Associate Editors
Air Pollution Control
H. E. HESKETH
Diesel and Gas Engine Power
F. PEKAR
Gas Turbine
R. A. HARMON
Power
D. T. BERUBE
Solar Energy
H. M. CURRAN
Energetics
J. B. COMLY
Fuels
R. E. BARRETT
Nuclear Engineering
M. S. OZKER

POLICY BOARD,
COMMUNICATIONS
Chairman and Vice-President
I. BERMAN

Members-at-Large
J. W. LOCKE
J. E. ORTLOFF
M. J. RABINS
W. J. WARREN

Policy Board Representatives
Basic Engineering, F. LANDIS
General Engineering, C. F. PHILLIPS
Industry, J. E. ORTLOFF
Power, R. E. REDER
Research, G. P. COOPER
Codes and Stds., L. L. ELDER
Computer Technology Com.,
A. A. SEIREG
Nom. Com. Rep.,
J. W. LOCKE

Business Staff
345 E. 47th St.
New York, N. Y. 10017
(212) 644-7789
Mng. Dir., Publ., J. J. FREY

OFFICERS OF THE ASME
President, CHARLES E. JONES
Exec. Dir. & Sec'y, ROGERS B. FINCH
Treasurer, ROBERT A. BENNETT

al of Engineering for Power (ISSN 0022-0825) is edited and published quarterly at the offices of merican Society of Mechanical Engineers, United ineering Center, 345 E. 47th St., New York, N. Y. 0017. ASME-TWX No. 710-581-5267, New York. ond Class postage paid at New York, N.Y., and at additional mailing offices.

NGES OF ADDRESS must be received at Society headquarters seven weeks before they are to be effective. Please send old label and new address.

PRICES: To members, $30.00, annually; to nmembers, $60.00. Single copies, $20.00 each. $5.00 for postage to countries outside the United States and Canada.

TEMENT from By-Laws. The Society shall not be sponsible for statements or opinions advanced in rs or . . . printed in its publications (B 13, Par. 4).

COPYRIGHT © 1981 by the American Society of hanical Engineers. Reprints from this publication be made on condition that full credit be given the TRANSACTIONS OF THE ASME—JOURNAL OF ENGINEERING FOR POWER, and the author, and date of publication be stated.

INDEXED by the Engineering Index, Inc.

Journal of Engineering for Power

Published Quarterly by The American Society of Mechanical Engineers
VOLUME 103 • NUMBER 1 • JANUARY 1981

1 Calculation of Windmilling Characteristics of Turbojet Engines (80-GT-50)
Zhao Qi Shou

13 An Evaluation of Steam Injected Combustion Turbine Systems (80-GT-51)
D. H. Brown and A. Cohn

20 Investigations of an Axial Compressor End-Wall Boundary Layer Prediction Method (80-GT-53)
J. De Ruyck and C. Hirsch

34 The Civic: A Concept in Vortex Induced Combustion for the Solar Gemini 10 kW Gas Turbine (80-GT-54)
J. R. Shekleton

43 The Interrelationship between Soot and Fuel NO_x Control in Gas Turbine Combustors (80-GT-76)
W. S. Blazowski, A. F. Sarofim, and J. C. Keck

49 Soot Formation in a Turbulent Swirl Stabilized Laboratory Combustor (80-GT-77)
D. P. Hoult and A. Ekchian

54 Ten Years of Digital Computer Control of Combustion Turbines (80-GT-78)
R. A. Yannone and J. F. Reuther

60 Effects of Free-Stream Turbulence Intensity and Frequency on Heat Transfer to Turbine Blading (80-GT-79)
F. J. Bayley and W. J. Priddy

65 Turbomachinery Design Considerations for the Nuclear HTGR-GT Power Plant (80-GT-80)
Colin F. McDonald and Murdo J. Smith

78 Comparison of Experimental and Computational Shock Structure in a Transonic Compressor Rotor (80-GT-81)
G. Haymann-Haber and W. T. Thompkins, Jr.

89 The Nuclear Closed-Cycle Gas Turbine (HTGR-GT)—Dry Cooled Commercial Power Plant Studies (80-GT-82)
Colin F. McDonald and Charles R. Boland

101 Demonstration of a Unified Approach to the Balancing of Flexible Rotors (80-GT-87)
M. S. Darlow, A. J. Smalley, and A. G. Parkinson

108 Influence of Acceleration on the Critical Speed of a Jeffcott Rotor (80-GT-88)
H. L. Hassenpflug, R. D. Flack, and E. J. Gunter

114 The Influence of Recent Heat Transfer Data on Gas Mixtures (He-Ar, H_2-CO_2) on Closed Cycle Gas Turbines (80-GT-89)
B. L. Pierce

118 Some Effects of Using Water as a Test Fluid in Fuel Nozzle Spray Analysis (80-GT-90)
H. C. Simmons and C. F. Harding

124 Interferometric Measurements in a Turbine Cascade Using Image-Plane Holography (80-GT-91)
P. J. Bryanston-Cross, T. Lang, M. L. G. Oldfield, and R. J. G. Norton

131 Structure and Decay Characteristics of Turbulence in the Near and Far-Wake of a Moderately Loaded Compressor Rotor Blade (80-GT-95)
A. Ravindranath and B. Lakshminarayana

141 Water-Cooled Gas Turbine Monometallic Nozzle Development (80-GT-97)
P. W. Schilke, W. S. Blazek, and W. F. Schilling

146 Low-Pressure Plasma-Spray Coatings for Hot-Corrosion Resistance (80-GT-98)
R. W. Smith, W. F. Schilling, and H. M. Fox

154 The Nutating Traction Drive (80-GT-99)
Y. Kemper

158 Aerodynamic and Geometric Design Criteria for the Performance of Low Powered Vehicular Gas Turbines (80-GT-117)
O. E. Balje

168 Hydrostatic Power Splitting Transmissions Design and Application Examples (80-GT-123)
J. Pichard and B. Besson

174 Experiments on the Vibration Characteristics of a Rotor With Flexible, Damped Support (80-GT-124)
Yan Li-Tang and Li Qi-Han

(*continued on page 19*)

Downloaded 03 Jun 2010 to 171.66.16.159. Redistribution subject to ASME license or copyright; see http://www.asme.org/terms/Terms_Use.cfm

180 A Statistical Investigation of Microstructure and Crack Growth in Titanium Alloys (80-GT-125)
D. A. Wilson and D. W. Hoeppner

188 The Control of Hot Corrosion in Marine Gas Turbines (80-GT-126)
J. F. G. Condé and C. G. McCreath

198 Gas Turbine Engine Disk Retirement-for-Cause: An Application of Fracture Mechanics and NDE (80-GT-127)
C. G. Annis, Jr., M. C. VanWanderham, J. A. Harris, Jr., and D. L. Sims

201 Nonaxisymmetric Blade Row Interaction in Axial Turbomachines (80-GT-133)
N. A. Mitchell

210 The Effect of the Axial Velocity Density Ratio on the Aerodynamic Coefficients of Compressor Cascades (80-GT-134)
J. Starke

220 Closed-Cycle Gas Turbine Working Fluids (80-GT-135)
J. C. Lee, J. Campbell, Jr., and D. E. Wright

229 The Hybrid Diffuser (80-GT-136)
R. C. Adkins, D. S. Matharu, and J. O. Yost

237 Boundary Layer Studies on Highly Loaded Cascades using Heated Thin Films and a Traversing Probe (80-GT-137)
M. L. G. Oldfield, R. Kiock, A. T. Holmes, and C. G. Graham

247 The Combined Effect of Axial Velocity Density Ratio and Aspect Ratio on Compressor Cascade Performance (80-GT-138)
U. Stark and H. Hoheisel

256 Information for authors

Downloaded 03 Jun 2010 to 171.66.16.159. Redistribution subject to ASME license or copyright; see http://www.asme.org/terms/Terms_Use.cfm

Zhao Qi Shou
Peking Institute of Aeronautics and Astronautics,
Peking,
Peoples' Republic of China

Calculation of Windmilling Characteristics of Turbojet Engines

The operation of a turbojet engine under windmilling conditions was analyzed and the relationship of engine speed and airflow has been derived. Replacing the efficiencies of compressor and turbine by a total pressure loss coefficient, the author was able to obtain the equations for matching the engine components and the universal curve of windmilling turbine characteristic based on theoretical analysis and experimental data. Based on the relations obtained, a simple method for calculating the windmilling characteristic of a turbojet engine was derived. In the absence of compressor and turbine characteristics under windmilling conditions, two approximate calculating methods were developed. The theoretical relations developed have been checked by experimental data. An example of the application of this approximate method is presented in the Appendix and the agreement between the prediction and experimental data is generally good.

I Introduction

Windmilling characteristics of aero gas turbine engines are required by the designers of aircraft and engines as well as flight operation and they are especially significant for combustor design. One of the major problems that must be considered in the design of an advanced combustion chamber is reliable relighting of the gas turbine engine under windmilling conditions at all altitudes. In order to solve this problem it is necessary to estimate the windmilling characteristics of a turbine engine and air parameters at the inlet of the combustion chamber. Few published papers deal with this problem. Alabin [1] discussed the calculation method utilizing the matching line in principle; however, up to now it has not been used practically.

Based on an analysis of the working process of a turbojet engine under windmilling condition, precise and an approximate methods of calculating windmilling characteristics have been derived.

The present paper is limited to turbojet engines, and more work would be required to analyze turbofan engines.

2 The Working Process of a Turbojet Engine under Windmilling Condition

In windmilling operation, by means of the dynamic pressure of the intake flow, the air flows through the engine and rotates the rotor. The direction of rotation is determined by the direction of resultant aerodynamic torques acting on the rotor. Because the airflow does work on the rotor to overcome the engine friction and as a result of the effect of the shape of blades, the direction of rotation remains the same as the original direction of rotation.

The rotational speed depends on the balance of aerodynamic torques acting on each stage of the rotor as well as the friction torques.

The air velocity (or air flow rate) within the engine mainly depends on the air passage area and the overall pressure losses through the engine.

In the compressor, the rear stage passage area appears excessively contracted in windmilling operation, as a result, the attack angles on the front and rear stages are off design. The friction torque is usually small relative to the aerodynamic torque. The attack angles on various stages of the compressor will vary about zero deg. The aerodynamic torque acting on the turbine in the windmilling operation increases with the increase of flight velocity, so that the attack angles in the compressor change towards positive value with the increase of flight velocity, as illustrated in Tables 1 and 2.

The values of attack angles listed in the tables were obtained from experimental data taken on windmilling operation at simulated high altitude test facilities.

It is obvious that the more the attack angles shift from zero attack angle, the greater the total pressure; and in an axial flow compressor, the stage with a large negative attack angle will work as a turbine. The net change of total pressure of air flow passing through the compressor is the result of three components, i.e.: the total pressure increase caused by transferring work to the passing air from some stages of the compressor, the total pressure loss due to losses, and the total pressure drop on several stages of the compressor which operate as a turbine.

In the turbine, because of the large swirl angle of the nozzle guide vanes and its convergent passage, the air flow always expands and delivers energy to the rotor during the windmilling operation. A part of this energy is consumed to overcome the friction and the remainder is delivered solely to the compressor and then transferred back to the air. Therefore, in the windmilling operation the total temperature of airflow rises through the compressor and drops through the turbine. The temperature of air after the turbine is nearly the same as the temperature at the engine intake, since the power absorbed due to the friction is relatively small.

As for combustor, afterburner and jet pipe, under the windmilling operation conditions only total pressure loss occurs with no change total temperatures.

The relations between the flight Mach number and the air parameters for several turbojet engines are shown in Fig. 1. Those parameters were obtained from experimental data under windmilling conditions at simulated high altitude test facilities.

Contributed by the Gas Turbine, Division and presented at the Gas Turbine Conference and Products Show, New Orleans, La., March 10–13, 1980 of THE AMERICAN SOCIETY OF MECHANICAL ENGINEERS. Manuscript received at ASME Headquarters December 11, 1979. Paper No. 80-GT-50.

Copyright © 1981 by ASME
Downloaded 01 Jun 2010 to 171.66.16.59. Redistribution subject to ASME license or copyright; see http://www.asme.org/terms/Terms_Use.cfm

Table 1 Axial flow compressor of six stages

Engine A $\pi_{c0} = 8.85$

Flight velocities M_H	0.314	0.62	0.913	1.075
Air velocities at compressor intake M_1	0.0528	0.1035	0.145	0.168
Attack angles on first stage at mean radius	+1°50'	+3°18'	+7°30'	+10°24'
Attack angles on sixth stage at mean radius	-19°	-17.5°	-13°	-8.5°

Table 2 Axial flow compressor of one stage and a centrifugal compressor

Engine B $\pi_{c0} = 5.5$

Flight velocities M_H	0.253	0.385	0.662	0.775	0.881
Air velocities at axial flow compressor intake M_1	0.036	0.055	0.090	0.101	0.114
Attack angles on axial flow compressor at mean radius	-5°20'	-1°40'	+3°50'	+7°20'	+8°20'
Attack angles on centrifugal flow compressor at mean radius	-22.7°	-18.5°	-14.5°	-12.3°	-10.3°

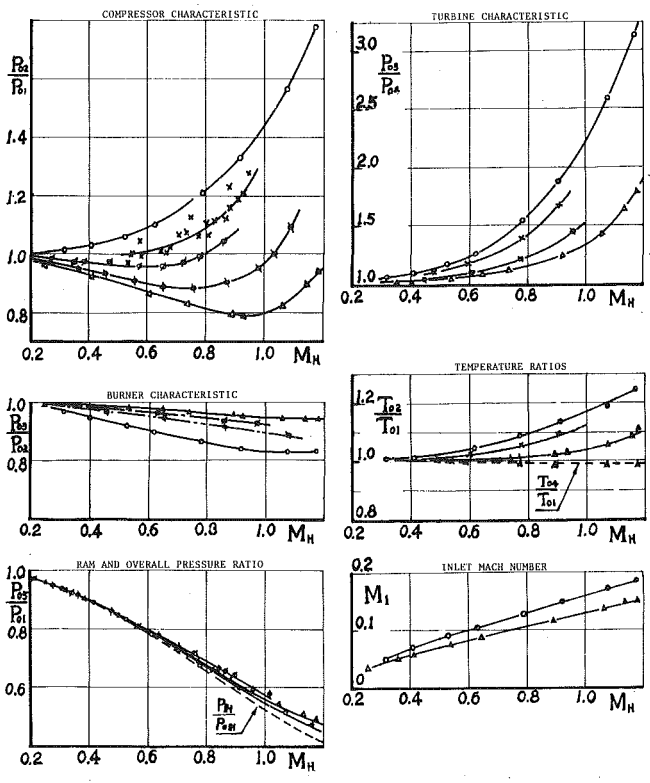

Fig. 1 Air parameters in the turbojet engine as a function of flight Mach number in windmilling operation

The shape of the curves in this figure can be understood by application to the above-mentioned principles.

Fig. 1 (*f*) indicates that the exit total pressure is approximately equal to the inlet static pressure for a given flight Mach number. This indicates the kinetic energy of the incoming air has been exhausted through the engine showing that the internal flow resistance in the engine is quite substantial. The P_{05}/P_{01} curves of different engines are close to each other.

Fig. 2 and Fig. 3 represent the airflow rate characteristics and the engine speed characteristics of turbojet engines under windmilling conditions.

3 The Analysis of the Windmilling Engine Speed Characteristics

When the engine speed is stable in windmilling operation the torques which act on the compressor and the turbine M_c and M_t should be balanced with the friction torque M_f, that is

Nomenclature

A = area (m^2)
C_P = specific heat at constant pressure (Kcal/Kg·K)
C = velocity of airflow (m/s)
D = diameter (m)
g = acceleration due to gravity (m/s^2)
J = mechanical equivalent of heat (Kcal/Kg·m)
M = Mach number
M_H = flight Mach number
M_f = friction torque of the transmission system (Kg·m)
M_t = aerodynamic torque acting on the turbine (Kg·m)
M_c = aerodynamic torque acting on the compressor (Kg·m)
m = airflow rate (Kg/s)
n = engine speed (rpm)
P = static pressure (Kg/m^2)
P_0 = total pressure (Kg/m^2)
$q(\lambda)$ = aerodynamic function:

$$q(\lambda) = \frac{A^*}{A} M \left(\left(\frac{2}{\gamma+1}\right) \times \left(1 + \frac{\gamma-1}{2} M^2\right)\right)^{\left(\frac{(\gamma+1)}{2(1-\gamma)}\right)}$$

i = enthalpy
ρ = density
R = gas constant (Kg·m/Kg·K)
T = static temperature (K)
T_0 = total temperature (°K)
U = circumferential velocity (m/s)
V = relative velocity (m/s)
W_f = friction power (Kg·m/s)
γ = specific heat ratio
ζ = total pressure loss coefficient
σ = total pressure recovery coefficient
π = pressure ratio

Subscripts

1 = at inlet of compressor
2 = at inlet of combustion chamber
3 = at exit of nozzle guide vanes
4 = at exit of turbine
5 = at exit of nozzle
c = compressor
cc = combustion chamber
ap = afterburner and jet pipe
H = ambient
i = air intake
r = rated
t = turbine
Σ = the whole engine
I = the general expression for the Ith stage

Downloaded 01 Jun 2010 to 171.66.16.59. Redistribution subject to ASME license or copyright; see http://www.asme.org/terms/Terms_Use.cfm

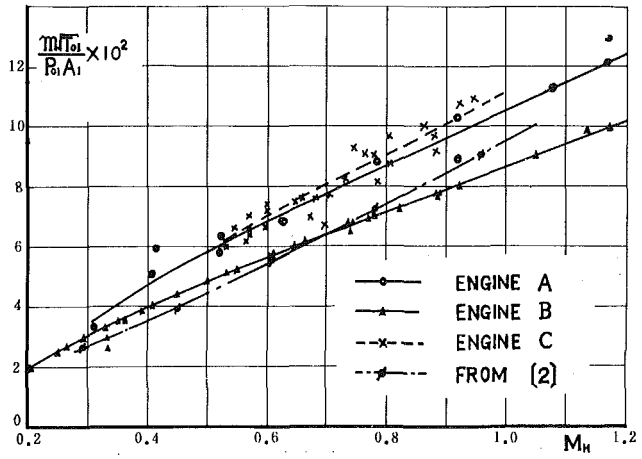

Fig. 2 Windmilling airflow rate characteristics for several turbojet engines

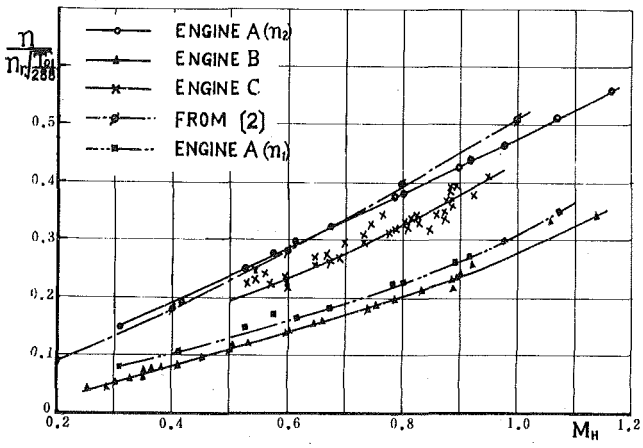

Fig. 3 Windmilling engine speed characteristics for several turbojet engines

$$M_f = M_c + M_t = M_{cI} + M_{cII} + \ldots + M_{tI} + M_{tII} + \ldots$$

The aerodynamic torque acting on the first stage of the compressor rotor M_{cI} (see Fig. 4 (a)) will be

$$M_{cI} = \int_{\text{root}}^{\text{top}} r \frac{dm}{g} \Delta C_{ul} \tag{3.2}$$

where

$$dm = 2\pi(P_1/RT_1)C_1 r dr$$

$$\Delta C_{ul} = C_{2u} = C_{2a} tg\beta_2 - U$$

$$U = 2\pi rn$$

Integrating equation (3.2) and expressing it by means of the parameters at mean radius, we obtain

$$M_c = \frac{D_c P_1 C_1 A_1}{2gRT_1}(a_1 C_1 tg\beta_{2m} - b_{I\pi D_c} n) \tag{3.3}$$

where

β_{2m} is the air flow angle at mean radius at outlet.

a_I is a factor, a function of tip-to-hub ratio $\overline{d}$, blade twist $\dfrac{tg\beta}{tg\beta_{2m}}$ and $\dfrac{C_{2a}}{C_1}$.

b_I is a factor, that is $b_I = (1 + d^{-2})/2$.

The aerodynamic torque acting on the rotor of second stage M_c is the same as equation (3.2). From the velocity triangles as shown in Fig. 4(b) and following the same procedures as mentioned above, we obtain

$$M_{cII} = \frac{D_c P_1 C_1 A_1}{2gRT_1}(a_{II}' C_1 tg\theta_m' + a_{II} C_1 tg\theta_{2m}' - b_{II}\pi D_c n) \tag{3.4}$$

The expressions of aerodynamic torque of the rear stages of the compressor and that of the turbine rotors are similar to equation (3.4). Substituting the equations (3.3), (3.4) and others into the equation (3.1), we obtain

$$M_f = \frac{DP_1 C_1 A_1}{2gRT_1}(KC_1 - Li\pi Dn) \tag{3.5}$$

where D is the diameter of engine, represented by the diameter of compressor or turbine.

$$K = (a_I tg\beta_{2m} + a_{II} tg\beta_{2m}' + \ldots + a_{II}' tg\theta_m' + \ldots)$$

$\beta_{2m'}$ $\beta_{2m''}$ θ_m' are the outlet airflow angles of each stage of rotor at mean radius for compressor and turbine, respectively.

$a_I' \ldots a_{II}'$ are the factors of the same property as a_1.

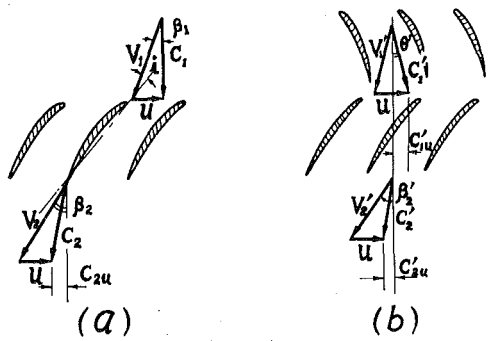

Fig. 4 Velocity triangles for first and second stages of compressor

i represents the number of stages of compressor and turbine.

$$L = \frac{1}{i}(b_I + b_{II} + \ldots) \text{ while } b_I' \, b_{II}' \ldots$$

are the function of the tip-to-hub ratio $\overline{d}$ of compressor and turbine, in general, $\overline{d} = 0.4 \rightarrow 0.8$, then L is approximately 0.7.

In equation (3.5), replacing the velocity C_1 with Mach number M_1, we obtain

$$\frac{2M_f}{\gamma DP_1 A_1 M_1} = (KM_1 - Li\pi Dn/\sqrt{\gamma gRT_1}) \tag{3.6}$$

Equation (4.3) is the basic relationship of engine speed characteristics of turbojet engine under windmilling condition. In this equation, the left side of the equation is far less than one term on the right hand side $Li\pi Dn/\sqrt{\gamma gRT_1}$, so the left hand side of the equation may be neglected, then

$$KM_1 = Li\pi Dn/\sqrt{\gamma gRT_1} \tag{3.7}$$

The ratio is

$$Z = \frac{2M_f}{\gamma DP_1 A_1 M_1}\frac{\sqrt{\gamma gRT_1}}{Li\pi Dn} = \frac{2gM_f}{0.7\pi niD^2 m} \tag{3.8}$$

The expression (3.8) shows that the larger the values of D, n and i, the smaller value of Z has. For example, Engine B is of small size, by experimental data we obtain $Z = 0.052$, when $H = 0$ (sea level), $M_H = 0.515$ while Engine A is of middle size, $Z = 0.005$, when $H = 0$, $M_H = 0.407$. Therefore, for the ordinary turbojet engine, equation (3.7) is the representation of the windmilling engine speed characteristics. It will be further simplified as follows.

As a rule, $M < 0.2$, thereby $T_1 \simeq T_{0H'}$ and $\pi D = U_r/n_r$ substituting them into equation (3.7), we obtain

$$\frac{KM_1}{LiU_r} = \frac{n}{n_r\sqrt{T_{0H}}} \tag{3.9}$$

Downloaded 01 Jun 2010 to 171.66.16.59. Redistribution subject to ASME license or copyright; see http://www.asme.org/terms/Terms_Use.cfm

where

n_r is the rated rpm of the engine.

U_r is the circumferential velocity at rotor tip at rated rpm.

According to equation (4.5), i.e.

$$M_1 = f\left(\frac{A_5}{A_1}, \frac{P_5}{P_{01}}, \zeta\Sigma\right)$$

M is merely a function of the flight Mach number M and the geometry and configuration of the engine, so left hand side of equation (3.9) is also the function of M_H and the geometry and configuration of the engine. Therefore $n/n_r\sqrt{T_{0H}}$ is the similarity parameter of engine speed characteristics under windmilling conditions, its nondimensional form $n/n_r\sqrt{T_{0H}/288}$ is appropriate to the coordinate of engine speed characteristic.

Equation (3.9) shows that the windmilling engine speed relationship does not vary with altitude. But in the case of a small engine, the friction torque has a definite influence on it, altitude will give effects on the curves. The relationship between them is as follows.

For the same engine, at the same flight Mach number M_H at different altitudes H_1 and H_2, which correspond to the different atmospheric pressures P_{H1} and P_{H2} at different air total temperature T_{0H1} and T_{0H2} at different engine speed n_1 and n_2, substituting them into the equation (3.6), we obtain

$$\frac{n_2}{n_r\sqrt{T_{0H2}}} = \frac{n_1}{n_r\sqrt{T_{0H1}}}\left(1 - Z_1\left(\frac{P_{H1}}{P_{H2}} - 1\right)\right) \tag{3.10}$$

where

$$Z_1 = \frac{2gM_f}{0.7\pi n_1 i D^2 m_1}$$

The comparison between the results calculated from equation (3.10) and the experimental data of Engine B is shown in Fig. 5. In this calculation the values of Z_1, and n_1, are obtained relative to the altitude $H = 0$. Fig. 5 shows that the calculated results agree with the experimental data, and at low Mach numbers, the stronger is the influence of friction torque and altitude.

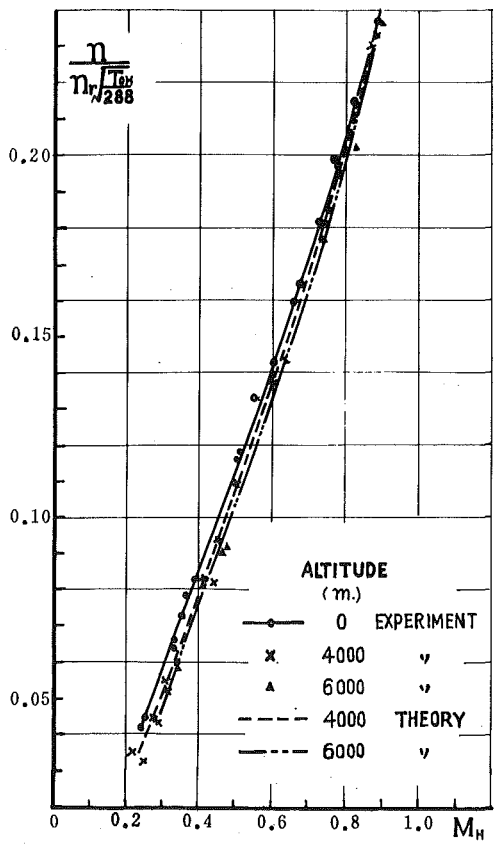

Fig. 5 Effect of altitude on windmilling engine speed characteristic for Engine B, comparison between values of prediction and experiment

In reference [3], the thrust of the engine is 1500 kg, which is 80 percent larger than the Engine B, so the experimental result of windmilling engine speed characteristic shows that the effect of altitude on the characteristic curve is smaller than that of Engine B.

4 The Analysis of Windmilling Airflow Rate Characteristic

When the airflow is stable in windmilling operation, the airflow passing through the engine must observe the following relationships:

$$\text{equation of continuity } m = A_1\rho_1 C_1 = A_5\rho_5 C_5 \tag{4.1}$$

$$\text{equation of state } \rho g = \frac{P}{RT} \tag{4.2}$$

$$\text{velocity at nozzle exit } C_5 = \sqrt{\frac{2gRT_5}{P_5}(P_{05} - P_5)}$$

$$\text{total pressure loss } \sigma_\Sigma = \frac{P_{05}}{P_{01}} = \left(1 - \frac{\gamma}{2}M_1^2\zeta_\Sigma\right)$$

we assume

$$T_1 = T_5 \text{ and } \frac{P_5}{P_1} = \frac{P_5}{P_{01}} \tag{4.4}$$

Solving the above simultaneous equations, using the equation of aerodynamic parameters $M_1 = C_1/\sqrt{\gamma g R T_1}$,

$$\frac{T_{01}}{T_1} = \left(1 + \frac{\gamma - 1}{2}M_1^2\right), \frac{P_{01}}{P_1} = \left(1 + \frac{\gamma - 1}{2}M_1^2\right)\gamma/(\gamma - 1)$$

neglecting higher-order term of M_1, we obtain

$$M_1^2 = \frac{2}{\gamma}\left(1 - \frac{P_5}{P_{01}}\right)\left(\frac{P_{01}A_1^2}{P_5A_5^2} + \zeta_\Sigma\right)^{-1} \tag{4.5}$$

and

$$\left(\frac{m\sqrt{T_{01}}}{P_{01}A_1}\right)^2 = \frac{2\frac{g}{R}\left(1 - \frac{P_5}{P_{01}}\right)}{\frac{P_{01}}{P_5}\left(\frac{A_1}{A_5}\right)^2 + \zeta_\Sigma + \frac{(\gamma + 1)}{\gamma}\left(1 - \frac{P_5}{P_{01}}\right)} \tag{4.6}$$

If $P_{01} = P_{0H}$ and $P_5 = P_H$ then equation (4.6) becomes

$$\left(\frac{m\sqrt{T_{0H}}}{P_{0H}A_1}\right)^2 = \frac{\frac{2g}{R}\left(1 - \left(\frac{a}{\sigma_i}\right)\left(\frac{P_H}{P_{0H}}\right)\right)}{\zeta_\Sigma + \left(\frac{A_1}{A_5}\right)^2\left(\frac{P_{0H}}{P_H}\right) + \frac{\gamma + 1}{\gamma}\left(1 - \frac{P_H}{P_{0H}}\right)} \tag{4.7}$$

When taking into consideration the flow loss at the air intake and the ejection in the exhaust nozzle, we have $P_{01} = \sigma_i P_{0H}$ and $P_5 = aP_H$. Equation (4.6) can be written as

$$\left(\frac{m\sqrt{T_{0H}}}{P_{0H}A_1}\right)^2 = \frac{\frac{2g}{R}\left(1 - \left(\frac{a}{\sigma_i}\right)\left(\frac{P_H}{P_{0H}}\right)\right)\sigma_i^2}{\zeta_\Sigma + \left(\frac{A_1}{A_5}\right)^2\left(\frac{\sigma i}{a}\right)\left(\frac{P_{0H}}{P_H}\right) + \frac{\gamma + 1}{\gamma}\left(1 - \left(\frac{a}{\sigma_i}\right)\left(\frac{P_H}{P_{0H}}\right)\right)} \tag{4.8}$$

Equations (4.7) and (4.8) are the relationships of windmilling airflow rare characteristics.

In deriving the above equations, some assumptions and simplification have been made. By error analyses we realized that the deviation caused by them is less than 1.5 percent. Fig. 6 shows the comparison between the experimental data $\zeta_{\Sigma exp}$ and the calculated data ζ_Σ. The calculated data are obtained from equation (4.7) and the experimental data are obtained from equation (4.4). Fig. 6 shows the correctness of equations (4.7) and (4.8). It should be noticed that here ζ_Σ is yet unknown. The method of calculating ζ_Σ will be shown later.

From equation (4.7), we see that the right hand side of it is only a function of flight Mach number and geometry and configuration of

Downloaded 01 Jun 2010 to 171.66.16.59. Redistribution subject to ASME license or copyright; see http://www.asme.org/terms/Terms_Use.cfm

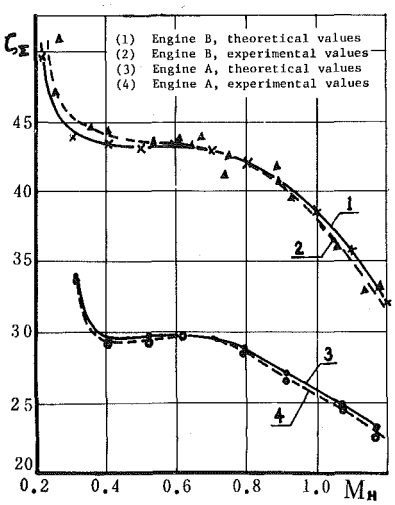

Fig. 6 Engine total pressure loss coefficients as function of flight Mach number, in windmilling operation, comparison between values of prediction and experiment

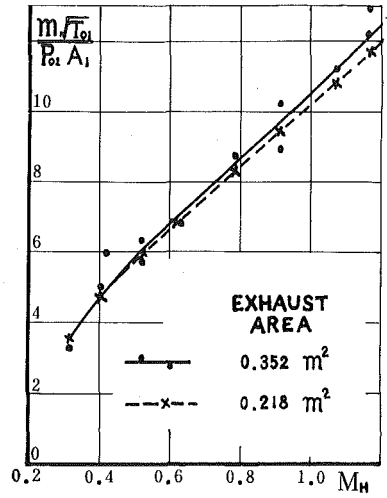

Fig. 7 Effect of nozzle area on windmilling airflow rate characteristic for Engine A

the engine. The values of ζ_Σ of similar engines are equal or close to each other; therefore, the left hand of equation (4.7) is a similarity parameter. It can be used as a proper parameter of the coordinate.

From equation (4.7) we know that for ordinary engines, $A_1/A_5 = 0.6 \rightarrow 1.8$, while $\zeta_\Sigma = 25 \rightarrow 50$, therefore the effect of the variation of exhaust nozzle area on the windmilling airflow rate characteristic is very small (see Fig. 7).

5 The Matching of Various Components under Windmilling Conditions

The thermodynamic process of an engine can be represented on the i—s diagram as shown in Fig. 8.

According to the principle of energy conservation we have

$$\Delta i_{0c} + \Delta i_{0f} = \Delta i_{0t} \tag{5.1}$$

where Δi_{0f} is the enthalpy increase corresponding to the friction power consumed in the transmission system that is

$$\Delta i_{0f} = \frac{JW_f}{m} = C_p(T_{01} - T_{04})$$

After transformation of equation (5.1), we obtain

$$\frac{T_{02}}{T_{01}} = \frac{T_{02}}{T_{04}}\left(1 - \frac{JW_f}{C_pT_{01}m}\right) \tag{5.2}$$

In Fig. 8 the air parameters of states 1 and 2 are only the function of the state, thereby the total enthalpy increase between state 1 and 2 can be represented by an isentropic process corresponding to the compression ratio P_{02iS}/P_{01}, that is

$$C_p(T_{02} - T_{01}) = C_pT_{01}\left(\left(\frac{P_{02iS}}{P_{01}}\right)\left(\frac{\gamma - 1}{\gamma}\right) - 1\right) \tag{5.3}$$

The entropy increase between state 1 and 2 can be represented by isoenthalpy process corresponding to the pressure ratio P_{02}/P_{02iS}, that is

$$\Delta S_c = -AR\ln\left(\frac{P_{02}}{P_{02iS}}\right) = -AR\ln\sigma_c$$

where σ_c is the total pressure recovery coefficient, solely due to the flow losses, thus $\sigma_c = P_{02}/P_{02iS}$, then

$$\frac{P_{02}}{P_{01}} = \frac{P_{02iS}}{P_{01}}\sigma_c$$

Following the same procedures we obtain that of the turbine

$$C_p(T_{02} - T_{04}) = C_pT_{04}\left(\left(\frac{P_{03}}{P_{04iS}}\right)\left(\frac{\gamma - 1}{\gamma}\right) - 1\right)$$

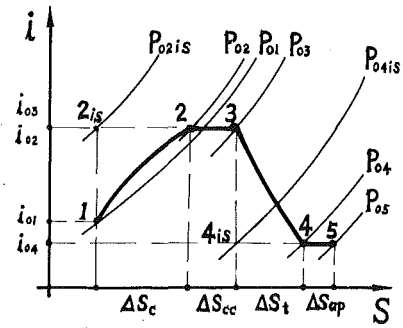

Fig. 8 The thermodynamic process of an engine in windmilling operation

$$\sigma_t = \frac{P_{04}}{P_{04iS}}$$

$$\frac{P_{03}}{P_{04}} = \frac{P_{03}}{P_{04iS}}\frac{1}{\sigma_t}$$

Combining the above equations after appropriate transformation, we obtain

$$\frac{P_{02}}{P_{01}} = \frac{P_{03}}{P_{04}}\sigma_c\sigma_t\left(1 - \frac{JW_f}{C_pT_{01}m}\right)\left(\frac{\gamma}{\gamma - 1}\right) \tag{5.7}$$

$$\frac{T_{02}}{T_{01}} = \left(\sigma_t\frac{P_{03}}{P_{04}}\right)\left(\frac{\gamma - 1}{\gamma}\right)\left(1 - \frac{JW_f}{C_pT_{01}m}\right) \tag{5.8}$$

$$\frac{T_{02}}{T_{04}} = \left(\sigma_t\frac{P_{03}}{P_{04}}\right)\left(\frac{\gamma - 1}{\gamma}\right) \tag{5.9}$$

$$\frac{P_{02}}{P_{01}} = \sigma_c\left(\frac{T_{02}}{T_{01}}\right)\left(\frac{\gamma}{\gamma - 1}\right) \tag{5.10}$$

$$\sigma_\Sigma = \frac{P_{05}}{P_{01}} = \frac{P_{02}}{P_{01}}\frac{P_{03}}{P_{02}}\frac{P_{04}}{P_{03}}\frac{P_{05}}{P_{04}} = \sigma_c\sigma_t\sigma_{cc}\sigma_{ap}\left(1 - \frac{JW_f}{C_pT_{01}m}\right) \tag{5.11}$$

Considering its very small value for ordinary engine, the term $JW_f/C_pT_{01}m$ can be neglected.

Here we use the total pressure recovery coefficients σ_c and σ_t to replace the usually used efficiencies η_c and η_t. It is convenient to use the total pressure recovery coefficients under windmilling conditions and it also gives a clearer picture.

6 The Characteristics of Engine Components

The characteristics of engine components are obtained mainly by experiments, but up to now the characteristics of compressors and turbines in the range of windmilling conditions (i.e., small rotational

Downloaded 01 Jun 2010 to 171.66.16.59. Redistribution subject to ASME license or copyright; see http://www.asme.org/terms/Terms_Use.cfm

speed and large airflow rate) are not available. To perform these experiments at existing compressor test facilities, it is necessary to add an additional equipment for air supply or suction. It is a lot of trouble but significant to obtain these characteristics, so that the air parameters at the inlet of the combustion chamber under windmilling conditions can be defined precisely. That is highly important for the combustion chamber design.

As for the combustion chamber, afterburner, jet pipe, etc., only the flow resistance characteristics are needed.

It is necessary to present the component characteristics in terms of the air parameters at engine intake for calculation later.

1 *The Resistance Characteristics of the Combustion Chamber.*

$$\text{Let } \sigma_{cc} = \frac{P_{03}}{P_{02}} = 1 - \frac{\gamma}{2}\zeta_{cc}M_1^2 \tag{6.1}$$

The total pressure loss coefficient of combustion chamber ζ_{cc0} which was obtained at cold air flowing test under the design condition is defined as the air parameters at the inlet of combustion chamber, that is:

$$\Delta P_{0cc} = \frac{\gamma}{2}P_2\zeta_{cc0}M_2^2 \tag{6.2}$$

also

$$\sigma_{cc} = 1 - \frac{\Delta P_{cc}}{P_{02}} = 1 - \frac{\gamma}{2}\zeta_{cc0}\left(1 + \frac{\gamma - 1}{2}M_2^2\right) - \left(\frac{\gamma}{\gamma - 1}\right)M_2^2$$

where ζ_{cc0} is known and can be considered a constant. From the simultaneous equations (6.1) and (6.2), and the continuity equation $A_1\rho_1c_1 = A_2\rho_2c_2$, after transformation and simplification, we obtain:

$$\zeta_{cc} = \left(\frac{A_1}{A_2}\right)^2\left(\frac{P_{01}}{P_{02}}\right)^2\left(\frac{T_{02}}{T_{01}}\right)\zeta_{cc0}\frac{\left(1 + 0.5\left(\frac{A_1}{A_2}\right)^2\left(\frac{P_{01}}{P_{02}}\right)^2\left(\frac{T_{02}}{T_{01}}\right)M_1^2\right)}{(1 + 1.2\,M_1^2)}$$

$$\zeta_{cc} \simeq \left(\frac{A_1}{A_2}\right)^2\left(\frac{P_{01}}{P_{02}}\right)^2\left(\frac{T_{02}}{T_{01}}\right)\zeta_{cc0}\frac{\left(1 + 0.5\left(\frac{A_1}{A_2}\right)^2 M_1^2\right)}{(1 + 1.2\,M_1^2)} \tag{6.3}$$

2 *The Resistance Characteristic of the Afterburner and Jet Pipe.*

Let

$$\sigma_{ap} = \frac{P_{05}}{P_{04}} = 1 - \frac{\gamma}{2}\zeta_{ap}M_1^2 \tag{6.4}$$

Following the same procedures as that for the combustion chamber, we can obtain the similar form as the equation (6.3). Since the value of ζ_{ap} is a small portion of ζ_Σ it can be further simplified as

$$\zeta_{ap} = \left(\frac{A_1}{A_4}\right)^2\left(\frac{P_{01}}{P_{04}}\right)^2\zeta_{ap0} = \left(\frac{A_1}{A_4}\right)^2\left(\frac{P_{01}}{P_{02}}\frac{P_{02}}{P_{03}}\frac{P_{03}}{P_{04}}\right)\zeta_{ap0}$$

$$\zeta_{ap} \simeq \left(\frac{A_1}{A_4}\right)^2\left(\frac{P_{01}}{P_{04}}\right)^2\zeta_{ap0} \tag{6.5}$$

3 *Characteristics of the Turbine.* In general, the characteristic of a turbine is represented by the variation of efficiency η_t and expansion ratio P_{03}/P_{04} with respect to $\overline{n}$ and $\overline{m}$, where $\overline{n}$ is the ratio of $n/\sqrt{T_{03}}$ to $(n/\sqrt{T_{03}})r$ and $\overline{m}$ is the ratio of $m\sqrt{T_{03}}/P_{03}$ $(M\sqrt{T_{03}}/P_{03})r$. The subscript r denotes the rated operation. One of the features of the turbine characteristic for ordinary turbojet engine is that the curves of $P_{03}/P_{04} = f(\overline{m})$ at different $\overline{n}$ are close to each other. But the published curves of turbine characteristic are only in a narrow tested range; i.e., $\overline{n} \geq 0.5$. We suppose that under windmilling conditions, since the values of $\overline{n}$ for different turbojet engines are nearly the same at the same M_H, and the flow losses are more or less the same due to the convergent passages of blades, large leading edge radius of blades and low velocity of airflow and low speed of the rotor, therefore the curves of P_{03}/P_{04} for different engines will be quite close to each other or even coincident.

In order to verify this point, it is necessary to examine the experimental data from turbojet engines under windmilling conditions and to derive the coordinate parameter represented by the parameters of windmilling characteristic, which will be explained as follows:

$$\overline{m} = \frac{\frac{m\sqrt{T_{03}}}{P_{03}}}{\left(\frac{m\sqrt{T_{03}}}{P_{03}}\right)_r} = \frac{q(\lambda_3)}{q(\lambda_3)_r}$$

Generally

$$q(\lambda_3)_r = 1, \text{ then } \overline{m} = q(\lambda_3).$$

By the equation of continuity we have

$$q(\lambda_3) = \frac{A_1}{A_3}\frac{P_{01}}{P_{03}}\frac{\sqrt{T_{02}}}{\sqrt{T_{01}}}q(\lambda_1)$$

$$= \frac{A_1}{A_3}\frac{P_{01}}{P_{04}}\frac{P_{04}}{P_{03}}\frac{\sqrt{T_{02}}}{\sqrt{T_{01}}}\frac{m\sqrt{T_{01}}}{P_{01}A_1}\frac{1}{0.3965} \tag{6.6}$$

where

$$\frac{P_{01}}{P_{04}} \simeq \frac{P_{01}}{P_{05}} = \frac{1}{\sigma_\Sigma}$$

from equation (5.8), we know

$$\sqrt{\frac{T_{02}}{T_{01}}} = f\left(\frac{P_{03}}{P_{04}}, \sigma_t\right)$$

where σ_t will not vary in a large range as will be shown later. Since P_{03}/P_{04} is a function of $q(\lambda_3)$, from equation (6.6) we obtain

$$\frac{P_{03}}{P_{04}} = f\left(\frac{A_1}{A_3}\frac{1}{\sigma_\Sigma}\frac{m\sqrt{T_{01}}}{P_{01}A_1}\right) \tag{6.7}$$

Taking the parameter $(A_1/A_3\,1/\sigma_\Sigma m\sqrt{T_{01}}/P_{01}A_1)$ as the abscissa and the parameter P_{03}/P_{04} as the ordinate, and making use of the experimental data from turbojet engines we could check the windmilling turbine characteristic. The calculation results can be seen in Appendix I and Fig. 9.

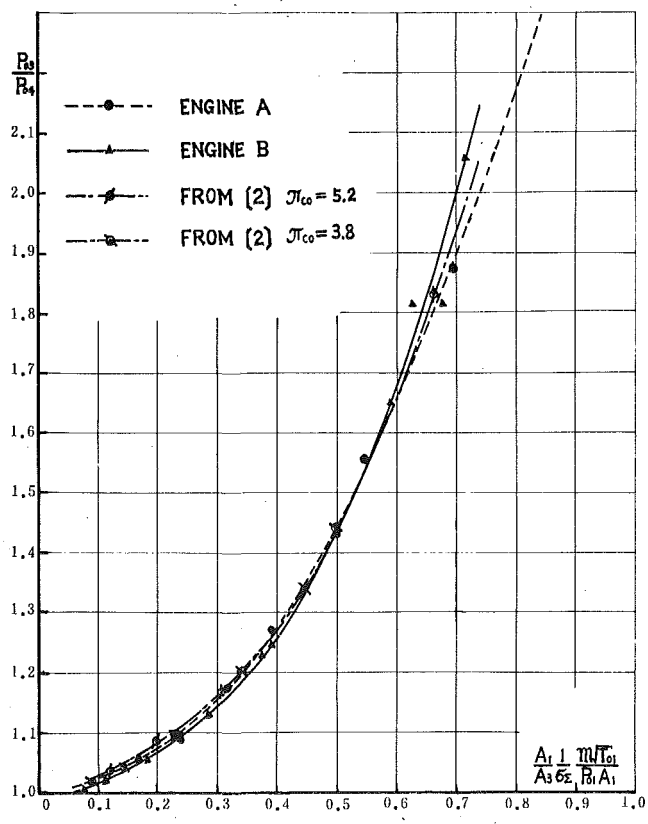

Fig. 9 Windmilling turbine characteristics for four turbojet engines

Downloaded 01 Jun 2010 to 171.66.16.59. Redistribution subject to ASME license or copyright; see http://www.asme.org/terms/Terms_Use.cfm

The turbine in those four turbojet engines is either of two stages and twin spool or single stage and single shaft. Fig. 9 shows that when $(A_1/A_3\ 1/\sigma_\Sigma\ m\sqrt{T_{01}}/P_{01}A_1) < 0.7$, it corresponds to $M \leq 0.9 \rightarrow 1.0$, the four curves are quite close to each other, thus we may draw a common curve, which approximately represents the universal curve of windmilling turbine characteristic. In the absence of characteristic of this component, this universal curve can be used approximately for the calculation.

The total pressure loss coefficient of turbine ζ_t is defined as

$$\sigma_t = 1 - \frac{\gamma}{2} M_1^2\, \zeta_t \tag{6.8}$$

Combining the equation (6.8) with the equation (5.8), and when $\gamma = 1.4$, the relationship between ζ_t and air parameters can be obtained,

$$\zeta_t = (0.7\ M_1^2)^{-1} \left(1 - \left(\frac{T_{02}}{T_{01}}\right)^{3.5} \left(\frac{P_{03}}{P_{04}}\right)^{-1} \left(1 - \frac{JW_f}{C_p T_{01} m}\right)^{-3.5}\right) \tag{6.9}$$

Figs. 10 and 11 give the windmilling ζ_t characteristic for two different turbojet engines, and show that the two curves are close to each other and the value of ζ_t does not vary much in the range of $0.4 \leq M_H \leq 1.0$. According to the aforementioned analysis, one considers that under windmilling conditions the loss coefficient characteristics of turbine of the ordinary turbojet engines are more or less the same, and $\zeta_t = 11 \rightarrow 13$.

The conversion relationship of σ_t to η_t under windmilling conditions is obtained from equation (5.9) with the definition of η_t, that is

$$\sigma_t = \left(\frac{P_{03}}{P_{04}}\right)^{-1} \left(1 - \eta_t \left(1 - \left(\frac{P_{03}}{P_{04}}\right)^{-0.286}\right)\right)^{-3.5} \tag{6.10}$$

4 *The Characteristics of the Compressor.* Up to now the universal curve of windmilling compressor characteristic which is applicable to different compressors is not available.

For convenience to calculate windmilling characteristic, we replace η_c by σ_c and it seems reasonable to use σ_c than η_c. The conversion relationship of σ_c to η_c under windmilling conditions is obtained by equation (5.10) with the definition of η_c. That is

$$\sigma_c = \left(\frac{P_{02}}{P_{01}}\right) \left(\left(\left(\frac{P_{02}}{P_{01}}\right)^{0.286} - 1\right) \eta_c^{-1} + 1\right)^{-3.5} \tag{6.11}$$

The total pressure loss coefficient ζ_c is defined as

$$\sigma_c = 1 - \frac{\gamma}{2} M_1^2\, \zeta_c \tag{6.12}$$

Combining the equation (6.12) with equation (5.10) and $\gamma = 1.4$,

$$\zeta_c = (0.7\ M_1^2)^{-1} \left(1 - \left(\frac{P_{02}}{P_{01}}\right)\left(\frac{T_{02}}{T_{01}}\right)^{-3.5}\right) \tag{6.13}$$

Fig. 12 shows the windmilling ζ_c characteristic for two different turbojet engines. Their difference is due to the different compressor types. If the compressor types are identical, the design compression ratio, the number of stages and the blade profile do not differ greatly, so the variation of air flow attack angle will be about zero deg, more or less the same; thereby the curves of windmilling characteristic are more or less the same too.

5 *The Total Loss Coefficient of Engine* ζ_Σ. With solving of the simultaneous equations (4.4), (5.11), (6.1), (6.4), (6.8), (6.12), neglecting $JW_f/C_P T_{01} m$ and the higher terms of M_1 we obtain

$$\zeta_\Sigma = (\zeta_c + \zeta_{cc} + \zeta_t + \zeta_{ap})X \times \left(1 - \frac{\gamma}{2} M_1^2\, B\, (\zeta_c + \zeta_{cc} + \zeta_t + \zeta_{ap})\right) \tag{6.14}$$

where

$$B = \frac{\zeta_c\zeta_{cc} + \zeta_c\zeta_t + \zeta_c\zeta_{ap} + \zeta_{cc}\zeta_t + \zeta_{cc}\zeta_{ap} + \zeta_t\zeta_{ap}}{(\zeta_c + \zeta_{cc} + \zeta_t + \zeta_{ap})^2}$$

for ordinary turbojet engine, $B = 0.25 \rightarrow 0.35$.

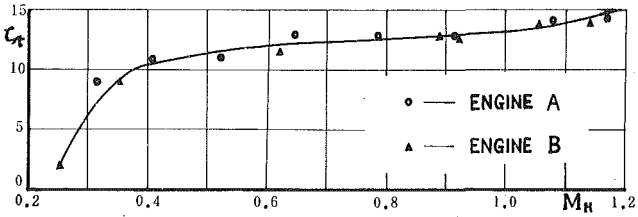

Fig. 10 Turbine total pressure loss coefficients as a function of flight Mach number in windmilling operation

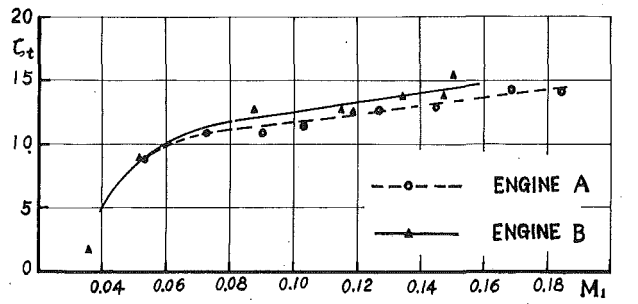

Fig. 11 Turbine total pressure loss coefficients as a function of Mach number at inlet of compressor in windmilling operation

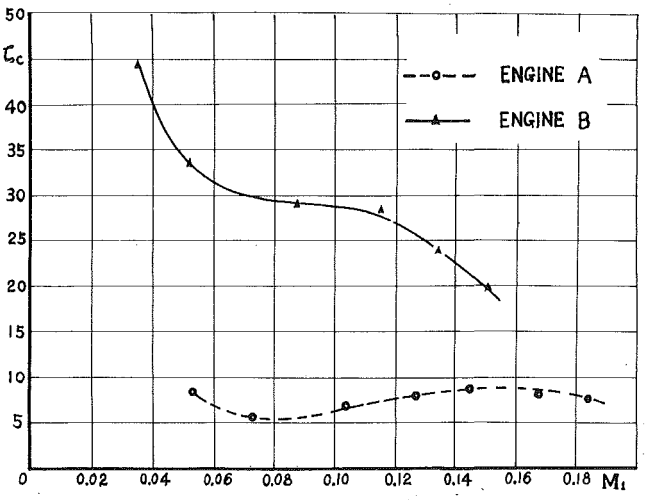

Fig. 12 Compressor total pressure loss coefficients as a function of Mach number at inlet of compressor in windmilling operation

Taking $B = 0.3$ and $\gamma = 1.4$, then equation (6.14) is

$$\zeta_\Sigma = (\zeta_c + \zeta_{cc} + \zeta_t + \zeta_{ap})X \times (1 - 0.21\ M_1^2(\zeta_c + \zeta_{cc} + \zeta_t + \zeta_{ap})) \tag{6.15}$$

In order to verify the equations derived in paragraphs 5 and 6, the experimental data of two turbojet engines are examined, that is to make a comparison between the $\zeta_{\Sigma cal}$ and $(P_{02}/P_{01})_{cal}$ calculated by above derived equations and the $\zeta_{\Sigma exp}$ and $(P_{02}/P_{01})_{exp}$ obtained from experimental data (see Appendix II).

This result shows that for Engine B the deviation of ζ_Σ is less that 1.5 percent. For Engine A its deviation is small too when M_H is small; but its deviation becomes apparent and up to 3 percent when $M_H > 1.0$. (The measurement accuracy of Engine A is less than Engine B, which is probably one of the reasons for larger deviation of Engine A.)

7 Calculation of Windmilling Characteristic

In order to calculate the windmilling characteristic and the air parameters at the inlet of every component, it is necessary to solve the simultaneous equations of all component characteristics, the equation for the matching of the components and the equality of the rotational speed and airflow rate of compressors and turbines. The

Downloaded 01 Jun 2010 to 171.66.16.59. Redistribution subject to ASME license or copyright; see http://www.asme.org/terms/Terms_Use.cfm

diagrammatic method may be used since the characteristics of compressors and turbines are represented only by the diagrams.

The key point fo the diagrammatic method is to draw the matching line on the compressor characteristic. The procedures are as follows.

First Step: Collecting Necessary Information.

1 The characteristic of compressors and turbines of this engine including those at low rpm range.

It should be represented by $m\sqrt{T_{01}}/P_{01}A_1$, P_{02}/P_{01}, $m\sqrt{T_{03}}/P_{03}A_3$, P_{03}/P_{04}, etc.

2 The total pressure loss coefficient and the characteristic of intake duct and ejector nozzle σ_i, a.

3 The cross-sectional areas of every components A_1, A_2, A_3, A_4 and A_5.

Second Step: Drawing the Matching line.

1 First choosing a value of n_1 from the compressor characteristic and having selected a value $(m\sqrt{T_{01}}/P_{01}A_1)_a$, the value $(m\sqrt{T_{03}}P_{03}A_3)_a$ can be obtained from the following conversion equation for the abscissa.

$$\left(m\sqrt{T_{03}}/P_{03}A_3\right) = \frac{A_1}{A_3}\left(\frac{T_{02}}{T_{01}}\right)^{0.5}\left(\frac{P_{02}}{P_{01}}\right)^{-1}\sigma_{cc}\left(\frac{m\sqrt{T_{01}}}{P_{01}A_1}\right) \tag{7.1}$$

where σ_{cc} is obtained from both equations (6.1) and (6.3).

P_{02}/P_{01}, T_{02}/T_{01} and σ_c are determined from the compressor characteristic corresponding to n_1 and $(m\sqrt{T_{01}}/P_{01}A_1)_a$.

In calculation, the value M_1 is obtained from the tables or graphs of aerodynamic parameters by the value of

$$q(\lambda) = \frac{1}{0.3965}\left(\frac{m\sqrt{T_{01}}}{P_{01}A_1}\right)$$

2 The values of $(P_{03}/P_{04})_a$ and σ_t can be determined by the values $(m\sqrt{T_{03}}/P_{03}A_3)_a$ and n_1 on the turbine characteristic.

From the conversion equation of the ordinate, i.e., equation (5.7), the value $(P_{02}/P_{01})_a$ can be calculated, then by the value $(m\sqrt{T_{01}}/P_{01}A_1)_a$ and $(P_{02}/P_{01})_a$, we can set a point "a" on the compressor characteristic (see Fig. 13).

3 Selecting an other value $(m\sqrt{T_{01}}/P_{01}A_1)_b$. The value $(P_{02}/P_{01})_b$ can be obtained by the same way as above, then according to values $(m\sqrt{T_{01}}/P_{01}A_1)_b$ and $(P_{02}/P_{01})_b$ another point "b" can be set on the compressor characteristic. Having set three points a, b, and c nearby the curve n_1, a curve may be drawn through these three points which intersects with the curve n_1 at S; S is the matching point.

The matching line can be thus formed by linking up those points.

Third Step: Calculating the P_{02}/P_{01}, T_{02}/T_{01}, P_{03}/P_{04}, σ_c, σ_t, σ_{cc}, σ_{ap} and σ_Σ Corresponding to the Value of $m\sqrt{T_{01}}/P_{01}A_1$.

1 Selecting a value of $m\sqrt{T_{01}}/P_{01}A_1$, the values of P_{02}/P_{01}, T_{02}/T_{01} and σ_c can be determined from the matching point on the compressor characteristic.

2 The value of σ_{cc} is given by both equations (6.1) and (6.3).

3 The values of (P_{03}/P_{04}) and σ_t are determined from the turbine characteristic by the value of $(m\sqrt{T_{01}}/P_{01}A_1)$.

4 σ_{ap} is obtained from both equations (6.4) and (6.5).

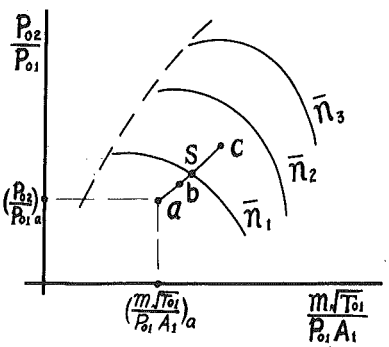

Fig. 13 Diagram of defining the matching line on compressor characteristic

5 σ_Σ is obtained from equation (5.11).

Fourth Step: Calculating the M_H Corresponding to the Value of $(m\sqrt{T_{01}}/P_{01}A_1)$. That is the windmilling characteristic.

From equation (4.7) or (4.8), the (P_H/P_{OH}) may be obtained, that is

$$\frac{P_H}{P_{OH}} = \frac{B + \sqrt{B^2 - 4AC}}{2\left(\frac{a}{\sigma_i}\right)A} \tag{7.2}$$

where

$$A = \frac{2g}{R} - \frac{\gamma+1}{\gamma}\left(\frac{m\sqrt{T_{01}}}{P_{01}A_1}\right)^2 = 0.669 - 1.714\left(\frac{m\sqrt{T_{01}}}{P_{01}A_1}\right)^2$$

$$B = A - \zeta_\Sigma\left(\frac{m\sqrt{T_{01}}}{P_{01}A_1}\right)^2$$

$$C = \left(\frac{A_1}{A_5}\right)^2\left(\frac{m\sqrt{T_{01}}}{P_{01}A_1}\right)^2$$

$$\zeta_\Sigma = (1-\sigma_\Sigma)(0.7M_1^2)^{-1}$$

then the value of M_H can be obtained from the tables or graphs of aerodynamic parameters.

8 Approximate Calculation of Windmilling Characteristics

If the compressor and the turbine characteristics within the low rpm range are not available, while the air parameters at the inlet of combustion chamber under windmilling conditions are necessary in the design, we can approximately calculate these parameters by utilizing the information from similar engines as a so-called reference engine. There are two approximate calculation methods according to the availability of existing information.

Approximate Method I. The reference engine should be of the same compressor type as that of the designed engine; moreover, the compression ratios, numbers of stages and blade profiles should not be very different in both engines; thus its compressor characteristic will be close to that of the designed engine.

Therefore, the foundation of this method is that the three curves $\sigma_c = f(m\sqrt{T_{01}}/P_{01}A_1)$, $\sigma_t = f(m\sqrt{T_{01}}/P_{01}A_1)$ and $P_{03}/P_{04} = f(A_1/A_3\ 1/\sigma_\Sigma\ m\sqrt{T_{01}}/P_{01}A_1)$ of the reference engine are taken for those of the engine to be designed.

The key of this method is drawing the matching line on the windmilling turbine characteristic. The procedures are as follows.

First Step: Collecting Necessary Information.

1 The reference engine's windmilling characteristic, air parameters at inlet of every components and A_1, A_2, A_3, A_4, A_5, ζ_{cc0}, ζ_{ap0}, etc.

2 For the engine to be designed:

$$A_1, A_2, A_3, A_4, A_5, \zeta_{cc0}, \zeta_{ap0}, \text{ etc.}$$

Second Step: Calculating the Three Characteristic Curves of the Reference Engine, i.e.

$$\sigma_c = f\left(\frac{m\sqrt{T_{01}}}{P_{01}A_1}\right),\ \sigma_t = f\left(\frac{m\sqrt{T_{01}}}{P_{01}A_1}\right) \text{ and } \frac{P_{03}}{P_{04}} = f\left(\frac{A_1}{A_3}\frac{1}{\sigma_\Sigma}\frac{m\sqrt{T_{01}}}{P_{01}A_1}\right)$$

Where the parameters which need to be calculated are σ_c from the equation (5.10) and σ_t from equation (5.8) or (5.9).

If the air parameters of Sections 3, 4 or 5 are not available, the parameters need to be calculated are σ_{cc} from both equations (6.1) and (6.3), σ_{ap} from both equations (6.4) and (6.5) and σ_Σ from both equations (4.4) and (4.8).

When M_H is small, since the error in the measurement value of T_{02}/T_{01} becomes large, the values of σ_c and σ_t may be calculated as follows

$$\sigma_c\sigma_t = \frac{\sigma_\Sigma}{\sigma_{cc}\sigma_{ap}}$$

Third Step: Calculating the Matching Point from the Windmilling Turbine Characteristic. At first we obtain the simulta-

Downloaded 01 Jun 2010 to 171.66.16.59. Redistribution subject to ASME license or copyright; see http://www.asme.org/terms/Terms_Use.cfm

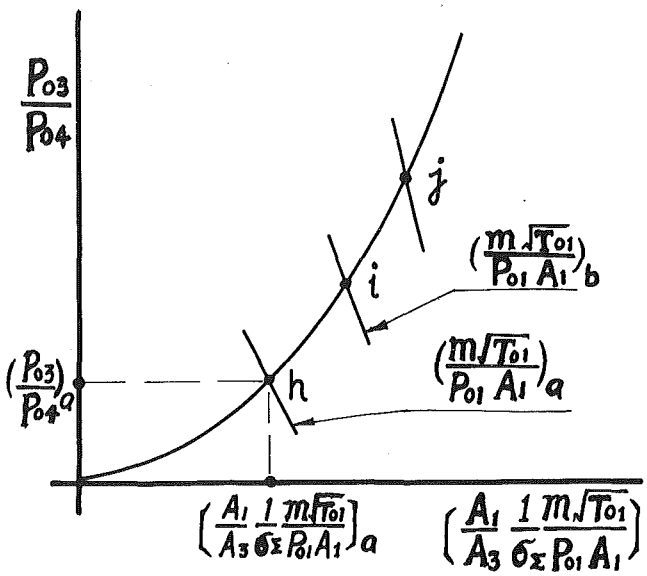

Fig. 14 Diagram of defining the matching points on windmilling turbine characteristic

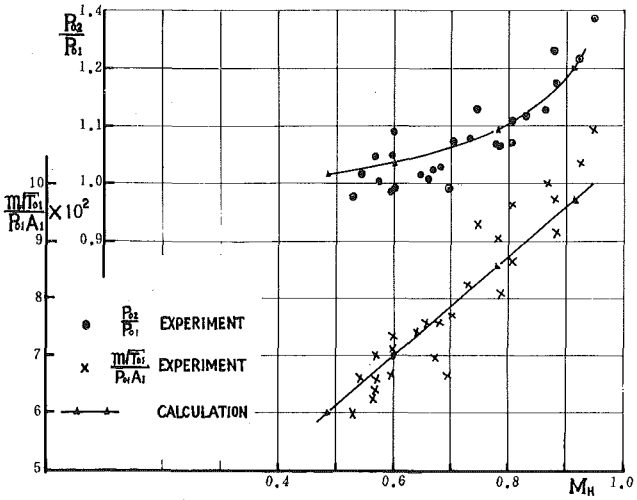

Fig. 15 Windmilling characteristic of airflow rate and compression ratio for Engine C, comparison between values of prediction and experiment

neous equations of all components except the turbine. Solving the simultaneous equations (5.7), (5.8), (5.11), (6.1), (6.3), (6.4) and (6.5), neglecting $JW_f/C_PT_{01}m$ and taking $\gamma = 1.4$, we obtain

$$\left(\frac{A_1}{A_3}\frac{1}{\sigma_\Sigma}\frac{m\sqrt{T_{01}}}{P_{01}A_1}\right) = \frac{A_1}{A_3}\left(\frac{m\sqrt{T_{01}}}{P_{01}A_1}\right)\left(B - 0.7M_1^2\left(\frac{A_1}{A_4}\right)^2\frac{\zeta_{ap0}}{B}\right)^{-1} \quad (8.1)$$

where

$$B = \sigma_c\sigma_t - 0.7M_1^2\left(\frac{A_1}{A_2}\right)^2\zeta_{cc0}\frac{\sigma_t^{0.286}\left(1 + 0.5\left(\frac{A_1}{A_2}\right)^2 M_1^2\right)}{\sigma_c\sigma_t\left(\frac{P_{03}}{P_{04}}\right)^{1.714}(1 + 1.2M_1^2)}$$

M_1 is obtained from the tables or graphs of aerodynamic parameters according to the value of $m\sqrt{T_{01}}/P_{01}A_1$.

The left hand side of equation (8.1) is also the abscissa of windmilling turbine characteristic too. Here it is a function of the unknown P_{03}/P_{04}. They can be obtained by means of solving the equation (8.1) in combination with the windmilling turbine characteristic.

According to the equation (8.1) and by selecting a value of $(m\sqrt{T_{01}}/P_{01}A_1)_a$, a curve can be drawn on the graph of windmilling turbine characteristic and intersects the original curve at h, which is the matching point of this selected value $(m\sqrt{T_{01}}/P_{01}A_1)_a$. (see Fig. 14).

Selecting the different values $(m\sqrt{T_{01}}/P_{01}A_1)_b$, $(m\sqrt{T_{01}}/P_{01}A_1)_c$, etc. we can obtain the different intersection i, j, etc. and the different value $(P_{03}/P_{04})_b$, $(P_{03}/P_{04})_c \ldots (A_1/A_3/1/\zeta_\Sigma\ m\sqrt{T_{01}}/P_{01}A_1)_b$, etc.

Fourth Step: Calculating the Values of P_{02}/P_{01}, T_{02}/T_{01} and σ_Σ Corresponding to the Value of $m\sqrt{T_{01}}/P_{01}A_1$.

The value of P_{02}/P_{01} is given by the equation (5.7).

The value of T_{02}/T_{01} is given by the equation (5.8).

The value of σ_Σ is given by the following equation.

$$\sigma_\Sigma = \frac{A_1}{A_3}\left(\frac{m\sqrt{T_{01}}}{P_{01}A_1}\right)\left(\frac{A_1}{A_3\sigma_\Sigma}\frac{1}{P_{01}A_1}\frac{\mu\sqrt{T_{01}}}{}\right)^{-1} \quad (8.2)$$

Fifth Step: Calculating the Windmilling Airflow rate Characteristic. From equation (7.2) we can obtain the value of M_H corresponding to the value of $m\sqrt{T_{01}}/P_{01}A_1$.

Having the values of $m\sqrt{T_{01}}/P_{01}A_1$, P_{02}/P_{01}, T_{02}/T_{01} and P_{03}/P_{04} in accordance with the value M_H, the values of air parameters such as flow rate, pressure and temperature at the inlet of combustion chamber or other components under windmilling conditions can be obtained easily.

In Appendix III, there is an example of application of this approximate method. The engine C calculated consists of a single—spool compressor of nine stages $\pi_{c0} = 7.14$. The reference engine is Engine B which contains a twin—spool compressor of six stages, $\pi_{c0} = 8.85$.

Figure 15 illustrates the comparison between the calculated results and the experimental data obtained from flight test. Although these two engines are not of full similarity, this figure shows that the calculated results basically agree with the experimental data.

In some turbojet engines, a bleed valve airflow control system which is open at low compression ratios is used for anti-surge purposes. So in windmilling operation, the airflow rate at compressor intake will be more than that at the inlet of the combustion chamber. But, in practice, i.e., in the range of flight Mach number for relighting, since the difference between the static pressures of the inside and the outside of the compressor is not large, the bleeding airflow is not large. Engine C is provided with a bleed valve airflow control system. According to the experimental data of P_{02}, P_2, etc., we can calculate the value of m_2. A comparison between m_1 and m_2 shows that the value of m_2/m_1 is about unity within the range of measurement accuracy.

Approximate Method II. If there is only the windmilling airflow rate characteristic of the reference engine and not the air parameters at the inlet of components, approximate method II can be used. It is basically the same as approximate method I. The difference lies in the second step of the calculation procedures.

The second step of method II is as follows:

1 Making use of the universal curve of windmilling turbine characteristic. (see Fig. 9 or 16)

2 Calculating ζ_Σ from the equation (4.8 and σ_Σ from the equation (4.4).

3 According to the equation (8.1), we have

$$\sigma_c\sigma_t = \frac{A + \sqrt{A^2 + B}}{2} \quad (8.3)$$

where

$$A = \frac{1}{2}\left(\sigma_\Sigma + \left(\sigma_\Sigma^2 + 2.8M_1^2\left(\frac{A_1}{A_4}\right)^2\zeta_{ap0}\right)^{1/2}\right)$$

$$B = 0.7M_1^2\left(\frac{A_1}{A_2}\right)^2\sigma_t^{0.286}\zeta_{cc0}\left(1 + 0.5\left(\frac{A_1}{A_2}\right)^2 M_1^2\right)X \times\left(\frac{P_{03}}{P_{04}}\right)^{-1.714}(1 + 1.2M_1^2)^{-1}$$

$\frac{P_{03}}{P_{04}}$ is determined from Fig. 16.

σ_t is calculated from equation (6.8) by taking $\zeta_t = 11 \rightarrow 13$.

The accuracy of approximate method II is less than that of approximate method I, since method II used the universal curve of

Downloaded 01 Jun 2010 to 171.66.16.59. Redistribution subject to ASME license or copyright; see http://www.asme.org/terms/Terms_Use.cfm

turbine and the approximation of ζ_t. If the compressor of the reference engine is similar to the compressor of the engine to be designed, the approximation of applying method II will be better.

When $M_H > 1.0$ the deviation of P_{03}/P_{04} from the universal curve of turbine is more than ±2.5 percent and the variation of ζ_t can be large, so method II is suitable to the range of $M_H \leqq 1.0$.

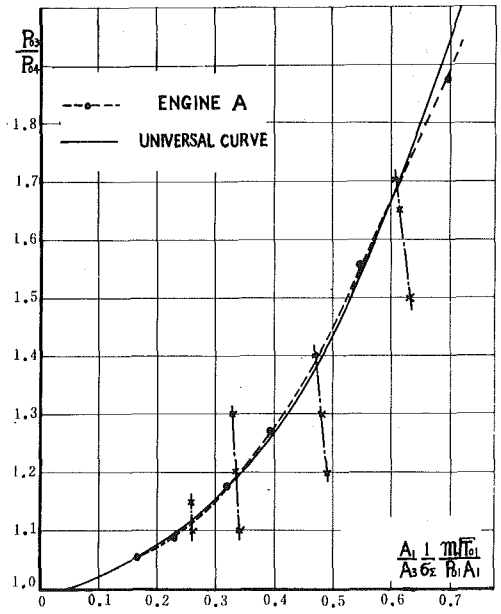

Fig. 16 Diagram of defining the matching points using universal curve of windmilling turbine characteristic

References

1 Alabin, M. A., et al., "Starting of Aircraft Gas Turbine Engines," AD-740291, 1972.

2 Wallner, L. E., and Welna, H. J., "Generalization of Turbojet and Turbine—Propeller Engine Performance in Windmilling Condition," NACA RM-E51J23, Dec. 1951.

3 Sobolushi, A. E. and Farely, J. M., "Steady State Engine Windmilling and Engine Speed Decay Characteristics of Axial-Flow Turbojet Engine," NACA RM-E51I06, 1951.

APPENDIX I

Check whether the curves of windmilling turbine characteristic for four turbojet engines are close to each other.

The ordinate of this characteristic is P_{03}/P_{04}.

The abscissa of this characteristic is $(A_1/A_3 \quad 1/\sigma_\Sigma \quad m\sqrt{T_{01}}/P_{01}A_1)$.

The values of all parameters should be given by experimental data, yet some of them are not available. They can be obtained as follows.

1 The experimental data P_{03} for Engine A and Engine B can be obtained from

$$P_{03} = P_{02}\left(1 - \frac{\gamma}{2} M_1^2 \zeta_{cc}\right)$$

where

P_2 is obtained from experimental data

ζ_{cc} is obtained from Appendix II.

In addition, the area ratio A_1/A_2 is known, $A_1/A_3 = 4.31$ for Engine A. $A_1/A_3 = 2.98$ for Engine B.

2 The design parameters of two turbojet engines taken from reference [2], were

$\pi_{c0} = 5.2$, $m = 44.1$ Kg/s (97 lb/s) and

$\pi_{c0} = 3.8$, $m = 26.4$ Kg/s (58 lb/s).

Table 3

M_H	$\frac{m\sqrt{T_{01}}}{P_{01}A_1}$	M_1	ζ_{cc}	σ_{cc}	P_{02}	P_{03}	P_{04}	$\frac{P_{03}}{P_{04}}$	σ_Σ	$\frac{A_1 m\sqrt{T_{01}}}{A_3\sigma_\Sigma P_{01}A_1}$
Engine A										
0.314	3.6×10^{-2}	0.0525	13.32	0.974	1.107	1.075	1.0156	1.058	0.935	0.166
0.407	4.88×10^{-2}	0.0725	13.90	0.950	1.161	1.105	1.0156	1.09	0.892	0.236
0.522	6.09×10^{-2}	0.0925	13.35	0.9235	1.30	1.20	1.0156	1.18	0.831	0.314
0.62	7.0×10^{-2}	0.1035	13.1	0.9014	1.44	1.295	1.0156	1.273	0.775	0.390
0.785	8.55×10^{-2}	0.1266	12.1	0.864	1.83	1.580	1.0156	1.555	0.678	0.544
0.913	9.7×10^{-2}	0.145	10.9	0.84	2.265	1.902	1.0156	1.875	0.60	0.695
1.075	11.25×10^{-2}	0.168	8.74	0.83	3.17	2.63	1.0156	2.59	0.515	0.94
1.17	12.2×10^{-2}	0.184	7.2	0.83	3.998	3.32	1.0156	3.262	0.471	1.115
Engine B										
0.254	2.44×10^{-2}	0.0358	2.87	0.9973	0.805	0.8025	0.7985	1.007	0.957	0.076
0.533	5.08×10^{-2}	0.075	3.37	0.987	0.8625	0.851	0.0855	1.058	0.8288	0.183
0.654	5.995×10^{-2}	0.088	3.63	0.9804	0.903	0.886	0.8105	1.093	0.7655	0.233
0.742	6.735×10^{-2}	0.099	3.90	0.9733	0.948	0.924	0.8165	1.132	0.7084	0.283
0.354	3.54×10^{-2}	0.052	3.0	0.9943	1.067	1.061	1.0375	1.024	0.915	0.114
0.922	7.99×10^{-2}	0.119	4.28	0.958	1.379	1.32	1.0605	1.247	0.608	0.391
1.053	9.08×10^{-2}	0.1343	4.13	0.9479	1.629	1.543	1.0775	1.435	0.544	0.497
1.135	9.95×10^{-2}	0.147	3.62	0.9453	1.899	1.796	1.0895	1.65	0.505	0.587
0.89	7.76×10^{-2}	0.115	4.38	0.9595	0.642	0.616	0.500	1.233	0.622	0.3725
1.175	9.96×10^{-2}	0.148	3.28	0.9497	1.082	1.03	0.568	1.815	(0.476)0.44	.675(.624)
1.28	10.8×10^{-2}	0.162	2.82	0.9482	1.362	1.292	0.628	2.058	0.45	0.715

Downloaded 01 Jun 2010 to 171.66.16.59. Redistribution subject to ASME license or copyright; see http://www.asme.org/terms/Terms_Use.cfm

Table 4

M_H	$\frac{m\sqrt{T_{01}}}{P_{01}A_1}$	M_1	$\frac{1}{\sigma_\Sigma}$	$\frac{P_{02}}{P_{01}}$	$\frac{P_{03}}{P_{02}}$	$\frac{P_{03}}{P_{04}}$	$\frac{A_1 m\sqrt{T_{01}}}{A_3\sigma_\Sigma P_{01}A_1}$
$\pi_{c0} = 5.2$							
0.2963	$2.597X10^{-2}$	0.0385	1.06	0.983	0.996	1.04	0.1196
0.4491	$3.947X10^{-2}$	0.058	1.145	0.962	0.986	1.09	0.197
0.6083	$5.523X10^{-2}$	0.083	1.262	0.96	0.971	1.172	0.304
0.7766	$7.20X\ 10^{-2}$	0.1062	1.42	0.995	0.952	1.342	0.446
0.9580	$9.10X\ 10^{-2}$	0.1361	1.663	1.135	0.926	1.83	0.660
$\pi_{c0} = 3.8$							
0.2963	$2.597X10^{-2}$	0.0385	1.06	0.965	0.994	1.02	0.0905
0.4491	$3.947X10^{-2}$	0.058	1.145	0.933	0.983	1.046	0.1489
0.6083	$5.523X10^{-2}$	0.083	1.262	0.897	0.965	1.102	0.2292
0.7766	$7.20X\ 10^{-2}$	0.1062	1.42	0.886	0.94	1.206	0.3364
0.9580	$9.10X\ 10^{-2}$	0.1361	1.663	0.94	0.911	1.44	0.4975

Engine B

M_H	m	n	M_1	M_f	$\frac{JW_f}{C_P T_{01} m}$
0.254	0.819	892	0.0358	0.18	$7.60X10^{-4}$
0.354	1.639	1509	0.052	0.20	$6.60X10^{-4}$
0.645	2.544	3324	0.088	0.25	$1.13X10^{-3}$
0.89	2.657	4940	0.115	0.31	$2.10X10^{-3}$
0.922	5.698	5351	0.119	0.33	$1.10X10^{-3}$
1.053	7.355	6860	0.1314	0.39	$1.30X10^{-3}$
1.135	8.7	8060	0.147	0.44	$1.57X10^{-3}$
1.175	4.905	8500	0.15	0.46	$3.30X10^{-3}$

Engine A

M_H	m	n	M_1	M_f	$\frac{JW_f}{C_P T_{01} m}$
0.314	6.32	892	0.0528	1.69	8.5×10^{-4}
0.407	10.2	1170	0.0725	1.98	7.3×10^{-4}
0.522	13.86	1500	0.0905	1.88	$7.35X\ 10^{-4}$
0.62	16.14	1790	0.1035	1.93	7.6×10^{-4}
0.785	23.88	2460	0.1266	2.16	7.9×10^{-4}
0.913	30.0	3000	0.145	2.3	8.1×10^{-4}
0.075	40.63	3900	0.168	2.58	8.8×10^{-4}
1.17	49.38	4600	0.184	2.82	9.2×10^{-4}

Table 5

$(\frac{P_{02}}{P_{01}})_{exp}$	$(\frac{T_{02}}{T_{01}})_{exp}$	$\frac{P_{03}}{P_{04}}$	$\zeta_{\Sigma exp}$	ζ_{cccal}	ζ_{apcal}	ζ_{ccal}	ζ_{tcal}	ζ_{tcal} $\frac{JW_f}{C_P T_{01} m} = 0$	$\Sigma\zeta_{cal}$	$\zeta_{\Sigma cal}$	$(\frac{P_{02}}{P_{01}})_{cal}$	K
0.963	1.0008	1.007	47.9	2.87	0.28	44.2	1.9	4.76	49.15	48.4	0.964	0.09
0.942	1.0016	1.024	44.7	3.0	0.305	33.6	9	9.55	45.9	44.5	0.944	0.215
0.852	1.0045	1.093	43.25	3.63	0.436	29.2	12.9	13.15	46.16	42.7	0.857	0.254
0.792	1.02	1.225	40.25	4.38	0.66	28.5	12.7	13.7	46.24	40.9	0.798	0.2678
0.793	1.023	1.243	39.9	4.28	0.69	27.0	12.6	13.0	44.57	39.3	0.798	0.27
0.822	1.047	1.435	36.8	4.13	0.875	23.9	13.8		42.7	36.5	0.824	
0.891	1.076	1.65	34.0	3.62	1.02		14.0					
0.942	1.092	1.815	32.7	3.28	1.12	20	15.6	16.3	40.0	32.6	0.948	0.266
1.017	1.009	1.057	33.8	13.32	0.68	8.16	9.0	10.35	31.16	32.1	1.019	0.33
1.032	1.015	1.10	29.4	13.9	0.715	5.496	10.81	11.4	30.76	29.6	1.036	0.32
1.061	1.027	1.175	29.45	13.35	0.77	5.66	10.92	11.35	30.70	29.1	1.062	0.325
1.10	1.043	1.265	29.9	13.1	0.84	6.9	11.35	11.42	32.19	29.2	1.10	0.318
1.208	1.084	1.545	28.8	12.1	0.96	7.8	12.6	12.65	33.46	29.3	1.205	0.33
1.33	1.128	1.885	27.2	10.9	1.09	8.67	12.8	12.9	33.46	27.7	1.35	0.34
1.57	1.195	2.59	24.6	8.75	1.27	7.95	14.1	14.2	32.07	25.4	1.6	0.32
1.785	1.25	3.262	22.3	7.2	1.44	7.75	14.0	14.1	30.39	23.0	1.84	0.33

Downloaded 01 Jun 2010 to 171.66.16.59. Redistribution subject to ASME license or copyright; see http://www.asme.org/terms/Terms_Use.cfm

Table 6

Chosen	According to $q(\lambda_1)=\frac{1}{.3965}\left(\frac{m\sqrt{T_{01}}}{P_{01}A_1}\right)$		From Fig. 12 for Engine A	From Fig. 11 for Engine A	From eq. (6.12)	From eq. (6.8)	Chosen	From eq. (8.1)	Drawn on Fig.16	Corresponding to the intersect point from Fig. 16		From eq. (8.2)	From eq. (4.4)	From eq. (5.7)	From eq. (5.8)	From eq. (7.2)	From aero. parameter table
$\frac{m\sqrt{T_{01}}}{P_{01}A_1}$	M_1	$0.7M_H^2$	ζ_c	ζ_t	σ_c	σ_t	$\frac{P_{03}}{P_{04}}$	$\frac{A_1 m\sqrt{T_{01}}}{A_3\sigma_\Sigma P_{01}A_1}$		$\frac{P_{03}}{P_{04}}$	$\frac{A_1 m\sqrt{T_{01}}}{A_3\sigma_\Sigma P_{01}A_1}$	σ_Σ	ζ_Σ	$\frac{P_{02}}{P_{01}}$	$\frac{T_{02}}{T_{01}}$	$\frac{P_H}{P_{OH}}$	M_H
.097	.145	.0147	8.5	13.0	.8750	.8090	1.5 1.65 1.7	.632 .615 .610	a-a	1.692	.611	.606	26.8	1.198	1.094	.584	.910
.0855	.1266	.0112	7.8	12.5	.9125	.8596	1.2 1.3 1.4	.491 .481 .4725	b-b	1.393	.473	.690	27.6	1.092	1.053	.6716	.780
.070	.1035	.0075	6.7	11.5	.9498	.9138	1.1 1.2 1.3	.340 .3352 .332	c-c	1.192	.337	.793	27.6	1.032	1.025	.7825	.600
.060	.090	.0056	5.8	10.0	.9671	.9434	1.1 1.15	.265 .263	d-d	1.115	.264	.860	25.4	1.016	1.017	.853	.485

Other data are obtained from the graphs and tables in the reference [2], and their parameters represented by $m\sqrt{\theta}/\delta A_1$, $V_H/\sqrt{\theta}$ and total pressure drop have been transformed into $m\sqrt{T_{01}}/P_{01}A_1$, M_H and total pressure ratio. In addition, the values of area A_1 and A_3 are calculated from the design values of m, π_c, A_1/A_5 and P_{04}/P_H in reference [2]. And choose $T_{03} = 1050$ K, $\eta_m = 0.98$, $\eta_c = 0.78$, $\sigma_{cc} = 0.95$, $q(\lambda_3) = 1$ and $q(\lambda_5) = 1$, we calculate the area;

Engine of $\pi_{c0} = 5.2$:

$$A_1 = 0.315\ m^2,\ A_3 = 0.0722\ m^2.$$

Engine of $\pi_{c0} = 3.8$:

$$A_1 = 0.194\ m^2,\ A_3 = 0.059\ m^2.$$

All the data checked are illustrated in Tables 3 and 4.

APPENDIX II

Verification of the Equations Derived in Paragraphs 5 and 6: i.e., to make a comparison between the values of $\zeta_{\Sigma cal}$ and (P_{02}/P_{01}) calculated from theory and the values of $\zeta_{\Sigma exp}$ and $(P_{02}/P_{01})_{exp}$ from experiment.

The value of $(P_{02}/P_{01})_{cal}$ can be calculated from both equations (5.7) and (5.11), that is,

$$\left(\frac{P_{02}}{P_{01}}\right)_{cal} = \frac{(1-0.7M_1^2\zeta_{\Sigma cal})\left(\frac{P_{03}}{P_{04}}\right)_{cal}}{(1-0.7M_1^2\zeta_{cccal})(1-0.7M_1^2\zeta_{apcal})}$$

where the values of every parameters are given by following equations:

$$\zeta_{\Sigma cal} \tag{6.16}$$

$$\zeta_{ccal} \tag{6.3}$$

$$\zeta_{apcal} \tag{6.5}$$

$$\zeta_{ccal} \tag{6.13}$$

$$\zeta_{tcal} \tag{6.9}$$

$(P_{03}/P_{04})_{cal}$ is obtained from Appendix I.

The known values for calculation are as follows: Engine A:

$$A_1 = 0.3069\ m^2,\ A_2 = 0.0636\ m^2,\ A_3 = 0.0713\ m^2,$$

$$A_4 = 0.277\ m^2,\ \zeta_{cc0} = 0.59,\ \zeta_{ap0} = 0.517.$$

Engine B:

$$A_1 = 0.0685\ m^2,\ A_2 = 0.05\ m^2,\ A_3 = 0.023\ m^2,$$

$$A_4 = 0.0764\ m^2,\ \zeta_{cc0} = 1.415,\ \zeta_{ap0} = 0.318.$$

In addition, the friction power W_f is given by the equation $W_f = M_f n/30$, where M_f can be obtained from the graph for this engine.

The values of $(P_{02}/P_{01})_{exp}$, $(T_{02}/T_{01})_{exp}$ and $\zeta_{\Sigma exp}$ are obtained from the curves drawn according to the experimental data. Table 5 illustrates the results of calculation and experiment.

APPENDIX III

Prediction of the Windmilling Airflow Rate Characteristic and the Values of P_{02}/P_{01}, T_{02}/T_{01}, P_{03}/P_{04}, etc. for Engine C Using Approximate Method I. Engine A is chosen as the "reference engine". Its relevant data are shown in Tables 3 and 5.

The known values of Engine C are as follow:

$$A_1 = 0.2139\ m^2,\ A_2 = 0/068\ m^2,\ A_3 = 0.056\ m^2,$$

$$A_4 = 0.1887\ m^2,\ A_5 = 0.1948\ m^2,\ \zeta_{cc0} = 1.048,$$

$$\zeta ap_0 = 0.412.$$

We take $\sigma_i = 1$ and $\alpha = P_5/P_H = 1$ (the air intake for flight testing was a subsonic intake).

The procedure and its results are shown in Table 6 and Fig. 16.

Downloaded 01 Jun 2010 to 171.66.16.59. Redistribution subject to ASME license or copyright; see http://www.asme.org/terms/Terms_Use.cfm

An Evaluation of Steam Injected Combustion Turbine Systems

D. H. Brown
Corporate Research and Development,
General Electric Company,
Schenectady, NY,
Mem. ASME

A. Cohn
Electric Power Research Institute,
Palo Alto, CA,
Mem. ASME

Performance and economic evaluation results are presented for steam injected combustion turbine systems. The steam injected gas turbine plant shows a potential for low capital cost and high efficiency for sites where water consumption is not a deterrent. Steam produced in a heat recovery steam generator is injected into the gas turbine combustor section to the extent of 0.155 pounds steam per pound of air flow. Water consumption is estimated to be 2.5 pounds per kWh (1.13 kg/kWh). When burning distillate fuel at 2200°F (1204°C), the potential efficiency is 40 percent as compared to 32 percent for a simple cycle gas turbine, and the specific output per pound of air flow is increased by 30 percent. The estimated capital cost per kilowatt is 3 percent greater than that for the simple cycle gas turbine.

Basic Steam Injected Gas Turbine (STIG)

In a modification of the simple cycle gas turbine, steam can be added to the compressed air at the combustion chamber so that the power is increased by the added mass flowing through the expansion turbine. The theoretical performance of such configurations has been evaluated by several authors [1–3]. The thrust of this evaluation was to determine the economic cost of electricity and the performance to be obtained when the component efficiencies were constrained to the level of present industrial gas turbine technology, when all rational parasitic losses were accounted, and when reasonable constraints on exhaust visibility were applied. To this end, the gas turbine component performance parameters presented in Appendix I were made identical to those for the gas turbines evaluated in the ECAS Phase I study of 1974 [4]. All gas turbines were evaluated at a common advanced firing temperature of 2200°F (1204°C) and a common air flow of 570 pounds per second (258 kg/s). The physical size and output of the turbine and generator would be increased to accommodate the increased mass flow and power produced by steam injection. The steam to air ratio and the compressor pressure ratio were primary variables. Each was evaluated through and beyond the range in which it would commonly be used. The cooling air flow for the gas turbine was adjusted in each evaluation to maintain the turbine metal temperatures at a fixed level.

A criterion for visual environmental intrusion was formulated, and is presented in Appendix II. The basis for the criterion is that the onset of a visible white steam-like exhaust plume for the gas turbine should correspond exactly to the onset of a similar plume for fossil-fired power plants that use wet flue gas scrubbers to remove sulfur dioxide. Gas turbine plant performance was limited by this criterion, and should be less optimistic than evaluations that omit such a constraint.

The basic STIG cycle is illustrated schematically in Fig. 1. The distinctive feature is that the gas turbine exhaust heat, otherwise lost from the cycle, is recovered in a heat recovery steam generator to produce superheated steam at relatively low pressure. This steam is introduced in the gas-turbine combustion system and heated to the rated turbine firing temperature. A significant increase in power output and cycle efficiency results relative to the simple cycle gas turbine. This cycle is distinguished from the combined cycle by the omission of a separate steam turbine and its heat rejection system, comprising a condenser and cooling tower.

Practical thermodynamic cycle evaluations of the steam injected gas turbine were made with parametric investigation of cycle efficiency and specific output variations as functions of compressor pressure ratios and steam injection rate. Pressure ratios were explored over a range of 8:1 to 30:1 and steam to air ratios were explored over the full range of plausible steam rates up to the maximum steam production capability of the heat recovery steam generator. The parameters of the heat recovery steam generator are presented in Appendix III.

The performance of the basic steam injected gas turbine at a pressure ratio of 16 is presented in Fig. 2. A number of parameters follow linear trends as the steam to air ratio increases. Gas turbine

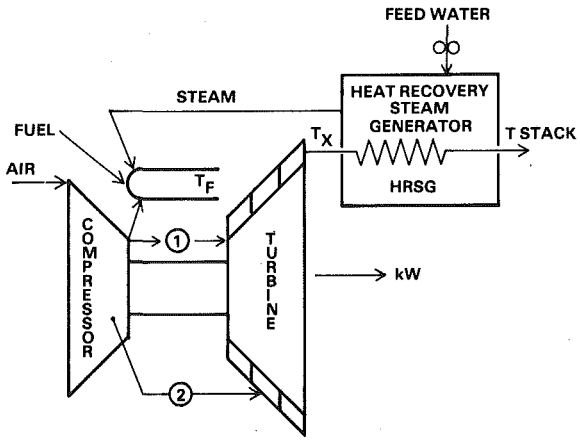

1. NONCHARGEABLE TURBINE AIR COOLANT
2. CHARGEABLE TURBINE AIR COOLANT

Fig. 1 Steam injected gas turbine

Contributed by the Gas Turbine Division and presented at the Gas Turbine Conference and Products Show, New Orleans, La., March 10–13, 1980 of THE AMERICAN SOCIETY OF MECHANICAL ENGINEERS. Manuscript received at ASME Headquarters December 11, 1979. Paper No. 80-GT-51.

Copyright © 1981 by ASME

Downloaded 01 Jun 2010 to 171.66.16.59. Redistribution subject to ASME license or copyright; see http://www.asme.org/terms/Terms_Use.cfm

specific power and exhaust temperature rise progressively. Steam superheat rises with gas turbine exhaust temperature until a steam to air ratio of 0.174 is reached at the pressure ratio of 16. Beyond that ratio superheat drops rapidly due to an insufficiency of enthalpy available to the heat recovery steam generator. The fuel rate increases linearly to the 0.174 steam to air ratio, and increases linearly but more rapidly thereafter due to the declining temperature of the steam being injected. These factors result in the efficiency peaking at the 0.174 steam to air ratio. The requirement for the exhaust plume visibility limit to be less than the stack temperature would constrain the steam to air ratio to 0.155. Beyond that ratio a visible steam-like plume would prevail in cold weather longer than the similar plumes produced by flue-gas-scrubbed power plant stacks. The turbine flow area would be increased by 24 percent to accommodate the combined flow of steam and combustion products.

The 30°F (16.7°C) pinchpoint for the heat recovery steam generator was just reached at the 0.174 steam to air ratio and prevailed from there to the extreme limit of 0.237 steam to air ratio. The stack temperature rose from 300°F to 314°F (149°C to 157°C) over this range of steam to air ratios.

The composite results of similar characteristics at various pressure ratios for the basic steam injected gas turbine cycle are summarized in Fig. 3. Several notable envelopes are detailed. At the extreme right is found the maximum specific output as limited by the ability to recover heat in a practical heat recovery steam generator while meeting the constraints of 50°F (27.8°C) superheat for steam injected at the gas turbine and a 30°F (16.7°C) minimum pinchpoint. The envelope of maximum efficiency (maximum steam superheat) shows that appreciable sacrifice in efficiency would have resulted had maximum specific output been the basis of design point selection.

The envelope of exhaust-plume visibility limit criteria lies close to the maximum efficiency envelope. Little sacrifice is entailed in design point selection by this criterion rather than by maximum efficiency.

The highest pressure ratio currently foreseen for single-shaft industrial gas turbines is 16. Although a pressure ratio of 20 would provide the highest efficiency, a pressure ratio of 16 was selected as the superior economic candidate for the basic steam injected gas turbine cycle. That point has been boldly encircled.

Simple Cycle Gas Turbine

Shown at the extreme left in Fig. 3 is the performance of the simple cycle gas turbine (steam to air ratio of zero). At this advanced firing temperature the maximum specific output occurs at a pressure ratio of 12. The efficiency increases for higher pressure ratios and peaks at a pressure ratio of 30. The selected performance point for comparison with other alternatives was made at the pressure ratio of 16, with an efficiency of 33 percent.

The simple cycle machines are presumed to use an advanced combustor that would control NO_x without need for either steam or water addition.

Combined Steam and Gas Turbine Cycles

The conventional combined cycle power plants produce high pressure steam in the gas turbine HRSG. These plants may aggregate several gas turbines, sending steam to a single condensing steam turbine. The steam is condensed and recycled to the HRSGs. The consumptive use of water is only for evaporative cooling tower makeup. Combined cycle plants have great operational flexibility and many operating points are at near-to-maximum efficiency.

Combined cycle performance appears in Fig. 3 at an efficiency level of 44 percent, with specific output in the range of 205 kW per pound per second of air flow. The pressure level of 12 was selected for cost determination and performance comparison with other alternatives.

STIG Combined with Noncondensing Steam Turbine

Another alternative for high pressure steam produced in the HRSG is to expand it through a noncondensing steam turbine to generate additional power before injecting it into the gas turbine. All of the

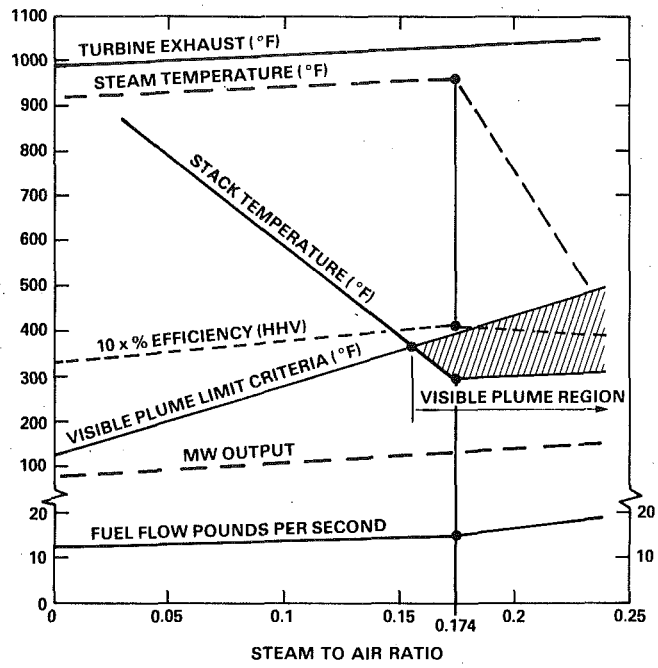

Fig. 2 Steam injected gas turbine characteristics (2200°F (1204 °C), 16 pressure ratio)

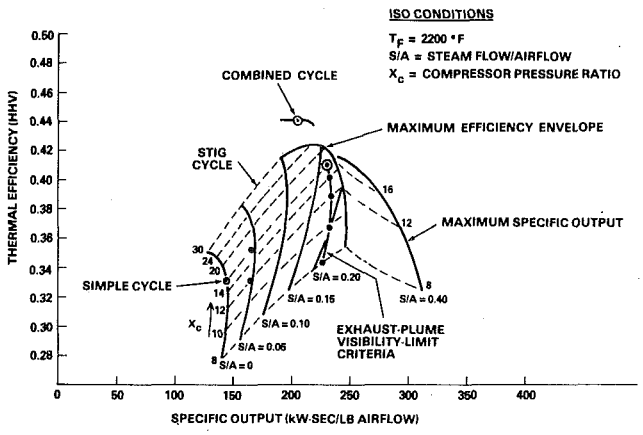

Fig. 3 Steam injected gas turbine cycle performance

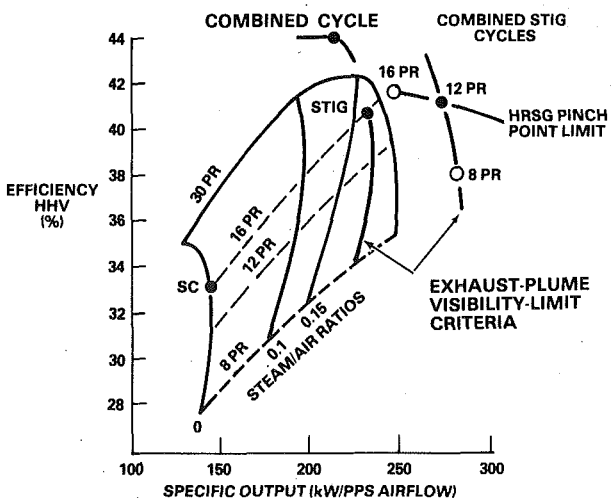

Fig. 4 Comparison of 2200°F (1204°C) gas turbine cycles

Downloaded 01 Jun 2010 to 171.66.16.59. Redistribution subject to ASME license or copyright; see http://www.asme.org/terms/Terms_Use.cfm

Table 1 Performance of selected 2200 °F (1204°C) gas turbine cycles

	Pressure Ratio	Efficiency HHV	kW Per PPS Air	Steam/ Air	Lb H_2O per kWh	Steam Condition	Limit Condition
Simple Cycle	16	33%	144	0	0	-	Pressure Ratio
Combined Cycle	12	44%	205	0	1.69	1450p/1000 °F	High Efficiency
STIG Cycle	16	41%	226	0.155	2.47	330p/952 °F	Plume Criteria
Regen. STIG	16	42%	202	0.131	2.33	330p/834 °F	Plume Criteria
Combined STIG	12	41%	270	0.185	2.47	1450p/1000 °F	HRSG & Plume

steam is finally discharged to the atmosphere and comprises a consumptive use of water. A comparison of this configuration with that of the combined cycle shows impressive simplifications. There is no condenser or heat rejection cooling tower. The steam turbine exhaust goes directly to the gas turbine. In combined cycle plants, however, a single steam turbine may receive steam from several gas turbines. That is not the case for STIG combined cycles. Several STIG gas turbines cannot share a single steam turbine exhaust because that would provide a pressure shunt between their combustion chambers. Combustion instability could result. The single steam turbine could have its own generator, or it could be shaft-connected to the gas turbine in the manner of conventional starting or booster steam turbines.

The calculations for the combined STIG cycle performance were made to find the conditions at which efficiency and specific output were maximum without violating HRSG constraints or the exhaust visibility limit criterion. Figure 4 shows the performance of the combined STIG cycles relative to the alternative gas turbine cycles. At a low pressure ratio such as 8, the exhaust visibility limit criterion governs; as pressure ratio increases, the HRSG pinchpoint begins to govern at a pressure ratio of 12. The three points shown represent the highest efffciency and output at each specific pressure ratio. The point at a pressure ratio of 12 was selected for economic appraisal. It makes a small efficiency sacrifice as compared with the 16 pressure ratio point, and a small specific output sacrifice as compared with the pressure ratio of 8 point. The STIG combined cycle efficiency is slightly better than the basic STIG cycle, but distinctly poorer than the combined cycle plant. The specific output is superior to all alternatives.

Regenerative STIG Gas Turbines

An alternative use for the gas turbine exhaust heat would be to regeneratively heat compressor discharge air prior to combustion. An HRSG would follow the exhaust regenerator to produce steam for injection into the gas turbine. It was found that the steam-producing capacity of the HRSG was appreciably reduced. As a result the specific output would be only 90 percent of that for the basic STIG cycle. The efficiency increased 1 percent. The added cost of the regenerator, in conjunction with the specific work reduction, rules out the regenerative STIG cycle as an economic alternative to the basic STIG cycle.

Performance Summary

Table 1 summarizes performance for each type of steam injected gas turbine plant and alternative gas turbine cycles. The selected points that were dictated by exhaust visibility limit criteria were all in the immediate vicinity of the highest efficiency achievable at the selected pressure ratio. The STIG combined cycle and the basic STIG cycle exhibit the greatest specific output. The water consumption was comparable at approximately 2.5 pounds per kilowatt hour (1.13 kg/kWh) for all STIG cycles. Water consumption comprised injected steam, HRSG blowdown, and evaporative cooling tower evaporation in the case of the combined cycle. By comparison, fossil-fired steam plants would require 3.8 pounds of water per kilowatt hour (1.7 kg/kWh) to replenish the wet cooling tower evaporation.

Table 2 Power output and auxillary power demands

	Simple Cycle	STIG Cycle	Combined STIG	Combined Cycle
Gas Turbines	1	1	1	4
Gas Turbine Output, MW	82	129	134	346.8
Steam Turbine Output, MW	0	0	20	145.8
BOP Auxiliaires, MW	-1.0	-1.0	-1.0	-14.4
Transformer Loss, MW	-0.4	-0.6	-0.8	-2.5
Net Station Output, MW	80.6	127.4	152.2	475.8
Net Station Efficiency (HHV)	32.4%	40.5%	40.9%	42.5%
Fuel Consumption, Btu/kWh net	10531	8425	8342	8028
Water Consumption, gal/kWh net	0	0.30	0.30	0.21

Net Power Plant Performance

The net power plant performance was evaluated by assignment of auxiliary-demands and is tabulated in Table 2. The combined cycle plant was configured with four gas turbines and a single steam turbine in order to secure the best economic evaluation. Cooling tower fans and circulating water pumps account for the large auxilliary demand of the combined cycle plant. Transformer losses were one-half percent of the net station output.

Economic Comparisons

To make these economic results directly comparable with the ECAS Phase I results [4], the component and installation costs were evaluated in 1974 dollars for the candidate STIG power plants and their alternatives. The combined cycle plant costs were identical to case 8 in that study. A 20 percent contingency was added to the subtotal costs to cover items not detailed when considering major components. Interest during construction amounted to 5 percent and 8.25 percent of construction costs for one- and two-year construction periods, respectively. Cost escalation during construction was omitted since this effect is accounted for by levelizing all costs as if all plants had a common start of service date in mid-1974. The capital cost distributions for the selected power plants are presented in Table 3. On the basis of dollars per kilowatt the STIG plant is comparable to the simple cycle gas turbine.

Cost of Electricity

Cost elements that vary annually with the amount of electricity generated are water acquisition and treatment costs, fuel cost, and operation and maintenance cost. Table 3 presents these costs in detail as compared in the year 1974. Their subtotal is termed variable costs in 1974. Over a 30-year plant life with all variable cost escalating at 6.5 percent and interest at 10 percent, the leveled cost would be 1.94 times the first year cost of the variable items [5] as shown in Table 4. The capital cost is accounted at a fixed charge rate of 18 percent annually to arrive at the total levelized cost of electricity. This cost element relates to the capacity factor which is the kilowatt-hours generated annually divided by the kilowatt capacity times 8760 hr per year.

Downloaded 01 Jun 2010 to 171.66.16.59. Redistribution subject to ASME license or copyright; see http://www.asme.org/terms/Terms_Use.cfm

Table 3 Capital cost distributions in million dollar units (mid-1974 dollars)

	Simple Cycle	STIG Cycle	Combined STIG	Combined Cycle
Gas Turbine-Generator	6.9	8.0	8.0	25.2
Installation	1.9	1.9	1.9	7.6
HRSG and Installation	-	4.1	5.0	20.0
Steam Turbine-Gen. and Installation	-	-	3.1	16.0
Water Treatment Installed	-	0.3	1.1	-
Condenser and Cooling Towers	-	-	-	5.5
Contingency at 20%	1.8	2.9	3.8	14.9
Interest During Construction	0.5	0.9	1.2	8.2
Total Capital Cost	11.8	19.2	25.6	107.4
Total Capital Cost, $/kW	138	142	158	202
Years to Construct	1	1	1	2

Table 4 Cost of electricity in mills per kilowatt-hour

Cost Factor		Simple Cycle	STIG Cycle	Combined STIG	Combined Cycle
Water at 30¢/1000 gal		-	0.09	0.09	0.06
Water Treatment		-	0.03	0.30	-
Fuel at $3/million Btu		31.6	25.3	25.0	24.1
Operation and Maintenance		2.0	2.0	2.0	2.0
Variable Cost in 1974		33.6	27.4	27.4	26.1
Variable Cost Levelized		65.2	53.1	53.2	50.7
Total Cost Levelized					
Capacity Factor	1.0	68.0	56.1	56.5	54.9
Capacity Factor	0.65	69.5	57.6	58.2	57.2
Capacity Factor	0.01	349	345	378	472

The STIG combined cycle has both a variable COE and a capital cost greater than the basic STIG cycle. It would be more complex and less flexible to operate. The basic STIG plant is marginally superior compared to the STIG combined cycle.

Compared to the simple cycle gas turbine, the STIG plant is marginally more costly and has an appreciable advantage in lower variable COE. Where water availability was not a deterrent, the STIG plant has potential economic advantage over the simple cycle gas turbine down to very low capacity factors (less than 0.01). The greater simplicity of the simple cycle gas turbine makes it more adaptable to unattended and remote operation.

As compared to the combined cycle plant with a condensing steam turbine, condenser and cooling towers the variable COE favors the combined cycle plant whereas the capital cost per kilowatt capacity favors the STIG plant. Economics would favor the STIG plant below 0.53 capacity factor, and would favor the STAG plant at higher capacity factors.

A screening curve based on these economics is presented in Fig. 5. The coal-fired steam power plant would burn pulverized coal and utilize a flue gas desulfurization.

Observations

The basic steam injected gas turbine at 2200°F (1204°C) firing temperature has potential advantages as compared to alternative gas turbine cycles. Its heat recovery steam generator operates at low pressure and would be tolerant of lower quality feedwater as compared to a high pressure power boiler. When compared to the conventional combined cycle there are no separate steam turbine, condenser or cooling towers. The water consumption is comparable to other alternatives, and the exhaust plume visibility would be no more evident than those of fossil-fired coal burning plants using flue gas scrubbers. The cost of electricity on the basis of levelized costs over the life of the plant are potentially competitive with both the simple cycle gas turbine for peaking service and the combined cycle for intermediate duty.

The alternative gas turbines have the advantage of being fully developed and commercially available at today's firing temperatures. Developments are underway to enable the simple cycle machine to operate without water for emissions control. The simple cycle gas turbine is capable of remote and unattended operation. The combined cycle gas turbine may aggregate several gas turbines sending steam to a single steam turbine and achieve many operating points at high efficiency. The steam injected gas turbine would require a 24 percent

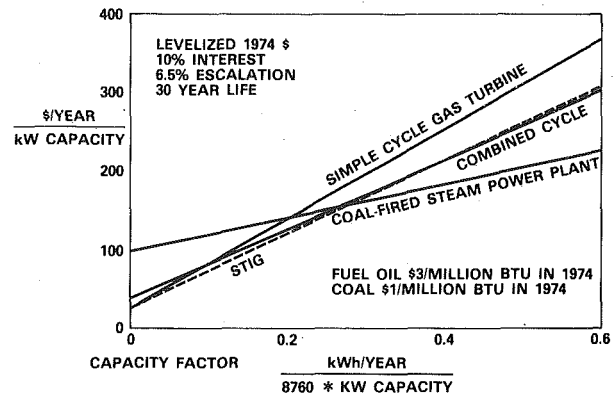

Fig. 5 Screening curves for 2200°F (1204°C) gas turbine options (mid-1974 dollars; levelized)

larger flow area for the turbine for a given compressor, and development in the areas of the combustor, the turbine aerodynamic and mechanical design, the turbine cooling, and the control system.

Conclusion

This evaluation demonstrates that when the steam injected gas turbine is constrained to levels of performance that are rational for heavy-duty industrial gas turbines and that do not offend environmental constraints, there are potential economic and performance benefits to be realized over a wide and relevant range of capacity factors. However, the economic benefit is small compared to the simple cycle at low capacity factors, and is small compared to the combined cycle at intermediate capacity factors. The STIG gas turbine would also require turbine and combustor developments.

Acknowledgments

This evaluation was made on behalf of the Electric Power Research Institute. Bruce Fick and Richard Sheldon of the General Electric Gas Turbine Division provided the detailed gas turbine analysis for the cycle performance evaluations.

References

1 Day, W. H. and Kydd, P. H., "Maximum Steam Injection in Gas Turbines," ASME Paper, No. 72-JPC-GT-1, Joint Power Conference, Boston, 1972.

2 Boyle, M. P. and Chen, M. S., "Optimization of Various Gas Turbine Cycles," *Proceedings of the Third Turbomachinery Symposium*, Texas A&M University Press, Oct. 1974.

3 Fraize, W. E. and Kinney, C., "Effects of Steam Injection on the Performance of Gas Turbine Power Cycles," ASME JOURNAL OF ENGINEERING FOR POWER, Apr. 1979, Vol. 101, 217–227.

4 Brown, D. H. and Corman, J. C., "Energy Conversion Alternatives Study, General Electric Phase I Final Report, Report No. NASA-CR-134948, Volume II, Advanced Energy Conversion Systems, Part 1, Open Cycle Gas Turbines," prepared for National Aeronautics and Space Administration, Energy Research and Development Administration, and National Science Foundation, Feb. 1976.

5 Pomeroy, B. D., Corman, J. C., Fleck, J. S., Fleming, R. B., Marsh, W. D., "Comparative Study and Evaluation of Advanced Cycle Systems, Phase 1 Report," EPRI AF-158, May 1976.

APPENDIX 1

Gas Turbine Parameters

Ambient:	ISO day, 59°F (15°C), 60 percent relative humidity
Configuration:	Heavy duty industrial single shaft gas turbines including generator and all auxiliaries.
Compressor:	570 pounds per second (258.5 kg/s) airflow. 4 in. (995 N/m^2) water inlet pressure drop, single shaft to 16 pressure ratio.

Downloaded 01 Jun 2010 to 171.66.16.59. Redistribution subject to ASME license or copyright; see http://www.asme.org/terms/Terms_Use.cfm

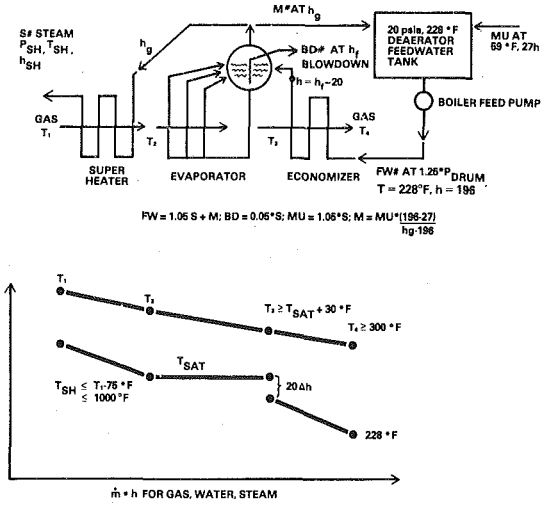

Fig. 6 Heat recovery steam generator—schematic and temperature profiles

Fuel: Distillate, 3 dollars per million Btu, 19663 Btu per pound higher heating valve (45728 kJ/kg), 18550 Btu per pound lower heating valve (43139 kJ/kg).

Combustor: 99 percent combustion efficiency, 3 percent pressure drop, combustor pressure is 14.5525 times the pressure ratio, injection steam 50°F (27.8°C) or more above saturation at combustor pressure.

Turbine: 2200°F (1204°C) total temperature at first stage, stage inlet at 1.0 Mach number, three stages, air cooled, exhaust pressure loss 5 in. water (1244 N/m^2) plus 15 in. water (3733 N/m^2) if HRSG and plus 8 in. water (1990 N/m^2) if regenerator in exhaust.

Regenerator: Air side pressure loss 2.2 percent, gas side pressure loss 2.0 percent, effectiveness related to air side 81 percent.

Turbine Cooling: Cooling air schedule varied with pressure ratio and steam injection rate.

APPENDIX II

Criteria for Exhaust Plume Visibility Limit

When any exhaust stream contains water vapor, its mixture with ambient air may create a white opaque condensate plume. Although the condensate is water (it is commonly called steam) its appearance can be mistaken for smoke. Virtually every stack discharge will exhibit such a visible plume on a cold winter morning. A suitable criterion would limit plume visibility to being no more frequent than for alternative power plant stacks. Since most coal-burning plants will require flue gas scrubbers, that was the exhaust chosen as the standard for comparison. Flue gas scrubbing saturates the flue gas with water vapor at 125°F (52°C). The gas is reheated to 175°F (79°C) prior to exhausting from the stack. A psychrometric diagram shows that similar plume visibility potential will exist for any atmospheric discharge meeting the following criterion:

$$\text{Minimum discharge temperature °F} = (50 + 1277*\text{Humidity})/(1 - \text{Humidity}).$$

Humidity is the weight fraction of water vapor in the stack gas. If the stack temperature exceeds this criterion, then its visible exhaust plume on cold days will start after the coal-fired stack plume has already been visible and will disappear before that plume disappears.

Table 5 Heat recovery steam generator parameters

Type Plant	Makeup	Steam Produced	Comments
STIG Cycle	635 gpm	330 P, 952 °F, 1499h	Injected Steam
Combined STIG	757 gpm	1450 P, 1000 °F, 1494h 183 P, 574 °F, 1309h	Out of HRSG Injected Steam
Combined Cycle	7 gpm	1450 P, 1000 °F, 1494h	2.5 in. Condenser

The criterion defines the stack temperature for exact parity with a coal-fired power plant with flue gas scrubbing on the basis of the appearance, duration, and disappearance of a visible white condensate in the exhaust plume.

APPENDIX III

Heat Recovery Steam Generator (HRSG)

Figure 6 shows a schematic of the heat recovery steam generator and the temperature profiles that limit heat recovery from the gas turbine exhaust gas. An additional constraint requires that the injection steam be at least 50°F (27.8°C) superheated relative to a saturation pressure equal to compressor discharge pressure. Only 99 percent of the gas turbine exhaust is accounted as flow through the HRSG to allow for bypass stack leakage. The bypass would be used during startup and to limit excess steam production. Unlike typical power boilers the HRSG units for STIG cycles operate with 100 percent makeup (MU). The deaerator is serviced by saturated steam (M) to produce feedwater (FW) at 228°F (109°C). A large 5 percent blowdown (BD) was assigned to limit drum water solids concentrations. The economizer heats the feedwater to within 20 Btu per pound (46.5 kJ/kg) of the drum saturated water enthalpy. The temperature pinch point limits are 75°F (41.7°C) at the superheater outlet, 30°F (16.7°C) leaving the evaporator section, and a 300°F (149°C) lower limit on stack gas temperature. From the drum to the gas turbine the pressure losses would be 5.8 percent in the superheater, 5 percent in the connecting steam line, and 35 percent in the high recovery control throttle at the gas turbine. The gas turbine combustor pressure was 14.5525 times the pressure ratio, and the resulting steam drum pressure would be 1.5 times the combustor pressure. A sodium zeolite water treatment would be used for the low pressure HRSGs. High pressure power boilers for the STIG combined cycle would require the more expensive complete demineralizer water treatment. Table 5 shows the parameters of the HRSGs for the selected gas turbine cycles of this study.

Downloaded 01 Jun 2010 to 171.66.16.59. Redistribution subject to ASME license or copyright; see http://www.asme.org/terms/Terms_Use.cfm

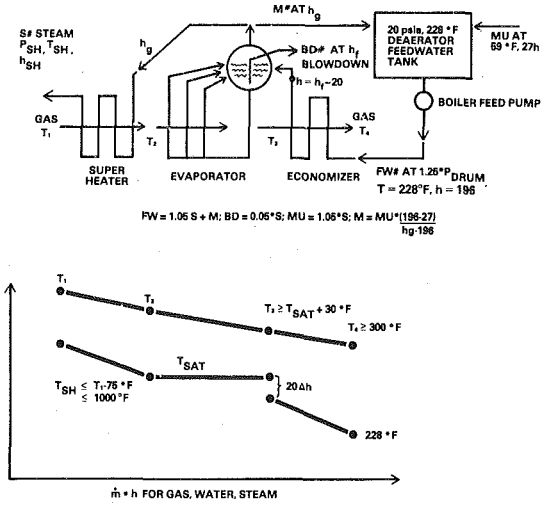

Fig. 6 Heat recovery steam generator—schematic and temperature profiles

Fuel: Distillate, 3 dollars per million Btu, 19663 Btu per pound higher heating valve (45728 kJ/kg), 18550 Btu per pound lower heating valve (43139 kJ/kg).

Combustor: 99 percent combustion efficiency, 3 percent pressure drop, combustor pressure is 14.5525 times the pressure ratio, injection steam 50°F (27.8°C) or more above saturation at combustor pressure.

Turbine: 2200°F (1204°C) total temperature at first stage, stage inlet at 1.0 Mach number, three stages, air cooled, exhaust pressure loss 5 in. water (1244 N/m^2) plus 15 in. water (3733 N/m^2) if HRSG and plus 8 in. water (1990 N/m^2) if regenerator in exhaust.

Regenerator: Air side pressure loss 2.2 percent, gas side pressure loss 2.0 percent, effectiveness related to air side 81 percent.

Turbine Cooling: Cooling air schedule varied with pressure ratio and steam injection rate.

APPENDIX II

Criteria for Exhaust Plume Visibility Limit

When any exhaust stream contains water vapor, its mixture with ambient air may create a white opaque condensate plume. Although the condensate is water (it is commonly called steam) its appearance can be mistaken for smoke. Virtually every stack discharge will exhibit such a visible plume on a cold winter morning. A suitable criterion would limit plume visibility to being no more frequent than for alternative power plant stacks. Since most coal-burning plants will require flue gas scrubbers, that was the exhaust chosen as the standard for comparison. Flue gas scrubbing saturates the flue gas with water vapor at 125°F (52°C). The gas is reheated to 175°F (79°C) prior to exhausting from the stack. A psychrometric diagram shows that similar plume visibility potential will exist for any atmospheric discharge meeting the following criterion:

$$\text{Minimum discharge temperature °F} = (50 + 1277*\text{Humidity})/(1 - \text{Humidity}).$$

Humidity is the weight fraction of water vapor in the stack gas. If the stack temperature exceeds this criterion, then its visible exhaust plume on cold days will start after the coal-fired stack plume has already been visible and will disappear before that plume disappears.

Table 5 Heat recovery steam generator parameters

Type Plant	Makeup	Steam Produced	Comments
STIG Cycle	635 gpm	330 P, 952 °F, 1499h	Injected Steam
Combined STIG	757 gpm	1450 P, 1000 °F, 1494h 183 P, 574 °F, 1309h	Out of HRSG Injected Steam
Combined Cycle	7 gpm	1450 P, 1000 °F, 1494h	2.5 in. Condenser

The criterion defines the stack temperature for exact parity with a coal-fired power plant with flue gas scrubbing on the basis of the appearance, duration, and disappearance of a visible white condensate in the exhaust plume.

APPENDIX III

Heat Recovery Steam Generator (HRSG)

Figure 6 shows a schematic of the heat recovery steam generator and the temperature profiles that limit heat recovery from the gas turbine exhaust gas. An additional constraint requires that the injection steam be at least 50°F (27.8°C) superheated relative to a saturation pressure equal to compressor discharge pressure. Only 99 percent of the gas turbine exhaust is accounted as flow through the HRSG to allow for bypass stack leakage. The bypass would be used during startup and to limit excess steam production. Unlike typical power boilers the HRSG units for STIG cycles operate with 100 percent makeup (MU). The deaerator is serviced by saturated steam (M) to produce feedwater (FW) at 228°F (109°C). A large 5 percent blowdown (BD) was assigned to limit drum water solids concentrations. The economizer heats the feedwater to within 20 Btu per pound (46.5 kJ/kg) of the drum saturated water enthalpy. The temperature pinch point limits are 75°F (41.7°C) at the superheater outlet, 30°F (16.7°C) leaving the evaporator section, and a 300°F (149°C) lower limit on stack gas temperature. From the drum to the gas turbine the pressure losses would be 5.8 percent in the superheater, 5 percent in the connecting steam line, and 35 percent in the high recovery control throttle at the gas turbine. The gas turbine combustor pressure was 14.5525 times the pressure ratio, and the resulting steam drum pressure would be 1.5 times the combustor pressure. A sodium zeolite water treatment would be used for the low pressure HRSGs. High pressure power boilers for the STIG combined cycle would require the more expensive complete demineralizer water treatment. Table 5 shows the parameters of the HRSGs for the selected gas turbine cycles of this study.

DISCUSSION

J. L. Jones, C. N. Chang, and J. Hamill[1]

This paper has been reviewed with great interest because of past work by IPT in the development of the Cheng Dual-Fluid Cycle (DFC) engine. The DFC engine was, in fact, discussed in detail with the General Electric Company in 1976. Only limited recognition of the benefits of steam injection in a gas turbine engine is given in this paper. Full benefit of the Dual-Fluid Cycle was not presented because of the argument on plume visibility. IPT's staff asserts that plume visibility should not be a real constraint on the DFC engine (called STIG in this paper). The Cheng Dual-Fluid Cycle engine maximizes waste heat recovery by critically metering steam-to-air ratio uniquely for a given set of gas turbine cycle parameters.

We would like to point out that the plume visibility limitation analysis cited in Messrs. Brown and Cohn's paper contains certain assumptions which made them conclude that the combined cycle offers better efficiency and cost benefits so long as utilities operate the combined cycle more than 1000 hr annually—a conclusion with which we disagree.

With reference to the paper, we wish to present our views.

1 Considering the plume visibility criterion presented in Ap-

[1] International Power Techonlogy, Inc., 506 Oakmead Parkway, Sunnyvale, Calif. 94086.

Copyright © 1981 by ASME

Downloaded 01 Jun 2010 to 171.66.16.59. Redistribution subject to ASME license or copyright; see http://www.asme.org/terms/Terms_Use.cfm

pendix II, it is clear that, for zero humidity, the minimum discharge temperature goes to 50°F, whereas 125°F was indicated in Fig. 2. When we plot the visible plume limit criteria (according to the equation presented in Appendix II and assuming humidity defined as wgt. steam/wgt. exhaust gas), using the same Fig. 2, we find it approaches the stack temperature at a steam-to-air ratio of about 0.165, which is near the peak efficiency condition identified in the authors' calculations. The visible plume region, thus, is barely a constraint on the STIG system defined by the authors.

If one accepts the authors' definition of humidity as wgt. steam/wgt stack gas, then the visible plume limit for the sample case extends to a steam-to-air ratio of 0.175 and no constraint is imposed on the DFC (STIG) system.

2 From a physical and thermodynamic point of view, plumes should not appear for a given moisture content if the exhaust temperature is above the equilibrium dew point. In reality, the plume appears when the exhaust gas mixture is cooled down faster than the diffusion rate of the steam. That is the reason why the plume generally appears a short distance away from the top of the exhaust stack and then disappears again further away from the stack. Hence, the plume visibility problem is more or less an engineering design problem of the stack rather than a limitation in physical principle.

The exhaust gas dew point limit as a criteria for plume visibility, when added to Fig. 2, is clearly well below the exhaust gas temperature over the range of steam-to-air ratios of interest.

3 Using the engine operating conditions defined in the paper, we have calculated the efficiency and power output for the Cheng Dual-Fluid Cycle engine. A special computational program, developed by IPT for the DFC engine, was used. This program was devised to locate the maximum efficiency peaks and identify the critical combinations of fuel, air and steam for these peaks according to IPT's patent on the Cheng-DFC engine (U.S. Patent No. 4,128,994). This calculation uses the same component losses as those employed by G.E. in 1976 and in this paper (see Table 1). For the DFC engine at 2200°F turbine inlet temperature and compression ratio 16:1 with 2.5 percent loss to blade cooling air, the thermal efficiency is 44.5 percent (HHV) or 47.5 percent (LHV) and the throughput is 291 KW/PPS air flow. For comparison to combined efficiency, see Fig. 4. The stack temperature is 251.5°F which is 98°F above the dew point temperature.

Table 1 Input conditions

Inlet pressure loss	$4''H_2O$
Compressor efficiency	88 percent
Pressure drop across combustor	3 percent
Combustion efficiency	99 percent
Turbine efficiency	90 percent
Turbine back pressure loss	$20''H_2O$
ΔT pinch	30°F
ΔT upper	75°F
Cooling air lost to the cycle	2.5 percent

This temperature differential is much higher than normally encountered during wet scrubber exhaust stack operation where reheating the exhaust gas by 35°F (T) is sufficient to eliminate the visible plume.

4 In reality, when a Cheng DFC engine is operating at 2200°F at a higher pressure ratio, say 20:1, the thermal efficiency will be over 50 percent (LHV) and with a reduced steam-to-air ratio; hence, the exhaust will be further away from the visible plume conditions.

The Cheng Dual-Fluid Cycle (STIG) engine has better thermal efficiency and lower unit capital cost ($/kW) than was cited by the authors. These improved characteristics would result from a correct interpretation of the plume problem, and the use of the optimum waste heat boiler pressure, plus the recognition of the increased power output that is used for cost normalization.

For example, the boiler pressure at 330 psig cited by the authors in the STIG system at a compressor pressure ratio of 16:1 has an over pressure of about 90 to 110 psig. This not only reduced the recoverable waste heat but also critically reduces the thermodynamic potential of the steam due to the resultant throttling requirement.

Actually, the real problem with exhaust gas plumes is not visibility due to water content, but the presence of pollutants, normally NO_x and SO_2. The injection of steam into the combustor of the DFC engine provides for the effective suppression of NO_x production to well within acceptable limits. In addition, IPT is developing a practical and effective method for the clean-up of sulfur compounds from the exhaust gas of plants burning coal-derived synfuel or other higher sulfur content fuels, to avoid the occurrence of acid rain or other pollution problems.

Authors' Closure

The discussers contend that the benefits of steam injection have been understated, and that plumes do not become visible unless the discharge gas is at its dew point. In their discussion they attribute no humidity to the ambient air and account no water vapor products from the combustion of fuel. Their simplified use of injected steam as the only source of humidity in the exhaust leads to the erroneous assertion that a simple cycle gas turbine exhaust can be cooled to 50°F without condensation and their own replot of Fig. 2 with a less restrictive plume parity criteria limit. The ambient air as defined in Appendix I has 0.0064 pounds of water vapor per pound of mixture, and combustion of distillate oil adds 1.39 pounds of water vapor per pound of fuel burned. The fuel flow and other data evaluated are detailed in reference [6]. The visible plume limit criterion of Fig. 2 is correct as presented.

The contention that dew point temperature is the sole criterion for plume visibility is not correct. Condensation plumes result from the mixing of two gases such as exhaust gas and ambient air. Figure 7 shows the psychrometry of that mixing with dashed lines showing visible plumes for both the STIG cycle and the Flue Gas Desulfurization-Coal Stack when the ambient air is at 20°F. When the ambient warms and reaches the plume criteria parity line, both stack plumes would become invisible simultaneously. The stack condition endorsed by the discussers of 251.5°F with 154°F dew point falls in the "worse than FGD zone" and would result in exhaust plumes being visible more frequently and for longer duration than the plants constrained to be on the plume criteria parity line. Plume visibility is more than

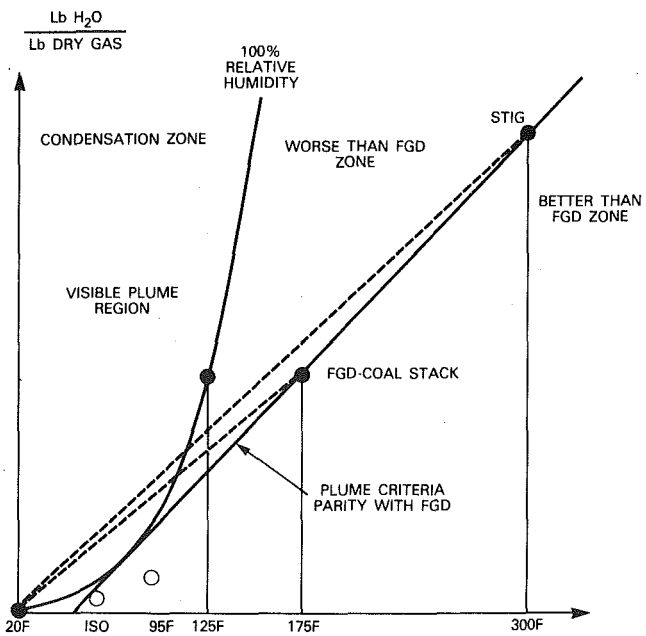

Fig. 7 Psychometry of visible plume formation and plume parity criteria

Downloaded 01 Jun 2010 to 171.66.16.59. Redistribution subject to ASME license or copyright; see http://www.asme.org/terms/Terms_Use.cfm

a stack design problem and dew point temperature of the exhaust is not an appropriate plume visibility criteria.

The performance presented by the discussers for the CDFC engine was evidently made without realistically accounting for the air chargeable for turbine cooling. Both the higher specific work and the higher efficiency claimed by the discussers appear to correlate with their assumption of 2.5 percent "lost" cooling air. It is unfortunate that the discussers compare their analytic results to the authors' performance estimates for the STIG and for combined cycle plants that are based on realistic values for chargeable cooling air flow. The air coolant schedule used conforms to reference [4] evaluations as a function of firing temperature, pressure ratio, and water vapor content of the expansion gases.

R. J. Boyle [7] examines the effects of inclusion and exclusion of cooling air on steam injection gas turbine cycles. The results with cooling air corroborate the findings of the authors' study, but even with uncooled turbines Boyle does not project the extremes of specific work and efficiency claimed for the CDFC cycle by the discussers.

A serious concern with steam injection is the margin to combustion instability in the gas turbine. The total steam pressure drop of 50 percent provides for the use of a high recovery control valve that precludes pressure feedback between the combustor and the boiler, and steam pipe and superheater pressure drops. Omission of these pressure drops would improve the STIG performance, but at the expense of being unrealistic for a viable design.

The STIG cycle chosen for cost and performance evaluation was close to optimum efficiency despite the limitation added by the plume criteria. For all of the cycles evaluated the performance and costs were derived in a manner identical to reference [4]. The evaluations were made as fairly as possible by adhering to reasonable constraints for component performance that could be expected with a moderate development effort.

Additional References

6 Brown, D. H., "Steam Injected Gas Turbine Study: An Economic and Thermodynamic Appraisal," EPRI AF-1186 TPS 77-737, Sept. 1979.

7 Boyle, R. J., "Effect of Steam Addition on Cycle Performance of Simple and Recuperated Gas Turbines," NASA Technical paper 1440, Apr. 1979.

Downloaded 01 Jun 2010 to 171.66.16.59. Redistribution subject to ASME license or copyright; see http://www.asme.org/terms/Terms_Use.cfm

J. De Ruyck
Research Assistant.

C. Hirsch
Professor.

Vrije Universiteit Brussel
Dept of Fluid Mechanics
Brussels, Belgium

Investigations of an Axial Compressor End-Wall Boundary Layer Prediction Method

A previously developed axial compressor end-wall boundary layer calculation method which requires the introduction of three-dimensional velocity profile models is summarized. In this method the classical three-dimensional velocity profile models were shown to present inherent limitations at stall limit, with regard to the range of transverse boundary layer thicknesses they are able to represent. A corrected profile model is presented which contains no more limitations without affecting the previous found overall results. Stall limit is predicted by limiting values of shape factor and/or diffusion factor. The new profile model containing also compressibility effects allows the calculation of boundary layers in machines with shrouded blades, by simulating the jump between rotating and non rotating parts of the walls. A corrected version of a force defect correlation is presented which is shown to give better agreement at high incidences. Some results on high and low speed machines are discussed. The model is applied to obtain an end-wall blockage correlation depending on geometry, flow coefficient, AVR, aspect ratio, solidity, diffusion factor, Reynolds number, axial blade spacing, tip clearance and inlet boundary layer thickness. A quantitative estimation of the losses associated with the end-wall boundary layers can be obtained using this analysis and therefore can be a useful tool in the design of an axial compressor stage.

Introduction

Turbomachinery flows are affected by secondary effects which are mainly due to interactions between blades and end-wall boundary layers. Several effects can be distinguished in these secondary flows and losses such as passage vortex, secondary stresses, mixing, corner vortices, leakage flows, etc. All these effects should be taken into account and this can be done in several ways.

The more classical way consists in defining correlations for the secondary losses as well as for the angle corrections and to distribute them in a certain way along the span. However, correlations for secondary losses are subject to a large uncertainty and various expressions for the secondary loss coefficients can be found in the literature [27].

In order to analyze secondary flow effects, two other approaches are actually being developed, namely the calculation of mainflow vorticity components through non viscous secondary flow theories, and the inclusion of all secondary flow effects in the end-wall boundary layer, under a pitch-averaged form. While the first way is important for understanding secondary flows, it will probably seldom be directly of use in the design of a multistage turbomachine and up to now, satisfactory results are obtained in cascades and single stage machines [6, 7]. Furthermore, it cannot take all the aforementioned effects into account. On the other hand, when using end-wall boundary layer calculation methods, the basic flow equations are integrated in the transverse direction (pitch averaging) and over the boundary layer thickness, simplifying considerably the amount of information which is to be analyzed, and concentrating all secondary flow effects in the end-wall boundary layer equations. While detailed information is lost by integration,the method is able to take into account all kind of secondary flow phenomena in an averaged form, and its output is a measure for all secondary losses, through an overall efficiency drop [1].

The present work is an investigation on the method presented in [1] and [2] which has its base in the method of Mellor and Wood [8] and Hirsch [4, 5]. Compressibility effects are fully introduced extending the field of application of the basic method. A detailed analysis is made of the force defects which are shown to be a dominant parameter in estimating the secondary flow effects in the end-wall boundary layer equations. The used models are shown to be in agreement with experimental data.

An end-wall blockage correlation is obtained based on the end-wall boundary layer equations. Through this correlation some basic properties such as quasi-equilibrium and exponential increase of blockage level clearly appear.

In the first section, the main equations and the basic properties of the previous work are summarized, while in the second section the compressibility corrections on the end-wall boundary layer calculations are introduced. In the next section, the velocity and density profiles are discussed followed by a detailed analysis of the force defect properties and assumptions. Finally, the end-wall blockage correlation is described and results of various calculations are presented and discussed.

Contributed by the Gas Turbine Division and presented at the Gas Turbine Conference and Products Show, New Orleans, La., March 10–13, 1980 of THE AMERICAN SOCIETY OF MECHANICAL ENGINEERS. Manuscript received at ASME Headquarters December 11, 1979. Paper No. 80-GT-53.

Copyright © 1981 by ASME
Downloaded 01 Jun 2010 to 171.66.16.59. Redistribution subject to ASME license or copyright; see http://www.asme.org/terms/Terms_Use.cfm

1 Theoretical Development [1, 2]

1.1 Boundary Layer Momentum Equations. Integrating the Navier-Stokes equations over a control volume with axial length dx, physical boundary layer thickness δ and pitch s, following vectorial boundary layer equation can be found [1] (Fig. 1)

$$\frac{d}{dx}\tilde{c}_{xe}{}^2\tilde{\bar{\theta}} + \tilde{c}_{xe}\tilde{\delta}_x{}^\star\frac{d\tilde{\bar{W}}}{dx} = \frac{\tilde{\bar{\tau}}_w}{\rho} + \frac{\bar{F}}{\rho} \tag{1}$$

where

$$\tilde{c}_{xe}{}^2\tilde{\bar{\theta}} = \int_0^\delta (\tilde{\bar{V}}_e - \tilde{\bar{V}})\tilde{c}_x dy \tag{2}$$

$$\tilde{c}_{xe}\tilde{\delta}_x{}^\star = \int_0^\delta (\tilde{c}_{xe} - \tilde{c}_x)dy \tag{3}$$

$$\bar{F} = \bar{F}_1 + \bar{F}_2 + \bar{F}_3 + \bar{F}_4 \tag{4}$$

$$\bar{F}_1 = \bar{1}_t\frac{1}{g}\int_0^\delta [p_e - p]_a{}^b dy \tag{5}$$

$$\bar{F}_2 = -\rho\frac{d}{dx}\int_0^\delta (\bar{V}_e{}'\bar{V}' - \bar{V}')c_x' dy \tag{6}$$

$$\bar{F}_3 = -\bar{1}_x\int_0^\delta \frac{d}{dx}(\tilde{p}_3 - \tilde{p})dy \tag{7}$$

$$\bar{F}_4 = -\bar{1}_m\frac{2}{g}\int_0^\delta (\tau_{be} - \tau_b)dy \tag{8}$$

A tilde ($\sim$) denotes a pitch averaged value and any flow parameter $g(x, z)$ can be written as

$$g(x, z) = \tilde{g}(x) + g'(x, z) \tag{9}$$

$$\int_a^b g'(x, z)dz = 0 \tag{10}$$

It is to be noted that equation (1) may be written in an arbitrary coordinate system and that it contains only two impulse thicknesses, $\bar{\theta}$. Unknowns of this relation are $\bar{\theta}$, $\delta_x{}^\star$, $\bar{\tau}_w$ and $\bar{F}$.

In the following, all variables will correspond to pitch averaged values and the tildas will be dropped.

The end-wall boundary layer theories differ essentially through different assumptions about two parameters: the direction of the force defect $\bar{F}$ and its magnitude. From equations (5–8) for the different force defect components, it follows that the direction of the total force defect is by no means easy to determine.

The force defect $\bar{F}$ contains all interaction terms between blades and boundary layer flow and represents the integrated difference in effective blade force over the boundary layer with respect to the blade force outside the end-wall boundary layer. Due to different approximations in averaging over the pitch, a slightly different expression

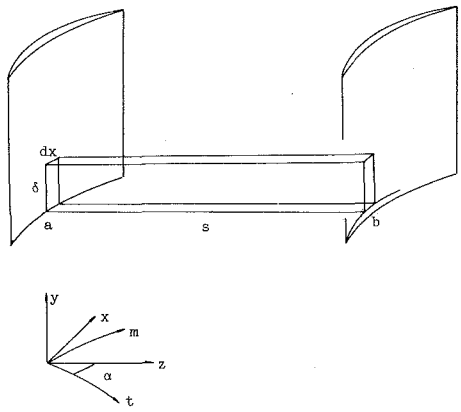

Fig. 1 Integration of Navier Stokes equations—coordinate systems

for $\bar{F}_2$, which contains the secondary stresses $\bar{V}'c'$ can be found

$$\bar{F}_2 = -\frac{d}{dx}\int_0^\delta (\bar{V}_e'c_{xe}' - \bar{V}'c_x')dy \tag{11}$$

equation (6) being obtained by first integrating over the boundary layer thickness [1] and equation (9) by first averaging the Navier Stokes equations [11].

In equation (8), τ_b denotes the skin friction along the blade profiles and [8]

$$\tau_b = (\tau_b)_{\text{pressure side}} = -(\tau_b)_{\text{suction side}} \tag{12}$$

1.2 Introduction of Complementary Relations. Since equation (1) contains more than two unknowns ($\bar{\theta}$, $\delta_x{}^\star$, $\bar{\tau}_w$ and $\bar{F}$), extra relations are to be supplied. A third differential equation is given by Head's entrainment equation obtained by integrating the continuity equation over the same volume as has been done for the Navier-Stokes equation [15].

$$\frac{1}{c_{xe}}\frac{d}{dx}c_{xe}(\delta - \delta_x{}^\star) = \frac{F(\mathrm{H}^\star)}{\cos\alpha} \tag{13}$$

where

$$F(\mathrm{H}^\star) = 0.0306(\mathrm{H}^\star - 3)^{0.653} \tag{14}$$

$$\mathrm{H}^\star = \frac{\delta - \delta_m{}^\star}{\theta_m} \tag{15}$$

$$\delta_m{}^\star = \int_0^\delta \left(1 - \frac{u}{u_e}\right)dy \tag{16}$$

$$\theta_m = \int_0^\delta \left(1 - \frac{u}{u_e}\right)\frac{u}{u_e}dy \tag{17}$$

Nomenclature

b = boundary layer parameter
c = velocity, chord
C_f = wall friction coefficient
C_L = lift coefficient
C_D = drag coefficient
F = force defect
f = blade force
g = staggered spacing
h = annular height
H = shape factor
$\mathrm{H}^\star$ = Head's shape factor
J = jacobian
m = mainstream coordinate
n = power
p = static pressure
p_t = stagnation pressure
r = radius, recovery factor
s = pitch
T = temperature
T_r = recovery temperature
T_t = stagnation temperature
t = transverse coordinate
t_c = tip clearance
U = wheel speed
u = mainstream velocity component
V = absolute velocity
v = radial velocity component
W = relative velocity
w = transverse velocity component
x = axial coordinate
y = coordinate normal to the wall
z = tangential coordinate
α = flow angle
β = blade angle
γ = stagger
δ = physical boundary layer thickness
$\delta^\star$ = displacement thickness
ϵ_w = wall skewing angle
θ = momentum thickness
ξ = axial blade spacing
ρ = static density
σ = solidity
τ = shear stress
φ = mass flow coefficient
ψ = pressure rise coefficient

Subscripts

m, y, t = in streamline coordinates
x, y, z = in cartesian coordinates
e = at the edge of the boundary layer
w = at the wall
k = kinematic

Downloaded 01 Jun 2010 to 171.66.16.59. Redistribution subject to ASME license or copyright; see http://www.asme.org/terms/Terms_Use.cfm

The shear stress $\bar{\tau}_w$ was calculated using the Ludwig-Tillman semi-empirical formula

$$C_f = 0.246\,\mathrm{Re}_{\theta_m}{}^{-0.268} e^{-1.56H} \tag{18}$$

where

$$H = \frac{\delta_m{}^\star}{\theta_m} \tag{19}$$

$$\tau_m = \frac{1}{2} u_e{}^2 C_f \tag{20}$$

$$\tau_t = \tau_m tg\epsilon_w \tag{21}$$

In order to estimate the defect forces, a defect force component [1, 2]

$$\frac{F_t}{\rho} = -\frac{k}{s} u_e{}^2 \theta_2 \tag{22}$$

was introduced in absence of tip clearance, where

$$\theta_2 = \bar{\theta} \cdot \bar{1}_t \cos\alpha \tag{23}$$

while a second contribution was given by

$$\frac{F_x}{\rho} = C_D \frac{u_e{}^2}{2} \frac{h}{g} \tag{24}$$

The last equation (24) is demonstrated by Cyrus [10] and contains the losses due to secondary stresses, mixing losses, corner vortices, leakage flows, etc. The loss coefficient C_D was written as [2]

$$C_D = C_{DS} + C_{DT} \tag{25}$$

where C_{DS} denotes the secondary loss coefficient and C_{DT} the tip clearance loss coefficient. The used empirical expressions for C_{DS} and C_{DT} were [2]

$$C_{DS} = \frac{L}{2} C_L{}^2 \frac{s}{h} \sigma \tag{26}$$

$$C_{DT} = K C_L{}^2 \frac{t_c}{h} \sigma \tag{27}$$

where

$$L = 0.02$$

and

$$K = 0.3$$

Equation (26) is obtained after Vavra [13] and $L/2$ indicates that the overall secondary losses are distributed over hub and tip end-wall boundary layer. Equation (27) is obtained after Laksminarayana [3].

A detailed discussion about the force defect assumptions will be given in Section 4.

Since different extra unknowns are introduced in the complementary relations ($\delta_m{}^\star$, θ_m, ϵ_w) other information is to be supplied in order to integrate the boundary layer equations. This is obtained by the introduction of three-dimensional velocity profile models [1], which are discussed in Section 3.

2 Compressibility Effects

Axial compressor end-wall boundary layer calculation procedures are affected by compressibility effects in several ways. The basic equations as well as the complementary relations (13) and (18) depend on density variations in both axial and spanwise directions and corrections are to be introduced.

2.1 Basic Equations. Taking both compressibility effects and variations of radii into account, equations (1) and (13) can be rewritten as follows [8]

$$\frac{1}{\rho_e r}\frac{d}{dx}\rho_e r c_{xe}{}^2\bar{\theta} + c_{xe}\delta_x{}^\star \frac{d\overline{W}}{dx} = \frac{\bar{\tau}_w}{\rho} + \frac{\overline{F}}{\rho} \tag{28}$$

$$\frac{1}{\rho_e r c_{xe}}\frac{d}{dx}\rho_e r c_{xe}(\delta - \delta_x{}^\star) = \frac{F(\mathrm{H}^\star)}{\cos\alpha} \tag{29}$$

The different thicknesses are now defined by following equations and depend on spanwise variations of density

$$\theta_x = \int_0^\delta \left(1 - \frac{c_x}{c_{xe}}\right)\frac{\rho}{\rho_e}\frac{c_x}{c_{xe}}dy \tag{30}$$

$$\theta_z = \int_0^\delta \left(\frac{c_{ze} - c_z}{c_{xe}}\right)\frac{\rho}{\rho_e}\frac{c_x}{c_{xe}}dy \tag{31}$$

$$\delta_x{}^\star = \int_0^\delta \left(1 - \frac{\rho}{\rho_e}\frac{c_x}{c_{xe}}\right)dy \tag{32}$$

$$\delta_m{}^\star = \int_0^\delta \left(1 - \frac{\rho}{\rho_e}\frac{u}{u_e}\right)dy \tag{33}$$

$$\theta_m = \int_0^\delta \left(1 - \frac{u}{u_e}\right)\frac{\rho}{\rho_e}\frac{u}{u_e}dy \tag{34}$$

The use of profile model equations as described in reference [1] is possible in compressible flows if besides a velocity profile model, a profile model is introduced for the density ratio ρ/ρ_e.

2.2 Density Profile Model Equation. Before integrating the rhs of equations (30–34) by use of three-dimensional velocity profile model equations, it is necessary to assume profiles for ρ/ρ_e.

When constant static pressure is assumed through the boundary layer, the density ratio can be related to the static temperature ratio through

$$\frac{\rho_e}{\rho} = \frac{T}{T_e} \tag{35}$$

The static temperature variations in a turbulent boundary layer are the subject of several studies [16, 17]. The quadratic temperature-velocity relationship used by Spence [16] given by

$$T = T_w + (T_r - T_w)\frac{u}{u_e} - (T_r - T_e)\left(\frac{u}{u_e}\right)^2 \tag{36}$$

can be shown to hold for turbulent boundary layers [16]. T_r is the "recovery" temperature and is defined as the total temperature at the wall. If the wall is assumed adiabatic, the recovery temperature T_r will coincide with T_w and equation (36) reduces to equation (37), together with equation (35)

$$\frac{\rho_e}{\rho} = \frac{T}{T_e} = \frac{T_r}{T_e} + \left(1 - \frac{T_r}{T_e}\right)\left(\frac{u}{u_e}\right)^2 \tag{37}$$

The recovery temperature is related to the recovery factor r defined as

$$r = \frac{T_r - T_e}{T_{te} - T_e} \tag{38}$$

giving for the recovery temperature

$$\frac{T_r}{T_e} = 1 + r\left(\frac{T_{te}}{T_e} - 1\right) \tag{39}$$

or

$$\frac{T_r}{T_e} = 1 + r\frac{\gamma - 1}{2} M_e{}^2 \tag{40}$$

The density ratio equation (37) can now be written as

$$\frac{\rho}{\rho_e} = \frac{1}{1 + r\dfrac{\gamma - 1}{2} M_e{}^2\left[1 - \left(\dfrac{u}{u_e}\right)^2\right]} \tag{41}$$

A value of $r = 0.89$ is generally accepted for turbulent boundary layers. In this way it is possible to relate ρ/ρ_e with a model equation for u/u_e and the profile model for ρ/ρ_e is given by equation (41).

It is to be noted that contributions $\overline{F}_1$ and $\overline{F}_3$ to the defect force $\overline{F}$ equations (5) and (7) arise from variations of static pressure in the boundary layer and therefore one can expect deviations in a turbomachine from the usual boundary layer assumptions. However it is

Downloaded 01 Jun 2010 to 171.66.16.59. Redistribution subject to ASME license or copyright; see http://www.asme.org/terms/Terms_Use.cfm

assumed that these variations do not greatly influence the compressibility effects and equation (35) is accepted.

2.3 Entrainment Rate and Skin Friction Coefficient. Sumner and Shanebrook [14] and Davis [12] presented an analysis of compressibility effects on equations (14) and (18) and showed their validity when applying it to high supersonic flows. Following Green [18] the "kinematic" Head's shape factor $H_k{}^\star$ was introduced in equation (14)

$$H_k{}^\star = \frac{\delta - \delta_{mk}{}^\star}{\theta_{mk}} = \frac{\int_0^\delta \frac{u}{u_e} dy}{\int_0^\delta \left(1 - \frac{u}{u_e}\right)\frac{u}{u_e} dy} \neq H^\star \tag{42}$$

With the reference temperature of Eckert $T^\star$ [19], a modified skin friction law is introduced through

$$C_f = 0.246\, R_{e_\theta}{}^{-0.268} \left(\frac{T_e}{T^\star}\right) e^{-1.56 H_k} \tag{43}$$

where H_k denotes the kinematic shape factor defined as

$$H_k = \frac{\delta_{mk}{}^\star}{\theta_{mk}} = \frac{\int_0^\delta \left(1 - \frac{u}{u_e}\right) dy}{\int_0^\delta \left(1 - \frac{u}{u_e}\right)\frac{u}{u_e} dy} \neq H \tag{44}$$

The reference temperature $T^\star$ for adiabatic walls is given by

$$\frac{T^\star}{T_e} = 1 + 0.72r \frac{\gamma - 1}{2} M_e{}^2 \tag{45}$$

Thus, two new parameters H_k and $H^\star{}_k$ are introduced and are to be estimated. This can be done from H and H through semi-empirical correlations which will be mentioned in the next section. However, the use of profile models for both velocity and density ratio's inside the end-wall boundary layer allows for the calculation of any integral boundary layer parameter such as H, H_k, $H^\star$, etc.; and equations (15) and (18) are easily replaced by equations (42) and (43), without use of extra correlations.

3 Velocity and Density Profile Models

Usually, in three-dimensional boundary layers, a two-dimensional velocity profile model (e.g., a power law model) is introduced in the mainstream direction and a cross flow model (e.g., Mager profile) in the transverse direction. This leads to the possibility of back flows in the axial direction of the turbomachine. As shown in [1], singular points appear when axial backflow occurs near the end-wall or when

$$|a + \epsilon_w| > \frac{\pi}{2} \tag{46}$$

which corresponds to det $(J) = 0$, where J denotes the jacobian matrix of the transformation between the integral boundary layer thicknesses and the boundary layer profile model parameters such as power, skewing, etc.

The boundary layer may be considered as separated when this situation is reached and equation (46) can even be used as a separation criterium. However, even in a more or less large domain around these singularities, serious numerical problems will appear, leading to an approach of the stall limit which will be laborious. For this reason, a profile model was introduced [2] which excludes any axial backflow. This is obtained by taking the axial direction x as the privileged two-dimensional one, and introducing a model equation for the axial component c_x/c_{xe}. For two-dimensional or collateral boundary layers, such a model is equivalent to the classical ones, and important differences will only occur at high flow- and skewing angles, which precisely corresponds to stall approach.

3.1 Velocity Profile Model Equation [1, 2]. Following profile model equation is used for the axial velocity ratio

$$\frac{c_x}{c_{xe}} = 1 - b(1 - y')^n \tag{47}$$

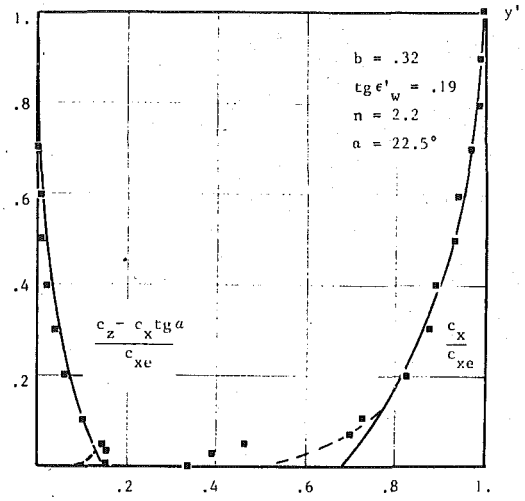

Fig. 2 Axial and tangential velocity profiles fitted with equations (47) and (50) ([20] point *K* inlet skewing)

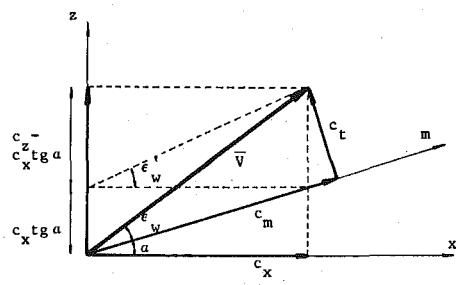

Fig. 3 Different velocity components inside the three-dimensional end-wall boundary layer

where

$$b = e^{-7n\sqrt{C_f}} \tag{48}$$

and

$$y' = y/\delta$$

b is the velocity defect at the edge of the small inner layer which is not considered when integrating over the boundary layer [1] (see Fig. 2). The second component is defined in the tangential direction z by defining a model equation for

$$\frac{1}{\cos^2 \alpha} \frac{w}{u_e} = \frac{c_z}{c_{xe}} - \frac{c_x}{c_{xe}} tg\ \alpha \tag{49}$$

which represents the difference between the three-dimensional component c_z and the corresponding two-dimensional component $c_x tg\ \alpha$. Following model equation is used

$$\frac{c_z - c_x tg\ \alpha}{c_{xe}} = (1 - b) tg\ \epsilon_w'(1 - y')^n \tag{50}$$

The power n is taken equal to the power of the axial profile equation (47). The use of equation (50) is illustrated on Fig. 2. A new parameter ϵ_w' is introduced defined as (see Fig. 3)

$$tg\ \epsilon_w' = \lim_{y \to 0} \frac{c_z - c_x tg\ \alpha}{c_x} \tag{51}$$

which can be related with ϵ_w through

$$tg\ \epsilon_w' = tg(\alpha + \epsilon_w) - tg\ \alpha \tag{52}$$

The use of equations (47) and (51) seems to imply that the secondary flow occurs in planes normal to the axial direction, which would be a questionable hypothesis. However this implication is not obvious; in fact the integration of equations (1) and (13) yields as output values of the integral boundary layer thicknesses $\bar{\theta}$ and $\delta_x{}^\star$, which contain

Downloaded 01 Jun 2010 to 171.66.16.59. Redistribution subject to ASME license or copyright; see http://www.asme.org/terms/Terms_Use.cfm

all three-dimensional effects. These three output values allow the introduction of model equations with maximum three independent parameters (n, b, $tg\ \epsilon_w'$) which always satisfy the values of $\bar{\theta}$ and $\delta_x{}^\star$. Thus, if the axial components θ_x and $\delta_x{}^\star$ are affected by secondary flow effects, this will be reflected in the shape of the axial velocity profile model, which in this way contains a secondary flow component. In fact this reasoning raises the well known problem of dividing a flow into "secondary" and "primary" flow, which is by no means obvious [6, 7]. When the present type of method is used no hypothesis is to be made about this division, since all information about the three-dimensional flow is included in the values of $\bar{\theta}$ and $\delta_x{}^\star$. Furthermore the three parameter profile models try to give the best representative averaged velocity profile corresponding with the values of $\bar{\theta}$ and $\delta_x{}^\star$, while in reality velocity profiles may be much more ill-shaped.

3.2 Entrainment and Friction Laws. In relations (42) for $H^\star{}_k$ and (43) for C_f mainstream thicknesses appear such as θ_{mk} and $\delta_{mk}{}^\star$ appear. These thicknesses are defined through equations (16) and (17). Using the profile models described in the previous section, these thicknesses can no more be considered as independent of the three-dimensional character of the boundary layer, since they are function of ϵ_w' through equations (16) and (17). Therefore it was decided to replace the suffix m by x in equations (42) and (43). This was substantiated [2] by experimental data [12] and by the fact that for two-dimensional or quasi-two-dimensional boundary layers, axial and mainstream thicknesses have nearly the same value.

$$\theta_x \cong \theta_m \tag{53}$$

$$\delta_x{}^\star \cong \delta_m{}^\star \tag{54}$$

when

$$\epsilon_w \ll \alpha \text{ or } \alpha \simeq 0$$

In this way, the entrainment and skin friction relations finally become

$$F(H^\star) = 0.0306\ (H^\star{}_k - 3)^{0.653} \tag{55}$$

$$C_f = 0.246\ R_{e\theta_x}{}^{-0.268} \left(\frac{T_e}{T^\star}\right) e^{-1.56 H_k} \tag{56}$$

where

$$H^\star{}_k = \frac{\int_0^\delta \frac{c_x}{c_{xe}}\, dy}{\int_0^\delta \left(1 - \frac{c_x}{c_{xe}}\right)\frac{c_x}{c_{xe}}\, dy} \tag{57}$$

and

$$H_k = \frac{\int_0^\delta \left(1 - \frac{c_x}{c_{xe}}\right) dy}{\int_0^\delta \left(1 - \frac{c_x}{c_{xe}}\right)\frac{c_x}{c_{xe}}\, dy} \tag{58}$$

3.3 Integral Boundary Layer Parameters. Using equation (28) projected in cartesian coordinates, equations (29, 55) and (56), the unknown boundary layer thicknesses are θ_{xk}, $\delta_{xk}{}^\star$, θ_x, θ_z and $\delta_x{}^\star$, which are defined through equations (2, 3, 30, 31) and (32), respectively. Using equation (47) following expressions are found for the first two thicknesses

$$\theta_{xk} = \delta b \left(\frac{1}{n+1} - \frac{b}{2n+1}\right) \tag{59}$$

$$\delta_{xk}{}^\star = \delta b \frac{1}{n+1} \tag{60}$$

while H_k and $H^\star{}_k$ are given by

$$H_k = \frac{1}{1 - b\,\frac{2n+1}{n+1}} \tag{61}$$

$$H_k{}^\star = H_k \left(\frac{n+1}{b} - 1\right) \tag{62}$$

Applying equation (41) to the definitions of θ_x and $\delta_x{}^\star$, following equations are obtained

$$\theta_x = \int_0^\delta \left(1 - \frac{c_x}{c_{xe}}\right)\frac{c_x}{c_{xe}} \frac{1}{1 + a\left[1 - \left(\frac{u}{u_e}\right)^2\right]} dy \tag{63}$$

$$\delta_x{}^\star = \int_0^\delta \left[1 - \frac{c_x}{c_{xe}} \frac{1}{1 + a\left[1 - \left(\frac{u}{u_e}\right)^2\right]} dy \right. \tag{64}$$

where

$$a = r\,\frac{\gamma - 1}{2} M_e{}^2 \tag{65}$$

In order to simplify these integrals, some approximations will be done. A series expansion is made of equation (41) around $u/u_e = 1$.

$$\frac{\rho}{\rho_e} = 1 - 2a\left(1 - \frac{u}{u_e}\right) + (a + 4a^2)\left(1 - \frac{u}{u_e}\right)^2 + 0\left[a^2\left(1 - \frac{u}{u_e}\right)^3\right] \tag{66}$$

Since in the mayor part of the boundary layer $(1 - u/u_e)$ is much less than 1 (minimum is $b < 1$) a reasonable accuracy can be expected from equation (66) when taking only the first three terms of the rhs, certainly when $a < 1$, or, with $\gamma = 1.4$ and $r = 0.89$, when $M_e < 4$.

Furthermore u/u_e will be approximated by c_x/c_{xe}, according to Sections 3.1 and 3.2. In this way, equation (66) reduces to

$$\frac{\rho}{\rho_e} \cong 1 - 2a\left(1 - \frac{c_x}{c_{xe}}\right) + (a + 4a^2)\left(1 - \frac{c_x}{c_{xe}}\right)^2 \tag{67}$$

and θ_x and $\delta_x{}^\star$ are found to be given by

$$\theta_x = \delta b (f_1 - a_1 f_2 + a_2 f_3 - a_3 f_4) \tag{68}$$

$$\delta_x{}^\star = \delta b (a_1 f_1 - a_2 f_2 + a_3 f_3) \tag{69}$$

where

$$f_i = \frac{b^{i-1}}{in + 1} \tag{70}$$

and

$$a_1 = 1 + 2a \tag{71}$$

$$a_2 = 3a + 4a^2 \tag{72}$$

$$a_3 = a + 4a^2 \tag{73}$$

Higher order terms can also be introduced, but f_i rapidly decreases through b^{i-1}. The last unknown thickness θ_z is given by, using equation (50)

$$\theta_z = \theta_x \left(tg\ \alpha - tg\ \epsilon_w' \frac{1 - b}{b}\right) \tag{74}$$

In Appendix I, a list is given of the different components of the jacobian matrix J of the transformation between θ_x, θ_z, $\delta - \delta_x{}^\star$ and n, b, $tg\ \epsilon_w'$.

In order to check the validity of equation (67) the different shape factors found using equations (61, 62, 68) and (69) are compared with some empirical correlations. In Fig. 4, a comparison is made between $H^\star{}_k$ found by equation (68) and the corresponding values of $H^\star{}_k$ found through Green's correlation [18] obtained by assuming equation (37) and a power law velocity profile

$$\frac{H^\star}{H^\star{}_k} = 1 + \frac{a\left(\frac{H^\star - 1}{H^\star + 1}\right)}{a + \frac{H^\star + 1}{2}} \tag{75}$$

Downloaded 01 Jun 2010 to 171.66.16.59. Redistribution subject to ASME license or copyright; see http://www.asme.org/terms/Terms_Use.cfm

$H^\star$ being obtained by its definition equation (15). The solid lines on Fig. 4 are obtained by taking various values for b and n. In Fig. 5, a comparison is made between H_k obtained through its definition equation (67) and corresponding values of $\overline{H}$ defined as

$$\overline{H} = \frac{\int_0^\delta \frac{\rho}{\rho_e}\left(1 - \frac{u}{u_e}\right) dy}{\theta_k} \tag{76}$$

According to experiments of Winter et al [21], $\overline{H}$ is found to satisfy equation (77), which is checked in Fig. 5.

$$\overline{H} \cong H_k \tag{77}$$

In Fig. 6 finally a comparison is made between H obtained through its definition and corresponding values of H obtained by

$$H = \frac{T_r}{T_e}(H_k + 1) \tag{78}$$

Equation (78) was obtained by Spence [16] by using equation (37) and assuming the following profiles

$$\frac{u}{u_e} = f\left(\frac{\eta}{\Delta}\right) \tag{79}$$

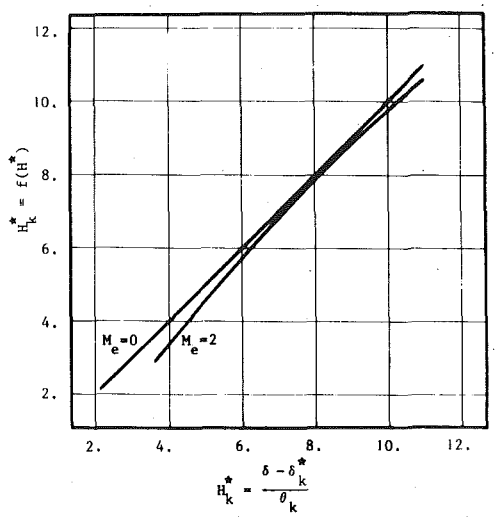

Fig. 4 Comparison of $H_k \star$ obtained with equation (68) and equation (75) using profile model equations (47) and (67)

where

$$\eta = \int_0^y \frac{\rho}{\rho_e} dy \tag{80}$$

$$\Delta = \int_0^\delta \frac{\rho}{\rho_e} dy \tag{81}$$

As can be seen from Figs. 4, 5 and 6, the use of the model equations is verified by the correlations (75, 77) and (78) up to $M_e = 2$ and they are in agreement with standard turbulent compressible boundary layer data.

3.4 Simulation of Jumps [2]. A profile model should be able to simulate jumps from rotating to non-rotating parts of the end-walls of a machine, as is the case when rotor tip and/or stator hubs are shrouded. If not, a method including profile model equations wouldn't be applicable to a large part of actual axial compressors.

When the mass flow through the shrouding seal is neglected, the jump conditions are easily deduced from equations (1) and (13)

$$\theta_x{}^r = \theta_x{}^{nr} \tag{82}$$

$$\theta_z{}^r = \theta_z{}^{nr} \tag{83}$$

$$\delta_x{}^{\star r} = \delta_x{}^{\star nr} \tag{84}$$

where the supscripts r and nr denote rotating and nonrotating parts of the walls at a jump, respectively. Assuming no discontinuity in the spanwise density ratio across the jump and according to [2], following relations can be found between the profile parameters before and behind the jump

$$n^r = n^{nr} \tag{85}$$

$$b^r = b^{nr} \tag{86}$$

$$tg\ \epsilon_w{}'^r = tg\ \epsilon_w{}'^{nr} + \frac{b}{1-b}(tg\ \alpha^{nr} - tg\ \alpha^r) \tag{87}$$

4 Force Defect Assumptions

The choice of adequate force defect assumptions is of primary importance in the end-wall boundary layer calculation methods. Three different aspects of the force defects can be considered in order to demonstrate this importance.

1 The defect force which appears when the momentum equations are pitch averaged contains all interaction effects between blades and end-wall boundary layer and in reality, all secondary flow effects are concentrated in these non-zero terms.

2 The possibility of a quasi-equilibrium of the end-wall blockage found in multistage compressors [22] can only be explained by the existance of negative axial defect force components. Furthermore,

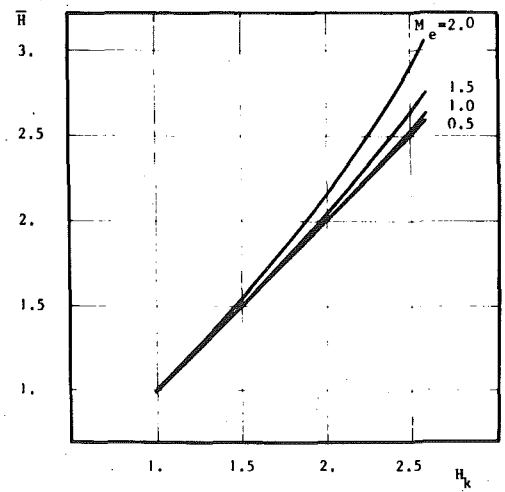

Fig. 5 Comparison between $\overline{H}$ equation (76) and H_k equation (61) using profile model equations (47) and (67)

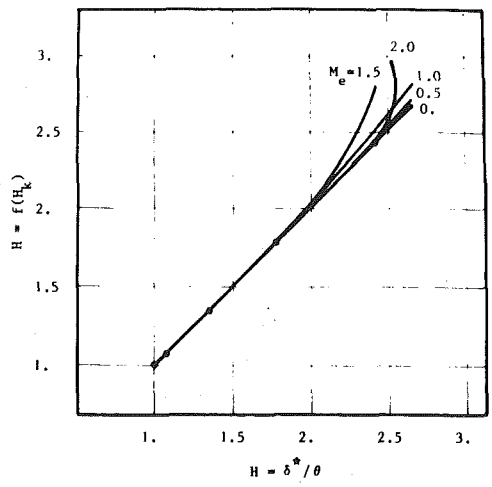

Fig. 6 Comparison of H obtained with equations (68) and (69), and obtained with equation (78), using profile model equations (47) and (67)

Downloaded 01 Jun 2010 to 171.66.16.59. Redistribution subject to ASME license or copyright; see http://www.asme.org/terms/Terms_Use.cfm

the equilibrium blockage level is directly determined by the different force defect levels, as will be discussed in Section 5.

3 Overall efficiency drop due to the presence of the end-wall boundary layer is directly related to blockage and tangential defect forces. Since blockage is directly affected by the defect force it can be said that these are the dominant parameter in the boundary layer calculation and the corresponding overall efficiency drops in axial turbomachinery.

4.1 Theoretical Aspects. In equation (4) different contributions to the defect forces appear: effects of blade loading variation, secondary stresses due to non-axisymmetry of the flow, variations of pressure gradient and blade shear stress in the end-wall boundary layer. It would be tempting to try to estimate each component separately. However this is a difficult task, while on the other hand it has proved to be efficient to introduce correlations for the total force defect.

As a first important step in this latter approach, Mellor and Wood [8] tried to estimate the direction of the total force defect. Assuming a constant stagnation pressure along a streamline and neglecting the shear stress term left in the basic equations, they found that the local blade force $\bar{f}$ is perpendicular to the pitch averaged streamlines inside the boundary layer, which is a well known perfect fluid property. Thus, if a collateral boundary layer is assumed, the effective defect force would be perpendicular to the averaged external streamline.

Cyrus [10] presented a more rigorous demonstration including the shear stress terms and total pressure losses in his equations. Neglecting c_y, the total pressure loss was found to be given by

$$\frac{d}{dx} p_t = f_x + f_z tg\ \alpha + \frac{\partial}{\partial y} (\tau_x + \tau_z tg\ \alpha) \tag{88}$$

Integrating equation (88) over the boundary layer, which is again assumed to be nearly collateral ($tg\ \alpha \cong cte$) yields after arranging [2, 10]

$$\int_0^\delta \frac{d}{dm} (p_{te} - p_t)\, dy = F_m + \tau_m \tag{89}$$

Relating the lhs of equation (89) with profile losses, secondary losses and skin friction losses, it can be rewritten as [2, 10]

$$\int_0^\delta \frac{d}{dm} (p_{te} - p_t)\, dy = -\frac{2}{g} \int_0^\delta (\tau_{be} - \tau_b)\, dy + C_{DS} \rho \frac{u_e^2}{2} \frac{h}{g} + \tau_m \tag{90}$$

and equation (89) reduces to

$$F_m = -\frac{2}{g} \int_0^\delta (\tau_{be} - \tau_b)\, dy + C_{DS} \rho \frac{u_e^2}{2} \frac{h}{g} \tag{91}$$

The first term of the rhs of equation (91) is found to be the contribution $\overline{F}_4$ in equation (4) and represents changes in profile losses through the end-wall boundary layer, while the second term is related to a span averaged secondary loss coefficient C_{DS} which includes losses due to secondary stresses, mixing losses, corner vortices, leakage flows, etc. Considering an overall secondary loss coefficient, equation (91) is rewritten as

$$F_m = \rho C_D \frac{u_e^2}{2} \frac{h}{g} \tag{92}$$

Thus, the mainstream defect force can be determined by an empirical loss coefficient such as equations (25, 26) and (27).

The determination of $\overline{F}$ is reduced to an estimation of F_t, which represents the defect in effective blade lift in the boundary layer. Two conflicting effects determine the value of F_t. Indeed, while a constant transverse pressure gradient is imposed by the external flow, creating the well known passage vortex, the presence of the blades will tend to impress the same path on each streamline in the boundary layer, limiting in this way the free development of the passage vortex. The last effect is certainly important when the end-wall boundary layer is highly skewed at inlet of a blade row, where a tangential force defect is necessary in order to reconstruct a quasi-collateral flow. These contributions can easily be seen in the transverse momentum equation obtained by projecting equation (1) in the transverse direction t:

$$\frac{d}{dx} u_e^2 \theta_2 = \frac{F_t}{\rho \cos \alpha} - c_{xe}^2 (\theta_x + \delta_x^\star) \frac{dtg\ \alpha}{dx} + \frac{\tau_t}{\rho \cos \alpha} \tag{93}$$

The second term in the rhs represents the pressure gradient impressed by the external flow creating a cross flow represented by θ_2, while the shear stress τ_t tends to restrain this cross flow. F_t will counterbalance the pressure gradient term and it is reasonable to assume that $u_e^2 \theta_2$ tends to a limiting value when the two mentioned effects exactly counterbalance and $d/dx u_e^2 \theta_2 = 0$. In this way, F_t tends to a limiting value given by, neglecting τ_t,

$$\frac{F_t^{\text{coll}}}{\rho \cos \alpha} \cong c_{xe}^2 (\theta_x + \delta_x^\star) \frac{dtg\ \alpha}{dx} \tag{94}$$

where coll stands for collateral. Equation (94) is a well known equation [9, 11]: if $F_t = F_t^{\text{coll}}$ and no cross flow is present at inlet ($\theta_2^{\text{in}} = 0$), then no cross flow will be predicted at outlet and the flow is always collateral.

Horlock and Perkins [11] added a defect force component to F_t^{coll} necessary to restore a collateral flow uniquely due to relative motion. This component was given by

$$\frac{F_t}{\rho \cos \alpha} = -\frac{(U c_{xe} \theta_x)_{\text{inlet}}}{\Delta x} \tag{95}$$

Δx being the length over which the collateral flow is to be restored. Indeed, if i and j denote absolute and relative system, it follows from the definition of $\bar{\theta}$ that

$$(u_e^2 \theta_2)^i = (u_e^2 \theta_2)^j - U c_{xe} \theta_x \tag{96}$$

and equation (95) corresponds to $(u_e^2 \theta_2)^j = 0$.

Principally, the same idea was adopted by Mellor and Wood by imposing

$$(\theta_2)_{\text{out}} = 0 \tag{97}$$

in absence of tip clearance. When equation (97) is used, equation (93) will automatically imply a defect force F_t which restores a collateral flow at outlet, for any inlet cross flow. As discussed in [1] the assumption $(\theta_2)_{\text{out}} = 0$ in absence of clearance is questionable. A next step was proposed by Hirsch [4] who improved Mellor and Wood's principle by introducing following correlation at outlet of a blade row, in absence of tip clearance

$$(\theta_2)_{\text{out}} = -Kc C_L^{1/2}\ \text{sign}\ \Delta c_z \tag{98}$$

However, equation (98) is a rough approximation of $(\theta_2)_{\text{out}}$, while this value should mainly be determined by equation (93). Inserting equation (22) in equation (93), one obtains a limiting value for θ_2

$$0 = -\frac{k}{g} (u_e^2 \theta_2)_{\text{lim}} = c_{xe}^2 (\theta_x + \delta_x^\star) \frac{dtg\ \alpha}{dx} + \frac{\tau_t}{\rho \cos \alpha} \tag{99}$$

or, when neglecting τ_t

$$(\theta_2)_{\text{lim}} \cong -\cos \alpha\ (\theta_x + \delta_x^\star) C_L\ \text{sign}\ \Delta c_z / 2k \tag{100}$$

Equation (100) has some resemblance to equation (98).

Equations (22, 95, 97) or (98) all tend to give similar variations for the axial defect forces and in particular can lead to quasi-equilibrium configurations in multistage compressors.

The last problem left is the determination of F_t in presence of a blade tip clearance. The above mentioned considerations for the case of no tip clearance are still valid, except that the outlet value of θ_2 written in the blade reference system will be affected by the leakage flow which is determined by both non-slip condition at the wall and pressure gradient across the clearance area. Mellor and Wood applied this principle by setting [8]

$$(\theta_2)_{\text{out}} = K t_c C_L^{1/2} \Delta c_z \tag{101}$$

which was improved by Hirsch through equation (98) to [5]

$$(\theta_2)_{\text{out}} = (K_1 t_c - K_2 c) C_L^{1/2}\ \text{sign}\ \Delta c_z \tag{102}$$

Downloaded 01 Jun 2010 to 171.66.16.59. Redistribution subject to ASME license or copyright; see http://www.asme.org/terms/Terms_Use.cfm

However, other effects are to be considered. Since there is no blade surface between wall and blade tip, f_t will vanish over the clearance, which corresponds to $[\Delta p]_b{}^a = 0$ in equation (5). In this way F_t can be rewritten as

$$F_t = \int_0^t c f_{te} dy + \int_{t_c}^{\delta} (f_{te} - f_t) dy \tag{103}$$

The first term is related to the external pressure gradient f_{te} which is determined by

$$f_{te} = \frac{f_{ze}}{\cos \alpha} = \frac{1}{\cos \alpha} c_{xe} \frac{dc_{ze}}{dx} \tag{104}$$

The interaction effects of the blades represented by the second term will decrease when t_c grows, since f_t is active only from $y = t_c$ to $y = \delta$, and disappear when $y = \delta$. This second term can be estimated from $(F_t)_{t_c=0}$ as follows. A power law similar to equation (47) is assumed for f/f_e

$$\frac{f_t}{f_{te}} \cong 1 - f_{tw}(1 - y')^{m-1} \tag{105}$$

where f_{tw} is found to be, after integration over the boundary layer of equation (105) and in absence of tip clearance

$$f_{tw} = \frac{1}{m} (F_t)_{t_c=0} \tag{106}$$

Application of equations (105) and (106) to the second term in the rhs of equation (103) yields

$$\int_{t_c}^{\delta} (f_{te} - f_t) dy \cong (F_t)_{t_c=0} \left(1 - \frac{t_c}{\delta}\right)^m \tag{107}$$

Application of equations (104) and (107) with equation (22) for $(F_t)_{t_c=0}$ gives as result for F_t

$$\frac{F_t}{\rho \cos \alpha} = \frac{t_c}{\cos^2 \alpha} c_{xe} \frac{dc_{ze}}{dx} - \frac{k}{g} u_e{}^2 \theta_2 \left(1 - \frac{t_c}{\delta}\right)^m \tag{108}$$

In the absence of transverse shear stresses (which is a rough approximation in presence of a tip clearance) a limiting value for θ_2 is found in the same way as equation (100)

$$(\theta_2)_{\text{lim}} = \cos \alpha \left[\frac{t_c}{\cos^2 \alpha} - (\theta_x + \delta_x{}^\star)\right] C_L \Delta c_z / 2k \left(1 - \frac{t_c}{\delta}\right)^m \tag{109}$$

Equation (109) has again some resemblance with the equation of Mellor and Wood equation (102). The use of equation (108) met some success when used by the authors, but better correlations between different test cases was found when simply setting $F_t = 0$ in presence of a tip clearance. This can be substantiated by equation (108) since in presence of an inlet cross flow essentially due to relative motion both terms of the rhs of equation (108) have a different sign and F_t may be of a lower order of magnitude.

4.2 Practical Aspects. Although a mainstream defect force is predicted through equation (92), only the axial component of it is used, equation (24), as was found empirically in [1]. The use of equation (92) instead of equation (24) does not affect a large part of the results presented in Section 6.

This can be explained by the fact that the tangential components of F_z predicted by equation (94) have an opposite sign in rotor and stator blade rows and nearly vanish over a stage, while the axial components given by equation (24) cumulate. Differences appear however at low mass flows where the outer casing boundary layer doesn't grow with decreasing mass flow when equation (94) is used. This phenomenon is not explained yet and may be tied to the use of $F_t = 0$ in presence of clearance, instead of an equation such as equation (108).

In conclusion, equations (22) and (24) are still used and the only practical improvement introduced concerning the defect forces with respect to reference [1] is the introduction of a secondary flow loss coefficient through equation (26). In this way, all secondary losses are concentrated in the end-wall regions.

5 Correlation for End-Wall Blockage

It would be of interest to obtain information on the end-wall blockage without having to perform detailed calculations of the type described in this paper. Therefore, an attempt is made to estimate the evolution of the blockage starting from the main geometry and flow parameters by integrating the end-wall boundary layer equations in an approximate way through each stage of the machine.

Projection of equation (1) in the axial direction yields the well known axial momentum equation

$$\frac{d}{dx} c_{xe}{}^2 \theta_x + c_{xe} \delta_x{}^\star \frac{dc_{xe}}{dx} = \frac{F_x}{\rho} + \frac{\tau_x}{\rho} \tag{110}$$

Integration over one blade row yields

$$\Delta\theta_x = \frac{1}{\tilde{c}_{xe}{}^2} \int_{\text{in}}^{\text{out}} \frac{\tau_x}{\rho} dx + \frac{1}{\tilde{c}_{xe}{}^2} \int_{\text{in}}^{\text{out}} \frac{F_x}{\rho} dx - \tilde{\theta}_x (2 + H) \frac{\Delta c_x}{\tilde{c}_x} \tag{111}$$

A tilde ($\sim$) denoting an average over the blade length Δ_x. When $\Delta\theta_x$ is taken over a complete stage, following approximate equation can be obtained

$$(\Delta\theta_x)_{\text{stage}} = p - q\tilde{\theta}_x \tag{112}$$

where p and q are calculated in Appendix II. These parameters are function of chord, stagger, solidity, flow coefficient, loading and axial velocity ratio and are given by

$$p = \sum_{R,S} \frac{c \cos \gamma}{2 \cos^2 \alpha_i} \left[C_f \left(1 + \frac{\xi}{c}\right) \cos \alpha_\infty + \Lambda C_L{}^2 \sigma\right] \tag{113}$$

$$q = 2(2 + H) \frac{\text{AVR} - 1}{\text{AVR} + 1} + \frac{\sin 2|\alpha_\infty|}{2} k_f \frac{1 - e^{-k\sigma}}{\varphi} \tag{114}$$

p/q is in general positive and θ_x tends as expected to a quasi-equilibrium value given by

$$\theta_x{}^{\text{eq}} = \frac{p}{q} \tag{115}$$

Equation (112) can be rewritten as

$$\frac{\Delta(\theta_x - \theta_x{}^{\text{eq}})}{\theta_x - \theta_x{}^{\text{eq}}} = -q \tag{116}$$

Equation (116) is the discretization of following equation

$$\theta_x - \theta_x{}^{\text{eq}} = (\theta_x - \theta_x{}^{\text{eq}})_{\text{inlet}} e^{-\sum_{\text{stages}} q} \tag{117}$$

or

$$\theta_x = \theta_x{}^{\text{eq}}[1 - e^{-(q_0 + \Sigma q)}] \tag{118}$$

where

$$e^{-q_0} = 1 - \frac{\theta_x{}^{\text{in}}}{\theta_x{}^{\text{eq}}} \tag{119}$$

Multiplication with a main value H yields finally as result for the contribution to the blockage due to one of the end-walls

$$\delta_x{}^\star = \delta_x{}^{\star\text{eq}}[1 - e^{-(q_0 + \Sigma q)}] \tag{120}$$

$$e^{-q_0} = 1 - \frac{\delta_x{}^{\star\text{eq}}}{\delta_x{}^{\star\text{eq}}} \tag{121}$$

$$\delta_x{}^{\star\text{eq}} = Hp/q \tag{122}$$

The overall blockage is obtained by adding the contribution of equation (120) for both hub and tip walls.

Equation (120) presents a remarkable similitude with the correlation of Grieb [23]. In this reference, an exponential expression is given for the total blockage through

$$\sum_{h,t} \frac{\delta_x{}^\star}{h} = a[1 - e^{-b[(\Delta p/q)_0 + \Sigma \Delta p/q]^c}] \tag{123}$$

where a, b and c were empirical constants and $\Delta p/q$ the dynamic head over a stage. The equilibrium blockage corresponding with this correlation is found to be a constant value and was given by a =0.2 and

Downloaded 01 Jun 2010 to 171.66.16.59. Redistribution subject to ASME license or copyright; see http://www.asme.org/terms/Terms_Use.cfm

thus the blockage in a multistage compressor would always tend to 20 percent of the annulus height. However, due to the low value of b and c, this limit is never approached in the test cases considered by Grieb.

Figure 7 is an illustration of equation (120) while a similar illustration of equation (123) can be found in [23]. In the same figure, equation (120) is compared with a fully calculated evolution of the axial displacement thickness of a six repeating stage compressor, in order to illustrate the correct exponential character of the blockage. Such a type of comparison was used in order to calibrate the coefficient k_f in equation (114) introduced in Appendix II. An application of equation (120) is shown in Section 6.

The correlation equation (120) contains the influence on blockage of effects such as mass flow coefficient, AVR, loading, tip clearance and geometrical blade parameters and allows the estimation of blockage without a detailed end-wall boundary layer calculation. A detailed analysis of this correlation will be published elsewhere.

6 Results

In [1] and [2] detailed results are presented of the end-wall boundary layer calculation method applied to some low speed multistage machines. Through several test configurations of the General Electric four stage compressor [24] it was shown that the method correctly predicts the effects of different aspect ratio's, tip clearances and axial blade spacings. These results are summarized in Figs. 8 and 9, where calculated overall properties of the compressor configurations are compared with experimental data.

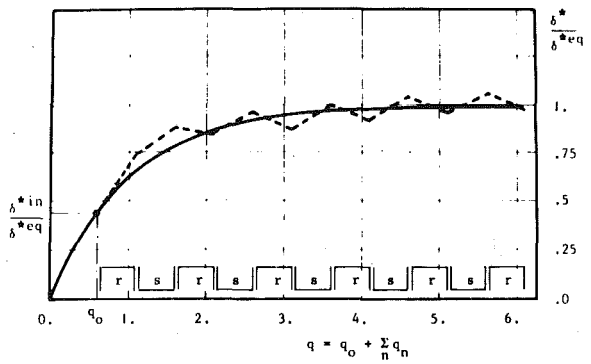

Fig. 7 Fit of end-wall blockage correlation equation (118). Solid line: equation (120), Dashed line: application of the end-wall boundary layer calculation method, N.G.T.E compressor, hub, $\varphi = .72$

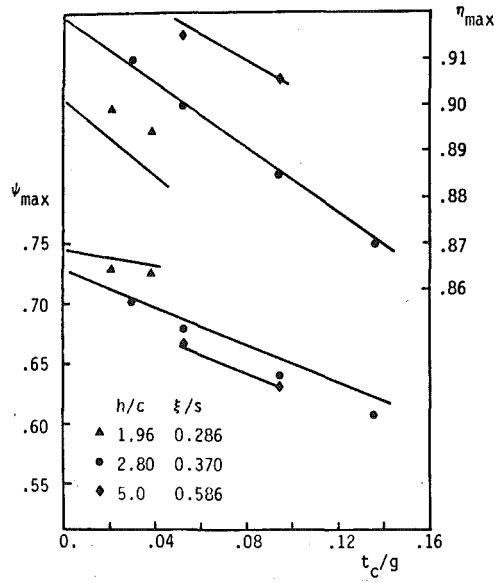

Fig. 8 General Electric four stage compressor—overall peak characteristics, solid lines: calculated

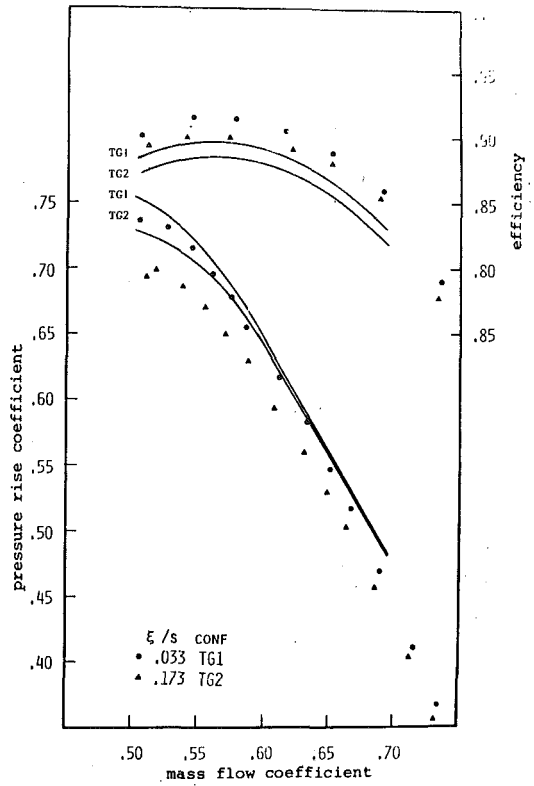

Fig. 9 General Electric four stage compressor—overall characteristics of TG1 and TG2 configurations, influence of axial blade spacing, solid lines: calculated

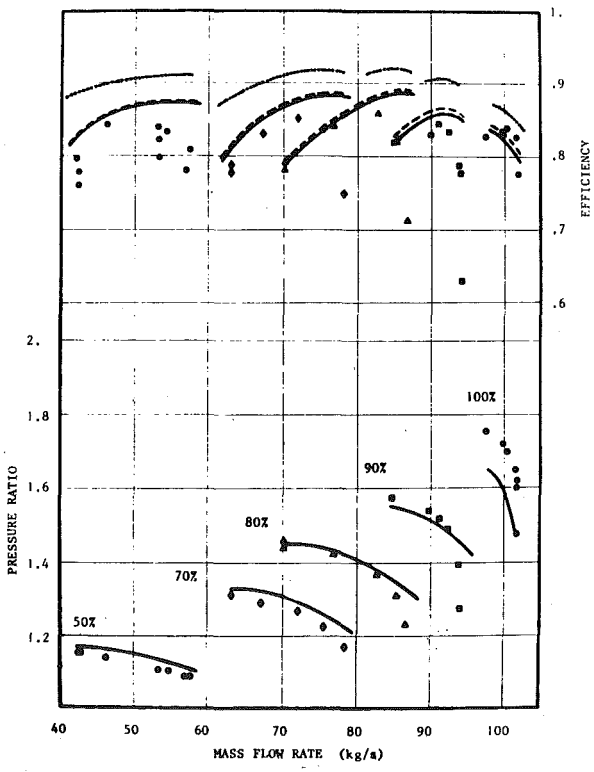

Fig. 10 Task II General Electric compressor—overall characteristics, solid lines: actual calculation method, dashed lines: calculation method without spanwise compressibility effects, dotted line: efficiency without taking end-wall losses into account

Downloaded 01 Jun 2010 to 171.66.16.59. Redistribution subject to ASME license or copyright; see http://www.asme.org/terms/Terms_Use.cfm

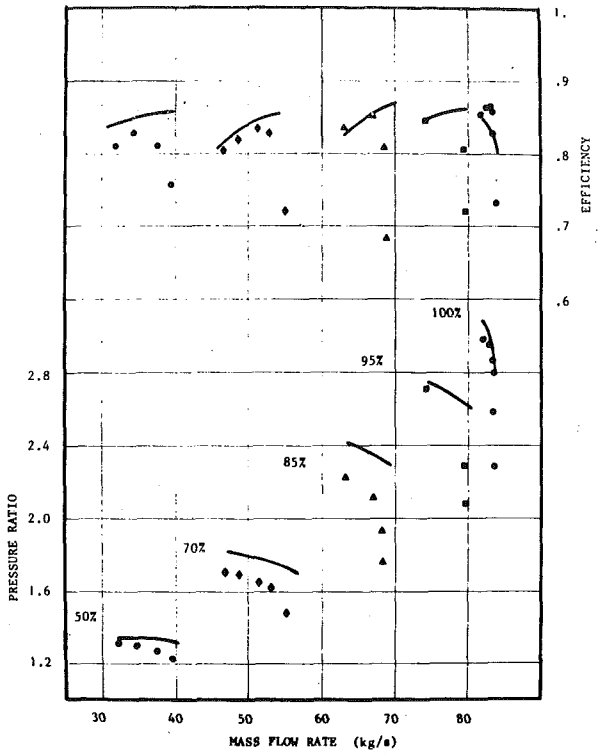

Fig. 11 Nasa two stage compressor—overall characteristics, solid lines: calculated

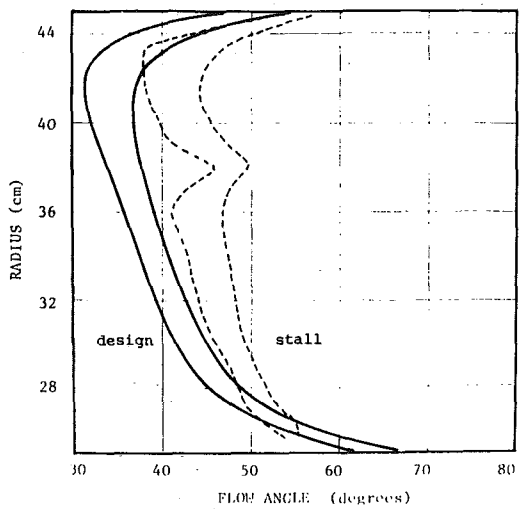

Fig. 12 Task II compressor. Absolute flow angle at rotor exit—solid lines: calculated, dashed lines: experiment

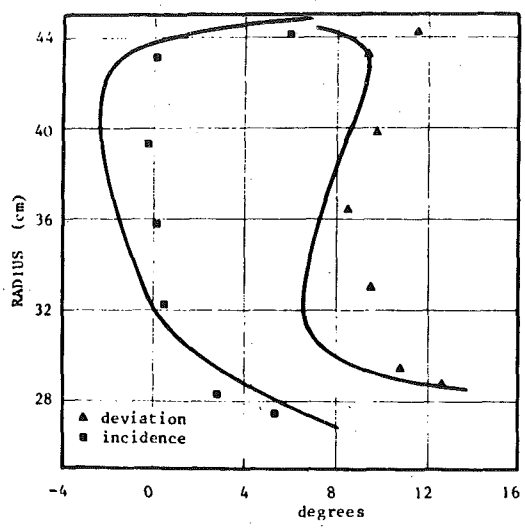

Fig. 13 Task II compressor. 0°/0° IGV/Stator schedule—stator incidence and deviation angles near design, solid lines: calculated

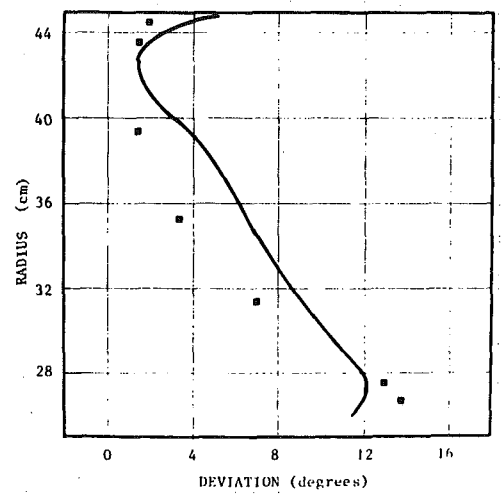

Fig. 14 Task II compressor. 0°/0° IGV/Stator schedule—rotor deviation angle, solid line: calculated

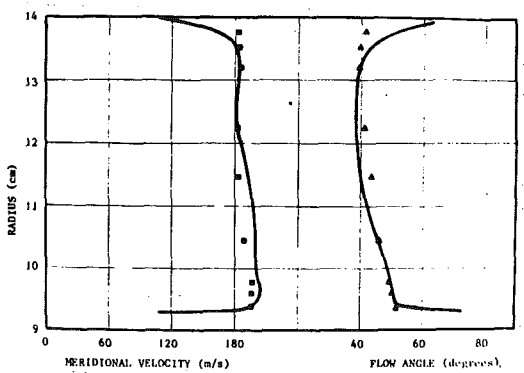

Fig. 15 Nasa TMX-3076 compressor—meridional velocity and absolute flow angle at exit of second rotor. Desing mass flow, solid lines: calculated

6.1 Compressibility Effects. The method with inclusion of compressibility effects is applied to two high speed test cases. The first one denoted as Task II is a General Electric 457 m/s tip speed transonic simple stage fan with variable geometry of IGV and stator [25]. The second is a NASA highly loaded two stage 442 m/s axial flow fan [26]. In Figs. 10 and 11 overall characteristics are shown of both test cases, and in Fig. 10 the results (solid lines) are compared with curves (dashed lines) obtained by excluding the spanwise compressibility effects, by setting $M_e = 0$ in equations (45) and (65). As can be seen in Fig. (10), a better approach of the experimental overall efficiencies is found, through a higher blockage level. In the same figure, it can be seen how this effect increases with increasing Mach number from 50 to 100 percent desing speed, giving a difference of 1 percent efficiency at the highest speed. In both figures, an overestimation is found at the high mass flow side of the efficiency characteristics. However this is related to an underestimation of overall off-design deviation angles at high mass flow rates. These overall deviations are determined by the loss correlations used in the radial equilibrium calculation program in which the end-wall boundary layer calculation method is included. This can be seen in Fig. 10 where the dotted lines represent efficiencies obtained without including the end-wall losses, and which does not drop at high mass flows. This effect is also found at low speeds as discussed in [1].

In Figs. 12–15 comparisons are made between some calculated spanwise flow parameter profiles and experimental data, including

Downloaded 01 Jun 2010 to 171.66.16.59. Redistribution subject to ASME license or copyright; see http://www.asme.org/terms/Terms_Use.cfm

the end-wall effects. As can be seen from these figures, the skewing effects on flow angle, deviations and incidence are quite well predicted in the end-wall regions for both test cases.

In Figs. 16 and 17 an evolution is shown of the axial displacement thickness (Fig. 16) and wall skewing angle (Fig. 17) at hub and tip of the TASK II compressor. In Fig. 17 the effects of jumps before and behind the rotor hub wall on the skewing angle can be seen, according to equation (87).

6.2 Defect Forces. In reference [24] experimental data are presented about defect forces. These experimental defect forces were defined as

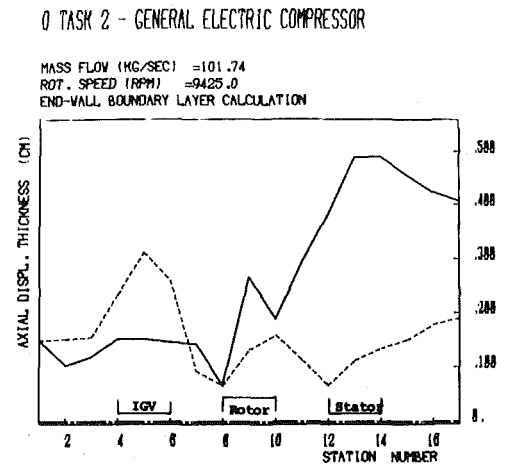

Fig. 16 Task II compressor. 0°/0° IGV/Stator schedule—calculated evolution of axial displacement thickness, solid line: tip, dashed line: hub

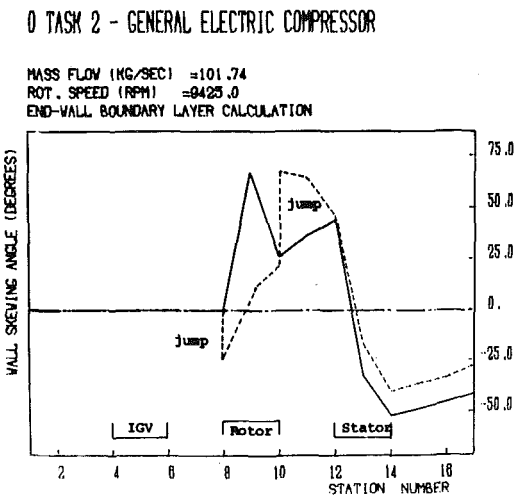

Fig. 17 Task II Compressor, 0°/0° IGV/Stator schedule—calculated evolution of wall skewing angle, solid line: tip, dashed line: hub

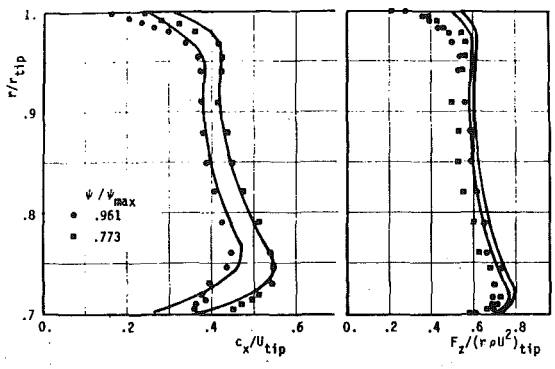

Fig. 18 Axial velocity and tangential force profiles at fourth rotor exit of the G.E. compressor, configuration 9, solid lines: calculated

$$\nu = \frac{1}{rf_{ze}} \int_r^{r+\delta} (f_{ze} - f_z) r \, dr \tag{124}$$

where

$$f_z = 2\pi r \rho c_{x2} \frac{r_2 c_{z2} - r_1 c_{z1}}{\bar{r}} \tag{125}$$

where 1 and 2 denote in and outlet of a blade row. The defect force defined through equation (124) does not necessarily include all the different force components discussed in Sections 1 and 4. However, ν can be deduced from the calculated results, since calculated axial and tangential velocity profiles are available. In Fig. 18, a spanwise evolution of axial velocity and corresponding tangential force defined by equation (125) is shown, compared with experimental data close to the stall limit of G. E. test configuration 9. Compared with the same result in [1], an improvement is found at hub, where better agreement is found with experimental data. This was mainly obtained by introduction of both secondary flow loss coefficient equation (26) and profile model equations equation (47) and equation (50), which affect the results of [1] close to the stall limit.

In Fig. 19 comparisons are made between experimental and calculated displacement thicknesses and force defects as function of different mass flow rates through ψ/ψ_{max}. The solid lines correspond with the solid symbols (third stator exit) and the dashed lines correspond with the open symbols (average of third and fourth rotor exit). From the experimental displacement thickness at both hub and tip, it follows that the end-wall boundary layer thickness decreases in absence of tip clearance, confirming the existance of important negative axial defect force components. This slope is correctly predicted by the calculation method, while the oscillations in boundary layer thickness are underestimated, indicating an underestimation of the difference in defect force between blade rows with and without tip clearance. This suggests the importance of an equation such as equation (108) in order to obtain improved detailed agreement. However, quite good detailed agreement is found with the actual method, as follows from [1] and [2]. From the lower pictures in Fig. 19, it follows that quite good levels for $\nu/\delta_x{}^\star$ are predicted, considering the important scatter on the experimental data. It is to be noted that if the flow is neither underturned nor overturned, it can be shown that

$$\frac{\nu}{\delta_x{}^\star} \cong 1 + \frac{1}{H} \tag{126}$$

Lower values correspond with overturned and higher values with underturned boundary layer flows. Thus it follows from Fig. 19 that both calculated and experimental data correspond with overturning, since all these values are less than 1, while $1 + 1/H$ is at least greater than 1.

6.3 Correlation for End-Wall Blockage. In Fig. 20 equation (120) is tested through some low speed repeating stage compressors. In order to apply the correlation, it was necessary to estimate inlet and outlet flow angles at each blade row. The outlet flow angles were approached by the outlet blade angles, and the corresponding values of inlet flow angle to each adjacent blade row was calculated. A little iterative procedure was necessary to obtain the results since C_f in equation (113) for p depends on θ_x. A constant value of 1.5 was taken for the shape factor H. In Fig. 20, it can be seen how an underestimation is found at tip of the G.E. test cases, however the detailed calculations also tend to underestimate this thickness, as can be seen from Fig. 19.

Conclusion

The present end-wall boundary layer calculation method which has its base in [1] is improved through the introduction of compressibility effects, an extra secondary flow loss coefficient in the defect force assumption and profile model equations without inherent limitations and allowing jumps on the end-walls.

The method is applicable on each type of axial compressor and quite good agreement is found for the different test cases analyzed up to now, as well for meridional and spanwise evolution of the end-

Downloaded 01 Jun 2010 to 171.66.16.59. Redistribution subject to ASME license or copyright; see http://www.asme.org/terms/Terms_Use.cfm

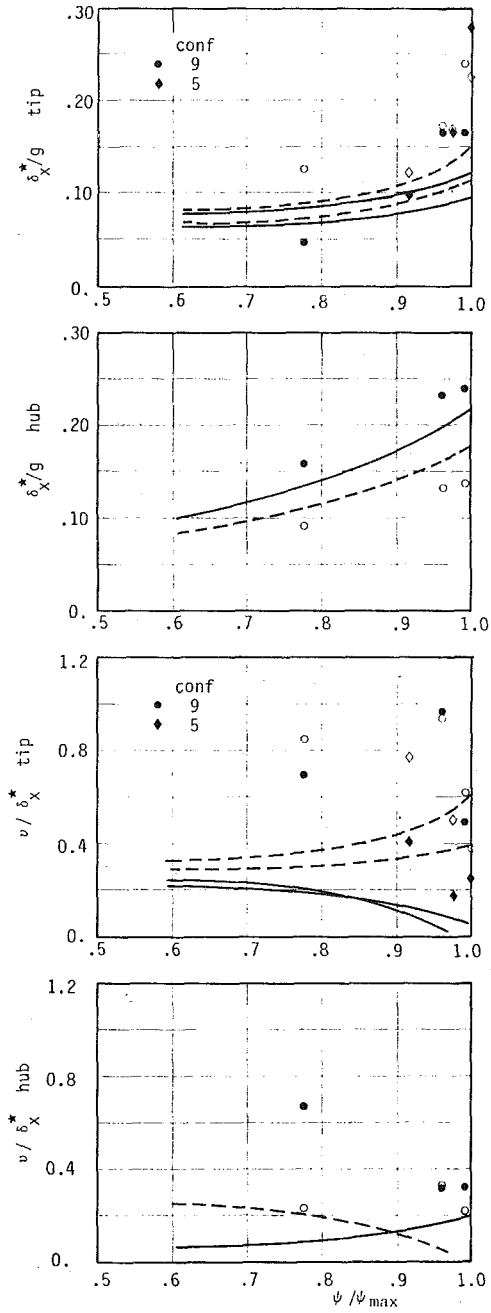

Fig. 19 General Electric compressor—axial displacement thickness and tangential force defect defined through equation (124), solid symbols and solid lines: experiment and calculated at third stator exit, open symbols and dashed lines: experiment and calculated average of third and fourth rotor exit

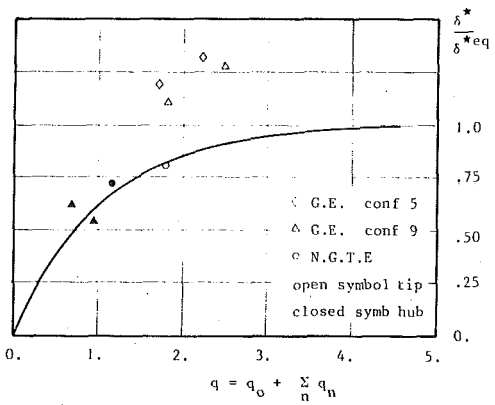

Fig. 20 End-wall blockage correlation—solid line: equation (120)

wall boundary layer parameters as for the overall properties of the compressors.

A correlation for end-wall blockage is also presented which is shown to be in good agreement with experimental data and contains the influence of various parameters. This correlation allows to assess the relative contributions from hub and tip walls to the overall blockage.

References

1 De Ruyck, J., Hirsch, C., Kool, P., "An Axial Compressor End-Wall Boundary Layer Calculation Method," ASME JOURNAL OF ENGINEERING FOR POWER, Vol. 101, No. 2, 1979, pp. 233–249.

2 De Ruyck, J., Hirsch, C., Kool, P., "Investigation on Axial Compressor End-Wall Boundary Calculations," International Joint Gas Turbine Congress and Exhibition, Israel, 1979.

3 Laksminarayana, B., "Method of Predicting the Tip Clearance Effects in Axial Flow Turbomachinery," ASME *Journal of Basic Engineering*, Vol. 92, 1970, pp. 467–482.

4 Hirsch, C., "Flow Prediction in Axial Flow Compressors Including End-Wall Boundary Layers," ASME JOURNAL OF ENGINEERING FOR POWER, Vol. 96, 1974, pp. 413–426.

5 Hirsch, C., "End-Wall Boundary Layers in Axial Compressors," ASME Paper No. 76-GT-72, 1976.

6 Horlock, J. H., Laksminarayana, B., "Secondary Flows Theory, Experiment and Application in Turbomachinery Aerodynamics," *Annual Review of Fluid Mechanics*, Vol. 5, 1975, p. 247.

7 De Ruyck, J., Hirsch, C., Kool, P., "Hot Wire Measurements in an Axial Compressor and Confrontation with Theoretical Predictions of Secondary Flows," Agard CP 214, 1978.

8 Mellor, G. M., Wood, G. L., "An Axial Compressor End-Wall Boundary Layer Theory," ASME *Journal of Basic Engineering*, Vol. 93, 1971, pp. 300–316.

9 Marsh, H., Horlock, J. H., "Wall Boundary Layers in Turbomachines," *Journal of Mechanical Engineering Sciences*, Vol. 14, 6, 1972, p. 411.

10 Cyrus, V., "Blade Defect Force in the Calculation Method of the End-Wall Boundary Layer," (Tchec) *Strojirenstvi* 28, Vol. 9, 1978, p. 515.

11 Horlock, J. H., Perkins, H. J., "Annulus Wall Boundary Layers in Turbomachines," Agard AG 185, 1974.

12 Davis, W. R., "Three-Dimensional Boundary Layer Computation on the Stationary End-Walls of Centrifugal Turbomachinery," ASME paper No. 76-FE-14, 1976.

13 Vavra, M. H., *Aero-Thermodynamics and Flows in Turbomachines*, John Wiley & Sons, N. Y., 1960.

14 Sumner, W. J., Shanebrook, J. R., "Entrainment Theory for Compressible Turbulent Boundary Layers on Adiabatic Walls," *AIAA Journal*, Vol. 9, No. 2, 1971, pp. 330–332.

15 Sumner, W. J., Shanebrook, J. R., "Entrainment Equation for Three-Dimensional Compressible, Turbulent Boundary Layers," *AIAA Journal*, Vol. 10, No. 5, 1972, pp. 693–694.

16 Spence, D. A., "The Growth of Compressible Turbulent Boundary Layers on Isothermal and Adiabatic Walls," R and M 3191, 1961, Aeronautical Research Council, London, England.

17 Shapiro, A. H., *The Dynamics and Thermodynamics of Compressible Fluid Flow*, Vol. 1, The Ronald Press Company, New York, 1953.

18 Green, J. E., "The Prediction of Turbulent Boundary Layer Development in Compressible Flow," *Journal of Fluid Mechanics*, Vol. 31, 1968, pp. 753–778.

19 Eckert, E. R. G., "Engineering Relations for Friction and Heat Transfer to Surfaces in High Velocity Flow," *Journal of Aeronautical Sciences*, Vol. 22, 1955, pp. 585–587.

20 Moore, R. W., and Richardson, D. L., "Skewed Boundary Layer Flow near the End-Walls of a Compressor Cascade," ASME paper No. 56-A-131, 1956.

21 Winter, K. G., Smith, K. G., Rotta, J. C., "Turbulent Boundary Layer studies on a Waisted Body of Revolution in Subsonic and Supersonic Flow," Agardograph 97, Pt. H 1965, pp. 933–961.

22 Bowen, J. F., Sabersky, R. H., Rannie, W. D., "Investigation of Axial Flow Compressors," Trans ASME, Vol. 73, 1951, pp. 1–15.

23 Grieb, H., Schäffler, A., "Seitenwandgrenzschichten in Axialverdichtern," *Vortrag anlässlich der Sitzung des Fachausschusses der DGLR für luftatmende Triebwerke*, Friedrichshafen, 1972.

24 Smith, L. H., "Casing Boundary Layers in Multistage Axial Flow Compressors," Brown Boveri Symposium, Flow Research on Blading, Elsevier, 1969.

25 Bilwakesh, K. R., Koch, C. C., Prince, D. C., "Evaluation of Range and Distorsion Tolerance For High Mach Number Transonic Fan Stages," NASA CR-72880, 1971.

26 Suggeri, R. S., Benser, W. A., "Performance of a Highly Loaded Two-Stage Axial Flow Fan," NASA TM X-3076, 1974.

27 Salvage, J. W., "Investigation of Secondary Flow Behaviour and End-Wall Boundary Layer Development Through Compressor Cascades," Van Karman Institute, technical note No. 107, 1974.

Downloaded 01 Jun 2010 to 171.66.16.59. Redistribution subject to ASME license or copyright; see http://www.asme.org/terms/Terms_Use.cfm

APPENDIX I

The different components of the jacobian matrix J are given by, according to equations (43, 48, 68, 69, 70) and (74)

$$\frac{\partial \theta_x}{\partial b} = -\theta_x \left[5.82\, H_k{}^2 \frac{f_2}{b f_1} + \frac{7.4626}{b \ln b} \right]$$

$$\frac{\partial \theta_x}{\partial n} = -\theta_x \left[5.82\, H_k{}^2 \frac{1}{f_1} \left(\frac{\partial f_2}{\partial n} - \frac{f_2}{f_1} \frac{\partial f_1}{\partial n} \right) - \frac{7.4626}{n} \right]$$

$$\frac{\partial \theta_x}{\partial tg\ \epsilon_w{}'} = 0$$

$$\frac{\partial \theta_x}{\partial x} = -\frac{\theta_x}{u_e} \frac{du_e}{dx}$$

$$\frac{\partial \theta_z}{\partial b} = \frac{\theta_z}{\theta_x} \frac{\partial \theta_x}{\partial b} + tg\ \epsilon_w{}' \frac{\theta_x}{b^2}$$

$$\frac{\partial \theta_z}{\partial n} = \frac{\theta_z}{\theta_x} \frac{\partial \theta_x}{\partial n}$$

$$\frac{\partial \theta_z}{\partial tg\ \epsilon_w{}'} = -\frac{1-b}{b} \theta_x$$

$$\frac{\partial \theta_z}{\partial x} = -\frac{\theta_z}{u_e} \frac{du_e}{dx} + \theta_x \frac{dtg\ \alpha}{dx}$$

$$\frac{\partial}{\partial b} (\delta - \delta_x{}^\star) = (\delta - \delta_x{}^\star) \left(\frac{1}{\theta_x} \frac{\partial \theta_x}{\partial b} + \frac{1}{\mathrm{H}^\star} \frac{\partial \mathrm{H}^\star}{\partial b} \right)$$

$$\frac{\partial}{\partial n} (\delta - \delta_x{}^\star) = (\delta - \delta_x{}^\star) \left(\frac{1}{\theta_x} \frac{\partial \theta_x}{\partial n} + \frac{1}{\mathrm{H}^\star} \frac{\partial \mathrm{H}^\star}{\partial n} \right)$$

$$\frac{\partial}{\partial tg\ \epsilon_w{}'} (\delta - \delta_x{}^\star) = 0$$

$$\frac{\partial}{\partial x} (\delta - \delta_x{}^\star) = -(\delta - \delta_x{}^\star) \frac{1}{u_e} \frac{du_e}{dx}$$

$$\frac{\partial H^\star}{\partial b} = \frac{\delta}{\theta_x} [-a_1 f_1 + 2a_2 f_2 - 3a_3 f_3 - \mathrm{H}^\star (f_1 - 2a_1 f_2 + 3a_2 f_3 - 4a_3 f_4)]$$

$$\frac{\partial \mathrm{H}^\star}{\partial n} = \frac{\delta b}{\theta_x} \left[-\mathrm{a}_1 \frac{\partial f_1}{\partial n} + a_2 \frac{\partial f_2}{\partial n} - a_3 \frac{\partial f_3}{\partial n} - \mathrm{H}^\star \left(\frac{\partial f_1}{\partial n} - a_1 \frac{\partial f_2}{\partial n} + a_2 \frac{\partial f_3}{\partial n} - a_3 \frac{\partial f_4}{\partial n} \right) \right]$$

APPENDIX II

Projection of equation (1) in the axial direction yields the well known axial momentum equation

$$\frac{d}{dx} c_{xe}{}^2 \theta_x + c_{xe} \delta_x{}^\star \frac{dc_{xe}}{dx} = \frac{F_x}{\rho} + \frac{\tau_x}{\rho} \tag{110}$$

Integration over the blade row yields

$$\Delta\theta_x = \frac{1}{\tilde{c}_{xe}{}^2} \int_{\text{in}}^{\text{out}} \frac{\tau_x}{\rho} dx + \frac{1}{\tilde{c}_{xe}{}^2} \int_{\text{in}}^{\text{out}} \frac{F_x}{\rho} dx - \tilde{\theta}_x (2 + H) \frac{\Delta c_x}{\tilde{c}_x} \tag{111}$$

A tilda denoting an average over the blade length Δx. The first term in the rhs of equation (111) is approximated through

$$\int_{\text{in}}^{\text{out}} \frac{\tau_x}{\rho} dx = \frac{u_e{}^2}{2} C_f \Delta x \cos \alpha_\infty \tag{127}$$

where

$$\alpha_\infty = \frac{\alpha_{\text{in}} + \alpha_{\text{out}}}{2} \tag{128}$$

C_f is given through equation (56), and the wall skewing angle is neglected. The last term in equation (111) is related to the axial velocity ratio at the wall and can be expressed through

$$\frac{\Delta c_x}{\tilde{c}_x} = 2 \frac{\mathrm{AVR} - 1}{\mathrm{AVR} + 1} \tag{129}$$

The force defect term in equation (111) finally contains two contributions, one from equation (92) depending on C_D and one from equation (22) projected in the x direction

$$\frac{F_x}{\rho} \cong C_D \frac{u_e{}^2}{2} \frac{h}{g} - \frac{k}{g} u_e{}^2 \theta_2 \sin \alpha \cos \alpha = \frac{F_{x1}}{\rho} + \frac{F_{x2}}{\rho} \tag{130}$$

Integration of the first contribution denoted as F_{x1} over Δx gives (equations (26, 27))

$$\int_{\text{in}}^{\text{out}} \frac{F_{x1}}{\rho} dx \cong \Lambda C_L{}^2 \sigma \frac{u_e{}^2}{2} \Delta x \tag{131}$$

where

$$\Lambda = K \frac{t_c}{s} + \frac{L}{2} \tag{132}$$

The second contribution denoted as F_{x2} will be evaluated using equation (22) through

$$\int_{\text{in}}^{\text{out}} \frac{F_{x2}}{\rho} dx \cong \sin \alpha_\infty \cos \alpha_\infty \int_{\text{in}}^{\text{out}} \frac{k}{g} u_e{}^2 \theta_2 dx \tag{133}$$

$u_e{}^2 \theta_2$ as function of x can be obtained by use of equation (93), where τ_t is neglected

$$\frac{d}{dx} u_e{}^2 \theta_2 \cong -\frac{k}{g} u_e{}^2 \theta_2 - \frac{F_t{}^{\text{coll}}}{\rho \cos \alpha} \tag{134}$$

integration with respect to x yields

$$u_e{}^2 \theta_2 = (u_e{}^2 \theta_2)^{\text{in}}\, e^{-k/gx} - \frac{g}{k} \frac{F_t{}^{\text{coll}}}{\rho \cos \alpha} (1 - e^{-k/gx}) \tag{135}$$

where x is taken zero at leading edge of the blade rows. Integration of equation (135) over Δx gives

$$\int_{\text{in}}^{\text{out}} u_e{}^2 \theta_2 dx = \frac{g}{k} (u_e{}^2 \theta_2)^{\text{in}} (1 - e^{-k\sigma}) - \frac{g}{k} \frac{F_t{}^{\text{coll}}}{\rho \cos \alpha} \Delta x \left(1 - \frac{1 - e^{-k\sigma}}{k\sigma} \right) \tag{136}$$

where

$$\sigma = \frac{c \cos \gamma}{s \cos \gamma} = \frac{\Delta x}{g} \tag{137}$$

and equation (133) becomes

$$\int_{\text{in}}^{\text{out}} \frac{F_{x2}}{\rho} dx = \frac{\sin 2\alpha_\infty}{2} \left[(u_e{}^2 \theta_2)^{\text{in}} (1 - e^{-k\sigma}) - \frac{F_t{}^{\text{coll}}}{\rho \cos \alpha} \Delta x \left(1 - \frac{1 - e^{-k\sigma}}{k\sigma} \right) \right] \tag{138}$$

The first term in equation (138) is a contribution from the inlet cross flow, while the second represents the counteracting effect of F_t against the transverse gradient in the blade row. It is to be noted that if Mellor and Wood's condition $\theta_2{}^{\text{out}} = 0$ is imposed instead of equation (22), the same equation (138) can be found where σ is taken infinite, which corresponds to very closed spacings. If $(u_e{}^2 \theta_2)^{\text{in}}$ is assumed to be defined mainly by the relative motion setting (equation (96))

$$(u_e{}^2 \theta_2)^{\text{in}} = -U c_{xe} \theta_x \operatorname{sign} \alpha_\infty \tag{139}$$

unphysical behavior of the blockage correlation equation (120) was obtained. In fact $\theta_2{}^{\text{in}}$ has a non-zero contribution from the previous blade rows depending on pressure gradient (through $F_t{}^{\text{coll}}$), skin friction and defect forces. An ad hoc expression is therefore attempted, neglecting the second term in the rhs of equation (138) and by introducing an empirical coefficient k_f through

Downloaded 01 Jun 2010 to 171.66.16.59. Redistribution subject to ASME license or copyright; see http://www.asme.org/terms/Terms_Use.cfm

$$\int_{\text{in}}^{\text{out}} \frac{F_{x2}}{\rho}\,dx = -\frac{\sin 2\alpha_\infty}{2} k_f U c_{xe} \theta_x \text{ sign } (1 - e^{-k\sigma})$$

$$= -\frac{\sin 2|\alpha_\infty|}{2} k_f c_{xe}{}^2 \frac{1}{\varphi} \theta_x (1 - e^{-k\sigma}) \quad (140)$$

Comparisons with numerical and experimental results suggested a value $k_f \simeq 0.5$. The increase of θ_x over a whole stage can now be written as (equations (127, 131) and (140))

$$(\Delta\theta_x)_{\text{stage}} = p - q\tilde{\theta}_x \quad (112)$$

where

$$p = \sum_{R,S} \frac{c \cos \gamma}{2 \cos^2 \alpha_\infty} [C_f \cos \alpha_\infty + \Lambda C_L{}^2 \sigma] \quad (141)$$

$$q = 2(2 + H) \frac{\text{AVR} - 1}{\text{AVR} + 1} + \frac{\sin 2\alpha_\infty}{2} k_f \frac{1 - e^{-k\sigma}}{\varphi} \quad (114)$$

The effect of axial spacing between blades can be introduced by expressing that the skin friction acts over an extra distance ξ between two adjacent blade rows and equation (141) becomes

$$p = \sum_{R,S} \frac{c \cos \gamma}{2 \cos^2 \alpha_\infty} \left[C_f \left(1 + \frac{\xi}{c} \right) \cos \alpha_\infty + \Lambda C_L{}^2 \sigma \right] \quad (113)$$

Downloaded 01 Jun 2010 to 171.66.16.59. Redistribution subject to ASME license or copyright; see http://www.asme.org/terms/Terms_Use.cfm

J. R. Shekleton,

Engineering Staff Specialist,
Control and Combustion Systems,
Solar Turbines International,
San Diego, CA 92138

The Civic: A Concept in Vortex Induced Combustion for the Solar Gemini 10 kW Gas Turbine

The Radial Engine Division of Solar Turbines International, an Operating Group of International Harvester, under contract to the U.S. Army Mobility Equipment Research & Development Command, developed and qualified a 10 kW gas turbine generator set. The very small size of the gas turbine created problems and, in the combustor, novel solutions were necessary. Differing types of fuel injectors, combustion chambers, and flame stabilizing methods were investigated. The arrangement chosen had a rotating cup fuel injector, in a can combustor, with conventional swirl flame stabilization but was devoid of the usual jet stirred recirculation. The use of centrifugal force to control combustion conferred substantial benefit (Rayleigh Instability Criteria). Three types of combustion processes were identified: stratified and unstratified charge (diffusion flames) and premix. Emphasis is placed on five nondimensional groups (Richardson, Bagnold, Damköhler, Mach, and Reynolds numbers) for the better control of these combustion processes.

Introduction

Small reciprocating engine driven generator sets are used in large numbers by the U.S. Army. A small gas turbine has potential advantage, including multi-fuel ability, light weight and portability, reliability, and excellent cold weather starting. Solar, under contract to the U.S. Army MERADCOM, developed and qualified such a small 10 kW gas turbine generator set. This paper describes the development of the combustor and discusses the scaling problems of small combustors.

Engine Description and Initial Development

A schematic of the single-shaft Gemini 10 kW engine is shown in Fig. 1. A radial compressor and turbine are mounted back-to-back on overhung bearings. Air is supplied from the compressor via a can combustor to the turbine. An alternate configuration was evaluated, using an annular combustor as shown in Fig. 2. Typical design point conditions for the engine are:

- Gross power – 11.19 kW
- Airflow – 0.195 kg/s
- Pressure – 345 kPa
- Fuel flow – 10.43 kg/hr

The engine is flat rated for a generator output of 10 kW in a range of ambient conditions from 325 K hot day to 219 k cold day and altitudes up to 2440 m. The principal fuel is diesel oil, but the engine must operate with equal facility on such fuels as kerosene, gasoline, JP4, JP5, and arctic diesel. Combustor maintenance is permitted every 500 hr and a 6000 hr life is required.

Fuel Atomization. The principal problem of small gas turbine combustors is fuel atomization. Fuel injector design to minimize re-

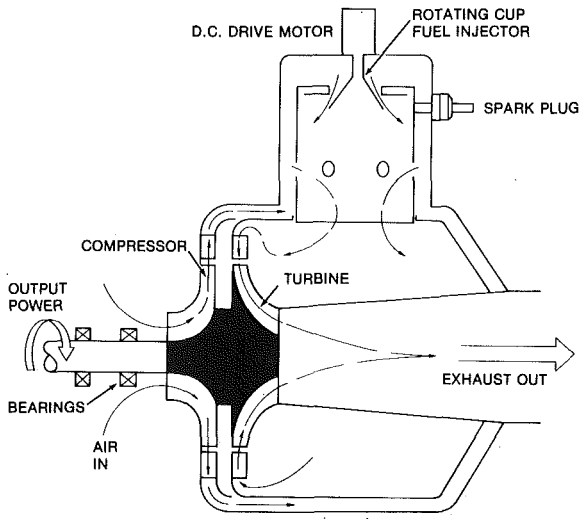

Fig. 1 10 kW engine with a can combustor

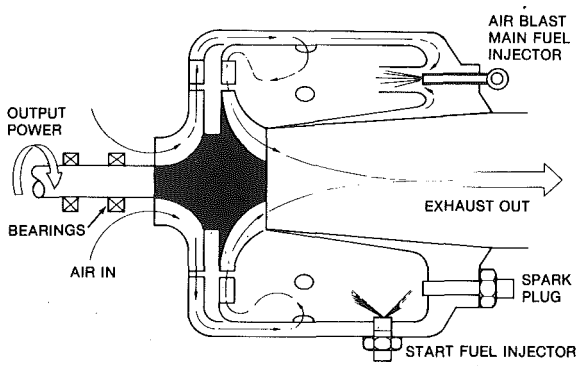

Fig. 2 10 kW engine with an annular combustor

Contributed by the Gas Turbine Division and presented at the Gas Turbine Conference and Products Show, New Orleans, La., March 10–13, 1980 of THE AMERICAN SOCIETY OF MECHANICAL ENGINEERS. Manuscript received at ASME Headquarters December 11, 1979. Paper No. 80-GT-54.

Copyright © 1981 by ASME

Downloaded 01 Jun 2010 to 171.66.16.59. Redistribution subject to ASME license or copyright; see http://www.asme.org/terms/Terms_Use.cfm

liability problems of small orifices, and small combustor dimensions that increase the need for small fuel droplet size both dominate the method of combustor design. As fuel temperature is lowered, its viscosity increases (prior to clouding) to values as high as:

Fuel	Ambient Temperature, K	Fuel Viscosity, CS
No. 2 Diesel	261	25
No. 1 Diesel	233	16.5
Arctic Diesel	228	60
JP4	219	12
Gasoline	219	1.5

Swirl pressure atomizing fuel injectors commonly used in gas turbines are sensitive to fuel viscosity effects at low fuel flows (Fig. 3). Data were obtained by using a variety of differently sized swirl pressure injectors and by establishing the fuel pressure required to obtain an ignitable spray in cold air, with a 0.1 Joule ignitor and differing viscosity oils. Viscous effects are negligible above a fuel flow of 16 kg/hr, but at a fuel flow of 5.0 kg/hr despite excessive fuel pressures, adequate fuel atomization cannot be obtained. The 10 kW being designed for light-off fuel flows down to 1.0 kg/hr could not use a swirl pressure injector. An alternate solution of a continuous air assist pump to atomize the fuel was ruled out on grounds of cost and reliability.

Annular Combustor. Solar's gas turbines are small and mostly use annular combustors for structural symmetry and integrity, good aerodynamics for low pressure loss and low turbine hot spots, and readily cooled compact ducting for high turbine temperature capability. Consequently, the need for a multiplicity of fuel injectors as used in annular combustors results in fuel flows considerably lower than the value of 16 kg/hr required to minimize viscous fuel effects. A typical solution is simple airblast main fuel injection as shown in Fig. 2. These injectors function similarly to an automobile carburetor. In larger engines, an air assist pump is used which acts on each injector for starting only. On smaller engines, however, a single small swirl pressure injector is used for starting only. The hot streak emanating from this single injector is not detrimental to small engines which attain full speed in a few seconds. The airblast main fuel injectors require a design point combustor pressure drop on the order of 4 percent in order to achieve air velocities high enough for acceptable fuel atomization. This pressure drop is higher than needed for combustion and mixing of air, and is a trade-off for using reliable, low fuel flow injectors with multi-fuel capability in small engines.

Start Injector Design. After considerable experimentation, an impingement start fuel pressure atomizing injector was developed for the annular combustor (Fig. 4). Effective fuel atomization was obtained, at a fuel flow rate of 2.0 kg/hr, up to a viscosity of 25 cs with 700 kPa fuel pressure. The goal of 60 cs for use of arctic diesel fuel was not achieved. The minimum fuel flow attainable of 2.0 kg/hr resulted in a small fuel metering orifice diameter of 0.15 mm which frequently plugged up. The high start fuel flow caused hot streaks through the turbine and proved to be unacceptable for the 10 kW engine.

Can Combustor. A rotating cup fuel injector has the ability to thoroughly atomize unusually low fuel flows with high fuel viscosities, and does not need either fuel pressure or small metering orifices. When driven by a small electric motor, the power consumption is negligible, which is indicative of the gross inefficiency of most fuel atomizing concepts. A schematic of the initial development of the can combustor, using the rotating cup fuel injector, is shown in Fig. 5. By flowing a small amount of air at high velocity over the lip of the cup, the injector becomes essentially a fuel filmed airblast injector, as commonly used in modern gas turbine combustors [1]. Unlike these injectors, it was unnecessary to flow high velocity air over both sides of the fuel film. The technique proved complex and also deteriorated flame stability. With the cup acting in the role of a baffle flame stabilizer [2], the high velocity air over the cup lip formed inner and outer hot combustion gas recirculation zones for the purpose of continuous ignition. The dome of the combustor was air impingement cooled while the spent air was used both for film cooling of the combustor walls and for combustion. A schematic of the method of driving the rotating cup is shown in Fig. 6. The cup was 20 mm in diameter and driven at 13,000 rpm. Combustor pressure drop was 2 percent but,

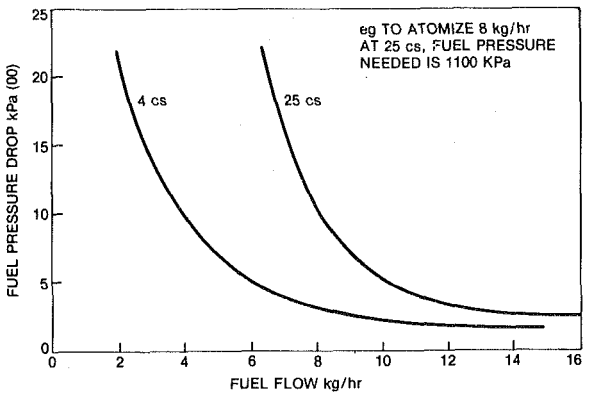

Fig. 3 Minimum fuel pressure for good fuel atomization

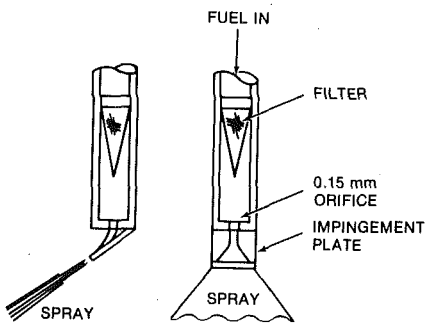

Fig. 4 Start injector for annular combustor

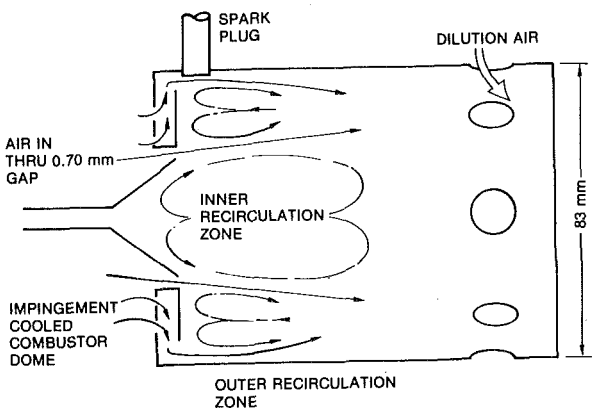

Fig. 5 Can combustor schematic

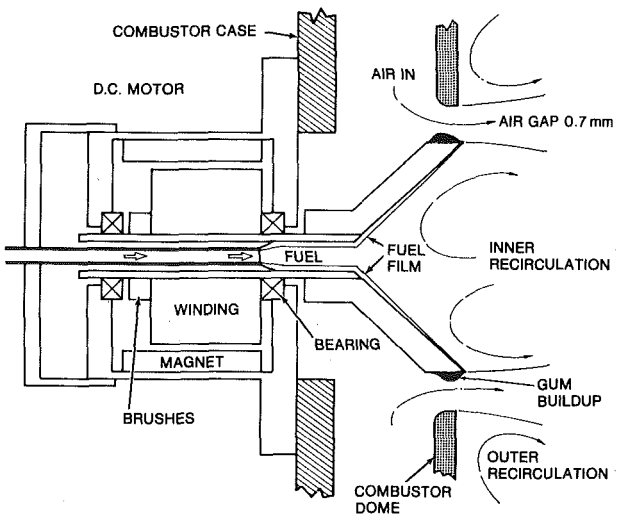

Fig. 6 Rotating cup and driving motor schematic

Downloaded 01 Jun 2010 to 171.66.16.59. Redistribution subject to ASME license or copyright; see http://www.asme.org/terms/Terms_Use.cfm

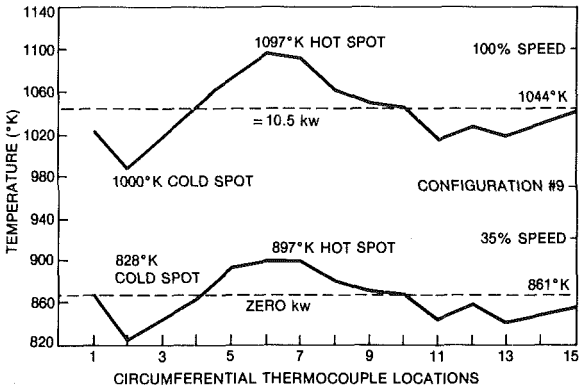

Fig. 7 Circumferential distribution of gas temperature at the turbine nozzle

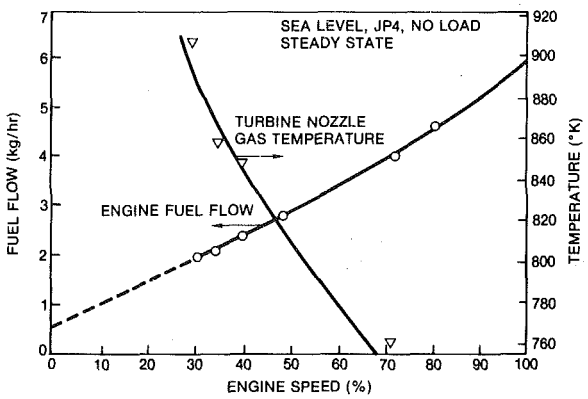

Fig. 8 Turbine nozzle inlet gas temperature and engine fuel flow

allowing for duct loss from the compressor to the turbine, the overall loss was 4 percent.

Can Combustor Development. The use of a can combustor caused maldistribution of air that resulted in nonuniform combustor and turbine nozzle temperatures. One solution was to increase combustor pressure drop; the preferred solution was to provide extra long mixing length between the combustor and the turbine. This length increase did not involve additional pressure loss because the relatively large combustor diameter of 83 mm results in low duct Mach numbers. As shown in Fig. 7, the turbine nozzle inlet temperature distribution was good over the whole speed range of the engine. Repeatability of this temperature distribution over such a wide speed range is attributable to the total dominance of the aerodynamics of the asymmetric ducting. Fig. 8 shows the steady-state turbine nozzle inlet gas temperature and engine fuel flow when the engine is operated with no load from 30 to 100 percent engine speed. The unusually low fuel flows are noteworthy. Due to the slow buildup of gums at the lip of the cup (Fig. 6) and the small air gap of 0.7 mm, carbon build on the combustor dome would occur after about 100 hr of engine operation when using diesel fuel. This carbon would lodge in the rather small turbine nozzle passageways and cause engine surge. Cleaning of the cup every 100 hr resolved this problem, and the engine was released for service testing.

Civic Combustor Design and Development

Field service experience indicated that three combustor problems required solution: field maintenance, such as cup lip cleaning, should be increased from 100- to 500-hr intervals; the life of the cup motor, limited by brush wear, should be increased from a 1500- to 2500-hr life; and the cold day light-off on arctic diesel should be improved. The two latter problems were readily resolved by use of a brushless dc motor and a higher energy (0.8 Joule) ignition system. After considerable experimentation to resolve the gum build on the cup lip, complete redesign of the combustor was decided upon, which is the major topic of this paper.

The approach used, called "concept in vortex induced combustion" (CIVIC) is largely based on low emission research and development done at Solar [3–6]. The principal aim was twofold: to thoroughly sweep the lip of the cup with high velocity air to inhibit the formation of gum; and to make the air gap at the lip much larger to reduce the sensitivity of the airflow through the gap to any gum buildup. By use of a conventional swirl stabilized flame, the flame stability could be significantly improved beyond that obtained with a simple baffle flame stabilizer. This would permit higher airflows over the cup, and hence a bigger gap, with the objective of providing all the combustion air over the cup.

Flame Stabilizing Mechanisms. Combustion similarities in furnaces, turbines, and reciprocating engines are many, as Swithenbank notes [7]. In a gasoline engine, ignition is initiated by a spark and the flame propagates out by turbulent supply of just burned hot combustion products, which serve as the subsequent ignition sources for the adjacent unburned fuel-air mixture. Excepting light-off, the

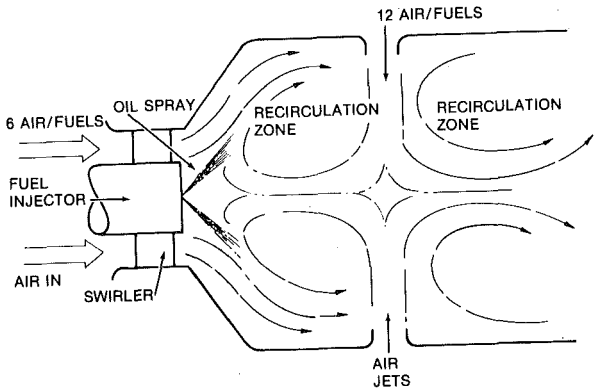

Fig. 9 Typical flame stabilization in a gas turbine

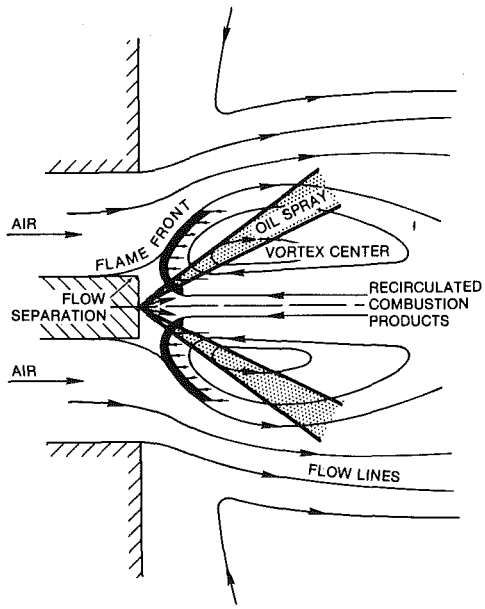

Fig. 10 Stabilization of pressure jet oil flames

ignition initiation source in the CIVIC is by recirculation of hot combustion products; otherwise, the flame similarly propagates by turbulent spread of just burned products into the adjacent fuel-air mixture. Two differing means of swirl stabilization by hot combustion product recirculation are used commonly in gas turbines [8] and furnances [9]. These are shown in Figs. 9 and 10, respectively. Generally, in the gas turbine, lack of flame stability permits little more than 10 percent of all the engine air to pass through the air swirler. Such combustors smoke when using swirl fuel pressure injection, and the use of airblast to reduce smoke further deteriorates flame stability [1]. The additional combustion air, supplied by impacting recircula-

Downloaded 01 Jun 2010 to 171.66.16.59. Redistribution subject to ASME license or copyright; see http://www.asme.org/terms/Terms_Use.cfm

tory air jets, is a probable means of quenching ignition and enhancing smoke. These air jets strip the film cooling air off the combustor walls and also act as flame holders to heat the walls downstream of these jets. This design approach was not attractive. Alternatively, the furnace flame passes all the combustion air through the air swirler and therefore provides the large air gap sought, although flame stability is not reported. Airflow separation occurred as shown in Fig. 10 and was found to enhance gum buildup on the cup. Tests with a fuel injector as shown produced copious amounts of exhaust soot even at atmospheric pressure. This may be desirable in a furnace, but not in a gas turbine. An alternate means of swirled flame stabilization was therefore pursued which appears well suited to smokeless furnace combustion.

CIVIC Flame Stabilizing Mechanisms. Flame stabilization refers to the method of fuel injection and to the method of initiation of flame ignition, as well as to the method of subsequent flame propagation and ignition. Three principal methods of flame stabilization are identified in the CIVIC concept. These three methods are named premix, stratified and unstratified charge fuel injection, as shown in Fig. 11. The means whereby the various flames are initially ignited and then propagated, by recirculation and turbulence respectively are shown in Fig. 12. The flame propagation is controlled by the centrifugal force effects of swirled flow. Experimental data are reported in references [3] and [6]. All three flames occurred at the same time in the 10 kW CIVIC combustor, although complete stratification was the goal. A fourth flame, with fuel in the recirculation zones, is to be avoided because it causes smoke.

Stratified Charge Fuel Injection. Rotating cup fuel injection is commonly used in furnaces [10]. In the 10 kW CIVIC, an extension of the combustor wall over the cup is used to prevent airflow separation and to provide a zone of primary hot gas inner recirculation for initial ignition and fuel evaporation (Fig. 11). Similar techniques appear to be used in other swirled gas turbine combustors, with more conventional fuel injectors and jet stirred recirculations [8]. Beér [11] describes the mechanisms whereby the resultant flame becomes laminarized due to centrifugal force effects. This is somewhat analogous to downward flame propagation in a tube [12]. Such a method of fuel ignition provides a means of extremely rapid fuel evaporation by heat supplied from the adjacent flame, due to centrifugal force effects (Fig. 12). It is essential that fuel atomization be fine enough so that the fuel evaporates before it can centrifuge through the flame and out of the evaporation zone. The consequent mixing inhibition of hot evaporated fuel and cool air provides a stoichiometric interface between fuel and air over a wide range of air/fuel ratios and hence provides excellent flame stability but with high NO_x. In order to burn the gasified, hot fuel, it must be mixed with cool air. This is achieved downstream by expanding the combustor outward to reduce centrifugal force effects (Fig. 11) which permits turbulent mixing and combustion. Any escape of fuel, even gas fuel [13], into the recirculation zone causes smoke. Therefore, the fuel droplets must be accurately located, as in a cup. For diesel oil, the flame is pale blue or invisible down to an overall air/fuel ratio of at least 10.

Unstratified Charge Fuel Injection. Unstratified charge fuel injection functions in exactly the opposite manner as stratified charge. In the 10 kW CIVIC, it occurs as a consequence of the small scale of the combustor, whereby some of the fuel droplets, centrifuging out of the stratification zone, are ignited by the outer hot gas recirculation. The centrifugal force effects, notably between the hot flame and cold air, provide fast inward mixing of the hot combustion products but with consequent poor flame stability and low NO_x. The high temperature gradients in such a flame enhance flame propagation, the phenomenon being analogous to upward flame propagation in a tube having similar air/fuel gradients [14]. A similar means of flame propagation is used in some diesel engines [15]. A blue or invisible flame is obtained unless the fuel droplet is too large and enters the outer recirculation.

In the stratified and unstratified charge modes of flame propagation, it is possible that the centrifugal force results in a preferential movement of light, hot combustion products and active species relative to the heavier fuel and air [16]. The hot products, being the

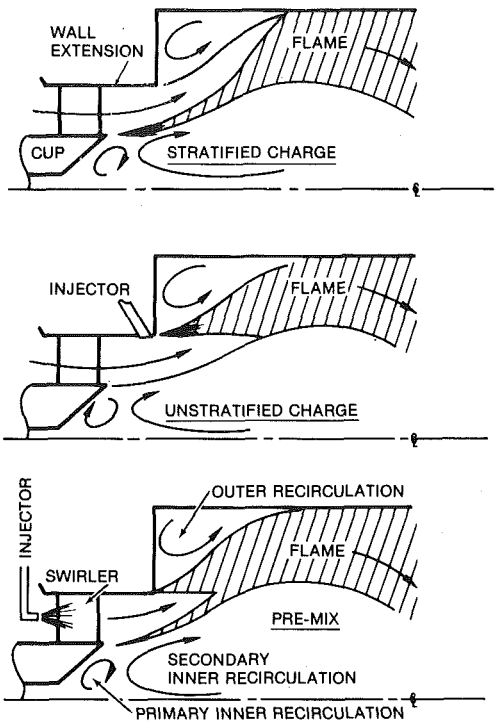

Fig. 11 Flame stabilization in the CIVIC fuel injector

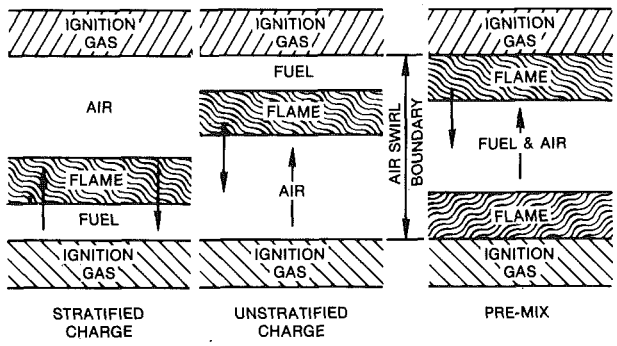

Fig. 12 Ignition and flame propagation in the CIVIC fuel injector

source of ignition to the cool unburned fuel-air mixture, are moved aerodynamically relative to this cool mixture, by centrifugal force effects in a "mixing controlled" fashion. In a "reaction controlled" system, such as a stirred reactor [17], these ignition species are supposed to be intimately mixed with the fuel-air mixture. Clearly, this mixedness is not likely in the above system. In the unstratified charge mode, the ignition species would tend to be preferentially disposed so as to ignite (on the average) a somewhat higher air/fuel ratio than that represented by the hot products of ignition. This would promote a cooler flame with lower NO_x [6]. In the case of the stratified charge flame, the opposite diffusion effect is likely [3, 6]. These phenomena may be of importance for NO_x control in reciprocating as well as continuous combustion processes.

Premix Fuel Injection. Premix fuel injection occurs in the 10 kW CIVIC when larger fuel droplets, which escape out of the stratification zone, evaporate and mix with the swirling air prior to reaching the unstratification zone. Ignition can be effected via either outer or inner recirculation zones, or both. Flame characteristics are similar to that of an unstratified flame; it is colorless and has low NO_x and poor flame stability. This is analogous to both upward and downward flame propagation in a tube [12], for outer and inner ignition respectively. For outer recirculation zone ignition, flame propagation is described in references [18–20].

CIVIC Combustor Development. The original CIVIC design, shown in Fig. 13, was used for preliminary evaluation. An acceptable

Downloaded 01 Jun 2010 to 171.66.16.59. Redistribution subject to ASME license or copyright; see http://www.asme.org/terms/Terms_Use.cfm

flame was observed at simulated (atmospheric) design conditions, but light-off could not be obtained. At typical low speed engine light-off, the air velocity through the air swirler was low and consequently the included angle of the fuel spray was near 180 deg [21]. The fuel impacted the overhanging extension of the combustor wall and prevented ignition. Using a radial inward flow swirler (Fig. 14) caused a somewhat unexpected delay in the outward expansion of the swirling air downstream of the cup. This provided an aerodynamic extension of the combustor wall and resolved the light-off problems.

The final version of the CIVIC concept (Fig. 15) incorporated refinements. Use of a baffle, thoroughly cooled by impingement of dilution air, prevented back flow of dilution air destructive to ignition in the stratification zone. This was expected from past experience [3]. Similarly, it proved undesirable to add film cooling air to the combustor wall in the region of the outer recirculation because this was also destructive to ignition of much of the fuel that had escaped the stratification zone. This problem was resolved through the use of external convective air cooling, then dumping the spent air downstream of the outer recirculation through a cooling strip. Extraneous air in either the inner or outer ignition zone caused smoke. In the CIVIC, the recirculation zones should be regarded only as a source of ignition and not as a place to burn fuel.

The engine was requalified using the CIVIC concept, higher energy spark plug, and brushless cup drive motor. Cup lip gum buildup was never entirely resolved, but being slow and with large amounts of air flowing through a large air gap (3.5 mm), cup lip cleaning is now done only at 500 hr increments and will probably move to less frequent intervals. The requalified 10 kW engine is now being prepared for production.

Problems of Scale in the Civic

The CIVIC has a simple form because the flow is two dimensional; it is not obscured by the three dimensional nonuniformities created by the typical air swirled and jet stirred combustor (Fig. 9). Thus, it is not only an attractive design for modeling, but it is also a practical combustor having a good flame performance. The eye can be used as a noninvasive probe, because the CIVIC has an ordinarily non-luminous combustion. As a consequence of the very high centrifugal forces (40,000 g and more) of small swirled combustors, fuel droplet centrifuge is a principal problem in achieving proper stratification. The 10 wK CIVIC is small for model work and is much smaller than most combustors. The use of a somewhat large combustor of more typical scale, with gas fuel for baseline information, presents intriguing possibilities for studying atomization and evaporation effects.

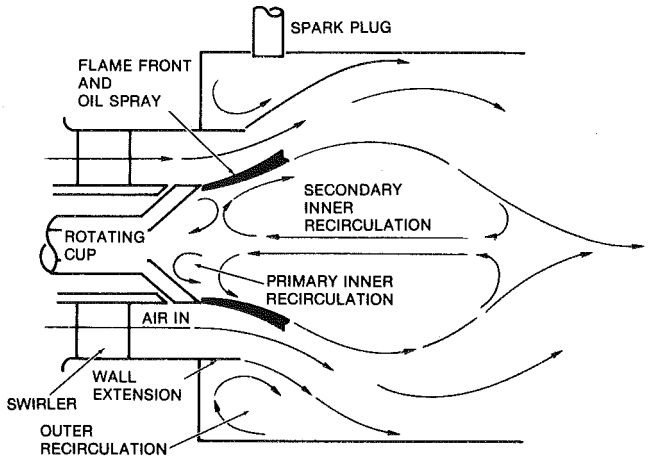

Fig. 13 Initial CIVIC combustor design

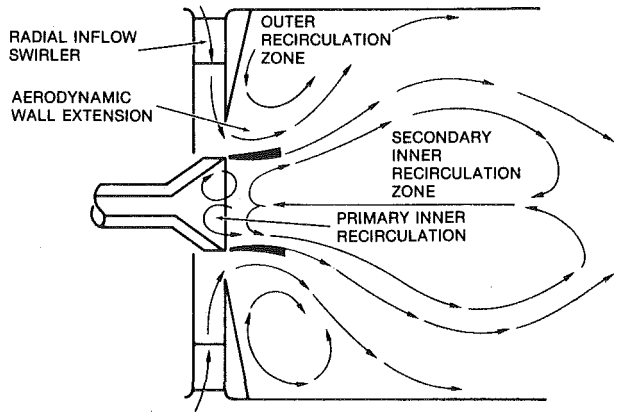

Fig. 14 Second CIVIC combustor design

Scaled Up CIVIC. Preliminary results at atmospheric pressure of an approximate 50 percent scale up of the CIVIC are shown in Figs. 16 and 17, using diesel oil and natural gas in the stratified charge mode. The geometric scaling involved is illustrated in Fig. 18. The flame was invisible for gas and pale blue for diesel oil. Visual flame observations also indicated no combustion in the unstratified charge mode, although the data suggest some premix mode combustion with diesel oil. The onset of high NO_x, as the flame zone air/fuel ratio approaches stoichiometric, is to be expected [22, 23] due to high flame temperature. The much lower NO_x levels at high air/fuel ratios is anticipated, from Solar's past experience, to increase approximately as the square root of the pressure ratio for pressure increases from this atmospheric test. The lower NO_x and lower range of efficient combustion seen for diesel oil, as compared to natural gas, is rationalized by the centrifuging out of the heavy liquid fuel drops, which results in less fuel stratification.

The flame stability and range of efficient combustion with gas is exceptional when considering that all the combustion air is flowing through the air swirler. The good flame stability and range of efficient combustion with diesel fuel should increase toward that obtained with natural gas when the air pressure is increased to normal engine levels. This is expected because of the higher degree of stratification from better evaporation and fuel atomization with airblast injection [1], rather than from any increase in reaction rate. The onset of high CO as the flame zone air/fuel ratio approaches stoichiometric is the result of disassociation and will not occur when an air dilution zone is used. The wide range of efficient combustion ensures essentially 100 percent combustion efficiency, with a short stable flame but with high NO_x, depending on the pressure ratio, over the operational range of an industrial gas turbine.

Nondimensional Groups. The Mach, Richardson, Reynolds, Bagnold, and Damköhler numbers are of some importance in the design of swirl flames in gas turbines, furnaces, and reciprocating engines, but especially when designing small combustors. The Mach and Bagnold numbers are the most important.

Mach Number. Mach number can be expressed for typical industrial combustors as follows (Appendix 1):

$$\frac{W\sqrt{T}}{AP} = C\sqrt{\text{Percent Pressure Loss}} = C_1 \text{ Mach number} \quad (1)$$

where W = combustor airflow, T = air temperature, P = air pressure,

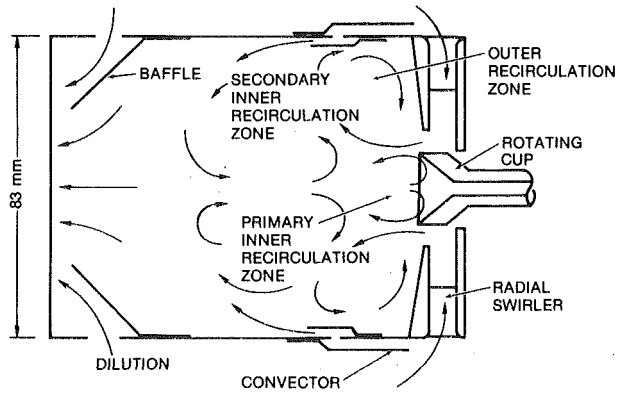

Fig. 15 CIVIC combustor design qualification test

Downloaded 01 Jun 2010 to 171.66.16.59. Redistribution subject to ASME license or copyright; see http://www.asme.org/terms/Terms_Use.cfm

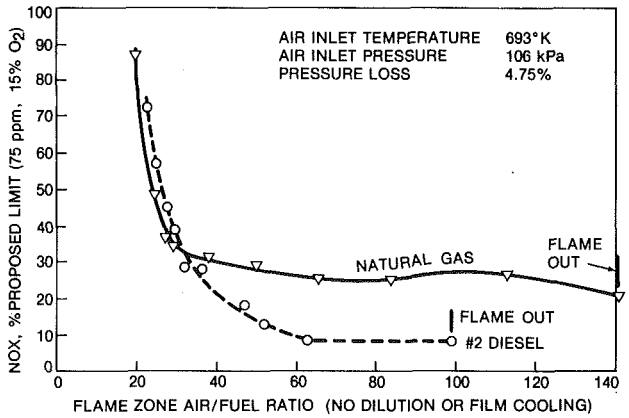

Fig. 16 NO_x emissions versus air-fuel ratio

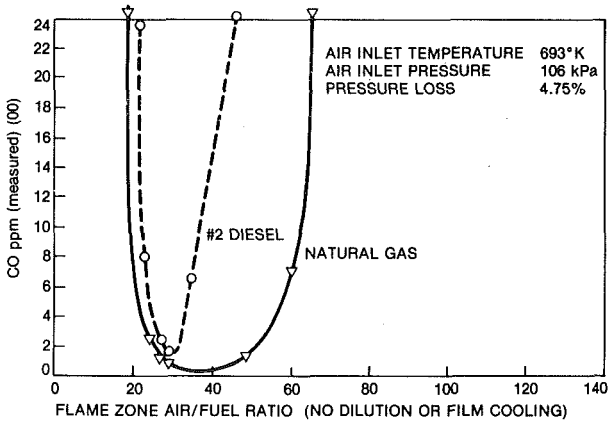

Fig. 17 CO emissions versus air-fuel ratio

A = effective hole flow area and C and C_1 = constants.

Fixing the percent pressure drop (or Mach number), with given airflow, temperature and pressure, establishes the hole flow area of the combustor. There is little latitude in sizing the flow area because an excessive pressure drop, due to a small flow area, is not acceptable for good engine performance. A large combustor having a large flow area has a low pressure loss. A low loss causes turbine hot spots, which induce air maldistributions and also poor liquid fuel atomization when using airblast atomization [1]. On this basis, for different combustor airflows, gas fueled can combustors can be scaled for design point operations as shown in Fig. 18.

Such a combustor is dominated by turbulent mixing even when using a premixed flame. The flame length remains more or less fixed, no matter what the flow throughput, and unacceptably high or low pressure loss is limiting. Penner [24] observed that, for a turbulent gas jet, the flame length is in good agreement with mixing length calculations. Flames of this sort are controlled by mixing and used in open-hearth furnaces. The rate of combustion is determined mainly by aerodynamic conditions [25]. Reciprocating engines operate on the same controlled mixing principles. Doubling the engine speed halves flame propagation time [15, 26]. Excessive engine speed limits air swallowing capacity and hence limits power output due to an excessive Mach number [27] just as in a gas turbine. In a mixing-controlled flame, the reaction rate can be assumed to be fast as compared to the mixing rate.

A further equation can be derived from the Mach number [28]:

$$\frac{\text{Combustor length with one injector}}{\text{Combustor length with } n \text{ injectors}} = \frac{\sqrt{n}}{1} = \frac{\text{Combustor volume with one injector}}{\text{Combustor volume with } n \text{ injectors}} \quad (2)$$

By this equation, combustor length and volume can be conserved considerably with a multiplicity of smaller combustors, which will speed up the mixing as velocity is fixed and length reduced. Although impractical in the 10 kW, this approach is commonly used in aero turbines using annular combustors and in reciprocating engines having multiple cylinders, and is a major criterion in the design of these machines.

Damköhler Number. The Damköhler number is defined by the ratio of the mixing time to the reaction time. With a very small combustor, or a multiplicity of scaled down combustors, the mixing rate is increased and the effects of reaction rate in terms of combustion efficiency and flame stability might start to become more dominant. In the cold starting conditions of arctic winter, or in high altitude light-off, centrifugal force clearly dominates fuel droplet trajectory and evaporation. The subsequent deleterious effects in influencing efficiency and stability of small swirl stabilized flames is powerful. Efficient starting in the stratified charge mode will ensure an extremely high reaction rate in normal engine operation. This is illustrated by the lack of pressure dependence on combustion efficiency and flame stability, at typical design conditions, in a small premix CIVIC flame [3].

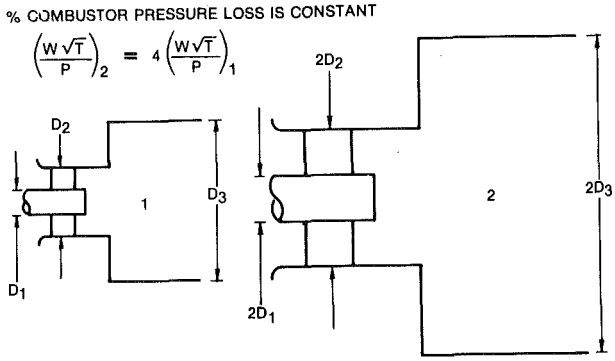

Fig. 18 Can combustor scale up

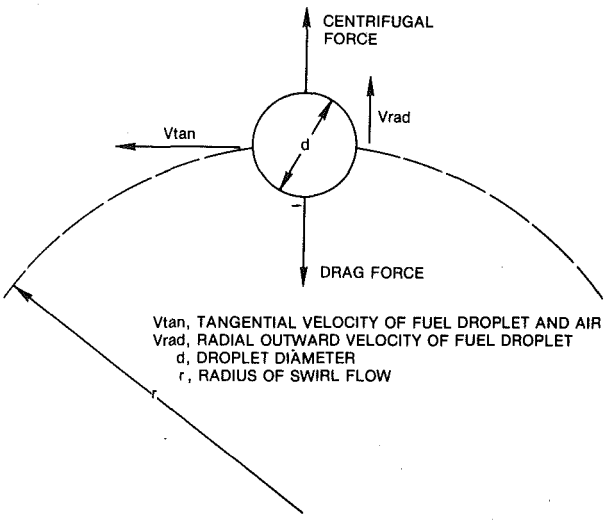

Fig. 19 Fuel droplet centrifuge in an axial air swirl flow

Bagnold Number. As used here, Bagnold number is the ratio of drag force to inertial force and is applicable to the flight of a fuel droplet in an air swirl induced centrifugal force field (Fig. 19). From a balance of drag and centrifugal forces acting on the fuel droplet, ignoring initial drop velocity change, the following equation can be derived (Appendix 2):

$$Vrad = C.d^2.G \quad (3)$$

where d = droplet diameter, G = centrifugal acceleration, $Vrad$ = radial out droplet velocity and, C = constant.

Obviously, when combustors are scaled down, the centrifugal force increases proportionately. In order to maintain geometric similarity in liquid fuel distribution, as is necessary for mixing control, the fuel droplet size must be reduced with scale down of the combustor. Again

Downloaded 01 Jun 2010 to 171.66.16.59. Redistribution subject to ASME license or copyright; see http://www.asme.org/terms/Terms_Use.cfm

ignoring the initial droplet velocity change as it is injected into the swirl flow, it can be shown (Appendix 3) that the fuel droplet must be scaled in the following proportions when the same combustor pressure drop is used:

$$\frac{Do}{do} = \sqrt{\frac{Ro}{ro}} \tag{4}$$

where Ro and ro = inner radii of the air swirler of the large and small combustors, respectively, and do and do = initial droplet sizes.

Similarly, it can be shown that for a fixed combustor size, mixing control is maintained, for an increase of airflow thoughput, when the droplet is scaled as follows:

$$\frac{Do}{do} = \sqrt{\frac{wo}{Wo}} \tag{5}$$

where Wo and wo = high and low airflows, respectively, and Do and do = corresponding droplet sizes.

For a very small combustor, droplet size and air velocity should be kept as small as possible. Fuel droplet size scale down is not possible in practice and consequently the problem of getting effective stratification at light-off is greatly enhanced in small combustors. Light-off problems are further increased when using less volatile fuels. Similar difficulties will occur in obtaining the proper spacial locations of the fuel, when using premix and unstratified charge fuel injection. The effects of high air pressure on fuel atomization and evaporation, which are beneficial with airblast atomizers [1], will reduce these deleterious small scale effects in normal engine operation. This might therefore confuse the effects of Damköhler, Bagnold, and Reynolds numbers in model work, but the use of gaseous fuel, which provides mixing control, would minimize such confusion.

Reynolds Number. When operating in turbulent flow, the influence of turbulence scale appears unimportant. Secondary effects of small scale in terms of Bagnold number and high air pressure on fuel evaporation are, of course, critical.

Richardson Number. This is the ratio of centrifugal to shear forces in swirl flow [11]. It is the means whereby the flame is dominantly propagated in swirl flow. Rather conveniently, the same scaling rules for the Mach number also apply for the Richardson number. It explains how the flame can be greatly speeded up or slowed down aerodynamically by appropriate location of the fuel relative to the air.

Summary

The use of swirl, without the customary jet stirred recirculation, shows potential advantage in combustion. The need for fine and accurately placed fuel droplets dominates the design of the typical small swirled combustor. Advantage may accrue from modeling the three combustion processes described and also applying these processes in gas turbines, furnaces, and reciprocating engines.

References

1 Bryan, R., et al., "Some Observations of the Atomizing Characteristics of Air-Blast Atomizers," *Combustion and Heat Transfer in Gas Turbine Systems,* Cranfield International Symposium Series, Vol. II, Norster, E. R., ed., Pergamon Press, Oxford, 1971, pp. 343–355.

2 Longwell, J. P., "Flame Stabilization and Flame Propagation in Ramjet Combustors," *Combustion Researches and Reviews,* Butterworths, London, 1955, pp. 58–71.

3 Sood, V. M. and Shekleton, J. R., "Ongoing Development of a Low Emission Industrial Gas Turbine Combustion Chamber," ASME Paper No. 79-GT-203.

4 Roberts, P. B., et al., "Advanced Low NO_x Combustors for Supersonic High-Altitude Aircraft Gas Turbines," ASME Paper No. 76-GT-12.

5 Duffy, T. E., et al., "Low Emissions Combustor/Vapor Generator for Automotive Rankine Cycle Engines," 7th Intersociety Energy Conversion Engineering Conference, San Diego, Calif. 1972, Paper No. 729129.

6 Sood, V. M. and Shekleton, J. R., "Ongoing Development of a Low Emission Axisymmetric Annular Vortex Combustor for an Industrial Gas Turbine," ASME 25th Annual International Gas Turbine Conference, New Orleans, La., 1980.

7 Swithenbank, J., "The Unknown Fluid Mechanics of Combustion," *Fluid Mechanics of Combustion,* Dussourd, J. L., et al., ed., ASME, New York, 1974, p. 4.

8 McKnight, D., "Development of a Compact Gas Turbine Combustor to Give Extended Life and Acceptable Exhaust Emissions," ASME Paper No. 78-GT-146, p. 3.

9 Beér, J. M., and Chigier, N. A., *Combustion Aerodynamics,* Halstead Press, New York, 1972, p. 192.

10 Gilchrist, J. D., *Furnaces,* Pergamon, London, 1963, pp. 24–27.

11 Beér, J. M., "Combustion Aerodynamics," *Combustion Technology: Some Modern Developments,* Palmer and Beér, ed., Academic Press, New York, 1974, pp. 75–86.

12 Gaydon, A. G. and Wolfhard, H. G., *Flames: Their Structure, Radiation and Temperature,* Chapman and Hall, London, 1970, p. 29.

13 Sood, V. M. and Shekleton, J. R., "Ongoing Development of a Low Emission Industrial Gas Turbine Combustion Chamber," ASME Paper No. 79-GT-203, p. 5.

14 Karim, G. A. and Tsang, P., "Flame Propagation Through Atmospheres Involving Concentration Gradients Formed by Mass Transfer Phenomena," *Fluid Mechanics of Combustion,* Dussourd, J. L., et al., ed., ASME, New York, 1974.

15 Lyn W. T., "Study of Burning Rate and Nature of Combustion in Diesel Engines," *Ninth Symposium (International) on Combustion,* Academic Press, New York, 1963, pp. 1069–1081.

16 Gaydon, A. G. and Wolfhard, H. G., *Flames: Their Structure, Radiation and Temperature,* Chapman and Hall, London, 1970, pp. 32–36.

17 Herbert, M. F., "A Theoretical Analysis of Reaction Rate Controlled Systems," *Combustion Researches and Reviews,* Mullins and Fabri, ed., Butterworths, London, 1957.

18 Lee, Y., "Flames Trajectory and Its Experimental Determination in Vortex Combustion," Dept., Mech. Eng., Penn State U., May 1963.

19 Lewis, G. D., "Centrifugal Force Effects on Combustion," *Proceedings of the Fourteenth Symposium on Combustion,* Combustion Institute, Pittsburgh, Pa. 1973.

20 Mestre, A. and Benoit, A., "Combustion in a Swirling Flow," *Proceedings of the Fourteenth Symposium on Combustion,* Combustion Institute, Pittsburgh, Pa. 1973.

21 Shekleton, J. R., "Rotating Cup Fuel Injector," United States Patent Number 3,933,133, Jan. 1976.

22 Fenimore, C. P., et al, "Formation and Measurements of Nitrogen Oxides in Gas Turbines," ASME Paper No. 70-WA/GT-3.

23 Singh, P. P., et al., "Formation and Control of Oxides of Nitrogen Emissions From Gas Turbine Combustion Systems," ASME Paper No. 72-GT-22.

24 Penner, S. S., "Diffusion Flames," *Chemistry Problems in Jet Propulsion,* Pergamon Press, London, 1957, p. 294.

25 Gaydon, A. G. and Wolfhard, H. G., "Diffusion Flames," *Flames: Their Structure, Radiation and Temperature,* Chapman and Hall, London, 1970, p. 152.

26 Smith, M. L. and Stinson, K. W., "The Process of Combustion," *Fuels and Combustion,* McGraw-Hill, New York, 1952, p. 152.

27 Taylor, C. F., *The Internal Combustion Engine in Theory and Practice,* Vol. 1, M.I.T., 1960, pp. 171–177.

28 Spalding, D. P., *Performance Criteria of Gas Turbine Combustion Chambers,* Bunhill, London, 1956, p. 10.

29 Godsave, G. A. E., "Studies of the Combustion of Drops in a Fuel Spray—The Burning of Single Drops of Fuel," *Fourth Symposium (International) On Combustion.*

APPENDIX 1

Percent Pressure Drop. Consider airflow through holes into a combustor. From Bernoulli's law,

$$\frac{P}{\rho} = \frac{V^2}{2g} + \frac{p}{\rho} \tag{6}$$

where P = total pressure outside the combustor, p = static pressure inside the combustor, ρ = air density, V = air velocity through the holes and, g = gravitational constant.

Assuming there is no pressure loss due to heat addition and that the combustor pressure loss is proportional to the dynamic head,

$$\frac{W\sqrt{T}}{A.P} = C\sqrt{\text{Percent Pressure Loss}} = \frac{V}{R\sqrt{T}} \tag{7}$$

where W = airflow rate through the holes, T = air temperature, A = effective flow area of the holes, C = constant and, R = gas constant.

Passing all the combustor air through one large combustor or a multiplicity of small combustors, with a fixed combustor pressure loss, equation (7) becomes

$$\frac{W\sqrt{T}}{A.P} = \frac{W_1\sqrt{T}}{A_1P} = C\sqrt{\text{Percent Pressure Loss}} \tag{8}$$

and, as $nW_1 = W$, and D^2 is proportionate to A,

Downloaded 01 Jun 2010 to 171.66.16.59. Redistribution subject to ASME license or copyright; see http://www.asme.org/terms/Terms_Use.cfm

$$\frac{W}{D^2} = \frac{W}{nD_1^2} \tag{9}$$

where W = airflow rate through one large combustor, n = number of small combustors, W_1 = airflow rate through one small combustor, D = basic dimension of the large combustor and, D_1 = basic dimension of a small combustor.

From equation (9),

$$\frac{D}{D_1} = \sqrt{n} \tag{10}$$

and so,

$$\left(\frac{D}{D_1}\right)^3 = (\sqrt{n})^3, \text{ or } \frac{D^3}{nD_1^3} = \sqrt{n} \tag{11}$$

Therefore,

$$\frac{D}{D_1} = \sqrt{n} = \frac{D^3}{nD_1^3} \tag{12}$$

which is to say that for a fixed airflow and pressure drop,

$$\frac{\text{The length of a single combustor}}{\text{The length of a multiplicity of small combustors}} = \frac{\sqrt{n}}{1} \tag{13}$$

$$\frac{\text{The combustor volume of a single combustor}}{\text{The total combustor volume of a multiplicity of small combustors}} = \frac{\sqrt{n}}{1} \tag{14}$$

APPENDIX 2

Ratio of Drag Force to Inertial Force. In the path of a fuel droplet (Fig. 19) moving in an axial air swirl (Fig. 14), assume the droplet is in uniform motion: Force of drag = centrifugal force. Hence,

$$\frac{C_d \cdot \rho_\alpha \cdot V_{\text{rad}}^2 \cdot \pi d^2}{2 \cdot 4} = \frac{\rho_\delta \pi\, d^3 \cdot V_{\tan}^2}{6 \cdot r} \tag{15}$$

where C_d = drag coefficient of the fuel drop, ρ_α = density of the air, V_{rad} = radial outward velocity of fuel drop, d = fuel drop diameter, ρ_δ = density of the liquid fuel drop, $V_{\tan}$ = tangential velocity of air and fuel drop and, r = radius of the swirl flow.

For small Reynolds Numbers and Stokesian flow,

$$C_d = 24/\text{Re} \tag{16}$$

and

$$\text{Re} = \rho_\alpha \cdot V_{\text{rad}} \cdot d/\eta \tag{17}$$

where Re = Reynolds number and η = air viscosity.

Therefore, by substitution,

$$\frac{24 \cdot \eta \cdot \rho_\alpha \cdot V_{\text{rad}}^2 \cdot \pi \cdot d^2}{\rho_\alpha \cdot V_{\text{rad}} \cdot d \cdot 8} = \frac{\rho_\delta \cdot \pi\, d^3 \cdot V_{\tan}^2}{6 \cdot r} \tag{18}$$

For fixed liquid and air properties and C_1 a constant,

$$V_{\text{rad}} = \frac{C_1 \cdot d^2 \cdot V_{\tan}^2}{r} \tag{19}$$

and

$$V_{\text{rad}} = C_1 d^2 G \tag{20}$$

where G = centrifugal acceleration.

APPENDIX 3

Fuel Droplet Scaling. From equation (19)

$$V_{\text{rad}} = \frac{C \cdot d^2 \cdot V_{\tan}^2}{r} = \frac{dr}{dt} \tag{21}$$

$$2rdr = C_1 \cdot V_{\tan}^2 \cdot d^2 \cdot dt \cdot 2 \tag{22}$$

From Godsave [29], for droplet evaporation,

$$d^2 = do^2 - C_2 t \tag{23}$$

where C_2 = constant, d = droplet diameter at time t and, do = droplet diameter at time zero.

Substituting for droplet diameter in the trajectory equation (22), the droplet diameter in the evaporation equation (23), and then integrating

$$\int_{ro}^{r} 2rdr = C_1 \cdot V_{\tan}^2 \int_0^t (do^2 - C_2 t) \cdot dt \cdot 2 \tag{24}$$

where ro = inner radius of air swirl and is the location of the fuel droplet at time zero, r = radius of the air swirl at which the droplet is located at time t.

Therefore,

$$r^2 - ro^2 = C_3 \cdot V_{\tan}^2 \left(do^2 \cdot t - \frac{C_2 t^2}{2}\right) \tag{25}$$

Fuel evaporation time must represent only a small proportion of the combustion time. Assuming t^2 is negligible.

$$r^2 - ro^2 = do^2 \cdot t \cdot C_3 \cdot V_{\tan}^2 \tag{26}$$

Equation (26) presents a relationship between time, scale, and droplet size. This applies to any scaling that can be examined. Assume a larger scale of combustor having the same pressure loss, and consider a droplet that has moved radially outward a fixed multiple of the inner radius, ro, and equal to $C_4 ro^2$ and $C_4 Ro^2$, where Ro and T refer to the larger scale of combustor:

$$C_4 ro^2 - ro^2 = do^2 \cdot t \cdot C_5 \tag{27}$$

$$C_4 Ro^2 - Ro^2 = Do^2 \cdot T \cdot C_5 \tag{28}$$

$$\frac{Ro^2}{ro^2} = \frac{Do^2 T}{do^2 t} \tag{29}$$

For mixing control, there must be geometric similarity of fuel droplet distribution in the two combustors, and assuming the same pressure drop,

$$\frac{T}{t} = \frac{Ro}{ro} \tag{30}$$

Substituting for time equation (30) into equation (29),

$$\frac{Ro^2}{ro^2} = \frac{Do^2}{do^2} \cdot \frac{Ro}{ro} \tag{31}$$

or

$$Do = \sqrt{\frac{Ro}{ro}} \cdot do \tag{32}$$

which is to say that, in a scaled up combustor, if the fuel droplet diameter is scaled up in proportion to the square root of the ratio of the scales, then the fuel droplet will centrifuge out in geometric similarity. For mixing control, permitting geometric scale up of the combustor as shown in Fig. 18, the air/fuel ratio at any geometrically similar point in space must also be the same in both combustors.

From the evaporation equation (23) for the two differing combustors,

$$d^2 = do^2 - C_2 t \tag{33}$$

$$D^2 = Do^2 - C_2 T \tag{34}$$

Substituting for Do from equation (32) and T from equation (30)

$$D^2 = \frac{Ro}{ro} \cdot do^2 - C_2 \cdot t \cdot \frac{Ro}{ro} \tag{35}$$

Therefore,

$$D^2 = \frac{Ro}{ro} \cdot d^2 \tag{36}$$

Downloaded 01 Jun 2010 to 171.66.16.59. Redistribution subject to ASME license or copyright; see http://www.asme.org/terms/Terms_Use.cfm

$$D = \sqrt{\frac{Ro}{ro}} \cdot d \tag{37}$$

and from equation (32),

$$\frac{Do}{do} = \sqrt{\frac{Ro}{ro}} = \frac{D}{d} \tag{38}$$

which is to say that, in a scaled up combustor, with the droplet scaled up in proportion to the square root of the ratio of the combustor dimensions, the droplet size will be reduced by evaporation but maintained in similar scale proportions at any geometrically similar point in space.

Assuming the same overall air/fuel ratio and the same combustor pressure loss, then the number of fuel droplets, n and N, for the combustor scales ro and Ro respectively, is given by

$$NDo^3 = \left(\frac{Ro}{ro}\right)^2 \cdot n \cdot do^3 \tag{39}$$

The ratio of the air/fuel ratios for the two combustors, denoted by $(A/F)_r$, at a geometrically similar point in space is

$$(A/F)_r = \frac{Ro^2}{N \cdot D^3} \cdot \frac{n \cdot d^3}{ro^2} \tag{40}$$

Substituting for N,

$$(A/F)_r = \frac{Ro^2}{ro^2} \cdot \frac{n \cdot d^3}{D^3} \cdot \frac{ro^2}{Ro^2} \cdot \frac{D^3}{nd^3} = 1 \tag{41}$$

which is to say that the air/fuel ratio, at any geometrically similar point in space, is equal for the two differing scales of combustor, when the droplet sizes are initially in proportion to the square root of the ratio of the combustor dimensions. In which case, the combustors are mixing controlled and in scale.

Downloaded 01 Jun 2010 to 171.66.16.59. Redistribution subject to ASME license or copyright; see http://www.asme.org/terms/Terms_Use.cfm

W. S. Blazowski
Exxon Research and Engineering Company, Linden, NJ

A. F. Sarofim
J. C. Keck
Massachusetts Institute of Technology, Cambridge, MA

The Interrelationship between Soot and Fuel NO_x Control in Gas Turbine Combustors

The decreased hydrogen content of future fuels will lead to increased formation of soot, while increased organically bound nitrogen in the fuel can result in excessive NO_x emission. Control concepts for these two problems are in conflict: prevention of soot requires leaner operation while control of emissions from fuel nitrogen requires fuel-rich operation. However, recent results of two DOE research programs point to both processes having a major dependence on "hydrocarbon breakthrough." Control of both fuel nitrogen conversion and soot formation can be achieved by primary zone operation at equivalence ratios just below that for hydrocarbon breakthrough. This paper reviews the evidence for the importance of hydrocarbon breakthrough, explains our current understanding of why hydrocarbon breakthrough is important, and offers suggestions of how these results might be applied.

Introduction

With increased emphasis on the utilization of U.S. energy resources for national self-reliance, alternative (synthetic) fuels are expected to play a major role in future energy developments. Future electric power generation with combined cycle gas turbines can make a major contribution to national energy goals if these systems could be made to accept synthetic liquid fuels having minimum upgrading [1–3]. Development of such fuel-flexible gas turbines will encourage the utilization of synthetic fuels as they enter the marketplace, have major impact on future conservation of petroleum supplies, and reduce the cost of power production.

Characteristics of the basic feedstocks from which future liquid fuels for gas turbines will be made are significantly different from typical petroleum properties. Liquid synfuels, especially those derived from coal, are likely to be more aromatic and have low hydrogen content. In the combustion system, these characteristics can be expected to promote the formation of soot. This can result in decreased combustor life due to enhanced flame radiation, increased smoke or visibility of the exhaust plume, increased emission of particulate material, and increased deposit forming tendency. Consequently, it is imperative that the process of soot formation within the combustion system be controlled.

Another significant difference between conventional petroleum and synthetic fuels is nitrogen content. Originally-bound nitrogen is effectively converted to NO_x[1] in conventional combustion systems. NO_x is also formed thermally by fixation of N_2 and O_2 from the air which participates in the combustion process but, for high nitrogen fuels such as synthetics with minimum upgrading, the NO_x due to fuel nitrogen is usually the dominant contribution. While existing stationary gas turbine standards make some allowance for fuel NO_x contributions [4], conventional combustors would not be capable of meeting the limitations if high nitrogen synthetic fuels are employed. The extent of fuel nitrogen conversion to NO_x must be reduced.

It is well known that soot production is reduced by operating combustion systems leaner (i.e., with more excess air) in the soot formation zone. In premixed systems or other processes not significantly influenced by droplet burning, the equivalence ratio[2] at which soot begins to form is greater than 1.0. Since the gas turbine combustion system operates with a low overall equivalence ratio ($\phi \sim 0.3$) it would seem that soot-free operation is routinely achievable. Unfortunately, stabilization of the combustion process requires a portion of the combustor, the primary zone, to be operated at stoichiometric or fuel rich mixture ratios. Further, reduction of fuel nitrogen-to-NO_x conversion requires fuel-rich operation (i.e., $\phi > 1.0$) in the first stage of the combustion process. Consequently, a working knowledge of the interrelationships between the soot formation and fuel nitrogen conversion processes during fuel-rich operation is vital to the development of future combustion systems capable of utilizing the lower hydrogen, higher nitrogen fuels of the future.

This paper presents research results of two organizations conducting independent programs for the U.S. Department of Energy which together provide important practical insight into the interrelationships between the soot formation and fuel nitrogen conversion problems. It has been found that both processes have a major dependence on the presence of hydrocarbons in the combustion process. The sooting limit corresponds to mixture conditions at which hydrocarbons are first observed in the first stage combustion products (the hydrocarbon breakthrough point) and the minimum fuel nitrogen conversion to NO_x occurs at the highest fuel-air ratio prior to the hydrocarbon breakthrough point. Strategies to prevent both soot formation and fuel nitrogen conversion should account for these important phenomena and control concepts might be based on this information.

[1] NO_x is the general symbol which represents the sum of NO and NO_2 emission from a source.

Contributed by the Gas Turbine Division and presented at the Gas Turbine Conference and Products Show, New Orleans, La., March 10–13, 1980 of THE AMERICAN SOCIETY OF MECHANICAL ENGINEERS. Manuscript received at ASME Headquarter December 13, 1979. Paper No. 80-GT-76.

[2] Equivalence ratio, ϕ, is the actual fuel-air ratio divided by the stoichiometrically correct fuel-air ratio. Values less than one correspond to lean operation while values greater than one indicate fuel-rich operation.

Copyright © 1981 by ASME
Downloaded 01 Jun 2010 to 171.66.16.59. Redistribution subject to ASME license or copyright; see http://www.asme.org/terms/Terms_Use.cfm

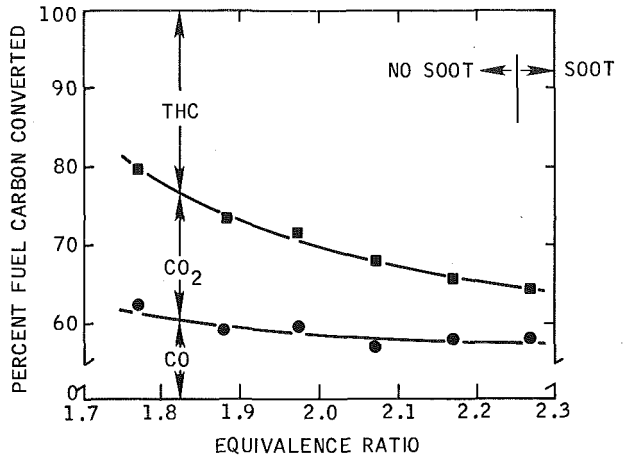

Fig. 1(*a*) Fraction of fuel carbon converted to each exhaust product for ethylene-air combustion [19]

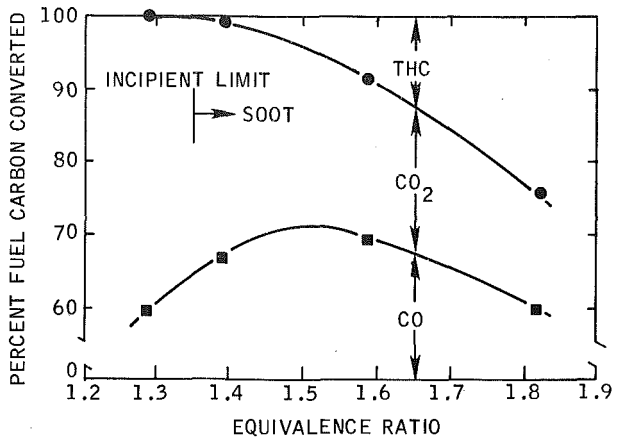

Fig. 1(*b*) Fraction of fuel carbon converted to each exhaust product for toluene-air combustion (air mass flow = 112.5 gm/min, inlet temperature = 300 °C) [19]

The balance of this paper is organized into three major sections. The first addresses current evidence that hydrocarbon breakthrough is critical to the soot formation and fuel nitrogen conversion processes. In general, the background work on soot formation was performed at Exxon Research while the fuel nitrogen conversion results were obtained at MIT. The second major section provides our current understanding of why hydrocarbon breakthrough is important to these processes. The third provides some insight on how these results might be applied in a gas turbine system. Use of the information could take the form of guidance for design, explanation of available results, or development of control concepts.

Evidence of Hydrocarbon Importance

Soot Formation. While both carbon formation and carbon consumption processes occur in continuous combustion systems, the latter are very much slower. The optimum approach for preventing hardware distress and avoiding serious environmental consequences is to develop combustion systems which avoid carbon formation while satisfying other system requirements (efficiency, gaseous emissions, hardware reliability, etc.).

The predominance of fundamental research activity has involved laminar premixed flames. Street and Thomas' work published in 1955 is extremely thorough in experimental detail and breadth of hydrocarbons examined [5]; it has become the classic paper in the field. Other publications are references [6–17]. Equilibrium calculations indicate that soot should not be present at fuel-air mixture conditions where the oxygen-to-carbon atomic ratio (O/C) is greater than one. That is, the general chemical equation:

$$CxHy + \frac{x}{2}O_2 \rightarrow xCO + \frac{y}{2}H_2 \qquad (1)$$

should define a soot formation threshold. However, all experimental results have shown soot formation at O/C substantially in excess of unity, thus proving that the process is kinetically controlled.

The most relevant work to the present interest—soot formation in gas turbine systems—has been recently conducted using a highly-backmixed, experimental combustor [18–20]. As noted above, most previous soot formation research had employed laminar premixed flames. The laminar aerodynamic situation is very different than that in the soot-forming region of continuous combustion devices like the gas turbine where combustion products are usually backmixed with incoming fuel and air in a strong, highly-turbulent recirculation zone. Therefore, soot formation experiments conducted in a highly-backmixed combustion environment are the most relevant here.

The highly backmixed combustion studies of soot formation have been conducted using the Jet Stirred Combustor. The device used was a modification of the Longwell-Weiss reactor [21] with hemispherical geometry. The reaction zone was 5.08 cm in diameter and had 25 radial exhaust ports of 3.2 mm dia. Combustion experiments were conducted at atmospheric pressure with a range of residence times of 0.6 to 4 ms. Fuel and air were metered separately, preheated to the desired inlet temperature prior to injection (liquid fuels are prevaporized), and injected into the reactor zone through forty small holes or sonic jets which stir the reactor contents and produce a mixture of essentially uniform temperature and composition. Measured quantities included gaseous species concentrations (CO, CO_2, THC[3], O_2), the incipient soot equivalence ratio, and soot production (mg/l). A complete description of the experiment can be found in references [18–20].

The previously reported Jet Stirred Combustor results [18–20] included an evaluation of the fuel-rich combustion and soot formation characteristics of a number of pure hydrocarbons. Groups of the hydrocarbons tested were found to behave similarly and three categories of hydrocarbons were defined The groupings were as follows:

Group 1	Group 2	Group 3
Ethylene	Toluene	1-methyl-naphthalene
Hexane	O-xylene	
Cyclohexane	M-xylene	
N-octane	P-xylene	
Iso-octane	Cumene	
1-octene	Tetralin	
Cyclo-octane	Dicyclopentadiene	
Decalin		

The first group produced large amounts of exhaust hydrocarbons (i.e., many percent based on equivalent flame ionization detector response to methane) without sooting and in no case was significant (i.e., measurable at the mg/l level) soot observed.

The second group produced measurable soot. For these fuels, the leanest mixture ratio at which soot is observed (the incipient soot limit) was found to correspond to the conditions at which significant concentrations of exhaust hydrocarbons were first detected (hydrocarbon breakthrough). In these cases, the measured hydrocarbon concentration was less than one percent at the incipient limit. Figure 1 compares the behavior of ethylene (from Group 1) and toluene (from Group 2). The illustration presents the portions of fuel carbon converted to CO, CO_2 and THC. Hydrocarbon concentrations are very significant at and even below the incipient soot limit in the case of ethylene combustion, but for toluene the soot limit corresponds to the hydrocarbon breakthrough equivalence ratio.

Another commonality in the second group is that the incipient soot limit of these fuels was about 1.4 and the amount of soot produced as fuel-air mixture ratio was increased beyond the incipient sooting limit was similar (within a factor of two) for all fuels in this group. 1-methyl-naphthalene was significantly different in this respect producing much higher soot quantities than those in the second category

[3] THC = Total hydrocarbons present in the exhaust products; expressed in volumetric concentration as if their composition was entirely methane.

Downloaded 01 Jun 2010 to 171.66.16.59. Redistribution subject to ASME license or copyright; see http://www.asme.org/terms/Terms_Use.cfm

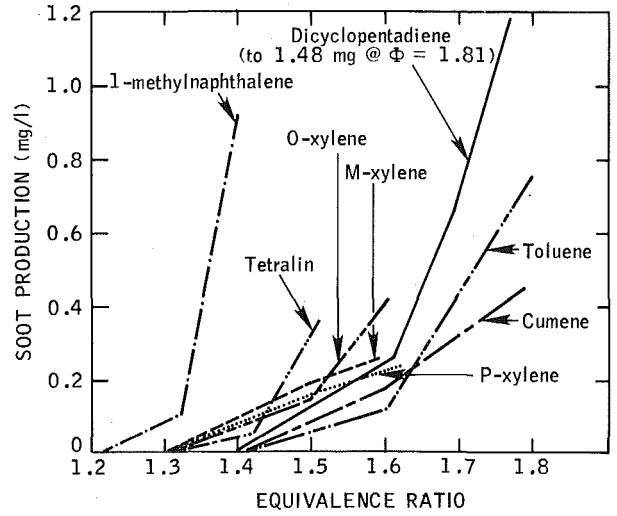

Fig. 2 Soot production for various pure hydrocarbons at 300°C inlet temperature and 112.5 gms/min air flow [19]

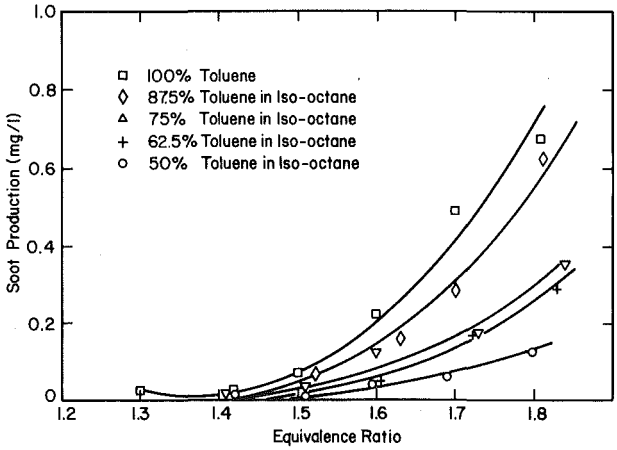

Fig. 3 Soot production versus equivalence ratio for toluene and toluene/iso-octane blends [20]

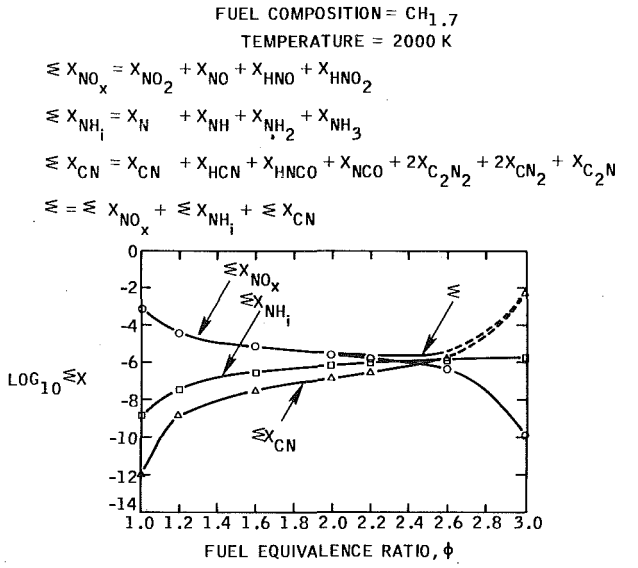

Fig. 4 Equilibrium fixed nitrogen species mole fractions as a function of fuel equivalence ratio. Fuel composition = $CH_{1.7}$, T = 2000 K [22]

Table 1 Combustion product hydrocarbon concentrations in jet stirred combustor experiments

	At Incipient Soot Limit		At Blow-out Point	
	ϕ	% HC	ϕ	% HC
100% Toluene	1.39	0.2	–	–
87.5% Toluene/ 12.5% Isooctane	1.41	0.15	–	–
75% Toluene/ 25% Isooctane	1.40	1.21	–	–
62.5% Toluene/ 37.5% Isooctane	1.49	0.82	–	–
50% Toluene/ 50% Isooctane	1.5	2.4	–	–
25% Toluene/ 75% Isooctane	–	–	1.61	7.12
10% Toluene/ 90% Isooctane	–	–	1.51	7.0

and having an even lower soot formation equivalence ratio (see Fig. 2). Consequently, this double-ring aromatic represents a third category of hydrocarbon soot forming characteristic.

Blends of iso-octane and toluene were tested to determine the behavior of a two-component mixture with Group 1 and Group 2 hydrocarbons. Results are shown in Fig. 3. Mixtures with 50 or more percent toluene produced soot while a 25 percent toluene blend did not. Clearly, for the mixtures which did soot, increases in the volume percent toluene result in increased soot production at all equivalence ratios.

It was also determined that with less toluene in the blend, the concentration of hydrocarbons at the incipient limit tended to be low for the highly sooting blends but increased sharply for those blends which did not soot (see Table 1). For example, with 50 percent toluene, the hydrocarbon concentration was 2.4 percent at the incipient soot limit, while with 100 percent toluene this value was 0.2 percent. These results indicate a combination of Group 1 and 2 behaviors and imply that a combination of the analytical descriptions for toluene and iso-octane might be a reasonable approach for prediction of the sooting characteristics of such fuel blends.

Taken together, these results allow us to develop the following conclusions concerning soot formation in gas turbines utilizing synthetic liquids:

- Future synfuels having low H-content due to high concentrations of single ring (Group 2) and double ring (Group 3) aromatics are capable of producing substantial quantities of soot.
- The amount of soot produced will be related to the amount of Group 2 and (especially) Group 3 compounds present in the fuel.
- Most importantly, in the case of highly aromatic fuels, the soot limit will correspond to the equivalence ratio at which hydrocarbons become a significant (~1 percent) combustion product.

As stated in the introductory section, the prevention of significant soot production should be accomplished in a combustion process which also minimizes fuel nitrogen conversion. The following subsection presents the evidence of the important influence of hydrocarbon breakthrough on this other process.

Fuel Nitrogen Conversion. It is well recognized that the production of nitric oxide by the combustion of fuels containing organically bound nitrogen can be suppressed by operating the first stage of the combustor fuel rich. The questions of what is the maximum attainable reduction in bound nitrogen conversion and what is the optimum first-stage equivalence ratio needed to achieve the maximum reduction are closely related to the presence of hydrocarbon species during the combustion process, that is, hydrocarbon breakthrough.

Consideration of the effect of increasing equivalence ratio on the *equilibrium* concentration of bound nitrogen species provides a measure of the constraints on the use of a staged combusion process to reduce NO_x emissions [22]. Representative calculations summarized in Fig. 4 for a flame temperature of 2000K and a fuel with an atomic hydrogen/carbon ratio of 1.7 show that increasing equivalence ratio decreases the concentration of nitrogen oxides (ΣX_{NO_x}) but increases that of amines (ΣX_{NHi}) and cyanides (X_{CN}). It is vital to design the first stage of the combustion process to minimize amines and cyanides as well as NO_x because, if formed, these species will al-

Downloaded 01 Jun 2010 to 171.66.16.59. Redistribution subject to ASME license or copyright; see http://www.asme.org/terms/Terms_Use.cfm

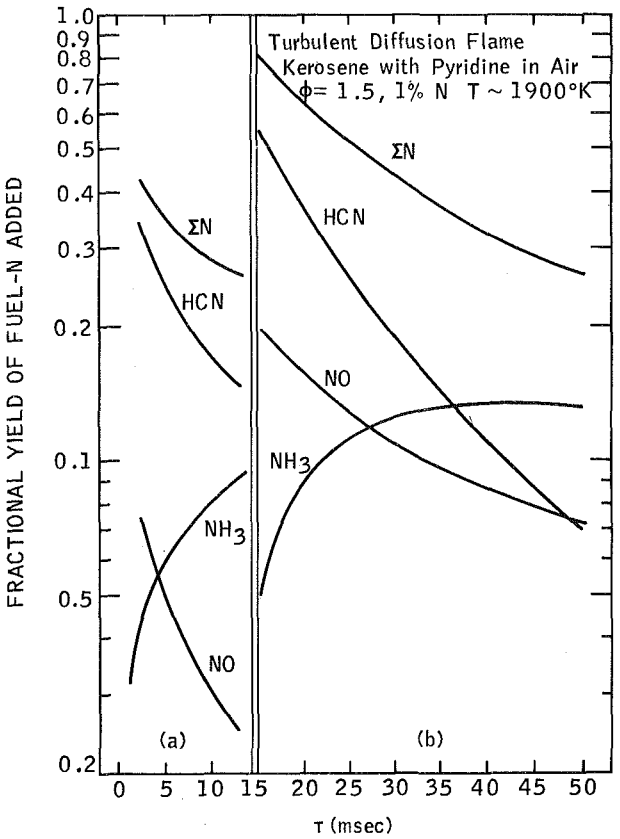

Fig. 5 Joint plot of laminar and turbulence diffusion flame data. (a) flat flame data for C_2H_4/O_2/He/Ar flame at $\varphi = 1.6$ with 2.5 percent N as NH_3. $T < 2120$ K (b) turbulent diffusion flame data for kerosene/air flame at $\varphi = 1.5$ with 1.0 percent N as pyridine. $T \sim 1900$ K [23]

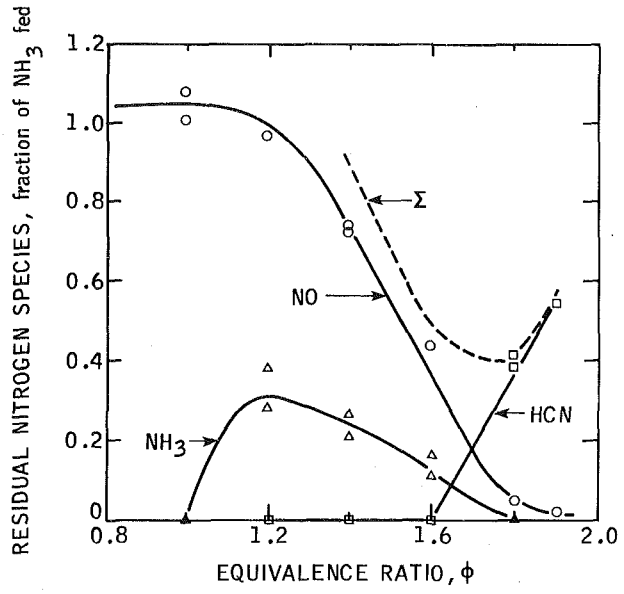

Fig. 6 Residual nitrogen species (dry basis) and temperature profiles as a function of fuel equivalence ratio, at 30 mm above the burner surface. C_2H_4/O_2/He flames doped with NH_3, $He/O_2 = 6.02$ [28]

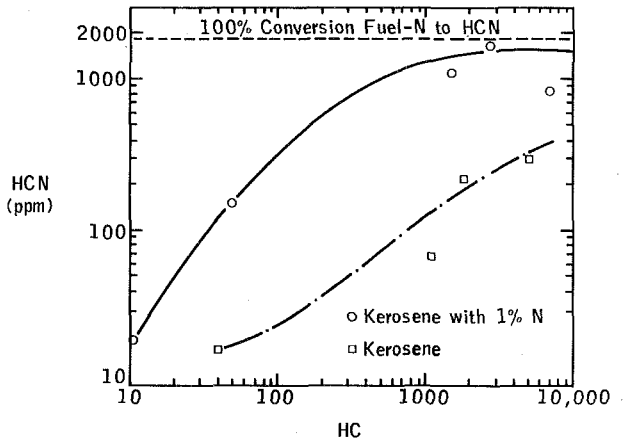

Fig. 7 HCN versus unburned hydrocarbons: $\varphi = 1.5$; $T_{inlet} = 600$ K; ⊙ Kerosene doped with Pyridine to 1 percent N by mass; ■ kerosene; $X/D = 5.0$ [23]

most completely convert to NO_x in the fuel lean second stage. The emission of total fixed or bound nitrogen ($\Sigma X_{NO_x} + \Sigma X_{NH_i} + \Sigma X_{CN}$) passes through a minimum at a ϕ of about 2.4.

The equilibrium concentration of bound nitrogen species at the minimum (slightly more than 1 ppm) is, however, not attained in practice. The factors which prevent the attainment of the equilibrium concentration are: (1) the relatively slow rate at which fuel nitrogen species are converted to the thermodynamically-stable and environmentally-preferred molecular nitrogen, (2) the interaction of hydrocarbon species with nitric oxide at higher equivalence ratios to form HCN which reacts even more slowly to N_2, thus providing an upper bound on the ϕ which can be used in practice, and (3) mixing constraints. Selected results from the program at MIT showing the importance of these three factors are presented below.

The kinetic constraints can be inferred from time-resolved measurement of HCN, NH_3, and NO obtained in the combustion products of a laminar flat flame of ethylene doped with ammonia (Fig. 5(*a*)) and the spray combustion of kerosene doped with pyridine (Fig. 5(*b*)). Several points need to be made. First, although the fuel nitrogen in the premixed flame was added to the flame as NH_3, most of the bound nitrogen at the first sampling point was in the form of HCN. It is only after the hydrocarbons decay that the ammonia concentration, that NH_3 to be found in the combustion products, begins to increase. Secondly, the rate of decay of the HCN and NO in the post flame gases shows the very slow rate of approach towards equilibrium. Finally, the behavior of the products of combustion for the pyridine-doped kerosene flame is qualitatively similar to that of the ethylene/NH_3 system, but the time frame is stretched due to the critical additional constraint of mixing in the spray flame.

Examining the effect of equivalence ratio on bound nitrogen species concentrations measured in the premixed flame (Fig. 6) suggests that the optimum value of ϕ is about 1.8. The difference between the experimentally observed ϕ for minimum fixed nitrogen and that calculated from equilibrium considerations (i.e., 1.8 versus 2.4) is attributable to the presence of hydrocarbons beyond $\phi = 1.8$ which allows substantial retention of fixed nitrogen as HCN. At these higher equivalence ratios HCN is by far the dominant species—the minima expresses a boundary where leaner operation is characterized by NO dominance and richer operation results in copious HCN. When at $\phi = 1.8$, this flame is still effective in consuming the initial fuel and no significant hydrocarbon concentrations are observed in the downstream portions of the flame system.

The equivalence ratio for minimum total fixed nitrogen is reduced to an even lower value in the spray flame where hydrocarbons persist at $\phi > 1.5$ due to unmixedness. The influence of hydrocarbons on the emission can be seen from the studies of reference [23] which concern the emissions from both kerosene and pyridine-doped kerosene flames. The values of HCN observed in the combustion products are plotted against the total hydrocarbon content (as measured by a flame ionization detector) in Fig. 7. It is clear that the levels of HCN for both doped and undoped fuels increased with increasing hydrocarbon content. Again it was found that the optimum ϕ for minimizing bound nitrogen emissions is determined by trade-offs between NO and HCN emissions; the optimum ϕ is close to the point at which hydrocarbons breakthrough and HCN shows a corresponding sharp increase at equivalence ratios beyond this point. For the kerosene spray combustor the ϕ for minimum emission of fixed nitrogen was in the range of 1.5.

Downloaded 01 Jun 2010 to 171.66.16.59. Redistribution subject to ASME license or copyright; see http://www.asme.org/terms/Terms_Use.cfm

Current Understanding

Soot Formation. Many mechanistic models for soot formation have been proposed and a number of references to these have been included. Generally, it is recognized that condensed ring aromatic hydrocarbons can produce soot via a different mechanism than do aliphatic hydrocarbons. A simplified mechanism following Graham, et al. [16,17] is shown in Fig. 8.

Aromatic hydrocarbons can produce soot via two mechanisms: (1) condensation of the aromatic rings into a graphite-like structure, or (2) breakup to small hydrocarbon fragments which then polymerize to form larger, hydrogen-deficient molecules which eventually nucleate and produce soot. Based on his shock tube studies of soot formation, Graham concludes that the condensation route is much faster than the fragmentation/polymerization route. Further, he has proposed that the mechanism by which an aromatic forms soot changes with temperature, below 1800 K the condensation path is favored while above this temperature the fragmentation/polymerization route is followed.

While the aliphatic soot formation process also involves complex reactions of the polynuclear species [15], these influences are far less dominant than for the aromatics. Accordingly, this simple model shows aliphatics producing soot predominantly through the slower fragmentation/polymerization mechanism. As a result, these hydrocarbons do not form the quantities of soot produced by the aromatics. Indeed, during the fuel-rich combustion of a fuel blend composed of aromatics and aliphatics, the aromatic hydrocarbons would produce the major portion of soot. Combustion of the aliphatic portions of the fuel influence temperature and hydrocarbon fragment concentration but soot formation via fragmentation/polymerization is small relative to that of aromatics.

The experimental results are consistent with this model. It has been observed that soot formation with Group 2 fuels commences with the initial presence of hydrocarbons in the exhaust. If we assume that these breakthrough hydrocarbons maintain their aromatic character, this observation may reflect the fast kinetics of the ring-building or condensation reactions. On the other hand, the aromatic molecule may be an effective source of C_2H_2 and high concentrations of acetylene as fuel pyrolysis occurs may be responsible for extensive soot production. Further, the results for 1-methylnaphthalene indicate that a double-ring aromatic provides the most rapid soot formation of the hydrocarbons studied. This observation can also be viewed as consistent with either the ring building view (i.e., the first ring-joining has already occurred) or the polymerization mechanism (i.e., even higher amounts of C_2H_2 present in the pyrolysis zone).

Fuel Nitrogen Conversion. The importance of the reactions of NO and hydrocarbons to form HCN has long been recognized [24–26]. Two of the reactions cited for HCN formation from NO are

$$CH_3 + NO \rightarrow HCN + H_2O \qquad (3)$$

$$CH + NO \rightarrow HCN + OH$$

These radical fragments will be present during the pyrolysis of most hydrocarbons and the NO-hydrocarbon reaction is therefore expected to be less sensitive to hydrocarbon type than soot formation. More data are needed to establish the extent to which NO-hydrocarbon reaction may be affected by the fuel type.

The conclusions regarding the importance of THC concentrations previously drawn are reinforced by these mechanistic considerations and the message to the combustor designer continues to be to operate a combustor at conditions that minimize hydrocarbons breaking through with the combustion products, i.e., minimize the reactants responsible for soot and HCN formation.

Application of Findings

THC Importance. Acceptable gas turbine combustion performance using low hydrogen, high nitrogen content fuels will require a fuel-rich first stage which promotes conversion of fuel N to N_2 while preventing excessive soot formation. This paper proposes that the first stage be thought of as a well-stirred reactor—a zone which is sufficiently mixed to be nearly homogeneous in temperature and composition. The incoming fuel-air mixture is assumed to be instantaneously mixed with the combustion products and the entire reaction zone is represented by one set of composition/temperature conditions. Soot and fuel nitrogen conversion in this system can be viewed as the products of the reaction between these components in the "well stirred pot" at rates determined by the existing temperature conditions.

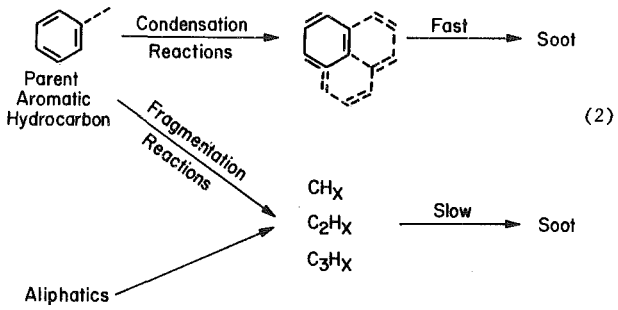

Fig. 8 Equation (2)

The distinction between the first stage operating as a plug flow reactor or as a stirred reactor is important. First, previous work has shown that the incipient soot formation limit in the stirred reactor configuration is richer than the plug flow case [27]. A further distinction is added through consideration of fuel nitrogen conversion. In the plug flow case, destruction of fuel nitrogen occurs where large concentrations of hydrocarbon fragments are present and formation of HCN can be extensive; low fixed nitrogen may be achieved by allowing the system to relax back towards equilibrium. On the other hand, at appropriate operating conditions the stirred reactor may allow fuel nitrogen destruction to occur at low hydrocarbon concentrations and the initial formation of HCN may be limited.

Soot will form in this well-stirred combustion zone if the initial fuel contains a substantial amount of single or double-ring aromatics and if the zone is operated in a manner which allows a significant concentration of hydrocarbons (unburned fuel fragments) to be present. Fuel nitrogen is minimized by operating the reaction zone as rich as possible without the presence of hydrocarbons. More oxidizing conditions allow the conversion of fuel N to NO_x to be more effective and the presence of hydrocarbons at richer operating conditions allows the formation of HCN in the first stage which will subsequently be oxidized to NO_x in the second, fuel-lean stage of the combustor. Consequently, these results imply that minimization of both NO_x and soot in gas turbines utilizing future fuels will require a staged combustion process designed for the richest possible operation without substantial hydrocarbon breakthrough. It is recommended that combustor designers utilize this information by analyzing THC concentrations within the fuel-rich first stage during combustor development testing.

The ability to operate fuel rich without soot formation is also influenced by the type of fuel being combusted (i.e., composition in terms of Group 1, 2, or 3). Lesser quantities of single-ring and double-ring compounds in the fuel will increase the incipient sooting ϕ and allow the THC concentration at the limit to increase. However, fuel nitrogen conversion is not likely to be as sensitive to fuel type—fixation of fuel nitrogen as HCN will coincide with the THC breakthrough regardless of the type of hydrocarbons present in the fuel. Consequently, the maximum operating equivalence ratio for fuels with a predominance of Group 1 hydrocarbons may be dictated more by considerations of fuel nitrogen conversion than soot formation.

A point which should be emphasized is that the JSC experiments on which these conclusions are based involves a premixed prevaporized system. The presence of fuel droplets in the first stage would be expected to seriously influence the results. Successful operation will require the pockets of fuel-rich mixture resulting from droplets in the first stage be avoided—otherwise the consequence of hydrocarbon breakthrough (soot formation and fixation of fuel nitrogen) will occur locally. Fuel injection, droplet-air mixing, and droplet vaporization must be accomplished in a manner which allows homogeneous con-

Downloaded 01 Jun 2010 to 171.66.16.59. Redistribution subject to ASME license or copyright; see http://www.asme.org/terms/Terms_Use.cfm

ditions approaching homogeneity to be achieved on a micro-scale within the first stage.

Finally, the second stage combustion process is also critical for achieving low levels of NO_x emission. Large quantities of thermal NO_x emission. Large quantities of thermal NO_x can be produced if the mixing process is too slow and allows regions of near-stoichiometric, high temperature reaction.

Control by THC or Radiative Characteristics. One important concern in the design of low NO_x combustion systems is the impact of load variation on operating characteristics. For example, a reduction in load causes a decrease in fuel-air ratio requirements and perhaps combustor inlet temperature. These changes can cause the system to operate in a manner substantially off the optimum operating point unless adjustments are made to key combustion parameters.

The evidence that THC is a critical indicator of optimum operation suggests that measurement of this parameter might be used to control conditions in the first stage. One can envision a flame ionization detector which monitors first stage gas composition to provide a signal proportional to first stage THC. This, in turn, could control air supplied to the first stage in a manner which assures optimum operation. In essence, this control scheme would attempt to have the combustor always operating at the "knee" of the THC versus equivalence ratio characteristic.

Alternative methods of monitoring THC which do not involve extraction of a physical sample might also be employed. Luminosity is a measure of soot formation but is more indicative of Group 2 and Group 3 hydrocarbon breakthrough than Group 1. It is therefore expected to be a useful measure of when THC breakthrough occurs but could overlook situations in which fuels with a low sooting potential are utilized. Alternatively, a spectroscopic analysis of flame emission or adsorption in a spectral region characteristic of hydrocarbons could be employed as the control signal.

Establishing the best method of sensing hydrocarbon breakthrough and controlling key combustor variables will require additional research and development. The appropriate THC concentration to use as a set point is not known and the ability to design first stage zones with controllable flows must be developed.

Conclusion

The effective use of future synthetic fuels in gas turbines will require the development of two-stage combustion systems which minimize both soot formation and the conversion of fuel-bound nitrogen to NO_x. Recent results show that incipient sooting limits for highly aromatic fuels correspond to mixture conditions at which hydrocarbons are first observed in the combustion products (the hydrocarbon breakthrough point) *and* that minimization of fuel nitrogen conversion requires operating at the highest fuel-air ratio prior to the hydrocarbon breakthrough point. This paper concludes that the first stage of an advanced combustion system should be operated as a fuel rich stirred reactor. The design of such a system must insure that hydrocarbons are not present in substantial quantities in the first stage and measurements of first stage THC could be an important part of future combustor development programs. This paper also concludes that some form of THC measurement (physical probe, emission, absorption, or luminosity) might be employed as an effective control to maintain optimum combustor performance over the entire range of engine operation.

Acknowledgment

This work was supported by the U.S. Department of Energy under contracts EC-77-C-03-1543 (at Exxon) and AER75-15916 (at MIT). Dr. J. Birkeland of DOE was the responsible Program Manager and Dr. J. Fischer of Argonne National Laboratory was the technical program monitor.

References

1 Cooper, V., and Duncan, R., "Baseload Reliability in a Combustion Turbine?," *EPRI Journal,* June 1978, pp. 17–21.

2 Longwell, J. P., "Synthetic Fuels and Combustion," 16th Symposium (International) on Combustion, 1976, pp. 1–15.

3 Pillsbury, P. W., Cohn, A., Mulik, P. R., Singh, P. P., and Stein, T. R., "Fuel Effects in Recent Combustion Turbine Burner Tests of Six Coal Liquids," ASME Paper 79-GT-137, 1979.

4 Dibelius, N. R., Ketterer, R. J., and Manning, G. B., "The Effect of Environmental Regulations on the General Electric Research and Development Program for Combustion Turbines Using Coal Derived Liquids," ASME Paper 79-GT-41, 1979.

5 Street, J. C., and Thomas, A., "Soot Formation in Premixed Flames," *Fuel,* Vol. 34, 1955, pp. 4–36.

6 Cullis, C. F., "Role of Acetylenic Species in Carbon Formation," *ACS Symposium Series,* Vol. 21, 1976, pp. 348–357.

7 Daniels, P. H., "Carbon Formation in Premixed Flames," *Combustion and Flame,* Vol. 4, 1960, pp. 45–49.

8 Fenimore, C. P., and Jones, G. W., "Comparative Yields of Soot from Premixed Hydrocarbon Flames," *Combustion and Flame,* Vol. 12, No. 3, 1968, pp. 196–200.

9 Fenimore, C. P., and Jones, G. W., "Coagulation of Soot to Smoke in Hydrocarbon Flames, *Combustion and Flame,* Vol. 13, No. 3, 1969, pp. 303–310.

10 Fennimore, C. P., Jones, G. W., and Moore, G. E., "Carbon Formation in Quenched Flat Flames at 1600°K," 6th Symposium (International) on Combustion, 1956, pp. 242–246.

11 Holderness, F. H., and MacFarlane, J. J., "Soot Formation in Rich Kerosene Flames at High Pressure," Paper No. 18, AGARD Conference Proceedings No. 125, *Atmospheric Pollution by Aircraft Engines,* 1973.

12 Homann, K. H., "Carbon Formation in Premixed Flames," *Combustion and Flame,* Vol. 11, 1967, pp. 265–287.

13 Howard, J. B., "On the Mechanism of Carbon Formation in Flames," 12th Symposium (International) on Combustion, 1968.

14 MacFarlane, J. J., Holderness, F. H., and Whiteher, F. S. E., "Soot Formation Rates in Premixed C_5 and C_6 Hydrocarbon-Air Flames at Pressure Up to 20 Atmospheres," *Combustion and Flame,* Vol. 8, 1964, pp. 215–229.

15 LaHaye, J., and Prado, G., "Formation of Carbon Particles from a Gas Phase: Nucleation Phenomenon," *Water, Air and Soil Pollution,* Vol. 3, 1974, pp. 473–481.

16 Graham, S. C., Homer, J. B., and Rosenfeld, J. L. J., "The Formation and Coagulation of Soot Aerosols Generated by the Pyrolysis of Aromatic Hydrocarbons," *Proceedings of the Royal Society of London,* A, Vol. 344, 1978.

17 Graham, S. C., Homer, J. B., and Rosenfeld, J. L. J., "The Formation and Coagulation of Soot Aerosols," International Shock Tube Symposium, 10th Proceedings, 1975.

18 Blazowski, W. S., Edelman, R. B., and Harsha, P. T., "Fundamental Characterization of Alternate Fuel Effects in Continuous Combustion Systems," First Annual Report, Contract EC-77-C-03-1543, Sept. 1978.

19 Blazowski, W. S., "Dependence of Soot Production on Fuel Structure in Backmixed Combustion," *Combustion Science and Technology,* to be published in 1979.

20 Blazowski, W. S., "Dependence of Soot Production on Fuel Blend Characteristics and Combustion Conditions," ASME Paper 79-GT-155, presented at 24th International Gas Turbine Conference, March 1979, to be published in the ASME JOURNAL OF ENGINEERING FOR POWER.

21 Longwell, J. P., and Weiss, M. A., "High Temperature Reaction Rates in Hydrocarbon Combustion," *Industrial Engineering Chemistry,* Vol. 47, No. 8, 1955, pp. 1634–1643.

22 Sarofim, A. F., Taylor, B. R., and Pohl, J. H., *AIChE Air Symposium Series, Air Pollution,* 1977.

23. Foster, D., Ph.D. Thesis—Mechanical Engineering, MIT, 1978 also to appear in a joint paper, "Investigation of Factors affecting NO_x formation in Nitrogen Containing Fuels."

24 Rees, Y., and Williams, G. H., *Advances in Free Radical Chemistry,* Vol. 3, 1968, pp. 199–230.

25 Myerson, A. L., 15th Symposium (International) on Combustion, 1974, Combustion Institute, p. 1085.

26 Haynes, B. S., *Progress in Astronautics and Aeronautics,* Vol. 62, 1977, pp. 359–395.

27 Wright, F. J., "The Formation of Carbon Under Well-Stirred Conditions," *12th Symposium (International) on Combustion,* The Combustion Institute, Pittsburgh, 1968, pp. 867–875.

28 Chon, H. W., m.a. thesis—Chemical Engineering, MIT, 1976.

Downloaded 01 Jun 2010 to 171.66.16.59. Redistribution subject to ASME license or copyright; see http://www.asme.org/terms/Terms_Use.cfm

D. P. Hoult
A. Ekchian
Massachusetts Institute of Technology, Cambridge, MA 02139

Soot Formation in a Turbulent Swirl Stabilized Laboratory Combustor

The effect of pressure and fuel composition on soot formation was studied using a high pressure, tubular laboratory burner with a swirl stabilized diffusion flame. A specially-designed water flushed probe was used to extract samples of soot and other combustion products for analysis. Measurements showed the expected increase of soot concentration with pressure only until a critical value of the Reynolds number was reached. After this point, no further increase of soot loading was observed with pressure rise. This behavior was found to be present when either kerosene or propane was used in the burner. At a suitably high Reynolds number, several fuels, closely related to JP-4, were tested in the burner. These fuel blends were constructed by adding cyclic compounds to the JP-4 so as to change its hydrogen-to-carbon ratio. It was found that the amount of soot formed scaled with this ratio, although the sooting effect of different blends with the same ratio were not identical.

Introduction

Particulate emissions from the gas turbine or the diesel engine have long been considered an aesthetic nuisance. With the recent realization of the carcinogenic and mutagenic potential of these pollutants, there has come about an urgent effort to limit their generation. However, the control of particulates is severely hampered by the fact that, in spite of extensive research, very little firm information is available on the kinetic scheme of soot formation in a typical combustion chamber [1]. In the past, experimental investigations aimed at developing a fundamental theory to explain the phenomenon of soot formation have been continuously frustrated by the complicated nature of both the chemistry and the fluid mechanics that are involved. A different approach, that may be used, is to identify critical parameters that affect the rate of soot formation and to develop predictive scaling laws that can be used to extrapolate available data to new situations without the need for fundamental kinetic considerations.

In this work, the objective was to study the effects of pressure and fuel composition on soot formation in a tubular burner with a swirl stabilized diffusion flame. The selection of these two parameters for consideration stems from the fact that gas turbine combustors are increasingly being called upon to operate at higher pressures and in the future may be required to operate with fuels of lower and lower hydrogen-to-carbon ratios [2].

Historically, there has been a significant amount of interest in the effect of pressure on soot formation in both diffusion and premixed flames. (For example see references [3–7].) The consensus is that, in general, soot production rates are directly proportional to pressure. Results that will be presented here indicate that, for the range of pressures studied, this trend does not continue indefinitely. Furthermore, if flow velocities are held constant, it is observed that a plateau is reached in soot generation, and there is no longer any change with increasing pressure. This effect was not observed in the work done by others such as Janota, et al. [3], Schirmer [4] and Toone [5]. The conclusions of this paper, although they represent about five years work, must be viewed as tentative, until documented with more experimental results.

This dichotomy could in part be due to the fact that it is difficult to change the pressure in a burner without affecting other important parameters. For example, Toone's [5] data show that the increased pressure not only increases mean soot levels leaving the combustor, but also alters the radial distribution of equivalence ratio and soot levels in the combustor. This could be indicative of a change in the injector spray pattern, the quality of atomization, or both. In fact, Toone [5] shows further that only slight changes in the cone angle, of the fuel injector, can have a significant influence on particulate levels in the exhaust. However, to be conclusive, more tests are needed which achieve the same Reynolds numbers, through independent variations in size, pressure level, or flow velocity.

In the same vein, it should be noted that work done by MacFarlane, et al. [6] shows that, even in their relatively simple combustor, pressure increase significantly alters the temperature distribution in the flame. It may be important, therefore, that before the effect of emissions from different types of flames is scaled, the effect of pressure on flame structure should be examined.

On the other hand it is heartening that some data, presented by Kadota, et al. [8] on single droplet combustion, show the same kind of plateau as was observed in the more complex flame structure discussed here. The results of MacFarlane, et al. [6] also imply a similar kind of effect for certain stoichiometries where pressure rise does not increase the amount of soot observed after a certain critical pressure is reached. As they suggest "... further increase in pressure cannot continue to produce ... (an) increase in soot formation ..., since the required amount of unoxidized carbon is just not available. For a given mixture strength therefore, soot formation ... can be expected to level off at some maximum value" [6].

The fuel compositions considered here suggest that the propensity of a hydrocarbon fuel to form soot is inversely proportional to the hydrogen-to-carbon ratio. Slight differences in soot emissions are also caused by using fuels with the same hydrogen-to-carbon ratios, but different chemical compositions. This implies that this ratio is not the sole scaling factor involved in using different fuels, and that a more

Contributed by the Gas Turbine Division and presented at the Gas Turbine Conference and Products Show, New Orleans, La., March 10–13, 1980 of THE AMERICAN SOCIETY OF MECHANICAL ENGINEERS. Manuscript received at ASME Headquarters December 13, 1979. Paper No. 80-GT-77.

Copyright © 1981 by ASME
Downloaded 01 Jun 2010 to 171.66.16.59. Redistribution subject to ASME license or copyright; see http://www.asme.org/terms/Terms_Use.cfm

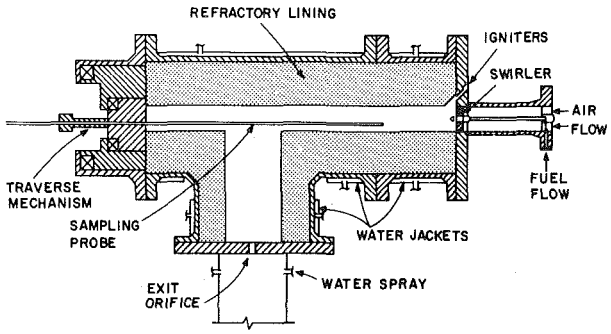

Fig. 1 Schematic cross section of high pressure burner

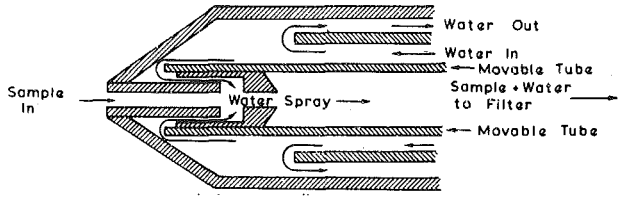

Fig. 2 Schematic of the tip of the cooled, water-flushed soot sampling probe

fundamental explanation may be necessary. As Schalla and MacDonald [9] suggest, the relative strengths of the carbon-to-hydrogen and carbon-to-carbon bonds may have to be accounted for in the scaling. It was felt that the spread in the results observed here was not large enough to warrant that investigation.

Description of Experimental Apparatus

A schematic of the continuous flow combustor used in this experiment is shown in Fig. 1. The burner combustion zone, which has a 7.6 cm i. d., is lined with refractory material to minimize heat loss. Combustion air enters through 45 deg swirler vanes which establish a recirculating flow field that stabilizes the combustion process. A fuel injection nozzle is located in the plane of the swirlers, and is supplied with fuel through aerodynamically streamlined struts positioned some three diameters upstream of this plane. The mass flow rate is controlled by means of a sonic orifice at the exit of the burner which also allows the burner pressure to be regulated up to about seven atmospheres.

Soot samples were collected from the burner for analysis by means of a specially designed, water flushed probe [10]. The probe was protected from the harsh environment in the burner by means of a water jacket. Some of the cooling water was allowed to enter the sample tube, at a controlled rate, so as to quench reactions in the exhaust gas sample and to prevent the probe from becoming blocked by soot deposits. Figure 2 shows a cross section of the tip of the probe.

The soot generated in the burner was separated from the mixture of exhaust gas and water flowing out of the probe by means of preweighed fiberglass filters. These filters were then desiccated and weighed to determine the amount of soot collected on them. Since the mass flow rate of combustion gases through the probe was measured independently, it was thus possible to calculate the concentration of soot inside the burner at the location of the tip of the probe. In separating the unburned hydrocarbons from the solid, carbonacious soot, a chemical separation process was used, as described in [10].

The composition of the gas phase of the combustion products sampled by the probe was also determined. These measurements were used to calculate the local stoichiometry at the point of sampling [11]. When these gas samples were taken, the flush water was temporarily turned off, but small amounts of leakage prevented reliable measurements of water vapor concentration from being made.

Experimental Results

In the design of this experiment, careful attention was paid to the aerodynamic detail of the geometry upstream of the nozzle, so as to maintain an axisymmetric flow field in the combustor. It is recognized that upstream nonuniformities can cause large variations in the distribution of combustion products in the burner [12]. Consequently, prior to studying the effects of scaling parameters on soot formation, the distribution of both the stoichiometry and the soot concentration in the burner was investigated. Figs. 3–5, which represent data collected at various axial locations, indicate that the distributions of these quantities are axisymmetric. In fact, at a distance of four burner diameters from the nozzle, the soot concentration is uniform across a cross-sectional plane.

In this burner the dependence of soot production on pressure, and consequently Reynolds number, was investigated using two different fuels [13]. The burner was first run at a fixed overall stochiometry of 1.25 with kerosene as a fuel. Its upstream and downstream geometries were held fixed, while the pressure was changed systematically by changing the size of the sonic orifice at the burner exit. The variation of the peak value of the soot concentration in the burner due to the change in this parameter was then monitored using the water quenched probe. The results in Fig. 6 suggest that the increase in soot production with Reynolds number, and pressure, reaches a plateau after which no further increase is recorded. Each plotted point is the average of three to six measurements and the accuracy is estimated at ±10 percent. Three different atomizing injectors had to be used in this experiment to cover the range of fuel flow rates that was required.

To eliminate the effect of changing injectors, the same experiment was repeated using propane. In this case, fuel was delivered in the form of a vapor jet, coaxial with the centerline of the burner, to the same location as was the liquid fuel in the previous experiment. The geometry of the burner was not altered. The results, shown in Fig. 7, indicate that soot production increases with Reynolds number (or pressure) until it levels off at a certain Reynolds number on the order of 15,000. As was observed in the previous case, these results imply an absence of pressure scaling of peak soot loading. All the remaining figures that will be presented here deal with measurements made at Reynolds numbers high enough to be in the range where the peak amount of soot is independent of Reynolds number. Tests carried out by the firm of Joseph Lucas, Burmley, England, suggest that over a considerable pressure range the cone angle was unaffected by pressure—i.e., the air flow dominates the fuel distribution process [14]. We believe that a similar result is valid for our rig.

In Figs. 6 and 7, the variation of the maximum concentrations of soot is assumed to be indicative of soot production in the entire burner. Figures 8 and 9 show that the axial gradients in soot concentration, that are obtained using four different fuels, are of similar shape. Within the accuracy of the data, the increase in soot levels to the peak values, at about 2.5 burner diameters, and the subsequent decay have essentially the same shape for the different fuels. This behavior and the symmetry of the soot distribution in the cross-sectional plane indicate that peak soot loading is in fact a representative quantity. However, it is clear the soot production is affected by the composition of the fuel that is used.

It is commonly believed that the hydrogen to carbon ratio is a good way to scale the amount of soot formed from different fuels. Measurements of the peak soot levels were made, in this burner, using different blends of fuels containing various percentages of hydrogen [13]. These measurements, shown in Fig. 10, support this belief.

Discussion of Results

A number of important nondimensional parameters are known to affect soot production in a burner of this type. Reynolds number, which was one of the parameters that was considered here, is known to be important in determining the turbulent motions in nonreacting flows. When the Reynolds number of a flow is high enough, the large scale turbulent mixing processes no longer depend on viscosity. That is, the turbulent diffusivity for the large scale eddies is Reynolds number independent. Also, it should be noted that, for pipe flows with no reactions, the friction factor on the wall is constant after a Reynolds number of about 20,000.

Downloaded 01 Jun 2010 to 171.66.16.59. Redistribution subject to ASME license or copyright; see http://www.asme.org/terms/Terms_Use.cfm

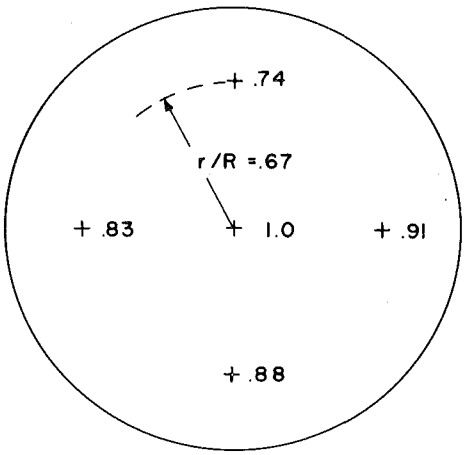

FUEL : JETA
ϕ = .8
Re = 17, 450
Z/D = 2.5

SOOT LOADINGS
NORMALIZED:
1.0 = 1850 mg/Sm^3
R = 3.8 cm

Fig. 3 Distribution of soot loading at a position 2.5 diameters downstream of injector, an axial location of peak soot loading

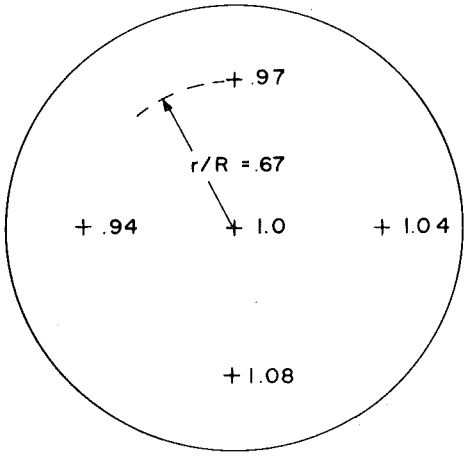

FUEL : JETA
ϕ = .8
Re = 17, 450
Z/D = 4.0

SOOT LOADINGS
NORMALIZED :
1.0 = 1650 mg / Sm^3
R = 3.8 cm

Fig. 4 Distribution of soot loading 4.0 diameters downstream of injector

In a diffusion flame burner, the Reynolds number can have an important affect in determining the rate of mixing of the fuel and air. An estimate of the ratio of the reaction time to this flow time (or mixing time) can be made for the operating conditions used here. Reaction times of one millisecond to reach peak soot concentration are reported by Prado [1] for a laminar burner at 20 torr. It can be assumed that soot reaction rates scale inversely with pressure, as does the flame thickness. This assumption is based on the fact that the soot seems to be formed at the same position in a laminar flame independent of pressure [1]. Using this estimate, the ratio of flow time to reaction time is calculated:

$$\tau = \frac{\text{flow time}}{\text{reaction time}} = \frac{1}{10^{-3}\,\text{s}} \times \frac{760\ \text{mmHg} \times \text{atm} \times D}{20\ \text{mmHg} \times U} = 10^3$$

here D is the burner diameter, while U is a typical gas velocity. This indicates that the flow time is much longer than the reaction time.

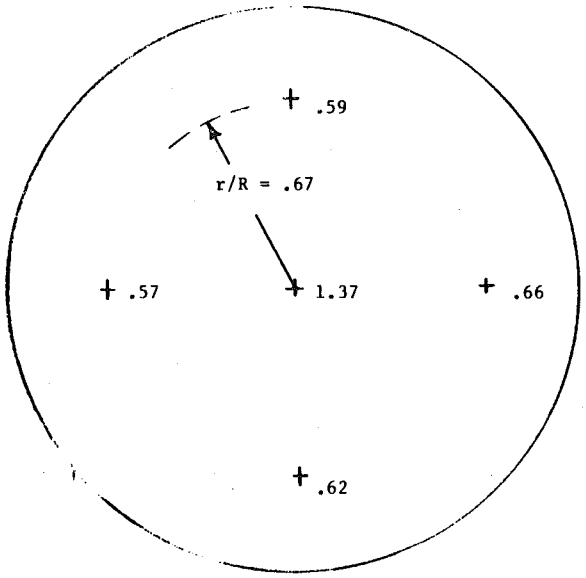

Fuel: Jet A
$\phi_{overall}$ = .8
Re = 17,450

R = 3.8 cm
Z/D = 1

Fig. 5 Distribution of soot loading one diameter downstream of injector

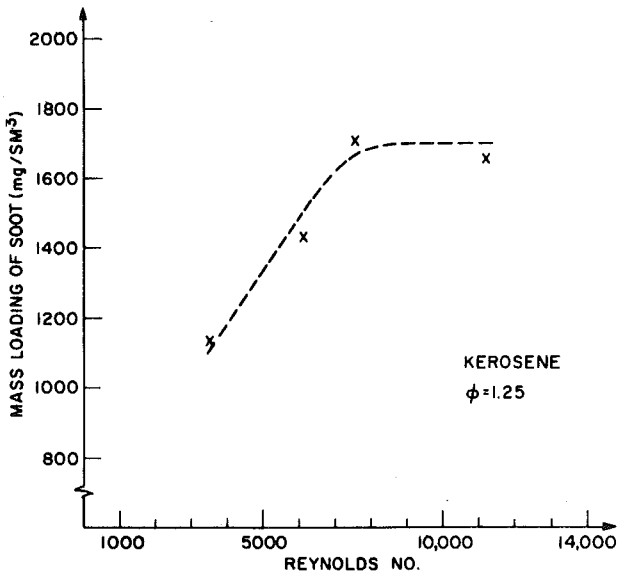

Fig. 6 Effect of Reynolds number or pressure on the peak soot concentration. Kerosene/air, equivalence ratio of 1.25, atomizing pressure

This supports the fact that the turbulent mixing process controls the amount of soot formed. Hence, there should be a Reynolds number scaling of soot production; but, in light of the previous discussion, it is feasible that soot levels do not increase indefinitely. It should be emphasized that the Reynolds number data would have been more complete if the variation of this parameter was achieved by changing either the flow rate or the pressure. In these experiments the variation was achieved solely by changing the pressure.

Fuel properties are more difficult to scale. Different parts of the *combustion process may have many reactions, and different fuels may* have different reaction schemes. However, the suggested mass ratio

Downloaded 01 Jun 2010 to 171.66.16.59. Redistribution subject to ASME license or copyright; see http://www.asme.org/terms/Terms_Use.cfm

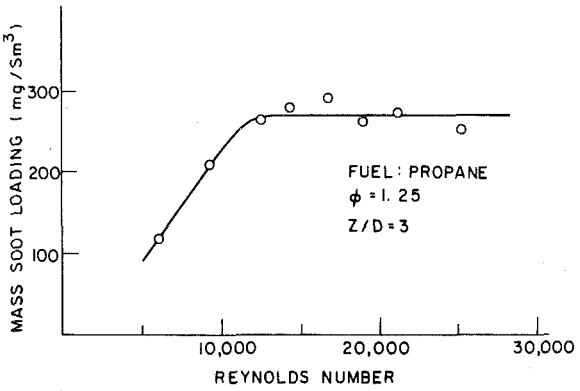

Fig. 7 Effect of Reynolds number on peak soot concentration from the combustion of propane

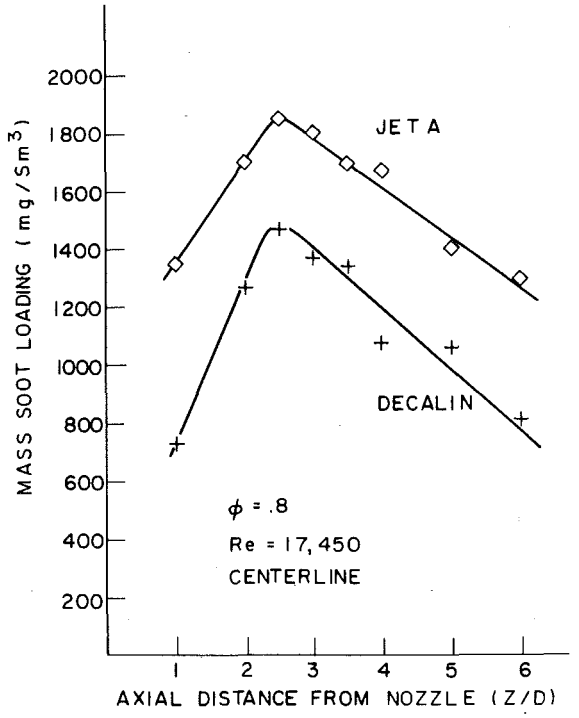

Fig. 8 Effect of fuel composition (jet A and decalin) on the axial profiles of soot concentration

of hydrogen to carbon in the fuel seems to be an effective global scaling factor.

Other nondimensional scaling factors that can be considered are equivalence ratio and swirl number. The effects of these two parameters were not studied here. Equivalence ratio was kept constant in any given experiment, while swirl number (for definition of swirl number see reference [15]) was typically kept constant at 0.8. The swirl number defines the size of the recirculation zone in the burner downstream of the swirler vanes.

If the parameters studied here or suggested as important are confirmed to be the critical scaling parameters for these types of combustors, possibilities for practical applications of these results seem important. For example, it may be possible to predict the amount of soot formed one or two diameters downstream of the swirler in a full scale engine, by studying an appropriately scaled swirler and injector.

References

1 Lahaye, J., and Prado, G., "Mechanisms of Carbon Black Formation," *Chemistry and Physics of Carbon,* Ed., P. Walker and P. Thrower, *14,* 1978, pp. 167–294.

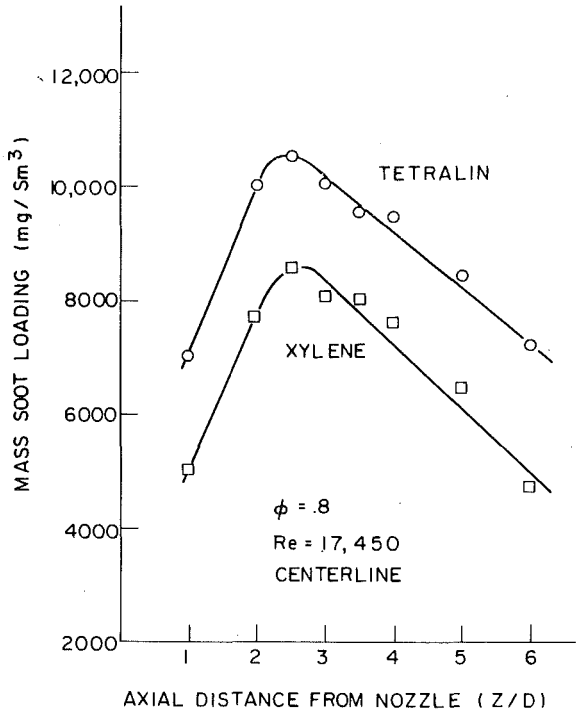

Fig. 9 Effect of fuel composition (tetralin and xylene) on axial profiles of soot concentration

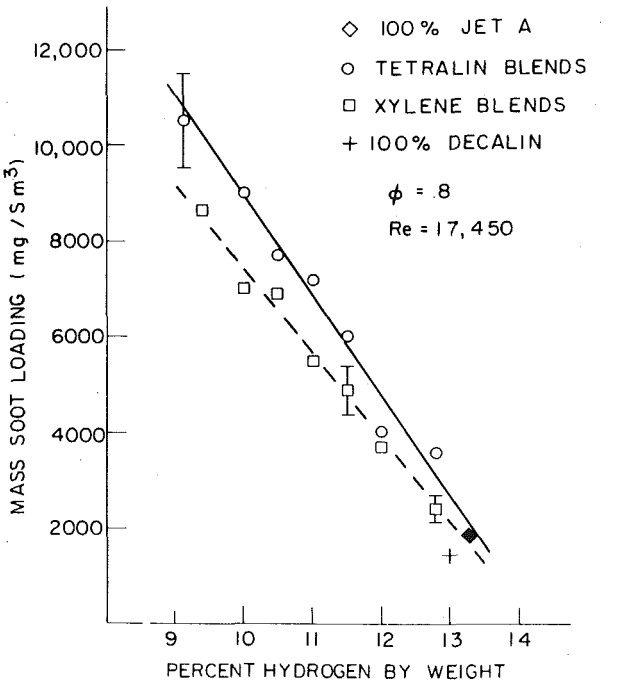

Fig. 10 Variation of peak soot loading as a function of the percent of hydrogen in the fuel

2 Longwell, J., "Jet Aircraft Hydrocarbon Fuels Technology," A Workshop held at the Lewis Research Center, Cleveland, Ohio. NASA Conference Publications 2033, 1978.

3 Janota, M. S., Crookes, R. J., Daie, S. J. Nazha, M. A. A., and Sodha, M., "Soot and Gaseous Pollutant Formation in a Burning Fuel Spray in Relation to Pressure and Air/Fuel Ratio," *Journal of the Institute of Fuel,* Vol. 50, No. 402, Mar. 1977.

4 Schirmer, R. M., *Effect of Fuel Composition on Particulate Emissions from Gas Turbine Engines,* Eds. W. Cornelius and W. G. Agnew, Plenum Press, N. Y. 1972, pp. 189–210.

5 Toone, B., "A Review of Aero Engine Smoke Emission," *Combustion in Advanced Gas Turbine Systems,* Ed. I. E. Smith, Pergamon Press, London, 1968, p. 271–296.

6 MacFarlane, J. J., Holderness, F. H., and Whitcher, F. S. E., "Soot

Downloaded 01 Jun 2010 to 171.66.16.59. Redistribution subject to ASME license or copyright; see http://www.asme.org/terms/Terms_Use.cfm

Formation Rates in Premixed C_5 and C_6 Hydrocarbon—Air-Flames at Pressures up to 20 Atmospheres," *Combustion and Flame,* Vol. 8, 1964, pp. 215–229.

7 Milberg, M. E., "Carbon Formation in an Acetylene-Air Diffusion Flame," *Journal of Physical Chemistry,* 1959, pp. 578–582.

8 Kadota, T., Hiroyasu, H. and Farazandehmehr, A., "Soot Formation by Combustion of a Fuel Droplet in High Pressure Gaseous Environments," *Combustion and Flame,* Vol. 29, 1977, pp. 67–75.

9 Schalla, R. L. and McDonald, G. E., "Mechanism of Smoke Formation in Diffusion Flames," *Fifth Symposium on Combustion,* 1955, pp. 316–324.

10 Prado, G., Lee, M. L., Hites, R. A., Hoult, D. P., and Howard, J. B., "Soot and Hydrocarbon Formation in a Turbulent Diffusion Flame," *16th International Symposium on Combustion,* 1976, pp. 649–661.

11 Irani, B., "Effects of Reynolds Number and Mixing on Soot Production in a Turbulent Diffusion Flame," Aug. 1977, MS Thesis in Mechanical Engineering, MIT, Cambridge, Mass.

12 Hoult, D. P., and Rife, J. M., "Laboratory Measurements in a Turbulent, Swirling Flow," submitted to NASA Lewis Research Center, Sept. 1979.

13 Hoover, J. A., "Soot Production in a Turbulent Diffusion Flame: Turbulent Scaling and Fuel Composition Effects," June 1978, MS Thesis in Mechanical Engineering, MIT, Cambridge, Mass.

14 Private Communication, Nov. 5, 1979, J. Odgers.

15 Beer, J. M., and Chigier, N. A., *Combustion Aerodynamics,* Applied Science Publishers, London, 1972.

Downloaded 01 Jun 2010 to 171.66.16.59. Redistribution subject to ASME license or copyright; see http://www.asme.org/terms/Terms_Use.cfm

R. A. Yannone

Fellow Engineer,
Combustion Turbine Systems Division,
Westinghouse Electric Corp.,
Concordville, Penn.

J. F. Reuther

Fellow Engineer,
Industry Systems Division,
Westinghouse Electric Corp.,
Pittsburgh, Penn.

Ten Years of Digital Computer Control of Combustion Turbines

This paper establishes the design criteria for the digital computer control systems first produced in 1969, and currently in the tenth year of history for startup, control, and monitoring of combustion turbine units in the 25-125 MW range, reviews the advantages of digital control and the fall-out obtained from the application of an advanced state-of-the-art control in the area of diagnostics and historic data handling, reviews the integration of the digital computer back-up system, composed of a solid-state fuel scheduler and logic sequencer provided for total system performance and reliability, and discusses the feasibility of a computer retrofit using existing software with the latest state-of-the-art microprocessor emulator.

Background

In 1969, a need was recognized for an advanced state-of-the-art design for automatic control of combustion turbines. The complexity of new turbine requirements for remote control operation, rapid starting transients and isolated system loading functions placed unusual demands on the existing control systems.

Reliability of performance for these functions and the protection of the turbine hot parts were prime considerations in design of the new systems.

Prior to 1969, the control systems had progressed from electro-hydraulic to electro-pneumatic and were progressing toward solid state design for the three basic control requirements of sequencing, protection and fuel scheduling.

Progress in miniaturizing computer hardware provided the stimulus to establish feasibility of packaging this type of system for turbine generator control. Limitations of space defined for control systems had to be reconciled with the need for adequate memory, input-output and control functions. Flexibility of control and economics pointed to the application of a computer, especially where two or more turbines could be controlled by one computer. The merits of the computer system were weighed against conventional controls by a task force which confirmed feasibility of computer control for combustion turbines.

The initial meeting held for the design of the present control system occurred in October 1967. The control that evolved is a hybrid analog/digital system providing centralized automatic speed, load and temperature control with monitoring and turbine protection at all stages of operation.

Design Criteria

It has always been a paramount design criterion to protect the turbine against malfunction of the controls under any of its failure modes and to cause fail-safe operation or shutdown of the turbine-generator. To this end, extensive study was devoted to determine the feasibility of detecting malfunction of the computer system and establishing the proper control response to analog scanning and memory problems.

A direct digital control with all computations managed by the computer was desirable. However, the existing state-of-the-art, 30 point per second analog to digital input system, made sampling of turbine speed impractical at the estimated required rate of ten times per second. Therefore, a hybrid system was developed, with the computer supplying a speed reference signal to a solid state PID droop speed controller. In addition to the analog hardware, a calculated software fuel limit was provided. This signal is a function of the low selected PID temperature controller output, the surge limit, the PID MW controller output and the load rate limiter.

The total system required that it be capable of reading and analyzing both digital and analog inputs and developing both analog and digital outputs. The integration of these signals was required to perform the essential turbine functions of sequencing, protection and fuel scheduling.

The engineering goal for the system was to create an intimate closed loop between the turbine, the auxiliaries, the fuel system and the computer, and to accomplish simultaneously the control of more than one turbine.

History

By the end of 1968, a prototype system was shipped to the combustion turbine manufacturing plant at Lester, Penn., for further simulation, debugging and testing with the actual turbine to be controlled (a 251AA rated to drive a nominal 25 MW generator).

The initial turbine generator units shipped to the field were dual controlled by one computer and installed at the site of Alabama Power—Demopolis, Ala. Field participation extended from August to November 1969, and during that period both combustion turbines were started simultaneously, manually synchronized, and loaded as required.

Additional work at VEPCO's Portsmouth Station, in December 1969, confirmed the automatic generator synchronizing program, remote unattended starting and automatic transfer of fuels under load.

The control later was applied to the larger 501 frame turbines, which at that time generated about 50 MW. The first start-up of this frame occurred at Cincinnati Gas and Electric—Miami Fort Plant, in December 1970. Larger frame sizes followed with the start-up at Abilene, Kan., in July 1973, and the start-up at Hutchinson, Kan., in June 1975. During this time the operating capacity of the turbine

Contributed by the Gas Turbine Division and presented at the Gas Turbine Conference and Products Show, New Orleans, La., March 10–13, 1980 of THE AMERICAN SOCIETY OF MECHANICAL ENGINEERS. Manuscript received at ASME Headquarters December 13, 1979. Paper No. 80-GT-78.

Copyright © 1981 by ASME

Downloaded 01 Jun 2010 to 171.66.16.59. Redistribution subject to ASME license or copyright; see http://www.asme.org/terms/Terms_Use.cfm

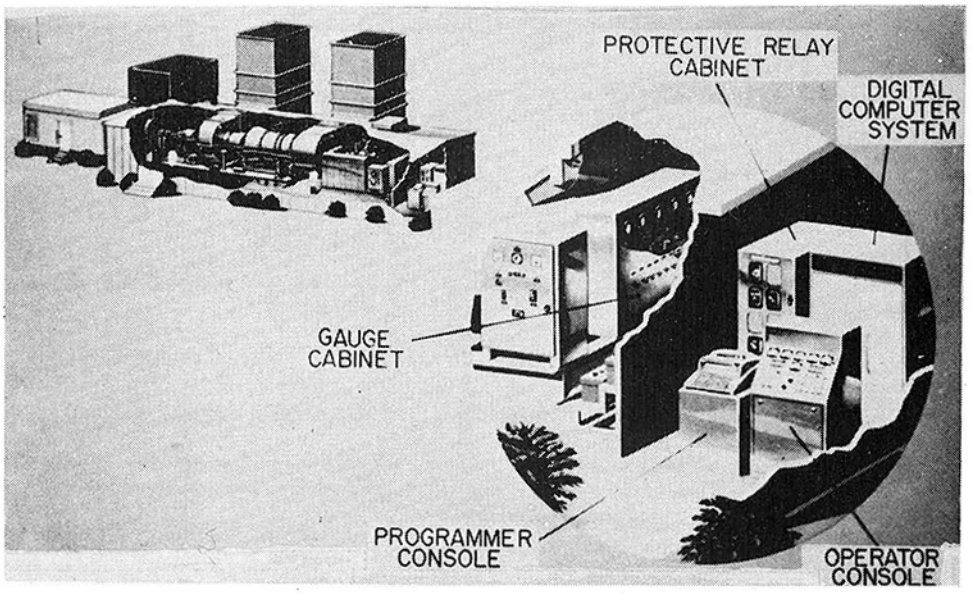

Fig. 1 Typical combustion turbine installation

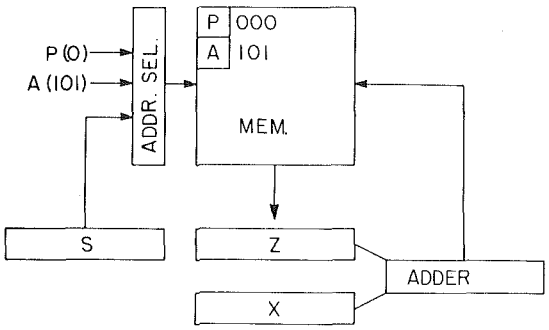

Fig. 2 Central processor block diagram

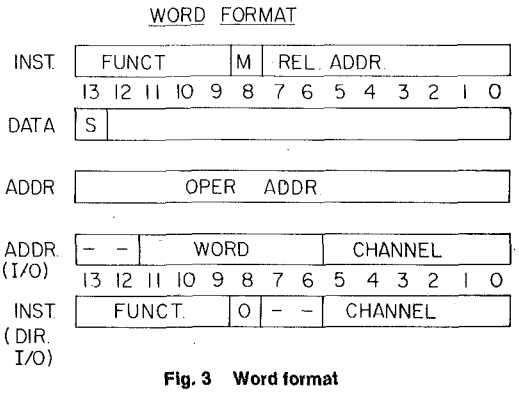

Fig. 3 Word format

generators increased from 50 to 129 MW.

Presently, there are approximately 200 computers controlling some 250 turbines at sites ranging from Alaska to Ecuador and from Taiwan, throughout the United States, and to Saudi Arabia.

A typical combustion turbine installation is shown in Fig. 1.

Hardware Description

Computer. The heart of the control system is the PRODAC 50 computer main frame using magnetic core memory of 16384 words (14 bit).

Although some integrated circuits are employed, most circuit boards utilize discrete components and some "cordwood" packaging techniques that were current practice when the system was introduced to the market in 1964.

The computer has the means to anticipate improper operation due to excessive ambient temperatures by reading its own temperature. At excessive control room temperature, it can make the decision to stop the turbine or turn control over to the backup system.

Numbers (instructions, addresses, values) are read out of core into a hardware Z register. It and another hardware register (X) are fed into an adder and the output of the adder is read back into core. The S, or storage register indicates the core location to be read and in addition the address of the program counter (P) or accumulator (A) may be selected (see Fig. 2). In all, a repertoire of 25 instructions may be executed.

To keep track of real time, the 60 cycle computer power source is fed to a synchronous interrupt circuit which interrupts the computer every 1/60 s. Thus, some programs where necessary for proper control run every 0.1 s, while others run at times ranging from every 1.2 s to every 2 h. This design makes it possible to provide a clock and calendar program to record time and the date for printed messages.

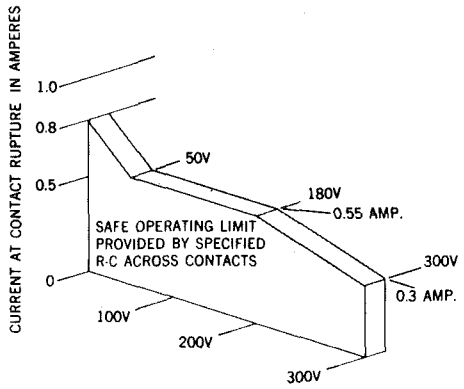

Fig. 4 Contact output rating

The system core cycle time is 4.5 μs and the average instruction execution time is 20 μs, slow by modern standards but adequate to control, monitor and protect two operating turbine-generator systems.

The word format for the computer programming which uses a 14 bit word length is shown in Fig. 3.

Contact Closure Outputs. Contact closure outputs are mercury-wetted, hermetically sealed bistable relays with two driver coils, one for set and one for reset. Should the computer stop, they retain their last position. The contacts have resistor-capacitor surge protection giving them a rating as shown in Fig. 4. Each word of 14 contacts requires 5 ms for execution.

Downloaded 01 Jun 2010 to 171.66.16.59. Redistribution subject to ASME license or copyright; see http://www.asme.org/terms/Terms_Use.cfm

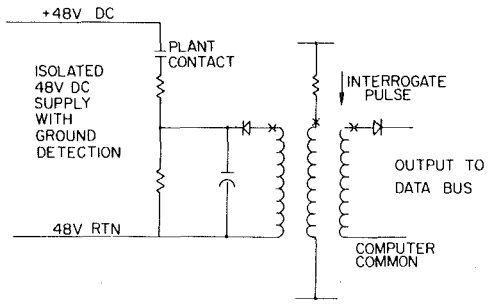

Fig. 5 Contact status input

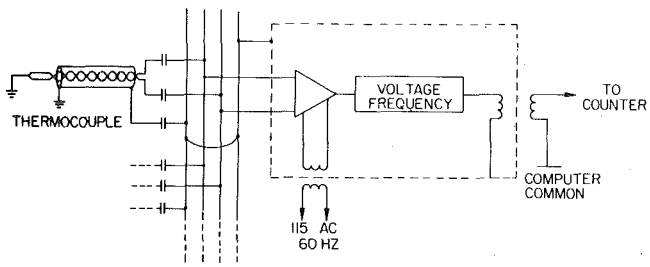

Fig. 6 Simplified analog input schematic

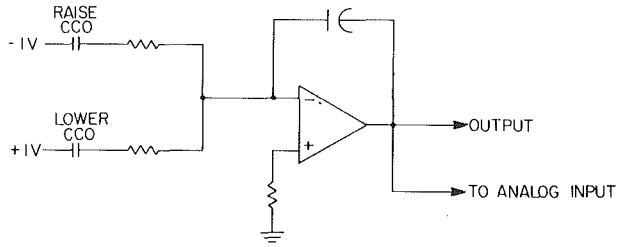

Fig. 7 Analog output schematic

Contact Inputs. A contact status input being "read" by the computer is referred to as contact closure input. Pulse transformers are used to provide electrical isolation between the plant and the computer with an RC filter of 2.5 ms time constant to avoid misreading the status due to voltage spikes.

Referring to Fig. 5, if the contact is open, the capacitor is uncharged. If an interrogate pulse is put on the primary winding, the capacitor acts as a short on the secondary winding keeping the voltage supplies for sampling on the data bus low. If the contact is closed on interrogation, the input diode is back biased and the capacitor appears as an open circuit on the secondary winding, allowing a logical one. The contacts are read 14 at a time into the accumulator where they may be used as the programmer sees fit.

Some input contacts are used as interrupts; that is, their closing causes the computer to execute one or more instructions out of order.

Analog Inputs. Analog inputs, voltages with a nominal 5 V range and a nominal 50 MV range are read into the computer using integrator and voltage/frequency converter techniques. Integration occurs over 1/60 s to reject 60 Hz noise, with the integration time determined by a high accuracy crystal controlled oscillator. Here again, electrical isolation between the plant signals and the computer is attained. The voltage/frequency converter is enclosed in a guard shield which is switched by relay to a representative ground point brought back on transducer input sheath wires while a point is being read.

Analog point selection relays also provide electrical isolation as they connect voltages to be read at the input of the voltage/frequency converter (see Fig. 6).

In reading the points, one cycle is used to integrate and another cycle is used to drop out and pick up the necessary relays, allowing 30 points to be read per second. Two of the points read are accurately calibrated voltages, one for each of the two ranges. Should the readings be out of range, the turbine will either be stopped or transferred to a backup system.

Scan time per point for individual analog signals vary from once every 1.2 s to once every 19.2 s. The odd times are due to the fact that the main programs are bid to run 50 times a minute.

Analog point cards reading thermocouples have open thermocouple detection hardware. A small current is circulated through the thermocouple in a reversed direction. It has negligible effect on the output voltage of a healthy thermocouple. However, if the thermocouple is completely open, the value is read as negative full scale. In practice, any thermocouple reading less than −50°F is considered open, causing an alarm indication and possible control rejection when used in calculations.

Analog Outputs. Analog outputs used for variables of speed reference, voltmeter settings, inlet guide vane positions and flow setting for water injection are implemented using holding amplifiers. Their output is measured as an analog input. If they are not at the proper level, input raise/lower contacts are pulsed an amount proportional to the error, causing them to integrate up or down toward the desired value (see Fig. 7).

Typical Integration of the Input/Output Signals. A simple control loop, for example turbine exhaust temperature control, can be traced through the system. Sixteen thermocouples are read into the computer such that no reading is older than 6 s when used. They are checked for limit, and those not open or shorted are averaged. Rate action is applied to the average and the resulting value is subtracted from a temperature reference which is a nonlinear function of the combustor shell pressure. The difference is processed by proportional and integral algorithms and becomes a maximum allowable fuel signal. If it is the lowest of several control outputs (surge, MW, load rate limiter, or temperature), it is used to set an analog output which determines the fuel valve setting. These calculations are re-evaluated 50 times a minute.

A typical algorithm used for rate action is called a differential block, but might better be described as a rate lag since it evaluates the transfer function $Y(S) = K(TS/(1 + TS)) * X(S)$. Using sampled data techniques, a Z transform will give the following algorithm:

$$Y(N) = ((2T - H)/(2T + H)) * Y(N - 1) + K * (2T/(2T + H)) * (X(N) - X(N - 1))$$

where $Y(N)$ and $Y(N - 1)$ are the new and old outputs respectively, $X(N)$ and $X(N - 1)$ are the new and old inputs respectively. H is the sampling time and T the time constant.

Operator Interface. In the standard system in addition to the computer, the two other major pieces of equipment are the programmer console and the operator console.

Programmer Console. The programmer console is a combination printer, keyboard, tape punch and tape reader in communication with the computer. It provides a direct means for the operator to interrogate the turbine generator performance. The operator, in seconds, can adjust control curves and set-points without any external instrument input or measured outputs required by conventional analog systems. It also enables the operator to change points on the hourly log, change control limits, update time and calendar, read any analog input or contact closure input, operate any contact closure output and trigger printing of a log containing historical data.

The impact of this function is to provide maximum availability of the turbine without scheduling costly outage for maintenance or control adjustments. Also of importance is the production of a hard copy printout which can be retained for comparison of turbine performance as well as for documentation of turbine-generator operation and alarm recording.

Local Operator Panel. The operator panel (see Fig. 8) consists of a series of lights, pushbuttons, voltmeters and a digit switch. Besides the expected functions as load and fuel selection and start-stop requests, the following is a list of noteworthy functions:

1 By means of the digit switch and two pushbuttons, as many as 80 analog quantities can be selected to be displayed on the panel instrumentation.

Downloaded 01 Jun 2010 to 171.66.16.59. Redistribution subject to ASME license or copyright; see http://www.asme.org/terms/Terms_Use.cfm

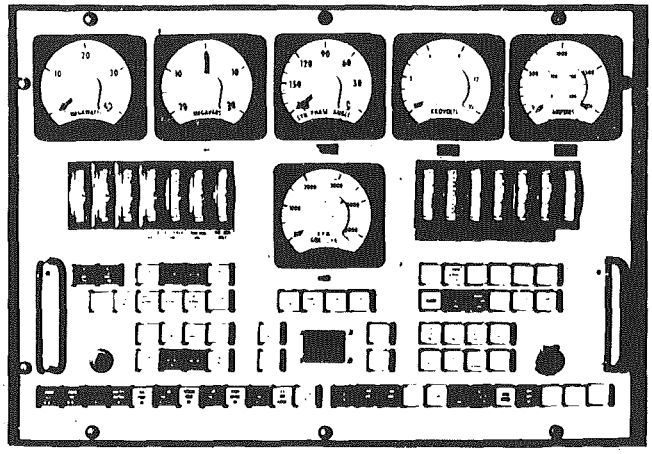

Fig. 8 Local operator panel

2 In addition to the alarm reset and horn silence buttons, a demand review button will initiate a hardcopy printout of all existing alarms.
3 A row of 24 lights indicates in sequence the start-up and loading progress.
4 Five of the lights are actually lighted pushbuttons. With the supervisory key switch turned on, the operator may select hold points for visual maintenance during the starting sequence.

Software Description

The software design is based on a two-level priority system defined as the dominant level and the secondary level. A dominant level program can interrupt the secondary level and a hardware interrupt can interrupt either level. There are several dominant level programs and their priority among themselves is based on the order in which they are bid.

There are 14 secondary sublevel programs. If several programs are bidding to run, the one with the highest priority level will run first, but once a secondary sublevel program starts to run, it cannot be interrupted by a higher priority secondary sublevel program. When no other program is running, a confidence check program runs within the computer.

Typically, a synchronous interrupt or a pushbutton interrupt may cause a program to run which will perform some vital function and then bid for a secondary sublevel program to perform more detailed operations.

The two major software programs are the sequence logic program and the control program. The former evaluates the six sheets of English logic describing the control sequence and protection. The sequence program also establishes which operating mode the control program should calculate. The latter sets the speed reference and the fuel limit. The modes are described as follows:

Mode 0—Initialization for Starting
Mode 1—Acceleration of Turbine
Mode 2—Synchronization of Generator
Mode 3—Load Control—Temperature Limited
Mode 4—Temperature Control—Load Limited

The other programs, in general, supply information to these two programs or perform functions requested by them. For instance, the synchronous interrupt program will bid a dominant level bidding subroutine which in turn will bid the sequence program every 1.2 s. When the analog scan program runs, it will read, for example, a bearing thermocouple and store the temperature in a value table. When the sequence program runs it will read this value and determine if it exceeds an alarm limit. Later the alarm program will sense this change and call the message writer subroutine to bid for the output device program to print the message.

With the application of software to the sequence and control programs, field retrofit improvements require little hardware change, but rather the addition of punched tape for the site. Also, special customer requirements can usually be easily implemented by existing cables. Special requirements may vary from a single external contact operation requiring an alarm, to the use of the turbine generator system as a synchronous condenser.

The great benefit derived from the application of the software for sequence and control has been the inherent reliability of repetitive performance.

Below is a list of the programs and a brief description of each:

Dominant Level Programs. (Priority is based on order of calling.)

1 (a) *Analog Output Pulser.* Generates raise and lower contact closure outputs as determined by the secondary sublevel analog output program.
(*b*) *Time Routine.* Increments real time in seconds, minutes, hours, days and years.
(*c*) *Bidding Subroutine.* Bids secondary sublevel programs, as required, on 1.2 second to greater than 2 hour intervals.
(*d*) *Span Adjust.* Recalibrates the analog/digital converter system and triggers an analog scan.
2 *Operator Console (one level for each unit).* Processes local and remote operator panel interrupts. Decides whether to process high priority pushbutton functions on this level or bid a secondary sublevel.
3 *Automatic Synchronizing.* Matches speed, voltage and phase. Decides when to initiate closing of generator breakers.
4 *Analog Scan.* Saves analog/digital converter readings after first compensating thermocouple readings to 32°F. This correction is determined by the secondary sublevel cold junction compensation program. It also determines which, if any, is the next analog input to be scanned.

Secondary Level Program. Several important programs of the 14 total are listed and briefly described below:

1 *Programmer Console.* Uses numeric load programs and reads core, reads tape, checks tape, punches tape, set limits, operates CCOs, reads CCIs, reads analog inputs, converts values for limit setting, and triggers post disturbance log printout.
2 *Operator Console.* Processes those local and remote pushbutton functions initiated by the operator, but not handled on the dominant level.
3 *Sequencer.* Evaluates the sequence logic and takes appropriate action to accelerate and load the turbine.
4 *Control.* Analyzes cycle temperatures and schedules fuel to the unit based on these and other analog readings in conjunction with the sequence program.
5 *Dead Computer.* Performs checks on computer hardware which can cause the action to transfer control to backup or cause turbine shutdown on sensing failure.
6 *Alarm and Logging.* Responds to the need to indicate malfunction and to cause analog variables to be periodically printed.

Special Programs. Several of the software programs are worthy of mention because of their uniqueness in the industry for the control of combustion turbines. Two of these, the sequence and control programs are responsible for the turbine acceleration, fuel limiting and unit protection.

These programs are run in series every 1.2 s. It has been field-proven that the computer system is fully capable of simultaneously controlling and protecting two combustion turbines using this increment of time to repetitively run programs. The original concept of controlling more than two turbines from one computer would have increased the program running time and was never attempted.

Sequence Program. The sequence program has defined MARCRO's for each basic logic block. If a three input "AND" is to be evaluated, the programmer writes ANN 3, A, B, C, where three logic conditions are represented by A, B, and C. The assembler would automatically choose the proper instructions to "AND" together with those three conditions and place the result in the sign bit of the accumulator. Thus, the programming is done directly from the English logic sheets.

The sequence of events for starting the combustion turbine as a

Downloaded 01 Jun 2010 to 171.66.16.59. Redistribution subject to ASME license or copyright; see http://www.asme.org/terms/Terms_Use.cfm

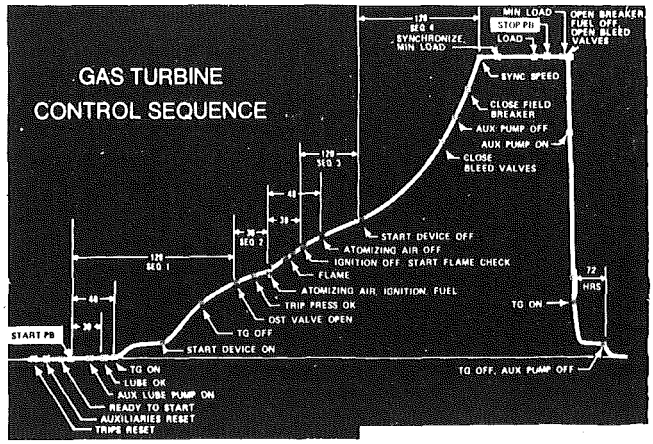

Fig. 9 Software logic sequence

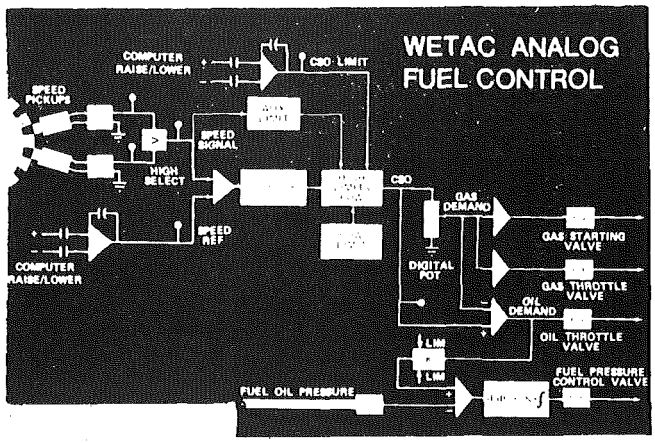

Fig. 10 Analog fuel control

function of time is displayed in Fig. 9.

Fuel Control Program. The control program has similar MACRO's for one and two input function generators, differentiators and integrators. The control system permits nonlinear loading curves to be evaluated, resulting in better heat rates while performing proportional plus reset plus rate function digitally. Time constants and gains can be easily changed, through the keyboard of the programmer's console, to provide maximum on-line facility.

The basic analog control signals of exhaust temperature, megawatts and speed are used to control fuel flow to the combustion turbine. The higher of two turbine speed signals is selected for control while their average is used to detect failure of one. The higher of two speed signals is compared with the computer set speed reference signal and the error is amplified to become the fuel demand signal limited by computer determined values.

The calculated fuel demand signal becomes the final control signal which is programmed to schedule fuel by positioning the gas or oil fuel valves. The computer is able to recognize an operator or control request for the desired fuel and will generate an orderly fuel control ramp to permit automatic transfer from one fuel to another while at load. See Fig. 10 for a schematic representation of the analog fuel control.

Generator Breaker Synchronizing Program. The automatic synchronizing program will rough match turbine speed based on frequency transducer readings. It then will take readings of hardware produced phase difference signals every 1.2 s. From these readings a check is made to see that the phase angle is varying linearly and that the slip frequency can be determined. Raise/lower pulses are generated to match speed and, if the slip frequency is satisfactory, the time to in-phase conditions can be calculated. Taking into account breaker closing time, the breaker can usually be closed within a window of 0 to 5 deg before in-phase condition and with a maximum allowable slip frequency of 0.1 Hz.

Diagnostics Program. The use of diagnostic programs to catch transients that have occurred at the instant of shutdown or prior to the shutdown is a form of computer type sophistication not available from conventional systems.[1] Its contribution in the solving of turbine or control problems by comparison of values or by analyzing historical data tables can provide the means of avoiding catastrophic damage through scheduling of prompt maintenance.

Post Disturbance Program. One of the most useful diagnostic tools developed for the computer system provides the capability to look back into history for 5 min on ten selected turbine variables.

The computer program, on demand, will tabulate and print out a chronological display of variables taken at 6 s and 1 min intervals for 5 min of history.

The program has been most useful in determining the turbine variable changes occurring under remote control or where operator attendance is limited. It is an effective means of providing engineering communication for the customer and the designer when developing problem solution.

Temperature Reasonability. An important design contribution to the analog measuring system has been the software program for determining the health of temperature signals derived from thermocouples.

Most thermocouple operated devices have a method of detecting open thermocouples, but do not have a means of automatically rejecting readings that are improper although not open circuited.

The computer makes use of a software program using design data and control history to establish bands of reasonability which are continuously compared to the actual temperature for out of bounds.

The net result of the usefulness of the reasonability program is to establish a superior level of confidence in those readings used for turbine hot parts performance and life.

Freeze Table. Another unique addition to the diagnostic family provides a snap-shot at the instant of turbine shutdown of nine selected analog variables and the contact position of every contact input from the field. The table is available on demand and can be instrumental in the tracking of transients that can cause control problems.

Local Maintenance Controller

Past practice indicates that combustion turbine controls have always been designed with a single unitized control system. There may be built-in, inherent redundancy or auctioneering loops which can define reasonability to run under failure. However, with all control systems, there is, at some point in time, reason to expect failure. It is the intent of most control systems to be fail-safe and, in the case of turbine control, where necessary, to cause shut-off of the fuel supply and stopping of the machine.

Many combustion turbines are used in the peaking mode which will permit maintenance during off-peak hours in contrast to base load machines where continuous operation is of more importance. Availability is of particular importance with turbine generator operation at base load control or on isolated systems where continuous running is necessary.

For those utility systems requiring the ultimate in availability, it is desirable that the computer have some means of transferring control in the event of failure.

In 1974, a unique add-on, designated a Local Maintenance Controller (LMC), was developed and installed to permit turbine operation in the event of computer failure. Those systems requiring maximum protection against loss of power availability were then provided with an alternate means of starting and loading the combustion turbine when the expertise for troubleshooting and maintaining the computer was not readily available.

[1] Overton, R. L. and Yannone, R. A., "Gas Turbine Computer Control as Compared to Wired Logic System," ISA-70 international conference paper 767-70, Oct. 26–29, 1970, Philadelphia, Pa.

Downloaded 01 Jun 2010 to 171.66.16.59. Redistribution subject to ASME license or copyright; see http://www.asme.org/terms/Terms_Use.cfm

The design of the LMC provides a completely independent backup system composed of an analog fuel scheduler and relay sequencer. It is able to make automatic on-line, bumpless transfers under full load operation and is unique in that the system can transfer in either direction in a second or two. Successful transfers to and from the computer are a result of the ability of each system to track and match the controlling fuel signal.

Transfers to LMC are indicated at the remote control station. Also annunciated remotely is the failure of the backup system to track the primary system, which acts to inhibit transfer. The "failure to track" signal allows the remote dispatcher to schedule maintenance on the backup system while maintaining load on the primary system.

Operation at the load transferred is maintained on speed regulation control by the backup controller, and will also permit the operator to change loads manually as necessary, within the temperature control limits.

The LMC provides simplified analog control and does not duplicate all the complexity of the primary functions. However, the controller can operate the turbine safely without operator attention for periods of several hours and for continuous operation with supervision or the minor addition of protective equipment.

The later series of computer systems for the combined cycle plants were designed with the provision for backup control to provide users more reliability.

Microprocessor Emulator

As with all systems, state-of-the-art advances have caused the 1969 system to assume some measure of obsolescence. It is true that the available input-output hardware and the analog scanning systems are essentially the same, but the design of new memory and logic functions has greatly improved reliability, physical size and cost.

The phenomenal improvement in electronics using large scale integration, miniaturization and microprocessors can best be illustrated by the fact that the original system of 50 separate cards is now duplicated by ten printed circuit cards.

The availability of a microprocessor retrofit design has given a second wind to the computer/LMC controls, extending the life of the total system. This progress is important because it allows the continuance of an advanced system in the existing physical confines, while providing the state-of-the-art improvement in hardware.

The development of the retrofit in progress today will provide greatly improved reliability, as well as a significantly reduced level of capability necessary for servicing.

The troubleshooting procedures to locate and repair circuit malfunctions within the PRODAC 50 are simplified. Problems with the microprocessor can be identified quickly and can usually be solved in minutes by inserting a replacement card. Because maintenance is simpler, trained customer personnel can learn to match the service capability of the most experienced factory servicemen.

Summary

One very important attribute of the digital computer system has been its excellent record in the protective control of the turbine against mechanical failure, confirming strongly that computers can control safely, as well as effectively. Many areas of patentability and design novelty were established by this system which offers a step change in the advancement of the state-of-the-art for combustion turbine control. It has been very adaptable to changes required for the turbine-generator and auxiliaries without the addition to the basic hardware of a single input, output or analog provision over a ten year period. This advantage was in part the result of the initial design planning, but also points specifically to the versatility of the software system to re-cycle input and output signals as required for turbine control.

Today, additional flexibility is available in the powerful new Fortran-like compiling techniques which further simplify the application of software programming for turbine requirements.

A negative aspect of the control, on the computer side of the hybrid system, has been the difficulties presented by the developing nations where provision for spare parts, travel time or expertise is a problem.

The mean time between failure for the computer over a ten year period, for all systems reporting, indicates the need for hardware expertise in the field. The addition of the computer backup LMC, however, provides a very acceptable 16,000 hr MTBF for the system where the demand for availability is paramount.

The difficulty of training customer personnel without previous in-house computer expertise, particularly, for remote areas of the world may present challenges. Since this area of power expansion represents the predicted major accumulation of future combustion turbine work, consideration must be given to using microprocessor techniques in the area of monitoring and alarming, data gathering, logging, post disturbance and temperature calculations. That is, for those functions of peripheral control where turbine operation is not dependent upon the microprocessor.

Modern microprocessor systems are comparable in computational horsepower in many ways to the PRODAC 50 computer. Improvements in the techniques used to measure analog inputs allow the scanning at a much faster rate, offering the possibility of direct digital control in the speed loop of the control system. Fuel valves could then be positioned directly by the microprocessor system, rather than using the computer to output a speed reference with the analog control providing closed loop speed droop control.

Ten years of combustion turbine control by digital computer systems has developed an appreciation of computer capability and the in-house expertise to use advantageously the existing microprocessor technology. The advancement in hardware design offers the opportunity to greatly enhance the reliability and availability of the combustion turbine controllers of the 1980's.

Downloaded 01 Jun 2010 to 171.66.16.59. Redistribution subject to ASME license or copyright; see http://www.asme.org/terms/Terms_Use.cfm

F. J. Bayley
Dean of Engineering.

W. J. Priddy
Research Fellow in Mechanical Engineering.

University of Sussex,
Brighton,
Sussex,
UK.

Effects of Free-Stream Turbulence Intensity and Frequency on Heat Transfer to Turbine Blading

This paper describes a continuing experimental program in which the frequency and amplitude of turbulence in the mainstream flow over a cascade of turbine blades are separately and controllably varied. The effects of these two characteristics of the flow are demonstrated showing the significant effect of each upon the rates of convection to most of the blade surface. A correlation following the predictions of the theoretical work of reference [2] *is shown to have some promise, although some modification is required to allou for changes in mainstream Reynolds number not accounted for by the usual normalizing procedure.*

Introduction

It is now generally accepted that significant differences are found between measurements of convective heat transfer to turbine blading in laboratory cascades and deductions from engine data. Qualitatively these differences are explicable through the different turbulence characteristics of the flows in cascades and those in the demanding environment of an engine, and certainly many workers have demonstrated experimentally and theoretically that different turbulence parameters have varying and usually significant effects upon local convective heat transfer rates. Quantitatively, however, the situation is less satisfactory, certainly from the designer's point of view, dictated by his requirement to make reliable predictions of blade life and thus of local temperatures around a blade surface. Not least the quantitative difficulties arise from the problems of measuring flows within an engine, but, even if these were overcome, uncertainties would remain as to the properties of real flows which characterise the turbulence and its effect upon local heat transfer. Turbulence intensity has traditionally been regarded as the principal turbulence parameter, but many workers have demonstrated that other factors are important and Dyban and Epik [1], for example, suggest that each of the three components of velocity fluctuation, the energy spectrum, the correlation coefficient, and the so called intermittency factor need to be known to define a turbulent flow.

Many modern turbine blade sections, even at the high Reynolds numbers at which they operate, manifest considerable areas over which the boundary layer remains laminar in a steady, low turbulence stream. The superimposition of main stream velocity fluctuations associated with artificially induced mainstream turbulence is known to affect dramatically heat transfer rates under such conditions, and Ishigaki [2] has shown theoretically that under such conditions the frequency of the perturbations, as well as their intensity or amplitude, is important in determining the enhancement of the convection process. Clearly such effects can be important in turbine blade design for, as rotor speed changes, so will the frequency of the perturbations in flow velocity which the blades experience.

Contributed by the Gas Turbine Division and presented at the Gas Turbine Conference and Products Show, New Orleans, La., March 10–13, 1980 of THE AMERICAN SOCIETY OF MECHANICAL ENGINEERS. Manuscript received at ASME Headquarters December 13, 1979. Paper No. 80-GT-79.

This paper describes a continuing program of research in the Mechanical Engineering Laboratories of the University of Sussex that is attempting to separate the effects of some of the different turbulence parameters. A previous paper describing this work [3] showed how in experiments on a modern rotor blade section there appeared to be a clear and separable effect of frequency, over parts of the blade section at least. This early work, however, involved intensities of turbulence generally higher than might be reasonably expected in an engine, and frequencies lower than would be typical of those experienced by rotor blades, for example, passing through the wakes of stator. In the present paper some of the deficiencies of the earlier work have been made good and some preliminary attempts are reported at correlating the magnitude of the observed effects following the predictions of the theoretical work of reference [2].

The Turbulence Generator

The cascade tunnel used for the present work typically yielded a turbulence intensity of less than one percent at the blade leading edges. This level of turbulence was enhanced for the test program by a generator of the general form described in reference [3]. This comprises a squirrel cage that can be rotated at varying speeds, thus producing a perturbation frequency determined by this speed and the number of bars in the cage, which for the current part of the program has been kept at thirty. The intensity of the turbulence is determined largely, again as described in detail in [3], by the diameter of the bars, but also by the distance downstream from the cage. Compared with the earlier apparatus of [3] the current design enables the distance between the cage and the leading edges of the blades in the cascade to be varied between 6.4mm and 38mm giving an additional control of the turbulence characteristics. Even more important, the facility to operate close to the cage has enabled the effects of the peak frequencies upon the heat transfer to be observed. Thus the current cage design, shown in the drawing of the apparatus, Fig. 1, which incorporates carbon fiber bars 2.4mm in diameter, can be rotated at up to 20,000 rev/min, giving a bar passing frequency, with 30 bars, of 10 kHz. In the earlier apparatus, with a fixed distance of 46mm between cage and blades, the high frequency perturbations were found not to persist in the flow over this distance, which was not, of course, typical of blade interrow spacing in modern engine design.

Copyright © 1981 by ASME
Downloaded 01 Jun 2010 to 171.66.16.59. Redistribution subject to ASME license or copyright; see http://www.asme.org/terms/Terms_Use.cfm

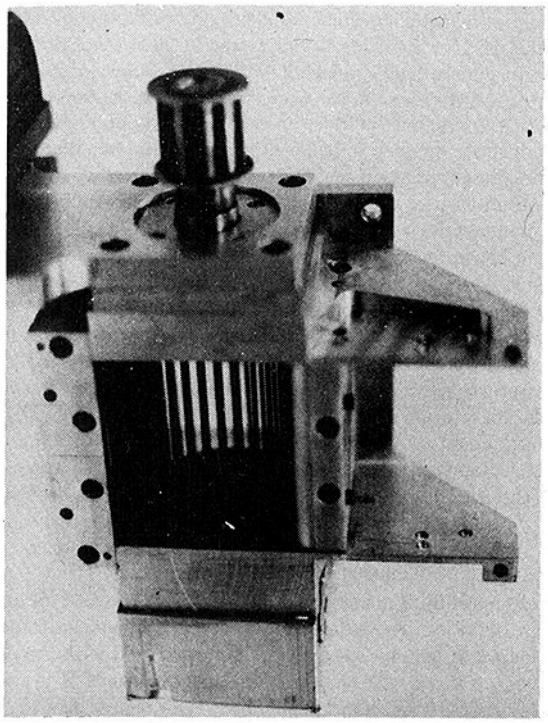

Fig. 1 Experimental set up

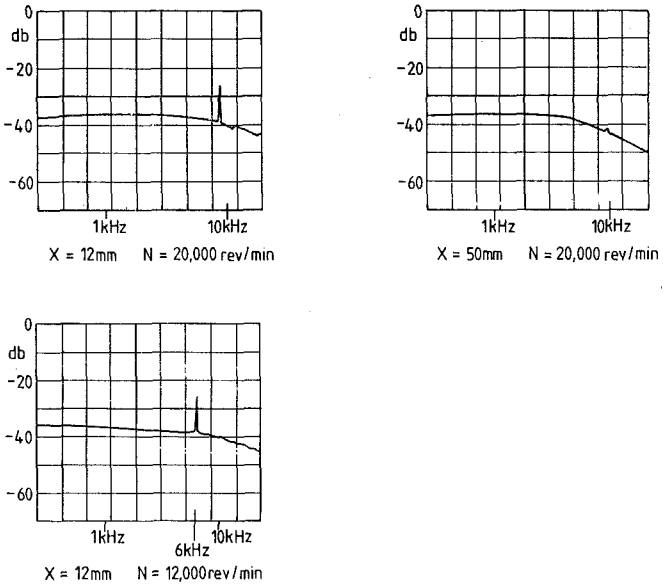

Fig. 2 Power spectra (dB: log f). Effect of speed and distance of cage

The turbulence characteristics of the flows behind the cage have been determined by a hot wire anemometer using a single filament set normal to the mainstream flow direction and traversed over the cascade entrance plane. The signals were analyzed by standard Disa anemometer circuitry to yield the usual turbulence intensity, defined as the rms streamwise velocity fluctuation expressed as a percentage of the average mainstream absolute velocity. In this phase of the work no attempt has been made to distinguish component fluctuations nor to attempt spatial correlation of the perturbations. The work has concentrated on the gross characteristics of the flow, and in particular its frequency characteristics. Determination of these has been facilitated in the current program of work, compared with the earlier, by the use of a Solartron 1510 spectrum analyser. This instrument analyzed the signals from the anemometer online to yield directly the power spectra of the fluctuating flow. Some typical examples of these are reproduced in Fig. 2 and in all cases the distinct "spike" at the bar passing frequency is noteworthy, and is now found to be distinguishable further downstream at the higher frequencies than was the case in the earlier program of work.

Figures 3(*a*), (*b*), and (*c*) show how independent the turbulence intensity of frequency and rate of mainstream flow were, as also was found in our earlier work [3], and the effect on this parameter of distance from the cage, which follows generally accepted trends.

For the whole program of work reported here measurements were made of turbulence characteristics only at the blade leading edges, for current instrumentation does not allow measurements through the blade passages.

Measurements of Heat Transfer

The present program of work has given the opportunity of comparing two different procedures for determining the distribution of convective heat transfer rate around a turbine blade section. In the past and for some of the present work use has been made of the method developed by our former colleague Dr. A. B. Turner [4]. In

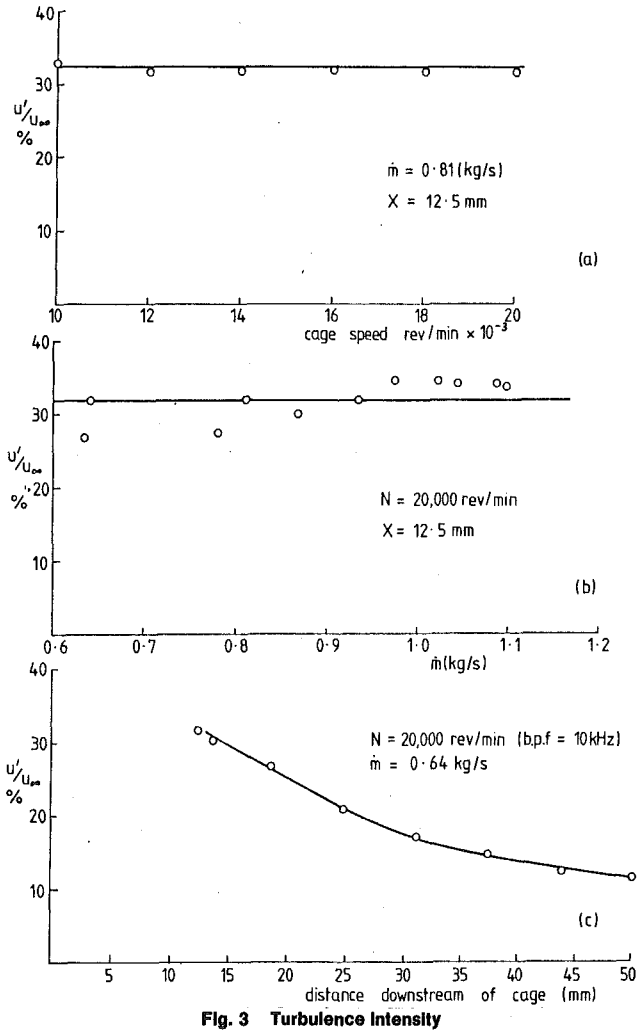

Fig. 3 Turbulence Intensity

Nomenclature

b.p.f. = blade passing frequency, Hz
c = blade chord, m
f_b = bar passing frequency, Hz
$\dot{m}$ = mainstream rate of flow, kg/s
M_2 = exit Mach number
N = rotational speed of cage, rev/min
Nu = Nusselt number
Nu_0 = Nusselt number in steady flow
u_∞ = mainstream velocity, m/s
u' = root mean square velocity fluctuation, m/s
Re = Reynolds number
x = distance around blade surface, m
X = distance of blade cascade from cage, mm

Downloaded 01 Jun 2010 to 171.66.16.59. Redistribution subject to ASME license or copyright; see http://www.asme.org/terms/Terms_Use.cfm

this, the Laplacian conduction equations are solved by a finite element method on a digital computer using boundary conditions of measured temperature distribution around the blade outer surface and heat transfer rates at the surfaces of internal passages conveying cooling air. The procedure yields the normal temperature gradient and hence the heat transfer rate at the outer surface. This has proved to be a powerful technique and is sensitive enough to show clearly sharp changes of heat transfer rate, as at the laminar-turbulent transition. It is, however, expensive of computer and user time and this is especially the case when blade sections with long thin trailing edges are examined, for, even with the largest computer at our disposal, it is difficult to arrange for sufficient elements for an accurate solution to be contained within these regions.

The alternative procedure, which has been adopted for most of the current program, is to model the blade section as a hollow shell, about 1-mm thick, in a metal-plastic composite material. This has a thermal conductivity of about 1 W/mK, so that the typical heat fluxes under the test conditions, in which the mainstream total temperature is about 90°C, and the cooling air temperature inside the shell about 20°C, produce temperature drops through the wall of the order 10°C. This can be accurately measured by thermocouples formed from fine (0.2mm dia) wires buried in the inner and outer surfaces. The differences between inner and outer temperatures are readily converted online to heat transfer coefficients by a simple data reduction program, and outputs like that of Fig. 4 can be obtained as the rig is running. This figure shows graphically the variation of the heat transfer distribution around the section under test as the velocity and hence the Reynolds number of the flow are increased under low mainstream turbulence conditions. The development of the laminar-turbulent transition region is particularly noteworthy.

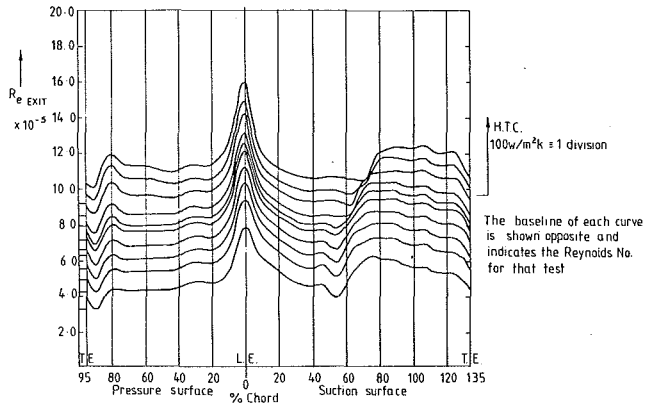

Fig. 4 Distribution of heat transfer in steady flow

The plastic metal shell technique has proved most convenient and effective, and for the blade section tested in the present program has produced data in good agreement with the Laplacian method; indeed significant differences in the observations from the two techniques have been found only in those areas of difficulty previously referred to, and we are inclined to believe the shell data to be more reliable.

In the present program some 160 tests have been made in which the distribution of heat transfer has been determined around the same rotor blade section as described in reference [3]. The distribution of velocity, shown in Fig. 5, changed little in the program in which the exit Reynolds number was varied between 2.5×10^5 and 7.5×10^5 (exit Mach numbers up to 0.9), turbulence intensity between 0.5 and 32 percent, and the characteristic fundamental frequency ranged in lkhz steps up to 10khz. The axis of rotation of the cage of the turbulence generator was parallel to the span of the blades, and reversal of the direction of rotation was found to have no effect. The blade incidence was maintained nominally at zero throughout the program, and the cascade comprized three blades, 64-mm chord and 80–mm span of which the center blade only was instrumented to provide heat transfer data.

Discussion of Results

The general form of the distribution of heat transfer around the present blade section under steady, low turbulence conditions has been shown in Fig. 4. These results are consistent with the data of other workers, and with simple flat plate correlations. The pressure surface remains in the laminar boundary layer regime over the whole range of Reynolds numbers covered, while transition to turbulence occurs rather later on the suction surface than would be predicted from any of the usual correlations as quoted for example by Brown and Martin [5]. The trends, however, are as might be expected with the transition starting point being slightly retarded by the greater accelerations at the higher Reynolds number in this constant density tunnel.

The effects of turbulence intensities which might not unreasonably be expected in an engine are shown in Fig. 6. The striking effect of the perturbations upon the heat transfer to the pressure surface in particular is noteworthy, and even the intermediate turbulence intensity more than trebles the convective coefficients on this surface. Effects are less on the suction surface and indeed downstream of the previously observed transition region, which is now almost wholly suppressed, there is little enhancement, as many other investigators have found [5]. Further upstream there is some increase in heat transfer, surprisingly more evident with the lower intensity represented in this figure.

The effect of frequency on the distribution of heat transfer, as the intensity of the perturbation and the mainstream Reynolds number

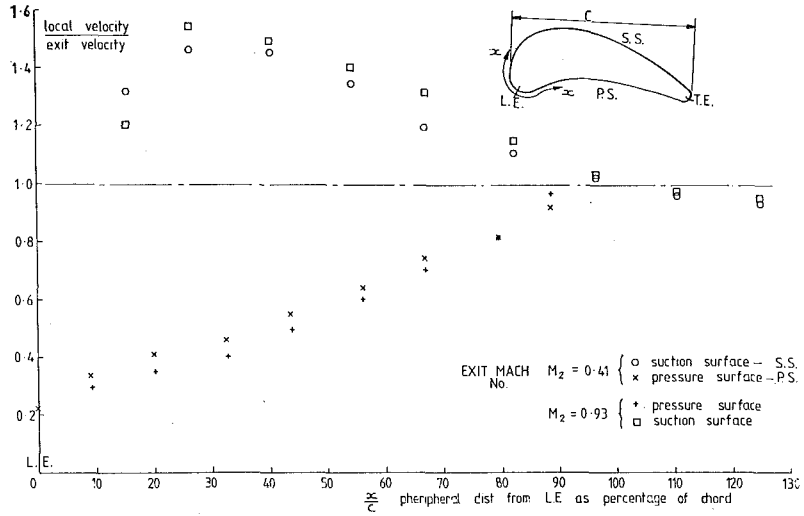

Fig. 5 Velocity distribution around blade

Downloaded 01 Jun 2010 to 171.66.16.59. Redistribution subject to ASME license or copyright; see http://www.asme.org/terms/Terms_Use.cfm

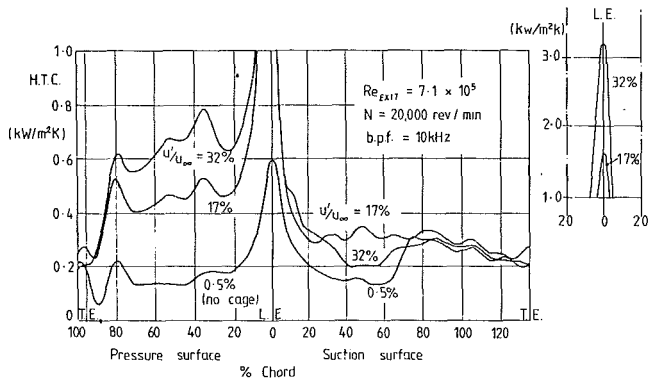

Fig. 6 Variation of heat transfer coefficient distribution with turbulence intensity

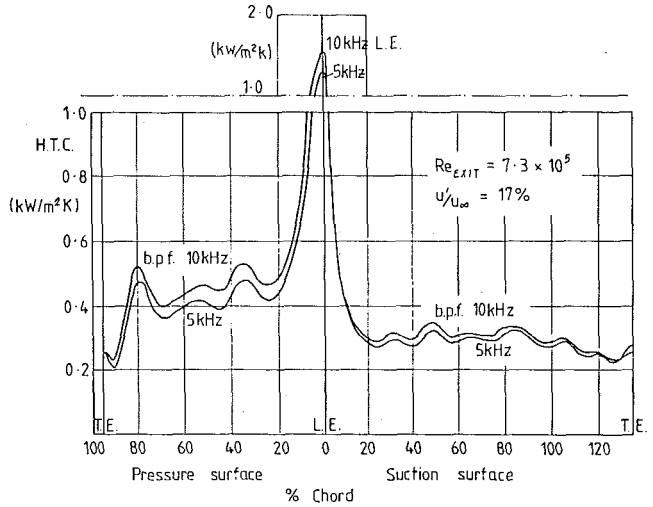

Fig. 7 Variation of heat transfer coefficient distribution with blade passing frequency

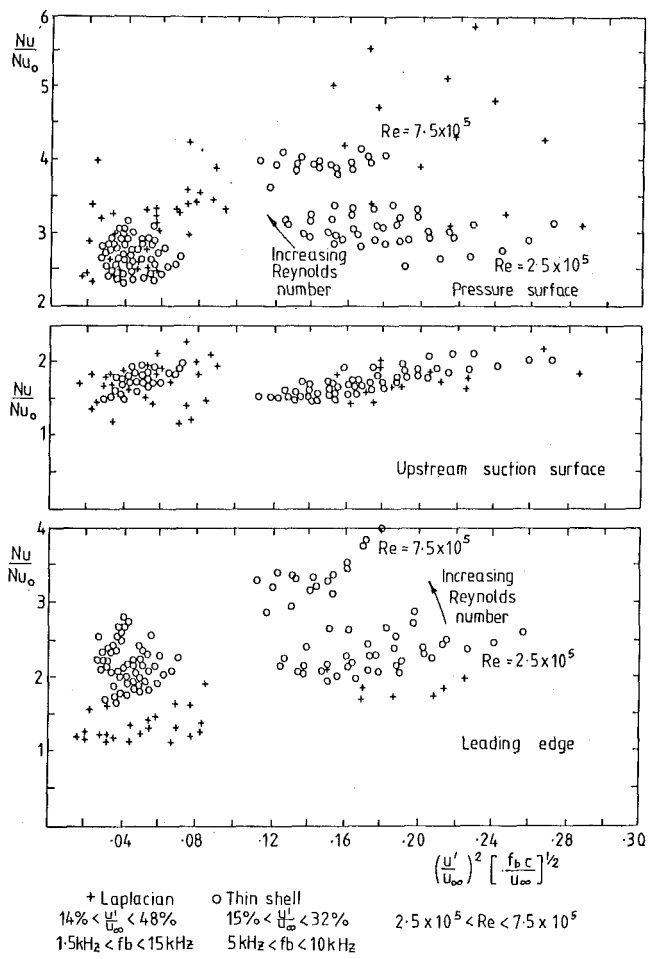

Fig. 8 Effect of combined turbulence parameter on Nusselt number

are held at about the values of Fig. 6, is shown in Fig. 7. Although the effects are less dramatic than those resulting from the change from a steady to an unsteady flow, there is nevertheless an increase in the rate of heat transfer to most of the blade surface as the characteristic fundamental frequency of the perturbations is raised.

Such an effect was predicted by Ishegaki [2], who derived from his theoretical analysis the parameter

$$\left(\frac{u'}{u_\infty}\right)^2 \left(\frac{f_b c}{u_\infty}\right)^{1/2}$$

in which u' is the rms velocity fluctuation superimposed on the mainstream velocity, u_∞, so that (u'/u_∞) is the usual turbulence intensity. The second group is the so-called Strouhal number in which f_b is the frequency of disturbance, in this case the blade passing frequency, and c a characteristic length, in this case the chord, or the appropriate fraction, of the blade.

Figure 8 shows the results from all of the present program represented in terms of this parameter. The heat transfer rate in the ordinate of the figures is represented in the normalized form as the ratio of the coefficient measured in the unsteady flow to that at the corresponding conditions in the unperturbed flow. This figure shows the enhancement of heat transfer in three of the four principal regions into which the whole blade surface can be, somewhat arbitrarily, divided. The downstream half of the suction surface has been omitted since, as has been observed, here the effects of the perturbations were small.

The remaining three regions, the pressure surface, the leading edge (approximate) semicircle, and the upstream half of the suction surface show effects which are not inconsistent with the trend suggested by Ishigaki's theoretical work [2]. The enhancement is much greater than he predicted, and the substantial scatter of the data shows that there are effects on the heat transfer rates not accounted for in this work and not removed by the normalizing procedure used in this figure. For instance, there appears to be a clear effect of Reynolds number, as indeed other investigators have observed.

Including the Reynolds number in the turbulence parameter of the abscissa produces for the three regions of the blade the result shown in Figure. 9. Here the exit Reynolds number has been used to characterize the pressure surface, the dimension and velocity at the downstream end of the upstream suction surface for this region, and the cascade inlet velocity and the radius of curvature for the leading edge. Because of the scale chosen, all the points for this latter region are compressed into a narrow region near the origin, and in Fig. 9 are represented as average points for the two turbulence intensities shown. The detailed variation in normalized heat transfer with the modified turbulence parameter for the leading edge region is shown in Fig. 10.

The correlations of these two figures are not discouraging and indeed Fig. 9 suggests that perhaps there is a unifying trend over the three areas of the blade, here separately considered. Nevertheless differences are apparent between the regions and the data currently available do not make clear whether this is perhaps due to inherent differences in, for example, the stability of the flow in the three regions of the blade, which is not accounted for by the turbulence parameter used. Alternatively, it is possible that the variations in turbulence characteristics around the blade, which currently we are not able to measure, account for the different effects in the areas examined. Further work is required to resolve this exciting possibility.

Conclusions

From the work reported in this paper the following principal conclusions may be drawn:

1 The rotating squirrel cage technique, first reported in reference

Downloaded 01 Jun 2010 to 171.66.16.59. Redistribution subject to ASME license or copyright; see http://www.asme.org/terms/Terms_Use.cfm

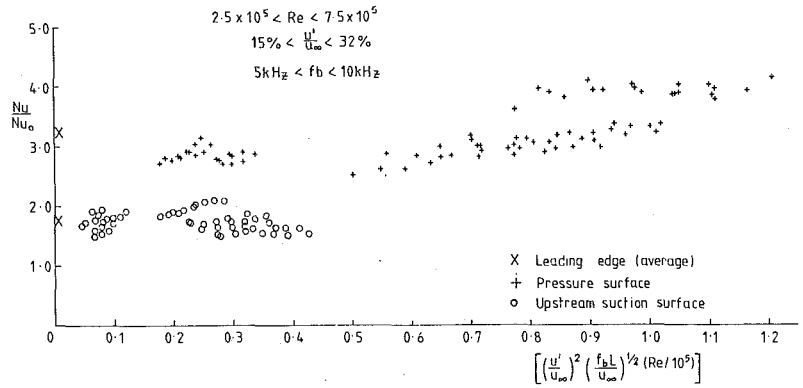

Fig. 9 Variation in heat transfer with turbulence over three blade regions

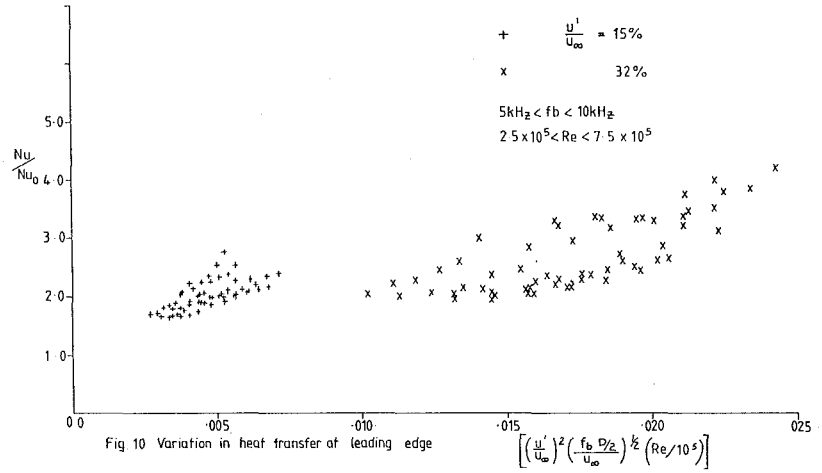

Fig. 10 Variation in heat transfer at leading edge

[3] has continued to prove a flexible and convenient means of applying controlled disturbances to a cascade of turbine blades. In particular, the use of carbon fiber bars has permitted the use of higher passing frequencies and the variable distance between the cage and blades has given further and closer control of turbulence intensity.

2 The adoption of the plastic metal shell model of the blade section has given results of comparable, indeed better, reliability than the earlier Laplacian finite element technique. Certainly it has simplified the data processing procedures and much increased the feasible rate of testing.

3 As in the previously reported part of this continuing program of work [3], the perturbations applied to the flow have shown how the rate of heat transfer is enhanced to all but the downstream half of the suction surface, beyond the normal laminar turbulent transition region, which is suppressed by the perturbations. The effects on the heat transfer coefficient are greatest on the pressure surface and the leading edge radius, and rather less on the upstream suction surface.

4 The effects of the frequency of the perturbations remain evident as in the earlier program [3]. Qualitatively the trends are not inconsistent with the theoretical predictions of Ishigaki [2], although the enhancement of heat transfer is greater.

5 There appears to be an effect of Reynolds number upon the enhancement of heat transfer above the rate associated with the corresponding unperturbed flow, and certainly a reasonably encouraging correlation is obtained by modifying the Ishigaki turbulence parameter to take account of this.

6 Nevertheless, clear differences between the different areas of the blade remain in their response to the perturbations, and further work is required to determine whether these can be accounted for by variations in the mainstream turbulence characteristics around the blade section, which currently cannot be measured.

Acknowledgments

Our thanks are due to Rolls Royce Ltd., for the company's continuing support of this work, and to the Science Research Council, for its capital funding of the Thermo-Fluid Mechanics Research Centre of the University of Sussex in which this work is carried out, and for the award of a Research Studentship to one of the authors (WJP).

References

1 Dyban, Y. E., and Epik, E., "Calculation of Convective Heat Transfer from Statistical Characteristics of Turbulence," *Heat Transfer Soviet Research,* Vol. 9, No. 4, 1977.

2 Ishigaki, H., "The Effect of Oscillation on Flat Plate Heat Transfer," *Journal Fluid Mechanics,* Vol. 47, 1971, p. 537.

3 Bayley, F. J., and Milligan, R. W., "The Effect of Free Stream Turbulence upon Heat Transfer to Turbine Blading," AGARD PEP conference on High Temperature Problems in Gas Turbine Engines, paper No. 37, 1977.

4 Turner, A. B., "Local Heat Transfer Measurements on a Gas Turbine Blade," I. Mech. E., *Jnl. of Mech. Eng. Sci.,* Vol. 13, No. 1, 1971.

5 Brown, A., and Martin, B. W., "Heat Transfer to Turbine Blades With Special Reference to the Effects of Mainstream Turbulence," ASME Gas turbine conference, paper No. 79-GT-26, 1979.

Downloaded 01 Jun 2010 to 171.66.16.59. Redistribution subject to ASME license or copyright; see http://www.asme.org/terms/Terms_Use.cfm

Turbomachinery Design Considerations for the Nuclear HTGR-GT Power Plant[1]

Colin F. McDonald
General Atomic Company,
Preliminary Design Department,
San Diego, CA

Murdo J. Smith
United Technologies Corporation,
Power Systems Division,
South Windsor, CT

For several years, design studies have been underway in the U.S. on a nuclear closed-cycle gas turbine plant (HTGR-GT). This paper presents design aspects of the helium turbomachine portion of these studies. Gas dynamic and mechanical design considerations are presented for helium turbomachines in the 400 MWe (non-intercooled) and 600 MWe (intercooled) power range. Design of the turbomachine is a key element in the overall power plant program effort, which is currently directed towards the selection of a reference HTGR-GT commercial plant configuration for the U.S. utility market. A conservative design approach has been emphasized to provide for maximum safety and durability. The studies presented for the integrated plant concept outline the necessary close working relationship between the reactor primary system and turbomachine designers. State-of-the-art technology from large industrial gas turbines developed in the U.S., considered directly applicable to the design of a helium turbomachine, particularly in the areas of design methodology, performance, materials, and fabrication methods, is emphasized.

Introduction

It is projected that by the end of the century closed cycle gas turbine (CCGT) power plants will be operational in the U.S. for electrical power generation because of (1) their adaptability to both nuclear and coal-fired heat sources, (2) very high fuel utilization efficiency, (3) potential for a high degree of reliability and availability and low maintenance, and (4) efficient cost-effective dry cooling where no cooling water is available. Further development is likely since this power conversion system seems well suited to projected fusion and solar power plants of the twenty-first century. The technology bases for CCGT plants are well established with 40 years of European operating experience. These European fossil-fired plants, with electrical power outputs of up to 50 MWe, have demonstrated high degrees of availability and reliability, with several of the units having operated successfully for over 100,000 hr.

The benefits of the nuclear gas turbine power plant are consistent with meeting national energy goals, and the high power conversion efficiency potential satisfies the increasingly important resource conservation demands. The helium turbomachine is the key element in the power conversion system, and this paper outlines the extensive program of design and development necessary in order to commercialize the HTGR-plant for utility service in the last decade of this century.

The design of a new power plant concept is an iterative process to satisfy the various performance, economic, safety, and reliability goals, and several plant configurations have evolved as the program has progressed in the last few years. The most recent design studies done by General Atomic are for a dry-cooled commercial plant in the 800 to 1200 MWe power range [1]. In these power plant studies both intercooled and non-intercooled variants are being investigated, both of these being based on dry-cooling to ensure maximum site selection flexibility within the U.S. Following earlier reported turbomachine work [2–4] this paper addresses design activities currently in progress in support of the aforementioned power plant studies.

For an integrated plant, with the power conversion system installed inside the reactor vessel, the turbomachine cannot be treated as an isolated component, and indeed the design of the machine and the resolution of the gas flow paths and interfacing duct connections, becomes an inherent part of the plant primary system development. In support of the plant configuration studies, turbomachine conceptual designs were done for machines in the 400, 500, and 600 MWe power classes, for both intercooled and non-intercooled types. To span the above power range and to illustrate the difference between the machine types, only the 400 MWe (non-intercooled) and 600 MWe (intercooled) design variants will be addressed in this paper.

To the non-specialist, gas turbines with the above power ratings may seem extremely large compared with open-cycle gas turbine experience, where units up to 100 MWe have been built. In point of fact, the high degree of pressurization associated with the closed-cycle system results in helium turbomachines that are of similar overall size to existing air-breathing industrial gas turbines, but of course exhibit much higher specific power because of the high density and specific heat of the working fluid. State-of-the-art technology from large industrial gas turbines developed in the U.S., considered directly applicable to the design of a helium turbomachine, particularly in the areas of design methodology, performance, materials, and fabrication methods, is emphasized in this paper.

Closed-Cycle Gas Turbine Background

While the closed-cycle gas turbine is not well known in the U.S. it

[1] Work supported by the U.S. Department of Energy, Contract DE-A703-76SF70046.

Contributed by the Gas Turbine Division and presented at the Gas Turbine Conference and Products Show, New Orleans, La. March 10–13, 1980 of THE AMERICAN SOCIETY OF MECHANICAL ENGINEERS. Manuscript received at ASME Headquarters December 13, 1979. Paper No. 80-GT-80.

Copyright © 1981 by ASME

Downloaded 01 Jun 2010 to 171.66.16.59. Redistribution subject to ASME license or copyright; see http://www.asme.org/terms/Terms_Use.cfm

has demonstrated very high fuel utilization efficiencies, and a high degree of reliability in the various European plants that have operated for almost a million hours. Since operation of the pioneer plant in 1939, the 40 years of experience have substantiated the claim that this prime-mover is well established [5]. Some 20 plants were built for combined electrical power and heat production, and details of the operating experience of those known to still be in operation have been discussed in reference [6].

With the helium turbomachine itself being the singularly most important power conversion loop component from the development standpoint it is germane to review the applicability of established technologies. The industrial technology bases from which the turbomachine can benefit are shown in Fig. 1, which illustrates existing hardware. The emphasis in this figure relates to the formidable world-wide resources, which if utilized on an international cooperative basis, will make near-term introduction of the nuclear gas turbine plant a reality.

While helium turbomachines are not well known in the U.S., the array shown in Fig. 2 is included to illustrate that helium axial flow turbomachines over an impressive power range have been constructed and operated successfully in Europe.

An important helium turbine plant is the fossil-fired 50 MWe Oberhausen 2 unit, which was built by Energieversorgung Oberhausen AG (EVO) in the Federal Republic of Germany [7, 8]. In addition to providing electrical power (50 MWe) and district heating (54 MWt), the tests carried out on the EVO plant are intended to supply information (for the European High Temperature Helium Turbine (HHT) Project) on the dynamics of the overall plant and on the long-term behavior of specific components. The selection of a relatively low system pressure for this power plant yields a larger volumetric flow of the helium working fluid, and accordingly the actual equipment size is comparable in size to a plant rated at over 200 MWe. An appreciation for the size of the turbine is given in Fig. 3 which shows details of the high pressure rotor from the EVO plant.

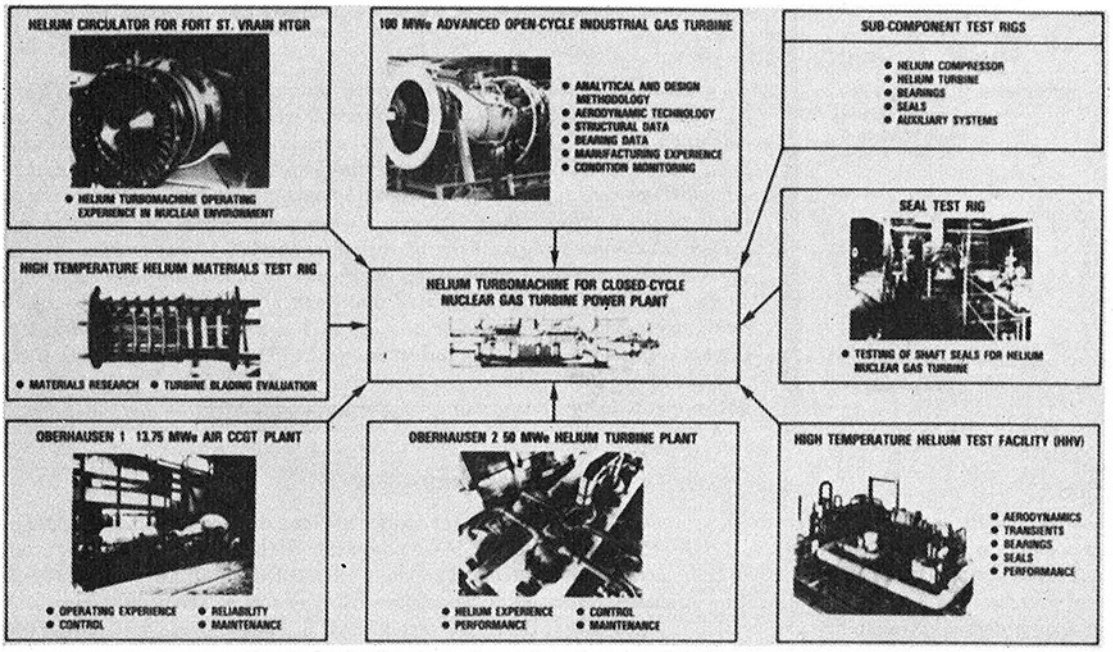

Fig. 1 Technology bases for nuclear closed-cycle helium turbomachine

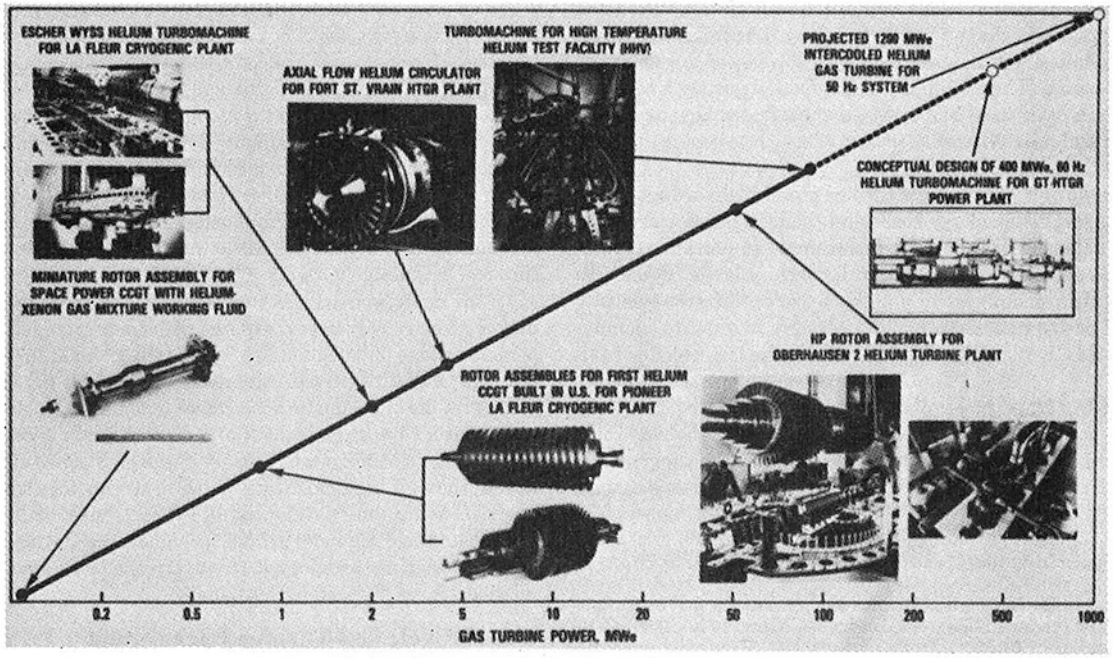

Fig. 2 Helium gas turbomachinery design evolution

Downloaded 01 Jun 2010 to 171.66.16.59. Redistribution subject to ASME license or copyright; see http://www.asme.org/terms/Terms_Use.cfm

Another important plant is the high temperature helium test facility (HHV) at the KFA in Julich in the Federal Republic of Germany. The operation of this helium test plant represents a central test within the European HHT Project. By this program essential characteristics of the turbomachine are to be verified. The turbomachine consists of two turbine stages which produce 45 MWe, and an eight stage compressor which absorbs 90 MWe, the difference being supplied by a 45 MWe synchronous motor. As a result of the compression work, the helium can be heated up to 1000°C (1832°F) so that a heater fired by fossil fuels has been eliminated. The combination of turbine and compressor and the thermodynamic conditions in the closed loop results in a turbomachine with dimensions representative of a helium turbine of approximately 300 MWe output. The rotor for the HHV plant shown in Fig. 4 has a bearing span of 5.7m (18.7 ft) and weighs about 66 tons (60,000 kg). The diameters of the bearings and seals are representative of a large commercial nuclear gas turbine plant.

A full account is given in reference [9] of the roles of the EVO plant and the HHV facility in the development of the European HHT project. The turbomachine design activities outlined in the following sections of this paper are for the HTGR-GT program in the U.S.; however, it should be mentioned that a formidable effort has also been expended in Europe on the design of the turbomachinery for the HHT project [10–13].

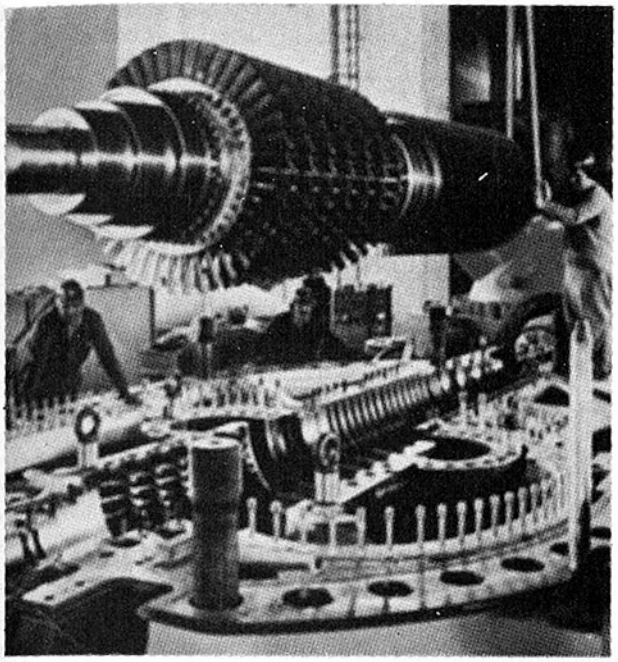

Fig. 3 High pressure rotor assembly for Oberhausen 2 Helium Turbine Plant (by courtesy Gutehoffnungshütte Sterkrade AG)

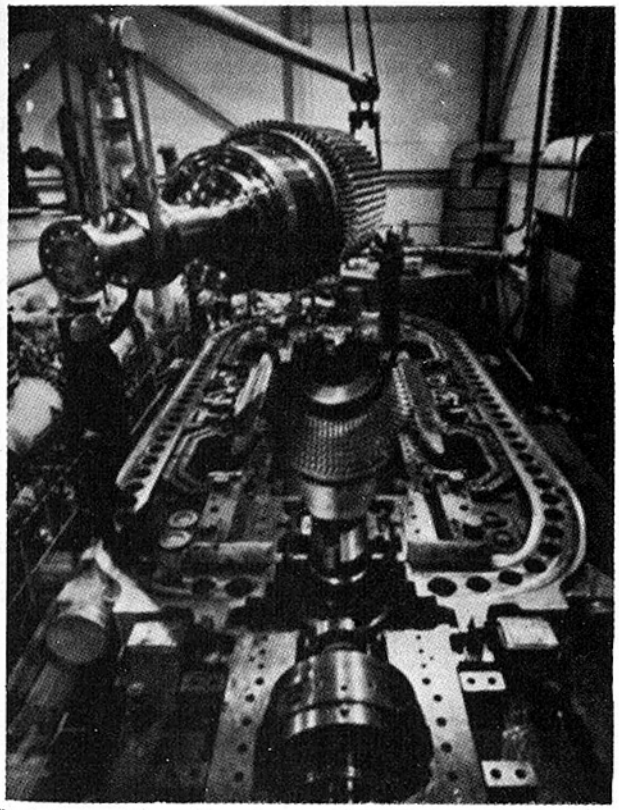

Fig. 4 Helium turbomachine rotor assembly for high temperature helium test facility (HHV) (by courtesy Brown Boveri Company)

HTGR-GT Plant Configuration

Since aspects of the overall plant design are presented in a separate paper at this meeting [1], only a brief description will be made here, the main point to be made being the significance of prime-mover integration in the PCRV on turbomachine design. As the plant configuration has evolved, from an earlier three-loop reference design [14] to the more recent two-loop arrangement, an integrated approach has been retained, and the degree to which the turbomachine is integrated in the PCRV can be clearly seen from Fig. 5.

In current studies of a two-loop plant both intercooled and non-intercooled variants are being evaluated, and for the purposes of this paper the overall features of the HTGR-GT plant concept can be most simply reviewed by addressing the non-intercooled version. The plan view of the PCRV on Fig. 6 shows the slightly offset core cavity and the two horizontal turbomachine cavities oriented in a chordal manner. The recuperator and precooler are positioned over the turbomachine cavity; and in the case of the intercooled variant the additional heat exchanger is positioned off to one side of the turbomachine. The elevation view through the PCRV shown in Fig. 7 gives details of the major components in the power conversion loop. An additional elevation view in Fig. 8 shows the hot gas duct in which the high temperature helium is transported from the reactor to the turbine.

From these figures it can be seen that the helium turbomachine is truly integrated in the reactor primary system, and thus cannot be designed as an isolated component. In addition, to the many mechanical interfaces in the horizontal cavity, the gas flow path directions in and out of a turbomachine play an important role in the development of the flow path geometries within the entire primary circuit.

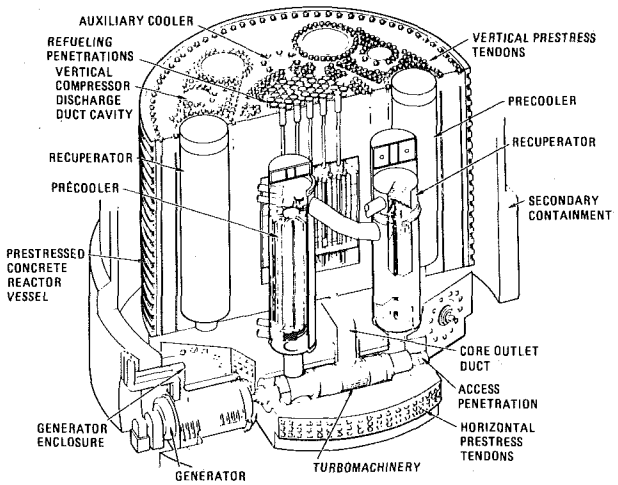

Fig. 5 Isometric view of HTGR-GT power plant primary system showing helium turbomachine integrated in the PCRV

Downloaded 01 Jun 2010 to 171.66.16.59. Redistribution subject to ASME license or copyright; see http://www.asme.org/terms/Terms_Use.cfm

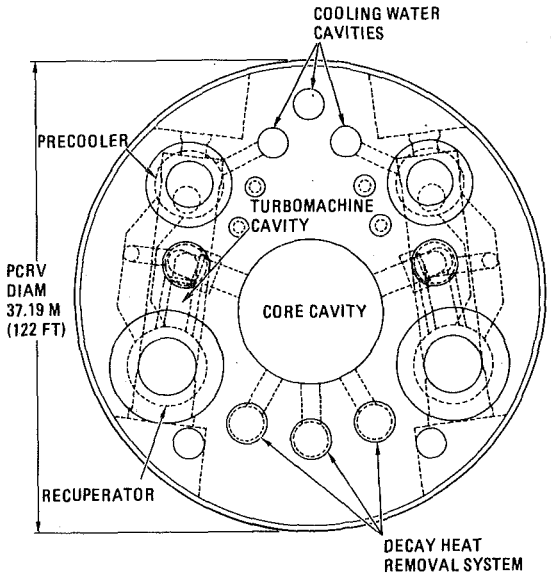

Fig. 6 Plan view of PCRV for two loop non-intercooled HTGR-GT plant showing orientation of major power conversion system components

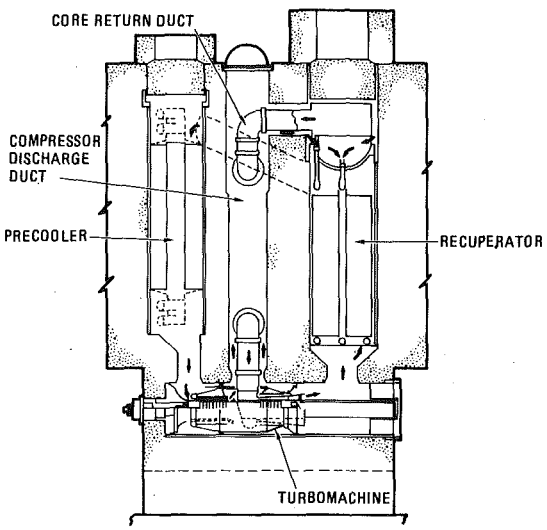

Fig. 7 Elevation view through power conversion loop showing turbomachine and heat exchanger(s) installation

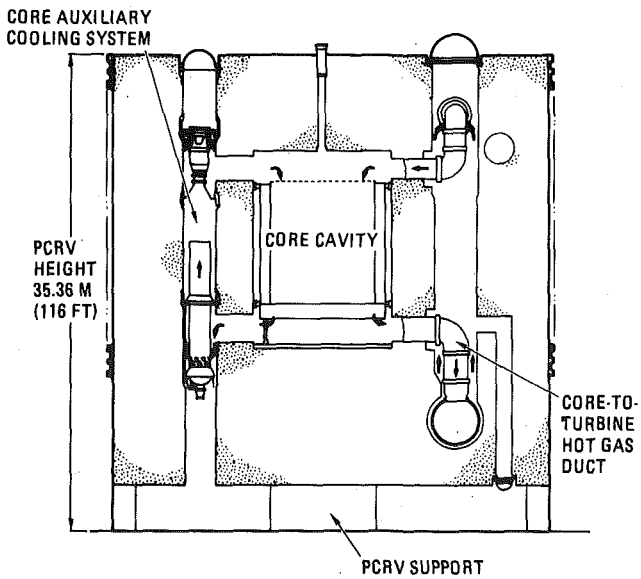

Fig. 8 Elevation view through PCRV showing core cavity and turbine inlet duct

Thermodynamic Cycle Data

As outlined in reference [15], studies have been conducted to select cycle parameters (for minimum power generating cost) for both intercooled and nonintercooled plant variants. For the purpose of initiating turbomachine conceptual designs in support of the plant configuration studies it was necessary to establish comparative cycle data. The tentative values used are shown on Table 1, and these data are felt to be very representative for turbomachine design purposes. The key differences between the two cycles are shown on the loop diagram for the non-intercooled plant (Fig. 9), and the flow path diagram for the intercooled variant (Fig. 10).

From Table 1 it can be seen that the compressor pressure ratio for the intercooled variant optimized out a little higher than for the non-intercooled cycle, and this results in an increased specific power. The maximum system pressure of 7.93 MPa (1150 psia) is the same for both cycles, and is related strongly to cost of the PCRV. An important parameter influencing the efficiency is the turbine inlet temperature, and for both cycles a value of 850°C (1562°F) was assumed. As shown in Fig. 11 this temperature is modest compared to that for most industrial gas turbines; it is below the level where turbine blade cooling is necessary, and it facilitates utilization of an existing nickel-base alloy which is used extensively in industrial gas turbines.

Turbomachine Gas Dynamic Design Considerations

For both the non-intercooled and intercooled machines simple and rugged arrangements consisting of single shaft, two bearing, direct-drive, turbomachine arrangements were chosen for the HTGR-GT plant, and simplified cross sections of the 400 MWe non-intercooled, and 600 MWe intercooled machines are shown in Figs. 12 and 13, respectively, and details are given in Table 2.

For an integrated plant arrangement, with a limitation on machine envelope, close cooperation between the turbomachinery and primary system designers is essential. Since high turbomachinery efficiencies are required, it is important that minimum loss ducts to and from the compressor and turbine be incorporated, this necessitating close attention to the interfacing of the gas turbine with the other components in the power conversion loop. Minimum loss ducts with carefully contoured geometries to give good flow distribution into the compressor and turbine tend to require large volutes and scrolls; however, with installation of the machine in the horizontal cavity in the PCRV, and the requirement of minimizing the bearing span to give satisfactory rotor dynamic characteristics (i.e., critical speed margin), large flow areas are not available (as can be seen in Figs. 12 and 13), and

Table 1 HTGR-GT plant(s) cycle data

Thermodynamic Cycle	Non-Intercooled	Intercooled
Heat Rejection Mode	Dry-Cooled	
Ambient Air Temp., °C (°F)	15 (59)	
Recuperator Effectiveness	0.90	0.90
Approx. System Pressure Loss (ΔP/P), %	9	11
Compressor Flow, kg/s/MW(t)	0.57	0.50
Compressor Inlet Temp., °C (°F)	26.7 (80)	26.7 (80)
Compressor Inlet Pressure, MPa (psia)	3.17 (460)	2.64 (383)/4.5 (653)
Compressor Pressure Ratio	2.50	3.0 (1.73/1.73)
Compressor Efficiency, %	89.8	90.8 LP, 90.2 HP
Turbine Inlet Temp., °C (°F)	850 (1562)	850 (1562)
Turbine Inlet Pressure, MPa (psia)	7.65 (1109)	7.56 (1096)
Turbine Expansion Ratio	2.34	2.74
Turbine Efficiency, %	91.8	92.2
Turbine Cooling Flow, %*	3.6	3.6
Precooler Water Outlet Temp., °C (°F)	132 (270)	87 (189)
Intercooler Water Outlet Temp,, °C (°F)	---	66 (150)
Approx. Cycle Efficiency, %	40.0	42.0

*The designs of both machines are based on utilization of uncooled turbine blades, and the cooling flows indicated (as a percentage of compressor discharge flow) are necessary for cooling the turbine rotor, structures, and casing to satisfy the 280,000-hr life requirement.

Downloaded 01 Jun 2010 to 171.66.16.59. Redistribution subject to ASME license or copyright; see http://www.asme.org/terms/Terms_Use.cfm

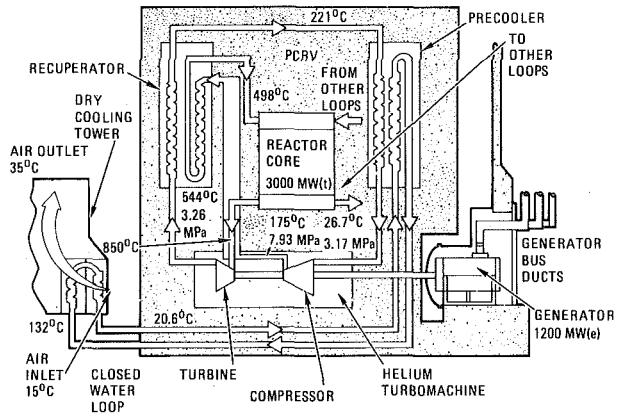

Fig. 9 Loop cycle diagram for non-intercooled dry-cooled HTGR-HT power plant

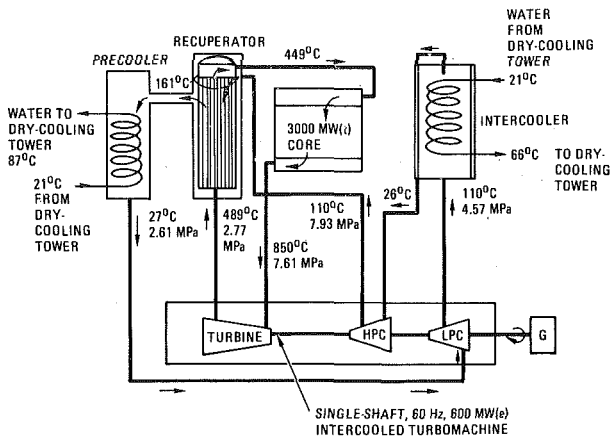

Fig. 10 Flow path diagram for intercooled HTGR-GT power plant

trade-offs are necessary to satisfy both aerodynamic and structural requirements for the selected primary system. Gas dynamic design considerations for the compressor and turbine are briefly discussed below.

Compressor Gas Dynamic Design Considerations. Since axial compressor aerothermodynamic design techniques have been well documented, it is not the intent to describe detailed analyses in this paper, but rather to outline how the fluid properties of helium influence the flow path geometries, and to emphasize that the gas dynamic procedures used are essentially identical to conventional air-breathing gas turbine practice.

The choice of working fluid affects the turbomachine primarily in two ways: (1) the number of stages for the attainment of the required compressor pressure ratio and high efficiency, and (2) the machine size for a high pressure closed system. The specific heat of helium is five times that of air, and since the stage temperature rise varies inversely as the specific heat (for a given limiting blade speed), it follows that the temperature rise available per stage when running with helium will be only one fifth that of air, and this of course results in more stages being required for a helium compressor. It is fortunate that the optimization (for maximum cycle efficiency) of a highly recuperated closed cycle system gives a relatively low pressure ratio, hence the number of compressor stages (18 and 16 for the non-intercooled and intercooled variants, respectively, as can be seen from Table 2) is comparable with existing open-cycle industrial gas turbines.

Substitution of helium for air greatly modifies aerodynamic requirements by removing Mach number limitations; the problem then becomes that of trying to induce the highest possible gas velocities that stress limited blades will allow. For the selected single-shaft arrangements outlined in Table 2, the compressor rotational speed is, of course, fixed at the generator synchronous speed of 3600 rpm for a 60 Hz machine. The size of the machine is thus dictated by the choice of blade speed, there being an incentive to use the highest values possible commensurate with stress limits to reduce the number of stages, since the stage loading factor is inversely proportional to the square of the blade speed.

For the specified thermodynamic conditions, detailed gas dynamic analyses were performed by United Technologies Corporation to identify optimum solutions for the HTGR-GT turbomachine. Details of the selected compressor designs are given in Table 2. Helium compressors for closed-cycle gas turbines are characterized by small blade heights, high hub-to-tip ratios, and low aspect ratios. An important parameter is the rear stage hub-to-tip ratio, and an accepted upper limit for high efficiency compressors is about 0.90. With high pressure helium, the blade heights are small and end-wall losses become significant; thus, careful mechanical design is necessary to minimize tip clearance effects. While the end-wall effects have an adverse effect on efficiency, two factors that will partially offset this are the very high Reynolds numbers (6×10^6), and the very low Mach number (0.40). The high efficiency design solutions given in Table 2 have acceptable gas dynamic loading factors characteristic of conservatively designed industrial gas turbines, and should give a satisfactory surge margin.

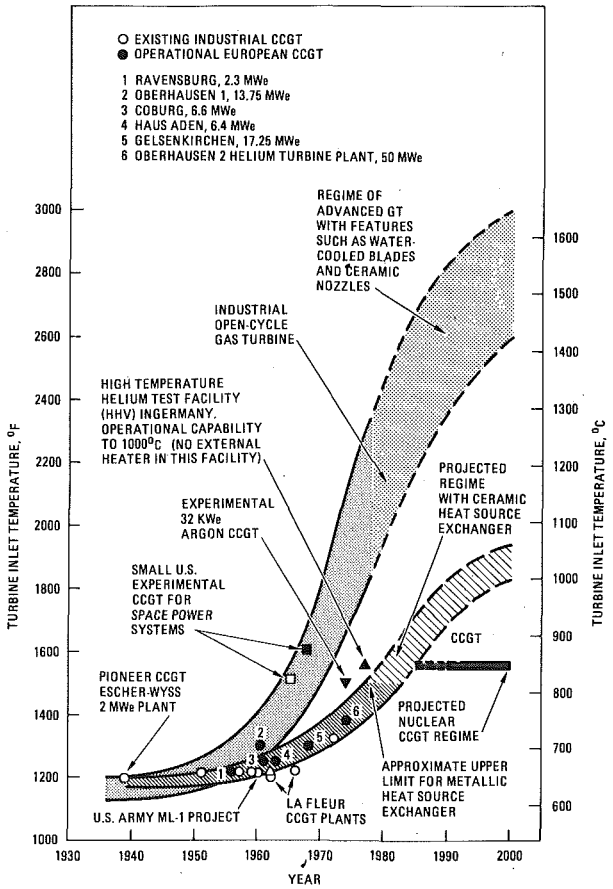

Fig. 11 Turbine inlet temperature trends for closed-cycle and open-cycle industrial gas turbines

Turbine Gas Dynamic Design Considerations. The properties of helium affect the turbine in very much the same way as they influence the compressor. That is to say for a given expansion ratio, the total number of stages for a helium turbine will be much greater than for an air-breathing gas turbine. Because it is desirable to have as high a blade speed as possible in order to reduce the number of stages to a minimum, the most critical stress conditions are those of the first stage since the rotor blade temperature is at the maximum value.

The turbine blade centrifugal stress (for a given blade geometry) is proportional to the $\text{rpm}^2 \times$ annulus area, and for a single shaft, 60 Hz machine, one degree of freedom is lost to the designer. A conser-

Downloaded 01 Jun 2010 to 171.66.16.59. Redistribution subject to ASME license or copyright; see http://www.asme.org/terms/Terms_Use.cfm

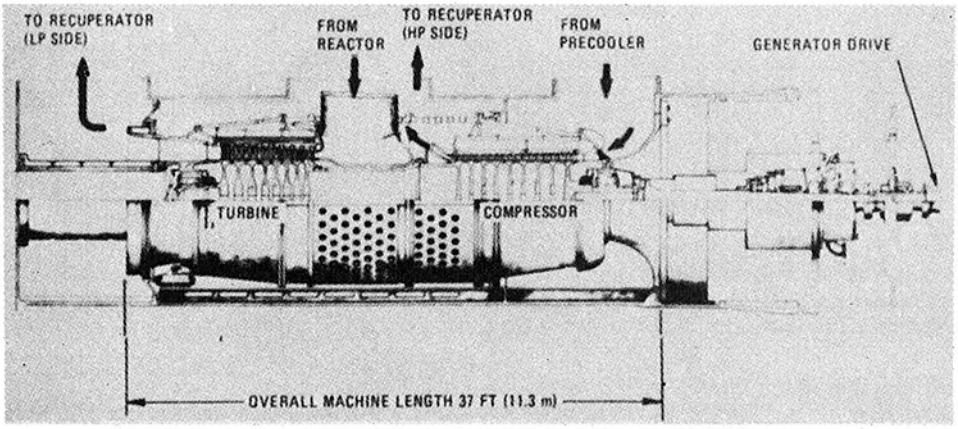

Fig. 12 Arrangement of 400 MWe, non-intercooled turbomachine for HTGR-GT plant

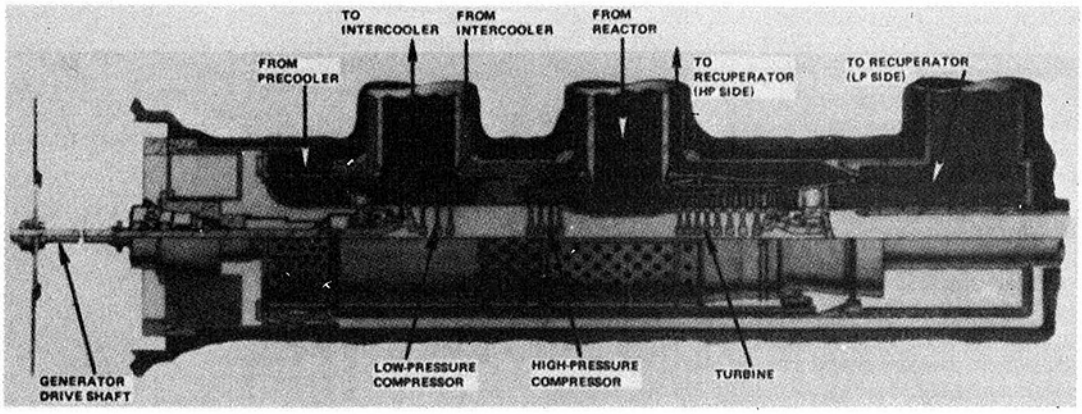

Fig. 13 Arrangement of 600 MWe, intercooled turbomachine for HTGR-GT plant

vative ground rule established for the HTGR-GT plant, is that the stress levels in the primary system components must be commensurate with the plant operating life of 280,000 hours (i.e., 40 years with a capacity factor of 80 percent). The preliminary turbine designs (with a gas inlet temperature of 850°C) performed by United Technologies Corporation, and outlined in this paper have been based on the use of an existing turbine blade nickel-base alloy that has been used extensively in open-cycle industrial gas turbines. The use of advanced materials (molybdenum alloys for example) or blade cooling may be desirable at some time in the future when reactor outlet temperatures are increased above the present-day value.

From Table 2 it can be seen that eight and nine stage turbine designs were selected for the non-intercooled and intercooled plant variants respectively. With tip speeds, conservative by modern industrial turbine practice, it can be seen that helium turbines are characterized by small blade heights. In fact the turbine is substantially smaller than an equivalent air-breathing turbine since the enthalpy drop in the helium turbine is many times greater (i.e., very high specific power).

Turbomachinery Performance Predictions. The performance predictions for the helium turbomachines discussed in this paper are based on established design methodology, and the high compressor and turbine efficiency values given in Table 2 reflect the influence of technology from a demonstrated advanced-technology industrial gas turbine (UTC 100 MWe FT-50 engine) as described in references [16] and [17]. The closed-cycle gas turbine plant is sensitive to small changes in compressor and turbine efficiencies as can be seen in Fig. 14, which illustrates performance data for the non-intercooled cycle.

Since the design of the helium turbomachinery for the HTGR-GT plant draws heavily on established industrial gas turbine practice, it is germane to compare design parameters. In Table 3 the salient features of the HTGR-GT turbomachine are compared with the FT-50, 100 MWe industrial gas turbine. Flow path geometries and gas dynamic features of these two machines are compared in Fig. 15. Mechanical design comparisons are discussed in the following section.

Table 2 Details of HTGR-GT plant turbomachine designs

Turbomachine Rating, MW(e)	400	600
Machine Type	Non-Intercooled	Intercooled
Machine Arrangement	Single-Shaft	Single-Shaft
Frequency, Hz	60	60
No. of Turbine Inlet Ducts	1	1
Turbine Inlet Temp., °C (°F)	850 (1562)	850 (1562)
Compressor Pressure Ratio	2.50	3.0 (1.73/1.73)
No. of Compressor Stages	18	8 + 8
Max. Compressor Tip Dia., m (in.)	1.83 (71.9)	2.18 (85.9)
Blade Height, mm (in.) (min./max.)	80.0/125.7 (3.1/4.9)	76.2/165.1 (3/6.5)
Comp. Adiabatic Efficiency (across blading), %	89.8	90.8 LP/90.2 HP
No. of Turbine Stages	8	9
Max. Turbine Tip Dia., m (in.)	2.18 (86)	2.40 (94.5)
Blade Height, mm (in.) (min./max.)	125.7/297.2 (4.9/11.7)	165.1/393.7 (6.5/15.5)
Turbine Isentropic Efficiency (across blading), %	91.8	92.2
Blading Life, hr	280,000	280,000
Blade Cooling	No	No
Turbine Blade Material	Nickel-Base Alloy, IN-100	
Generator Drive End	Compressor	
Rotor Burst Shield	Yes, Integral Part of Machine Structure	
Thrust Bearing Position	External to PCRV	
No. of Journal Bearings	2	2
Journal Bearing Man Access	Yes	Yes
Type of Rotor Construction	Welded Rotor	Welded Rotor
Machine Casing Diameter, m (ft)	4.0 (13.1)	4.0 (13.1)
Machine Length, m (ft)	11.3 (37)	15.8 (52)
Machine Weight, kg (ton)	276,770 (305)	317,600 (350)
Design Technology Base	Large Industrial Open-Cycle Gas Turbines	

Turbomachine Mechanical Design Considerations

Design criteria, unique to the nuclear application, had a strong influence on the overall design of the helium turbomachine, and the two variants shown in Figs. 12 and 13 are of similar enough overall

Downloaded 01 Jun 2010 to 171.66.16.59. Redistribution subject to ASME license or copyright; see http://www.asme.org/terms/Terms_Use.cfm

construction to be addressed together as follows. Because the machine will become contaminated in service the overall design of the casings and structures must be such that remote handling, decontamination, and maintenance procedures are applicable. At first sight the above requirements could be well satisfied with an arrangement having a full length split casing design. For such a configuration (as shown in Figs. 3 and 4 for example) the cases could be separated and the rotor removed as a single unit. An important element in the design of the turbomachine is the incorporation of containment rings around the rotor bladed sections to contain fragments and missiles in the unlikely event of a rotor failure. Use of a full length split casing design would require incorporation of split containment rings, which as will be discussed below are not felt to be viable.

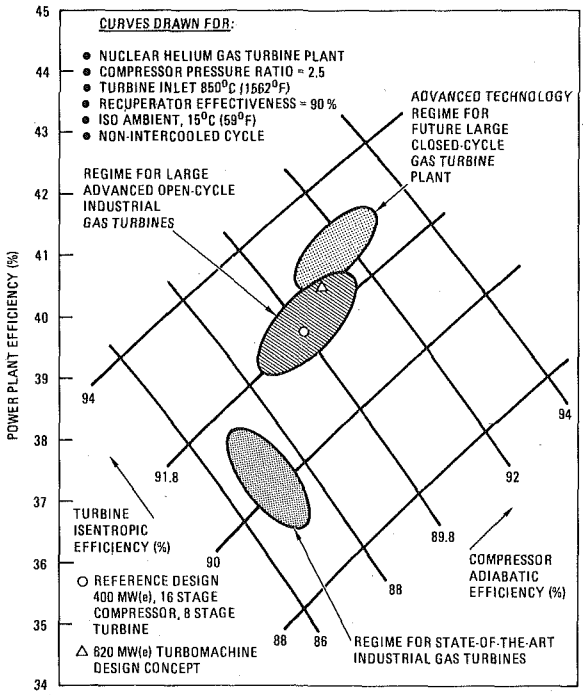

Fig. 14 Array showing influence of compressor and turbine efficiencies on performance of non-intercooled HTGR-GT power plant

As shown in Figs. 12 and 13 the turbomachine casing are of the double-wall type in which the stator blades of the turbine and compressor are supported on an inner high temperature resistant casing and the alignment between the bearing housing and the high temperature casing is maintained by the cooled outer casing. The overall structure can best be appreciated by studying Fig. 16, which shows the separation sequence for a candidate intercooled machine. The way in which the casings are split satisfies the aforementioned requirements of (1) remote disassembly capability, and (2) full circumferential containment rings. Key elements of the helium turbomachine mechanical design are discussed below.

Turbomachine Rotor. A simple two-bearing arrangement was selected for the turbomachine rotor, and man access cavities have been provisioned in the PCRV for inspection and limited work on the journal bearings. Detailed rotor dynamic analyses have confirmed the adequacy of the two bearing arrangement, and satisfactory critical speed margins have been identified for the overspeed condition.

The rotor is of welded construction. Welded rotors have a long successful history in Europe. The view of the compressor rotor (for the non-intercooled machine) in Fig. 17 shows the welded disc construction, the tangential blade attachments, and the dual blade rows mounted on each disk. This design minimizes weight, machining time, and number of parts compared with more traditional bolted-up rotor assemblies. The turbine design shown in Fig. 18 also employs the welded rotor concept. It has an insulated case to reduce materials cost and give tip clearance control. Tangential blade attachments are used to minimize turbine secondary cooling requirements and improve performance.

Unlike fossil-fired open-cycle gas turbines (aircraft and industrial) low cycle fatigue and hot corrosion are not design factors, however,

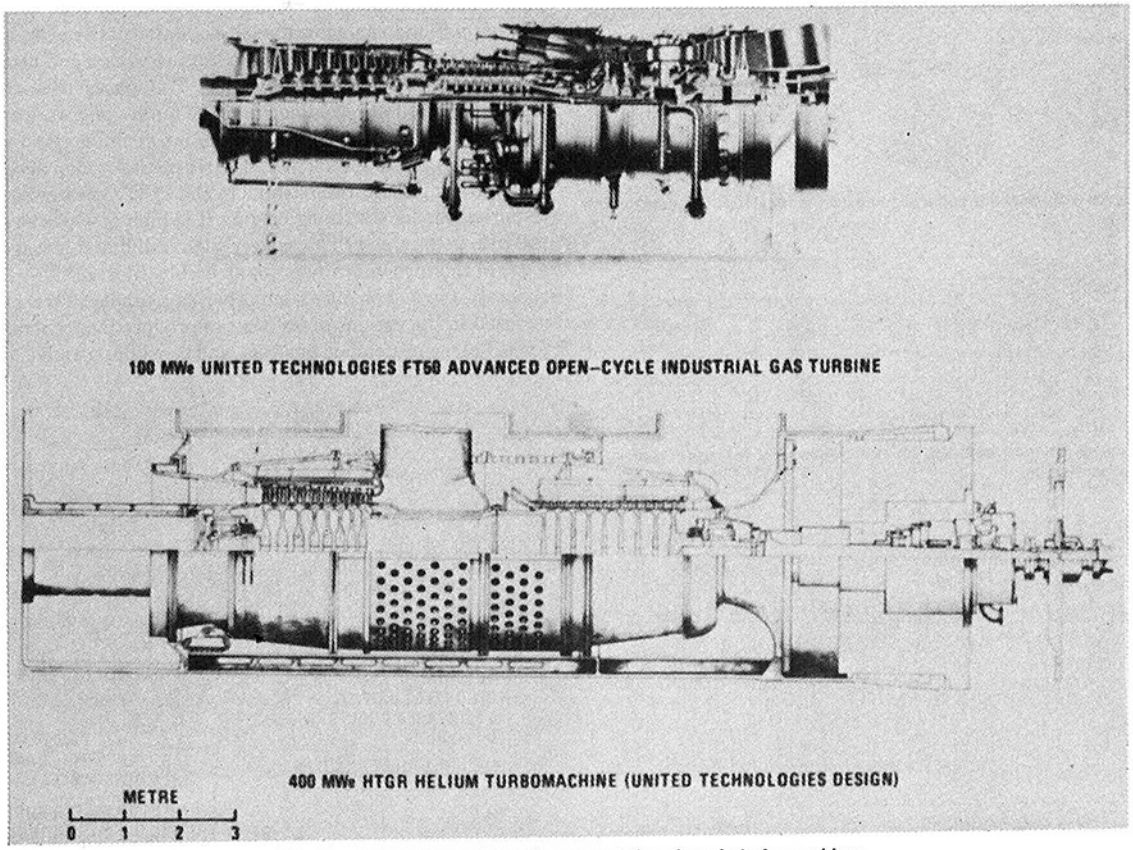

Fig. 15 Comparative sizes of open and closed-cycle turbomachines

Downloaded 01 Jun 2010 to 171.66.16.59. Redistribution subject to ASME license or copyright; see http://www.asme.org/terms/Terms_Use.cfm

creep rupture and high cycle fatigue are design considerations. For the turbine blading, creep is the life limiting factor. In the case of the turbine discs, fracture mechanics are the controlling design criteria. A total bleed flow from the compressor of 3.6 percent of the total flow is required for cooling of the hot-end structures. The turbine casing requires 0.6 percent of the flow, and 3.0 percent is distributed in the turbine welded rotor assembly to give an average disk temperature of 315°C (600°F). For the turbine blading (uncooled) the stress level is well within the limits for 1 percent creep of the nickel-base alloy IN-100 at 280,000 hours, which is the design life of the blading.

Aircraft and industrial gas turbines are designed so that in the event of a blade failure the fragments are contained within the machine casings. The casings of these machines, however, are not designed for containment of a failed rotor for reasons of weight limitation for the aircraft application, and economic considerations in the case of industrial applications. This design practice has proved to be sound since rotor failures in modern gas turbines are rare events.

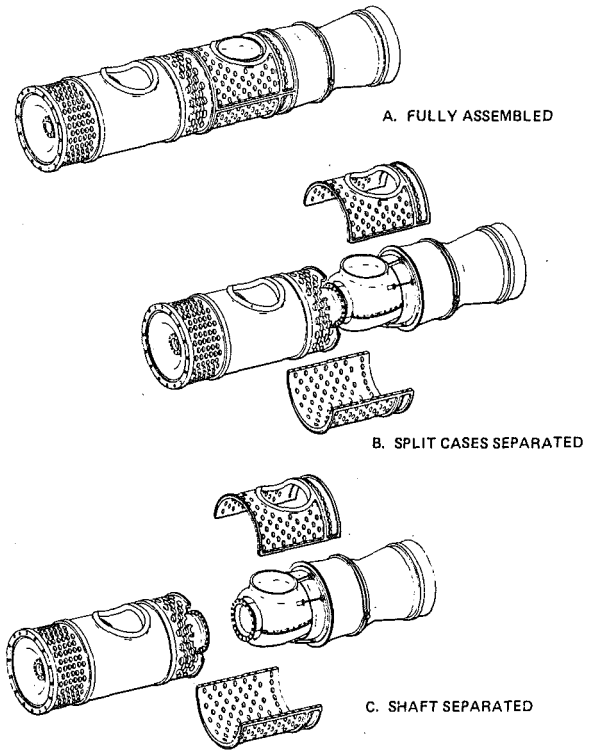

Fig. 16 Example of assembly separation sequence for HTGR-GT plant helium turbomachine

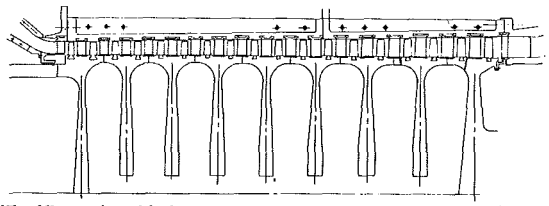

Fig. 17 View of welded compressor rotor assembly for non-intercooled HTGR-GT turbomachine

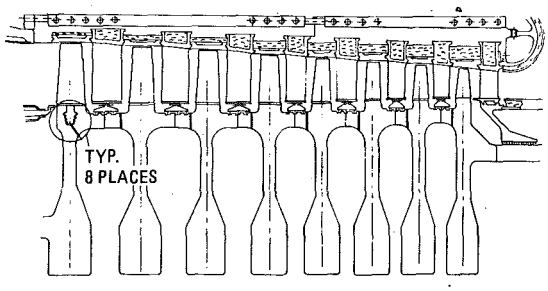

Fig. 18 View of welded turbine rotor assembly for HTGR-GT turbomachine

For the HTGR-GT plant, with the turbomachine installed inside the reactor vessel, it was felt not only to be prudent, but in fact a safety requirement, that fragments and missiles generated in the unlikely event of a rotor failure, would be contained within the turbomachine casing. As mentioned previously, rotor burst protection is incorporated in the machine design in the form of containment rings (sometimes referred to as burst or missile shields) around the compressor and turbine rotor bladed sections [18]. The procedure outlined in reference [19] was used to analyze the mechanics of containment of the eighth stage disk in the 400 MWe helium turbomachine at the minimum burst speed condition, which for this machine is 150 percent of the 3600 rpm operating speed. The analysis showed that a containment ring of 178mm (7 in.) in thickness should be adequate to contain an eighth stage disk failure. The nature of the energy absorption process, which depends upon large plastic strain in the containment ring, precludes the use of any sort of axial mechanical joints in the ring, and as mentioned earlier negates the use of a full-length horizontally split casing configuration.

Bearings. Oil-lubricated journal bearings were chosen since, in general, minimum film thicknesses for oil bearings were found to be about twice as great as those for water bearings with the same length/diameter ratio, and maximum allowable misalignments were found to be more flexible than for water bearings. Similarly gas and magnetic bearings were not considered feasible for such large systems, with rotor weights in excess of 60,000 Kg (66 Ton). The journal bearings are subjected to high radial loading during normal operation and must be capable of withstanding temporary overload due to a seismic event.

Tilting pad bearings were selected because of their self-aligning stability. Details of the journal bearings for the 400 MWe machine are shown in Fig. 19. The bearings are five-pad tilting pad designs with a shaft journal diameter of 508mm (20 in.) and a length of 406mm (16 in.). For the 600 MWe machine the diameter is 600mm (24 in.), and as shown in Table 3 these values compare with 381mm (15 in.) for a 100 MWe open-cycle industrial gas turbine. Referring to Fig. 19 the pads are supported on pivots offset from the pad center in the direction of rotation to enhance the self-actuation of the pads. Man access cavities are provided in the PCRV for inspection and limited maintenance work on the journal bearings. The spaces in which the bearings are located are isolated from the main cycle working fluid by shielding (purge gas from the helium purification system is used to give an acceptable radiological environment for man access).

Integrating the turbomachine in the PCRV creates some unique requirements for the thrust bearing. The high pressure level at which the plant operates produces very high individual forces in various parts of the turbomachine rotor assembly. Most of these forces, fortunately, tend to balance each other, but small differences in areas exposed to the various pressures can produce large changes in axial force. Following detailed analyses, and providing an adequate margin

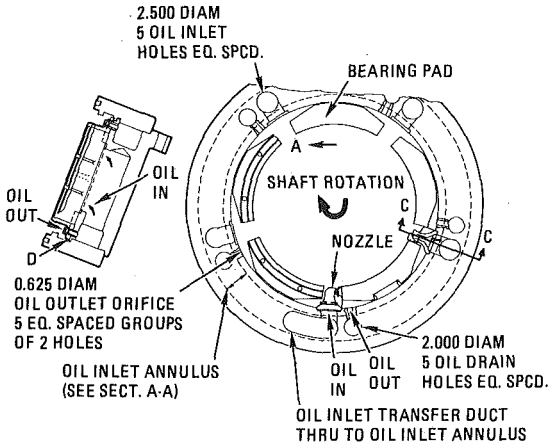

Fig. 19 Journal bearing details for helium turbomachine

Downloaded 01 Jun 2010 to 171.66.16.59. Redistribution subject to ASME license or copyright; see http://www.asme.org/terms/Terms_Use.cfm

of safety, the design load for the 400 MWe machine was taken to be 90,745 Kg (100 tons). To meet this loading requirement a double-acting tilting pad bearing with a thrust collar diameter of 762mm (30 in.) and eight pads per side was designed. The drive to the generator is from the compressor end of the turbomachine, and this permits the thrust bearing to be located external to the PCRV. The motivation for external positioning of this bearing is twofold; (1) inspection and maintenance are eased, and (2) it keeps to a minimum the number of oil lubrication systems inside the reactor vessel. With an outer diameter of 762mm (30 in.) and a rotational speed of 3600 rpm, the thrust bearing is slightly beyond current thrust bearing experience. However, it is the opinion of bearing manufacturers who have been consulted that the design is attainable with little more in the way of development than a demonstration test.

Bearing Compartment Seals. With the journal bearings enclosed within the primary coolant system of the reactor an important aspect of the turbomachine design is the prevention or minimization of the ingress of lubricants into the primary system. Ingress of oil into the primary system is to be avoided or minimized since it can react in a deleterious manner with the reactor core, or be deposited in the thermal insulation or on the heat exchanger surfaces. A requirement was established that the bearing compartment leakage should not exceed 0.028 m^3 (1 ft^3) per year. Primary coolant must also be excluded from the bearing compartment since it carries quantities of radioactive material which would contaminate the lubrication system. A detailed study (following an initial investigation outlined in [3]) of the bearing compartment seals and service systems identified a sealing system which appears to be feasible on the basis of experience with industrial gas turbines.

Table 3 HTGR-GT-industrial gas turbine comparison

Application	Nuclear Closed-Cycle Gas Turbine		Industrial Open-Cycle Gas Turbine
Power Plant	HTGR-GT		FT-50
Turbomachine Status	Conceptual Design		Operational
Turbomachine Type	Single-Shaft		Split Shaft
Power Output, MW(e)	400	600	100 Non-Intercooled
	Non-Intercooled	Intercooled	
Working Fluid	Helium	Helium	Air
Rotational Speed, rpm	3600	3600	LP Compressor 3520 HP Compressor 4200 Power Turbine 3600
Turbine Inlet Temp., °C (°F)	850 (1562)	850 (1562)	1121 (2050)
Turbine Blade Temp., °C (°F)	816 (1500)	816 (1500)	816 (1500)
Compressor Pressure Ratio	2.50	3.0	16.0
No. of Compressor Stages	18	8 + 8	17
No. of Turbine Stages	8	9	4
Max. Compressor Disk Dia., mm (in.)	1575 (62)	1854 (73)	1321 (52)
Max. Turbine Disk Dia., mm (in.)	1600 (63)	1600 (63)	1575 (62)
Max. Blade Height, mm (in.)	297 (11.7)	394 (15.5)	635 (25)
Max. Turbine Tip Speed, m/s (ft/sec)	412 (1350)	453 (1485)	536 (1760)
Max. Journal Bearing Dia., mm (in.)	508 (20)	600 (24)	381 (15)
Max. Engine Dia., m (ft)	4.0 (13.1)	4.0 (13.1)	3.2 (10.5)
Overall Length, m (ft)	11.3 (37)	15.8 (52)	11.6 (38)
Assembly Weight, kg (ton)	276,770 (305)	317,600 (350)	113,430 (125)

The selected configuration consists of three seals mounted in series. The inner two are helium-buffered labyrinth seals which are backed up by a failure-actuated collar seal. Details of the bearing lubrication and buffering system are given in Fig. 20. The source of buffering helium is two parallel supply tanks, each with its own isolation valve. Two helium-buffered labyrinth seals are positioned in both the compressor and turbine journal bearing compartments. A view of a single element of the seal is shown schematically in Fig. 21. The seal shown is a multistage labyrinth type with the stages in radial steps. These seals are similar to the Ljungstrom seals used successfully by the Swedish turbine industry for many years. In normal operation, purified helium is pumped into the inlet cavity of each seal and flows in two directions through the seal assembly. Approximately 95 percent of the buffering helium flows through the large number of knife-edge seals and leaks into the primary coolant flow so as to prevent backflow of contaminated primary helium into the bearing casing. The bearing compartment is sealed off and permits no through flow, except for a small amount of oil and helium mixture which flows back to the separation system.

Inside the aforementioned twin buffer seals a collar seal has been incorporated. This is basically a collar around the shaft at a clearance slightly greater than that of the labyrinth seals. The purpose of this seal is to prevent oil leakage into the main helium stream in the event of destructive failure of the labyrinth seals due to bearing or shaft failure. In addition, the system includes an oil return pump. It is designed so that during catastrophic failure the high-flow supply pump

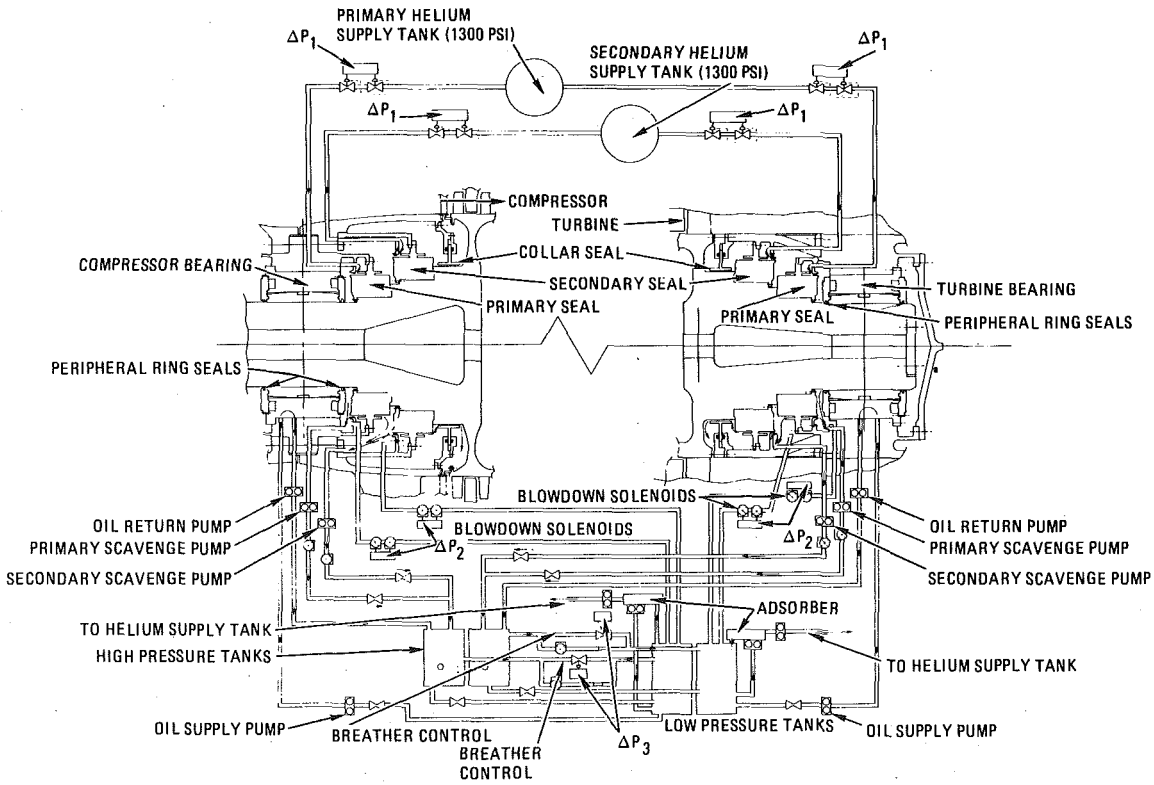

Fig. 20 Bearing lubrication and buffering system for helium turbomachine

Downloaded 01 Jun 2010 to 171.66.16.59. Redistribution subject to ASME license or copyright; see http://www.asme.org/terms/Terms_Use.cfm

could be shut down while the return pump scavenges the bearing compartment, thus leaving a smaller quantity available for possible ingress into the primary system. A failure mode and effect analysis was performed on the journal bearings lubrication and buffering system, and it revealed no significant concerns.

Turbomachine Cavity Seals. With installation of the turbomachine into the horizontal cavity in the PCRV there are two possibilities for machine-to-primary system interface; (1) flanged connections, and (2) compartmentalizing the cavity by means of circumferential seals. Flanged joints require very close tolerance control between the turbomachine and the vessel (both of which are subject to deflection due to thermal and creep effects over the life of the plant) and remote mechanisms for coupling and uncoupling. Early primary system studies indicated the preference for the seal concept (as shown schematically in Figs. 12 and 13) based on the following: (1) advantage

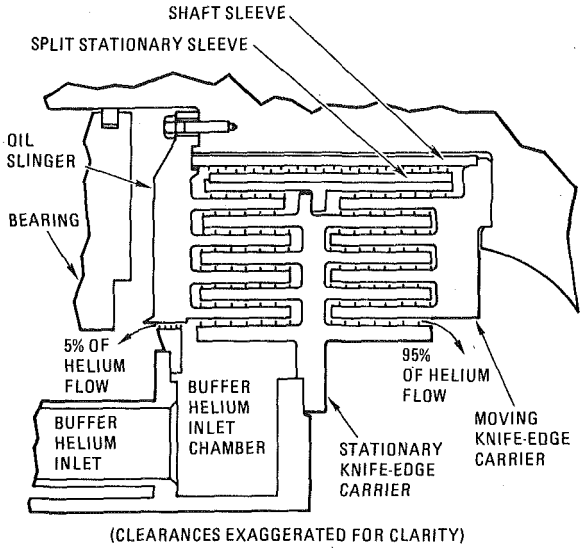

Fig. 21 Details of labyrinth seal in bearing compartment of helium turbomachine

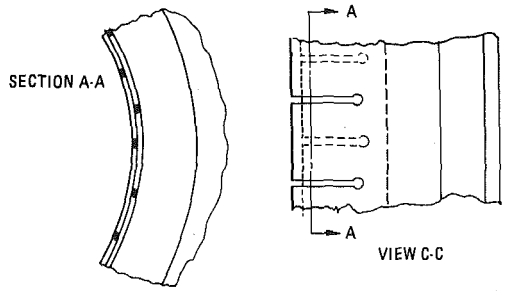

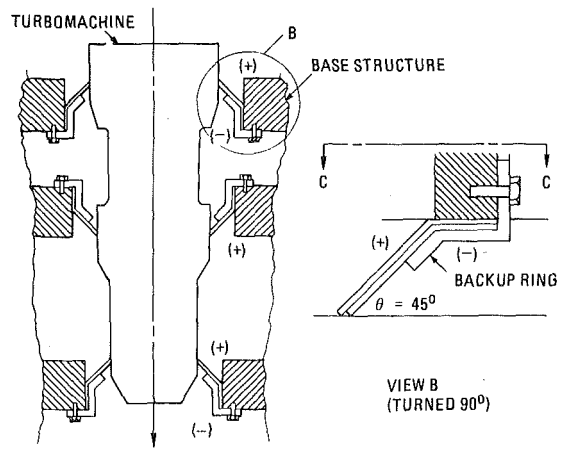

Fig. 22 Details of turbomachine-to-cavity circumferential case seal design concept

was taken of the cavity compartmentation in that the cavity itself was utilized as the flow boundary, this effectively reducing the turbomachine inlet and exit losses by virtue of the increased area associated with the "integral" plenum, (2) tolerance flexibility, and motion compliance between the PCRV and the turbomachine, and (3) eased maintenance procedure (i.e., elimination of remote retraction and back-up systems).

It was recognized in early investigations that the design of large circumferential seals with minimum leakage characteristics represented a formidable task. The present conceptual design includes utilization of segmented piston ring seals for isolation of the various flow plenums. Although performance of this type seal is well known and documented, and can be used as a standard against which other types may be compared, concern exists over use of piston rings of very large size. Current investigations are aimed at the possibility of using a leaf type seal which can be attached to the basic support structure and seals against the machined outer diameter of the engine cases. More confidence exists in establishing the roundness of this case than one incorporated into the support structure.

As shown in a simple form in Fig. 22, the seal arrangement consists of overlapping leaves in two layers fixed at one end to the support structure with the flexible leaves seated against the case ring. The system utilizes the pressure differential across it to create additional sealing force at the interface, thus minimizing leakage.

Materials Selection for Helium Turbomachine Design. At the onset of HTGR-GT plant studies a philosophy was established based on conservatism of design and safety, that the power conversion system components would be designed for the full operating life of the plant of 280,000 hours (40 years at 80 percent capacity factor). It was recognized, that in the case of the turbomachine, the turbine blading for example could be replaced in the 40 year time. Nevertheless, the aforementioned criteria were adopted, and the stress levels in the turbomachine are commensurate with the 280,000 hr operating life. Thus, while the turbine inlet temperature is modest compared with current industrial gas turbine practice, the long life requirement necessitates utilization of high grade alloys.

While the HTGR-GT plant is a long-term project (from concept selection to commercialization) the aforementioned conservatism was extended to material selection, and it was felt prudent to base the design on existing materials (i.e., no reliance is made for materials breakthroughs in the design). From Table 4 it can be seen that for the various elements of the turbomachine, existing materials have been selected. It is recognized that as better materials are developed and qualified for utility service, they will be factored into the program in a prudent manner.

The long-term behavior of materials under a representative reactor environment is being characterized and the environmental effects on material properties quantitatively established. The General Atomic materials screening program represents only a part of an overall effort being carried out by several countries to establish materials data for

Table 4 Materials selected for HTGR-GT plant turbomachine

Component	Material
Compressor	
Disks	Ladish D6AC Low Alloy Steel
Hubs	9 Ni - 4 Co - 0.2 C Steel
Blades, Vanes	AMS 6414 (AISI4340) Low Alloy Steel
Cases	ASTM A-515 Gr 55 Carbon Steel
Mounts	ASTM A-387 Gr 12 / ASTM A-217 WC6 — Low Alloy Steels
Ducts	
Containment Ring	AMS 5613 (AISI 410) Stainless Steel
Turbine	
Disks	Ladish D6AC Low Alloy Steel
Hubs	9 Ni - 4 Co - 0.2 C Steel
Blades	PWA 658 (IN-100) Ni-Base Alloy
Vanes	PWA 1447 (MAR-M-247) Ni-Base Alloy
Blade Tip Seals, High-Temperature Ducts	AM 5783 (Hastelloy S) Coated
Cases	ASTM A-515 Gr 55 Carbon Steel
Mounts	ASTM A-387 Gr 12 / ASTM A-217 WC6 — Low Alloy Steels
Ducts	
Containment Ring	AMS 5613 (AISI 410) Stainless Steel
Insulation	PWA 385 (Kaowool)

Downloaded 01 Jun 2010 to 171.66.16.59. Redistribution subject to ASME license or copyright; see http://www.asme.org/terms/Terms_Use.cfm

advanced gas-cooled reactor systems. To date over 25,000 hr have been accumulated on creep and corrosion tests at elevated temperature in a representative helium environment of the HTGR-GT primary circuit. Particularly encouraging are the results for the baseline candidate nickel-base turbine blade/vane alloy (IN-100) which shows no apparent degradation in properties.

Fabrication-Related Design Considerations. Following the theme mentioned in earlier sections of conservatism in design, utilization of existing materials, and established technology, it was an obvious goal to establish a turbomachine design that did not require advancements in the state-of-the-art as regards fabrication technology. (e.g., disk diameter exceeding current forging limits, and casings larger than have been cast todate)

For a single-shaft helium turbomachine (with a rotational speed of 3600 rpm) in the power range of 400–600 MWe, the rotating section is compact (characterized by small blade heights) and as outlined in Table 3 is substantially smaller than an equivalent air-breathing machine because of the high degree of pressurization of the helium working fluid (particularly at the turbine exit). The external dimensions of the helium turbomachines discussed in this paper are in fact quite similar (as can be seen in Fig. 23) to those of an existing air-breathing, advanced, open-cycle industrial gas turbine in the 100 MWe range. The fact that the helium turbine (particularly the rotor assembly and casings) is comparable in size with existing machines substantiates the claim that conventional fabrication methods and facilities can be used. An appreciation for the overall assembly size of the FT-50 100 MWe open-cycle industrial gas turbine can be seen in Fig. 24.

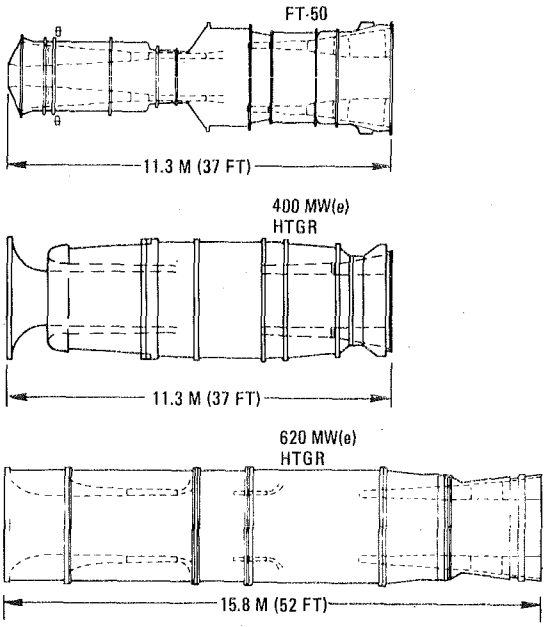

Fig. 23 Overall turbomachine envelope comparison for open-cycle and closed-cycle gas turbines

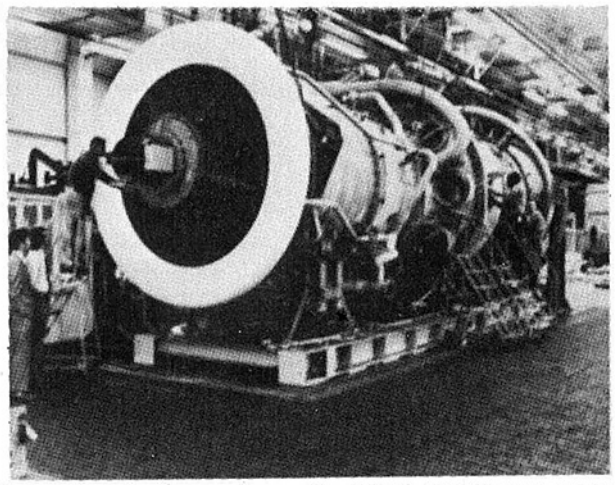

Fig. 24 View showing overall assembly of FT-50, 100 MWe open-cycle industrial gas turbine

Turbomachine Maintenance Considerations

For the integrated system it is important that turbomachine maintenance aspects be considered during the plant conceptual design phase. The primary objective of the HTGR-GT maintenance plan is to provide facilities, equipment, and components of reasonable cost that will yield good plant availability. It is therefore a matter of policy to design the reactor and conversion system installation, as well as the related maintenance facilities, for practical operation for both planned and unplanned maintenance.

The turbomachine will be serviced on scheduled inspection and maintenance programs that are intended to minimize maintenance costs while still providing assurance that the equipment is functioning within design structural and performance limits. Major maintenance will be performed on a six year interval. While removal of the turbomachine is considered to be a scheduled maintenance operation, current maintenance philosophy for a mature commercial plant is that the turbomachine will be removed only if the condition monitoring system indicates a problem. The reliance on diagnostics to indicate operating problems, together with turbomachine maintenance philosophy, is summarized in Table 5.

It is recognized that the turbomachine internal surfaces will become radioactively contaminated by deposition of helium-borne condensable fission products; thus, a procedure must be established for remote removal of a failed machine and replacement with a spare unit. For a multiloop plant, downtime will be held to a minimum by performing turbomachine change-out during a scheduled refueling period. Following a preliminary maintenance study [20]), an in-depth investigation has been carried out by General Atomic and United Technologies Corporation to establish a procedure (and the necessary equipment) for remote handling maintenance. It has been determined that essentially all disassembly and decontamination can be handled remotely, and since this will be a topic of a forthcoming paper, it is merely summarized below.

The turbomachine is being designed to permit easy disassembly and rebuilding. A procedure has been established for remote disassembly of the machine, and the view shown in Fig. 25 represents an initial operation in an on-site maintenance facility. Parts of the turbine and compressor stator cases are of split design, and this together with other design features permits the compressor and turbine rotor assemblies to be split into modules as illustrated in Fig. 16. Decontamination of each rotor can be carried out separately, as it is expected that fission product plate-out will be more severe on the turbine rotor

Table 5 HTGR-GT turbomachine maintenance philosophy

• Reliance on Diagnostics To Indicate Operating Problems	
– Temperatures	On-Line Computer System for Condition Monitoring
– Pressures	
– Vibration Monitors	
– Visual (Fiber Optics)	
– Direct Contact and Gas-Coupled Emission Transducers	
– Clearances and Eccentricities	
– Magnetic Metal Chip Detectors in Lubrication System	
– Oil Spectrometric Analysis	
– Primary System Chemistry	
• Turbomachine installation and removal procedures are established. Current design requires man access into the purged areas for connection/disconnection of drive coupling, service system line flanges.	
• For a mature commercial plant, the turbomachine will be replaced only if the diagnostic system indicates problems.	
• Stress levels in the turbomachine are commensurate with the full 280,000-hr plant operating life (i.e., no life-limited subcomponents).	
• Journal bearing areas are accessible for inspection and maintenance (bearing pad replacement, etc.).	
• In situ balancing of rotor is considered possible by UTC.	
• Alignment of the turbomachine-generator is not considered a problem.	
• For many maintenance operations, experience from industrial gas turbines is directly applicable.	

Downloaded 01 Jun 2010 to 171.66.16.59. Redistribution subject to ASME license or copyright; see http://www.asme.org/terms/Terms_Use.cfm

than on the compressor components. Following decontamination of the major subassemblies, the separate rotor sections and split stator cases can be disassembled to detail parts without the need for remote manipulators. A goal for the rebuilding of a used turbomachine, with replacement of sub-components as necessary (perhaps turbine blades in the first stages), would be to perform this operation in a straightforward hands-on manner.

For the direct-cycle HTGR-GT plant the issue of Inservice Inspection (ISI) has added importance since all the power conversion system components are installed inside the PCRV and are thus not accessible for direct visual inspection. ISI requirements are continually becoming more demanding to satisfy various code requirements, regulatory guides, licensing commitments, and to meet utility owner's needs. It is prudent therefore to consider ISI requirements during the plant conceptual design and to pursue a policy of providing inspectable designs where required. While in a very early stage of development, an on-going study has been aimed at identifying the type of inspection envisioned for key elements in the major components. Provisions are incorporated in the turbomachine design to permit borescope inspection of highly stressed areas while the turbomachine remains installed in the PCRV cavity. A summary of the ISI examination and testing possibilities for the turbomachine is given on Table 6. It should be emphasized that these possibilities are tentative and will require special attention in developing a program of ISI and testing as the turbomachine and plant designs mature.

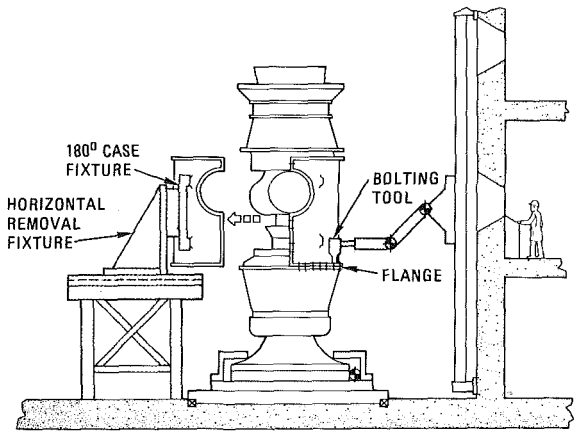

Fig. 25 View showing an initial operation in the remote disassembly of a contaminated helium turbomachine

Turbomachine Development

While no furthering of turbomachinery state-of-the-art is needed, several years of in-depth design work, in conjunction with a comprehensive development effort is necessary to realize the goal of progressing from the present conceptual design stage to plant commercialization in about 15 years. In this paper the formidable technology bases for the design of the helium turbomachine have been emphasized. Another point that should be made is the conservative nature of the turbomachine by virtue of the following:

- Low turbine inlet temperature
- Low rotor speed
- Known materials
- Low stress levels
- Uniform temperatures
- Non-corrosive working fluid
- Modest load following operation cycle
- All known technologies
- Industrial design practice

The development of the turbomachine will essentially consist of extensive component testing and installation check out in the PCRV. The following component testing is planned:

- Bearing and seal tests
- Lubricating system tests
- Flow distribution tests
- Compressor Rig Tests—1/2 scale
- Turbine Rig Tests—1/2 scale
- Disc and rotor burst tests—blade loss tests
- Shaft seal tests
- Materials compatibility
- Full scale spin test

The installation check out (at zero power) in the PCRV will consist of the following:

- Pressurization checks
- Turbomachine spin and balance test
- Motoring check out
- System simulator test
- Lubrication/Buffering system checks
- Instrumentation

The rise to full temperature operation will be done over a period of a few months with nuclear heat input. If problems are encountered with the turbomachine during this period it is projected that they can be remedied in a straightforward and timely manner since the contamination level will be very low, as evidenced by experience at the

Table 6 HTGR-GT turbomachine inservice inspection possibilities

Region or Subcomponent	Type of Examination	Method	Design Impact	Remarks
Bearings	Visual	From man access areas Borescopes Fiber optics	Access space environment	Development of specialized ISI methods necessary
	Direct contact	Acoustic emission transducers Oil analysis	Shielding	Experience from industrial gas turbine applicable
Blading	Visual	Remote	Viewing device accessibility	Proposed in-place exam by borescope for gross deformation
Rotor Disks Shaft Couplings Coupling bolts	Visual Surface and volumetric Direct contact	Direct, manual Gas coupled acoustic Emission transducers	Removability of turbomachine unit for shop examination	Existing equipment and techniques generally applicable
Structures and supports	Verification of continuing integrity	Visual in-place or design redundancy with monitoring	Accessibility for viewing in place or instrumented to detect change	Existing equipment
Seals	No specific ISI requirements, visual exam desirable			
Welds	Volumetric of primary boundaries	Remote ultrasonic	Accessibility to locate transducer over welds	Adaptation of existing equipment
Service system piping and welds	Surface or volumetric	Manual	Access to welds	Adaptation of existing equipment
Instrumentation and sensors	No specific ISI requirements; however, should be capable of detecting change in unit performance.			
Mechanical closures (Primary boundaries)	Volumetric for stud bolts > 50.8 mm (> 2 in.) Visual for stud bolts ≤ 50.8 mm (≤ 2 in.)	Remote ultrasonic Remote	Accessibility to locate transducer over stud Stud removability	Adaptation of existing equipment from light water reactors

Downloaded 01 Jun 2010 to 171.66.16.59. Redistribution subject to ASME license or copyright; see http://www.asme.org/terms/Terms_Use.cfm

Fort St. Vrain HTGR plant where maintenance work was performed on the helium circulators without difficulty.

Summary

Since closed-cycle gas turbines are not well known in the U.S., a predominant theme in this paper has been to emphasize, that in fact, helium turbomachines of large power rating (400–600 MWe) bear a close resemblance to existing large open cycle industrial gas turbines. The aerodynamic procedures used for a helium turbomachine are essentially identical to conventional air-breathing gas turbine practice. The high degree of pressurization in the closed-cycle system results in a compact arrangement, and it has been shown that helium turbomachines in the 400–600 MWe range are of similar overall size to existing industrial gas turbines in the 100 MWe class. In addition to existing mechanical design methodology being applicable, an important aspect of the above size comparison is that conventional fabrication methods and facilities can be used for the helium turbomachine.

Emphasis has been made of the formidable technology bases from which the design and development of the helium turbomachine can benefit. While this paper has been predominantly design-related, it was felt prudent to comment on existing hardware, and to point out that large multistage, axial-flow helium turbomachines have operated successfully in Europe.

Between now and the year 2000, when it is projected that the HTGR-GT plant could become a commercial option, it is postulated that significant technology advancements (materials, aerodynamic, etc.) could impact on the performance of the plant. During the conceptual design of the plant, however, it was felt prudent to use existing state-of-the-art technology, and in the case of the turbomachine, the conservative nature of the design (and performance estimates) reflects the influence of technology from demonstrated industrial gas turbines. Advancements in materials, design methodology and improved component efficiencies, will be factored into the plant as the design matures.

For the HTGR-GT plant an extensive program of design, development, and testing is necessary to achieve the performance and structural integrity to qualify the equipment for nuclear power generation. This paper has emphasized salient factors related to the helium turbomachine, since it represents the singularly most important component in the plant. Critical elements of the turbomachine, such as bearings and seals have been identified, and in these areas development work is necessary. The formulation of test plans and the design of specialized rigs, from which data will be needed for the final machine design, are in progress.

In closing, it is projected that rigorous development attention must be given to areas that impact the operation of the machine when installed inside the reactor vessel (i.e., bearings, seals, structural integrity, etc.), but when put into perspective, the overall simplicity and modest operating temperature of the helium turbomachine, is not regarded as being any more difficult than the development of a new high-temperature aircraft gas turbine.

Acknowledgments

Appreciation is hereby expressed by the authors to the managements of General Atomic Company and United Technologies Corporation for permission to publish this paper. Work on the HTGR-GT plant turbomachine has been supported by the U.S. Department of Energy under Contract DE-AT03-76SF70046. Design work on the helium turbomachine has been done by the Power Systems Division and Pratt and Whitney Aircraft Division of United Technologies Corporation, under subcontract to General Atomic Company.

References

1 McDonald, C. F., and Boland, C. R., "The Nuclear Closed-Cycle Gas Turbine (HTGR-GT)—Dry Cooled Commercial Power Plant Studies," ASME JOURNAL OF ENGINEERING FOR POWER, This issue, pp. 89–100.

2 Adams, R. G., and Boenig, F. H., "The Design of the Turbomachinery for Gas Turbine High Temperature Gas Cooled Reactor Power Plant," ASME Paper No. 77-GT-38, 1977.

3 Adams, R. G., et al., "Bearing Compartment Seal Systems for Turbomachinery in Direct Cycle HTGR Power Plants," ASME Paper No. 78-GT-38, 1978.

4 McDonald, C. F., "The Nuclear Closed-Cycle Gas Turbine (GT-HTGR)—A Utility Power Plant for the Year 2000," AIAA Paper 79-0191, 1979.

5 Keller, E., "Forty Years of Experience on Closed-Cycle Gas Turbines," *Annals of Nuclear Energy,* Vol. 5, Pergamon Press, 1978, p. 404.

6 McDonald, C. F., "The Closed-Cycle Gas Turbine—Present and Future Prospectives for Fossil and Nuclear Heat Sources," ASME Paper No. 78-GT-102, 1978.

7 Zenker, P., "The Oberhausen 50 MWe Helium Turbine Plant," *Combustion.* Vol. 47, No. 10, pp. 21–25.

8 Weber, D., "Helium Turbine Explores Future Nuclear Application," *Energy International,* Apr. 1978.

9 Noack, G., et al., "Significance of the Helium Turbine Plant at Oberhausen (EVO) and of the High Temperature Test Facility at Julich (HHV) for the Development of the HTGR Direct Cycle System (HHT)," paper presented at a Symposium on Gas-Cooled Reactors with Emphasis on Advanced Systems, Julich, Germany, Oct. 1975.

10 Haselbacher, H., and Eiermann, A., "Development of Helium Gas Turbine Systems in the Nuclear Field," ASME Paper No. 74-GT-123, 1974.

11 Endres, W., "Large Helium Turbines for Nuclear Power Plant," ASME Paper No. 70-GT-99, 1970.

12 Haselbacher, H., et al., "HHT Helium Turbine and the HHV Plant," Paper No. A4/21 presented at Nuclex 78, Basel, Switzerland, Oct. 3–7, 1978.

13 Haselbacher, H., "Closed-Cycle Gas Turbines for HTR Nuclear Power Plants and LNG Regasification Plants," *Brown Boveri Review* 66, 2–79, pp. 120–129.

14 McDonald, C. F., et al., "Primary System Design Studies for Advanced Direct Cycle Nuclear Gas Turbine Plant," ASME Paper No. 77-GT-25, 1977.

15 Kammerzell, L. L., "HTGR-GT Systems Optimization Studies," Paper to be presented at 25th ASME International Gas Turbine Conference, New Orleans, Mar. 1980.

16 Dvorak, H. G., and Rogers, W. H., "An Advanced Industrial Gas Turbine for Utility Generation," *Proceedings of the American Power Conference,* Vol. 37, 1975 p. 352.

17 de Biasi, D., "FT 50 Design Shortcut to 1980 Technology," *Gas Turbine World,* Nov. 1975.

18 Chmielewski, R., et al., "Fault Analyses of the Gas Turbine HTGR," ASME Paper 76-GT-99, 1976.

19 Hagg, A. C., and Sankey, G. O., "The Containment of Disk Burst Fragments by Cylindrical Shells," Trans ASME, Apr. 1974, pp. 114–223.

20 McDonald, C. F., and Paget, J. A., "Maintenance Considerations in the Design of the Direct-Cycle Nuclear Gas Turbine Power Plant," ASME Paper No. 79-GT-116, 1979.

Downloaded 01 Jun 2010 to 171.66.16.59. Redistribution subject to ASME license or copyright; see http://www.asme.org/terms/Terms_Use.cfm

Comparison of Experimental and Computational Shock Structure in a Transonic Compressor Rotor

G. Haymann-Haber
Research Engineer,
General Electric Corporation,
Lynn, MA 01910

W. T. Thompkins, Jr.
Assistant Professor,
Dept. of Aeronautics and Astronautics,
Massachusetts Institute of Technology,
Cambridge, MA
Assoc. Mem. ASME

Measurement of passage shock strength in a transonic compressor rotor using a gas fluorescent technique revealed an unexpected variation in shock strength in the radial direction. An axisymmetric idealization would normally predict that the passage shock strength would gradually weaken when moving radially inward until disappearing at the sonic radius. However, the measurements indicated a sharp peak in strength at the nominal sonic radius. Blade boundary layer separation originating at this point accounts for about one half of the total rotor losses. A numerical computation of the three-dimensional inviscid flow, using time-marching techniques, has accurately predicted in general the radial and tangential variations in passage shock strength and in particular the sharp pressure peak at the nominal sonic radius. The overall shock strength was somewhat overpredicted, but this overprediction may be the result of boundary layer separation in the experiment. This paper presents comparisons between the optical density measurements and computational results and in addition a short analytical discussion which demonstrates that the sharp shock strength rise may occur in many transonic compressor rotors.

Introduction

Techniques for unobtrusive optical sensing of turbomachinery flow properties have been developed and are now supplying high quality data for blade flow analysis and development. The most common technique, that of Laser Anemometry, has been successfully applied by several workers [1–3]; another technique [4] uses gas fluorescence to determine the instantaneous intra-blade static density. The gas fluorescence technique is particularly well suited to studying the turbomachinery shock structures, since unambiguous measurements of shock position and strength can be obtained.

A detailed analysis of passage as well as bow shock strength obtained for a compressor rotor with tip Mach number of 1.2 and a stagnation pressure ratio near 1.6 using the gas fluorescent technique was presented in reference [5]. The experimental data collected in this analysis is reproduced in Fig. 1, which plots shock density ratio against radius for points on each shock near the blade pressure surface and near the blade suction surface. These flow visualization measurements showed that for radius ratios (r/r_t) larger than 0.78 a passage shock existed whose strength varied strongly with radial as well as tangential position. For radius ratios less than 0.78, a steep diffuse compression exists; the approximate pressure ratio across these regions is shown in Fig. 1 and can be seen to be much less sensitive to radial or tangential position. Also shown here is a reference shock strength level derived from a typical streamline curvature calculation, using measured losses, by assuming that a normal shock would occur at the maximum relative approach Mach number. This simple axisymmetric shock strength is included only as a guide to the general level and trend of shock strength to be expected in the absence of exceptional events.

The derived streamline curvature reference shows the expected monotonic decrease in shock strength with decreasing radius; however, the experimental data show two important deviations from the streamline curvature prediction. Along the suction surface for ($r/r_t > 0.83$), the shock density ratio falls rapidly rather than increasing as it does at mid-passage and near the pressure surface. At these locations on the suction surface, the flow visualization photographs clearly show a shock-boundary layer interaction which is felt to cause this lower shock strength. Photographs at these radii are reproduced in Fig. 2. Near the shock termination radius ($r/r = 0.78$), there appears to be a local maximum in shock strength for all tangential positions whose level is much larger than would be expected from the streamline curvature calculations. Away from the suction surface, the shock strength follows the streamline curvature prediction approximately for $r/r > 0.83$, but then jumps up to a value of 1.25 to 1.40 at $r/r_t = 0.80$ where the streamline curvature calculation would predict a value of 1.15.

It was argued in reference [5] that the experimentally observed shock strength variation is required for a consistent flow field solution in which the passage shock terminates away from a solid surface. This paper reports on a new numerical procedure applied to the test rotor which reproduces rather well the observed shock strength variation and on an improved analytical assessment of possible shock-termination configurations which support the conclusions presented in reference [5].

Numerical Solution Techniques

A numerical solution for the three-dimensional, isentropic flow in

Contributed by the Gas Turbine Division and presented at the Gas Turbine Conference and Products Show, New Orleans, La., March 10–13, 1980 of THE AMERICAN SOCIETY OF MECHANICAL ENGINEERS. Manuscript received at ASME Headquarters December 13, 1979. Paper No. 80-GT-81.

Copyright © 1981 by ASME
Downloaded 01 Jun 2010 to 171.66.16.59. Redistribution subject to ASME license or copyright; see http://www.asme.org/terms/Terms_Use.cfm

the test rotor was reported in reference [6]. Because of the coarse finite difference grid used in this calculation, it was difficult to determine conclusively if the shock termination phenomenon described in the introduction was properly described. The test rotor flow has, therefore, been recomputed with improved simulation procedures, described in reference [7], which provide improved finite difference grid resolution as well as relaxing the isentropic flow assumption by including the inviscid energy equation in the simulation equations. These new calculations resolved this localized but important phenomena as well as improved predictions of blade pressure distributions. The equations solved in the new simulations are the full three-dimensional Euler equations which consist of the continuity equation:

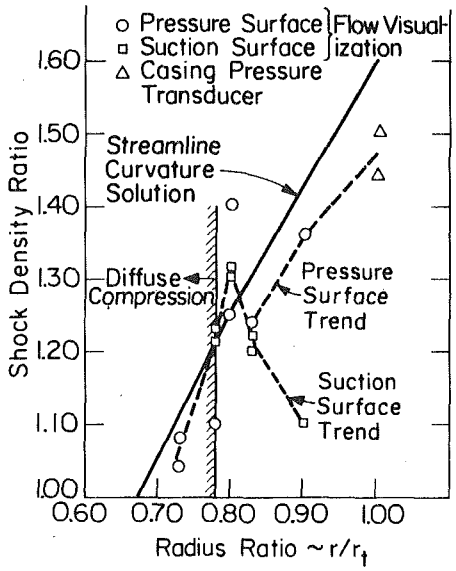

Fig. 1 Passage shock density ratios determined by fluorescent flow visualization for the M.I.T rotor

$$\frac{\partial \rho}{\partial t} + \nabla \cdot (\rho \bar{V}) = 0 \tag{1}$$

inviscid momentum equation,

$$\frac{D\bar{V}}{Dt} = -\frac{1}{\rho}\nabla P \tag{2}$$

and inviscid energy equation with no heat transfer,

$$\frac{Dh}{Dt} = \frac{1}{\rho}\frac{DP}{Dt} \text{ or } \frac{Dh_0}{Dt} = \frac{1}{\rho}\frac{\partial P}{\partial t} \tag{3}$$

where h and h_0 are the static and stagnation enthalpies. These equations expressed in weak conservation law form for a cylindrical coordinate system rotating with the compressor are:

$$\frac{\partial U}{\partial t} + \frac{\partial F}{\partial r} + \frac{\partial G}{\partial \theta} + \frac{\partial H}{\partial Z} = K$$

where

$$U = \begin{bmatrix} r\rho \\ r\rho u_r \\ r\rho u_\theta \\ r\rho u_z \\ rE_t \end{bmatrix} \quad F = \begin{bmatrix} r\rho u_r \\ r(\rho u_r^2 + P) \\ r\rho u_r u\theta \\ r\rho u_r u_z \\ ru_r(E_t + P) \end{bmatrix}$$

$$G = \begin{bmatrix} \rho u_\theta - wr\rho \\ \rho u_r u_\theta - \omega r \rho u_r \\ \rho u_\theta^2 + P - \omega r \rho u_\theta \\ \rho u_\theta u_z - \omega r \rho u_z \\ u_\theta(E_t + P) - \omega r E_t \end{bmatrix} \quad H = \begin{bmatrix} r\rho u_z \\ r\rho u_r u_z \\ r\rho u_\theta u_z \\ r(\rho u_z^2 + P) \\ ru_z(E_t + P) \end{bmatrix} \quad K = \begin{bmatrix} 0 \\ \rho u_\theta^2 + P \\ -\rho u_\theta u_z \\ 0 \\ 0 \end{bmatrix}$$

$$E_t = \rho(e + V^2/2) \qquad V^2 = u_r^2 + u_\theta^2 + u_z^2 \qquad P = \rho e(\gamma - 1)$$

ω = rotational speed of blade row

These equations are then nondimensionalized by a_0, T_0 and ρ_0, the upstream stagnation speed of sound, temperature and density on the

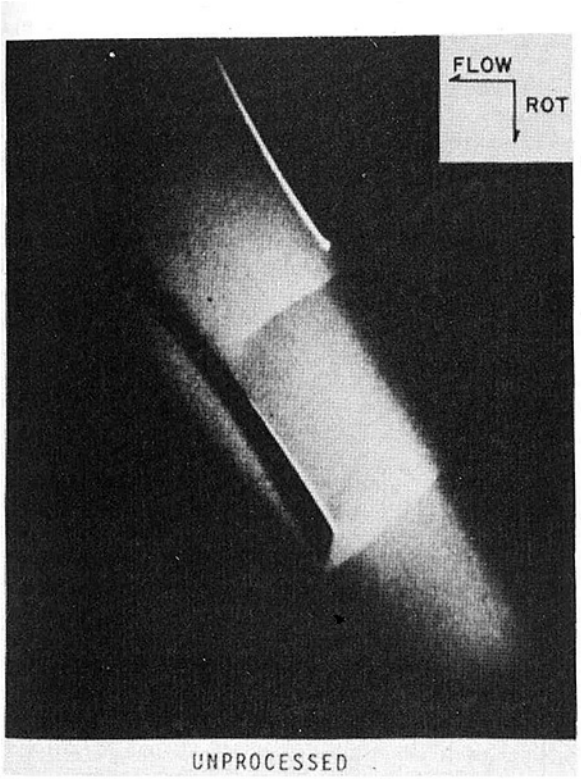

Fig. 2(*a*) Flow visualization photograph at radius ratio of 0.88 illustrating shock-boundary layer interaction on blade suction surface

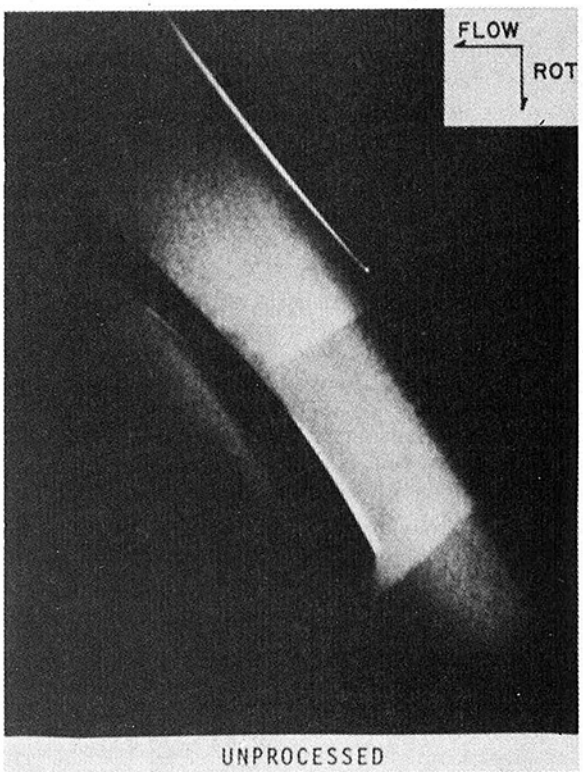

Fig. 2(*b*) Flow visualization photograph at radius ratio of 0.83 illustrating shock-boundary layer interaction on blade suction surface

Downloaded 01 Jun 2010 to 171.66.16.59. Redistribution subject to ASME license or copyright; see http://www.asme.org/terms/Terms_Use.cfm

tip casing streamline, and r_t, the rotor tip radius. In addition, γ, the specific heat ratio, is assumed constant.

It is important to note that even though the coordinate system is fixed to the rotor, all physical quantities, including the velocities, are those seen in the absolute coordinate system.

For inviscid simulations with uniform upstream flow properties, the flow may be assumed to be periodic with blade spacing, and only the region bounded by the pressure and suction surface of two adjacent blades needs to be considered. The physical space is sufficiently complex to render a finite difference solution impractical in that domain and is mapped into a computational domain, which is a rectangular box in which the grid lines form an evenly spaced mesh, thus allowing for easy implementation of a finite difference scheme.

The mapping functions are specified as a double set of simple analytical functions. First, one which regularizes the domain, and second, one that locally increases mesh density within the blade passage and around the leading and trailing edges.

The first set of mappings is given by:

$$R = \frac{r - r_h(z)}{r_t(z) - r_h(z)} \tag{5}$$

r_h = radial location of the hub

r_t = radial location of the tip

$$\theta = \frac{\theta - \theta_p(r,z)}{\theta_s(r,z) - \theta_p(r,z)} \tag{6}$$

where θ_p and θ_s describe the pressure and suction surface of the blades respectively, and their prolongations upstream and downstream of the blade row.

Inside the blade row

$$\xi = \frac{z - z_{le}(r)}{z_{te}(r) - z_{le}(r)} \tag{7}$$

Outside the blade row

$$\xi = \frac{z - z_{le}) + (z_{le_0} - z_{te})e^{(az^*)}}{(z_{te_0} - z_{le_0}) + [(z_{te} - z_{te0}) + z_{le_0} - z_{le})]e^{(az^*)}} - 0.5 \tag{8}$$

where z_{le} and z_{te} are the axial locations of the leading and trailing edges, z_{le_0} and z_{te_0} are constants to be chosen in a way to make the mapping function derivatives continuous at the leading and trailing edges, and z^* is given by:

$$z^* = \begin{cases} z - z_{le} & \text{upstream of the blade row} \\ z_{te} - z & \text{downstream of the blade row} \end{cases}$$

These mappings regularize the domain, align the grid lines with the leading and trailing edges, and allow them to become z = constant lines far away from the blades.

The mesh packing function is given by

$$\xi = A_x \sinh(K_x X) + B_x \tan^{-1}[\sinh(K_x X)] \tag{9}$$

where

$$A_x = \frac{A_x^*}{2\{A_x^* \sinh h(K_x) + B_x^* \tan^{-1}[\sinh h(K_x)]\}}$$

$$B_x = \frac{B_x^*}{2\{A_x^* \sinh h(K_x) + B_x^* \tan^{-1}[\sinh h(K_x)]\}}$$

A_x^* and B_x^* are arbitrary constants and K_x is a free parameter that controls mesh packing. Full details of this last transform are given by Merrington [8].

The introduction of these mappings modifies the original partial differential equations. Using the chain rule, equation (4) becomes

$$\frac{\partial U}{\partial t} + \left(\frac{\partial F}{\partial R}\frac{\partial R}{\partial r} + \frac{\partial H}{\partial R}\frac{\partial R}{\partial z}\right) + \left(\frac{\partial F}{\partial \theta}\frac{\partial \theta}{\partial r} + \frac{\partial G}{\partial \theta}\frac{\partial \theta}{\partial \theta} + \frac{\partial H}{\partial \theta}\frac{\partial \theta}{\partial z}\right) + \left(\frac{\partial F}{\partial X}\frac{\partial X}{\partial r} + \frac{\partial H}{\partial X}\frac{\partial X}{\partial z}\right) = K \tag{10}$$

since $(\partial R/\partial\theta)$ and $(\partial X/\partial\theta)$ are identically zero.

Equation (10) is the final form of the equations before the differencing is applied. The members of the Jacobian matrix of the transform, together with the radial locations of the grid points, and curvatures of the solid boundaries, contain all the geometry information needed to solve the problem.

The resulting grid structure is shown in Figs. 3 and 4. There are 100 points in the axial direction, 36 of which are within the blade passage, 18 points in the radial direction and 17 in the circumferential direction, totaling 30,600 grid points.

It is important to note that the grid lines rotate following the blade twist as one moves radially outwards; thus, the grid lines are approximately aligned with the relative flow direction.

Solid and periodic boundaries are placed between two adjacent grid lines, allowing for the easy application of boundary conditions and periodicity. The grid lines extend about five blade chords upstream of the leading edge, and about three downstream of the trailing edge, in order to permit the application of far field boundary conditions as far away from the blades as possible and thus reduce possible oscillations at the boundaries.

The grid lines in the circumferential direction are at a constant axial position, thus simplifying the application of periodicity boundary conditions. However, shocks that may appear in the flow are then usually not aligned with the grid lines, as shown in Fig. 4, resulting in poorer shock resolution.

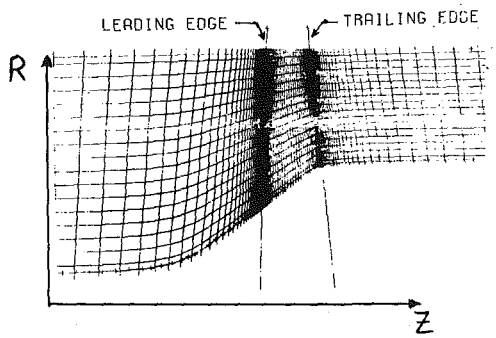

Fig. 3 Finite difference grid structure in the *R-Z* plane

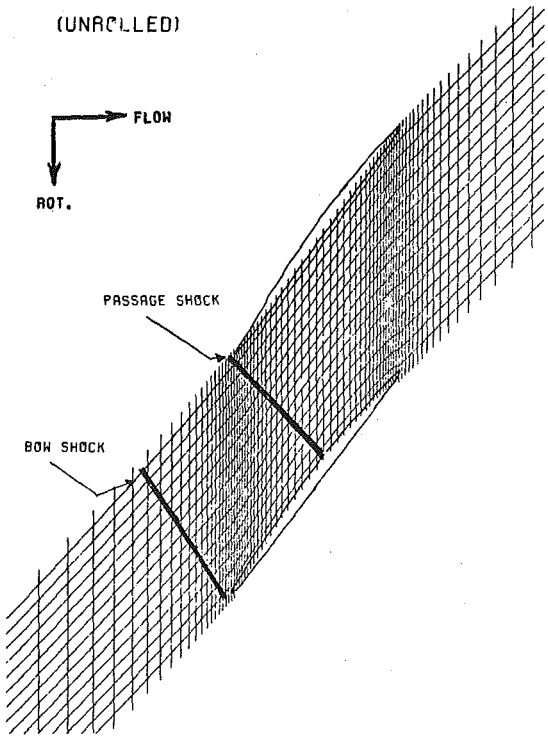

Fig. 4 Finite difference grid structure in the θ. $-$ Z plane

Downloaded 01 Jun 2010 to 171.66.16.59. Redistribution subject to ASME license or copyright; see http://www.asme.org/terms/Terms_Use.cfm

Several attempts were made to model a spinner, including one that would smoothly merge with the centerline, but these attempts were unsuccessful. High radial velocities tended to build up at the points close to the centerline, resulting in mass flow defects of the order of 5 percent. Since $r = 0$ is a singular point in a cylindrical coordinate system, the implementation of boundary conditions at the centerline poses some problems. Solutions to this problem have been suggested in references [9] and [10] but for the results to be presented the spinner was replaced by a cylindrical center body with $r/r_t = 0.3$.

Equation (10) is solved using MacCormack's split operator finite difference scheme. This is a two step, explicit, second order accurate, conditionally stable scheme. The difference equation in the R direction, for instance, would be:

$$U^*_{j,k,l} = U^n_{j,k,l} - \frac{\delta t}{\delta R}\left[(F^n_{j,k,l+1} - F^n_{j,k,l})\frac{\partial R}{\partial r} + (H^n_{j,k,l+1} - H^n_{j,k,l})\frac{\partial R}{\partial z}\right] + \delta t A K^n_{j,k,l} \quad (11)$$

$$U^n_{j,k,l} = \frac{1}{2}\left\{U^n_{j,k,l} + U^*_{j,k,l} - \frac{\delta t}{\delta R}\left[(F^*_{j,k,l} - F^*_{j,k,l-1})\frac{\partial R}{\partial r} + (H^*_{j,k,l} - H^*_{j,k,l-1})\frac{\partial R}{\partial z}\right] + \delta t A K^*_{j,k,l} + Z^n_{j,k,l}\right\} \quad (12)$$

where j, k, and l, respectively, identify the axial, circumferential and radial coordinate of a grid point, n indicates the time step, and * indicates an intermediate provisional time step. Here

$$F^* = F(U^*),\ H^* = H(U^*),\ K^* = K(U^*) \text{ and } A = [0\ 1\ 0\ 0\ 0].$$

Equation (11) is the forward step, while (12) is the backward step. The forward-backward sequence was permutated on succeeding time steps. Each of the operators was run with a time step as close to the stability limit as possible and was combined in a symmetric sequence as described in reference [11].

In order to stabilize the solution along steep gradients of the flow quantities, such as across shock waves and near the leading and trailing edges, artificial viscosity terms were introduced which increase the damping of the scheme. The form of these terms for the R step is:

$$Z^n_{j,k,l} = \kappa\{[u^n_{rj,k,l} - u^n_{rj,k,l-1}](U^n_{j,k,l+1} - U^n_{j,k,l}) - [u^n_{rj,k,l+1} - u^n_{rj,k,l}](U^n_{j,k,l} - U^n_{j,k,l-1})\} \quad (13)$$

where κ is a parameter that controls the strength of the artificial viscosity terms. Low values of κ produce sharp shocks, but result in unacceptable oscillations downstream of the shock. High values of κ yield smooth solutions, but also very wide shocks and strong distortions to the inviscid field. A value of κ equal to 0.4 was used.

No through flow conditions at solid boundaries are implemented in the staggered grid system using essentially reflection in a locally orthogonal coordinate system which includes the effect of surface curvatures on the normal pressure gradient. As discussed in references [7] and [12], this procedure results in first order accurate but consistent boundary formulations.

Outside the blade passage, periodicity is applied in the circumferential direction. This is particularly simple for the system of offset points since there are no points on the symmetry boundary itself and thus no assumptions have to be made regarding the value of the flow quantities at those locations. Also, the fact that circumferential grid lines are at constant axial location avoids the need for interpolations.

The upstream boundary condition is applied at the first axial grid plane by using a program developed by Berenfeld [13]. The program uses the predicted flow conditions at the second axial grid plane and calculates the flow quantities at the first axial grid plane using a linearized potential flow analysis developed by Tan [14]. In order to apply this theory, the flow upstream of the second grid plane must be assumed to be compressible, inviscid, isentropic and steady. This flow can then be described by linearized potential flow equations if upstream running waves are weak. Far upstream boundary conditions are uniform, non-swirling flow. Three-dimensional perturbations proved to be very small when initially calculated and were neglected. The upstream boundary condition procedures are quite similar to those suggested in reference [15].

The downstream boundary condition, applied at the last axial plane, assumes an axisymmetric radial equilibrium solution with the same total momentum as that in the previous axial plane. The static pressure at the hub is specified. The downstream boundary condition has several inadequacies, among them that it ignores three-dimensional perturbations which do not decay far downstream, and further work is required on this area.

The Kutta condition is applied at the last axial points on the blades. At these points the usual no-through flow boundary conditions are applied, except for the pressures, which are set as though it were a periodic boundary. In this way, the points at the trailing edge, although physically only one set, are logically two sets of points and the pressures are identical at the "fictitious" points. No attempt is made to directly set the velocities at the trailing edge, since there are no points on the trailing edge itself.

Numerical Results

Computer codes which implement these procedures were developed and run on a dedicated minicomputer, a Digital Equipment Corporation model PDP 11/70. Use of the minicomputer allowed solutions for large grids to be computed at low cost, but required long run times. A fully converged solution requires about 120 hr run time at a total cost of about 400 dollars. The low computer costs make the minicomputer system very useful in a research environment like a university, where low cost is more important than solution run time.

The parameters specifying the operating point of the compressor are the upstream stagnation temperature and pressure, the rotor speed, and the downstream pressure. The mass flow is a result of the computation and is not explicitly specified anywhere. Consequently, a uniform mass flow at all axial planes is a good criterion for the convergence of the solution. This convergence was obtained to an acceptable degree, with about 1 percent variation in mass flow between any two axial planes in the flow domain.

The computed average total pressure ratio across the compressor was about 1.8, as compared to the nominal design point of 1.6 at which the experiments were conducted. This difference is felt to reflect the smaller deviation angles normally found when a purely inviscid calculation is compared to a real flow with separation at or before the blade trailing edge. In reference [16], this change in deviation angle was shown to be about 5 deg over the blade span.

The initial computed values for the overall efficiency of the compressor were below the experimental ones, which is opposite to what would be expected from an inviscid solution, where shocks are the only source of losses. One source of this inefficiency is the artificial viscosity terms. These terms are large wherever steep flow gradients exist, regardless of whether they are compressions or expansions. Consequently, regions such as the suction surfaces near the leading edges and where the hub has a strong curvature, are subjected to higher than necessary losses. In order to reduce these effects, the artificial viscosity terms were strongly attenuated away from sonic lines and stagnation points, which are the regions where numerical instability occurs. The solution remains stable in these cases. Figure 5 shows a sample plot of Mach number versus axial position for the attenuated viscosity case. Here a shock is resolved over about 5 grid lines which is acceptable for the purposes of this paper but may not be adequate for design type calculations.

In MacCormack's method, shocks are resolved as regions of steep gradients in the flow quantities. This makes it difficult to distinguish between shocks and compression waves, and the boundary between them is not clear cut. Another characteristic of MacCormack's method is that shocks are preceded by an overshoot and followed by an undershoot of the Mach number, see Roache [12] and Taylor [17]. This effect is usually a good indication of the starting and termination points of a shock. For the present case, however, the shock is preceded by a strong expansion and correspondingly fast increase in the Mach number, and followed by a continuing compression as the passage extends toward the trailing edge. In most cases these compressions and expansions are strong enough to completely blur out the expected

Downloaded 01 Jun 2010 to 171.66.16.59. Redistribution subject to ASME license or copyright; see http://www.asme.org/terms/Terms_Use.cfm

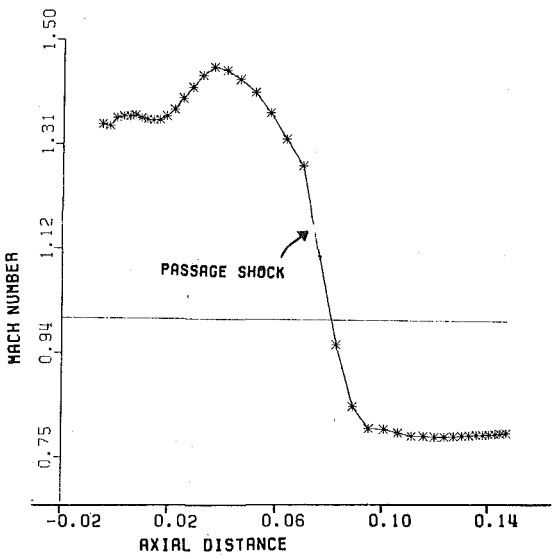

Fig. 5 Computed mach number along a streamwise running grid to line

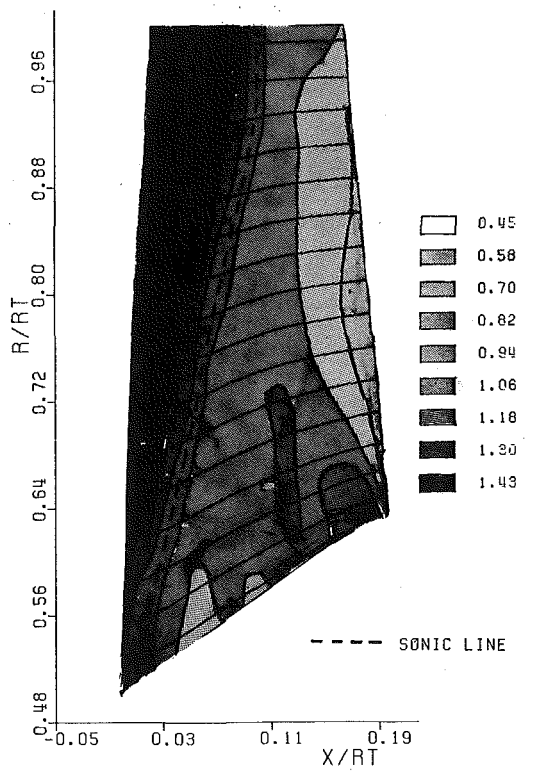

Fig. 6 Mach number contour plot for hub-to-tip stream surface near blade suction surface

overshoots, resulting in an uncertainty in shock strength and position. The problem is clearly seen in Fig. 5. The criteria adopted here is to consider the shock to lie in the steepest part of the compression curve.

Figure 6 shows the computed Mach number distribution for a hub to tip stream surface (S1 surface) close to the suction surface. The streamlines on that surface are also shown. The shock appears as a region of steep gradient in the Mach number, and the difficulty of determining where it weakens into a compression wave becomes clear. The striking feature on this stream surface is that the flow is supersonic virtually all the way down to the hub, whereas the axisymmetric theory predicts a nominal sonic line at about 80 percent radius. Note the curving of the streamlines within the shock, as required for oblique shocks. It is also interesting to note that since the flow becomes supersonic virtually all the way down to the hub, whereas the design intent was for a nominal sonic line at about 80 percent radius. Note the curving of the streamlines within the shock, as required for oblique shocks. It is also interesting to note that since the flow is subsonic behind the shock, it is a strong oblique shock, and that as required it becomes normal to the casing as it approaches the tip.

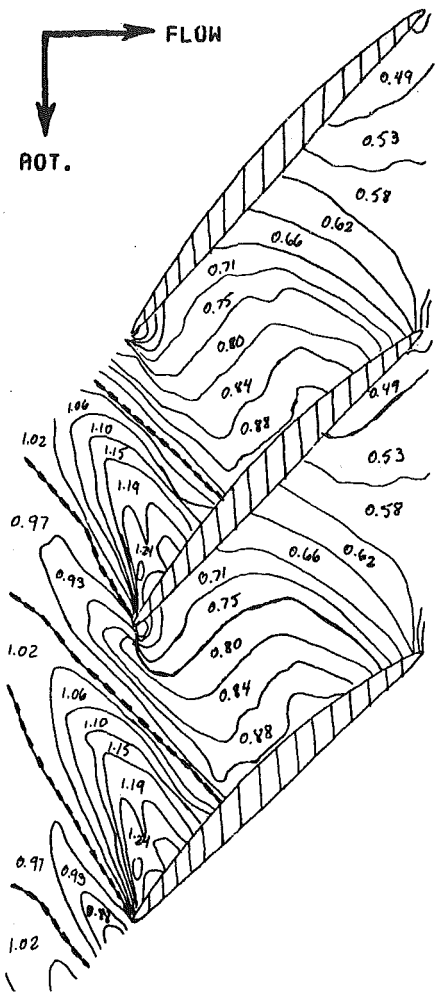

Fig. 7 Isomach contour lines for conical blade-to-blade surface near hub casing. L. E. radius = 0.70, T. E. radius = 0.76, - - - - - sonic line

Figures 7–9 show isomach contours for a series of conical sections around the compressor, chosen so as to apprxoimately follow the streamlines at any given leading edge radius. The source of the high Mach numbers becomes apparent as a strong expansion around the suction surface behind the leading edge. At a radius of 0.70 a double compression wave forms, one ahead of the passage, and one inside. At a radius of 0.80 the isomachs are probably close enough to warrant assuming a shock exists. The shock is clearly detached, although it is not clear whether the side extending ahead of the passage forms a box shock or a compression wave. At a slightly higher radius of 0.85 the shock strength from the suction surface to mid-passage does not seem to increase much, and it is not until a radius of 0.95 that the Mach number ahead of the shock picks up its increase trend again. Because of the strong expansion around the leading edge, the Mach number ahead of the shock is 20 percent larger than free-stream at a radius of 0.80 and about 10 percent larger at 0.95, originating an unexpectedly strong shock at what would have been the nominal sonic line.

In connection with this observation, Fig. 11 shows the Mach number ahead of the passage shock or compression wave versus radius. On the pressure surface only a mild flattening at a radius of about 0.86 is observed for the otherwise monotonic Mach number increase, but

Downloaded 01 Jun 2010 to 171.66.16.59. Redistribution subject to ASME license or copyright; see http://www.asme.org/terms/Terms_Use.cfm

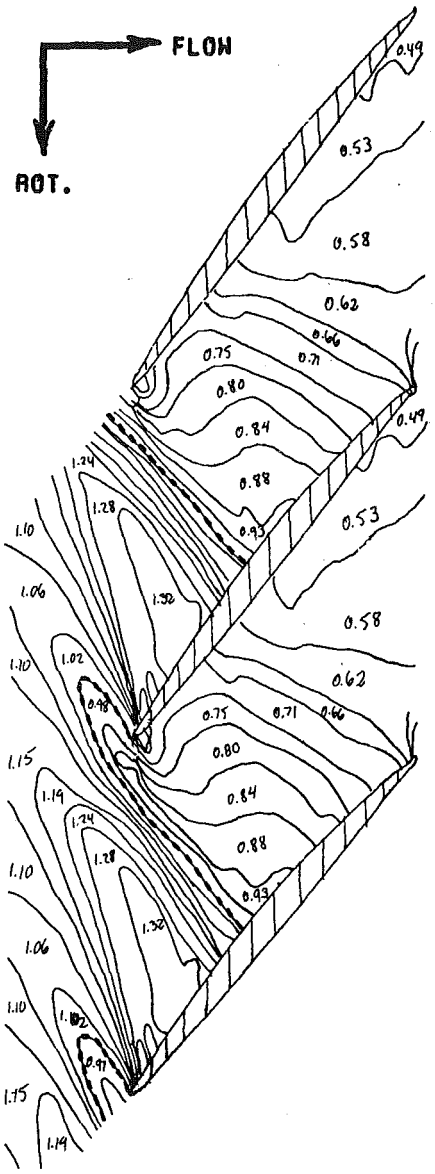

Fig. 8 Isomach contour lines for conical blade-to-blade surface near stack strength maximum. L. E. radius = 0.80, T. E. radius = 0.85, - - - - - sonic line

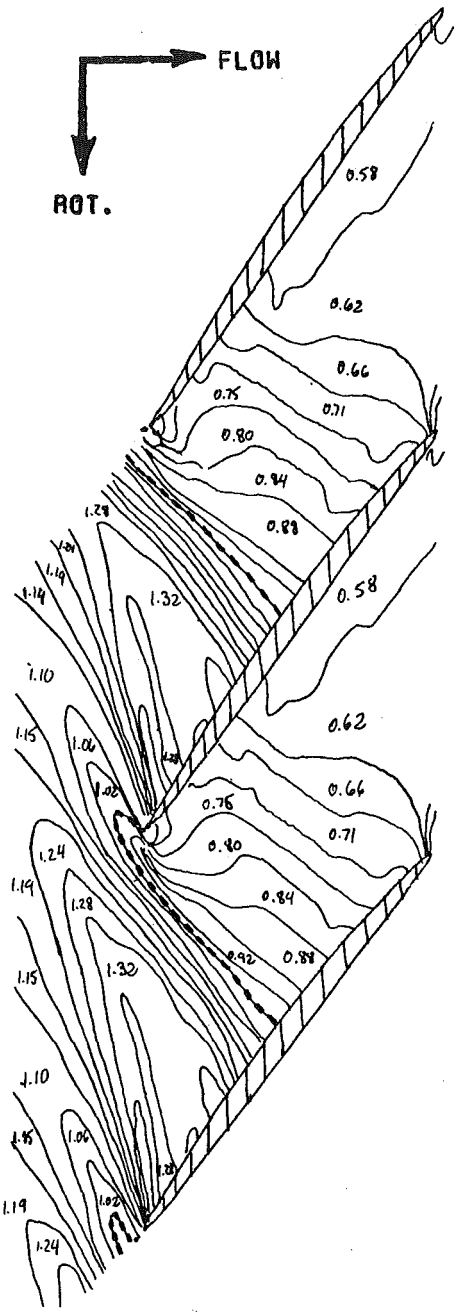

Fig. 9 Isomach contour lines for conical blade-to-blade surface just above local shock strength maximum. L. E. radius = 0.85, T. E. radius = 0.90, - - - - - sonic line

definite peaks appear at a radius of 0.80 midway between the blades, and at 0.77 on the suction surface. This is the first evidence of the shock structure mentioned in the introduction. Also shown in this figure is the axisymmetric predicted variation in relative Mach number. The Mach number in front of the shock or diffuse compression wave may be seen to be quite higher than the relative inlet Mach number computed from the streamline curvature solution.

Comparison with Experimental Data

Figures 12–14 compare the density ratios across the passage shock or compression wave as predicted by the computations and as shown by the flow visualization. The starting and termination points of the compression waves are difficult to determine given the resolution available from the flow visualization. Therefore, there may be some vertical shift in the values of the density ratios. Experimental data is scarce close to the blades, and therefore the experimental curves in Figs. 13 and 14 (pressure and suction surfaces) are only approximate. At mid-passage (hub to tip casing surface midway between blade suction and pressure surfaces), the comparison between predicted and measured compression ratios is excellent. The predicted local density ratio maximum occurs at the proper radius with nearly the proper size. Compression ratios at other radii are also predicted well except that the computed pressure ratios appear to rise too rapidly near the tip radius. Along the pressure surface, the computed compression ratios agree well all across the blade span. Comparison of the local maximum at $r/r_t = 0.80$ is complicated by the variability in experimental measurements, measured density ratios of 1.33 and 1.40 in two successive tests. At the present time it is not known whether this experimental measurement difference is due to true blade to blade flow variations or some other source. Compression ratios along the suction surface are predicted well only for $r/r_t < 0.80$. At larger radii, a shock-boundary layer interaction evident is in Fig. 2, and a pure inviscid calculation cannot reproduce accurate detailed flow results at these radii.

Much more information than the local shock strength can be recovered from flow visualization photographs like Fig. 2 by use of image processing. Such images may be digitized and corrected for errors in

Downloaded 01 Jun 2010 to 171.66.16.59. Redistribution subject to ASME license or copyright; see http://www.asme.org/terms/Terms_Use.cfm

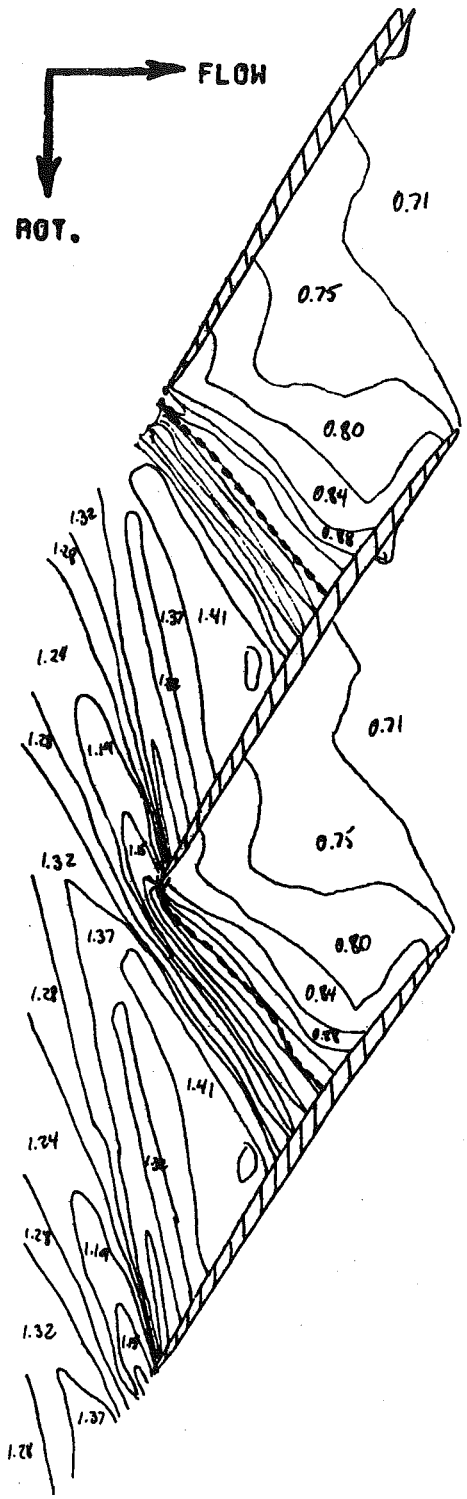

Fig. 10 Isomach contour lines for conical blade-to-blade surface near tip casing. L. E. radius = 0.95, T. E. radius = 0.98, - - - - - sonic line

the imaging system as discussed in reference [4] so that relative density values across the entire blade passage may be determined with an accuracy of about ±5 percent. These digitized and corrected flow pictures can be compared directly with the numerical computations as is shown in Figs. 15–17. Much of the sharpness of the visualized shock is unavoidably lost in digitizing process as may be seen by comparing the flow visualization photograph in Fig. 3 with its digitized and corrected counterpart, Fig. 15. Relative density variations are much more evident in the corrected images than in the original photographs.

Comparisons of the detailed computed and experimental results for three radial positions, $r/r_t = 0.88$, 0.83 and 0.80, are shown in Figs. 15–17. At all three positions the suction surface expansion is properly predicted both in the shape of the constant density contours and the amount of suction surface expansion; thus, the Mach number in front of the passage shock may be expected to be properly predicted. The computed passage shock may be seen to lie somewhat further upstream than the experimentally determined position, but its location is satisfactorily predicted. The most serious defect of the computed solution is in the prediction of the bow wave shape at an $r/r_t = 0.88$. The wave is weaker and does not stand as far off the leading edge as it does in Fig. 2 or 15. The mechanism producing the very large stand-off distance shown in Fig. 2 remains unknown.

Discussion

The most obvious conclusion to be drawn from comparing the computed and flow visualization results is that the unusual shock structure revealed in Fig. 1 does indeed have an inviscid origin. While not all details of the shock strength variation with position are predicted, the agreement between predicted and experimental values as illustrated in Figs. 12–14 seems adequate to establish that the major effects of a quite local flow phenomenon are properly accounted for by the inviscid computation except where flow separation is of overwhelming importance. More resolution in both the experiments and the computations would be desirable but seems unlikely to change this conclusion.

In reference [5] the necessity for a local shock strength maximum was demonstrated by showing that if the usual assumptions of axisymmetric flow theory plus an assumption of constant axial Mach number were made, a discontinuity appears in the radial momentum balance at the point where the shock terminates. The computed three-dimensional solution indicates that this discontinuity is in fact resolved by a local strength maximum, but requires an axial Mach number distribution quite different from the axisymmetric theory, see Fig. 11, or the assumption of constant axial Mach number.

It was shown in reference [16] that in fact the computed velocities and streamline curvatures observed in Fig. 6 resolve the potential pressure discontinuity and are consistent with the equations of motion. The required variation in relative Mach number can be found by requiring that the radial momentum balance be continuous everywhere and by recognizing that the projection of the shock on an S2 stream-surface and the incoming streamlines must be normal to each other at the shock termination as sketched in Fig. 18.

For simplicity, the supersonic blade sections will be idealized as flat plates with no camber; therefore, all the work in these outer sections is done by the deceleration provided by the shock alone. Furthermore, the blades will be assumed to be very close together, so that the flow is virtually axisymmetric.

Upstream of the "compressor" zero swirl and uniform total pressure and temperature are assumed. The subscript 1 will be used to refer to the flow just ahead of the shock, whereas 2 will denote the flow just behind it. Prime superscripts denote quantities referred to the rotating coordinate system.

The radial momentum equation in cylindrical coordinates can be written:

$$\frac{Du_r}{Dt} = \frac{u_\theta^2}{r} - \frac{1}{\rho}\frac{dP}{dr} \tag{14}$$

The ideal gas equation for the flow behind the shock can be written in nondimensional form as

$$\rho_2 = \gamma P_2 \frac{T_1}{T_2}\left(1 + \frac{\gamma - 1}{2} M_1^2\right) \tag{15}$$

If a parameter ϕ is defined as

$$\phi = \left(1 + \frac{\gamma - 1}{2} M_1^2\right) \tag{16}$$

and since

$$M_1^2 = M_1'^2 - (\omega r)^2 \left(1 + \frac{\gamma - 1}{2} M_1^2\right) \tag{17}$$

Downloaded 01 Jun 2010 to 171.66.16.59. Redistribution subject to ASME license or copyright; see http://www.asme.org/terms/Terms_Use.cfm

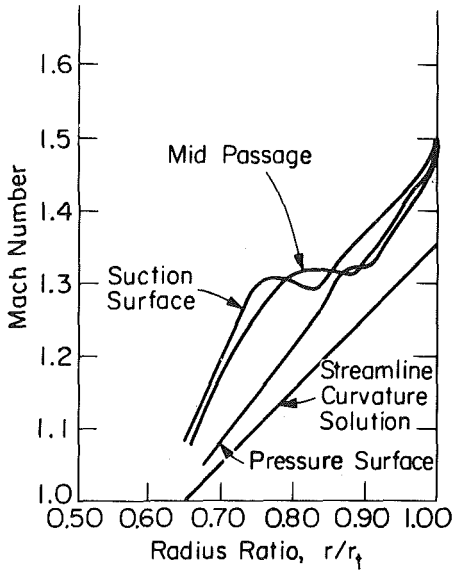

Fig. 11 Computed Mach number ahead of passage shock or compression wave

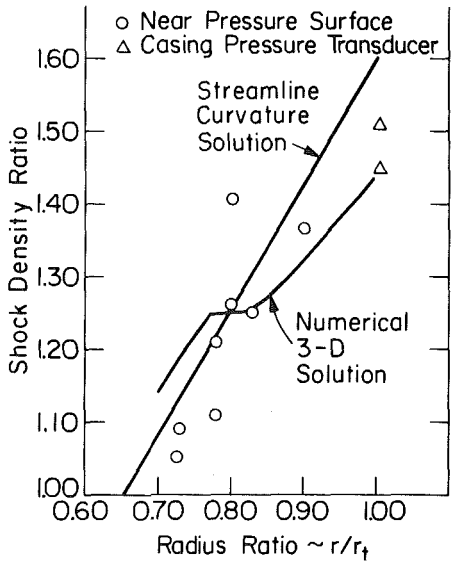

Fig. 12 Comparison of computed and experimental shock density ratios near blade pressure surface

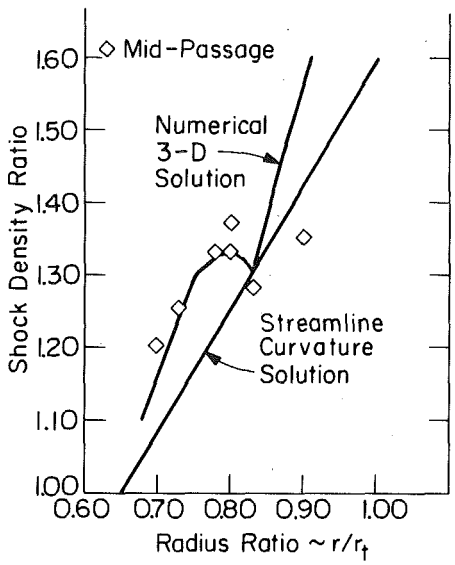

Fig. 13 Comparison of computed and experimental shock density ratios at mid-passage

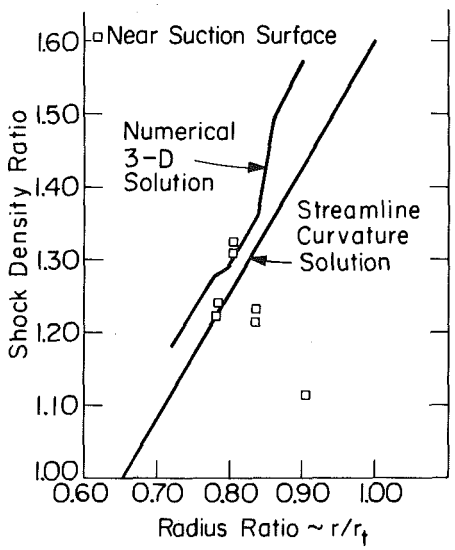

Fig. 14 Comparison of computed and experimental shock density ratios near blade suction surface

then (16) can also be expressed as

$$\phi = \frac{\left[1 + \frac{\gamma - 1}{2} M_1'^2\right]}{\left[1 + \frac{\gamma - 1}{2} (\omega r)^2\right]} \tag{18}$$

Behind the shock equation (14) can be written

$$\frac{Du_{r_2}}{Dt} = \frac{(V_2' \sin \alpha_2 - \omega r)^2}{r} - \frac{T_2}{T_1} \frac{1}{\gamma P_2 \phi} \frac{dP_2}{dr} \tag{19}$$

which can be accomplished by replacing ρ_2 by the expression (15) and u_{θ_2} by $V_2' \sin \alpha_2 - \omega r$, as explained in Fig. 19.

If constant upstream stagnation pressure, P_{0_1}, is assumed and since $P_1 = P_{0_1} \phi^{\gamma/\gamma-1}$ and $\omega r = V_1' \sin \alpha_1$, equation (19) can be written as

$$\frac{Du_{r_2}}{Dt} = \omega^2 r \left[\frac{V_2'}{V_1'} - 1\right]^2 - \frac{T_2}{T_1} \frac{P_1}{P_2} \frac{\phi \gamma/\gamma - 1}{\gamma \phi} \frac{d}{dr} \left[\left(\frac{P_2}{P_1}\right) \phi \gamma/\gamma - 1\right] \tag{20}$$

Using the fact that for a perfect gas $(T_2/T_1)(P_1/P_2) = \rho_1/\rho_2$, and finding the derivative with respect to r one obtains

$$\frac{Du_{r_2}}{Dt} = \omega^2 r \left[\frac{V_2'}{V_1'} - 1\right]^2 - \frac{\rho_1}{\rho_2} \frac{1}{\gamma \phi} \left[\frac{d(P_2/P_1)}{dr} - \frac{\gamma}{\gamma - 1} \frac{P_2}{P_1} \frac{1}{\phi} \frac{d\phi}{dr}\right] \tag{21}$$

For a normal shock the following relations hold:

$$\frac{P_2}{P_1} = \frac{2\gamma}{\gamma + 1} M_1'^2 - \frac{\gamma - 1}{\gamma + 1} \tag{22}$$

$$\frac{V_2'}{V_1'} = \frac{\gamma - 1}{\gamma + 1} + \frac{2}{\gamma + 1} \frac{1}{M_1'^2} \tag{23}$$

$$\frac{\rho_1}{\rho_2} = \frac{(\gamma - 1) M_1'^2 + 2}{(\gamma + 1) M_1'^2} \tag{24}$$

From equations (18) and (22) it can be shown that

$$\frac{1}{\phi} \frac{d\phi}{dr} = (\gamma + 1) \left[\frac{M_1'(dM_1'/dr)}{\left[1 + \frac{\gamma - 1}{2} M_1'^2\right]} - \frac{\omega^2 r}{\left[1 + \frac{\gamma - 1}{2} (\omega r)^2\right]}\right] \tag{25}$$

$$\frac{d(P_2/P_1)}{dr} = \frac{4\gamma}{\gamma + 1} M_1' \frac{dM_1'}{dr} \tag{26}$$

Using equations (18, 20) and (22–26), and some manipulation one obtains for the shocked region

Downloaded 01 Jun 2010 to 171.66.16.59. Redistribution subject to ASME license or copyright; see http://www.asme.org/terms/Terms_Use.cfm

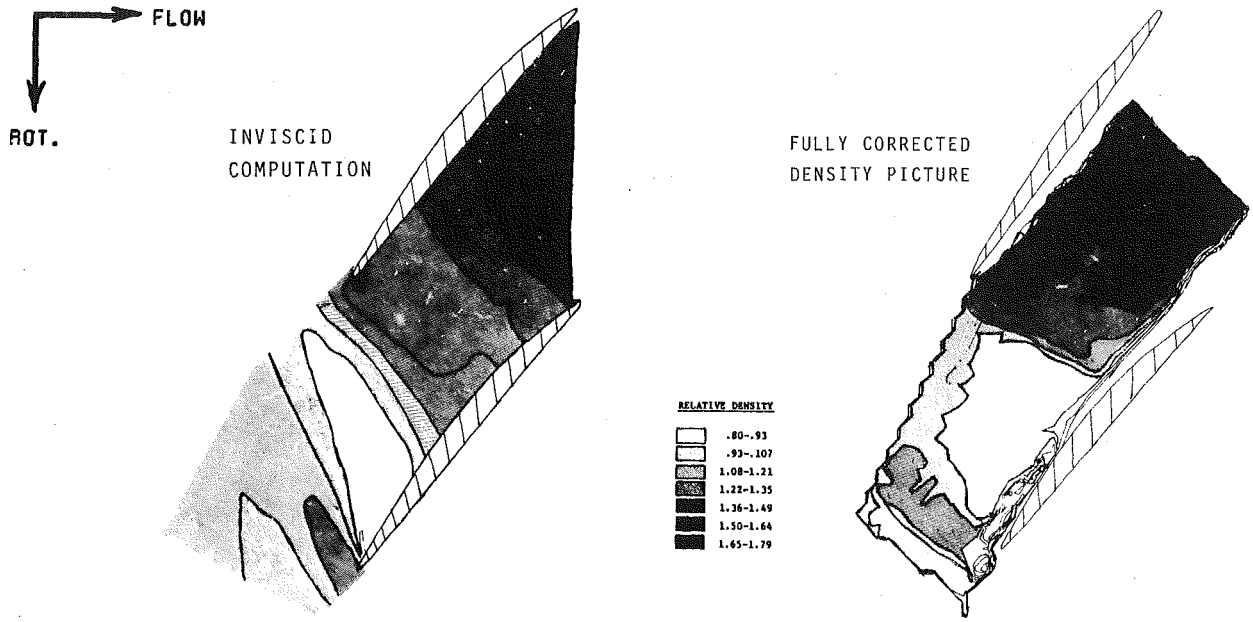

Fig. 15 Comparison of computed and experimental density distributions on blade-to-blade surface near local shock strength maximum

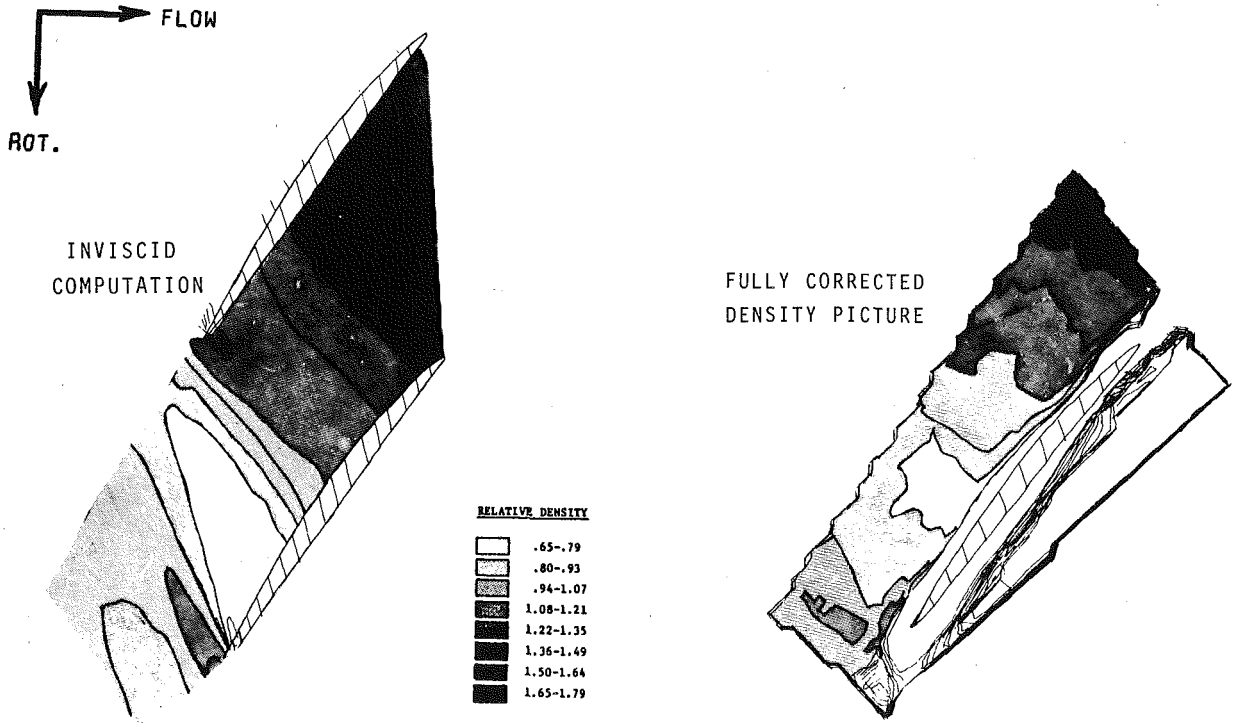

Fig. 16 Comparison of computed and experimental density distributions on blade-to-blade surface just above local shock strength maximum

$$\frac{[(\gamma-1)M_1'^2+2]\left[1+\frac{\gamma-1}{2}(\omega r)^2\,3+\gamma-2M_1'^2\right]}{\left[1+\frac{\gamma-1}{2}M_1'^2\right]}M_1'^3\left(\frac{dM_1'}{dr}\right)_{\substack{\text{shocked}\\\text{region}}}$$

$$=\omega^2 r[4+4(\gamma-1)M_1'^2-(4+4\gamma-(\gamma-1)^2)M_1'^4-2(\gamma^2-1)M_1'^6]$$

$$-(\gamma+1)^2\left[1+\frac{\gamma-1}{2}M_1'^2\right]M_1'^4\left\{\frac{Du_{r_2}}{\mathrm{Dt}}\right\}_{\substack{\text{shocked}\\\text{region}}} \quad (27)$$

and below the shock one obtains, since all ratios are unity and also $d(P_2/P_1)/dr \equiv 0$

$$\left(\frac{Du_{r_2}}{Dt}\right)_{\substack{\text{below}\\\text{shock}}}=\frac{\left[1+\frac{\gamma-1}{2}(\omega r)^2\right]}{\left[1+\frac{\gamma-1}{2}M_1'^2\right]}M_1'\left(\frac{\mathrm{dM}_1'}{\mathrm{dr}}\right)_{\substack{\text{below}\\\text{shock}}}-\frac{\omega^2 r}{\left[1+\frac{\gamma-1}{2}M_1'^2\right]} \quad (28)$$

Assuming now that at the shock termination point the flow is axial in the absolute coordinate system, it is clear that Du_{r_t}/Dt has to be continuous at that point, since otherwise streamline splitting will occur. There is no loss of generality by the above simplification, since

Downloaded 01 Jun 2010 to 171.66.16.59. Redistribution subject to ASME license or copyright; see http://www.asme.org/terms/Terms_Use.cfm

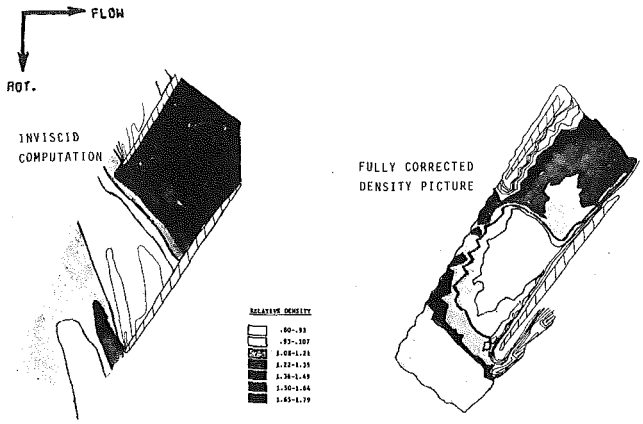

Fig. 17 Comparison of computed and experimental density distributions on blade-to-blade surface near tip casing

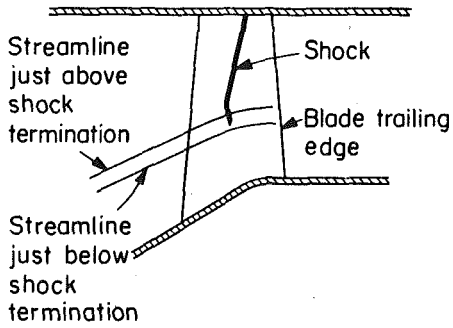

Fig. 18 Sketch of one possible shock-stream line intersection showing shock to be normal to local streamline direction at termination

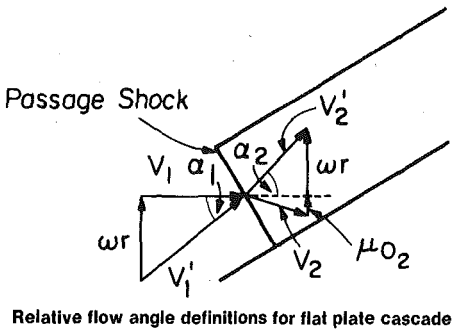

Fig. 19 Relative flow angle definitions for flat plate cascade analysis

if this is not true Euler's equation can be expressed in a coordinate system aligned with the flow. Therefore

$$\left(\frac{Du_{r_2}}{Dt}\right)_{\substack{\text{just}\\ \text{below shock}}} = \left(\frac{Du_{r_2}}{Dt}\right)_{\substack{\text{just}\\ \text{above shock}}} \tag{29}$$

Using equations (28) and (29) we can then write

$$\frac{\left[1+\frac{\gamma-1}{2}(\omega r)^2\right]}{\left[1+\frac{\gamma-1}{2}M_1'^2\right]} M_1'^2 \left\{[(\gamma-1)M_1'^2+2][3+\gamma-2M_1'^2]\left(\frac{dM_1'}{dr}\right)_{\substack{\text{above}\\ \text{shock}}} + (\gamma+1)^2 M_1'^2 \left(\frac{dM_1'}{dr}\right)_{\substack{\text{below}\\ \text{shock}}}\right\}$$

$$= \omega^2 r[4+4(\gamma-1)M_1'^2 - 2(2\gamma+1-\gamma^2)M_1'^4 - 2(\gamma^2-1)M_1'^6] \tag{30}$$

The right hand side of (30) is negative for M_1' greater than one (for the usual values of γ, the specific heat ratio), and zero for $M_1' = 1$. Let us consider each case separately.

If the shock terminates where M_1' equals 1, the right hand side of equation (30) vanishes and the equation is reduced to

$$\left(\frac{dM_1'}{dr}\right)_{\substack{\text{above}\\ \text{shock}}} = -\left(\frac{dM_1'}{dr}\right)_{\substack{\text{below}\\ \text{shock}}} \tag{31}$$

Three possible variations in dM_1'/dr exist:

1 dM_1'/dr greater than zero below the shock.—This implies that dM_1'/dr is less than zero above the shock. Since the shock is at the sonic line, the Mach number would have to be subsonic on both sides of the shock, and no shock exists.

2 dM_1'/dr equal to zero below the shock—in this case dM_1'/dr is also zero above the shock (and thus continuous). Taking the derivative of equation (30) it can be shown that then d^2M_1'/dr^2 is also zero at termination. Consequently an inflection point occurs for this case.

3 dM_1'/dr is less than zero below the shock—dM_1'/dr is then greater than zero above the shock, and thus the Mach number has a minimum at shock termination, while the flow is supersonic on both sides.

The other possible case is when the shock does not terminate where M_1' equals 1, but at a higher Mach number. In this case the right hand side of (30) is negative. All other terms on the left hand side are positive, except the polynomial $(3+\gamma-2M_1'^2)$ that multiplies dM_1'/dr above the shock. For $\gamma = 1.4$, this term is negative only if M_1' is greater than 1.48. Since it is unlikely that the flow has not shocked at that Mach number in a compressor stage, it is safe to assume that all terms on the left hand side of (30) are positive.

Two more possible variations of dM_1'/dr exist:

4 dM_1'/dr is greater than zero below the shock—Then dM_1'/dr is less than zero above the shock, which is now possible since the flow is supersonic below shock termination. A Mach number maximum appears at the shock termination point.

5 dM_1'/dr is less than zero below the shock—dM_1'/dr could be greater or less than zero above the shock, depending on the value of the different parameters entering the equation. For the test rotor geometry, a maximum for the Mach number in the unshocked region is expected, assuming the present case is feasible.

This discussion illustrates that arbitrary Mach number variations about the passage shock termination point are not possible, but rather are constrained by a requirement that the radial acceleration be continuous there. Consistent variations appear to have either local maxima or at least a plateau at the shock termination point rather than a monotonic increase with radius. In addition, the shock may terminate at a radius where the approach Mach number is much larger than 1.0. These analytical predictions are to be compared to the numerically computed Mach number profiles shown in Fig. 11. Here the predicted profile shape shows up clearly along the suction surface and at mid-passage and somewhat less clearly along the pressure surface. The close agreement between computed and measured shock strengths as well as between computed and analytically predicted Mach number profiles further confirms the conclusion that the local shock strength maximum is an inviscid phenomena.

It must be emphasized that, while the Mach number profiles for the test compressor do lead to local pressure maxima, this situation is not the only possible case. In reference [5] it was demonstrated and substantiated by the discussion of equation (31), that no pressure maximum need exist if the shock terminated at $M_1' = 1.0$ and $dM_1'/dr = 0$ there, case 2. If the passage shock is oblique to the streamlines in the meridional plane rather than normal still further Mach number profiles exist for which no pressure maximum is expected. Such oblique shock cases are discussed in reference [17].

Acknowledgment

This research was sponsored by NASA Lewis Research Center under Grant NGL 22-009-383 and monitored by Drs. William McNally and Roderick Chima.

References

1 Wisler, D. C., and Massey, P. W., "Gas Velocity Measurements Within a Compressor Rotor Passage Using the Laser Doppler Velocimeter," ASME JOURNAL OF ENGINEERING FOR POWER, Vol. 95, Apr. 1973, p. 91.

2 Walker, D. A., Williams, M. C., and Hourse, R. D. "Intrablade Velocity Measurements in a Transonic Fan Utilizing a Laser Doppler Velocimeter,"

Downloaded 01 Jun 2010 to 171.66.16.59. Redistribution subject to ASME license or copyright; see http://www.asme.org/terms/Terms_Use.cfm

Minnesota Symposium on Laser Anemometry, Univ. of Minnesota, Minneapolis, Oct. 22–24, 1975.

3 Dunker, R. J., Strinning, P. E., and Weyer, H. B. "Experimental Study of the Flow Field Within a Transonic Axial Compressor Rotor by Laser Velocimetry and Comparison with Through-Flow Calculations," ASME JOURNAL OF ENGINEERING FOR POWER, Vol. 100, April 1978, p. 279.

4 Epstein, A. H., "Quantitative Density Visualization in a Transonic Compressor Rotor," ASME JOURNAL OF ENGINEERING FOR POWER, Vol. 99, July 1977, pp. 460.

5 Epstein, A. H., Kerrebrock, J. L., and Thompkins, Jr., W. T., "Shock Structure in Transonic Compressor Rotors," *AIAA Journal,* Apr. 1979.

6 Thompkins, W. T. and Epstein, A. H., "A Comparison of the Computed and Experimental Three-Dimensional Flow in a Transonic Compressor Rotor," AIAA Paper 76-368, July 1976.

7 Thompkins, W. T., "Three-Dimensional Flow Solution Program for Transonic Compressor Blade Rows," NASA Contractor's Report to be published Jan. 1980.

8 Merrington, G. L., ARL Report/ME, No. 146.

9 Roberts, D. W. and Forester, C. K., "Parabolic Procedure for Flows in Ducts with Arbitrary Cross Sections," *AIAA Journal,* Vol. 17, Jan. 1979, pp. 33.

10 Griffin, M. D., Jones, E., Anderson, T. D., "A Computational Fluid Dynamic Technique Valid at the Centerline for Non-Axisymmetric Problems in Cylindrical Coordinates," *Journal of Computational Physics,* Vol. 30, Mar. 1979, pp 352.

11 MacCormack, R. W., "Computational Efficiency Achieved by Time Splitting of Finite Difference Operators," AIAA Paper 72-154, 1972.

12 Roache, P. J., *Computational Fluid Dynamics,* Hermosa Publishers, 1976, pp 230–240.

13 Berenfeld, S., "A Study of Boundary Conditions for Three-Dimensional Transonic Compressor Rotors," SM Thesis, MIT, June 1979.

14 Tan, C. S., "Three-Dimensional Vorticity-Induced Flow Effects in Highly Loaded Axial Compressors," PhD Thesis, MIT, 1978.

15 Rae, W. J. and Lordi, J. A., "A Study of Inlet Conditions for Three-Dimensional Compressor Flows," XE-6129-A-4, June 1978, Calspan Corporation, Buffalo, NY.

16 Haymann-Haber, G., "A Computational Study of the Flow in a Transonic Axial Compressor Using an Inviscid, Three Dimensional Finite Difference Calculation," SM Thesis, MIT, June 1979.

17 Taylor, T. D., Ndefo, E. and Masson, B. S., "A Study of Numerical Methods for Solving Viscous and Inviscid Flow Problems," *Journal of Computational Fluid Physics,* Vol. 9, 1976, pp. 261–286.

Downloaded 01 Jun 2010 to 171.66.16.59. Redistribution subject to ASME license or copyright; see http://www.asme.org/terms/Terms_Use.cfm

Colin F. McDonald
Mem. ASME

Charles R. Boland

General Atomic Company,
San Diego, CA 92138

The Nuclear Closed-Cycle Gas Turbine (HTGR-GT)—Dry Cooled Commercial Power Plant Studies[1]

Combining the modern and proven power conversion system of the closed-cycle gas turbine (CCGT) with an advanced high-temperature gas-cooled reactor (HTGR) results in a power plant well suited to projected utility needs into the twenty-first century. The gas turbine HTGR (HTGR-GT) power plant benefits are consistent with national energy goals, and the high power conversion efficiency potential satisfies increasingly important resource conservation demands. Established technology bases for the HTGR-GT are outlined, together with the extensive design and development program necessary to commercialize the nuclear CCGT plant for utility service in the 1990s. This paper outlines the most recent design studies by General Atomic for a dry-cooled commercial plant of 800 to 1200 MW(e) power, based on both nonintercooled and intercooled cycles, and discusses various primary system aspects. Details are given of the reactor turbine system (RTS) and on integrating the major power conversion components in the prestressed concrete reactor vessel.

Introduction

The advantages of the gas turbine high-temperature gas-cooled reactor exemplified many times in recent years [1–4], consist of the following: (1) plant simplification, (2) improved economics, and (3) siting flexibility. An extensive design and development program for the HTGR-GT components is necessary to commercialize the plant for utility service in the last decade of this century. This paper discusses design aspects of the HTGR-GT plant in its present conceptual design stage and outlines the established technology bases for this new power plant concept. The existence of operating experience from both gas-cooled reactors and closed-cycle gas turbine (CCGT) power conversion systems makes the HTGR-GT plant a potential commercial reality for the late 1990s.

In the current period of energy consciousness, the utility companies are reviewing their nuclear capacity, including the important element of power plant rating. This paper reports on studies based on differing plant variants in the 800 to 1200 MW(e) range. The multiloop power conversion system affords flexibility toward future utility needs and increases plant availability, since operation can be sustained with a loop shut down. Design studies for both nonintercooled and intercooled cycles are underway to maximize plant cost effectiveness and resource conservation.

The excellent cogeneration capabilities of the HTGR-GT plant, made possible by the sensible heat rejection of the CCGT, have been well documented [5–7]. However, it is the siting flexibility of dry-cooled plants (covered in this report) that has attracted utility attention both in the U.S. and Europe. Dry cooling relieves plant location from being tied to rivers and bodies of water that may well have already reached their assigned thermal effluent capacity. The HTGR-GT plant also takes advantage of limited cooling water via wet/dry cooling. For the sites with cooling water in the next century, it is projected that bottoming cycle cogeneration will be available as an option to the utility owner.

Compliance with nonproliferation guidelines and changing and more demanding safety considerations have had increasingly important impact on nuclear power plant design. The HTGR-GT plant is adaptable to high-, medium-, and low-enrichment fuel cycles. This paper outlines power plant studies based on the medium-enriched uranium (MEU) fuel cycle, which are thus in compliance with the current U.S. nonproliferation goals. A conservative design approach has been emphasized for the multiloop plant concept to provide for maximum safety and durability. The HTGR is an inherently safe reactor type by virtue of its graphite-moderated core, single-phase working fluid, and containment of all the nuclear equipment in a prestressed concrete reactor vessel (PCRV).

This paper reports only part of the rapidly increasing international efforts to combine the gas turbine and nuclear energy within the next two decades. The extraordinary role of the HTGR-GT in meeting international energy goals is significant. The studies reported in this paper represent an important step towards the selection of an optimized HTGR-GT plant configuration for the U.S. commercial marketplace.

Background of HTGR-GT Plant Studies

As HTGR-GT plant design studies have progressed (since initiation in 1972), the thermodynamic cycle and plant configuration have evolved from investigations of the best means to satisfy the various performance, economic, safety, and operational goals. Many papers have been published in the open literature in the last seven years; a summary of the design evolution is given in reference [8]. During this period, external assessments of the HTGR-GT plant have been car-

[1] Work supported by U.S. Department of Energy Contract DE-AT03-76SF70046.

Contributed by the Gas Turbine Division and presented at the Gas Turbine Conference and Products Show, New Orleans, La., March 10–13, 1980 of THE AMERICAN SOCIETY OF MECHANICAL ENGINEERS. Manuscript received at ASME Headquarters December 13, 1979. Paper No. 80-GT-82.

Copyright © 1981 by ASME

Downloaded 01 Jun 2010 to 171.66.16.59. Redistribution subject to ASME license or copyright; see http://www.asme.org/terms/Terms_Use.cfm

ried out by the government and by specialist consulting companies. From the technical and economic standpoints, these reviews have been favorable, as exemplified by the most recent assessment done by NUS Corporation under contract from Electric Power Research Institute (EPRI) [9].

An extensive program of design, development, and testing on the nuclear gas turbine plant is necessary to achieve performance and structural integrity and to qualify the equipment for nuclear power generation. This program is a main part of an international cooperative program currently underway. A dialogue has been in effect for several years between the U.S. program (General Atomic) and the European High Temperature Helium Turbine (HHT Project) partners. This effort intensified in 1977–78 relative to the definition of a European-sited demonstration plant. Such a demonstration plant is considered an attractive approach to creating the necessary technical base from which follow-on commercial plants could be engineered with a high degree of commonality for both 60 Hz United States and 50 Hz European power systems.

Figure 1 presents qualitatively the relations between the U.S. plant studies, the European (HHT) demonstration project, and possible U.S. and European follow-on commercial plants. Initial details of the HHT demonstration plant concept have been discussed previously [10]. The main features of the demonstration plant will be finished in late 1979, and an extensive international effort will be initiated to meet the goal of demonstration plant operation by about 1990. It is recognized that complete design convergence between the U.S. and European plant variants is not possible because of (1) the fundamental frequency difference, (2) differing codes and standards, and (3) different safety and licensing criteria. It is further recognized, however, that commonality in the main features of the plants, together with a strong technology exchange effort, would be a move in the direction of minimizing overall cost and lowering development risks, by utilizing worldwide technology.

Work on the HTGR-GT plant over the last few years has been supported by the U.S. Department of Energy and a group of electrical utilities, with participation by industrial companies. A key element in the formulation of a new power plant concept is participation by utility organizations right from the onset, and indeed, such a rapport has been in existence on the HTGR-GT program since 1972. With the formation of the Gas Cooled Reactor Associates (GCRA), the utility inputs to plant design are now more formalized. With regular meetings of the GCRA Technical Advisory Committee (TAC), the utility directives can be factored into the plant design on an on-going basis right from the conceptual design stage.

Until recently, work in the U.S. at General Atomic, had been directed towards the design, performance, and economic assessment of a HTGR-GT plant in the 1200-MW(e) class with capability of being adapted to both smaller and larger units. A 1200-MW(e) reference plant established in 1977–78, based on a nonintercooled cycle and embodying three power conversion loops (PCLs), has been described previously [11].

Over the last few years, plant layout studies have been done for a wide range of power levels. These studies have consisted essentially of varying the number of PCLs, sizing the major components, evaluating the impact of component orientation on PCRV diameter, computing plant efficiency, and estimating costs (capital and power generating costs). The range of plants studied in a conceptual manner and the impact on PCRV diameter (which is regarded as a major capital cost indicator) are shown on Fig. 2.

Inputs from TAC indicate a trend away from the larger plants envisioned a few years ago for operation towards the end of this century. Studies are now aimed at plants in the range of 800 to 1200 MW(e), and this paper outlines configurations in this range based on both nonintercooled and intercooled cycles and with differing numbers of PCLs.

Technology Bases for HTGR-GT Plant

The technology resources from which the HTGR-GT plant can draw are formidable and are briefly outlined in this section. The necessary technologies stem from several sources, as shown in Fig. 3,

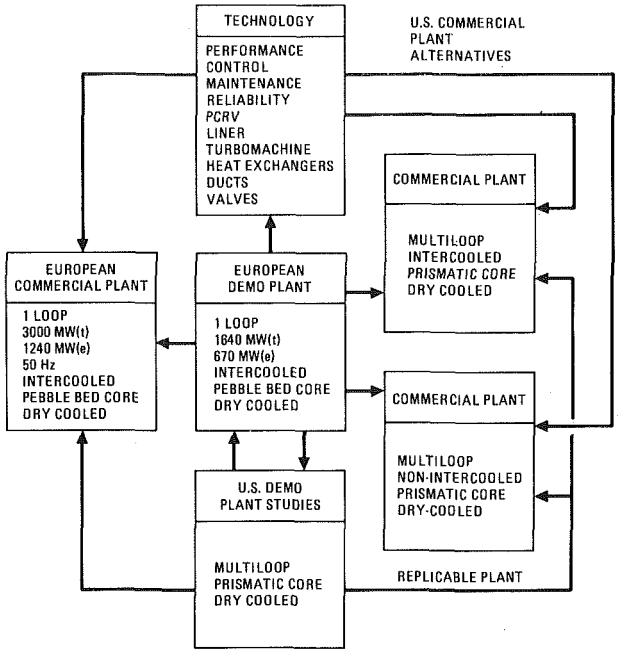

Fig. 1 Demonstration-commercial plant relationships

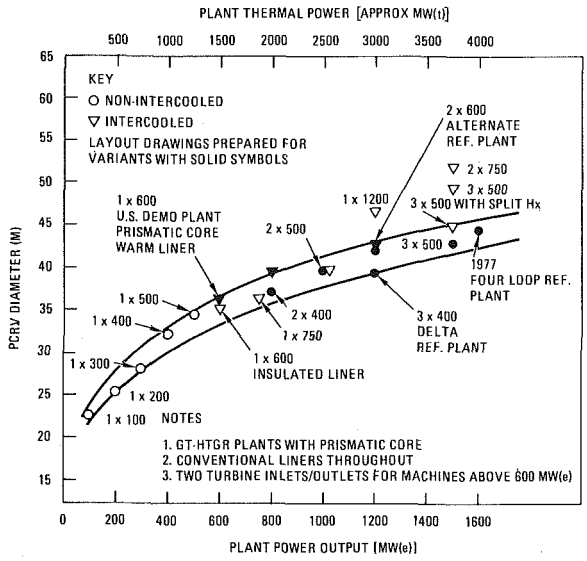

Fig. 2 Impact of HTGR-GT plant power rating on PCRV diameter

and when combined, form the bases from which a successful nuclear gas turbine plant can be designed, developed, and introduced into utility service with a high degree of confidence that the performance, economic, safety, and reliability goals will be realized.

From the reactor standpoint, there is extensive operating experience for gas-cooled reactors, and in particular, for the helium-cooled high temperature reactor. Valuable pioneering experience from the experimental high temperature reactors in the United Kingdom (Dragon Project), in the U.S. (UHTREX), and in the Federal Republic of Germany (AVR) formed the basis for the first HTGRs entering commercial service: the Peach Bottom and Fort St. Vrain reactors in the U.S. and (in the near future) the THTR plant in Germany. These HTGRs, while based on a steam-cycle power conversion system, provide valuable utility operating experience input to the HTGR-GT program.

While the CCGT is not well known in the U.S., it has demonstrated very high fuel utilization efficiencies and a high degree of reliability in the various European plants. Since operation of the pioneer plant in 1939, the 40 years of experience have substantiated the claim that

Downloaded 01 Jun 2010 to 171.66.16.59. Redistribution subject to ASME license or copyright; see http://www.asme.org/terms/Terms_Use.cfm

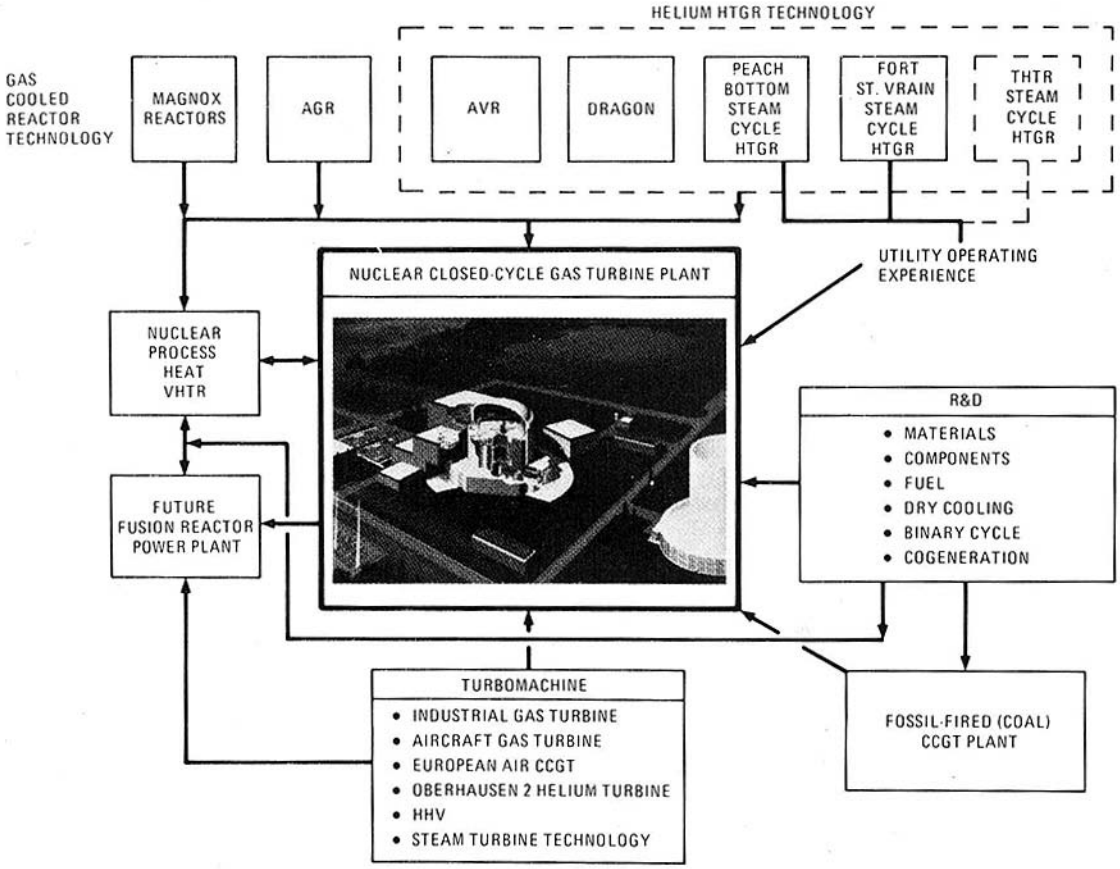

Fig. 3 Technology bases for HTGR-GT plant

this prime-mover technology is well established [12]. With the helium turbomachine itself being the singularly most important PCL component from the development standpoint, the applicability of established technologies from (1) European CCGT plants, (2) helium test facilities, (3) HTGR components and steam-cycle plant operating experience, and (4) advanced open-cycle industrial gas turbines are recognized. The industrial technology bases from which the turbomachine can benefit are shown on Fig. 4, which illustrates existing hardware. The emphasis here relates to the available comprehensive world-wide resources, which if utilized on an international cooperative basis, will make near-term introduction of the nuclear gas-turbine plant a reality.

An important helium turbine plant is the fossil-fired 50 MW(e) Oberhausen 2 unit which was built by Energieversorgung Oberhausen AG (EVO) in the Federal Republic of Germany. Many reports and papers have been written describing the EVO plant construction and operation [13–15]. In addition to providing electrical power [50 MW(e)] and district heating [54 MW(t)], the tests carried out on the EVO plant are intended to supply information (for the nuclear gas-turbine program) on the dynamics of the overall plant and on the long-term behavior of specific components. Another important plant is the high temperature helium test facility (HHV) at the Kernforschungsanlage (KFA) in Jülich. The operation of this helium test plant represents a central test within the European HHT project. By this program, essential characteristics of the turbomachine are to be verified. Furthermore, this plant serves for tests of prototype components for the HHT demonstration plant. A full account is given in reference [16] of the roles of the EVO plant and HHV test facility in the development of the European HHT project.

Emphasis of the formidable technology bases for the HTGR-GT plant has been made in this section of the paper, because this adds credibility to the claim that a new power plant type such as the HTGR-GT, while now only in the conceptual design stage, could become a commercial reality for utility service by the year 2000.

Thermodynamic Cycle(s) and Performance

A detailed account of the systems-related studies leading to the selection of an optimized set of cycle parameters is reported in a separate paper [17], so only a brief summary of the impact these have on plant layout and design will be covered here. In the HTGR-GT plant studies done over the last few years by General Atomic, there has been a strong motivation to use the nonintercooled cycle for the following reasons: (1) plant simplicity in both turbomachine and primary system and (2) high reject temperature for economical dry cooling and optional bottoming cycle. In Europe, on the other hand, the intercooled cycle has always been favored because (1) it has higher efficiency, (2) the reject water temperature is well suited to district heating, and (3) there is a carry-over from the European fossil-fired CCGT plants, which have all been intercooled.

In any compression process involving a multistage system, cooling between the stages reduces the compression work, and in the case of the CCGT, the plant efficiency is increased by virtue of the higher net turbine output. On a purely thermodynamic basis, an increase of about three percentage points can be computed for the intercooled cycle. When the additional pressure losses in the intercooler and in the more complex ducting arrangement are taken into account, the gain in efficiency is reduced to about two percentage points. Nevertheless, such a gain over the 40-year operating life of the plant has significant economic implications, and hence, the current study of plant designs is based on both intercooled and nonintercooled cycles. Some of the major factors involved in the issue of intercooling versus nonintercooling are outlined on Table 1.

As mentioned previously, efforts are underway for both plant variants to select the cycle parameters for minimum power generating cost. For the purpose of component sizing and plant configuration layout studies, it was necessary to establish early comparative cycle data. The tentative values used are shown on Table 2, and these data are felt to be very representative for design purposes. The key differences between the two cycles are shown on the loop diagram for the

Downloaded 01 Jun 2010 to 171.66.16.59. Redistribution subject to ASME license or copyright; see http://www.asme.org/terms/Terms_Use.cfm

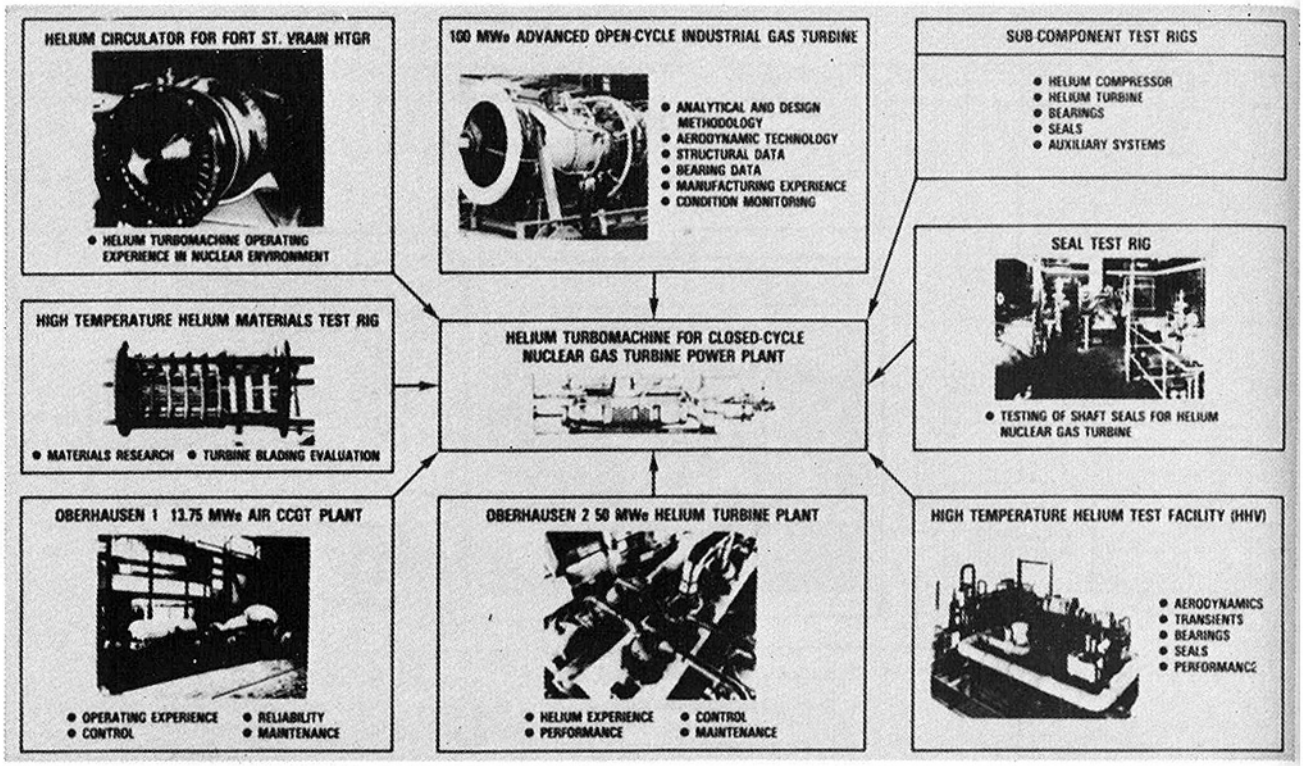

Fig. 4 Technology bases for nuclear closed-cycle helium turbomachine

Table 1 Major factors relating to the issue of intercooling

Non-intercooled Plant

1. Simpler turbomachine (shorter rotor, less duct connections)
2. Simpler gas flow paths and primary system layout
3. Less complex system implies improved availability and reliability
4. High reject temperature well suited for cogeneration (i.e., binary cycle, process steam, district heating, etc.)
5. Reduced plant construction time (simpler PCRV)
6. Reduced complexity and risk

Intercooled Plant

1. Increased cycle thermodynamic efficiency
2. Reduced helium mass flow rate (i.e., smaller components)
3. *Source of cooler high-pressure gas available for* cavity liner cooling
4. Reduced core inlet gas temperature
5. Possible use of additional water-to-helium heat exchanger (intercooler) for decay heat removal
6. Heat rejection split between two water-to-helium exchangers (precooler and intercooler) results in smaller unit assemblies
7. Utilization of European experience from the small fossil-fired CCGTs
8. Water outlet temperature well suited for district heating
9. Additional maintenance requirements
10. Increased plant capital cost
11. Additional potential source of water ingress to primary system

Table 2 HTGR-GT cycle data used in plant configuration comparison studies

Thermodynamic Cycle	Non-intercooled	Intercooled
Heat rejection mode	Dry-cooled	Dry-cooled
Turbine inlet temp, °C	850	850
Ambient air temp, °C	15	15
Compressor inlet temp, °C	26.7	26.7
Max system pressure, MPa	7.93	7.93
Compressor pressure ratio	2.50	3.0 (1.73/1.73)
System pressure loss (ΔP/P), %	∿9	∿11
Compressor flow kg/s/MW(t)	0.57	0.50
Recuperator effectiveness	0.90	0.90
Compressor efficiency, %	89.8	90.8 LP, 90.2 HP
Turbine efficiency, %	91.8	92.2
Precooler water outlet temp, °C	132	87
Intercooler water outlet temp, °C	--	66
Cycle efficiency, %	∿40.0	∿42.0

non-intercooled plant (Fig. 5) and on the flowpath diagram for the intercooled variant (Fig. 6).

An important parameter influencing the efficiency of the closed-cycle plant is the turbine inlet temperature. For the power plant studies outlined in this paper, a turbine inlet temperature of 850°C has been assumed. This temperature is modest compared to that for most industrial gas turbine practice [18]; it is below the level where turbine blade cooling is necessary, and it facilitates utilization of an existing nickel-base alloy which is used extensively in industrial gas turbines. The impact of turbine inlet temperature, together with other important parameters, is shown in Fig. 7 for a nonintercooled cycle. Projected operating regimes for various CCGT plant applications are shown on this plot. It is clear from Fig. 7 that the CCGT offers significant potential for high levels of plant efficiency when dry cooled.

Plant Configuration Studies

Three-Loop, 1200-MW(e) Nonintercooled Plant Concept. As previously mentioned, this 1200-MW(e) plant variant has received

Downloaded 01 Jun 2010 to 171.66.16.59. Redistribution subject to ASME license or copyright; see http://www.asme.org/terms/Terms_Use.cfm

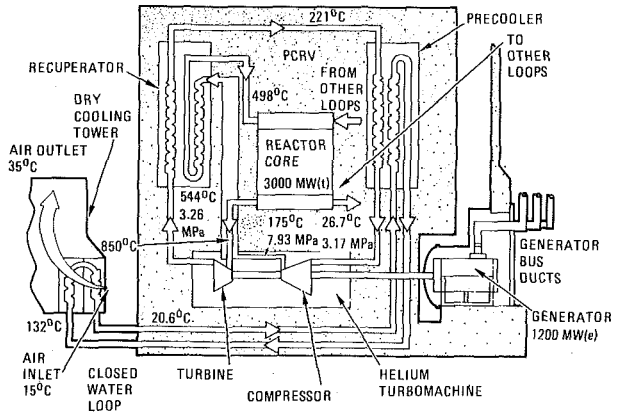

Fig. 5 Loop cycle diagram for non-intercooled dry-cooled HTGR-GT power plant

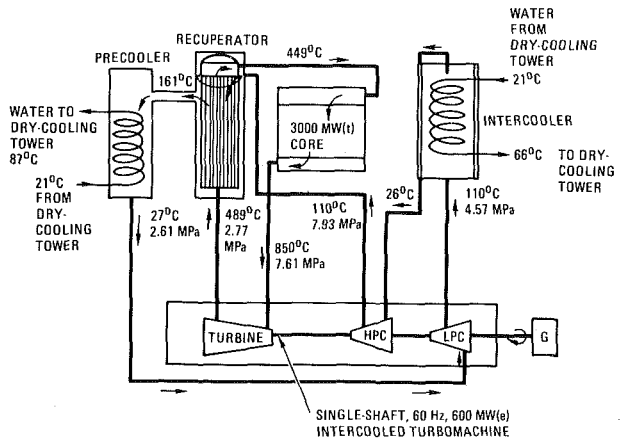

Fig. 6 Flow path diagram for two-loop intercooled HTGR-GT plant

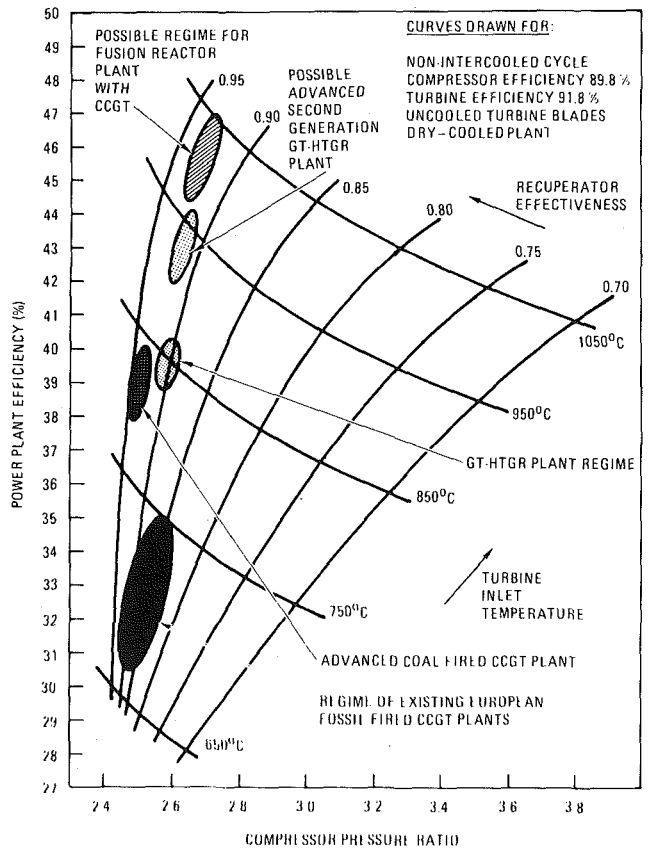

Fig. 7 Representative cycle parameter array for nonintercooled HTGR-GT plant

the most design attention in recent years, and in terms of performance and cost, forms the base case for comparison with other plant concepts. An isometric view given in Fig. 8 shows the major elements of the power conversion system integrated inside the PCRV. The compact nature of the installation is shown on the plan view of the PCRV (Fig. 9). An obvious goal in all plant design and layout studies is the minimization of the PCRV diameter because of its economic impact. The arrangement shown on Fig. 9 has the following main features: (1) centralized core cavity, (2) delta orientation of the three turbomachines, and (3) recuperator and precooler positioned over the turbomachine cavity. This arrangement represents a very good utilization of space within the reactor vessel, and in fact, satisfies the economic goal of PCRV diameter minimization. The delta orientation of the PCLs, as shown in Fig. 9, is well suited to the non-intercooled cycle. Incorporation of intercoolers is not attractive in this three-loop arrangement, since they must be positioned radially outwards from the turbomachine cavity, and this results in an unacceptably large increase in PCRV diameter. As will be outlined in the following sections,

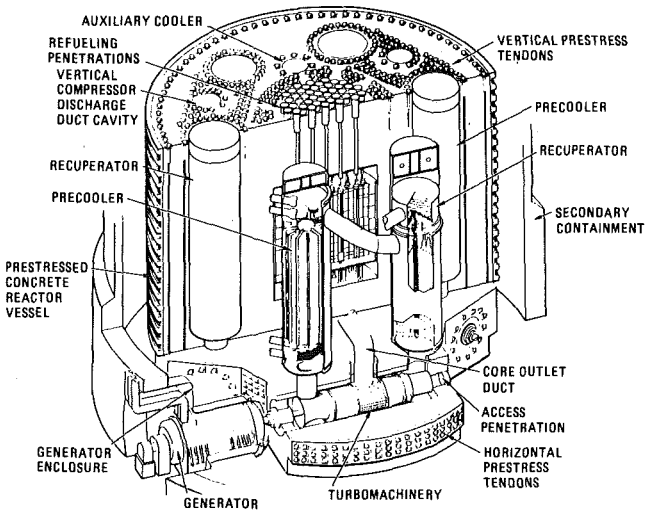

Fig. 8 Integrated HTGR-GR plant based on 3 PCLs and nonintercooled cycle

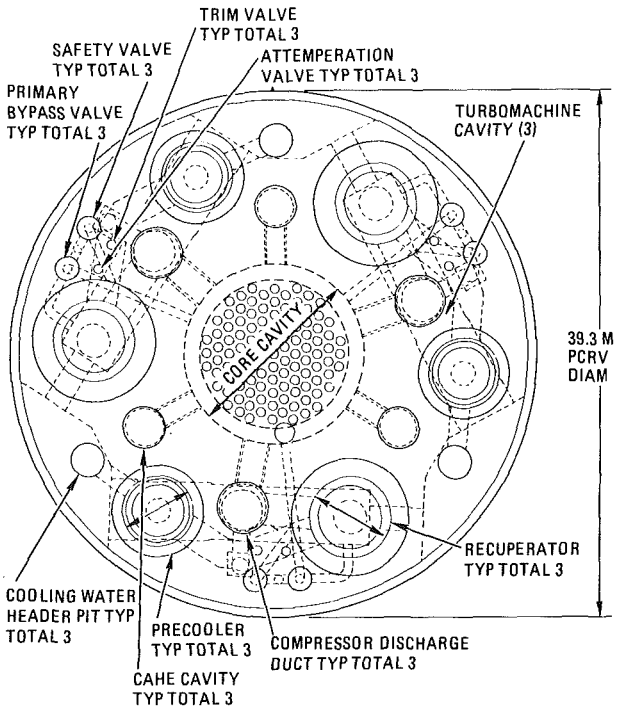

Fig. 9 PCRV plan view for 3 × 400-MW(e) nonintercooled HTGR-GT plant

Downloaded 01 Jun 2010 to 171.66.16.59. Redistribution subject to ASME license or copyright; see http://www.asme.org/terms/Terms_Use.cfm

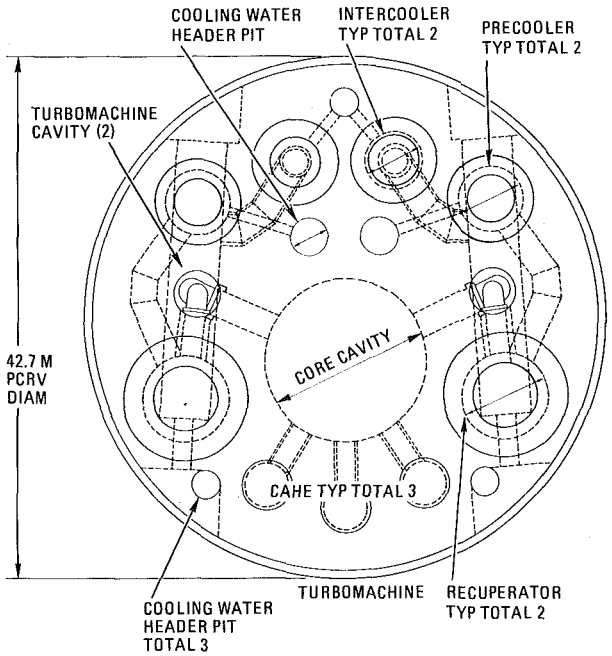

Fig. 10 PCRV plan view for 2 × 600-MW(e) intercooled HTGR-GT plant

evaluation of the intercooled cycle is being done for two-loop plant variants.

Two-Loop, 1200-MW(e) Intercooled Plant Concepts. The motivations for the study of a two-loop plant included the following: (1) potential capital cost reduction, (2) flexibility in power range, (3) adaptability to intercooling, (4) maximization of technical interchange between U.S. and European programs, and (5) simplified turbomachine maintenance. Accordingly, studies in the last year have involved the conceptual design and layout of two-loop plant variants based on both intercooled and non-intercooled cycles.

A representative layout of a two-loop intercooled plant is shown on the PCRV plan view given on Fig. 10. While studies have been performed for PCL ratings of 400, 500, and 600 MW(e), the main features of the plant are essentially the same, and the view shown on Fig. 10 for a 2 × 600 MW(e) concept can be considered representative. Again, as in previous studies, efforts were expended to minimize the diameter of the PCRV, and this was achieved by a combination of the following: (1) offsetting the core cavity, (2) chordal positioning of the two horizontal turbomachine cavities, (3) positioning the recuperator and precooler over the turbomachine cavity, and (4) establishing simplified gas flow paths within the primary system. Layout studies led to the positioning of the two intercoolers and three decay heat removal systems, as shown on Fig. 10, to give an acceptable arrangement from the standpoints of gas flow paths and PCRV structural considerations. It is recognized that with more in-depth studies the positioning of the major components within the vessel (and the angle of the turbomachine cavities) may change; however, the general arrangement shown on Fig. 10 is regarded as the optimum for a two-loop intercooled plant. The elevation view through the PCRV on Fig. 11 shows the simple gas flow paths between the turbomachine and the heat exchangers (it should be noted that the intercooler is not shown in this particular sectional view). The gas flow paths to and from the reactor core cavity are shown on Fig. 12. Also shown on this figure is a section through the core auxiliary cooling system (CACS), and the gas flow paths to and from the core cavity and in the heat exchanger and circulator can be clearly seen.

Two-Loop Nonintercooled Plant Concepts. As part of the study to compare the designs, economics, performance, and availability of intercooled versus non-intercooled plants, a layout study was performed to identify the main features of a two-loop nonintercooled plant variant.

A representative layout of a two-loop nonintercooled plant is shown on the PCRV plan view given in Fig. 13. While studies have been

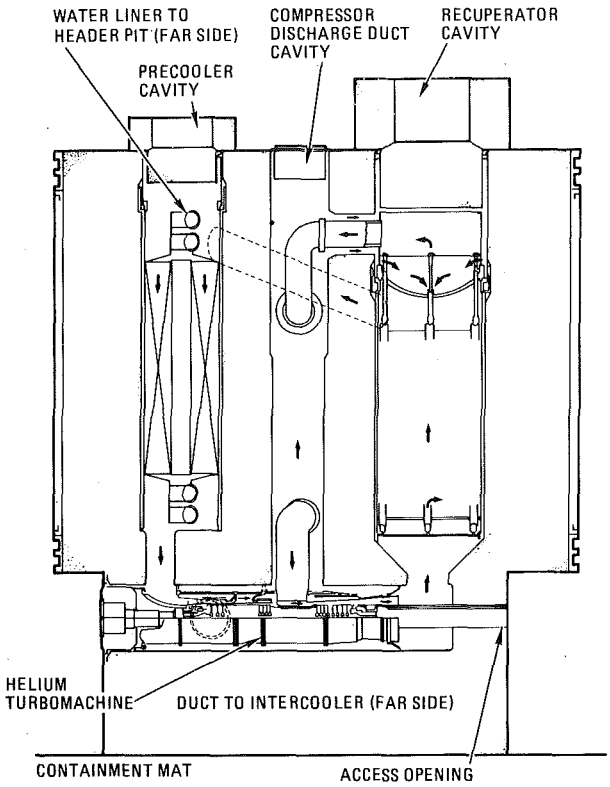

Fig. 11 View through PCL for two-loop HTGR-GT plant

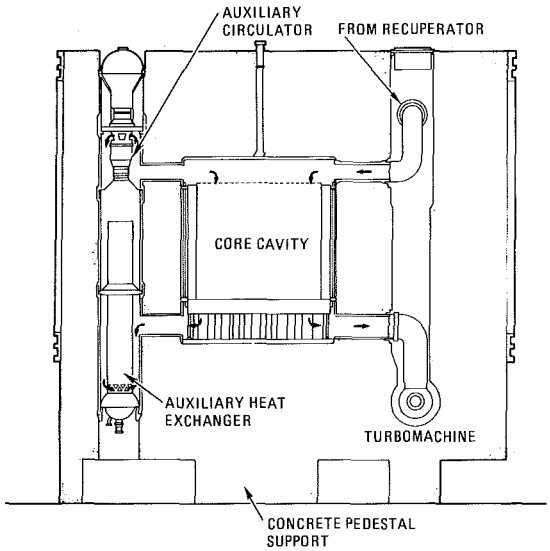

Fig. 12 Elevation through PCRV showing core cavity and decay heat removal system

performed for PCL ratings of 400, 500, and 600 MW(e), the main features of the plant are essentially the same, and the view shown on Fig. 13 for a 2 × 500 MW(e) concept can be considered representative. Several layout variants were developed for the nonintercooled plant, and the one shown in Fig. 13 has the following characteristics: (1) centralized core cavity, (2) chordal turbomachine cavity orientation, and (3) recuperator and precooler positioned over the turbomachine cavity. The positioning of the three CACS units (in a different orientation from the aforementioned intercooled variant) is conducive to good gas flow paths, PCRV structural considerations, and minimization of the vessel diameter. The main characteristics of the elevation views through the PCRV (shown previously for the intercooled variant in Figs. 11 and 12) are near identical for the two-loop nonintercooled plant.

Downloaded 01 Jun 2010 to 171.66.16.59. Redistribution subject to ASME license or copyright; see http://www.asme.org/terms/Terms_Use.cfm

Table 3 Comparison of HTGR-GT plant conceptual designs

Loop Rating, (MW(e)	400		500	600	400
Thermodynamic cycle	Non-intercooled	Intercooled	Non-intercooled	Intercooled	Non-intercooled
No. of loops	2	2	2	2	3
Plant output, MW(e)	800	800	1000	1200	1200
Plant efficiency, %	∿40.0	∿42.0	∿40.0	∿42.0	∿40.0
Core rating, MW(t)	2000	1905	2500	2860	3000
Plant type	Power conversion system integrated in PCRV				
Heat rejection	Dry-cooled				
Liner type	Conventional, insulated, and water-cooled				
Core type	HTGR prismatic fuel elements				
Fuel type	MEU				
Fuel cycle, yr	3				
Core power density, W/cm^3	6.8				
Core position	Offset	Offset	Central	Offset	Central
Turbomachine position	Chordal	Chordal	Chordal	Chordal	Delta
No. of recuperators	2	2	2	2	3
No. of intercoolers	--	2	--	2	--
No. of precoolers	2	2	2	2	3
No. of major cavities	12	14	12	14	16
PCRV diam, m	37.2	39.6	39.6	42.7	39.3
PCRV height, m	35.4	35.4	35.4	35.4	35.4
No. of CACS units	3	3	3	3	3
Design status	Conceptual	Conceptual	Conceptual	Conceptual	Conceptual

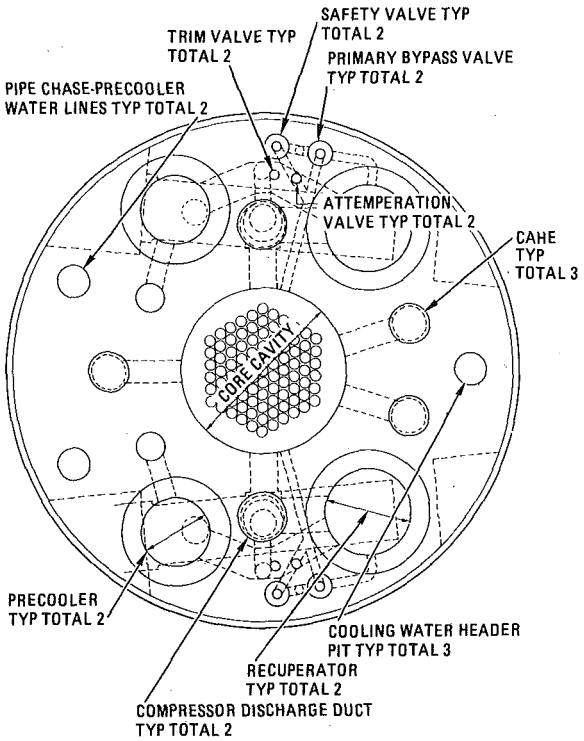

Fig. 13 Plan view of PCRV for 2 × 500-MW(e) nonintercooled HTGR-GT plant

Summary of Plant Layout Studies. Two major decisions in the HTGR-GT program will be made in 1979: (1) the power plant rating, and (2) the issue of intercooling versus nonintercooling. As will be mentioned in the following sections, a decision has been made to proceed with a plant embodying two PCLs. The plant layout studies presented in this paper are in support of the overall evaluation that will lead to the selection of a new reference plant concept.

Table 4 Motivating factors for a two-loop commercial plant configuration

1. Efficient PCRV design of small diameter strongly impacts cost.
2. Simplified vessel (tendon layout eased in bottom head).
3. Intercooling can be utilized with no major impact on PCRV size.
4. Non-intercooled efficiency of 40%, and intercooled value of 42% possible.
5. Simplified gas flow paths within PCRV (pressure loss ≯ 12%).
6. Ease of maintenance, since generator does not have to be moved to replace the turbomachine.
7. Spare machine approach by utility group/organization ensures high plant availability.
8. Plant operation on one loop considered possible (impact on availability and heat supply).
9. Flexibility in power range advantage for different utilities.
10. Growth potential possible from conservatively designed power conversion equipment.
11. Main loop cool-down perhaps eased by duplication of turbomachines.
12. Commercial plant can be replicated from the first-of-a-kind plant.
13. No scaling from demo to commercial plant necessary.
14. Reduced development risk and cost.
15. Simplified electrical system since all of the high voltage connections are at one end of the plant.

As shown in Fig. 2, design studies have been performed for a wide range of plant variants. However, the most recent work done (and reported in this paper) has centered on (1) two- and three-loop concepts, and (2) PCL ratings of 400, 500, and 600 MW(e). A summary of the salient features of some of the plant concepts studied is given on Table 3. The main disadvantages of the three-loop plant are (1) inflexibility of power rating (i.e., it is better suited to plants of 1200 MW(e) and higher), (2) not attractive as an intercooled variant (i.e., complex gas flow paths and large PCRV diameter), (3) high capital cost associated with the large number of components, and (4) an operational problem exists in that the generator must be moved before a turbomachine can be replaced.

From Table 3 and the layout concepts presented, it can be observed that the two-loop plant offers a simplified PCRV arrangement and has rating flexibility in the range of 800 to 1200 MW(e). It is also significant that an intercooler can be embodied without a major impact on PCRV diameter. The motivations for utilization of a two-loop plant layout concept are given in Table 4.

Downloaded 01 Jun 2010 to 171.66.16.59. Redistribution subject to ASME license or copyright; see http://www.asme.org/terms/Terms_Use.cfm

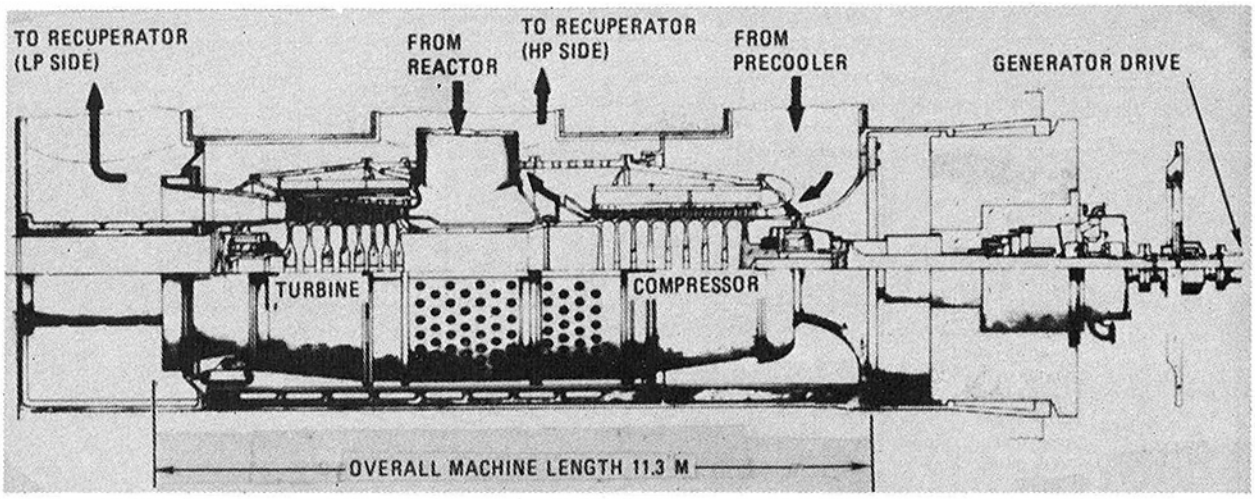

Fig. 14 400-MW(*e*) nonintercooled turbomachine for HTGR-GT plant

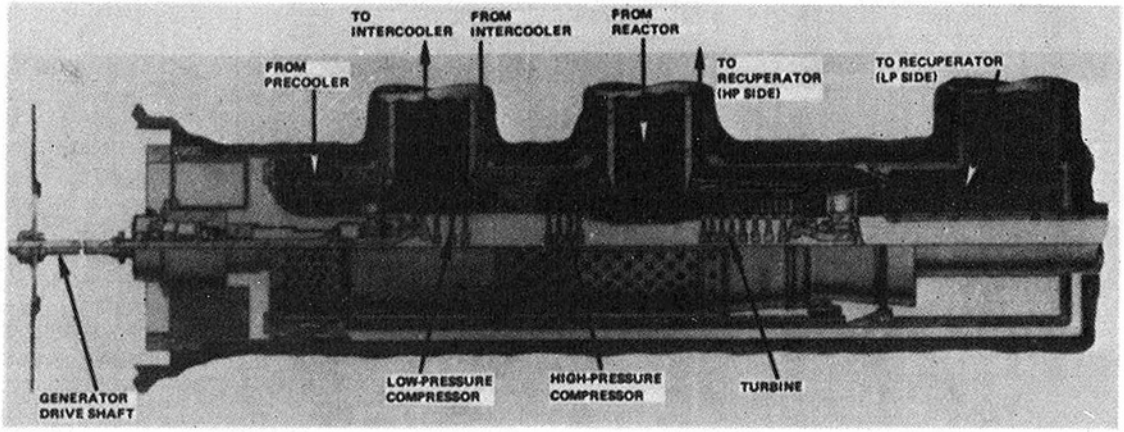

Fig. 15 600-MW(*e*) intercooled turbomachine for HTGR-GT plant

Component Design Considerations

It is not the purpose of this paper to describe in detail the design considerations for the major components of the HTGR-GT plant, since as noted below, these have been reported previously. However, for an integrated plant, the PCL components cannot be treated as isolated units, and indeed, their design and the resolution of the interconnecting gas flow path geometries must be considered during the establishment of the plant primary system configurations. During the aforementioned primary system design studies, extensive layout work was done to identify the most attractive installation and orientation of the major components. The main PCL components which have a strong influence on the primary system design are the turbomachine and the heat exchangers, and brief descriptions of these are given below.

Helium Turbomachine. The most recent turbomachinery design work for the HTGR-GT power plant has been done by the Power Systems Division and Pratt and Whitney Aircraft Division of United Technologies Corporation (UTC). General Electric and Brown Boveri Company were earlier participants in the HTGR-GT program. Since details of the helium turbomachine have been described previously [18–21], only a very brief summary will be given in this paper.

In support of the plant configuration studies, turbomachine conceptual designs were done for machines in the 400, 500, and 600 MW(e) power classes for both intercooled and nonintercooled types. To span the above power range and to illustrate the difference between the machine types, only the 400 MW(e) (nonintercooled) and 600 MW(e) (intercooled) variants will be addressed in this paper. Details of the 400 and 600 MW(e) turbomachines are shown in Figs. 14 and 15, respectively, and the salient features are summarized in Table 5. As will be discussed below, the two machines embody similar features in many areas. The design and performance predictions for these machines reflect the influence of technology from a demonstrated advanced technology industrial gas turbine in the 70 to 100 MW(e) power size (22).

An extremely simple arrangement consisting of a single-shaft direct-drive arrangement was chosen for both machines. The use of a two-bearing rotor, feasibility of which has been confirmed by rotor dynamic analyses to insure adequate critical speed margin, maintained the smallest number of individual parts and tended to minimize the overall cost of the machine, and to ease inspection and maintenance requirements.

Aerothermodynamic analysis showed that for both the 400 and 600 MW(e) machines a single turbine inlet duct (from the reactor) could be utilized, and the pressure losses and flow inlet geometry to the turbine bladed section were satisfactory. In the plant layout studies, it was found that a key element (from the standpoint of effective PCRV volume utilization) is the embodiment of a turbomachine with a single turbine inlet duct. For machine sizes above 700 MW(e), studies have shown the need for two turbine inlet ducts; for a plant embodying two such gas turbines, the gas flow paths are unduly complex, and the PCRV diameter is excessive.

The 400-MW(e) nonintercooled machine (Fig. 14) has 18 compressor stages and eight turbine stages. In the 600-MW(*e*) machine (Fig. 15), intercooling necessitates splitting the compressor into two eight-stage sections, and a high-efficiency nine-stage turbine is utilized. For both machines, the rotors are of welded construction. Welded rotors have a long successful history in Europe for both gas and steam turbines. The stress levels in the turbine blades are commensurate with a life of 280,000 hr (i.e., 40 years at 80 percent capacity factor). For the turbine inlet temperature of 850°C, blade cooling is not necessary, and an existing-nickel-base alloy (IN-100), which has been used extensively in open-cycle industrial gas turbines, was selected for the turbine blading.

Downloaded 01 Jun 2010 to 171.66.16.59. Redistribution subject to ASME license or copyright; see http://www.asme.org/terms/Terms_Use.cfm

Table 5 Details of HTGR-GT plant turbomachine designs

Turbomachine Rating, MW(e)	400	600
Machine type	Non-intercooled	Intercooled
Machine arrangement	Single-shaft	Single-shaft
Frequency, Hz	60	60
No. of turbine inlet ducts	1	1
Turbine inlet temp, °C	850	850
Compressor pressure ratio	2.50	3.0 (1.73/1.73)
No. of compressor stages	18	8 + 8
Max compressor tip diam, m	1.83	2.18
Blade height, mm (min/max)	80.0/125.7	76.2/165.1
Compressor adiabatic efficiency (across blading), %	89.8	90.8 LP/90.2 HP
No. of turbine stages	8	9
Max turbine tip diam, m	2.18	2.40
Blade height, mm (min/max)	125.7/297.2	165.1/393.7
Turbine isentropic effic. (across blading), %	91.8	92.2
Blading life, h	280,000	280,000
Blade cooling	No	No
Turbine blade material	Nickel-base alloy, IN-100	
Generator drive end	Compressor	
Rotor burst shield	Yes, integral part of machine structure	
Thrust bearing position	External to PCRV	
No. of journal bearings	2	2
Journal bearing man access	Yes	Yes
Type of rotor construction	Welded rotor	Welded rotor
Machine casing diam, m	4.0	4.0
Machine length, m	11.3	15.8
Machine weight, kg	276,770	317,600
Design technology base	Large industrial open-cycle gas turbines	

The casing diameter for both machines is 4.0 m, but of course, the higher helium mass flow rate for the 600-MW(e) machine results in an increased annulus flow area and larger blade heights, as shown on Table 5. The overall lengths of the 400-MW(e) (nonintercooled) and 600-MW(e) (intercooled) machines are 11.3 m and 15.8 m, respectively. Since the turbomachine is installed inside the reactor vessel, rotor burst protection is incorporated in the machine design in the form of containment rings around the compressor and turbine rotor bladed sections.

Man-access provisions are provided in the PCRV for inspection and limited maintenance work on the journal bearings, which are of the multiple, tilting pad, oil-lubricated type. The spaces in which the bearings are located are isolated from the main cycle working fluid by shielding (purge gas from the plant helium storage system is used to give an acceptable radiological environment for man-access). The drive to the generator is from the compressor end of the turbomachine, and the thrust bearing is located external to the PCRV to facilitate inspection and maintenance and to limit the number of oil-systems in the primary system to a minimum. Diagnostic condition monitoring, in-situ inspection, and maintenance features are designed into the turbomachine system [23].

For a single-shaft helium turbomachine (with a rotational speed of 3600 rpm) in the power range of 400 to 600 MW(e), the rotating section is compact and is substantially smaller than an equivalent air-breathing machine because of the high degree of pressurization (particularly at the turbine exit) and the high specific power associated with the helium working fluid. The external dimensions of the helium turbomachines discussed in this paper are, in fact, quite similar to those of an existing air-breathing, advanced, open-cycle industrial gas turbine in the 70 to 100 MW(e) range. The fact that the helium turbine (particularly the rotor assembly and casings) is comparable in size with existing machines substantiates the claim that conventional fabrication methods and facilities can be used.

The aforementioned helium turbomachine design activities have been done in support of the HTGR-GT plant for the U.S. market (60 Hz system); however, it should be pointed out that a formidable effort has also been expended in Europe for the HHT plant [10], and details of the turbomachine for this 50-Hz system have been reported in references [24–26].

Heat Exchangers. While details of the heat exchangers have been discussed previously [27], it is meaningful to discuss them briefly in the context of this paper, since they are large components and have a significant influence on the integrated primary system. The combined effects of size constraint (integration in the PCRV side-wall cavities), in-service inspection (ISI), in-situ repair, and maintenance and fabrication considerations have a significant effect on the choice of surface geometry, flow configuration, and mechanical design.

In the conceptual design phase of the HTGR-GT plant, the thermalhydraulic sizing and analysis of the heat exchangers was performed by General Atomic, and the mechanical design work was done by Combustion Engineering. In support of the plant configuration studies, heat exchanger conceptual designs were done for units with PCL ratings of 400, 500, and 600 MW(e) for both intercooled and nonintercooled types. To span the above power range and to illustrate the major differences between the two cycle types only, the exchangers for the 400-MW(e) (nonintercooled) and 600-MW(e) (intercooled) variants are discussed in this paper. The salient features of the recuperators, precoolers, and intercooler are given in Table 6.

The heat exchanger types selected for the HTGR-GT plant conceptual design have a sound technology base, and in this regard can be considered to be conservative. The helium-to-helium recuperator concept (shown on Fig. 16) remains unchanged from that reported

Downloaded 01 Jun 2010 to 171.66.16.59. Redistribution subject to ASME license or copyright; see http://www.asme.org/terms/Terms_Use.cfm

Table 6 Details of HTGR-GT plant heat exchanger designs

PCL Rating, MW(e)	400 MW(e) Non-intercooled		600 MW(e) Intercooled		
Exchanger	Recuperator	Precooler	Recuperator	Precooler	Intercooler
Exchanger configuration	Counterflow	Multipass cross counter-flow	Counterflow	Multipass cross counterflow	
Construction type	Straight tube modular	Helical bundle	Straight tube modular	Helical bundle	
Heat duty/unit, MW(t)	918	581	1253	533	337
LMTD, °C	42.5	30.5	44.3	27.3	19.3
Effectiveness	0.898	0.972	0.898	0.961	0.939
Tubes per exchanger	66,483	827	94,668	1196	1118
Tube o.d., mm	11.1	28.6	11.1	28.6	28.6
Wall thickness, mm	1.1	2.9	0.8	2.9	2.9
Modules per exchanger	83	1	161	1	1
Exchanger diam, m	5.64	4.72	6.8	4.9	4.7
Effective tube length, m	12.2	105	12.8	82.3	76.2
Effective bundle ht, m	12.2	12.5	12.8	13.7	10.97
Exchanger assy. ht, m	20.4	19.8	21.1	21.1	18.3
Exchanger assy. wt, tonnes	726	435	998	490	363
Max metal temp, °C	515	177	465	125	89
Max internal ΔP, MPa	4.62	1.83	5.08	1.3	3.2
Materials	Ferritic 2 1/4 Cr-1 Mo	Low-alloy 1/2 Cr	Ferritic 2 1/4 Cr-1 Mo	Low alloy, 1/2 Cr	
ISI/repair level	Module	Individual tubes	Module	Individual tubes	
Assembly location	Factory/ optional	Factory	Factory/ optional	Factory	
Transportation mode	Barge	Barge	Barge	Barge	
ASME code class	Section VIII	Section VIII	Section VIII	Section VIII	
Design status	Conceptual				
Technology status	State-of-the-art-technology				

previously in reference [28], namely, a straight-tube, counterflow arrangement, with an overall assembly made up from a multiplicity of contiguous hexagonal modules. In the case of the helium-to-water exchangers (precooler and intercooler), an extensive study led to a change in concept from the previous straight-tube, counterflow, modular approach [28], to a multipass cross-counterflow helical bundle configuration as typified in Fig. 17. The helical approach has the advantages of higher water velocity, considerably fewer tubes, larger tube diameters, more straightforward headering, and better ISI accessibility than the straight-tube counterflow variant.

The recuperator, precooler, and intercooler assemblies are well integrated in the PCRV, and the interfaces have received attention during the conceptual design phase to insure the viability of the selected mechanical design approaches. The axial counterflow recuperator (embodying tubes of small diameter) bears a close resemblance to units that have operated trouble-free for over half a million hours in the European fossil-fired CCGT plants. The multipass cross-counterflow helical bundle approach selected for the precooler and intercooler has been used extensively for steam generators in gas-cooled reactors. Thus, in adopting the aforementioned conservative design approach, it can be stated that the exchanger design types selected for the HTGR-GT plant have a proven background in the utility power-generating industry.

Another obvious issue related to the size and weight of the heat exchangers is the technology for handling, transporting, and installing the units in the reactor vessel. It has been shown [27] that the heat exchangers for the HTGR-GT are, in fact, no longer or heavier than units being built for contemporary steam plants, and that existing and proven methods of handling and transportation are indeed applicable.

For a long-term program such as the HTGR-GT, there is an obvious incentive to maintain the competitiveness of the plant by utilizing technology advancements in a prudent manner. Improvements in the heat exchangers will be continually sought, such as the adoption of advanced surface geometries, and the obvious goals that will be addressed in the future include (1) increased reliability/availability, (2) cost reduction, (3) size reduction, and (4) improved ISI capability and maintenance approaches.

The aforementioned heat exchanger design activities have been pursued in support of the HTGR-GT plant for the U.S. market; however, it should be pointed out that a formidable effort has also been expended in Europe for the HHT plant and details of these heat exchangers have been reported in reference [29].

Balance of Plant Design

The main point of this paper has been a discussion of the reactor turbine system (RTS) for differing power plant concepts. In addition to the RTS, which is integrated in the reactor vessel, an important task in the design process is the establishment of the overall plant configuration, and this essentially involves the design of all the balance of plant equipment and buildings. Since this is a comprehensive task and the subject of a forthcoming paper, balance of plant design will only be highlighted in this paper, but the importance of the task should be noted since a significant percentage of the overall plant cost is associated with the balance of plant items. In addition, many of the plant operational requirements, such as service systems, purification trains, refueling schemes, and on-site maintenance facilities, strongly impact the balance of plant features and economics.

Details of the overall plant plot for the three-loop nonintercooled plant have been discussed previously [23], so only the recent work associated with the two-loop variant will be mentioned here. As shown on Fig. 18, a reactor containment building (RCB) encloses the PCRV, and while the configuration illustrated is in a conceptual stage for the 2×600 MW(e) intercooled plant variant, it can be considered representative for the HTGR-GT plant. The secondary containment building and the PCRV incorporate safety features that limit loss of primary coolant and minimize damage in the event of failures in the turbomachine, shaft seals, heat exchangers, generator, or PCRV cavity closures.

A significant change from previous plant conceptual designs in-

Downloaded 01 Jun 2010 to 171.66.16.59. Redistribution subject to ASME license or copyright; see http://www.asme.org/terms/Terms_Use.cfm

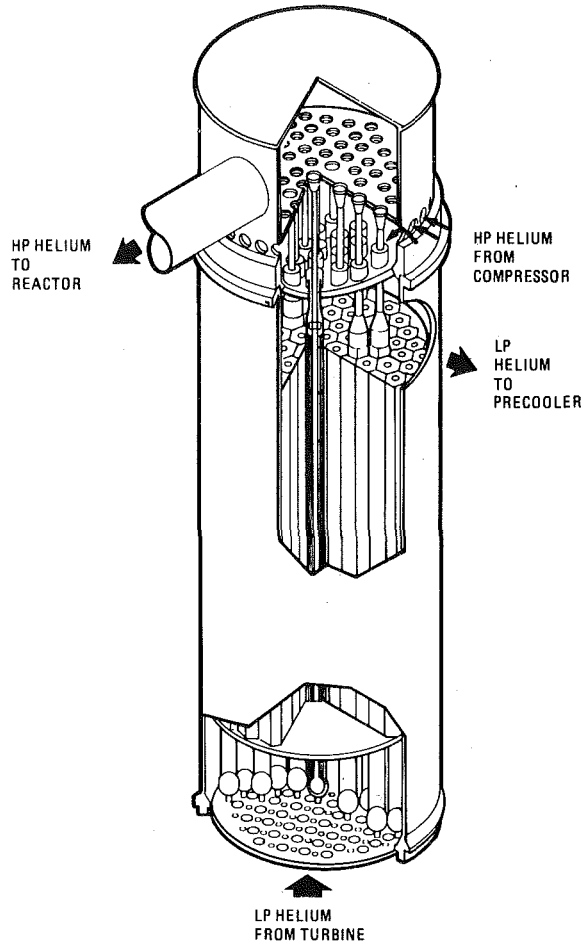

Fig. 16 Straight-tube, modular, counterflow recuperator concept for HTGR plant

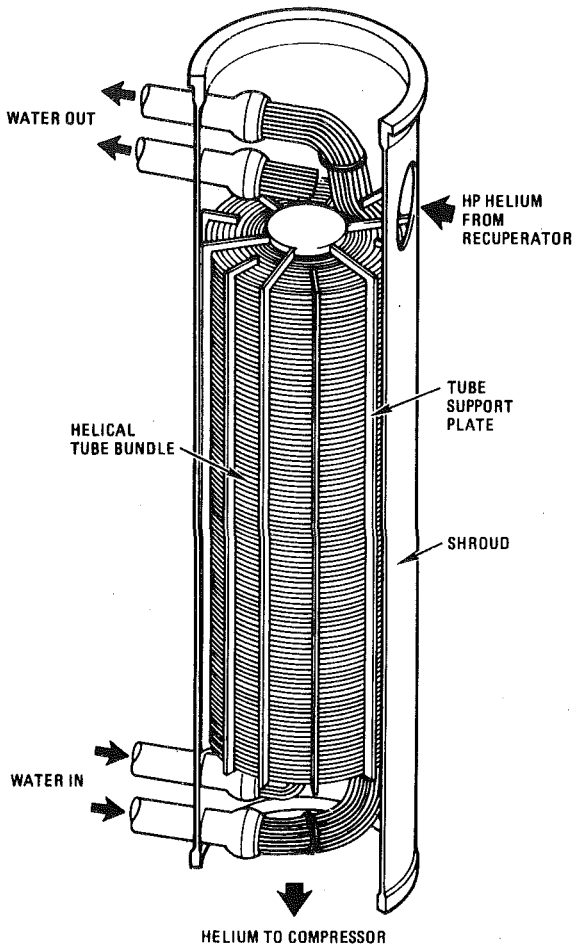

Fig. 17 Helical-bundle, cross-counterflow, helium-to-water heat exchanger concept (precooler and intercooler) for HTGR-GT plant

volves the utilization of all water-cooled generators of the type that have been extensively used in Europe for many years. The former hydrogen-cooled generator involved installation in local generator cells (which increased the complexity and cost of the RCB) to prevent the possibility of a hydrogen explosion within the containment building in the event of a gas leakage from the generator internals. As can be seen from Fig. 18, a simpler concept is now proposed with the generator located within the containment building. This eliminates the concern over a secondary containment rotating seal penetration. A tentative plant arrangement concept for a two-loop plant is shown on Fig. 19. This scheme illustrates the general layout of the various buildings, and indepth studies are currently underway by the architect/engineer to further define the balance of plant facilities to satisfy all of the plant requirements.

Summary

The work reported in this paper is only one part of the widespread international efforts to combine the gas turbine and nuclear energy. The benefits of the HTGR-GT plant are such that the worldwide efforts to bring it into use should increase rapidly. It is projected that with a dedicated effort the demonstration plant could be introduced into commercial utility service in the late 1990s, and the first commercial plant (essentially replicated from the demo plant) could be on-line around the turn of the century.

For the next generation of nuclear power plants, the dominant criteria in all design endeavors is to establish unquestionable safety features. The HTGR with its graphite-moderated core, single-phase gaseous working fluid, and integration of the equipment within a PCRV offers unprecedented safety characteristics. In addition to this vital element, the prospective advantages of the HTGR-GT to utilities include plant simplification, improved economics, and siting flexibility.

The work reported in this paper has outlined design-related studies which are in progress and directed towards the selection of a commercial plant reference design. A companion paper [17] has addressed systems-related studies leading to the selection of optimized parameters for minimum power generating cost. As discussed, a decision has been made to proceed with the design of a two-loop commercial plant configuration. This paper presents design-related studies which are important to deciding on the definition of two vital HTGR-GT features: (1) rating of the PCLs and (2) the choice of intercooled or non-intercooled cycle. These decisions will be made in 1979, and the definition of the reference commercial plant concept will be presented in a future paper.

Acknowledgments

Appreciation is hereby expressed by the authors to the management of General Atomic Company for permission to publish this paper. Work on the HTGR-GT plant has been supported by the U.S. Department of Energy under Contract DE-AT03-76SF70046, and by a dedicated group of electric utility companies. The contribution of Hans Amtmann of General Atomic is gratefully acknowledged. The authors wish to acknowledge work done by United Technologies Corporation, Combustion Engineering, and the European HHT Project.

References

1 Keller, C., and Schmidt, D., "Industrial Closed-Cycle Gas Turbines for Conventional and Nuclear Fuel," ASME Paper No. 67-GT-10, 1967.

2 Bammert, K., "A General Review of Closed-Cycle Gas Turbines Using Fossil, Nuclear, and Solar Energy," *Thiemig Paperback*, Vol. 57, Munich, Sept. 1975.

3 McDonald, C. F., "The Closed-Cycle Gas Turbine—Present and Future Prospectives for Fossil and Nuclear Heat Sources," ASME Paper No. 78-GT-102, 1978.

Downloaded 01 Jun 2010 to 171.66.16.59. Redistribution subject to ASME license or copyright; see http://www.asme.org/terms/Terms_Use.cfm

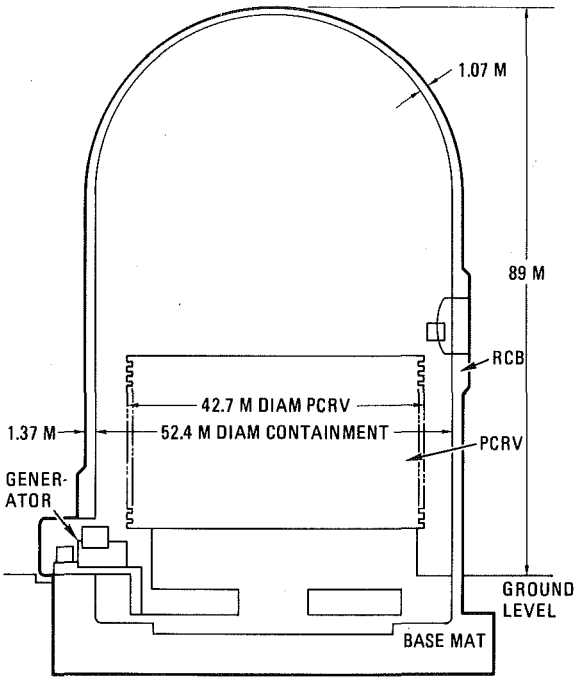

Fig. 18 Elevation view through RCB for two-loop HTGR-GT plant

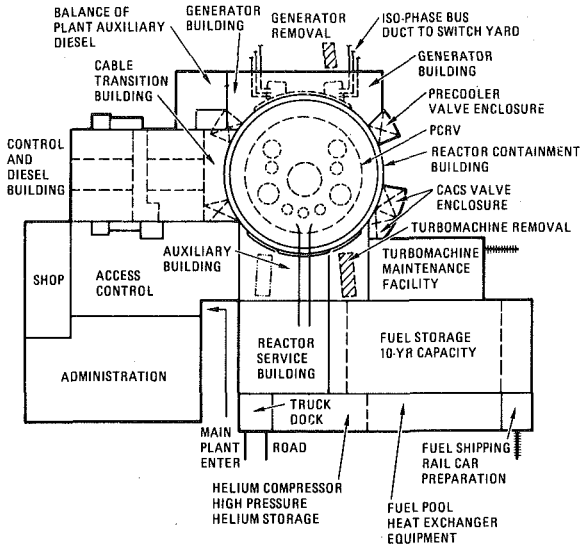

Fig. 19 Tentative overall arrangement for two-loop HTGR-GT plant

4 McDonald, C. F., and Krase, J. M., "Nuclear Gas Turbine Power Plant Activities in the United States," ASME Paper No. 77-JPGC/GT-5, 1977.

5 Goodjohn, A. J., and Law, S. H., "GT-HTGR—A Total Energy Utilization Option," AIAA/IEEE Conference on New Options in Energy Technology, San Francisco, CA, Aug. 2–4, 1977.

6 McDonald, C. F., "The Closed-Cycle Gas Turbine—A Proven Cogeneration Plant Adaptable to Fossil, Nuclear, and Solar Heat Sources," Conference on Energy Conservation, Sponsored by U.S. Department of Energy, Milan, Italy, Mar. 26–29, 1979.

7 Frutschi, H. U., "The Relationship of Power and Heat Production with Closed-Cycle Gas Turbines," ASME Paper No. 79-GT-103, 1979.

8 McDonald, C. F., "Large Closed-Cycle Gas Turbine Plant," Lecture Series on Closed-Cycle Gas Turbines at the Von Karman Institute for Fluid Dynamics, Sponsored by North Atlantic Treaty Organization, Brussels, Belgium, May 9–13, 1977.

9 "Technology Assessment of the Gas Turbine—High-Temperature Gas-Cooled (Helium) Reactor," EPRI NR-805, Project 900, Interim Report, Electric Power Research Institute, June 1978.

10 Arndt, E., et al., "HHT-Demonstration Plant," paper presented at European Nuclear Conference, Hamburg, W. Germany, May 6–11, 1979.

11 McDonald, C. F., et al., "Primary System Design Studies for Advanced Direct-Cycle Nuclear Gas Turbine Plant," ASME Paper No. 77-GT-25, 1977.

12 Keller, C., "Forty Years of Experience on Closed-Cycle Gas Turbines," *Annals of Nuclear Energy,* Vol. 5, No. 8–10, 1978, pp. 405–422.

13 Bammert, K., and Deuster, G., "Layout and Present Status of the Closed-Cycle Helium Turbine Oberhausen," ASME Paper No. 74-GT-132, 1974.

14 Zenker, P., "The Oberhausen 50 MW(e) Helium Turbine Plant," *Combustion,* Vol. 47, No. 10, Oct. 1976, pp. 21–25.

15 Weber, D, "Helium Turbine Explores Future Nuclear Application," *Energy International,* Vol 15, No. 4, Apr. 1978, pp. 47–50.

16 Noack, G., et al., "Significance of the Helium Turbine Plant at Oberhausen (EVO) and of the High Temperature Test Facility at Jülich (HHV) for the Development of the HTGR Direct-Cycle System (HHT)," *Symposium on Gas-Cooled Reactors with Emphasis on Advanced Systems, Jülich, Federal Republic of Germany, Oct. 1975,* Vol. II, IAEA, Vienna, Austria, May 1976, pp. 189–200.

17 Kammerzell, L. L., "HTGR-GT Systems Optimization Studies," 25th ASME International Gas Turbine Conference, New Orleans, Louisiana, Mar. 1980, to be presented.

18 McDonald, C. F., "The Nuclear Closed-Cycle Gas Turbine (GT-HTGR)—A Utility Power Plant for the Year 2000," AIAA Paper 79-0191, 1979.

19 Adams, R. G., and Boenig, F. H., "The Design of the Turbomachinery for the Gas Turbine HTGR Power Plant," ASME Paper No. 77-GT-38, 1977.

20 Adams, R. G., et al., "Bearing Compartment Seal Systems for Turbomachinery in Direct-Cycle HTGR Power Plants," ASME Paper No. 78-GT-38, 1978.

21 McDonald, C. F., and Smith, M. J., "Turbomachinery Design Considerations for the Nuclear HTGR-GT Power Plant," ASME JOURNAL OF ENGINEERING FOR POWER, This issue, pp. 65–77.

22 de Biasi, D., FT-50 Design Shortcut to 1980 Technology," *Gas Turbine World,* Nov. 1975, pp. 9–15.

23 McDonald, C. F., and Paget, J. A., "Maintenance Considerations in the Design of the Direct-Cycle Nuclear Gas Turbine Power Plant," ASME Paper No. 79-GT-116, 1979.

24 Haselbacher, H., and Eiermann, A., "Development of Helium Gas Turbine Systems in the Nuclear Field," ASME Paper No. 74-GT-123, 1974.

25 Haselbacher, H., et al., "HHT Helium Turbine and the HHV Plant," Nuclex 78, Basel, Switzerland, Oct. 3–7, 1978, Paper No. A4/21.

26 Haselbacher, H., "Closed-Cycle Gas Turbines for HTR Nuclear Power Plants and LNG Regasification Plants," *Brown Boveri Revue,* Vol. 66, No. 2, Feb. 1979, pp. 120–129.

27 Van Hagan, T. H., McDonald, C. F., and Creek, R. B., "Heat Exchanger Designs for Gas Turbine HTGR Power Plant," ASME Paper No. 79-WA/GT-2, 1979.

28 McDonald, C. F., Van Hagan, T. H., and Vepa, K., "Heat Exchanger Design Considerations for Gas Turbine HTGR Power Plant," ASME JOURNAL OF ENGINEERING FOR POWER, Vol. 99, Apr. 1977, pp. 237–245.

29 Naegelin, R., et al., "Heat Exchangers for HHT Plants, Nuclex 78, Basel, Switzerland, Oct. 3–7, 1978, Paper No. A4/16.

Downloaded 01 Jun 2010 to 171.66.16.59. Redistribution subject to ASME license or copyright; see http://www.asme.org/terms/Terms_Use.cfm

Demonstration of a Unified Approach to the Balancing of Flexible Rotors

M. S. Darlow
Consultant,
Assoc. Mem. ASME

A. J. Smalley
Manager,
Mem. ASME
Machinery Dynamics Section,
Mechanical Technology, Inc.,
Latham, NY 12110

A. G. Parkinson
Lecturer,
Department of Mechanical Engineering,
University College, London,
London, England

A flexible rotor balancing procedure, which incorporates the advantages and eliminates the disadvantages of the modal and influence coefficient procedures, has been developed and implemented. This new procedure, referred to as the Unified Balancing Approach, has been demonstrated on a supercritical power transmission shaft test rig. The test rig was successfully balanced through four flexural critical speeds with a substantial reduction in effort as compared with the effort required in modal and influence coefficient balancing procedures. A brief discussion of the Unified Balancing Approach and its relationship to the modal and influence coefficient methods is presented. A series of tests which were performed to evaluate the effectiveness of various balancing techniques are described. The results of the Unified Balancing Approach tests are presented and discussed. These results confirm the superiority of this balancing procedure for the supercritical shaft test rig in particular and for multiple-mode balancing in general.

1 Introduction

Rotor balancing procedures are classified according to the type of rotor for which they are designed, rigid or flexible. When rigid rotors are balanced, the shape of the centroidal axis as a function of speed does not change. For flexible rotors, the shape of the centroidal axis, and thus the unbalance distribution, does change with speed. In general, rigid rotor balancing procedures and tools are not applicable to the balancing of flexible rotors. The procedures for balancing rigid rotors are well established and accepted. However, the same is not true for the current flexible rotor balancing procedures. These procedures can be classified into two groups, modal balancing and influence coefficient balancing. In the past, these two general balancing methods have competed, each with the inherent advantages and disadvantages of the other. In both cases, the disadvantages have been significant enough to prevent widespread acceptance of the balancing procedure. Consequently, most flexible rotor balancing is currently done by trial and error procedures, which are inefficient.

A unified approach to the balancing of flexible rotors [1] which bridges the gap between modal and influence coefficient balancing is described. This new balancing method (hereafter referred to as the Unified Balancing Approach) combines the advantages of modal and influence coefficient balancing and eliminates the disadvantages of the two current procedures. At the same time, the Unified Balancing Approach provides a straightforward, practical approach to flexible rotor balancing, is well-suited to both production and field balancing. A glossary of terms is provided in an appendix as an aid to the reader.

A series of tests have been conducted to compare influence coefficient balancing, modal balancing and the Unified Balancing Approach. The tests were conducted using a supercritical power transmission shaft test rig. In all cases, the test rig was successfully balanced through four flexural critical speeds. However, the Unified Balancing Approach resulted in the fastest, easiest and most precise balancing of the three methods. Although the results of a single test cannot be conclusive, the indication is that the Unified Balancing Approach has tremendous potential, and further tests are certainly warranted. These tests were more searching than some because the test shaft was not grossly unbalanced at the start of the tests. After all, most methods will produce a large improvement when a rotor has a large initial unbalance!

2 Review of Modal and Influence Coefficient Balancing

Briefly, the influence coefficient method [2] seeks those correction masses in a predetermined set of planes which will minimize measured vibration (readings) at a series of sensors and speeds as predicted by influence coefficients, relating vibration reading to mass additions. The influence coefficients are normally determined by a series of trial mass tests.

The modal method [3] seeks to balance the rotor, one mode at a time, with a set of masses specifically selected to leave previously balanced lower modes undisturbed. Sensitivity to this combination of masses as a set is determined empirically by a series of trial mass tests.

Specific advantages and disadvantages, identified with each method, take on different relative importance according to the requirements of a particular balancing process. The principal advantages and disadvantages of modal balancing are listed in Table 1.

The only trial mass runs that are required at the highest balancing speed involve the combined weight sets for modal response. Individual trial mass runs are not required. Since, by design, the lower modes are not affected by a modal trial mass set, this mass set can be made large enough to assure good sensitivity at the mode being balanced. Elim-

Contributed by the Gas Turbine Division and presented at the Gas Turbine Conference and Products Show, New Orleans, La., March 10–13, 1980, of THE AMERICAN SOCIETY OF MECHANICAL ENGINEERS. Manuscript received at ASME headquarters December 17, 1979. Paper No. 80-GT-87.

Copyright © 1981 by ASME

Downloaded 01 Jun 2010 to 171.66.16.59. Redistribution subject to ASME license or copyright; see http://www.asme.org/terms/Terms_Use.cfm

inating the danger of upsetting the condition of previously balanced modes generally simplifies the balancing of higher modes. Only a basic understanding of the dynamics of the rotor system is needed to select locations for vibration sensors and balancing planes. It is not necessary to have prior knowledge of the system. Modal balancing does, of course, assume that the response of the rotor system is linear and that the vibration sensors are sufficiently accurate.

Modal balancing sometimes requires analytical procedures for selecting the sets of trial masses used for correcting specific modes [4]. Not only does the requirement for this analysis complicate the balancing procedure but any inaccuracies in this analytical model (which are inherent in any analytical representation of real components) reduce the effectiveness of the balancing procedure. Analytical procedures are not necessary, however, and several proponents of modal balancing employ empirical procedures to determine the modal trial mass sets. (See, for example, reference [3].) This empirical procedure has disadvantages, also. It requires substantial operator insight into the modal character of the whirl of a rotor due to unbalance, and this requirement inhibits the efficiency of production balancing techniques. Balancing a rotor to eliminate vibration as measured by a single sensor may not result in minimum vibration for the rotor as a whole, particularly when mode shapes are distorted or non-planar. Difficulty may also occur as a result of vibration from other modes not previously balanced. Methods have been developed to correct this problem (see, for example, reference [5]), but once again operator insight is required.

The principal advantages and disadvantages of influence coefficient balancing are listed in Table 2. Influence coefficient balancing is an entirely empirical procedure, its effectiveness limited only by the linearity of the rotor system and the resolution of the vibration sensors. Only a minimum knowledge of the rotor system is required for specifying the locations of the vibration sensors and balancing planes (for the application of correction masses).

Influence coefficient balancing provides for the simultaneous balancing of more than one mode, provided that the necessary sensitivity information (influence coefficients) is available. This feature can reduce the required number of balancing runs but does require measurement of the rotor vibration at speeds near the relevant critical speeds. It may not be safe to run through one of these critical speeds to make measurements at higher speeds. The empirical nature of this procedure and the modest skills required of the operator, along with the required calculation form, make this procedure ideally suited for computerizing and automating [6]. Least-squares minimization of vibration data allows for balancing criteria, based on reducing the vibration for a number of points in the rotor system and for any number of modes [7]. This feature of influence coefficient balancing can often be used to compensate for distorted or non-planar mode shapes and the effect of other unbalanced modes. Additional data manipulation techniques, designed to compensate for measurement errors inherent in any realistic application of rotor balancing [8], are available.

Since individual trial mass runs must be made at the highest balancing speed (as at all balancing speeds) when using influence coefficient balancing, the total number of runs required for this speed is substantially more than for modal balancing. In addition, the sizes of the individual trial masses used at the higher balancing speeds may be limited by the response of lightly damped lower modes to these trial masses. The initial unbalance present for the higher modes may make it impossible to acquire sensitivity data, using a restricted trial mass, at a speed close enough to a higher critical speed to produce a significant effect from this trial mass. That is, if the largest possible trial mass is small compared to the initial unbalance at the higher mode, the resolution of the sensitivity data acquired for this trial mass may be substantially reduced.

When a particular mode is balanced after a number of other modes have been balanced, a large quantity of data may be required. This requirement can ultimately affect the accuracy and convenience of the balancing procedure.

The inadvertent use of nonindependent balance planes can result in singular, or nearly singular, influence coefficient matrices. In the case of a singular matrix, the operator is notified and instructed to change the balancing configuration. Because of the noise in the vibration data signals and the effect of other unbalanced modes, it is virtually impossible for the influence coefficient matrix to be exactly singular. However, this matrix can be nearly singular (i.e., can have a very small determinant). This near singularity results in the calculation of large correction masses. These essentially cancel each other in their effect on the mode being balanced.

Due to their inherent disadvantages, neither modal nor influence coefficient balancing has gained widespread acceptance. Consequently, most practical flexible rotor balancing uses one of a number of trial and error procedures which are generally inefficient and often ineffective.

Table 1 Advantages and Disadvantages of Modal Balancing

Advantages	Disadvantages
• Minimizes number of runs at highest balancing speed	• Is not valid for systems with substantial damping
• Retains good sensitivity at highest balancing speed	• Requires a high degree of operator insight
• Leaves lower modes unaffected	• Usually considers vibration at only one or two sensors
• Can be entirely empirical	• Is not easily automated

Table 2 Advantages and Disadvantages of Influence Coefficient Balancing

Advantages	Disadvantages
• Is entirely empirical	• May require a large number of runs at highest balancing speed
• Balances two or more modes simultaneously	• May not provide good sensitivity at higher modes
• Is readily computerized and automated	• Requires data for previously balanced modes
• Provides least-squares minimization of data from multiple sensors	• Use of non-independent balance planes may result in impractical correction masses
• Provides compensation for measurement errors	
• Requires minimal operator insight	

3 Unified Balancing Approach

The Unified Balancing Approach (UBA) is intended to incorporate the advantages of both the influence coefficient and modal balancing methods, while eliminating the disadvantages of both methods. That is, the Unified Balancing Approach uses a modal method of applying correction masses in modal sets using data derived in an empirical manner and requiring a minimum of prior knowledge of the dynamics of the rotor. Essentially, the technique involves the calculation of modal trial mass sets based on the computerized influence coefficient procedure of taking trial mass data, as outlined in reference [9]. Generally, these modal trial mass sets are determined in such a way as to affect the mode of interest while not affecting the lower modes that have already been balanced. However, if appropriate data are available from previous tests or from numerical predictions, a modal trial mass set can be constructed that will have no effect on any general set of modes (including modes above and below the mode being excited). In general, the number of planes required for the modal trial mass set is one more than the number of modes which must not be affected.

As a result, the Unified Balancing Approach is not restricted to planar modes; it requires a minimum number of high speed runs; it permits good sensitivity of trial mass data at all speeds; and it is ideally suited to automated production balancing.

4 Test Program

A series of tests was conducted to compare the three balancing methods discussed above. Influence coefficient balancing was performed first. The second series of tests used an enhanced modal bal-

Downloaded 01 Jun 2010 to 171.66.16.59. Redistribution subject to ASME license or copyright; see http://www.asme.org/terms/Terms_Use.cfm

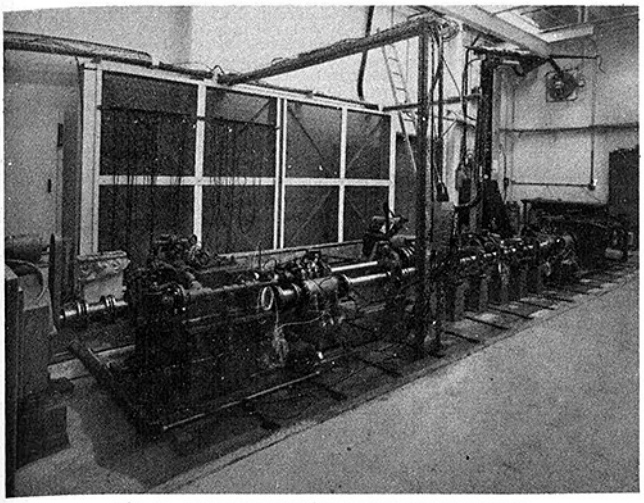

Fig. 1 Photograph of supercritical shaft test rig

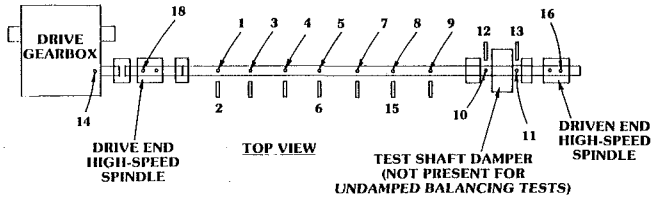

Fig. 2 Sketch showing displacement probe locations as referred to by probe numbers

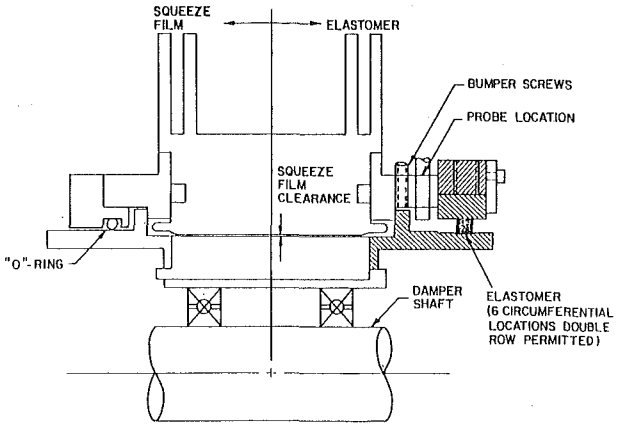

Fig. 3 Side by side sketch of squeeze film and elastometer dampers designed to suppress vibrations in a supercritical power transmission shaft

ancing procedure. These enhancements included some of the data manipulation and least-squares minimization tools generally associated with influence coefficient balancing. This first step in the development of the Unified Balancing Approach, culminated in the verification of a fully developed UBA procedure and computer program in the third set of tests. Details of the test rig and the test results follow.

Test Rig Description. The balancing tests were conducted using a test rig model of an advanced helicopter power transmission shaft (Fig. 1). The principal components of the test rig are a long, flexible shaft with an unsupported span (about 3.7 meters or 12 ft) and a short stub shaft (0.5 m), supported by a damper. The stub shaft is attached to the main shaft at the opposite end from which the main shaft is driven. During previous tests the damper was needed to control inherently unstable, subsynchronous vibrations which occurred at speeds slightly above the first critical speed. The addition of damping also makes balancing easier by broadening the resonant peaks and reducing the response to a set level of unbalance.

The main shaft was 3.7 m (12 ft) long with an outside diameter of 7.62 cm (3 in.), and a wall thickness of 3.175 mm (0.125 in.). The shaft had seven balancing rings adjacent to the displacement probes shown in Fig. 2. The probes were numbered as in the figure and the balancing planes (rings) were numbered consecutively from one to seven beginning at the drive end of the shaft. The shaft is attached to the driving and damper shafts by flexible disk couplings.

Two damper types were used at different stages of the test program. A squeeze-film damper was used during the influence coefficient and modal balancing tests; an elastomer damper was used during the UBA tests. A split sketch showing the two damper designs is presented in Fig. 3. The response of the system with the elastomer damper did not differ from that with the squeeze-film damper except for a slight change in the critical speeds. The shapes of the resonant peaks and the sensitivity of the test rig to unbalance was not noticeably affected by the change in damper configuration. Thus, the type of damper is not a significant factor in the comparisons of balancing test results. Additional details of the design and analysis of the test rig, as well as a more complete description of the hardware, can be found in references [1] and [10].

Influence Coefficient Balancing Tests. The first set of balancing tests involved the use of an influence coefficient balancing procedure. An on-line computer program was used to handle data acquisition and balancing calculations [11]. The balancing calculation portion of the program was based on the work of Lund [8].

This series of tests is described in detail in reference [1]. Briefly, the test shaft was balanced for the first and third critical speeds with no difficulty. However, the first attempt at balancing for the fourth critical speed resulted in substantial degradation of the balance condition for the first and third critical speeds. After rebalancing at the first and third critical speeds, the test shaft was successfully balanced through the fourth critical speed to over 10,000 rpm. A summary of the balancing runs is presented in Table 3, and a plot of the test rig response is presented in Fig. 4.

Table 3 Balancing Masses and Vibration Data for Influence Coefficient Balancing Tests

		Initial Vibration			Correction Masses						Subsequent Vibration		
					Plane 2		Plane 4		Plane 6				
Run No.	Mode No.	Data Speed (rpm)	Amplitude [mm(mils)-P-P]	Angle (deg)	Mass (grams)	Angle (deg)	Mass (grams)	Angle (deg)	Mass (grams)	Angle (deg)	Amplitude [mm(mils)-P-P]	Angle (deg)	Probe No.
1	1	901	2.15(84.6)	−169	–	–	5.787	−63.2	–	–	1.33(52.3)	175	5
2	1	901	1.33(52.3)	175	–	–	4.555	−79.9	–	–	0.33(13.5)	132	5
3	1	901	0.34(13.5)	152	–	–	1.070	−120.0	–	–	0.14(5.7)	73	5
4	3	3200	0.22(8.5)	−151	1.632	−82.3	1.571	102.7	0.627	−113.2	0.07(2.7)	−148	3
5	4	6800	1.34(52.9)	−58	4.45	−66.1	6.04	119.4	3.77	−49.7	0.27(10.7)*	−32*	5
6	3	3200	0.16(6.2)	−33	0.273	90.0	0.26	0.0	1.27	−127.9	0.03(1.3)	140	3
7	3	3200	0.03(1.3)	140	0.45	−75.7	0.63	133.0	0.65	−54.6	~0.01†	†	3
8	4	6800	0.27(10.7)	−32	1.30	−39.5	1.16	132.3	0.44	5.5	0.05(1.9)	17	5
9	4	6800	0.13(5.1)	149	0.31	60.0	1.02	129.9	0.26	38.6	0.05(2.0)	151	3
10	4	6800	0.05(2.0)	151	0.35	150.0	0.17	105.0	0.14	150.0	~0.03†	†	3
11	3	3200	0.11(4.2)	−166	0.74	131.9	0.48	−6.7	0.38	−150.9	~0.04†	†	8

* These data were taken after run 7, the first time that 6800 rpm could be reached again.
† Exact data not available.

Downloaded 01 Jun 2010 to 171.66.16.59. Redistribution subject to ASME license or copyright; see http://www.asme.org/terms/Terms_Use.cfm

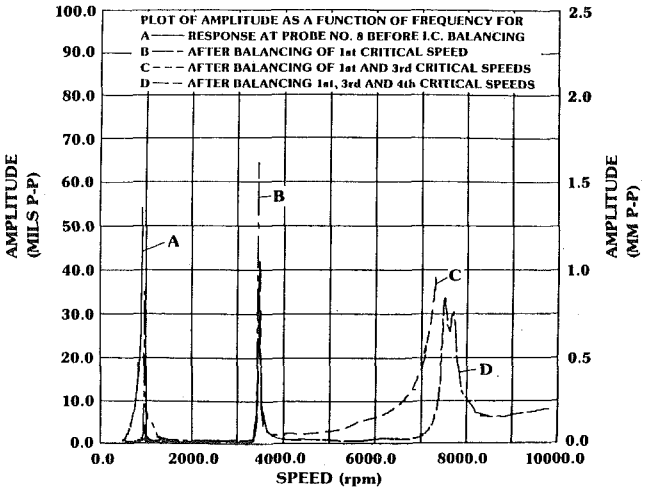

Fig. 4 Response at probe No. 8 during influence coefficient balancing

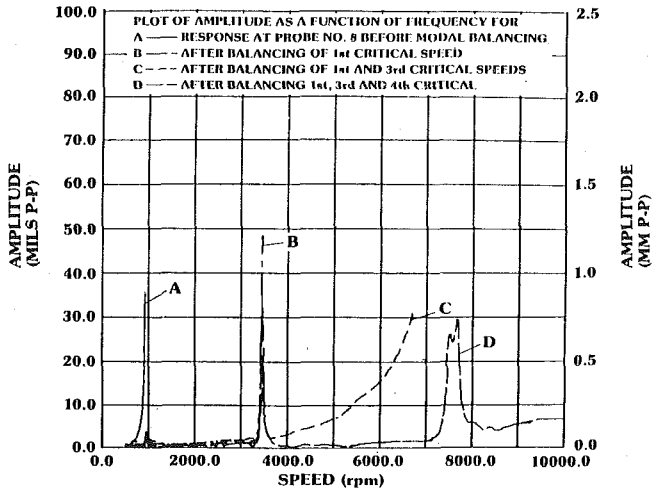

Fig. 5 Response at probe No. 8 during enhanced modal balancing

Table 4 Balancing Masses and Vibration Data for Enhanced Modal Balancing Tests

		Initial Vibration			Correction Masses						Subsequent Vibration		
					Plane 2		Plane 4		Plane 6				
Run No.	Mode No.	Data Speed (rpm)	Amplitude [mm(mils)-P-P]	Angle (deg)	Mass (grams)	Angle (deg)	Mass (grams)	Angle (deg)	Mass (grams)	Angle (deg)	Amplitude [mm(mils)-P-P]	Angle (deg)	Probe No.
1	1	901	0.89(35.1)	165	–	–	3.51	−97.0	–	–	0.03(1.0)	22	5
2	2	3200	1.17(46.1)	−16	5.52	160.7	–	–	5.52	−19.3	0.17(6.5)	121	3
3	2	3200	0.17(6.5)	121	0.32	−59.7	–	–	0.32	120.3	0.09(3.5)	125	3
4	3	6400	1.20(47.4)	−53	8.50	−57.5	11.89	122.5	8.50	−57.5	0.07(2.9)	76	5
5	1	901	0.21(8.1)	63	–	–	0.80	160.9	–	–	† ~0.6	†	5

† Exact data not available.

Enhanced Modal Balancing Tests. An enhanced modal balancing procedure was used for the second set of tests. The basic procedure is based on the work of Bishop and Parkinson [3]. The on-line computer program described in the previous section was also used for data acquisition and some of the balancing calculations for these tests. This program enhanced the standard modal balancing procedure. In particular, extra trial mass runs compensated for measurement errors, and a least-squares solution improved the correction mass calculations for multiple sensor locations. These features are not generally associated with modal balancing.

This series of tests is also described in detail in reference [1]. The test shaft was successfully balanced through the first, third and fourth critical speeds. The correction for the fourth critical speed did not have a substantially detrimental effect on the response at either the first or third critical speed. The mode shapes were observed to be nearly, but not exactly, planar. The test rig was again run to over 10,000 rpm. A summary of the balancing runs is presented in Table 4 and a plot of the test rig response is presented in Fig. 5.

Unified Balancing Approach Tests. The third set of balancing tests verified the Unified Balancing Approach (UBA). These tests used an on-line computer program similar to that used for the first two sets of balancing tests. However, the software was reconfigured for the procedure and the computations of the UBA [12]. Details of the theory and procedure for the UBA are presented in reference [9]. In general, these tests were successful, and the superiority of the UBA (at least for this test rig) was evident. Details of these tests follow.

The initial condition of the rotor was such that the first critical speed could not be negotiated. (The test rig could not be operated safely above 900 rpm.) The initial condition was comparable to the unbalance condition that existed prior to each of the earlier test programs. Since a large correction mass was anticipated for the first critical speed, the correction was spread to three balance planes (2, 4 and 6) by installing three trial masses simultaneously. (Note: the procedure for balancing the first mode is essentially identical for the three balancing methods.)

Uncorrected rotor and modal trial mass (equal masses in planes 2, 4 and 6) data were taken for the first mode at 890 rpm. A correction mass of about 2.3 grams at about 330 deg in each of planes 2, 4, and 6 was calculated. These masses were fabricated and installed.

The test rig was run and check balance data were taken at 893 rpm (the closest steady speed to 890 rpm). The net synchronous vibration of the rotor was reduced by more than 40 percent, but the first critical speed was not yet negotiable. A trim correction of about 1.3 g at about 270 deg in each of the planes 2, 4 and 6 was calculated. These correction masses were fabricated and installed. The response of the rotor at the first critical speed was reduced tremendously and the first critical speed was negotiated easily. Check balance data which indicated the presence of measurable residual vibration were then taken. Based on these data, a set of trim corrections of about 0.6 g at 165 deg in each of planes 2, 4 and 6 was calculated. These correction masses were also fabricated and installed.

With the third set of correction masses installed, the test rig was run and check balance data were taken at 889 rpm. These data indicated a substantial improvement (better than a 95 percent reduction of the synchronous vibration as compared to the unbalanced condition). The vibration at the first critical speed was well controlled and the test rig was capable of safe operation up to about 7800 rpm.

Clearly, the second critical speed (about 2500 rpm), while no longer critically damped, was heavily damped and nearly unresponsive to unbalance. The third critical speed, on the other hand, although fairly heavily damped, did evidence some response to unbalance. Thus, the balancing procedure was continued with the third critical speed (treated as the second mode). Again, the on-line computer program was used to take data and perform the Unified Balancing Approach calculations. During the individual trial mass portion of the balancing procedure, planes 2 and 4 were mistakenly used, instead of planes 2 and 6 as originally intended. Thus, the modal trial mass set that was calculated by the programs was not longitudinally symmetric, as it was expected to be. That is, it was anticipated that the modal trial mass set for planes 2 and 6 would be composed of a mass in plane 2 approximately equal in magnitude and opposite in direction to that in plan 6. However, the use of planes 2 and 4 resulted in a modal trial

Downloaded 01 Jun 2010 to 171.66.16.59. Redistribution subject to ASME license or copyright; see http://www.asme.org/terms/Terms_Use.cfm

mass set composed of a mass in plane 2 approximately 50 percent larger in magnitude than that in plane 4, with the angle of the two masses differing by about 170 deg. Clearly, the combination of planes 2 and 4 was not the optimum plane combination to be used for balancing the second mode (third critical speed). However, it was anticipated that the use of such non-ideal planes might provide an interesting test of the Unified Balancing Approach. Consequently, the modal trial mass set composed of planes 2 and 4 was used for balancing the second mode (third critical speed). This test was very successful, as the modal correction mass set that was calculated and installed resulted in a substantial improvement of the response at the third critical speed (better than a 70 percent reduction) while having virtually no effect on the response at the first critical speed. A trim correction was calculated but it was not installed because it was quite small and the response at the third critical speed was already very well controlled.

The test rig was not run again until the following day. Without adding or removing any trial or correction masses, the test rig was run up to a speed of about 7800 rpm. Although the synchronous response at the second and third critical speeds was virtually unchanged from the previous run, the response at the first critical speed was much worse. Apparently something in the shaft or test rig had changed spontaneously to alter the amount or distribution of unbalance or the amount of damping. It is possible that the change in the test rig response was due to a change in the shape or support (that is, a shift) of the test shaft or a set in the elastomer damper due to the test shaft weight. In any case, the balancing procedure was continued with a trim balance at the first critical speed.

The computer program was again used to apply the Unified Balancing Approach. This time a data speed of 911 rpm was used for balancing the first mode. Since this speed is closer to the first critical speed than the balancing speed of 890 rpm used during earlier runs, more sensitive balancing data could be acquired. A balancing run for the first critical speed was conducted as described above for a change in the balancing speed. Also, the trial mass (and subsequently the correction mass) was composed of just a single mass in plane 4 rather than distributed between planes 2, 4 and 6. The uncorrected rotor data taken during this balancing run indicated that the synchronous response of the test rig near the first critical speed was more than double that at the end of the previous run. For the first mode, a correction mass of about 1.7 g at about 44 deg in plane 4 was calculated and installed. The improvement in the response at the first critical speed was dramatic. A set of check balance data for the first mode was taken and a reduction in synchronous response as measured by the various probes of between 75 and 93 percent was indicated. This correction mass had virtually no effect on the response at the third critical speed (second mode). This absence of effect was not surprising in light of that fact that the second mode had a node very near to the location of plane 4.

It was not necessary at this point to do any more balancing at any of the first three critical speeds. Before continuing balancing with the fourth critical speed (treated as the third mode) several test runs were conducted and the synchronous response of the test rig was observed, particularly around the first critical speed. The response was repeatable except around the first critical speed where some substantial variations in response were observed. These variations were small (within 25 percent of the "balanced" response). However, at one point the rotor data at the first critical speed increased by more than a factor of two, only to return to its "balanced" response on the following run. There appeared to be a shift in the test shaft followed by a shift back. After this run the test rig response became more repeatable.

Uncorrected rotor data were taken for the first three modes (first, third and fourth critical speeds), followed by a series of individual trial mass runs in planes 2, 4 and 6. Data for these trial mass runs were taken in the vicinity of the first and third critical speeds to permit the calculation of a modal trial mass set for the third mode (fourth critical speed). The modal trial mass set calculated for the third mode consisted of a mass of 1.0 g at 0 deg in plane 2 (reference plane), a mass of about 1.4 g at about 191 deg in plane 4, and a mass of about 1.16 g at about 3.6 deg in plane 6. Note: this modal trial mass set is almost but not quite planar. A balancing run was conducted for the third mode (fourth critical speed) using this modal trial mass set. The modal trial mass set had no noticeable effect on the response at any of the first three critical speeds (neglecting the run-to-run variations at the first critical speed). A modal correction mass set was calculated for the third mode. This set consisted of a mass of about 1.3 g at 30 deg in plane 2, 1.8 g at 221 deg in plane 4, and 1.5 g at 34 deg in plane 6. These masses were fabricated and installed. When the test rig was run, a remarkable improvement was witnessed at the fourth critical speed. The fourth critical speed was negotiated easily; there was no noticeable effect on the response at either the second or third critical speed, and any change in the response at the first critical speed could easily be attributed to run-to-run variation in that response. (The observation of the operators was that the response at the first critical speed after this balancing run was not noticeably different from the response immediately prior to installing the correction masses). A set of check balance data taken at the balancing speed for the fourth critical speed (7620 rpm) indicated a reduction in synchronous rotor response of better than 90 percent. A trim balance mass set was calculated, but the masses were impractically small (0.1 g), and the rotor response was so good that the trim was not installed. This was clearly the best balanced condition that had ever been achieved with this test rig. Recalling that at least two days and six balance runs were required to balance just the fourth critical speed during the initial influence coefficient balancing procedure, the one run balance accomplished using the Unified Balancing Approach impressively demonstrated the benefits in balancing efficiency to be gained from the UBA.

The modal mass set ratios are listed in Table 5 and are illustrated schematically in Figs. 6 and 7. The axial distribution of the trial masses is shown in Fig. 6; the angular distribution is shown in Fig. 7. Note that the sets are almost but not quite planar. A tabulation of the correction masses that were added and the resultant change in vibration at key speeds during this series of tests is presented in Table 6. The sequence of balancing operations is illustrated in Fig. 8 by a series of vector plots, pairs of which show the correction mass added in the reference plane for each mode and the resulting change in vibration for the corresponding mode. A set of typical rotor response plots is presented in Fig. 9.

5 Discussion of Results

The results of the three test programs are compared in Table 7. Since the three procedures were essentially the same for balancing the first mode (first critical speed), it is not surprising that the corresponding results were very similar. However, the results for balancing of the second and third modes (third and fourth critical speeds) indicate that the Unified Balancing Approach is superior to the other two methods in terms of both efficiency and effectiveness.

Specifically, the UBA required many fewer total runs and highest-speed runs than did influence coefficient balancing. Also, UBA did not require any rebalancing at the lower critical speeds and obtained good sensitivity near the fourth critical speed with no difficulty, as did influence coefficient balancing. In addition, the final balance condition obtained using the UBA was substantially better than that obtained using influence coefficient balancing.

While the results obtained using the Unified Balancing Approach were superior to those obtained using the enhanced modal procedure, the difference was not as dramatic as the comparison with influence coefficient balancing. However, this does not indicate that modal balancing is superior to influence coefficient balancing, since the

Table 5 Modal Mass Set Ratios

Mode No.	Plane 2 mass (grams)	Plane 2 angle (deg)	Plane 4 mass (grams)	Plane 4 angle (deg)	Plane 6 mass (grams)	Plane 6 angle (deg)
1	—	—	1.0*	0	—	—
2	1.0	0	0.666	−170.6	—	—
3	1.0	0	1.393	−169.4	1.165	3.6

* The plane with the unit mass is the reference plane.

Downloaded 01 Jun 2010 to 171.66.16.59. Redistribution subject to ASME license or copyright; see http://www.asme.org/terms/Terms_Use.cfm

Table 6 Balancing Masses and Vibration Data for Unified Balancing Approach Tests

Fig. 8, ref.	Mode No.	Initial Vibration: Data Speed (rpm)	Initial Vibration: Amplitude [mm(mils) P-P]	Initial Vibration: Angle (deg)	Correction Masses: Plane 2 Mass (grams)	Plane 2 Angle (deg)	Plane 4 Mass (grams)	Plane 4 Angle (deg)	Plane 6 Mass (grams)	Plane 6 Angle (deg)	Subsequent Vibration: Amplitude [mm(mils) P-P]	Subsequent Vibration: Angle (deg)	Subsequent Vibration: Probe No.
(a)	1	890	1.88(74.19)	299.3	–	–	2.305*	−32.6	–	–	1.10(43.40)	−44.2	5
(b)	1	890	1.10(43.40)	−44.2	–	–	1.344*	−90.0	–	–	0.45(17.67)	−141.2	5
(c)	1	890	0.45(17.67)	−151.2	–	–	0.591*	165	–	–	0.06(2.30)	24.8	5
(d)	2	3820	0.32(12.50)	−149	1.263*	177.6	0.841	6.9	–	–	0.10(4.08)	−116.2	3
(e)	1	911	1.11(43.83)	60.6	–	–	1.692*	43.5	–	–	0.07(2.91)	171.3	5
(f)	3	7620	0.90(35.34)	−53.3	1.283*	30	1.787	−139	1.495	34	0.07(2.94)	106.6	5

* Denotes reference plane.

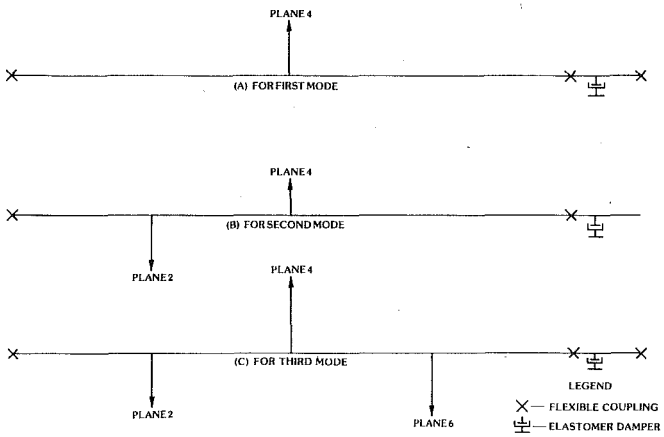

Fig. 6 Longitudinal distribution of model mass sets

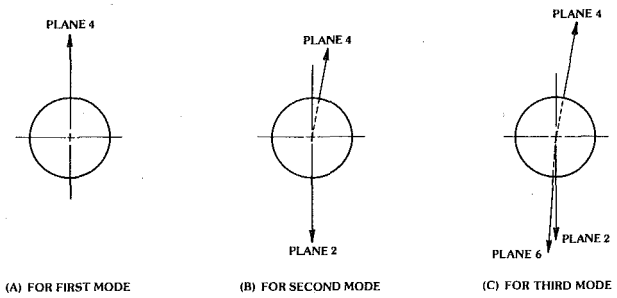

Fig. 7 Angular distribution of model mass sets

enhanced modal procedure incorporated some of the features of influence coefficient balancing and was, in fact, the first step in the development of the UBA. In general, the final balance condition was better using the UBA than the enhanced modal balancing. Also, the UBA was more straightforward and less intuitive than that of the enhanced modal procedure.

6 Summary and Conclusions

Modal and influence coefficient balancing each have specific advantages and disadvantages, as discussed above. The Unified Balancing Approach has been designed to incorporate the advantages of both modal and influence coefficient balancing and to eliminate their disadvantages.

Some of the advantages of the Unified Balancing Approach are as follows:

1 No prior knowledge of the dynamics of the rotor to be balanced is required. The necessary information is determined empirically.
2 As with modal balancing, the modes can be balanced individually, not affecting the balancing of other modes that have already been balanced.
3 In particular cases where the lower modes are more lightly

Table 7 Number of Balancing Runs

Mode No.	Balancing Trys	Total Runs	Data Sets	Highest Speed Runs	Residual Vibration mm (mils) P-P
1 IC*	3	5	5	5	1.0(39)
1 EM**	2	4	4	4	0.2(8)
1 UBA***	3	5	5	5	0.5(20)
2 IC	4	10	20	10	1.2(46)
2 EM	2	8	8	4	0.8(32)
2 UBA	1	7	7	3	0.2(7)
3 IC	4	10	30	10	1.6(62)
3 EM	1	9	9	3	1.2(49)
3 UBA	1	9	9	3	0.2(9)

* During influence coefficient balancing
** During enhanced modal balancing
*** During use of the Unified Balancing Approach

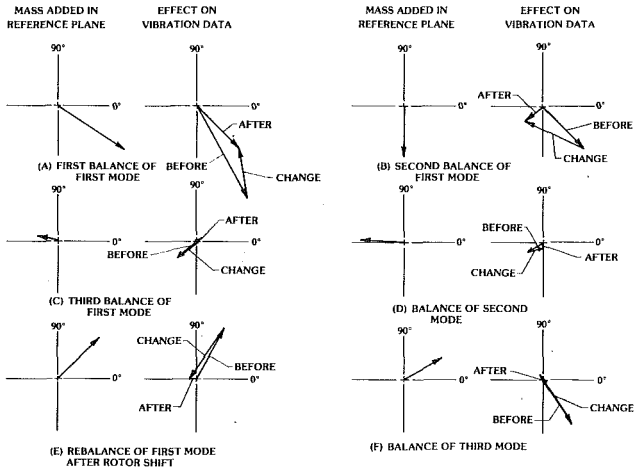

Fig. 8 Effect of balance masses on vibration data (scales: mass, 1 in. = 2 g; vibration, 1 in. = 50 mils peak to peak)

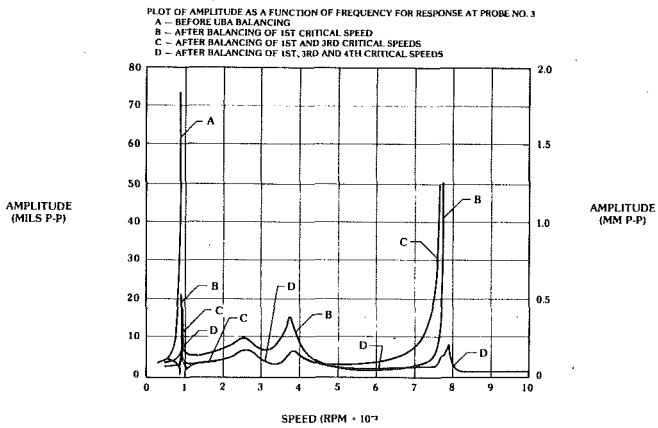

Fig. 9 Response at probe No. 8 during use of Unified Balancing Approach

Downloaded 01 Jun 2010 to 171.66.16.59. Redistribution subject to ASME license or copyright; see http://www.asme.org/terms/Terms_Use.cfm

damped than the higher modes, the use of modal trial mass sets allows the application of substantial trial masses at the insensitive modes without aggravating the response of the lower modes.

4 Using the Unified Balancing Approach, a smaller number of runs is required at the highest speeds of the rotor than would be required for influence coefficient balancing with individual trial mass runs.

5 In many cases, the balancing of a particular mode begins well below the corresponding critical speed, and the response at the balancing speed is reduced to the point where, even though no additional improvement can be made (because of limited vibration pickup sensitivity), the critical speed can still not be negotiated. Using the Unified Balancing Approach, only a single trial mass run is required at the higher balancing speed. However, using influence coefficient balancing, a complete new set of trial mass runs is required at the higher speed. Thus, use of the Unified Balancing Approach substantially reduces the number of balancing runs.

6 Production balancing of a series of identical rotors can be greatly simplified through the use of empirically determined and statistically averaged standard modal influence coefficients. The trial mass runs become small or even nonexistent.

Much effort has been expended in the literature to contrast the modal and influence coefficient balancing techniques and to proclaim the superiority of one or the other. Each method has distinct advantages and disadvantages. A Unified Balancing Approach has been formulated from the most useful aspects of both the modal and influence coefficient techniques.

A series of tests has been conducted to compare modal and influence coefficient balancing with the Unified Balancing Approach. The results of these tests indicate the superiority of the Unified Balancing Approach both in precision and ease of balancing. The feasibility of this balancing technique, both theoretical and practical has been shown.

References

1 Parkinson, A. G., Darlow, M. S., Smalley, A. J., and Badgley, R. H., "An Introduction to a Unified Approach to Flexible Rotor Balancing," ASME Paper No. 79-GT-161, presented at the ASME Gas Turbine Conference, Mar. 1979.

2 Tessarzik, J. M., and Badgley, R. H., "Experimental Evaluation of the Exact Point-Speed and Least-Squares Procedures for Flexible Rotor Balancing by the Influence Coefficient Method," ASME *Journal of Engineering for Industry,* 1974, Vol. 96, p. 633.

3 Bishop, R. E. D., and Parkinson, A. G., "On the Use of Balancing Machines for Flexible Rotors," ASME *Journal of Engineering for Industry,* 1973, Vol. 94, 561.

4 Kellenberger, W., "Should a Flexible Rotor be Balanced in N or (N + 2) Planes?" ASME *Journal of Engineering for Industry,* 1972, Vol. 94, p. 548.

5 Bishop, R. E. D., and Parkinson, A. G., "On the Isolation of Modes in the Balancing of Flexible Shafts" *Proceedings of the Institution of Mechanical Engineers,* London, 1963, Vol. 177, p. 407.

6 Badgley, R. H., "The Potential Impact of Multiplane-Multispeed Balancing on Gas Turbine Production and Overhual Costs," ASME Paper No. 74-GT-96, presented at the ASME Gas Turbine Conference and Products Show, Zurich, Switzerland, Apr. 1974.

7 Goodman, T. P., "A Least-Squares Method for Computing Balance Corrections," ASME *Journal of Engineering for Industry,* 1964, Vol. 86, p. 273.

8 Lund, J. W., and Tonnesen, J., "Analysis and Experiments on Multiplane Balancing of Flexible Rotors," ASME *Journal of Engineering for Industry,* 1972, Vol. 94(B), p. 233.

9 Darlow, M. S., Smalley, A. J., and Parkinson, A. G., "Procedures for a Unified Approach to the Balancing of Flexible Rotors," MTI Technical Report 79TR61, June 1979, to be published in the open literature at a joint conference on "Vibrations in Rotating Machinery" in Cambridge, England, Sept. 1980.

10 Zorzi, E. S., Burgess, G., and Cunningham, R., "Elastomer Damper Performance—A Comparison with a Squeeze Film for a Supercritical Power Transmission Shaft," paper to be presented at the 1980 ASME Gas Turbine Conference, Mar. 1980.

11 Darlow, M., and Fanuele, F., "User's Manual for MTI Balancing Programs," *MTI Computer Program User's Manual,* 1977.

12 Darlow, M., "Analysis and Interim Computer Program User's Manual for the MTI Unified Balancing Approach," MTI Technical Report 79TR41, Mar. 1979.

APPENDIX

Unified Balancing Approach: Glossary of Terms

Balance Mass Plane (Balance Plane). Axial position on rotor of location for making balance mass corrections.

Check Balance. Data taken at the balancing speed after the addition of a modal correction mass set. If the improvement in the balance is not sufficient, new modal influence coefficients and an additional modal correction mass set may be calculated using the check balance data.

Individual Trial Mass. A single trial mass used to generate influence coefficients for individual balance mass planes; used for calculating modal trial mass set ratios.

Influence Coefficients. Complex values representing the effect of the addition of the trial masses on the rotor responses.

Modal Correction Mass Set. A group of correction masses used to balance a particular critical speed while having no effect on other particular critical speeds. The number of masses (and balance planes) in this set is greater than or equal to the mode number of the critical speed being balanced. The magnitude ratios and relative angles of the masses in the set are the same as for the modal trial mass set used to excite the same critical speed, but the actual magnitudes and angles are calculated using rotor response data from the modal trial mass runs.

Modal Influence Coefficients. Complex values representing the effect of the addition of the modal trial mass sets on the rotor response.

Modal Trial Mass Set. A group of trial masses used to excite a particular critical speed while having no effect on other particular critical speeds. The number of masses (and balance planes) in this set is greater than or equal to the mode number of critical speed being excited. The magnitude ratios and relative angles of the masses in the set are calculated using rotor response data from individual trial mass runs, but the actual magnitudes and angles are arbitrary.

Mode. Shape of response of rotor-bearing system at a critical speed.

Mode Number. Generally, the order in which critical speeds occur when the speed of the rotor-bearing system is increased. For generally-rigid bearings, this number refers to the number of anti-nodes in the mode shape. For generally-flexible bearings with distinctly separate rigid body modes, this number will be one for the first rigid body mode and one greater than the number of rigid body modes (not including additional modes due to bearing asymmetry) for the first flexural mode. When balancing the nth mode, there are n-1 modes at lower speeds, at which the vibration must be controlled. Critically damped modes are not counted.

Trial Mass. A single mass or group of masses of known magnitude installed in a rotor at a specific balance plane and angle, to generate data used for calculating influence coefficients of the rotor-bearing system for this balance mass location (or combination) at speeds at which data were taken.

Two Trial Masses Per Plane (Alternately referred to as 0 and 180 deg trial masses). Trial mass data taken with a trial mass (or set of masses) located at the specified trial mass angle (or angles) and then moved to 180 deg from that position (or those positions). The additional data are used to calculate the measurement error inherent in the test data and to correct for that error.

Uncorrected Rotor. Rotor condition at the beginning of a balancing step, with no trial or correction masses installed.

Downloaded 01 Jun 2010 to 171.66.16.59. Redistribution subject to ASME license or copyright; see http://www.asme.org/terms/Terms_Use.cfm

H. L. Hassenpflug
Research Associate.

R. D. Flack
Assistant Professor.

E. J. Gunter
Professor.

Department of Mechanical and Aerospace Engineering,
School of Applied Science and Engineering,
University of Virginia,
Charlottesville, VA 22901

Influence of Acceleration on the Critical Speed of a Jeffcott Rotor

The effects of angular acceleration on a Jeffcott rotor have been examined both theoretically and experimentally. The equations of motion were solved via numerical integration. The rotor's response to unbalance was predicted for a number of cases of acceleration and damping. Both amplitude and phase responses were studied. In addition, techniques were developed for identifying system damping from data taken during accelerated runs. The results of the analysis indicate that for high acceleration rates the amplitude response at the critical speed may be reduced by a factor of four or more. The speed at which the peak response occurs can also be shifted by 20 percent or more. Experimentally, a small lightly damped rotor ($\zeta = 0.0088$) was run for several acceleration rates. The peak responses typically agree within 6 percent of theoretical predictions. Also, a beat frequency was observed both theoretically and experimentally after the rotor had passed through the critical speed.

Introduction

The high speed operation of many modern machines necessitates their passing through resonances to attain a specified operating speed. In many cases, to insure that a machine safely traverses a critical speed, the machine is rapidly accelerated. However, the transient nature of the passage through the critical speed generally limits the availability of data concerning the fundamental resonant behavior of the system. A change in operating speed or rate of acceleration can strongly influence the machine's maximum response to unbalance and the speed at which it occurs.

In many cases a rotor is rapidly accelerated from rest to operating speed, thus reducing the destructive effect of the presence of critical speeds. However, the deceleration rates on many machines are not controllable. Since deceleration rates are generally slower than acceleration rates, resonant problems may be encountered on run-down, where they may have been avoided on run-up, causing machine damage.

The phenomenon of acceleration through resonance was investigated analytically via a convolution integral by Lewis [1]. His solution displays the amplitude of vibration as a function of non-dimensionalized operating speed. He employed a forcing function of constant amplitude; i.e., it did not vary with speed as in a real unbalance force. When mass unbalance is considered as a forcing function, the amplitude varies as the square of the operating speed. As a result, his results may lead to significant errors when applied to a rotor system. Furthermore, Lewis deals only with the amplitude of response and does not address the phase relationship between unbalance and rotor response.

Baker [2] studied the acceleration of a rotor using a mechanical analog to solve the model equations. However the range of acceleration rates which he employed was out of range for most machinery. Also, he did not include any predictions for very lightly (but nonzero) damped cases. Unfortunately, these are the machines on which acceleration has the most pronounced effect. Phase relations were also not considered in reference [2].

Meuser and Weibel [3] studied accelerating systems with nonlinear spring rates via a mechanical analog. A constant forcing function was used similar to that in reference [1]. Primarily, this paper deals with the effects of nonlinearities rather than acceleration rates.

Gasch, et al. [4] consider acceleration of a rotor under the assumption of constant torque, allowing the acceleration to vary as torque is absorbed in resonant response. Their work avoids the range of practical application by assuming large unbalance eccentricity and very large acceleration rates. Both of these assumptions fall outside of the realm of most machine applications. Reference [4] also only presents results for the amplitude of the response; phase is not considered, nor is the speed at which maximum response occurs.

In all of the previous works, the thrust of the analysis was on predicting rotor response during acceleration. The objective of this paper is twofold. In addition to looking at rotor response during acceleration, a parameter identification method is developed using data from rotors during acceleration. Particularly, the system damping ratio is determined from the phase angle measurement of an accelerated rotor. It may also be determined by observing the speed shift in maximum response for a known acceleration.

Furthermore, experimental data for a rotor system have not been previously presented (although mechanical analogs were used). Thus, another aim of this paper is to present results from a rotor rig demonstrating the effects of acceleration.

Acceleration rates (and deceleration rates) range from zero to a maximum which has been seen in modern applications. The range of damping covers rotors from the heavily damped ($\zeta = 0.25$) to very lightly damped as might be encountered in a system on ball-bearing supports ($\zeta = 0.01$).

The theoretical solution employs a model based on a speed dependent forcing function as is the case in rotating equipment. Only small values for unbalance eccentricity (and hence constant acceleration rates) have been considered here. This assumption is in general

Contributed by the Gas Turbine Division and presented at the Gas Turbine Conference and Products Show, New Orleans, La., March 10–13, 1980 of THE AMERICAN SOCIETY OF MECHANICAL ENGINEERS. Manuscript received at ASME Headquarters December 14, 1979. Paper No. 80-GT-88.

Copyright © 1981 by ASME

Downloaded 01 Jun 2010 to 171.66.16.59. Redistribution subject to ASME license or copyright; see http://www.asme.org/terms/Terms_Use.cfm

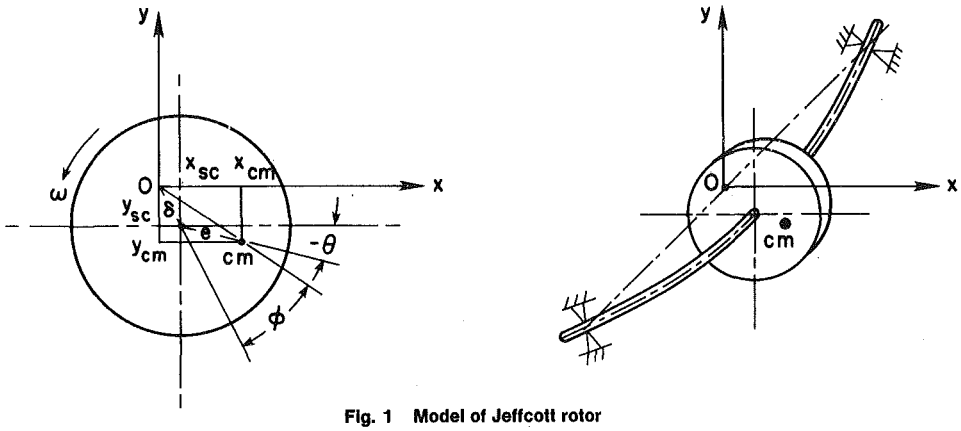

Fig. 1 Model of Jeffcott rotor

quite reasonable. High values of unbalance are quite destructive to machinery and balancing techniques do exist to limit the unbalance in a system to levels where vibration has little effect on acceleration rates. Overall, the aim of this paper is to present results in the range of practicability and applicability to gas turbine rotors and similar systems.

Theoretical Model and Solution

The theoretical model employs a single unbalanced disk, centrally mounted on an elastic shaft which is, in turn, mounted symmetrically on rigid bearings (see Fig. 1). By application of Newton's second law to the system, the following equations of motion are obtained:

$$-KX - CdX/dt = Md^2X_{cm}/dt^2 \tag{1}$$

$$-KY - CdY/dt = Md^2Y_{cm}/dt^2 \tag{2}$$

The coordinates of the disk center of mass, X_{cm} and Y_{cm}, expressed in the fixed coordinates X, Y are

$$X_{cm} = X + e\cos\theta \tag{3}$$

$$Y_{cm} = Y + e\sin\theta \tag{4}$$

Differentiating each of the above equations twice and substituting into equations (1) and (2), the equations of motion are expressed entirely in the fixed coordinate system:

$$\ddot{X} + C\dot{X}/M + KX/M = e(\omega^2\cos\theta + \alpha\sin\theta) \tag{5}$$

$$\ddot{X} + C\dot{Y}/M + KY/M = e(-\omega^2\sin\theta + \alpha\cos\theta) \tag{6}$$

The equations of motion previously derived were simultaneously integrated in time using a standard Euler integration scheme. A similar set of equations was solved by Lewis [1], using a convolution integral. However, the numercial solution has several advantages, one of which is ease of execution. Furthermore, the numerical technique provides versatility in the types of acceleration functions which can be employed (only constant acceleration is presented here). Also, it allows for the solution of phase angle, a formidable analytical problem. The techniques developed here may be applied in more advanced systems with several degrees of freedom for which the convolution integral would be impossible.

The integration procedure used a time step yielding approximately 1/500 revolution per step. Numerical stability was checked by varying step size to as little as 1/25,000 revolution. Results differed by less than one percent.

The results of the integration are expressed in polar coordinates. The instantaneous amplitude of vibration is $\delta = \sqrt{X^2 + Y^2}$. An angle, β, is defined as $\tan^{-1}(Y/X)$. The phase angle, ϕ, is defined as $\phi = \beta - \theta$, which represents the phase difference between the rotor response and unbalance.

The initial conditions for the integration procedure are taken as the unaccelerated or steady-state conditions for a Jeffcott rotor. This technique has the effect of operating for an extended period at some initial speed and then accelerating abruptly.

Unbalance in the system is considered to be small. Non-dimensionally it is represented by e/r_g, where r_g is the disk radius of gyration. For this model, e/r_g was of the order of 10^{-3}. For this range of eccentricity, constant acceleration may be associated with a constant driving torque. Consequently, the energy balance which yields angular acceleration rate as a function of applied torque becomes trivial and is not considered here. Large magnitudes of unbalance ($e/r_g = 0.10$) are examined by Gasch et al. [4], but are in general not representative of unbalances in real machinery. A variety of acceleration rates, both positive and negative, were used here. Also, several cases with different values of system damping were run to demonstrate the effect of damping on the acceleration response.

Theoretical Results

In the previous section, equations were derived for the response of a Jeffcott rotor as it accelerates through the critical speed. In this section, typical results are presented. First, the predicted unbalance response of the rotor is presented for several system parameters cases. Second, it is shown how results from accelerated runs can be used for system parameter identification.

Critical Speed Response. Results of the numerical analysis are presented in several formats. In Figs. 2–5, nondimensionalized amplitude is plotted against the speed ratio, Ω. Each plot has on it several curves, each representing runup at different acceleration rate. The angular acceleration is given nondimensionally by an acceleration ratio, $\gamma = \alpha/\omega_{cr}^2$. Each of the figures covers a different system

Nomenclature

A = amplification factor, δ/e
A_{cr} = critical speed amplification factor at no acceleration, $M\omega_{cr}/C$
A_{max} = maximum amplification factor during acceleration
C = system damping coefficient
e = unbalance eccentricity
K = shaft stiffness
M = mass of the disk
r_g = radius of gyration of the disk
X, Y = shaft displacements
$\dot{X}$, $\dot{Y}$ = velocities
$\ddot{X}$, $\ddot{Y}$ = accelerations
α = angular acceleration
γ = acceleration ratio, α/ω_{cr}^2
δ = shaft deflection, $\sqrt{X^2 + Y^2}$
ζ = normalized damping, $1/(2A_{cr})$
θ = angular displacement
ϕ = phase angle
ϕ_{node} = phase angle at "node" (51 or 141 deg)
Ω = speed ratio, ω/ω_{cr}
Ω_{node} = speed ratio at node
ω = angular velocity
ω_{cr} = undamped system critical speed, $\sqrt{K/M}$
ω_{max} = operating speed at A_{max}
ω_{op} = instantaneous operating speed

Downloaded 01 Jun 2010 to 171.66.16.59. Redistribution subject to ASME license or copyright; see http://www.asme.org/terms/Terms_Use.cfm

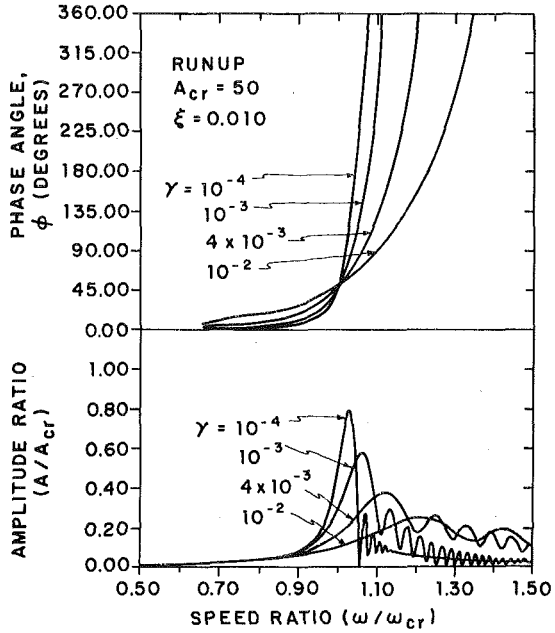

Fig. 2 Critical speed response for runup for $\zeta = 0.010$

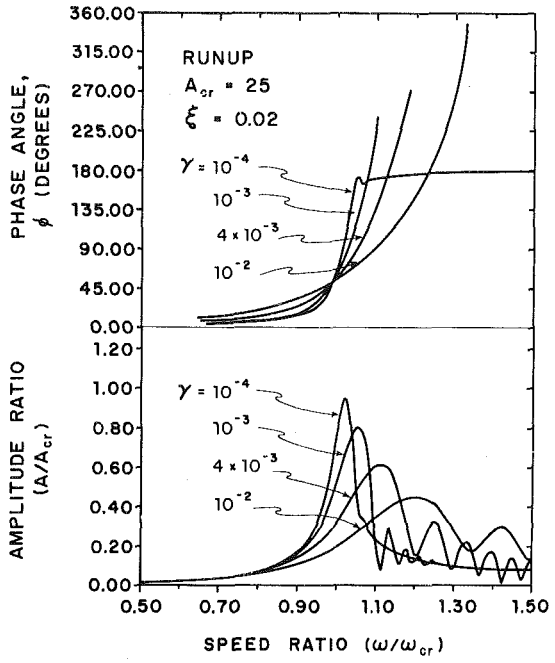

Fig. 3 Critical speed response for runup for $\zeta = 0.02$

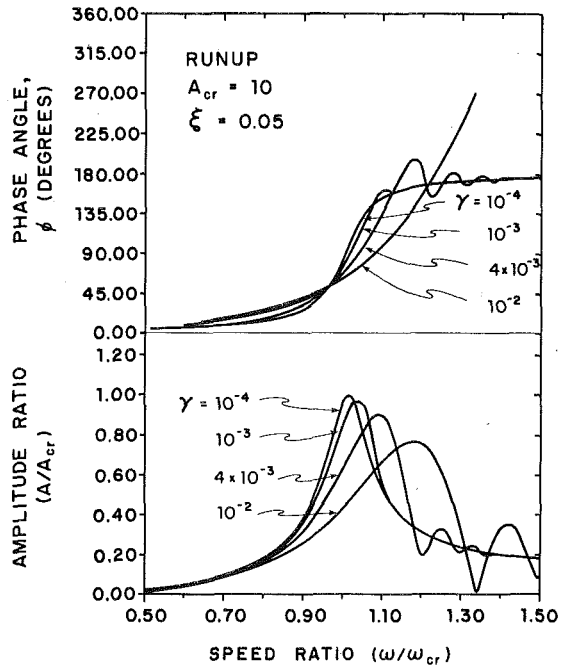

Fig. 4 Critical speed response for runup for $\zeta = 0.05$

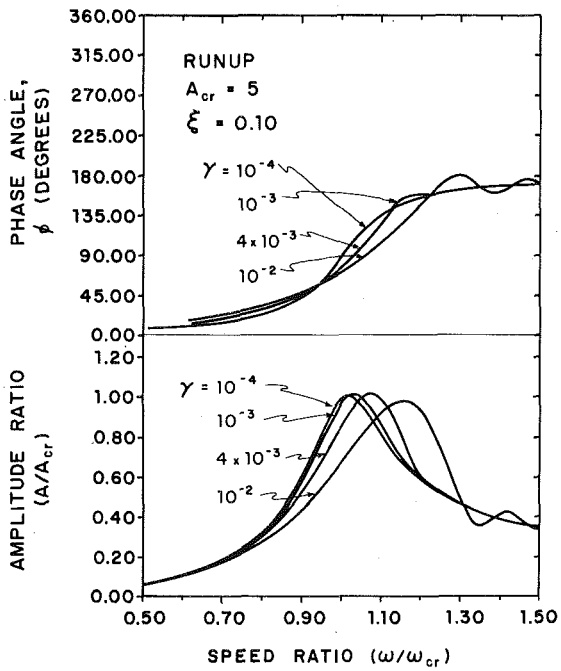

Fig. 5 Critical speed response for runup for $\zeta = 0.10$

damping ratio: $\zeta = 0.10$, 0.020, 0.05, and 0.10. Also in Figs. 2–5, the phase angles are shown, which correspond to the various speeds and acceleration rates. In Fig. 6, several cases of deceleration are considered for a system with a damping ratio, $\zeta = 0.020$. The results are presented in the same manner as in Figs. 2–5.

In each of the amplitude vs speed plots, several phenomena are observed. First, the maximum amplitude of vibration is reduced with the introduction of acceleration or deceleration. Lightly damped systems show the most pronounced reductions in amplitude. Also, the speed at which the maximum amplitude occurs (ω_{max}) is increased with positive acceleration and decreased with deceleration. This effect also is more outstanding in a lightly damped rotor. These phenomena are summarized in Figs. 7 and 8 and are discussed later in this section.

Another peculiarity exhibited by accelerated rotors which is shown by the amplitude plots is a "beating" frequency or harmonic oscillation in the amplitude of vibration, itself. While this behavior has been shown analytically by Lewis [1] and with the aid of a mechanical analog system by Baker [2], neither of their works offers a qualitative explanation of the effect.

This type of rotor behavior is easily explained by the interaction of a free vibration at the system natural frequency, which is excited as the rotor passes through the resonance and a forced vibration at the instantaneous operating speed. Precise measurement of the "beat" frequency shows it to be equal to the difference in operating speed and the critical speed ($\omega_{op} - \omega_{cr}$). The frequency of the "beating" is, therefore, independent of both damping and the acceleration rate. In Figs. 2–6 the beating frequency appears to be dependent on γ. However, one should remember that in these figures, the value of ω_{op} is dependent on both γ and time and thus, the abscissa is not a constant multiple of time for all of the curves.

Downloaded 01 Jun 2010 to 171.66.16.59. Redistribution subject to ASME license or copyright; see http://www.asme.org/terms/Terms_Use.cfm

Only the amplitude of the beat depends on damping. The beating phenomenon is inherently transient as is the free vibration at the critical speed. This is why the beating only occurs in the region of the amplitude plots which follows the critical speed in time, and in heavily damped rotors it is barely noticeable. The accuracy of these results is demonstrated experimentally in the following section.

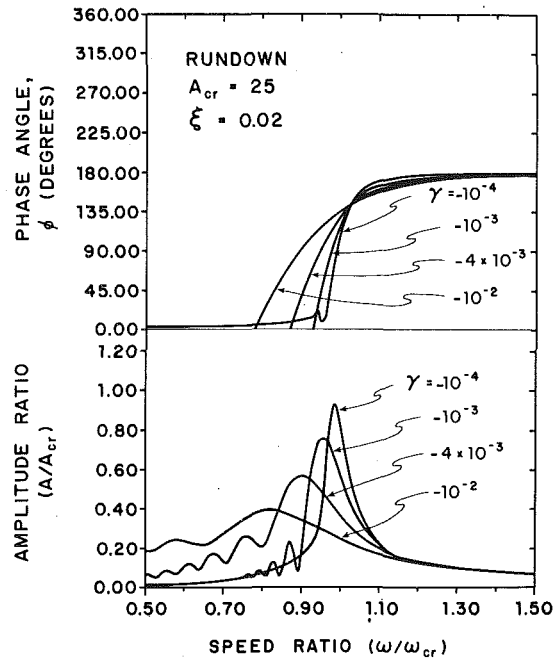

Fig. 6 Critical speed response for rundown for $\zeta = 0.02$

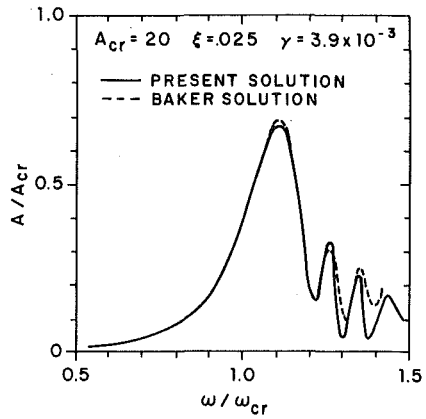

Fig. 7 Comparison of present and Baker [2] critical speed response predictions for runup for $\zeta = 0.025$

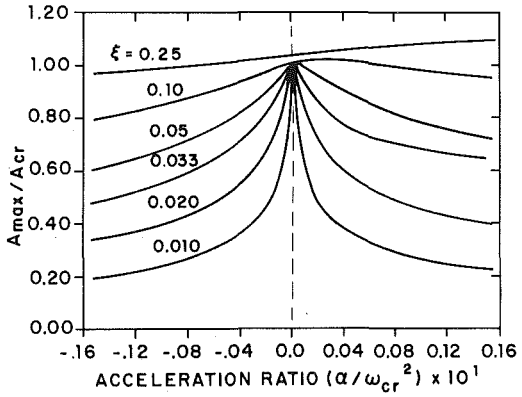

Fig. 8 Summary of maximum amplitude dependence on acceleration rate and damping

The present solution for one case is compared to the analog solution of Baker [2]. Results are shown in Fig. 7 for $\zeta = 0.025$ and $\gamma = 3.9 \times 10^{-3}$. As can be seen, very good agreement is obtained. The difference between the two peak responses is less than 2 percent. The "beating" also occurred at the same frequency.

Looking at the phase relations in Figs. 2–6, several more phenomena can be identified. Unlike the unaccelerated rotor, systems with acceleration do not typically show a 90 deg phase angle at the critical speed. Instead, the phase diagrams show "nodal" points at which the phase is independent of the acceleration rate. One will notice for the case of rundown (Fig. 6) a nodal point occurs above the critical speed, whereas for the cases of runup (Figs. 2–5), the nodal point occurs below the critical speed. In cases of heavy damping both nodal points are seen in both runup and rundown.

Although it has not been proven analytically or numerically, these results strongly suggest that two phase nodal points exist for any system and will be shown unless the phase measurement is obscured by transient vibration as is the case when a rotor undergoes beating. Furthermore, the nodal points are found at $\phi = 51$ deg and $\phi = 141$ deg regardless of damping. The use of these nodal points for system parameter identification will be discussed in the next subsection.

For several of the cases, the phase angle of the total motion is seen to be undefined after the rotor passes through the critical speed. This phenomenon is due to the beating frequency previously described. Two dominant frequencies are present in the system during the beating process. Since the phase angle represents the angle of the synchronous vibration component only, determination of the phase angle of the total motion becomes meaningless; i.e., the predominant frequency of vibration is nonsynchronous.

The results of the rotor response calculations are summarized in Figs. 8 and 9. Figure 8 illustrates the maximum nondimensionalized excursion that a shaft undergoes as a function of acceleration ratio. Several values of system damping are included. Figure 8 represents the vibrational amplitude suppression (or in some cases the magnification) capabilities that accelerating a rotor through a critical speed presents. In Fig. 9, the nondimensionalized speed at which the maximum vibration occurs is presented as a function of α/ω_{cr}^2 for several damping ratios. Figure 9 thus represents the effect rotor acceleration has on the "observed critical speed."

For example, for a rotor with an acceleration ratio of 0.001 and a damping ratio of 0.05, one can expect a maximum response of 78 percent of an unaccelerated case and expect the maximum response at 1.17 times the critical speed. These effects are even more pronounced for lower values of ζ.

Also of interest from Figs. 8 and 9 are the cases with large values of damping. For no acceleration ($\alpha/\omega_{cr}^2 = 0$) and a damping value of $\zeta = 0.25$, the value of A_{max}/A_{cr} is 1.04. The damped critical speed is at 1.07 times the undamped critical speed. As a result of the constant forcing function used by Lewis [1], he found a depressed critical speed. Baker [2] studied only very high acceleration rates ($\gamma \leq 4 \times 10^{-3}$) and, thus, cannot be used for comparison here.

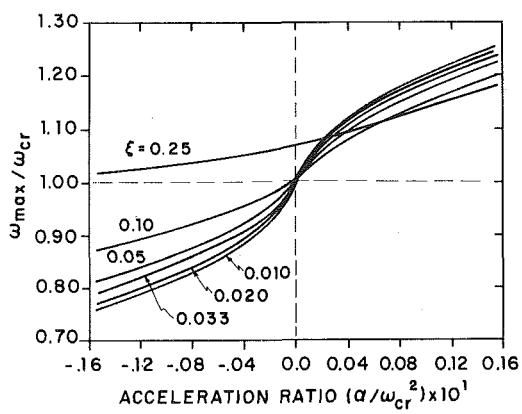

Fig. 9 Critical speed shift as a function of acceleration rate and damping

Downloaded 01 Jun 2010 to 171.66.16.59. Redistribution subject to ASME license or copyright; see http://www.asme.org/terms/Terms_Use.cfm

System Parameter Identification. In the previous subsection the occurrence of "nodal" points on the phase diagrams was determined. These nodes occurred at $\phi = 51$ deg and 141 deg regardless of the value of ζ. In this subsection the use of these conditions to determine the system damping will be discussed.

At the nodal points the relationship for phase is the same as for steady state operation (since all curves for one value of ζ pass through the same point on a ϕ versus ω/ω_{cr} diagram), namely:

$$\tan(\phi_{\text{node}}) = C\,\omega_{\text{node}}/(K - M\omega_{\text{node}}^2) \tag{7}$$

Thus, the damping can be calculated by:

$$\zeta = [(1 - \Omega_{\text{node}}^2)/2\,\Omega_{\text{node}}]\tan(\Omega_{\text{node}}) \tag{8}$$

where $\Omega = \omega/\omega_{cr}$.

To apply the above equations, one must first obtain response plots from a rotor for any acceleration. One next determines the value of the nondimensionalized rotational speed at $\phi = 51$ deg or 141 deg, i.e., Ω_{node}. Once the value of Ω_{node} is determined, ϕ_{node} and Ω_{node} are substituted into equation (8) such that ζ is found.

This method is most easily applied to rotors of significant damping ($\zeta \geq 0.020$). For more lightly damped systems, the nodal points are less than two percent removed from the critical speed and are difficult to accurately distinguish experimentally.

Experimental Results

Critical Speed Response. To demonstrate the accuracy of the results, an experimental analysis was completed. The experimental rig and data analysis system are shown in Fig. 10. The test rotor consisted of a single mass (1.63 kg) centrally located on a 9.53 mm steel shaft. The bearing span was 40.6 cm. The rotational speed was controlled with a ⅙ hp d-c motor. The first critical speed of the rotor was 1730 rpm. On run-up the acceleration rates were constant within 5 percent and on run-down the deceleration rates were constant within 1 percent.

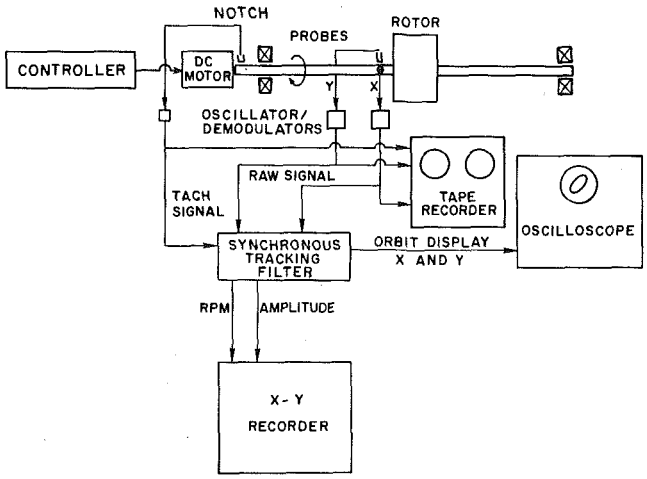

Fig. 10 Test rotor and instrumentation

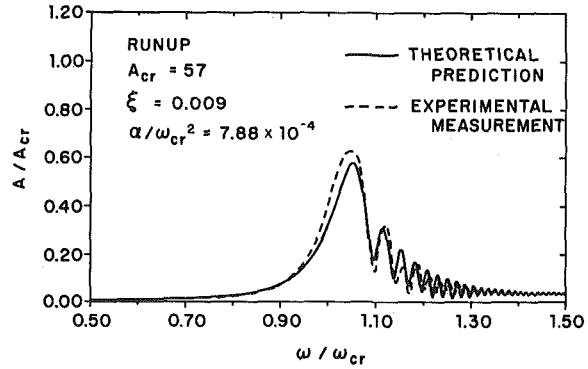

Fig. 11 Typical experimental critical speed response and theoretical predictions

The rig was instrumented with three displacement transducers. Two were located near the mass and the third was placed over a notch on one end of the shaft. The two central probes were calibrated and particular probes were chosen such that the two calibration curves were matched. Thus, direct comparison of the outputs of the X and Y probes was possible.

Data was analyzed using a synchronous tracking filter. The notch on the shaft was used as the trigger for the tracking filter. Outputs from the tracking filter included total or synchronous amplitude and synchronous phase angle (measured with respect to the notch). Reduced data was plotted using an analog plotter. Raw signals from the displacement probes were recorded on an FM tape recorder so that permanent records were obtained.

The rig was first run for no acceleration. A mass unbalance vector of 0.010 mm was used and the bow vector was less than 0.003 mm. From this base run, the system damping was determined. First, the response at the critical speed was divided by the response at four times the first critical speed. The latter corresponds to the mass unbalance vector. This generated a nondimensionalized critical speed response of 59.0, which corresponds to a damping ratio of 0.0085. Secondly, the slope of the phase angle versus speed curve was used to calculate ζ by:

$$\zeta = (d\phi/d\omega)_{cr}^{-1} \times \omega_{cr}^{-1} \tag{9}$$

From equation (9), the value of ζ was found to be 0.0091. Thus, since a difference of less than 7 percent was found, an average of the two methods was used to define the damping: $\zeta = 0.0088$, $A_{cr} = 57$. The bow and unbalance vectors were held constant for the remainder of the tests.

Several tests were performed including acceleration and deceleration runs. One typical run is presented here. For the particular run presented, the value of α/ω_{cr}^2 is 7.88×10^{-4}. The total motion data is presented in Fig. 11. Also presented in Fig. 11 is the theoretical prediction. The damping ratio determined from the baseline case is used in the prediction. As can be seen in Fig. 11, excellent agreement is obtained. First, the theoretical and experimental maximum responses are seen to occur at the same rotational speed ($\omega/\omega_{cr} = 1.050$) and the beating is seen to occur experimentally at the same frequency as predicted. Also, the maximum amplitude (A/A_{cr}) is observed to be 0.62, as compared to the predicted value of 0.58, which results in a difference of 6 percent. Results from other tests were similar and are not presented for brevity.

System Parameter Determination. As a last step, experimental data are presented for a larger rotor mounted in pressure dam journal bearings and the vibration data are used to identify the system damping by three methods. The rotor was a 25.4 mm shaft with single mass of 13.55 kg centrally located. The critical speed of this rotor was 3300 rpm. The motion at the center of the shaft was monitored, and a typical response plot is presented in Fig. 12. The rotor response as well as the test rotor itself is described in reference [5] in detail. In Fig. 12, both the relative phase and magnitude (mm) of the rotor are presented, and this figure is for an acceleration ratio of $\gamma = 1.3 \times 10^{-4}$.

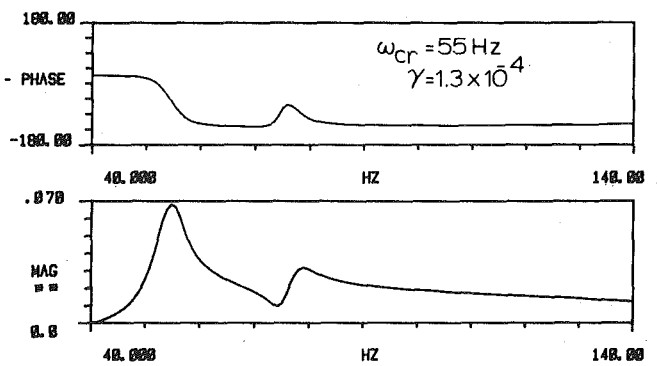

Fig. 12 Data from reference [5] used to demonstrate parameter identifcation

Downloaded 01 Jun 2010 to 171.66.16.59. Redistribution subject to ASME license or copyright; see http://www.asme.org/terms/Terms_Use.cfm

The data for this rotor are analyzed by three methods so that the system damping could be determined. First, the amplification factor was determined at low acceleration rates to be 12.2, by the ratio of the response at the critical speed to the rotor unbalance eccentricity, i.e., $\zeta = 0.041$. Second, the slope of the phase diagram at low acceleration rates yielded a value of ζ from equation (9) to be 0.044. And finally, using the nodal method for $\phi_{node} = 51$ deg (measured with respect to low speeds) yields a ratio of $\Omega_{node} = 0.967$ from Fig. 12. Using these data in equation (8) yields a value of $\zeta = 0.042$. As can be seen, very good agreement is seen with differences less than 5 percent being present between the nodal method and either of the other methods.

Conclusions

Overall, a Jeffcott rotor has been modeled theoretically, and the response (amplitude and phase) of the system as it was accelerated through the critical speed was predicted. A numerical technique was used to solve the equations of motion. If more complex multimass systems are to be examined, such numerical techniques will be necessary as convolution methods will not be practical. Also, experimental data were presented to demonstrate the accuracy of the method. Ranges of system damping, acceleration rates and unbalance eccentricity were studied which are typical in gas turbines and similar machinery. Specific conclusions include:

1 A beating frequency is observed after a rotor passes through the critical speed. The beating represents the difference between the operating and critical speeds.

2 High acceleration rates are seen to affect systems with low damping ratio the most. For systems with $\zeta \lesssim 0.25$, the maximum response varies by less than 10 percent for practical ranges of acceleration. The speed at which the maximum response is realized is dependent on the acceleration rate, again strongly so for low system damping.

3 A method was developed such that one can use a response phase plot for an accelerated rotor to easily determine the system damping. Such a method was previously not available.

4 Experimental results are presented to demonstrate the accuracy of the predicted responses. Differences between the theoretical and experimental results are less than 6 percent.

5 Experimental results are presented to demonstrate the method of parameter identification for an accelerated rotor. Differences between the presented methods for an accelerated rotor and conventional methods for the same unaccelerated rotor are less than 5 percent.

Acknowledgment

The authors wish to thank Dr. P. E. Allaire for his helpful discussions during this investigation. This research was sponsored by the Department of Energy under contract DE-ACOL-79ET-13151, under the direction of Dr. D. W. Lewis, and the Industrial Supported Program for the Dynamic Analysis of Turbomachinery at the University of Virginia, under the direction of Dr. E. J. Gunter.

References

1 Lewis, F. M., "Vibration During Acceleration Through a Critical Speed," ASME *Journal of Applied Mechanics*, Vol. 54, 1932, pp. 253–257.

2 Baker, J. G., "Mathematical-Machine Determination of the Vibration of an Accelerated Unbalanced Rotor," ASME *Journal of Applied Mechanics*, Vol. 61, 1939, pp. A 145–A 150.

3 Meuser, R. B. and Weibel, E. E., "Vibration of a Non-linear System During Acceleration through Resonance," ASME *Journal of Applied Mechanics*, Vol. 15, 1948, pp. 21-24.

4 Gasch, R., Markert, R., and Pfützner, H., "Acceleration of Unbalanced Flexible Rotors through the Critical Speeds," *Journal of Sound and Vibration*, Vol. 63, No. 3, 1978, pp. 393–409.

5 Flack, R. D., Leader, M. E., and Gunter, E. J., "An Experimental Investigation on the Response of a Flexible Rotor Mounted in Pressure Dam Bearings," accepted for publication in ASME *Journal of Mechanical Design*, 79-JMD-10.

Downloaded 01 Jun 2010 to 171.66.16.59. Redistribution subject to ASME license or copyright; see http://www.asme.org/terms/Terms_Use.cfm

B. L. Pierce

Westinghouse Advanced Energy Systems Division,
P.O. Box 10864,
Pittsburgh, Penn. 15236

The Influence of Recent Heat Transfer Data on Gas Mixtures (He-Ar, H_2-CO_2) on Closed Cycle Gas Turbines

Previous studies have been made on the composition of an optimal working fluid for closed cycle gas turbines. Those studies were based on the assumption that the objective could be achieved by mixing helium with a gas of higher molecular weight. The results of those calculations, based on heat transfer data of pure gases and air, indicated the possibility of significant cost advantages of gas mixtures relative to pure helium. Recent heat transfer measurements of low Prandtl number gas mixtures indicate that existing scaling laws for normal Prandtl number (~0.7) gases do not adequately represent the heat transfer characteristic of these gas mixtures. In this paper the influence of these gas mixture heat transfer data on closed cycle gas turbine coolers, recuperators and heat source exchangers is presented. The characteristic dimensions (flow area, surface area, and length) of these heat exchangers utilizing pure gases and gas mixtures are compared.

Introduction

The closed Brayton cycle has been proposed for application to the generation of electric power, for propulsion of ships, aircraft, buses and rail units; for power systems in satellites, space stations, and undersea. In many of these applications, investigations [1–4] have been carried out to determine the influence of using helium mixed with a higher molecular weight gas on system cost, performance and/or weight-volume. Helium possesses good heat transfer properties, but requires many stages in the turbomachinery. The higher molecular weight gases, due to their lower thermal conductivity, require considerably more heat transfer surface area, but a fewer number of stages in the turbomachinery. The results of the above mentioned investigations are that for certain gas mixtures of helium and higher molecular weight gases, cost advantages or minimum weight/volume can be obtained relative to pure gases. However, most of these investigations have assumed that the heat transfer correlations, primarily based on experimental data for gases with Prandtl numbers of approximately 0.7, are applicable to these gas mixtures with Prandtl numbers as low as 0.2. Numerical analyses [5] predicted that the existing scaling laws for gases with Prandtl numbers around 0.7 would not represent the heat transfer adequately. Measurements with helium-argon [5, 6] and hydrogen-carbon dioxide [7] confirmed that prediction for turbulent flow in circular tubes.

Helium Gas Mixtures

In a closed cycle gas turbine the compressor may require up to over half of the turbine work. To reduce this compression work, it is desirable to use a dense working fluid; by increasing the molecular weight and pressure of the gas, its density can be increased. However, heat exchanger size and weight are adversely affected by the use of high molecular weight gases. However, this disadvantage can be reduced markedly by the use of gases mixed with helium, primarily due to a distinct improvement in thermal conductivity of the gas mixture over the pure gases (Fig. 1). Also, a continuous range of average molecular weights is possible with the mixtures, compared to the discrete molecular weights of pure gases. The Prandtl number variation of helium-xenon mixtures is shown in Fig. 2, which shows a minimum of about 0.22 and is relatively flat over a large portion of the curve. Helium mixed with other gases produce curves of the same shape, but

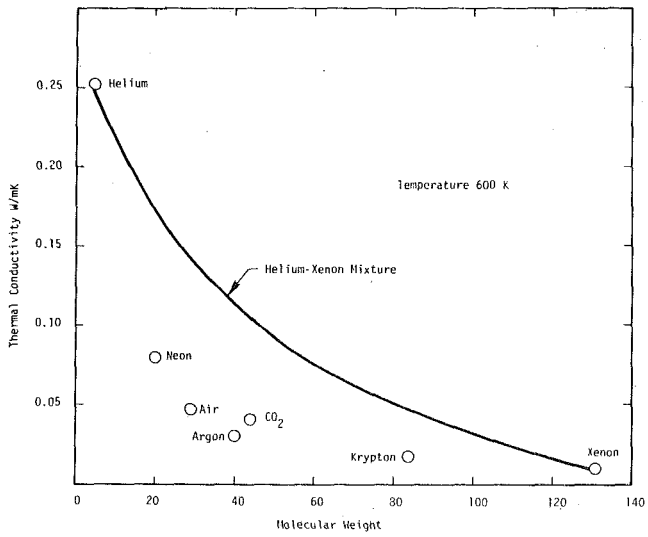

Fig. 1 Thermal conductivity of various gases and helium-xenon mixtures

Contributed by the Gas Turbine Division and presented at the Gas Turbine Conference and Products Show, New Orleans, La., March 10–13, 1980 of THE AMERICAN SOCIETY OF MECHANICAL ENGINEERS. Manuscript received at ASME Headquarters December 17, 1979 Paper No. 80-GT-89.

Copyright © 1981 by ASME

Downloaded 01 Jun 2010 to 171.66.16.59. Redistribution subject to ASME license or copyright; see http://www.asme.org/terms/Terms_Use.cfm

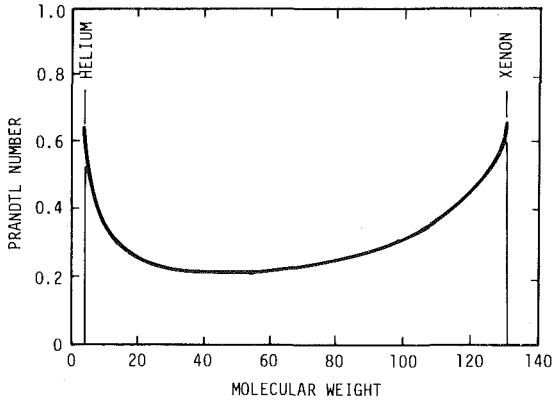

Fig. 2 Variation of prandtl number versus mixture molecular weight for helium-xenon at 283 K

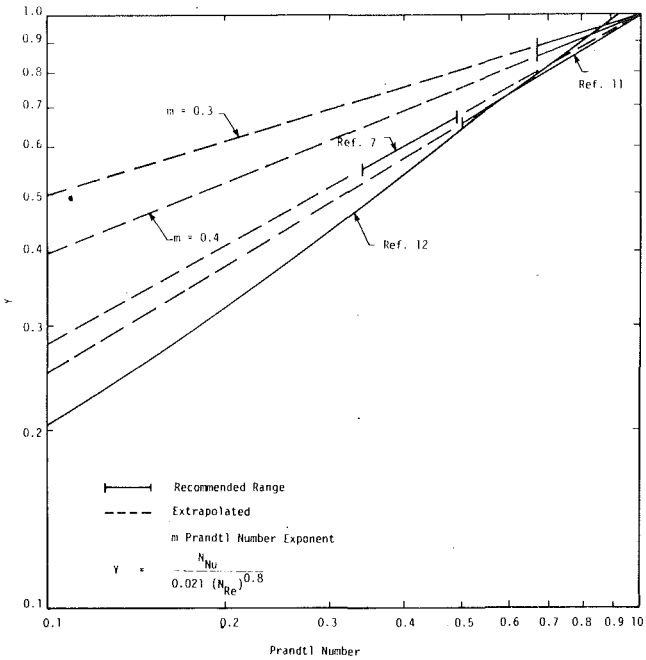

Fig. 3 Ratio of Calculated Nusselt Numbers to 0.021 $(N_{Re})^{0.8}$ versus Prandtl Number

their minima are greater than the helium-xenon mixture. Therefore, the Prandtl number range of interest for this investigation is from 0.2 to 0.7.

Heat Transfer Correlation

The following Nusselt heat transfer equation for turbulent gas flow in tubes has been recommended by many authors:

$$N_{Nu} = C(N_{Re})^n(N_{Pr})^m \quad (1)$$

Most of the authors use 0.8 as the exponent on the Reynolds number and slightly different constant factors (C), but exponents of the Prandtl number vary from 0.3 to 0.4. A few authors recommend correlations for gases with Prandtl number <0.7 with exponents of the

Table 1 Experimental Parameter Range

GAS	HYDROGEN	HELIUM	HELIUM-ARGON	HYDROGEN-CARBON DIOXIDE
Reynolds Number	7400-549000	5600-40500	18600-100000	21000-86000
Prandtl Number	0.67-0.70	0.67	0.42-0.49	0.34
T_w/T_b	1.1-3.0	1.3-3.0	1.1-1.8	1.2-1.8
x/D	4.9-114	3.9-66	2.1-82	2.0-50
References	8,9,10	8,9	6	7
Number of Data Points	361	45	236	80

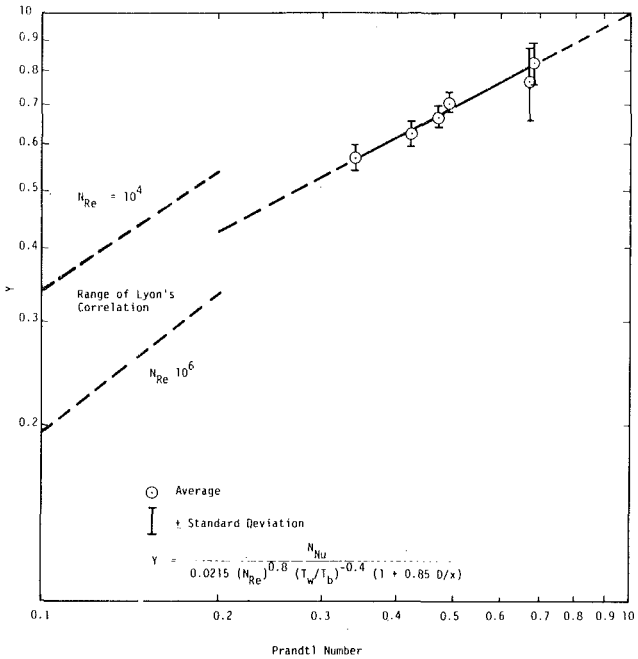

Fig. 4 Ratio of experimental local Nusselt numbers to 0.0215 (N_{Re})-$0.8(T_w/T_b)^{-0.4}(1 + 0.85\ D/x)$ versus Prandtl number

Prandtl number varying from 0.55 to 0.8. Figure 3 shows the effect of Prandtl number on the calculated Nusselt number for various correlations. At a Prandtl number of 0.7 the range of the correlations is 12 percent, however at a Prandtl number of 0.2, the range of the correlations is 90 percent. This figure demonstrates the danger of extrapolating heat transfer correlations based on experimental data at Prandtl numbers around 0.7 down to the lower range of interest for this investigation.

Experimental local heat transfer data for low Prandtl number gases [6, 7], hydrogen [8–10] and helium [8, 9] were analyzed to determine if a single correlating equation could be developed that adequately represented the experimental data and could be extrapolated to Prandtl numbers as low as 0.2. The range of parameters for the experimental data used is shown in Table 1. Fig. 4 shows the dependence of heat transfer on the Prandtl number. The best fit constant factor (C) is 0.0215 and the Prandtl number exponent (m) is 0.53 for all the experimental data which cover the Prandtl number range from 0.34 to 0.7. This constant factor and Prandtl number exponent compare favorably to reference [7] ($C = 0.021$, $m = 0.55$).

Nomenclature

A = cross-sectional area
C = constant
C_p = specific heat at constant pressure
D = hydraulic diameter
f = friction factor
g = gravitational constant
h = heat transfer coefficient
k = thermal conductivity
K_p = molar specific heat at constant pressure
L = axial length
m = Reynolds number exponent
M = molecular weight
n = Prandtl number exponent
N = dimensionless number
P = pressure
Q = thermal power
R = universal gas constant
S = surface area
T = temperature
v = specific volume
W = mass flow rate
x = distance in direction of flow
δ = difference, inlet-outlet
Δ = difference, wall-bulk
μ = viscosity

Downloaded 01 Jun 2010 to 171.66.16.59. Redistribution subject to ASME license or copyright; see http://www.asme.org/terms/Terms_Use.cfm

In the Prandtl number range from 0.7 to 1.0 the influence of the Prandtl number exponent ($0.3 < m < 0.6$) is within ± one standard deviation of the data. Therefore, the correlating equation can be extrapolated to a Prandtl number of 1.0 with confidence that any error introduced by the Prandtl number exponent would be small. Also shown in Fig. 4 is the extrapolation of the correlating line down to a Prandtl number of 0.2, as well as the extrapolated range covered by Lyon's [13] correlation for liquid metals. Lyon's correlation, based on experimental data, compares well with Martinelli's theoretical results [13]. At a Prandtl number of 0.2 the extrapolation of the gaseous correlation intersects the range of the extrapolation of Lyon's correlation at about the mid-point. Therefore, the following equation for constant property, fully developed conditions

$$N_{Nu} = 0.0215\,(N_{Re})^{0.8}(N_{Pr})^{0.53} \tag{2}$$

can be used to predict Nusselt numbers in the Prandtl number range of 0.2 to 1.0 with reasonable accuracy.

Gas Property Effects on Heat Exchanger Characteristics

Consider a coolant channel with axial turbulent flow. The following correlations may be applied to any flow cross section that can be described adequately by a hydraulic diameter (D):

$$D = \frac{4Al}{S} \tag{3}$$

The heat transfer area (S)

$$S = \frac{Q}{h\Delta T} \tag{4}$$

and the pressure drop (ΔP)

$$\Delta P = f\frac{L}{D}\frac{v}{2g}\left(\frac{W}{A}\right)^2 \tag{5}$$

The heat transfer coefficient (h) may be expressed by equation (2) for moderate ratios of surface of bulk temperature

$$h = 0.215\frac{k}{D}\left(\frac{WD}{A\mu}\right)^{0.8}(N_{Pr})^m \tag{6}$$

The specific volume (v) is calculated from the perfect gas equation of state

$$v = \frac{RT}{MP} \tag{7}$$

The thermal power (Q) transferred is

$$Q = WC_p\delta T \tag{8}$$

For turbulent flow, the friction factor (f) may be approximated by (N_{Re} from 5000 to 200,000 [14])

$$f = \frac{0.184}{\left(\frac{WD}{A\mu}\right)^{0.2}} \tag{9}$$

The specific heat per mole (K_p)

$$K_p = C_pM \tag{10}$$

The three characteristic dimensions of the coolant channel, flow cross section area A, length L, and heat transfer surface area S, are obtained from equation (1–8):

$$A = (N_{pr})^{0.51(1-m)}\frac{\sqrt{M}}{K_p}\left[\frac{RT}{gP}\frac{1.07}{\delta T\Delta T\Delta P}\right]^{1/2}Q \tag{11}$$

$$L = \frac{(N_{Pr})^{0.9(1-m)}(M)^{0.1}}{\mu^{0.2}}\left[\frac{gP\Delta P}{RT}\right]^{0.1}\left[\frac{\delta T}{\Delta T}\right]^{0.9}\frac{D^{1.2}}{0.0866} \tag{12}$$

$$S = \frac{(N_{Pr})^{1.4(1-m)}(M)^{0.6}}{\mu^{0.2}K_p}\left[\frac{RT}{gP\Delta P}\right]^{0.4}\frac{\delta T^{0.4}QD^{0.2}}{\Delta T^{1.4}0.0837} \tag{13}$$

The effect of fluid properties (N_{Pr}, M, K_p, and μ) on matrix volume or surface area according to equations (11–13) is shown in Fig. 5 with

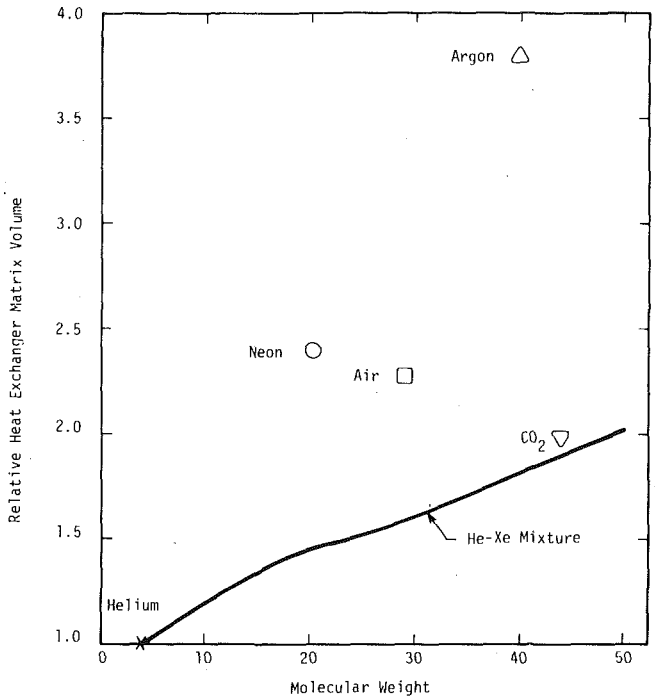

Fig. 5 Relative heat exchanger volume for pure gases, air, and binary mixtures (same gas on both tube and shell side)

the Prandtl number exponent (m) equal to 0.53. Helium is used as the reference, because it is best in regard to all three characteristic dimensions. To minimize volume ($\sim AL$), it is desirable for the gas to have low molecular weight, low Prandtl number, and high molar specific heat.

The fluid state (P/RT) has a weak influence on length, while both flow area and heat transfer area are influenced by temperature and pressure level. The thermal power level does not affect length, while both surface and flow areas are proportional to it. The gas temperature difference (δT equal to absolute difference between inlet and outlet temperature) is almost proportional to length, while flow area decreases and surface area increases with increasing δT. An increase in the temperature difference ΔT between the channel surface and gas gives a very significant reduction in surface area, a strong reduction in length and a slight reduction in flow area. An increase in pressure drop produces a reduction in flow and surface area and a very slight increase in length. The effect of hydraulic diameter is significant on length, is weak on surface area and does not appear in the flow area equation [11].

Fig. 6 shows the magnitude of the underestimation of heat exchanger characteristic dimensions using the ratio of equation (2) to a Colburn [13] or Stanton number [15] heat transfer correlation with m equal to ⅓ as a function of Prandtl number assuming molar specific heat and viscosity are constant. At a Prandtl number of 0.7 the underestimation of surface area and volume is only 10 percent, within design factors. However, at Prandtl numbers around 0.2 the surface area and volume are underestimated by 57 percent by using heat transfer correlation developed for normal Prandtl number (0.7) gases. Figure 6 is typical for closed cycle recuperators with gas mixtures on both shell and tube sides.

In fossil fired heat exchangers, the combustion gas side heat transfer coefficient and fouling factor control the overall heat transfer coefficient, so that the closed cycle gas turbine working fluid has a small effect on the required heat transfer surface area. However, in the recuperators, coolers, and bottoming cycle heat exchangers the working fluid can have a significant effect on the required heat transfer surface area.

Since the experimental heat transfer measurements with gas mixtures [5–7] have shown that existing scaling laws for gases with Prandtl numbers around 0.7 do not adequately represent the gas

Downloaded 01 Jun 2010 to 171.66.16.59. Redistribution subject to ASME license or copyright; see http://www.asme.org/terms/Terms_Use.cfm

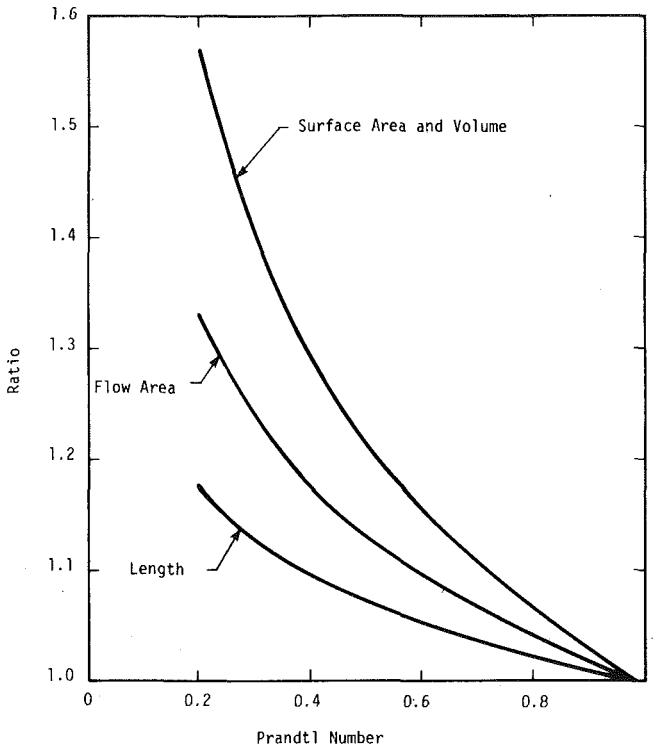

Fig. 6 Ratio of heat exchanger characteristic dimensions with equation (2) to a Colburn correlation

mixture heat transfer for turbulent flow in circular tubes, the existing heat transfer correlations for cross flow should be investigated to determine if the cross flow correlations are adequate for gas mixtures with low Prandtl numbers.

Summary

Equation (2) for constant property, fully developed conditions is recommended for use to predict Nusselt numbers for gases with Prandtl numbers in the range from 0.2 to 1.0. Previous investigations using gas mixtures with low Prandtl numbers may have underestimated the required heat transfer surface area.

References

1 Bammert, K., and Klein, R., "The Influence of He-He, He-N_2 and He-CO_2 Gas Mixtures on Closed-Cycle Gas Turbines," Gas Turbine Conference, ASME Paper 74-GT-124, Apr. 1974.

2 Telel'baum, S. D., "Mixtures of Gases as Future Working Media for Closed Cycle Gas Turbine Plant," *Teploenergetike*, 6, 1974.

3 Thompson, R. E., et al., "Nuclear Bi-Brayton System for Aircraft Propulsion Study," Contract F33615-77-C-0116, Westinghouse Advanced Energy Systems Division, Report No. WAES-TNR-234, Mar. 1978.

4 Coombs, M. G., and Norman, L. W., "Application of the Brayton Cycle to Nuclear Electric Space Power Systems," *Space Power Systems Engineering*, Academic Press, New York, 1966.

5 Taylor, M. F., et al., "Convection in the Closed Brayton Cycle," Office of Naval Research Contract No. N00014-75-C-00694, Second Annual Summary Report, University of Arizona, Apr. 1976.

6 Pickett, P. E., "Heat and Momentum Transfer to Internal, Turbulent Flow of Helium-Argon Mixtures in Circular Tubes," University of Arizona, July 1976.

7 Serksnis, A. W., "Convective Heat Transfer for Ship Propulsion," Office of Naval Research Contract No. N00014-75-C-0694, Fourth Annual Summary Report, University of Arizona, Apr. 1978.

8 Taylor, M. F., "Experimental Local Heat-Transfer and Average Friction Data for Hydrogen and Helium Flowing In a Tube at Surface Temperatures Up to 5600°R," NASA TN D-2280, Apr. 1964.

9 Taylor, M. F., "Experimental Local Heat-Transfer Data for Precooled Hydrogen and Helium at Surface Temperatures Up to 5300°R," NASA TN D-2595, Jan. 1965.

10 Hendricks, R. C., et al., "Experimental Heat-Transfer Results for Cryogenic Hydrogen Flowing in Tubes at Subcritical and Supercritical Pressures to 800 Pounds Per Square Inch Absolute," NASA TB D-3095, Mar. 1966.

11 Kays, W. M., *Convective Heat and Mass Transfer*, McGraw-Hill, New York, 1966.

12 Sleicher, C. A., and Rouse, M. W., "A Convenient Correlation for Heat Transfer to Constant and Variable Property Fluids in Turbulent Pipe Flow," *International Journal Heat Mass Transfer*, Vol. 18, 1975.

13 Jakob, M., *Heat Transfer*, Vol. II, John Wiley and Sons, New York, 1957.

14 McAdams, W. H., *Heat Transmission*, Third edition, McGraw-Hill, New York, 1954.

15 Kays, W. M., and London, A. L., *Compact Heat Exchangers*, McGraw-Hill, New York, 1958.

Downloaded 01 Jun 2010 to 171.66.16.59. Redistribution subject to ASME license or copyright; see http://www.asme.org/terms/Terms_Use.cfm

H. C. Simmons
Director of Engineering.

C. F. Harding
Project Engineer.

Gas Turbine Fuel Systems Division,
Parker Hannifin Corporations,
Cleveland, OH 44112

Some Effects of Using Water as a Test Fluid in Fuel Nozzle Spray Analysis

A systematic investigation was made of the differences in atomizing performance between water and kerosene fuel for six simplex fuel nozzles of small flow capacity. A large number of tests was run using two methods of spray analysis, to determine the effect of nozzle liquid pressure drop (ΔP_F) on Sauter Mean Diameter (SMD). It was found that there is a clearly-defined relationship dependent on both the relative values of surface tension and also on a Weber Number calculated for conditions in the liquid film at the nozzle discharge orifice. It is concluded that large errors in estimating SMD for modeling programs are possible if results observed with water are assumed to be representative of behavior with kerosene fuel.

Introduction

Gas turbine fuel nozzles are routinely tested to determine whether their performance meets specifications both for flow rates and spray quality. It is a common practice to use standardized liquids for this purpose in lieu of the actual fuel to be employed in service use and kerosene-type hydrocarbons such as MIL-F-7024 type 2 are generally employed. However there has always been an interest in using water as the test liquid since it is readily available in pure form and also has the advantage of being nonflammable. The latter point has recently become more significant with the increasing use of spray-analysis equipment involving lasers, such as light-scattering devices, where the problems of safety of operation are increasingly important.

In the course of attempts to correlate spray analysis results obtained by different methods it was found that some small-size simplex nozzles exhibited large and variable differences in Sauter Mean Diameter (SMD) between kerosene and water at comparable conditions of operation, and it was decided to investigate the effect on a systematic basis.

Methods of Spray Analysis

The data given in this paper were obtained using the Malvern Droplet Size Distribution Analyzer type ST1800 and the Parker High-Speed Analyzer Mark 2 (coded here as PH2), both located in the Cleveland, Ohio, Laboratories of Parker Hannifin Corporation. The Malvern equipment has been described in principle by Swithenbank, et al. [1]; it works by analysing the diffraction pattern produced by a continuous laser beam passing through the spray cloud and fitting the data to a Rosin-Rammler distribution from which the Sauter Mean Diameter (SMD) is easily calculated. The instrument is quite suitable for fuel nozzles, especially those of small flow capacity, and gives a result in a few minutes for each test condition. There was an operational advantage originally in using water as the test liquid, but later kerosene fuel could also be used.

The Parker Analyzer has been described previously [2]; it is essentially a "stop-action" flash-illuminated tele-microscope using a T.V. camera and automatic scanning of the drop shadows to size and count individual drops. It is used to traverse the spray, taking 100 frames at each of about 50 stations; the data are then summed and area-weighted to give a numerical size-by-class distribution from which all other statistics including SMD are computed and printed-out. A single test condition takes about 20 min to run but produces much more information than the Malvern instrument; it is particularly useful in investigating variations in spray quality as a function of position in the spray whereas the Malvern equipment gives an averaged estimate of spray quality for the entire spray. Arrangements were made to run tests on given fuel nozzles on both analyzers with both fuel and water. After it was shown that similar results were obtained with both analyzers additional tests were confined to the Malvern. This paper is not, however, to be regarded as a definitive comparison between the two analyzers.

Relative Physical Properties of Liquids

The physical properties of interest with regard to atomization are given in Table 1 for water and kerosene-type calibrating fluid (hereafter described as kerosene or fuel) at the temperature (80°F) normally used in fuel nozzle testing. It will be noted that the absolute viscosities are almost the same; there is a 30 percent difference in density but the surface tension is higher by a factor of 3 for water.

The effect of liquid density on the flow rate th rough a simplex nozzle is well understood. Following the analysis given in reference [3] it is clear that the discharge coefficient of the nozzle is uniquely related to the spray angle so if two liquids of different densities ρ_1 and ρ_2 exhibit similar spray angles it can be assumed that they would give the same volume flow rate $\dot{Q}$ for the same average exit velocity V. Since however, the nozzle pressure drop $\Delta P_F \propto \rho V^2$ it follows that $\dot{Q}_2/\dot{Q}_1 = \sqrt{\rho_1/\rho_2}$ for a comparison at the same ΔP_F. Similarly, the mass flow rate $\dot{W} \propto \rho$ for the same V but $\dot{W}_2/\dot{W}_1 = \sqrt{\rho_2/\rho_1}$ for the same ΔP_F.

Contributed by the Gas Turbine Division and presented at the Gas Turbine Conference and Products Show, New Orleans, La., March 10–13, 1980 of THE AMERICAN SOCIETY OF MECHANICAL ENGINEERS. Manuscript received at ASME Headquarters December 17, 1979. Paper No. 80-GT-90.

Copyright © 1981 by ASME
Downloaded 01 Jun 2010 to 171.66.16.59. Redistribution subject to ASME license or copyright; see http://www.asme.org/terms/Terms_Use.cfm

It is generally found that the spray angles are in fact identical between water and kerosene fuel so since $\rho_{water}/\rho_{fuel} = 1{\cdot}30$, $\dot{Q}_{water}/\dot{Q}_{fuel} = 0{\cdot}88$ and $\dot{W}_{water}/\dot{W}_{fuel} = 1{\cdot}14$.

Since these differences are not large it was decided to compare the behavior of the two liquids at given values of ΔP_F. (It should be noted, however, that this procedure would not be appropriate when the performance of a given nozzle is to be determined for alternative fuels of different physical properties; in this case it would be more usual to compare spraying performance at identical mass flow or heat unit rates.)

If any significant differences in spray performance between kerosene and water at similar ΔP_F are noted it is probable that they can be attributed to the differences in surface tension rather than the density.

Description of Nozzles Studies

Data are reported here for six fuel nozzles, coded A – F, all of the simplex pressure-atomizing type and all of the small flow number (F_N) capacity; the spray angles varied from 45 to 115 deg, and were essentially identical for both liquids. The nozzles were samples from current experimental or production gas turbine applications. The leading particulars are given in Table 2 which includes calculated values of liquid film thickness and a Weber Number which will be discussed later.

All nozzles gave acceptable symmetrical sprays free from streaks or voids. The spray measurements were made approximately 2 in. from the nozzle. Using the Malvern ST1800 the 6mm dia laser beam passed through the center of the spray; with the PH2 the normal technique of scanning a number of positions traversing a diameter of the spray was followed.

Test Results

The curves shown in Fig. 1 for the type A nozzle are quite typical in showing the decrease in SMD with increasing ΔP and clearly show the increase in SMD when using water. The degree of repeatability of these tests is also indicated by the small spread of the points. It is standard practice to plot data on log-log scales as in Fig. 2, and when this is done it is apparent that there is a well-defined change of slope in each case, the point of inflection being at a higher ΔP_F for water. A large number of tests was run to define the exact shape of these curves and not all the test points are shown.

This graph makes it clear that the use of water rather than fuel as the test fluid gives very different SMD results with this nozzle, which could be very misleading in modeling studies. It also demonstrates a previously unsuspected effect in that the nozzle exhibits a deterioration in SMD at low ΔP's even with kerosene. On the same graph the data obtained with the same nozzle on the PH2 analyzer is also shown and although the PH2 tended to give slightly higher SMD values, the agreement of the slopes was considered sufficiently good that only a few other confirmatory tests were made with the PH2.

Table 1 Properties of liquids at 80°F (26.7°C)

Liquid	Specific Gravity	Viscosity Absolute centipoises	Viscosity Kinematic centistokes	Surface Tension (dynes/cm.)
Water	0.996	0.87	0.87	73
Kerosene*	0.765	0.92	1.20	25

* MIL-F-7024 Type II Calibrating Fluid

\+ or density in g/cm³

Table 2 Dimension characteristics of the simplex nozzles tested

Type	F_n lb/√psi.hr	D_o Inch	2θ Degrees	t_F* µm	t_F µm	ΔP (We = 1) psi Water	ΔP (We = 1) psi Fuel
A	1.68	0.016	70°	51	62	67	18
B	0.28	0.007	85°	19	26	158	41
C	0.52	0.012	100°	21	32	128	34
D	1.2	0.014	60°	41	48	87	23
E	6.5	0.028	45°	112	121	34	9
F	2.5	0.022	115°	55	102	41	11

The results with the other five nozzles are given in Figs. 4–8 and it can be seen that the same general characteristics of change of slope were established in every case, resulting in large differences in SMD at low ΔP_F but comparatively small differences at high ΔP_F. It was evident therefore, that a common basis might be found to correlate the results.

Correlation of Results

Earlier unpublished work at Parker Hannifin had shown that the values of a Weber number (We) calculated in a particular manner (see Appendix 1) for the liquid film leaving the discharge orifice were in the region of 1 (the critical value) for fuel at low nozzle ΔP_F, and that We $\propto \Delta P_F/\rho_F\sigma$. When the calculations were made for the present nozzles it was found that We at the points of inflection of the SMD/ΔP_F curves was in every case close to 1; in other words the SMD changed more rapidly with We below the critical value than above. It was decided however, to fit the data by lines on the log-log plots for the two regions of We and accept the resulting value of We at the in-

Nomenclature

SMD = Sauter mean diameter, µm, µm,[1]
ρ = liquid density, g/cm³, kg/m³, 10^{-3} g/cm³
ρ_a = air density
σ = surface tension, dynes/cm, N/m, 10^{-3} dynes/cm
η = absolute viscosity, centipoise, mPa·s, 1 centipoise
$\dot{W}$ = mass flow rate, lb/hr, kg/hr, 2.205 lb/hr
$\dot{Q}$ = volume flow rate
V = liquid velocity, ft/s, m/s, 3.281 ft/s
ΔP = liquid pressure drop through nozzle, psi, kPa, 0.145 psi
F_I = inertial force
F_N = flow number ($=\dot{W}/\sqrt{\Delta P_F}$), lb/(√psi·hr), kg/(√kPa·hr), 5.79 lb/(√psi·hr)
We = Weber number
We_c = critical Weber number,
t_F = estimated actual film thickness (for calculation of We), µm, µm
t_F* = hypothetical film thickness (as used in equation (SF7), µm, µm
n = exponent in Rosin-Rammler equation
D_0 = Orifice diameter of simplex nozzle, in. mm, .0394 in.
D_A = air-core diameter
A_0 = orifice area
A_A = air core area
A_F = flow area
θ = included spray angle/2, deg, deg

Subscripts

F = liquid
K = kerosene fuel
a = air
c = critical value
* = actual units are not required in this paper.
W = water

[1] Units indicated are conventional units, SI units and conversion—1 SI unit =, respectively.

Downloaded 01 Jun 2010 to 171.66.16.59. Redistribution subject to ASME license or copyright; see http://www.asme.org/terms/Terms_Use.cfm

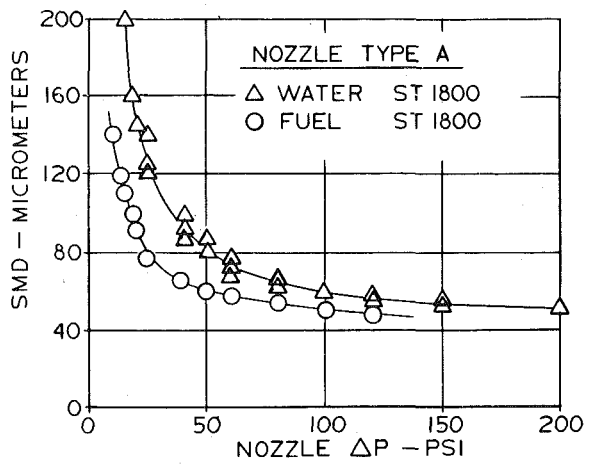

Fig. 1 Comparison of atomization performance of a simplex nozzle using water and kerosene fuel

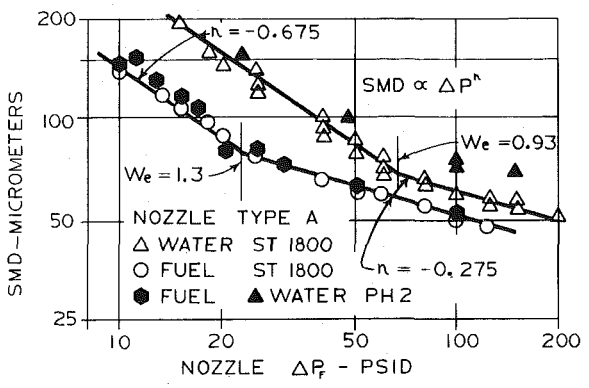

Fig. 2 Effect of test fluids on SMD with type A nozzle using two methods of spray analysis

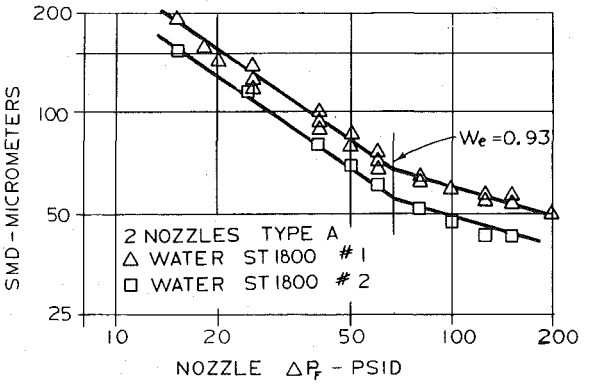

Fig. 3 Variation in SMD between two nozzles of the same design (Type A)

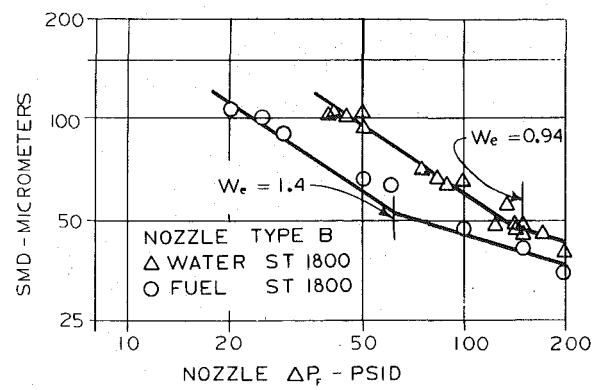

Fig. 4 SMD/ΔP_F relationship, nozzle type B, using fuel and water

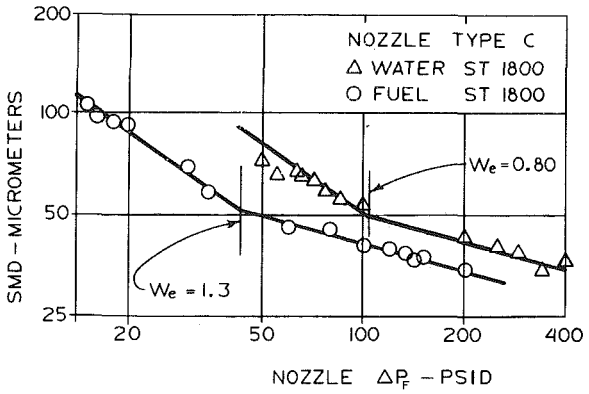

Fig. 5 SMD/ΔP_F relationship, nozzle type C, using fuel and water

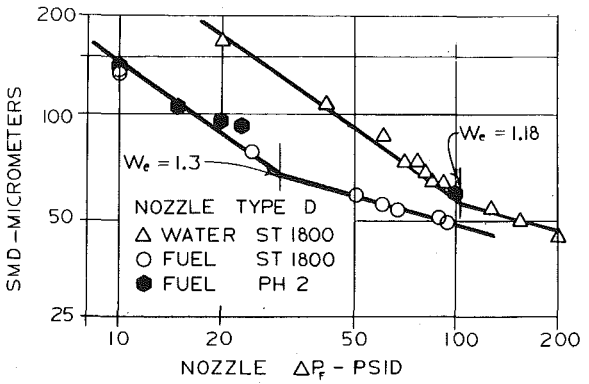

Fig. 6 SMD/ΔP_F relationship, nozzle type D, using fuel and water

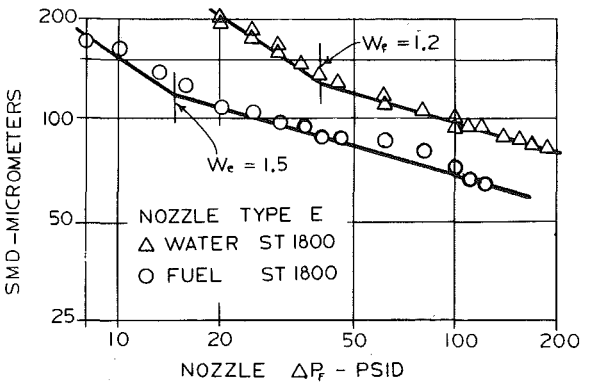

Fig. 7 SMD/ΔP_F relationship, nozzle type E, using fuel and water

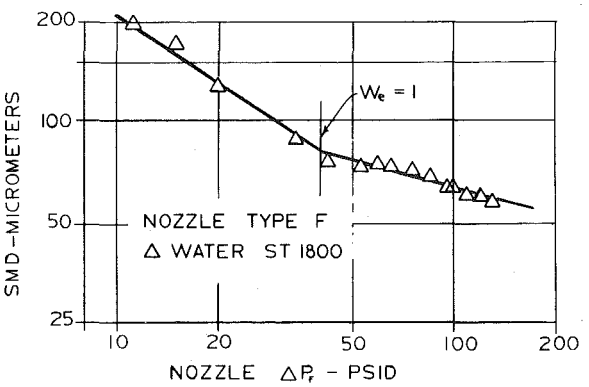

Fig. 8 SMD/ΔP_F relationship, nozzle type F on water

Downloaded 01 Jun 2010 to 171.66.16.59. Redistribution subject to ASME license or copyright; see http://www.asme.org/terms/Terms_Use.cfm

tersection. For all the higher We (ΔP_F) data the slope chosen was that given by Simmons in reference [4], based on a large amount of previous data.

$$[\text{for We} > 1]\ \text{SMD} \propto \Delta P_F^{-0.275} \tag{1}$$

For the low We (ΔP_F) values it was found that a common slope giving a good fit to the data was

$$[\text{for We} < 1]\ \text{SMD} \propto \Delta P_F^{-0.675} \tag{2}$$

The values of critical We determined in this manner are shown on the graphs and also given in Table 3 from which it is seen that they are remarkably close to 1, bearing in mind the somewhat indirect methods used. The values for the fuel tests were generally slightly higher than for water.

The results given in Fig. 3 are interesting as showing that two nominally similar nozzles exhibited the same slopes and inflection point although the SMD levels differed by as much as 15 percent.

The general agreement amongst all the data is shown clearly by Fig. 9 in which the test points are normalized to the SMD and Weber number at the points of inflection.

It is noteworthy that for We > the critical value (≈ 1) the data fit the SMD prediction equation (SF7) given in reference [3], not only in terms of ΔP but also the liquid film thickness t_F*, values of which are tabulated in Table 2. Equation (22) of reference [3] can be written as

$$\text{SMD} \propto t_F^{*0.375} \cdot \Delta P^{-0.275} \tag{3}$$

and Fig. 10 shows the agreement of the first term with data from the range of nozzles used. It also indicates the mean difference in SMD between water and fuel at a fixed ΔP above the critical Weber Number, this being about 20 percent. If this difference is expressed in the usual relationship of SMD to surface tension σ it is equivalent to

$$\text{SMD} \propto \sigma^{0.16}\ [\text{for We}_K, \text{We}_w > 1] \tag{4}$$

and Fig. 11 shows that this value fits other comparative test points selected from the data for the We > 1 cases. For any pair of curves such as in Fig. 2 we have three definable regions: (1) We > 1 for both liquids (2) We < 1 for water but > 1 for fuel and (3) We < 1 for both liquids. Figure 11 shows that for the last case

$$\text{SMD} \propto \sigma^{0.51}\ [\text{for We}_K, \text{We}_w < 1] \tag{5}$$

which is more than a 70 percent increase from fuel to water. There is no doubt therefore that for simplex nozzles in this range of flow capacity serious errors are possible if it is assumed that the results with water are representative of those with fuel.

It should be noted that if the results are compared at equal mass flow rates instead of equal ΔP_F the exponent in equation (4) changes only from 0.16 to 0.19 which is not significant for our purpose.

Prediction of the Weber Number Effect

The slope of the SMD/ΔP line for We < 1 is shown to be −0.675, so this portion of the curve can be represented by

$$[\text{for We} < 1]\ \text{SMD} \propto \Delta P^{-0.275} \cdot \text{We}^{-0.40} \tag{6}$$

which provides in conjunction with equation (3) a means of predicting with fair accuracy the shape of the curve for a given simplex nozzle after calculating the Weber Number by the method of Appendix 1. It is also possible to predict performance on kerosene fuel from data obtained using water by the use of equations (3–6) as appropriate which may be of value in some cases. It should be noted that the Weber Number effect with fuel occurs only for a limited range of small nozzle sizes (since there is little practical interest in sprays having SMD > 150 μm and Fig. 7 shows that only a small part of the range

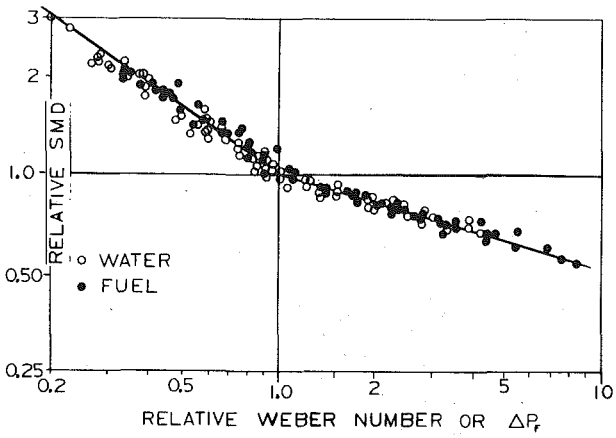

Fig. 9 Nondimensional correlation of effect of Weber number on SMD

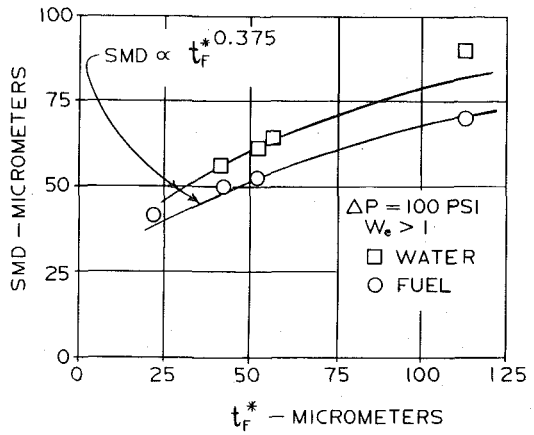

Fig. 10 Correlation of test results with SF7 prediction equation [4]

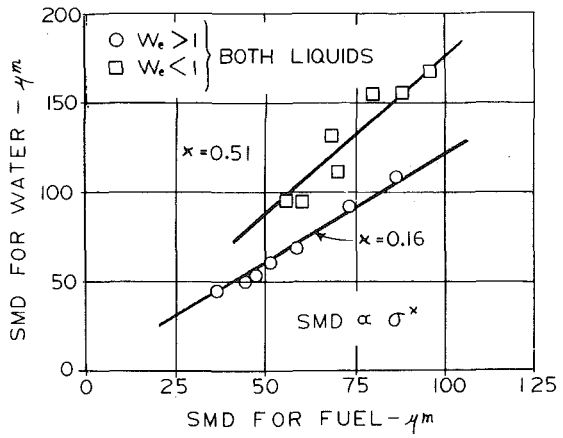

Fig. 11 Relationship of SMD and surface tension for different Weber number regions

Table 3 Weber number at point of inflection of SMD/ΔP_F curves. (We_c) nozzle ranked in order of increasing t_F

Type	t_F, μm	We_c Water	We_c Fuel
B	26	0.94	1.4
C	32	0.80	1.3
D	48	1.18	1.3
A	62	0.93	1.3
F	102	1.0	-
E	121	1.2	1.5

Downloaded 01 Jun 2010 to 171.66.16.59. Redistribution subject to ASME license or copyright; see http://www.asme.org/terms/Terms_Use.cfm

of the type E nozzle (F_N = 6-5) is affected. However, for the smaller nozzles the low We region extends into the operating flow range and can have a significant effect on spray quality.

Effect on Drop-Size Distribution

An interesting aspect of the test results obtained by the ST1800 Analyzer is that in every test series for a given nozzle there was a variation of the Rosin-Rammler exponent "n" with ΔP. Typical results are given in Fig. 12 and show essentially constant values of "n" for We > 1 but increasing below We < 1 corresponding to the higher SMD readings. It is characteristic of the Rosin-Rammler equation that higher values of "n" represent narrower distributions so the indications from Fig. 12 are that the higher SMD's resulting from low Weber Numbers are associated with a reduction in the range of drop sizes. A possible interpretation of this effect is that when the surface tension forces are significantly greater than the inertial forces the process of atomization by comminution is terminated earlier, thus giving fewer small-size drops. The constant value of "n" for We > 1 is in agreement with the findings of reference [3] that all drop-size distributions observed for good quality fuel nozzles are similar on a nondimensional basis; those results were all obtained using kerosene or hydrocarbon fuels and all were above the critical Weber number.

Summary and Conclusion

An interesting aspect of the work reported here is that it is doubtful if the effects of Weber number demonstrated would have been elucidated without running the large number of test points (over 350) made possibly by the Malvern ST1800 Analyzer. By comparison all other methods described in the literature for use with fuel nozzles are relatively slow and in some cases provide more data than are required for parametric investigations of this kind. The limited data obtained in repeat testing using the Parker PH2 Analyzer was in quite good agreement with the data obtained with the Malvern ST1800 Analyzer.

It has been shown that for a number of simplex fuel nozzles of small flow number and a range of spray angles there are significant differences in atomizing performance (SMD) between kerosene fuel and water. These differences are related to surface tension and results can be correlated by the use of a calculated Weber Number for the liquid film at the discharge orifice.

Serious errors may be introduced into modeling calculations if it is assumed that SMD data obtained using water are representative of performance with kerosene fuel. An equation is given for prediction of SMD allowing for a change in surface tension and Weber Number.

Acknowledgments

The authors wish to thank the Parker Hannifin Corporation and in particular Mr. C. J. McKeon, General Manager of the Gas Turbine Fuel Systems Division, for permission to publish this paper.

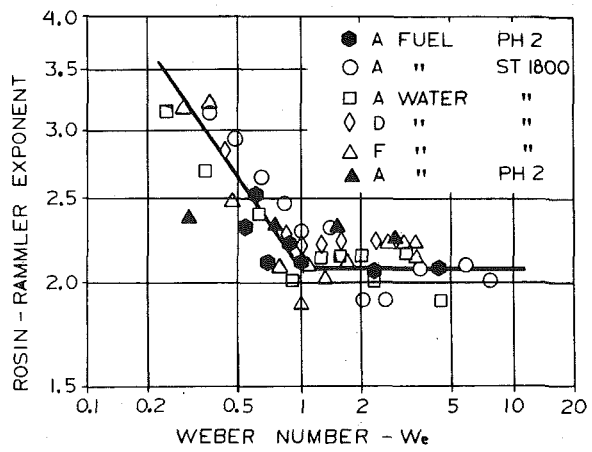

Fig. 12 Correlation of Rosin-Rammler exponent "n" and Weber number

References

1 Swithenbank, J., et al., "A Laser Diagnostic Technique for the Measurement of Droplet and Particle Size Distribution," University of Sheffield, England, 1976.

2 Simmons, H. C., "The Correlation of Drop-Size Distributions in Fuel Nozzle Sprays," ASME JOURNAL OF ENGINEERING FOR POWER, Vol. 99, July, 1977.

3 Giffen, E. and Muraszew, A., *The Atomization of Liquid Fuels*, John Wiley & Sons, New York, 1953, P. 108.

4 Simmons, H. C., "The Prediction of Sauter Mean Diameter for Gas Turbine Fuel Nozzles of Different Types," ASME Paper No. 79-WA/GT-5, Dec. 1979.

APPENDIX

Calculation of Weber Number We in the Liquid Sheet at the Nozzle Orifice Edge

I Derivation of Weber Number. Weber Number is defined as the ratio of inertial forces to surface tension forces.

If $F_{I_a} \equiv$ inertial force due to the air which is proportional to the pressure equivalent of velocity multiplied by an area then $F_{I_a} \propto \rho_a V_R{}^2 L t_F$ where Lt_F is the area and t_F is the liquid sheet thickness or lamina leaving the orifice, ρ_a is the air density and V_R is the relative velocity between the air and liquid which equals the liquid velocity in the case of a simplex nozzle.

If σ is the surface tension of the liquid which is defined as force/unit length then the surface force F_σ is equal to σL where L is a chosen length normal to the direction of the force.
Thus the Weber number We,

$$\text{We} = \frac{F_{I_a}}{F_\sigma}$$

$$= \rho_a V_R{}^2 L t_F / \sigma L$$

$$= \rho_a V_R{}^2 t_F / \sigma \tag{1}$$

or in terms of pressure since $V_R{}^2 = V_F{}^2$ where V_F is the liquid velocity,

$$\text{We} = \rho_a 2 g_c \Delta P_F t_F / \rho_F \sigma \tag{2}$$

II Derivation of $t_F \sim$ Liquid Sheet Thickness. A typical simplex fuel nozzle is shown diagrammatically in Fig. 13.

let A_A = air core area

$$= \pi D_A{}^2/4$$

let A_o = orifice area

$$= \pi D_0{}^2/4$$

let A_F = the flow area

$$= A_o - A_A$$

$$= \pi D_0{}^2/4 - \pi D_A{}^2/4$$

but $D_A = D_0 - 2t_F$

therefore

$$A_F = \pi D_0{}^2/4 - \pi(D_0 - 2t_F)^2/4$$

$$= \pi D_0{}^2/4 - \pi D_0{}^2/4 + \pi D_0 t_F - \pi t^2$$

$$= \pi D_0 t_F \text{ For } t_F \ll D_0 \tag{3}$$

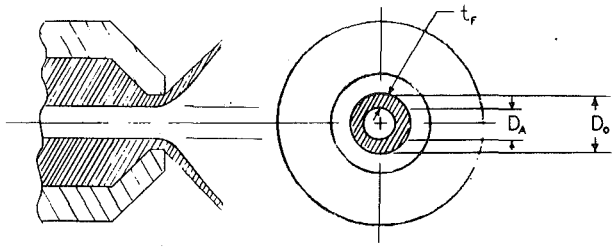

Fig. 13 Diagrammatic sketch of a typical simplex nozzle

Downloaded 01 Jun 2010 to 171.66.16.59. Redistribution subject to ASME license or copyright; see http://www.asme.org/terms/Terms_Use.cfm

The coefficient of discharge C_d for a simplex nozzle is defined on the assumption that the entire ΔP_F is converted to axial velocity and ignores the tangential component. However, if both C_d and the spray angle 2θ are identical for two cases (e.g. two different liquids in a given nozzle) then the air core diameter D_A is the same. As between kerosene fuel and water reference [3] reported no significant difference in C_d or 2θ and this was confirmed by the present tests. This can also be shown by the following:

let C_d = orifice discharge coefficient

then $A_F = C_d Ao/\cos\Theta$

but $A_F = \pi D_0 t_F$ (from equation (2))

therefore

$$\pi D_0 t_F = C_d \pi D_0^2/4 \cos\Theta$$

$$\text{or} \quad t_f = C_d D_0/4 \cos\Theta \tag{4}$$

Hence it is seen that the film thickness is independent of the differences in properties between fuel and water. In conventional units it is shown by reference [4] that for either liquid flowing through the nozzle,

$$t_F = .48\, F_N^*/D_0 \cos\Theta\ \mu\text{m} \tag{5}$$

where F_N^* = The nozzle flow number

$[LB_M/HR/\sqrt{PSI}]$ determined

For standard calibrating

fluid (Sp. Gr. = .77)

where D_0 = orifice diameter ~ in.

Θ = (included spray angle)/2 deg

and in S.I. units,

$$t_F = 71.2\, F_N^*/D_0 \cos\Theta\ \mu\text{m} \tag{6}$$

where

F_N^* has the same meaning as above but in different units ~ $\text{kg/hr}/\sqrt{KP_a}$

where D_0 is in mm

Note: In reference [4] and in the body of this paper a hypothetical film thickness t_F^* is used in the SMD prediction equations. t_F^* ignores the effect of spray angle, i.e., $t_F^* = t_F \cos\Theta$.

III Simplified Weber Number Equation for both Water and Fuel (from equation (1)). Note: The air density used in the following equations is that for 60°F (15.5°C) and standard atmospheric pressure.

In conventional units using fuel (kerosene),

$$\text{We} = 4.28 \cdot 10^{-4}\, \Delta P_K F_N^*/D_0 \cos\Theta \tag{7}$$

where

ΔP_K = fuel pressure drop

and for water,

$$\text{We} = 1.12 \cdot 10^{-4}\, \Delta P_W F_N^*/D_0 \cos\Theta \tag{8}$$

where

ΔP_W = water pressure drop

In S. I. units using fuel,

$$\text{We} = 9.05 \cdot 10^{-3}\, \Delta P_K F_N^*/D_0 \cos\Theta \tag{9}$$

and for water,

$$\text{We} = 2.38 \cdot 10^{-3}\, \Delta P_W F_N^*/D_0 \cos\Theta \tag{10}$$

therefore, using equation (7) as an example, the critical pressure ΔP_{K_c} at which the Weber number is unity,

$$\Delta P_{K_c} = D_0 \cos\Theta/4.28 \cdot 10^{-4}\, F_N^* \tag{11}$$

Downloaded 01 Jun 2010 to 171.66.16.59. Redistribution subject to ASME license or copyright; see http://www.asme.org/terms/Terms_Use.cfm

Interferometric Measurements in a Turbine Cascade Using Image-Plane Holography

P. J. Bryanston-Cross
T. Lang
The Advanced Research Laboratories,
Rolls-Royce Ltd.,
Derby, U.K.

M. L. G. Oldfield
R. J. G. Norton
Department of Engineering Science,
Oxford University,
Oxford, U.K.

A holographic technique used to produce image plane interferograms with white light reconstruction is described. This was used to study the transonic flow in a passage of a turbine stator cascade at a typical Reynolds number, Mach number, and free stream to blade surface temperature ratio. Both absolute holographic interferograms (fringes of constant flow density) and differential holographic interferograms (changes of density in 100 μsecs) are presented showing fine details in the boundary layer flow, trailing edge shocks, and wake structure. By counting the fringes on the interferograms, the free stream and surface Mach numbers and boundary layer temperature gradients can be determined.

1 Introduction

A basic tool for gas turbine aerodynamic research is the two-dimensional cascade tunnel, using a repertoire of measuring techniques. These commonly include surface pressure measurements, the use of traversing pressure probes and schlieren or shadowgraph for flow visualization. Optical techniques have an advantage over other methods in that they are noncontacting and do not introduce disturbances into the airflow. As a measurement technique holographic interferometry visualizes changes of density in the airflow. It can be used to give both a complete description of the free stream Mach number distribution and diagnostically to investigate local perturbations in the flow.

Although it is normally considered that the benefits of holography are associated with the production of three-dimensional images, interferograms of this type tend to be of limited resolution and exhibit speckle effects. This paper describes some preliminary experiments in a transient cascade tunnel using a two-dimensional technique and white-light reconstruction which produces high resolution interferograms of the flow.

2 Cascade Tunnel

The Oxford cascade tunnel [1, 2] is an isentropic light piston tunnel which generates a flow having a stagnation temperature of 430 K over a cascade of blades at 290 K. Full scale Reynolds and Mach numbers are achieved for a flow duration of 0.4 s.

The transient nature of the tunnel is an advantage for holographic work as reference exposures can be made only a few seconds before the run. Preliminary tests using a fast response displacement transducer on all three axes showed that the working section displacements during the run were at most ±0.16 mm.

Because the working section moves as a whole, and the windows are parallel and of schlieren quality, movement does not change the optical pathlength, and hence does not introduce spurious holographic fringe shifts or degrade the resolution. However, movements in a plane perpendicular to the optical path produce a corresponding (0.16 mm maximum) overlapping of the blade images formed from the two exposures used in the holographic technique.

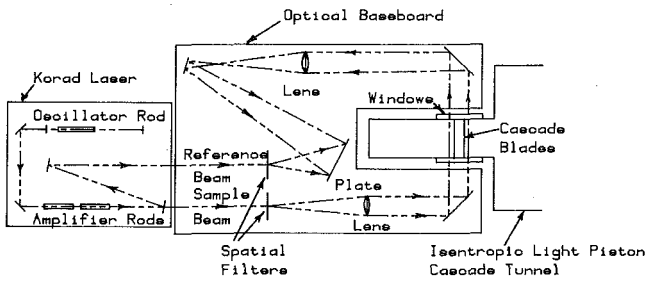

Fig. 1 Optical system used to obtain image plane holograms of the cascade flow

3 Holographic System

The holographic techniques employed in this work are commonly referred to as: dark field, off axis, image plane, white light reconstructed double exposure holograms [3–7].

The optical system (Fig. 1) used consisted of a rigid table which fitted around the tunnel test section but was mechanically isolated from it. Onto this table were mounted the optical components and a Korad double pulse ruby laser. The output beam from the laser was split into two parts, 65 percent forming the sample beam and the remainder the reference beam. The collimated sample beam was spatially filtered [8], and then expanded by a lens to form a 5 in. dia parallel beam. By the use of two mirrors the beam was directed through the test section parallel to the blade surface and perpendicular to the direction of flow. A second relay lens imaged the blade onto a holographic plate. This optical layout is more commonly associated with schlieren work [9] than interferometry. It was also noted that if a magnified image is projected onto the holographic plate, the focusing of the blade image is more easily optimized. The path length of the reference beam was increased by internal reflection inside the laser

Contributed by the Gas Turbine Division and presented at the Gas Turbine Conference and Products Show, New Orleans, La., March 10–13, 1980 of THE AMERICAN SOCIETY OF MECHANICAL ENGINEERS. Manuscript received at ASME Headquarters December 17, 1979. Paper No. 80-GT-91.

Copyright © 1981 by ASME
Downloaded 01 Jun 2010 to 171.66.16.59. Redistribution subject to ASME license or copyright; see http://www.asme.org/terms/Terms_Use.cfm

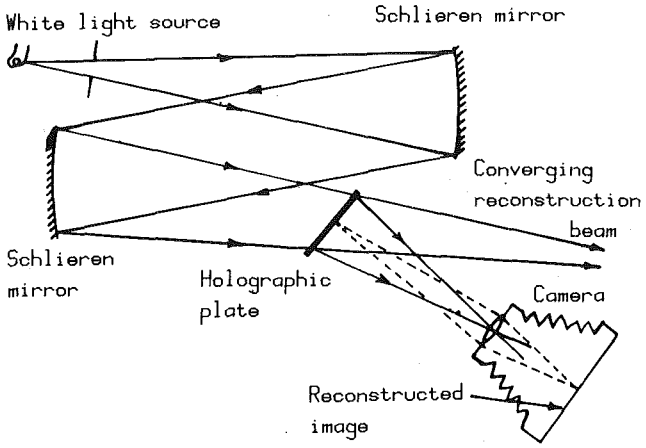

Fig. 2 White light reconstruction system

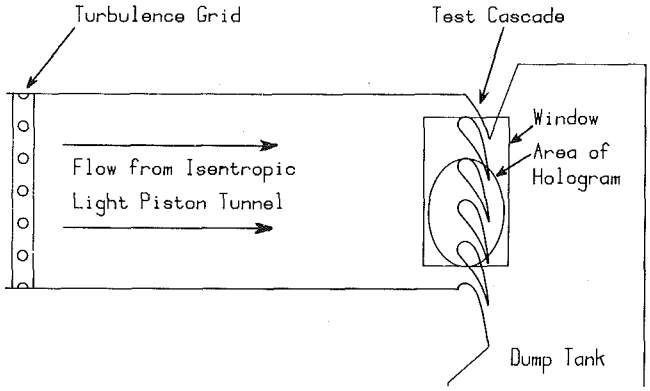

Fig. 3 General arrangement of test cascade

to match that of the sample beam. The reference beam was also spatially filtered and then combined with the sample beam to form an image plane hologram.

A white light method of reconstruction was used, similar to that described by Johoda and Sieman [6]. As shown in Fig. 2, a convergent beam of white light was projected through the holographic plate in the same direction as the original reference beam. The conjugate diffraction image [11] produced a wavefront corresponding to that of the original sample beam. By placing a lens at the point where the rays focus, an image of the flow field was projected onto a photographic plate. In using this method of reconstruction the speckle pattern normally associated with holographic images is avoided.

Two types of holograms were taken using this system:

1 **Absolute Hologram.** A reference exposure is made by firing the laser just before the tunnel run and a second exposure is taken during the run. The interference fringes on the image reconstructed from the hologram can be interpreted as contours of constant density in the cascade passage. These interferograms are equivalent to those obtained with a Mach Zender interferometer with the path lengths matched over the whole field of view.

The advantage of a holographic interferometer is that the reference and sample beams are separated in time, but use the same optical path. It is, then, only sensitive to changes in the flow and not to imperfections in the optical system. With a Mach Zender the two beams traverse different optical paths which must be accurately matched to within a wavelength if background fringes are to be eliminated. This requires high quality optics and precise adjustments to obtain absolute interferograms.

2 **Differential Hologram.** The two exposures (or laser pulses) are separated by 100 μs (which can be varied) and interference fringes represent contours of constant density change in 100 μs. This is not possible with a Mach Zender system with an incoherent light source.

4 Test Cascade

A test cascade of transonic turbine stator blades (Fig. 3) was used for the test. These provided a useful variety of flow types in the area of flow observed; in addition cooling air (at 290 K) was ejected from a row of 50 holes in the suction surface of the blades.

Table 1 Cascade Test Conditions

Upstream total pressure P_t	= 516 KPa
Upstream total temperature	= 432 K
Initial blade temperature	= 290 K
Inlet Mach Number	= 0.16
Stagnation density ρ_t	= 4.16 kg/m^3
Reynolds Number (exit conditions, true chord)	= 3.5×10^6
Upstream turbulence level	= 4.4 percent
Number of passages	= 5

The blades had a chord of 73 mm and a span of 76 mm. All the results shown here were obtained under conditions described in Table 1. Surface pressure distributions had been obtained during a previous test.

5 Holograms of Cascade Flow

The flow over a portion of the suction surface of a cascade blade with coolant ejection, from a spanwise row of holes, is shown in Fig. 4. In Fig. 5 there is no coolant flow although the holes are still present.

Figure 4(a) is an absolute hologram, Fig. 4(b) a differential (100 μs) hologram, and Fig. 4(c) is an enlargement of a conventional spark Schlieren photograph included for comparison. Figures 5(a), 5(b), and 5(c) are the corresponding set without coolant ejection.

Figure 6 is a highly enlarged reconstruction of an absolute hologram of the trailing edge flow of the blade.

In examining these holograms the following should be kept in mind:

1 The mounting of the blades in the windows was more flexible than intended, and the lift on the blade during the run displaced the trailing edge slightly towards the suction surface between the reference and flow exposures on the absolute holograms. This is evident in Fig. 6. The darker trailing edge outline is due to the reference exposure just before the run, but the lighter outline to the right shows the actual displaced position with flow present.

2 The optimum position of the image plane to minimize diffraction effects is not necessarily the same as that to minimize image shift due to refraction in regions of strong density gradient. The holograms shown here were optimized to reduce diffraction, and consequently there are refraction effects close to the surface. This effect may be observed near the injection holes on the holograms, but not on the schlieren.

Nomenclature

C = Dale-Gladstone coefficient, m^3/kg
Cax = cascade blade axial chord
L = optical path length, m
ΔL = change in optical path length
M = Mach number
N = fringe number
P = pressure, kPa
R = universal gas constant
s = optical path length, m
T = temperature, K
x, y, z = orthogonal spatial coordinates
γ = ratio of specific heats
δ = 100 percent boundary layer thickness
λ = wave length, m
μ = refractive index
$\bar{\mu}$ = mean refractive index along the optical path
ρ = density, kg/m^3

Subscripts

b = boundary layer
f = freestream
0 = reference value
s = static
t = stagnation value
w = wall

Downloaded 01 Jun 2010 to 171.66.16.59. Redistribution subject to ASME license or copyright; see http://www.asme.org/terms/Terms_Use.cfm

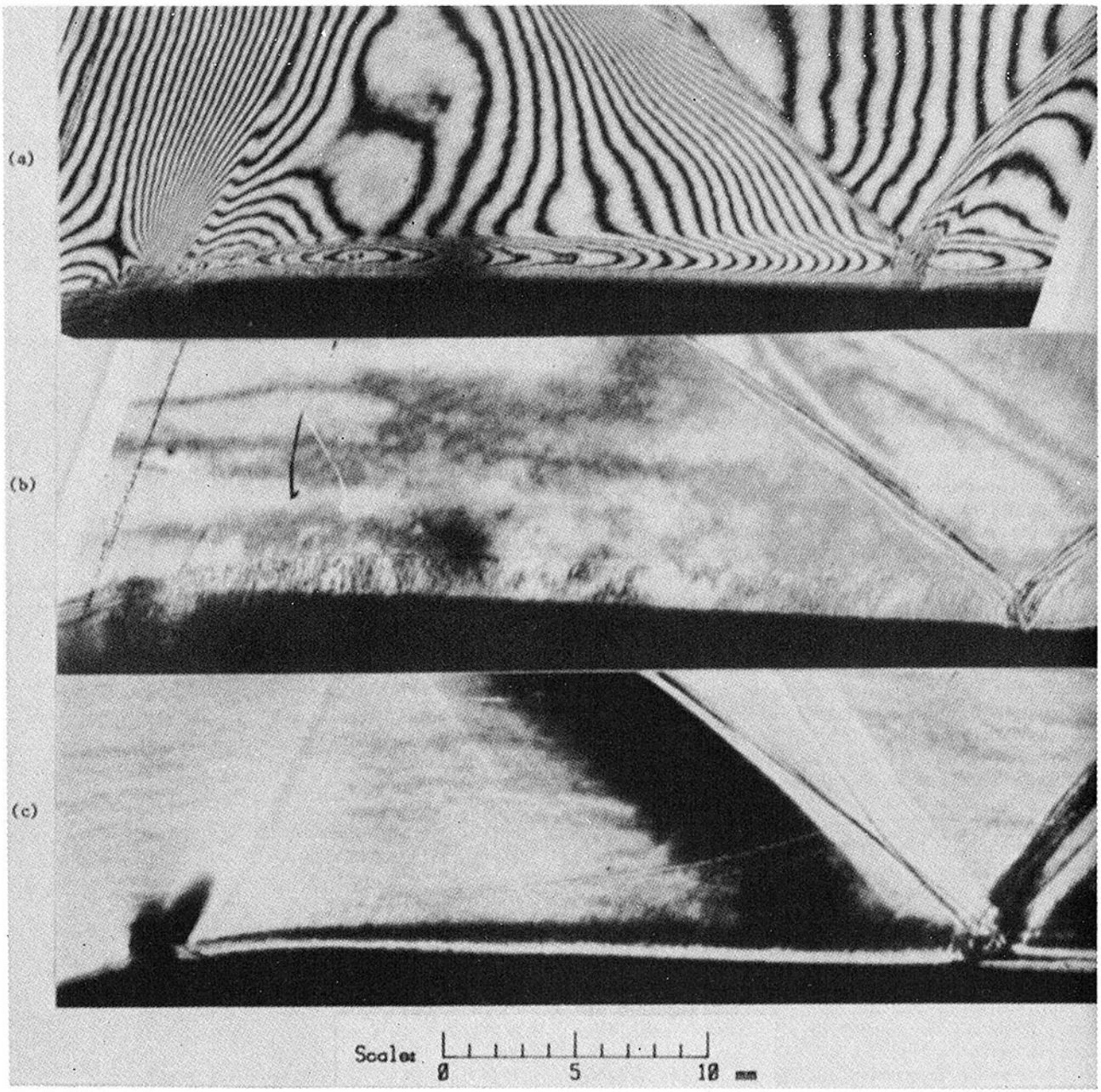

Fig. 4 Blade suction surface with coolant ejection. Flow from left to right. (*a*) absolute hologram, (*b*) differential hologram, 100 μs pulse separation, (*c*) schlieren

3 Although the holograms covered a complete blade passage, the prints shown here are taken from reconstructions of only part of the passage, in order to demonstrate the resolution obtained.

4 By making enlarged reconstructions from small areas of the image plane hologram (this is not the same as enlarging a photographic negative of the whole flow field) a fringe spacing of 40 μm was resolved.

In Fig. 6 this high resolution is not affected by the greater tunnel and blade movements.

5 Fluctuations in the exit flow, inherent in cascade experiments, cause perturbations in the position of the trailing edge shocks during the run. Figures 4 and 5 give six instantaneous pictures of the flow on different runs and hence do not show the shock waves in exactly the same positions.

6 It might be thought that the temperature profile in the sidewall boundary layers on the tunnel windows would appreciably change the mean integrated optical path length compared with the physical blade span.

In fact this effect is small. For the sidewall boundary layers upstream of the cascade the free-stream temperature is 432 K and the wall temperature is 288 K.

The Appendix shows that under these conditions the increase of optical path length in each boundary layer is given by

$$\Delta L = 0.045\ \delta,$$

where δ is the turbulent boundary layer thickness. For these tests, δ = 9 mm, and so for a physical path length (blade span) of 76 mm, the total increase of integrated optical path length through both boundary layers is 0.8 mm, corresponding to a change of only 1 percent. In the cascade passage the pathlength error will be similarly small except in regions of strong secondary flow.

In examining the holograms the following regions of the flow are of interest:

1 Free stream. In the freestream passage flow in Figs. 4(*a*) and 5(*a*) the fringe pattern can be interpreted as lines of constant Mach

Downloaded 01 Jun 2010 to 171.66.16.59. Redistribution subject to ASME license or copyright; see http://www.asme.org/terms/Terms_Use.cfm

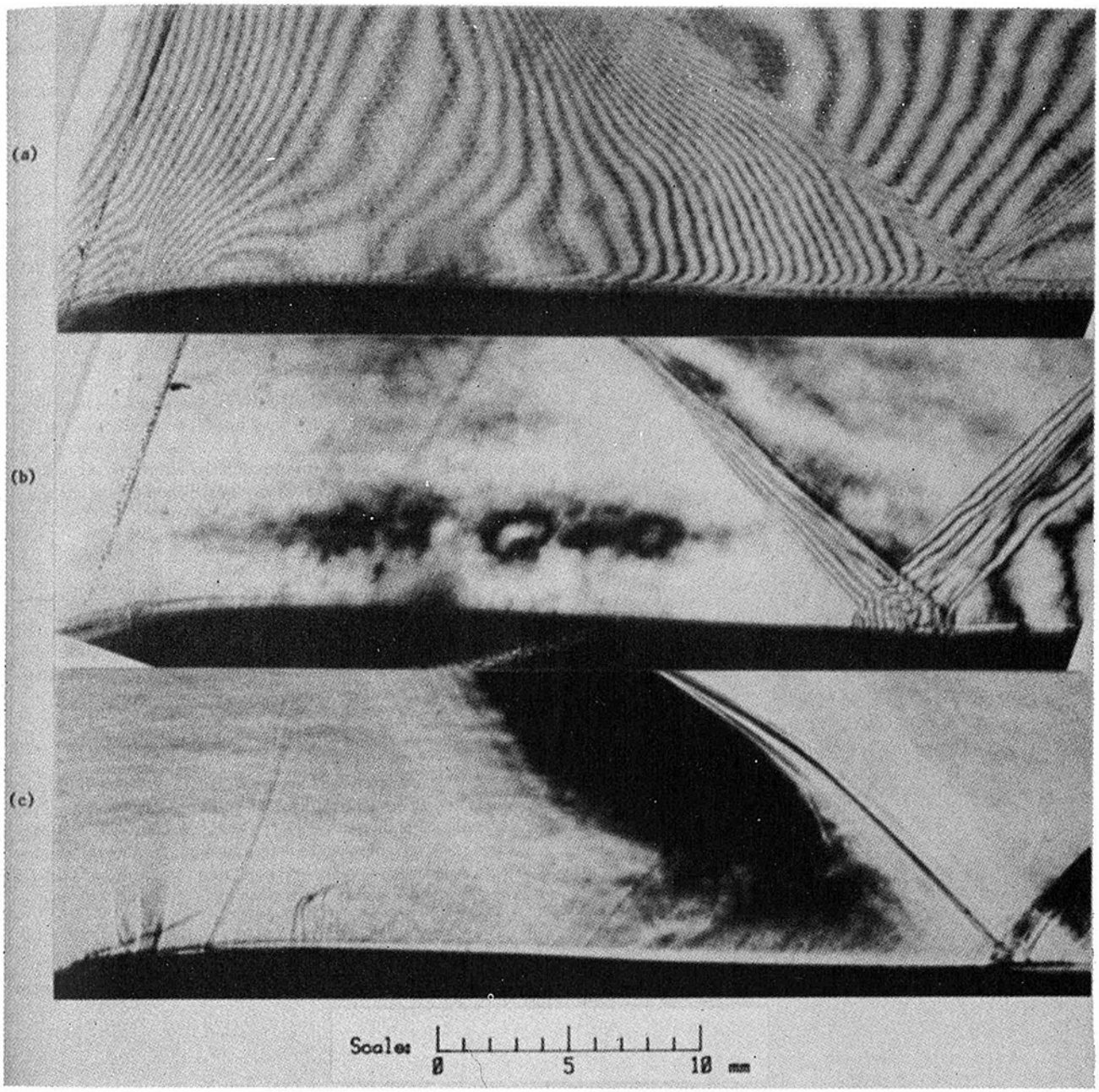

Fig. 5 Blade suction surface without coolant ejection. (*a*) absolute hologram, (*b*) differential hologram, 100 μs pulse separation, (*c*) schlieren

number upstream of the trailing edge shock (see Section 6). This shock wave is slightly nonplanar and hence appears to have finite thickness in both the holograms and schlieren prints. The steepness of the density change across the shock results in a large fringe shift and the closely spaced fringes are obscured by a superimposed diffraction pattern. Consequently the fringe count is lost through the shock. The conditions behind the shock could be recovered by solving the shock equations. Fringe counting could then resume.

In the differential (100 μs) holograms the only freestream disturbances visible upstream of the shock wave are slight perturbations due to turbulent fluctuations in both the main flow and in the sidewall boundary layers.

The large density gradient across the trailing edge shock wave renders it visible with only a small change of position in 100 μs.

2 Suction Surface Boundary Layer. In Fig. 5(*a*) the fringes indicate a decrease in density near the surface, and this is confirmed in Fig. 5(*c*). This is due to the recovery of total temperature in the slower moving boundary layer gas. The expected cooled layer next to the blade surface is obscured.

3 Coolant Ejection. Comparison of Fig. 4(*a*) with Fig. 5(*a*) shows a change of fringe pattern, and hence freestream Mach number, as the passage flow accommodates the added coolant mass flow. The coolant gas forms a denser cold layer in a thickened boundary layer, with a temperature stratification which is maintained downstream even through the shock-boundary layer interaction region. The differential hologram (Fig. 4(*b*)) shows this layer of coolant gas to be turbulent.

4 Wake Region. In Fig. 6, an enlarged view of the trailing edge region, the near wake and the shock structures are clearly visible. The shock positions and wake width agree with those obtained from schlieren prints, but greater detail of the fine structure is visible. In addition the holograms contain qualitative wake density information obtained without the interference of a wake probe.

There is a suggestion of periodic vortex structures in the wake similar to that observed [12] in other cascade flows even at high Reynolds and Mach numbers.

Downloaded 01 Jun 2010 to 171.66.16.59. Redistribution subject to ASME license or copyright; see http://www.asme.org/terms/Terms_Use.cfm

Fig. 6 Enlarged absolute holographic reconstruction of the trailing edge and near wake

6 Fringe Interpretation

For any qualitative analysis of absolute holograms it is necessary to assign an unambiguous fringe number to each fringe.

Usually this is done by counting away from a known leading edge stagnation point.

Alternatively, the fringe count may be referenced to a point of known Mach number (perhaps from a surface pressure measurement), using known stagnation conditions. In regions where the density has maximum or minimum values, as in and just above the coolant flow in Fig. 4(*a*), there may be an uncertainty as to the direction of increasing fringe number. This may be resolved by counting around the region of uncertainty and then tracing known fringes back. It is sometimes possible to confirm the fringe count by counting to the same fringe by two different routes, or by using spot Mach numbers from surface pressure tappings as a check.

The theory for computing Mach number has been based upon work covered in reference [10].

For a ray path s through a region of varying refractive index the optical path length is given by

$$\bar{\mu}s = \int_0^s \mu(x, y, z)ds \tag{1}$$

where $\mu(x, y, z)$ is the local refractive index and $\bar{\mu}$ is the mean refractive index along the path. For a two dimensional flow field, $\mu = \mu(x, y)$, illuminated by a parallel beam in the z direction, the ray path $ds = dz$ if the deflection of rays by refraction is small. The optical path length is simply $\mu(x, y)L$ where L is the total path length. A change in refractive index between two holographic exposures results in interferometric fringes. This can be expressed as

$$(\bar{\mu}_0 - \bar{\mu}_1)L = N\lambda \tag{2}$$

where N is the fringe number and λ the wavelength of the laser light. A bright fringe is produced if N is an integer and a dark fringe if N takes a half integer value. In this case $\lambda = 0.6943$ μm (ruby red). In order to obtain gas dynamic information the refractive index of the test gas must be related to the density by the Dale-Gladstone equation

$$\frac{\mu - 1}{\rho} = C \tag{3}$$

where μ is the refractive index of air of density ρ and the Dale-Gladstone coefficient $C = 2.25 \times 10^{-4}$ m^3/kg for air at $\lambda = 0.6943$ μm. By combining equations (2) and (3) the fringe order can be expressed in terms of a density change. Hence the fringes can be considered as lines of isodensity

$$\frac{N\lambda}{LC} = \rho_0\left(1 - \frac{\rho_1}{\rho_0}\right) \tag{4}$$

Except in the shock region the mainstream flow can be considered isentropic and the compressible flow equations can be used. If the density at the stagnation point is ρ_t, then the local free stream density ρ at a position in the flow can be determined by counting the number of fringes N between a stagnation point and the position. The local density along fringe number N is given by

$$\frac{\rho}{\rho t} = 1 - \frac{N\lambda}{\rho_t LC} \tag{5}$$

It should be remembered that in isentropic flow ρ_t is the maximum density and so

$$\frac{\rho}{\rho_t} < 1$$

for N fringes away from a stagnation region.

Using the Mach number-density equation

$$\frac{\rho}{\rho_t} = \left[1 + \frac{\gamma - 1}{2}\mathrm{M}^2\right]^{-1/(\gamma-1)}$$

where M is the Mach number at fringe N and γ is the ratio of specific heats, we get

$$\mathrm{M} = \sqrt{\frac{2}{\gamma - 1}\left(\left(1 - \frac{N\lambda}{\rho_t LC}\right)^{-(\gamma-1)} - 1\right)} \tag{6}$$

For air, $\gamma = 1.4$ and so

$$\mathrm{M} = \sqrt{5\left(\left(1 - \frac{N\lambda}{\rho_t LC}\right)^{-0.4} - 1\right)} \tag{7}$$

$(\lambda/\rho_t LC)$ is a constant for any given cascade tunnel condition. For the cascade test conditions $\lambda/\rho_t LC = 1/102.8$ and equation (7) simplifies further to

$$\mathrm{M} = \sqrt{5\left(\left(1 - \frac{N}{102.8}\right)^{-0.4} - 1\right)} \tag{8}$$

Equation (8) can be used to calculate the blade surface Mach number distribution by counting fringes from either the leading edge stag-

Downloaded 01 Jun 2010 to 171.66.16.59. Redistribution subject to ASME license or copyright; see http://www.asme.org/terms/Terms_Use.cfm

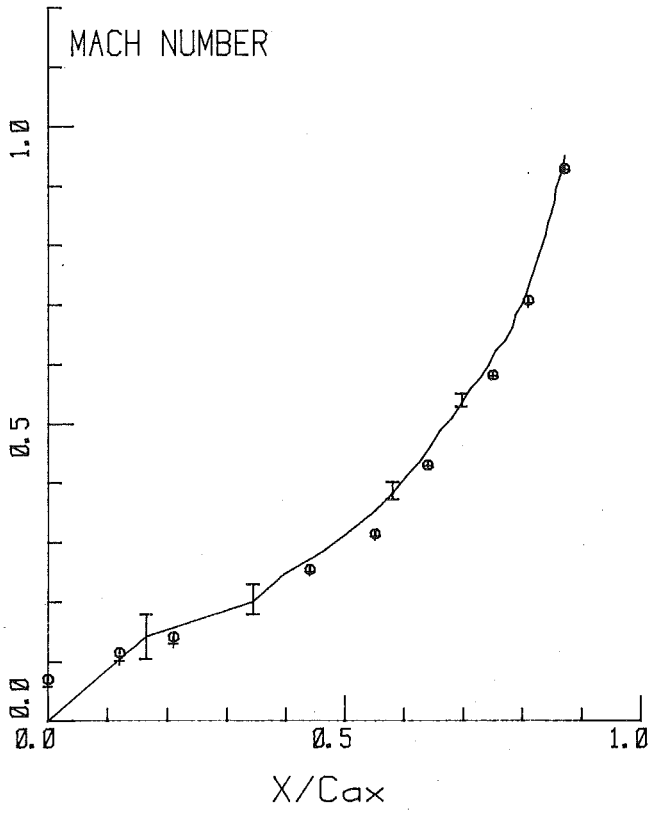

Fig. 7 Comparison of measured pressure-surface Mach number distributions. The continuous line is obtained from a fringe count on an absolute hologram and the symbols are from surface pressure measurements. The error bars represent ±0.5 fringes

nation point, or from any other point of known Mach number.

The accuracy of the fringe number N at a given surface point is limited to about ±0.5 by the following constraints:

- The difficulty of determining exactly the reference fringe at the stagnation point
- The difficulty of extrapolating from the boundary layer edge to the surface
- The effect of the window boundary layers

This ±0.5 uncertainty in N gives rise to percentage errors in Mach number which decrease markedly as N and M increase, and the technique is thus much more accurate at higher fringe numbers. For example $N = 2 \pm 0.5$ gives $M = 0.199 \pm 0.025$ (13 percent) and $N = 40 \pm 0.5$ gives $M = 1.044 \pm 0.009$ (0.09 percent).

The surface Mach numbers obtained by counting fringes and using equation (8) agree well with those obtained from surface pressure measurements to an accuracy of greater than that corresponding to a 0.5 fringe error on both surfaces. This agreement is shown in Fig. 7, which gives the Mach number distribution on the pressure surface.

Equations (6, 7) and (8) apply to isentropic flow and thus do not apply in the boundary layers and in regions where the free stream and injected coolant flows mix.

However along any line of constant pressure, the temperature is inversely proportional to the density, and hence can be obtained from the fringe count.

This can be used to obtain temperature profiles in the boundary layers by counting fringes from the free stream.

If ΔN is the fringe shift from the boundary layer edge (conditions T_s and ρ_s) to a point in the boundary layer (conditions T_b and ρ_b), then from equation (4) the temperature difference, $T_b - T_s$, is given by

$$T_b - T_s = T_s\left(\frac{T_b}{T_s}\right) - T_s$$

$$= T_s\left(\frac{\rho_s}{\rho_b} - 1\right)$$

$$= T_s\left(\frac{1}{\left(1 - \dfrac{\Delta N\lambda}{\rho_s LC}\right)} - 1\right) \tag{9}$$

In Fig. 5(a), without blowing, the maximum visible shift of +3 fringes in the boundary layer corresponds to a temperature rise, $T_b - T_s = 22.9$ K. This contrasts with the maximum fringe shift of −2 in the cooled flow of Fig. 4(a). This gives a temperature drop, $T_b - T_s = -13.6$ K.

In this manner the mixing of the coolant and the free stream can be studied.

7 Conclusions

The high quality of the interferograms of turbine blade cascade flow produced by using image plane holography with white light reconstruction has made possible quantitative measurements of the flow field, including constant Mach Number contours in the free stream. Additionally the technique gives much qualitative information in the boundary layer and wake regions of the blade.

With some further refining the technique offers an alternative to multiple blade pressure tappings to obtain surface and passage pressure distributions. Suggested improvements would include:

1 Observation of several complete passages simultaneously in a hologram to check repeatability and to enable fringe counting from one passage to another

2 Mount blades rigidly

3 Optimize optical system to minimize refraction and diffraction

4 A hologram is an image of the flow field at one instant of time: when there are fluctuations present, this must be related to the time averaged flow field.

8 Acknowledgments

The cascade testing at Oxford University and the development of the holographic system at Rolls-Royce Advanced Research Laboratory were supported by the Ministry of Defence (Procurement Executive). The authors gratefully acknowledge the permission of both Rolls-Royce Ltd., and the National Gas Turbine Establishment to reproduce the data included in this report and their advice and encouragement in this work.

Thanks are also due to those members of Rolls-Royce and the Oxford University Cascade group whose support made this work possible.

References

1 Schultz, D. L., Jones, T. V., Oldfield, M. L. G., and Daniels, L. C., "A New Transient Cascade Facility for the Measurement of Heat Transfer Rates," AGARD-CCP-229, 1977.

2 Oldfield, M. L. G., Jones, T. V., and Schultz, D. L., "On-Line Computer for Transient Turbine Cascade Instrumentation," *IEEE Transactions on Aerospace and Electronic Systems*, Vol. AES-14, No. 5, Sept. 1978, pp. 738–749.

3 Clarke, J. A., "Holographic Visualization of Acoustic Fields," *Journal Sound and Vibration*, Vol. 56, 1978, pp. 169–174.

4 Leith, E. N., and Upatnieks, J., *Journal Optical Society of America*, Vol. 54, 1964, p. 1295.

5 Surget, J., "Etude Quantitative d'un Ecoulement Aerodynamique par Interferometric Holographic," *Recherche Aerospatiale*, Vol. 13, Mar./June 1973, p. 161.

6 Jahoda, F. C., and Sieman, R. E., "Holographic Interferometry Cookbook," Los Alamos Scientific Laboratory Report No. UC37, Oct. 1972.

7 Radlay, Jr., R. J., and Havener, A. G., "The Application of Dual Hologram Interferometry to Wind Tunnel Testing," *AIAA Paper No. 73-210*, 11th Aerospace Sciences Meeting, Washington, D.C., Jan. 1973.

8 Bryanston-Cross, P. J., "An Investigation into the Airflow Over Heated Disruptive Surfaces by Holographic and Mathematical Technniques," Ph.D. Thesis, University of Aston in Birmingham, 1977.

9 Holder, D. W., and North, R. J., "Schlieren Methods," NPL notes on Applied Science No. 30, 1963.

10 Sinclair, D. W., and Whitfield, D. L., "Holographic Interferometry Measurements of Subsonic Turbulent Boundary Layers," ARO Inc., Arnold

Downloaded 01 Jun 2010 to 171.66.16.59. Redistribution subject to ASME license or copyright; see http://www.asme.org/terms/Terms_Use.cfm

ARS, Tenn. AIAA 11th Fluid and Plasma Dynamics Conference, July 1978.
11 Smith, H. M., "Holographic Recording Material," Vol. 20, *Topics in Applied Physics*, Springer-Verlag, 1977, pp. 1–20.
12 Lawaczeck, O., and Heinemann, H. J., "Von Karman Vortex Streets in the Wakes of Subsonic and Transonic Cascades," AGARD-PEP Meeting, Unsteady Phenomena in Turbomachinery, *AGARD-Conference Proceedings*, No. 177, 1975.
13 Schlichting, H., *Boundary-Layer Theory*, 6th Ed., McGraw-Hill, New York, 1968.

APPENDIX

Optical Path Length Changes Due To Sidewall Boundary Layers. An approximate analysis is presented here. For an incompressible turbulent flat plate boundary layer, the turbulent Prandtl number can be taken as unity [13] and the temperature profile is then identical to the velocity profile.

Assuming a 1/7th power law boundary layer profile on a flat plate of wall temperature T_w, with a free-stream static temperature T_f, the nondimensional temperature profile is

$$\frac{T - T_w}{T_f - T_w} = \left(\frac{y}{\delta}\right)^{1/7} \tag{10}$$

where y is the perpendicular distance from the plate and δ is the boundary layer thickness.

Assuming constant pressure through the boundary layer, the density profile is then given by

$$\frac{\rho_f}{\rho} = \frac{T}{T_f} = \frac{T_w}{T_f} + \left(1 - \frac{T_w}{T_j}\right)\left(\frac{y}{\delta}\right)^{1/7}$$

The optical path length change introduced by the presence of the boundary layer is then

$$\Delta L = \frac{1}{\rho_f}\int_0^\delta \rho dy - \delta$$
$$= \delta\left(\int_0^1 \frac{\rho}{\rho_f} d\left(\frac{y}{\delta}\right) - 1\right)$$

or

$$\Delta L = \delta\left(\int_0^1 \frac{1}{\left(\frac{T_w}{T_f} + \left(1 - \frac{T_w}{T_f}\right)\left(\frac{y}{\delta}\right)^{1/7}\right)} d\left(\frac{y}{\delta}\right) - 1\right) \tag{11}$$

For the flow upstream of the cascade described in this paper, the Mach number is 0.16, and hence $T_f \doteq T_t = 432$ K.

For a cold sidewall at $T_w = 288$ K, $T_w/T_f = 0.667$.

Using this value, equation (11) can be integrated numerically to give

$$\Delta L = 0.045\,\delta \tag{12}$$

Downloaded 01 Jun 2010 to 171.66.16.59. Redistribution subject to ASME license or copyright; see http://www.asme.org/terms/Terms_Use.cfm

Structure and Decay Characteristics of Turbulence in the Near and Far-Wake of a Moderately Loaded Compressor Rotor-Blade[1]

A. Ravindranath
Graduate Assistant.

B. Lakshminarayana
Professor.

Department of Aerospace Engineering,
The Pennsylvania State University,
University Park, Penn. 16802

The wake of a turbomachinery rotor-blade is turbulent, highly three-dimensional, and nonisotropic with appreciable curvature in the trailing-edge and near-wake regions. The characteristics of the turbulence vary considerably with radius, blade loading, free-stream turbulence, Reynolds number, and the rotor-blade geometry. This paper is concerned with the turbulence properties of a moderately loaded compressor blade, particularly near the blade trailing-edge. The tangential variation of the axial, tangential and radial intensities and stresses across the wake, as well as their decay characteristics were measured with a tri-axial hot-wire probe in the rotor frame of reference. The decay of intensities and stresses were found to be very rapid in the trailing-edge and near-wake regions and slow in the far-wake region. The effects of inlet-guide-vane and the hub-wall boundary layers on the rotor wake turbulence spectra are also discussed. Similarity rules for the three components of intensity are also derived and presented in this paper.

1 Introduction

The mean velocity defect and turbulence in a rotor wake contribute to the overall noise production, aerodynamic performance (losses, efficiency, etc.) and vibration characteristics of a turbomachinery. The study of the turbulence structure downstream of a rotor blade row is important since it introduces unsteadiness and affects the boundary layer behavior in the succeeding blade row. Recent investigations have revealed that the turbulence property in the boundary layer and the wake of a rotor blade contribute significantly to the unsteady blade forces, performance deterioration and to the noise generated in a turbomachine. Therefore, a thorough knowledge of the turbulence quantities in a compressor rotor wake is crucial to its improved design, reduced losses and improved efficiency and performance.

Available literature on the structure of turbulence in a turbomachinery stage is very limited and the only available data concern a very lightly loaded fan rotor, particularly in the far-wake region. No data are available for a moderate or heavily loaded compressor rotor, in the trailing-edge region in particular; this is the main objective of the paper.

The investigation of the turbulence structure behind a compressor rotor using a rotating hot wire probe is reported in this paper. Spectra of turbulence which show the effect of inlet-guide-vane wakes on the rotor wake turbulence characteristics are also given. Attempts have also been made to correlate the turbulence quantities and to examine the similarity characteristics.

This is a companion paper to reference [1], in which the mean properties of the wake and their decay characteristics were discussed.

2 Test Facility and Instrumentation

The investigation of the structure of turbulence behind a compressor rotor was carried out using the axial flow compressor facility at The Pennsylvania State University. A complete description of the facility is given in reference [1]. A schematic of the facility is shown in Fig. 1. The rotor wake measurements were carried out with a tri-axial hot-wire probe rotating with the rotor. The axial and radial measurement locations are tabulated in reference [1]. A rotating probe traverse mechanism was used to traverse the probe across the wake while the rotor is in motion (Fig. 1). A description of this mechanism as well as the data transmission, acquisition and reduction techniques are given in references [1] and [2]. This experimental program enabled the determination of three components of mean velocity and, three components of turbulence intensities, and Reynolds stresses across the wake. The mean velocity data outside the end wall boundary layers are presented and discussed in reference [1], the wakes inside the end wall boundary layers are discussed in reference [2].

3 Experimental Results, Interpretation and Correlation

Three mean voltages and six fluctuating voltages (rms values) from the rotating hot wire provide sufficient information to derive the three components of mean velocities and six components of turbulence stresses (including normal stresses). Details of the technique are given in reference [3] and an error estimate is carried out in reference [2].

[1] This is a companion paper to reference [1]. Mean flow properties were presented in reference [1]; this paper deals with the corresponding turbulence properties.

Contributed by the Gas Turbine Division and presented at the Gas Turbine Conference and Products Show, New Orleans, La., March 10–13, 1980 of THE AMERICAN SOCIETY OF MECHANICAL ENGINEERS. Manuscript received at ASME Headquarters December 19, 1979. Paper No. 80-GT-95.

Copyright © 1981 by ASME
Downloaded 01 Jun 2010 to 171.66.16.59. Redistribution subject to ASME license or copyright; see http://www.asme.org/terms/Terms_Use.cfm

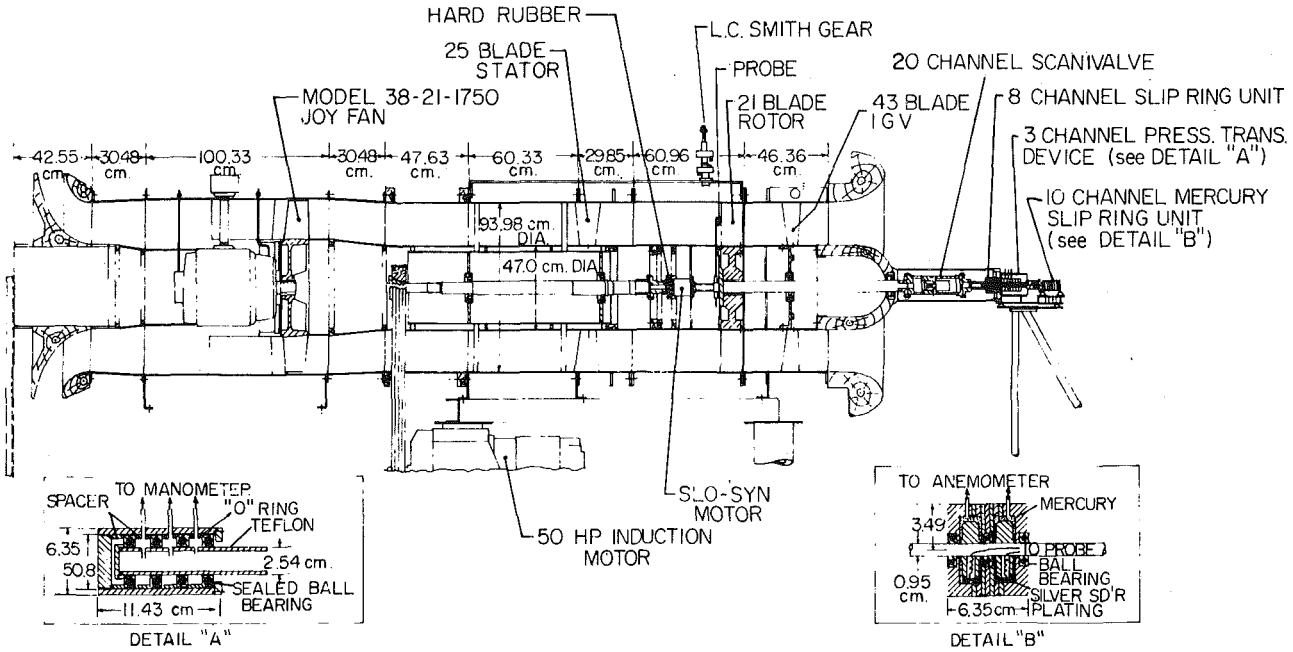

Fig. 1 PSU axial flow compressor facility and data transmission systems

The hot wire data are processed in streamwise (s, n, r) and cylindrical coordinate systems (r, θ, z). The most convenient system, from the point of view of physical interpretation, for the shear stress is the streamwise system. Hence the shear stress data are presented in the s, n, r system and the turbulence intensity data in the r, θ, z coordinate system.

All the data presented in this paper are in the relative (or rotor) frame of reference.

3.1 Turbulence Intensity Profiles.

3.1.1 Axial Turbulence Intensity. Axial turbulence intensity profiles for the rotor-wake at radii $R = 0.6581, 0.7297$ and 0.7973 and at various distances downstream of the blade are shown in Figs. 2–4. The turbulence intensity has been nondimensionalized by the local mean velocity, since turbulence is dependent on local flow conditions. The abscissa in the figures represent the tangential distance normalized by half the blade spacing.

The axial turbulence intensity profiles show very high values[2] in the trailing-edge region. In the near- and far-wake regions the magnitude reduces considerably. The very high values in the trailing edge region are attributed to the presence of trailing vortices as well as the production of turbulence in this region. Very high values of intensity near the wake center at the first axial station should be taken as an indication of the qualitative trend as the error is appreciable at this particular location.

The axial turbulence intensity profiles are asymmetrical in the trailing edge region and tend to become symmetrical beyond half-a-chord downstream. The asymmetry in the profile results from the differential growth of turbulence on the suction- and pressure-surfaces of the blade. In the near-wake plots of Figs. 2 and 4, the turbulence intensity profiles show a dip near the wake center and that the peak value occurs on either side of the wake center. This type of trend is expected in the trailing edge region as the turbulence intensity must be zero on the blade surface and the maximum value occurs slightly away from the surfaces. The profile for $R = 0.7297$ (Fig. 3) does not

[2] Large intensities near the trailing edge, apparent in Figs. 2–10, are caused by the fact that the intensities are normalized by the *local* velocities, which are very small. Substantial error due to the viscinity of the trailing edge (aerodynamic interference with the probe) and the presence of oscillating vortices may be present in the data. The turbulence would then include not only random fluctuations, but also periodic fluctuations in mean velocity due to the movement of the trailing vortex. This reasoning is only speculative and is not supported by detailed measurements near the trailing edge. Hence, at least for now, the turbulence intensities near the trailing edge (first station) should be viewed with caution.

Nomenclature

c = blade chord
e = fluctuating voltage
l_s, l_p = wake width at half the depth of turbulence intensity profile on the rotor-blade suction- and pressure-surface of the wake, respectively
n = exponent
R = radius ratio = (r/r_T)
r = local radius
(r, θ, z) = rotating cylindrical coordinate system (radial, tangential and axial coordinate directions)
S = blade spacing
(s, n, r) = natural coordinate system (streamwise, normal, and radial coordinate directions)
u = peripheral speed
W = total relative velocity
w' = fluctuating component of relative velocity
y = tangential distance
$\left(\frac{2y}{S}\right)$ = tangential distance normalized by half the blade spacing ($y = 0$ at wake center)
Z = axial distance from blade trailing-edge normalized by rotor blade chord
ϕ = mass average flow coefficient (W_z/U_T)
β_0 = blade outlet angle
$\tau_z, \tau_r, \tau_\theta$ = normalized turbulence intensities in the axial, radial and tangential directions, respectively $(\sqrt{\overline{w_z'^2}}/W, \sqrt{\overline{w_r'^2}}/W, \sqrt{\overline{w_\theta'^2}}/W)$
$\tau_{sn}, \tau_{rn}, \tau_{sr}$ = normalized streamwise, radial Reynolds stress, and stress correlations, respectively $(\overline{w_s'w_n'}/W_s^2, \overline{w_r'w_n'}/W_s^2, \overline{w_s'w_r'}/W_s^2)$

Subscripts

c = value at wake center
max = maximum value in the wake
0 = freestream value
p = pressure-surface
ref = reference value
(r, θ, z) = radial, tangential and axial directions
s = suction-surface
(s, n, r) = streamwise, normal and radial directions
T = value at rotor tip
1, 2, 3 = wire number one, two, and three
TE = trailing edge

Superscripts

$\overline{\ }$ = average value
$'$ = fluctuating quantity

Downloaded 01 Jun 2010 to 171.66.16.59. Redistribution subject to ASME license or copyright; see http://www.asme.org/terms/Terms_Use.cfm

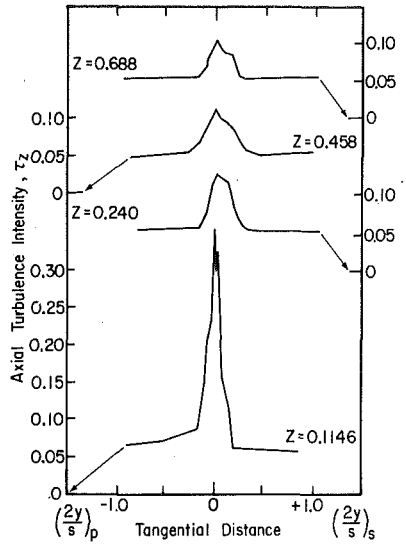

Fig. 2 Axial turbulence intensity profiles, $R = 0.6581$, $\phi = 0.56$

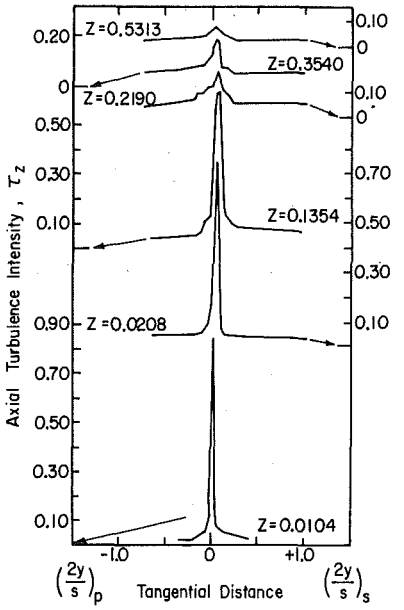

Fig. 3 Axial turbulence intensity profiles, $R = 0.7297$, $\phi = 0.56$

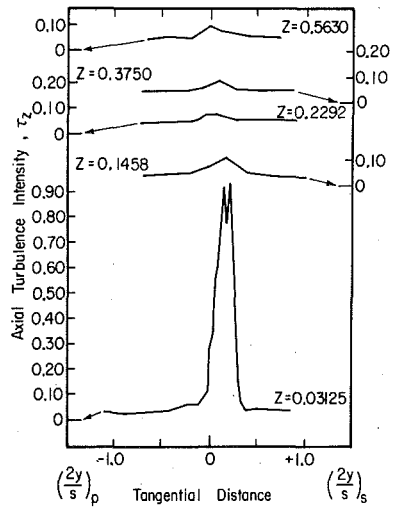

Fig. 4 Axial turbulence intensity profiles, $R = 0.7973$, $\phi = 0.56$

reveal this trend very clearly. This might be due to the region being too narrow and the consequent spatial error.

The magnitude of the axial turbulence intensity is about 0.85 at $Z = 0.0104$ (and $R = 0.7297$) which reduces to less than 0.15 at $Z = 0.5313$. This implies that the decay of intensities is very rapid in the trailing-edge region and slows down considerably beyond 0.2 chords downstream. The same trend is observed for the other radii $R = 0.7972$ and 0.6581. The rapid decay of turbulence intensities indicates that there is a very rapid redistribution of turbulent energy in these regions.

The axial turbulence intensity measured before the inlet-guide-vanes was about 0.5 percent and this is amplified to 2 to 5 percent after the passage through the rotor blade row. Free stream axial turbulence intensity far downstream of the rotor was found to be around the same order of magnitude in the region outside the rotor wake at all radii.

The effect of blade loading on the axial turbulence intensity can be seen by comparing the authors' results with those of reference [4]. The free stream axial turbulence intensity for both the rotors were of the same order of magnitude but very near the blade trailing edge the turbulence intensities are nearly 80 percent for the heavily loaded rotor while the intensities are about 30 percent for the lightly loaded fan blade. Thus the effect of loading is to increase the turbulence level in the wake in the trailing edge region. Increase in blade loading not only increases the decay rate as well as the turbulence levels.

The intensities are also found to decay much more rapidly with an increase in radius (compare Figs. 2 and 4).

3.1.2 Tangential Turbulence Intensity. Tangential turbulence intensity profiles for the radii $R = 0.6581$, 0.7297 and 0.7973 are plotted in Figs. 5–7 for varying axial distances. In these plots the ordinate represents the tangential turbulence intensity normalized by the local mean velocity.

The tangential turbulence intensity profiles are asymmetrical as in the case of axial component. The profiles exhibit a tendency to become symmetrical beyond half-a-chord downstream, the last measuring station using the rotating probe. These data seem to agree, qualitatively, with the argument on symmetry put forth in references [4] and [5].

Unlike the axial component of turbulence intensity, no dips in the turbulence profiles were found at the wake centerline. This indicates a complex phenomena, wherein a rapid redistribution of turbulence energy occurs in the tangential direction at the blade trailing-edge. The magnitude of both axial and tangential intensities are about the same in the trailing-edge region; but in the far-wake region the tangential intensities are smaller than axial intensities indicating that the tangential component of intensity decays faster than the axial component.

The effect of blade loading on the turbulence intensity can be seen by comparing the authors' results with those of reference [4]. For a heavily loaded rotor the maximum turbulence intensity near the trailing edge is nearly 60 percent while for a lightly loaded fan blade the maximum value is less than 30 percent. Increase in blade loading not only increases the turbulence levels, but also increases the decay rate.

3.1.3 Radial Turbulence Intensity. Radial turbulence intensity profiles for the radii $R = 0.6581$, 0.7297 and 0.7973 and at various axial locations are shown plotted in Figs. 8–10. These radial locations are outside the end-wall boundary layers. The ordinate represents the radial turbulence intensity normalized by the local mean velocity.

Radial turbulence intensity profiles are asymmetric in the trailing edge and near-wake regions. Not only do the profiles show marked changes from one radius to another, so does the decay rate.

Radial intensities in the free stream are found to be approximately 2 to 4 percent for all the radii. The radial intensities are larger than the axial and tangential components. At the wake center, in the trailing edge region, the radial intensities are very high and reach nearly the same value as axial intensities. The existence of these large radial components of intensities exhibit the three-dimensional nature and the effects of Coriolis force on the rotor wake. Reference [6] also reports dominant radial component in measurement of boundary layer on helical inducer blades.

Downloaded 01 Jun 2010 to 171.66.16.59. Redistribution subject to ASME license or copyright; see http://www.asme.org/terms/Terms_Use.cfm

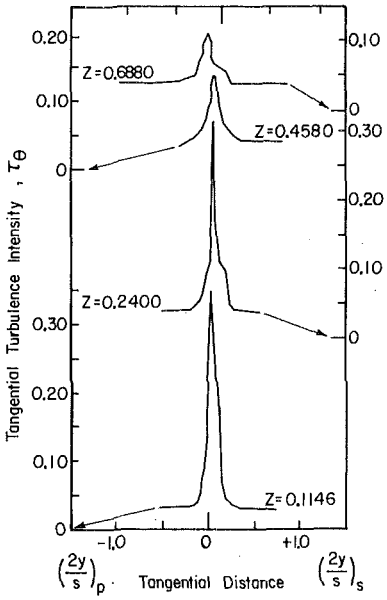

Fig. 5 Tangential turbulence intensity profiles, $R = 0.6581$, $\phi = 0.56$

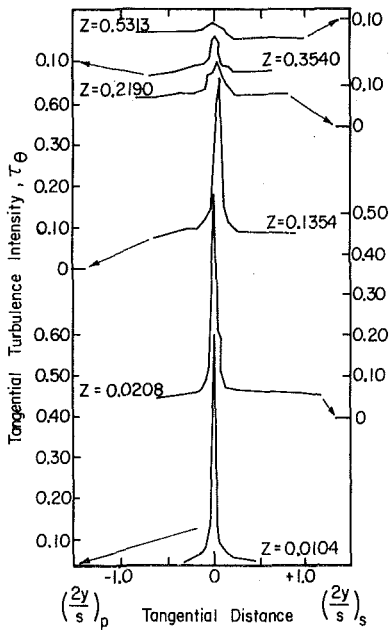

Fig. 6 Tangential turbulence intensity profiles, $R = 0.7297$, $\phi = 0.56$

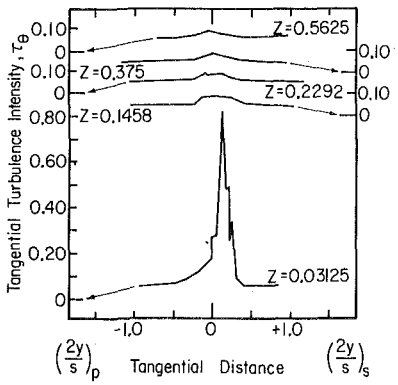

Fig. 7 Tangential turbulence intensity profiles, $R = 0.7973$, $\phi = 0.56$

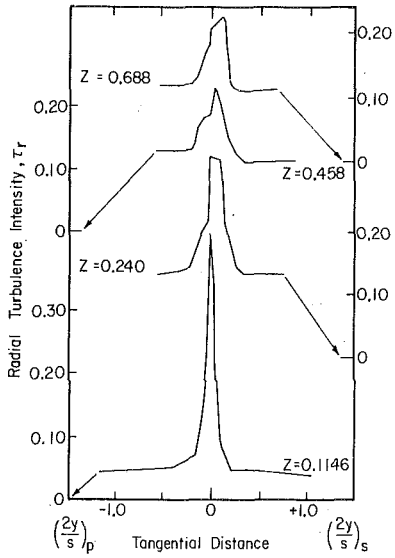

Fig. 8 Radial turbulence intensity profiles, $R = 0.6581$, $\phi = 0.56$

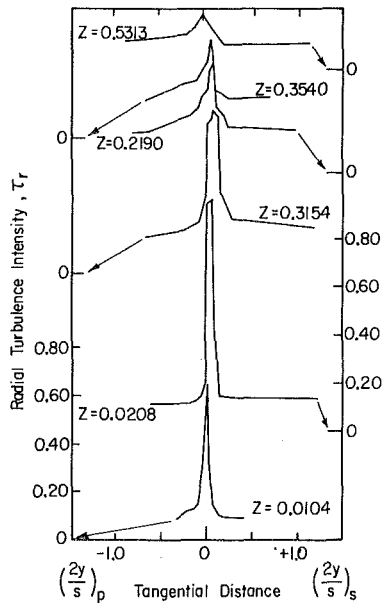

Fig. 9 Radial turbulence intensity profiles, $R = 0.7297$, $\phi = 0.56$

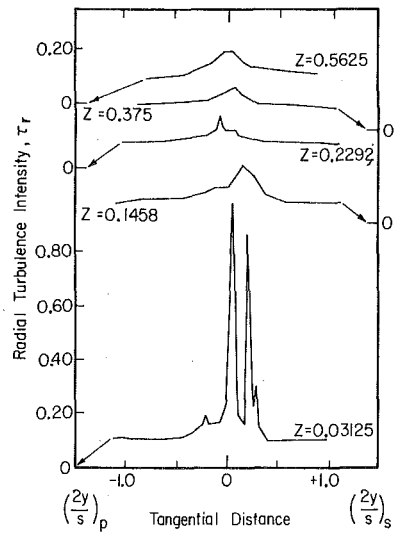

Fig. 10 Radial turbulence intensity profiles, $R = 0.7973$, $\phi = 0.56$

Downloaded 01 Jun 2010 to 171.66.16.59. Redistribution subject to ASME license or copyright; see http://www.asme.org/terms/Terms_Use.cfm

It is noted by comparison that the radial turbulence intensity decay is by far the slowest compared to the axial and tangential turbulence intensities. This indicates that the rotation effects are significant in the turbulence intensity structure of the rotor wake.

As seen from Fig. 9, for $R = 0.7297$ and $Z = 0.0104$, the radial turbulence intensity has a peak value of 0.65 which increases to 0.96 at $Z = 0.0208$. This indicates the effect of the trailing vortex on the radial turbulence intensity. The increase in turbulence intensity at these two locations might indicate the development of the vortex which initially grows stronger before it starts to decay. At $Z = 0.1354$ the value of the radial component of turbulence intensity is about 0.65 and beyond that the radial turbulence intensity decreases monotonically and reaches a value of nearly 0.25 at half-a-chord downstream.

References [4] and [5] provide a theoretical explanation of the redistribution of energy between the three components of fluctuating velocities and have shown that the effect of Coriolis force is to redistribute the energy such that $\tau_r \geq \tau_s$ in a compressor. This trend is true in this case, with the axial and radial intensities of the same order of magnitude. In a nonrotating case, $\tau_s > \tau_r$. It is also seen that beyond half-a-chord downstream of the blade the turbulence becomes isotropic with all the three components of velocities having nearly the same value.

3.2 Turbulence Shear Stress Profiles.

3.2.1 Streamwise Stress (τ_{sn}). The streamwise (τ_{sn}) component of the Reynolds stress is shown plotted in Figs. 11–13 at $R = 0.6581$, 0.7297 and 0.7973, respectively. Only the data in the s, n, r (natural coordinates) are given as they are the ones which are of practical interest. All the Reynolds stresses given here are normalized by the local dynamic pressure based on total relative mean velocity. The tangential distances are normalized by half the blade spacing. The streamwise stresses (τ_{sn}) are very small in the free stream and increase in magnitude near the wake center, where they reach a maximum value. This type of trend is to be expected as the production of stresses is brought about by velocity and turbulence intensity gradients.

The streamwise stress profiles (Figs. 11–13) show the expected reversal of stress at the wake center. This positive and negative stress distribution results from opposite gradients of streamwise mean velocity about the wake center. The profiles are asymmetrical about the wake center with the pressure-surface stresses being higher than the suction-surface stresses. The location of the zero streamwise Reynolds stress occurs slightly away from where the $\partial W/\partial n$ is zero. This characteristic has been measured and reported in reference [4]. A stationary hot wire probe and an ensemble average technique was used in references [7] and [8] to evaluate the wake properties. It is reported by these authors that the zero streamwise Reynolds stress occurs slightly away from where $\partial W/\partial n$ is zero. This implies that this characteristic is inherent for the wake and does not arise due to spatial resolution of the hot wire probe.

The profiles are asymmetric about the wake center and the decay of the stresses is extremely rapid in the trailing edge region, at all the radii. The shear stresses are nearly zero in the far wake region. This rapid decay can be expected as the steep gradient in mean velocity that exists in the trailing-edge region becomes very small for $Z > 0.15$. Further it is seen that at most of the radii the stresses in the freestream have a value other than zero, which might be due to the upstream inlet-guide-vane wakes.

3.2.2 Radial stress (τ_{rn}). The radial component of Reynolds stress for the three radii under consideration is shown plotted in Figs. 14–16. The radial stresses are opposite in sign to those of the streamwise stress. This is consistent with the mean velocity data presented in reference [1], where it was noted that the streamwise component of velocity increases on either side of the wake while the radial component of velocity decreases. In the free stream the value of the radial Reynolds stresses is around zero.

As the radial velocities and their gradients are much smaller than the streamwise velocities, it has to be expected that the ratio of the radial stress to streamwise stress be much less than unity. But in the present case, their ratio is greater than unity (at trailing edge and near-wake locations) indicating the effect of rotation on the stresses.

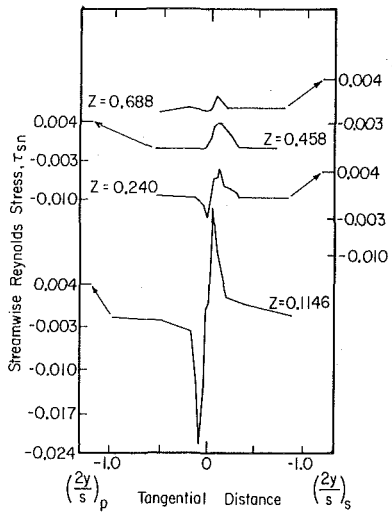

Fig. 11 Streamwise Reynolds stress profiles, $R = 0.6581$, $\phi = 0.56$

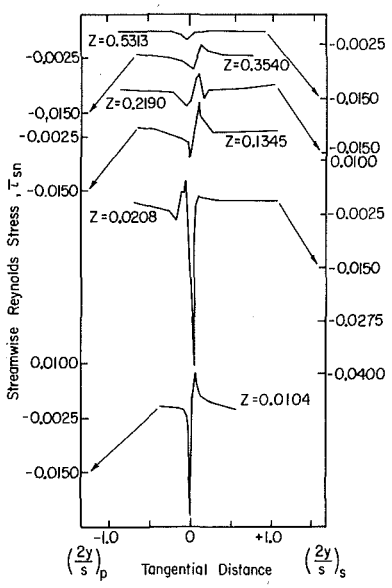

Fig. 12 Streamwise Reynolds stress profiles, $R = 0.7297$, $\phi = 0.56$

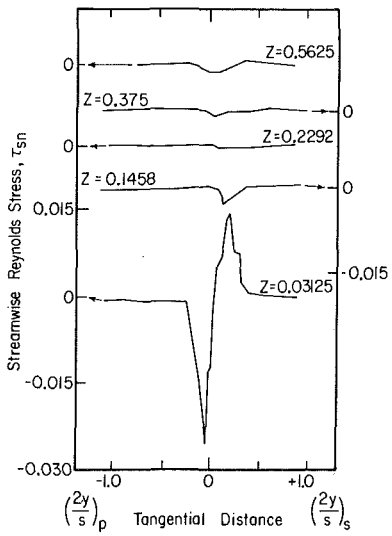

Fig. 13 Streamwise Reynolds stress profiles, $R = 0.7973$, $\phi = 0.56$

Downloaded 01 Jun 2010 to 171.66.16.59. Redistribution subject to ASME license or copyright; see http://www.asme.org/terms/Terms_Use.cfm

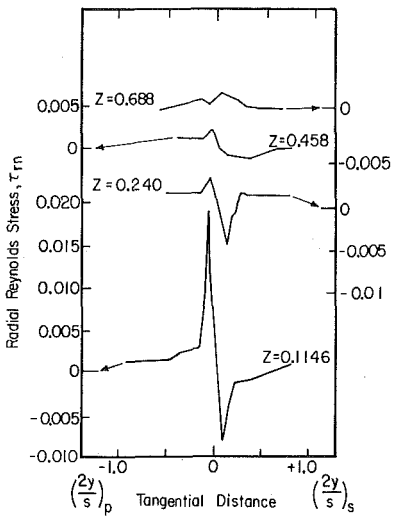

Fig. 14 Radial Reynolds stress profiles, $R = 0.6581$, $\phi = 0.56$

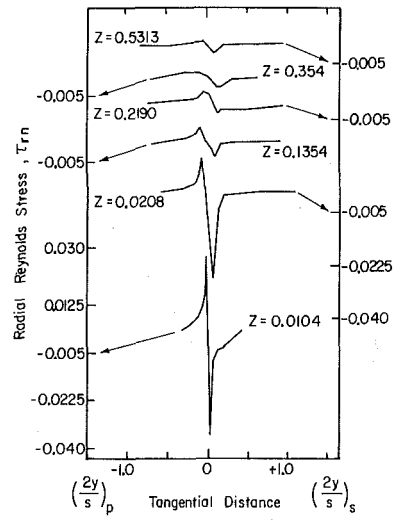

Fig. 15 Radial Reynolds stress profiles, $R = 0.7297$, $\phi = 0.56$

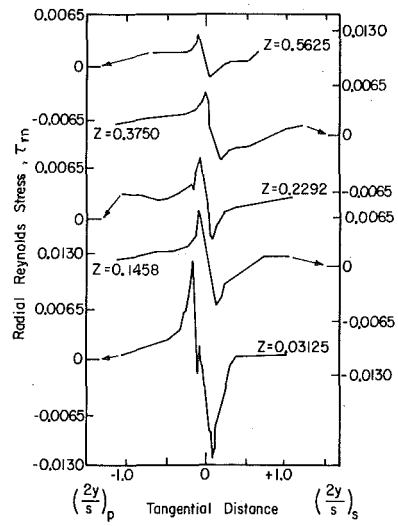

Fig. 16 Radial Reynolds stress profiles, $R = 0.7973$, $\phi = 0.56$

This can be argued on the basis of the Reynolds stress equation in the rotating coordinate system [4] wherein the effect of rotation is to attenuate the streamwise stress component (τ_{sn}) and amplify the radial stress component (τ_{rn}). In the trailing edge region the situation tends to be far more complicated because of the trailing vortex system dominating the flow. Their effect seems to make the radial velocity gradients highly steep. In the trailing edge and near-wake regions for $R = 0.7297$, the ratio of τ_{rn}/τ_{sn} is approximately 1.04. This ratio represents deviation of the total stress vector from the streamwise direction.

The effect of loading on this deviation can be seen by comparing the present data with those of reference [4]. Higher loading induces greater deviation of the stress vector from the streamwise direction. This is to be expected as higher loading results in higher radial components of velocity gradient and consequently larger radial stresses.

3.2.3 Stress correlation τ_{sr}. The stress correlations τ_{sr} are shown plotted in Figs. 17–19 for the radii $R = 0.6581$, 0.7297 and 0.7973. It is seen that the magnitude of this correlation is of the same order as that of streamwise stress. It has the same sense on either side of the wake. This correlation decays very rapidly in the trailing edge region and the decay is very slow in the far wake region.

The Reynolds stress data presented in this section must be studied with some caution. It is possible that the results are subjected to spatial errors which are inherent in a tri-axial hot wire probe. However, the contribution to stress from eddies larger than the distance between the probe sensors is measured accurately. An estimate of the scales of flow and the expected orders of error are given in Appendix A2 and A3 of reference [2].

3.3 Decay of Rotor Wake Turbulence Intensity and Stress with Downstream Distance.

3.3.1 Decay of Maximum Turbulence Intensities. Decay of maximum axial, tengential and radial turbulence intensities normalized by the local mean velocity is shown plotted in Fig. 20 for the wakes outside the annulus and hub wall boundary layers. It is seen that the intensities are very high in the trailing edge region and that they decay very rapidly in the vicinity of the blade.

Reference [4] gives a qualitative analysis on the effects of rotation on turbulence. It is shown that the turbulence structure of a rotor wake is quite different compared to a stationary case. The radial intensities are likely to be higher than the axial and tangential components. The present data seems to confirm this analysis only at higher radius. Furthermore, the data also confirm the analysis of reference [5], which shows that if the gradient of the radial component of mean velocity across the wake is much larger than the angular velocity of the machine, then

$$\tau_r > \tau_\theta > \tau_z$$

But the data at lower radii do not agree with this reasoning.

Not only the magnitudes of the turbulence intensities at each radii are different, so also are their decay rates. It is seen from Fig. 20 that the decay of the axial and tangential components are about the same while the radial intensity decays very much more slower.

Comparing the authors' results with those of reference [4], it is seen that the effect of loading is to increase the maximum axial, tangential and radial intensities in the wake. The decay of intensities is also rapid with increased blade loading.

The radial component is higher than the axial and tangential components far downstream and shows tendency to become isotropic beyond one chord length.

3.3.2 Decay of Maximum Shear Stresses. The decay of the maximum turbulence shear stresses are shown plotted in Fig. 21. The stresses are very high in the trailing edge region decaying very rapidly downstream of the trailing edge. The rate of decay seems to follow the same trend for all the radii outside the annulus and hub wall boundary layers. The decay, shown in Fig. 21, for the streamwise (τ_{sn}), radial (τ_{rn}) and shear stress correlation (τ_{sr}) seems to exhibit wide scatter for different radii. This is to be expected as the wake development and decay are different at different radii.

Normalizing the stresses by the corresponding values at the trailing

Downloaded 01 Jun 2010 to 171.66.16.59. Redistribution subject to ASME license or copyright; see http://www.asme.org/terms/Terms_Use.cfm

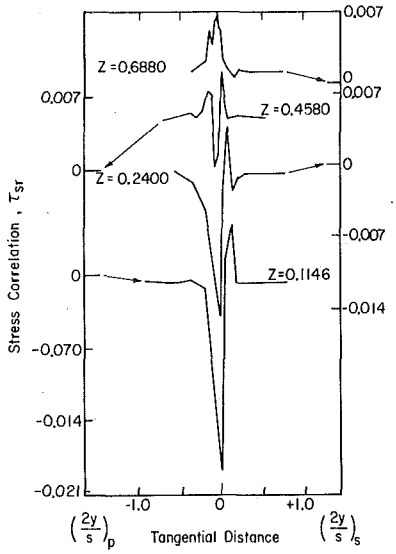

Fig. 17 Stress correlation profiles, $R = 0.6581$, $\phi = 0.56$

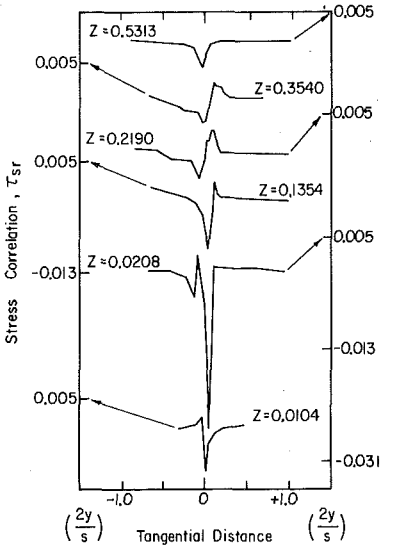

Fig. 18 Stress correlation profiles, $R = 0.7297$, $\phi = 0.56$

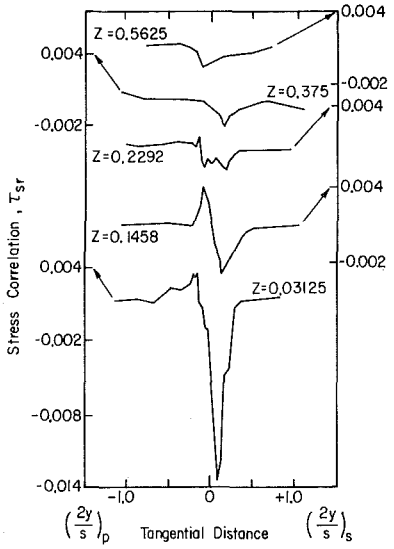

Fig. 19 Stress correlation profiles, $R = 0.7973$, $\phi = 0.56$

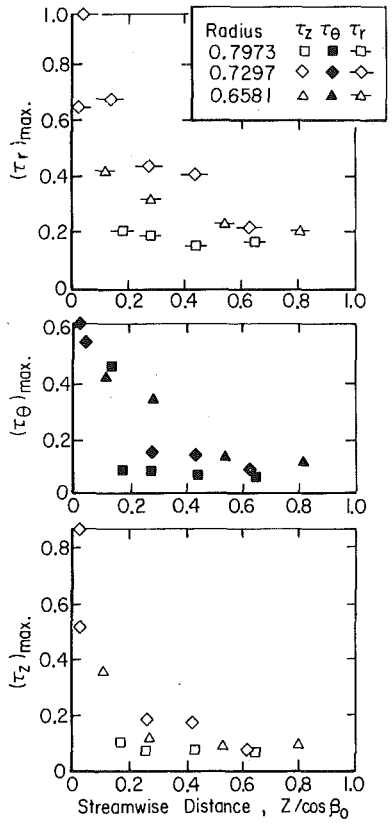

Fig. 20 Decay of maximum axial, tangential and radial turbulence intensity

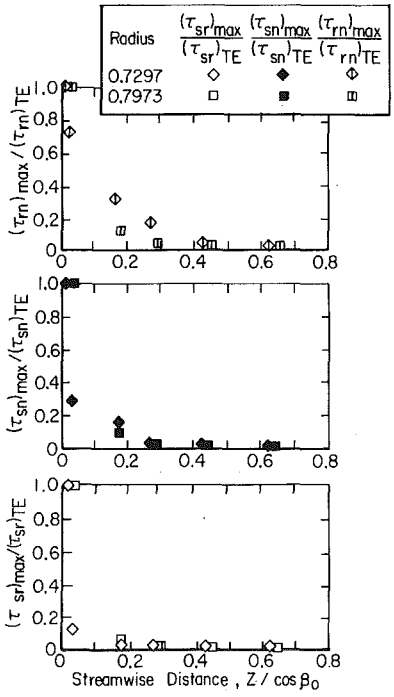

Fig. 21 Decay of maximum shear stress with streamwise distance

edge should collapse all the data on to a single curve, provided the stresses, like the intensities and velocities, depend only on their initial value. This correlation is attempted below.

Raj and Lakshminarayana [7] have shown that the decay of the stresses can be represented in the form

$$\tau_{ij} = K\left(\frac{z}{\cos\beta_0}\right)^n$$

Downloaded 01 Jun 2010 to 171.66.16.59. Redistribution subject to ASME license or copyright; see http://www.asme.org/terms/Terms_Use.cfm

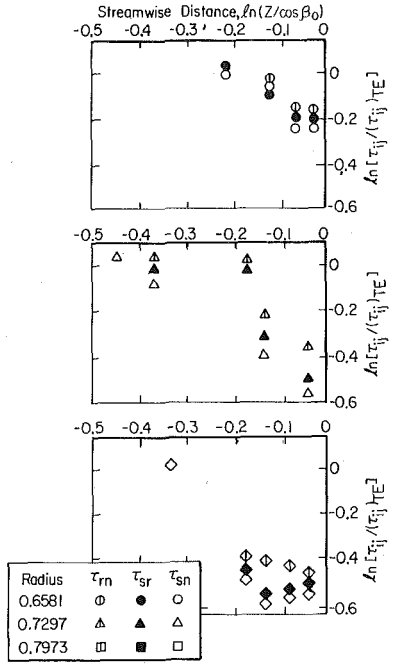

Fig. 22 Decay of normalized shear stress with downstream distance

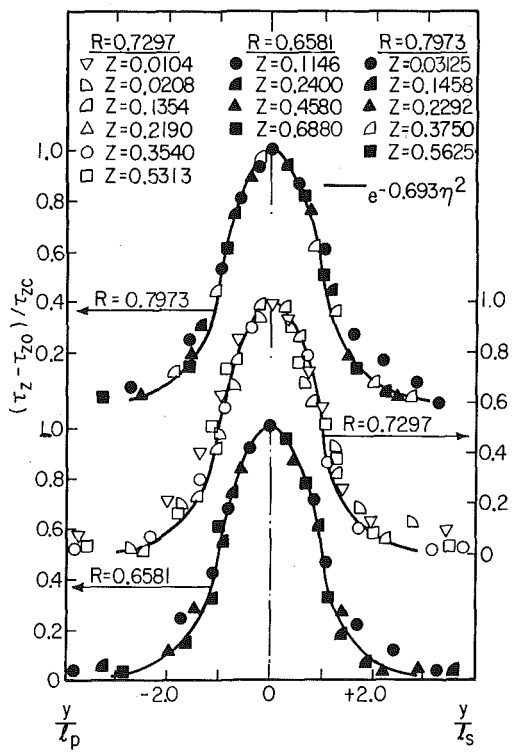

Fig. 23 Similarity for axial turbulence intensity profile

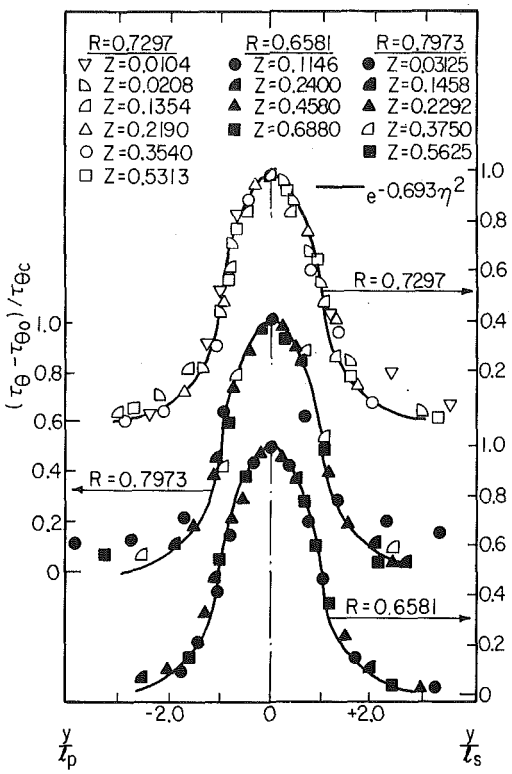

Fig. 24 Similarity for tangential turbulence intensity profile

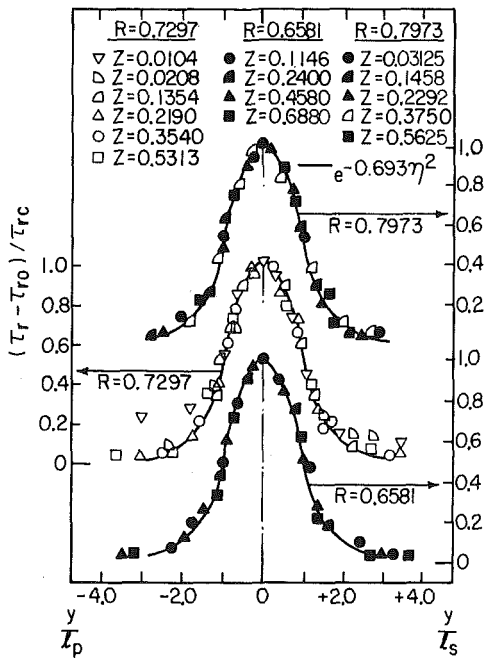

Fig. 25 Similarity for radial turbulence intensity profile

where the exponent n assumes different values for the three components of stress. This plot is shown in Fig. 22. A close look at the present data indicates that the exponent n assumes different values for different radii. Other normalizing factors to include radial variations of mean-velocity, turbulence intensities, and section drag coefficient might collapse the data into a universal curve and lead to a reasonably good correlation.

3.4 Similarity of Turbulence Intensity Profiles. The similarity rule was examined for axial, tangential and radial components of turbulence intensity for the entire wake region and these are plotted in Figs. 23–25. In these plots the turbulence intensity has been normalized by the maximum turbulence intensity. In situations where a "dip" was noticed at the wake center, an extrapolated peak intensity near the wake center was taken. To study the intensity profiles in the wake alone, the free stream value was subtracted from the local values. The distance from the wake centerline to the location where the maximum turbulence intensity minus the free stream value is half was taken as the characteristic length scale l_p and l_s, on the pressure and suction side, respectively. Using this technique which is very similar to the one employed to examine the velocity profile similarity [1], similarity was tried for the axial, tangential and radial components of turbulence intensity.

Downloaded 01 Jun 2010 to 171.66.16.59. Redistribution subject to ASME license or copyright; see http://www.asme.org/terms/Terms_Use.cfm

Similarity was found for all the three components of intensity for the entire wake region. As in the case of velocity profile similarity [1], the discrepancy from the Gaussian curve was noticed in the outer region of the flow as well as for the wakes in the trailing edge region. For the wakes inside the annulus and hub wall boundary layer the deviation from the Gauss' curve was considerable, particularly for the wakes in the trailing edge and near wake regions. This is to be expected as the turbulence structure in these regions is markedly affected by the tip vortex, secondary flow and the interaction of the wake and annulus and hub wall boundary layers.

3.5 Turbulence Structure.

3.5.1 Correlation Coefficient. The shear correlation coefficient, defined as $[\tau_{sn}/(\tau_s \cdot \tau_n)]$, where τ_s, τ_n are turbulent intensities in streamwise and normal directions, respectively, depends on the nature of turbulence. For the rotor wake this coefficient is shown plotted in Fig. 26 at various downstream locations for the radius $R = 0.7297$. Ermshaus [9] has given this correlation coefficient for the far-wake of axisymmetric bodies in a two-dimensional flow. The data indicate that this coefficient varies from 0.6 to −0.6 across the wake. It is known that a value of ±0.45 represents an isotropic turbulence structure. Comparison of the data from reference [9] with the author's data (Fig. 26) reflects the highly nonisotropic, inhomogeneous and asymmetric nature of turbulence, particularly in the near wake region. Beyond $Z = 0.5313$ the coefficient becomes almost constant across the rotor wake indicating the trend towards isotropy.

Outer regions of the wake display isotropic turbulence with the value around 0.4 (Fig. 26). In the inner regions of the wake where the radial intensities are dominant compared to streamwise and normal components, the correlation coefficient takes on very high values indicating the highly non-isotropic nature of turbulence. Outside the wake, as expected, the correlation coefficient reaches nearly zero values.

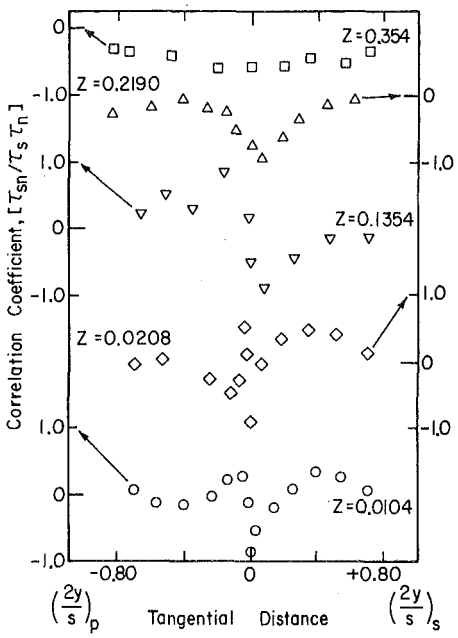

Fig. 26 Variation of the correlation coefficient across the rotor wake, $R = 0.7297$, $\phi = 0.56$

3.5.2 Turbulence Spectra. Real time spectrum analysis was carried out to evaluate the spectral content of the turbulence in the flow behind the rotor blades. Such an energy spectrum was taken at various axial, radial and tangential positions behind the rotor from a rotating hot wire. The spectrum in the free stream (between blades) as well as inside the wake (at the wake center) are presented and discussed in this section.

It is known that the slope of the energy spectrum is $-5/3$ in the inertial range of isotropic turbulence and -1 in the viscous convective range. It is of interest to know whether the rotor wake spectrum also follow this boundary layer spectrum.

Figure 27 shows the spectrum taken at four representative radii in the free stream. The spectrum of fluctuating voltages from each of the three wires are shown in these plots. The spectrum show peaks at the blade passing frequency. Plotted on a linear scale, the area under the peaks would represent the fraction of the total fluctuating energy contained in the periodic oscillations due to the upstream inlet-guide-vane wakes, while the area of the lower band would represent the fraction of the energy contained in the turbulence fluctuations. It is seen from Fig. 27 that most of the energy in turbulence outside the wake is confined to the low frequency range (less than 2 KHz) with peak at blade passing frequency (based on number of IGV

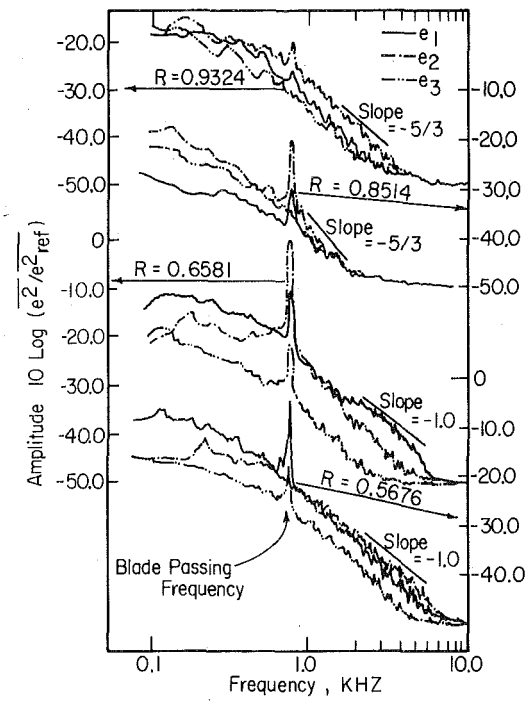

Fig. 27 Turbulence energy spectra in the relative frame of reference (outside the wake region)

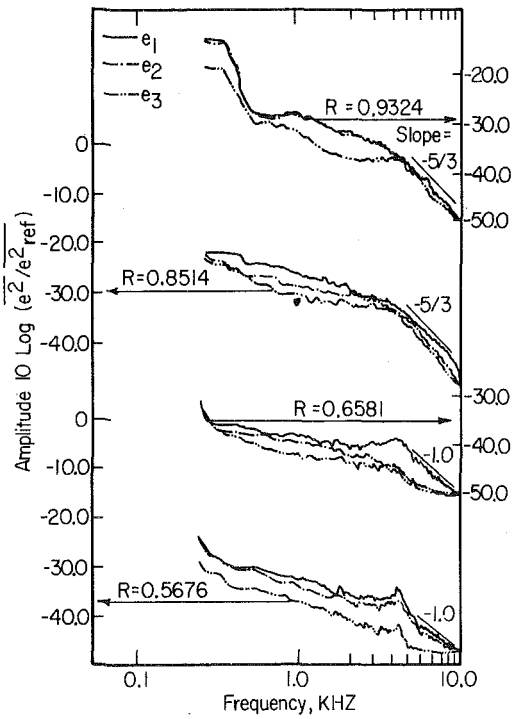

Fig. 28 Turbulence energy spectra in the relative frame of reference (at the wake center)

Downloaded 01 Jun 2010 to 171.66.16.59. Redistribution subject to ASME license or copyright; see http://www.asme.org/terms/Terms_Use.cfm

blades) corresponding to the inlet-guide-vane wakes. This value is 0.74 for this case (Fig. 27).

It is evident that the rotating hot wire senses the inlet-guide-vane wakes as a source of turbulence and hence its effect appears in the spectrum. The amplitude of the peak represents the magnitude of the velocity defect that persists in the inlet-guide-vane wakes after its passage through the rotor blade. The figure also shows the radial variation of the IGV wake velocity defect which is sensed by the rotating wire as a fluctuating velocity. The maximum defect seems to occur in the mid-radius region decreasing towards the end wall zones.

Figure 28 shows the spectrum taken at different radii at the center of the wake. The effect of radius on the spectral content can be seen from this figure. The energy content in the turbulence fluctuations increases with increasing radius. Further there are no "peaks" in the energy spectrum indicating that the inlet-guide-vane wakes undergo substantial changes in the transport properties as it passes through the boundary layer of the rotor blade. The spectrum also exhibits typical energy distribution that exists in turbulent flows with most of the energy contained within 10 KHz.

The energy in the spectrum is given by

$$E(k) = I_{(k)} f_{(k)}^{-n}$$

where $I_{(k)}$ = constant depending on the wave number, $f_{(k)}$ = frequency of the turbulent fluctuation and, n = exponent.

For the present case, the spectra taken in the blade passages (Fig. 27) show a slope of -1 for the wakes in the lower radius region and $-5/3$ in the higher radius region. For the spectra taken at the wake center (Fig. 28) the slopes are $-5/3$ at higher radii and -1 at lower radii. The $(-5/3)$ law is characteristic of an isotropic structure of turbulence.

It is of interest to note that the length scales of eddies in the above spectra. The eddy lengths in the frequency range shown in Figs. 27 and 28 lie between 0.14 cm to 1.52 cm.

4 Conclusions

The turbulence characteristics of the wake of a moderately loaded compressor rotor blade was investigated experimentally. The main emphasis was in the trailing edge and near wake regions. All the measurements were obtained using a rotating triaxial hot wire probe. The major conclusions that can be derived on the basis of this investigation are as follows:

1 Very high turbulence intensities were measured in the trailing edge region and is attributed to the trailing vortex system.

2 The intensity profiles were asymmetrical in nature. Increased blade loading seems to sustain the asymmetry to a much larger downstream distance.

3 The turbulence stress profiles are asymmetrical about the wake center with the stresses near the pressure-surface being higher than those near the suction-surface. The zero streamwise Reynolds stress occurs slightly away from the location of minimum velocity.

4 Decay of intensities and stresses are very rapid in the trailing edge region and it slows down in the far wake region. The rapid decay in the trailing edge region is attributed to the trailing vortex system.

5 The radial turbulence intensity decays slowest compared to axial and tangential components. The radial intensities were also found to be the largest and these phenomena are attributed to rotation effects.

6 The free stream turbulence for the wakes outside the end wall boundary layers are about the same at all radii.

7 The turbulence structure of the rotor wake is highly asymmetric, nonisotropic and inhomogeneous in the trailing edge region and becomes isotropic and asymmetric in half a chord downstream.

8 The spectra of turbulence taken in the blade passages and in the wake center show a slope of -1 at lower radii and $-5/3$ at higher radii.

9 Similarity was also found for all the three components of turbulence intensity. Discrepancy from the Gaussian curve was observed only in the outer regions of flow as well as far wakes in the trailing edge region.

Acknowledgments

This work was supported by the National Aeronautics and Space Administration through grant NSG 3012, with M. F. Heidmann as the Technical Monitor.

References

1 Ravindranath, A., and Lakshminarayana, B., "Mean Velocity and Decay Characteristics of the Near- and Far-Wake of a Compressor Rotor Blade of Moderate Loading," ASME Paper No. 79-GT-202 (to be published in the ASME JOURNAL OF ENGINEERING FOR POWER).

2 Ravindranath, A., "Three Dimensional Mean and Turbulence Characteristics of the Near Wake of a Compressor Rotor Blade," M.S. Thesis, Department of Aerospace Engineering, The Pennsylvania State University, Nov. 1979.

3 Gorton, C. A., and Lakshminarayana, B., "A Method of Measuring the Three Dimensional Mean Flow and Turbulence Quantities Inside a Rotating Turbomachinery Passage," ASME JOURNAL OF ENGINEERING FOR POWER, Vol. 98, No. 2, 1976, pp. 137–146.

4 Lakshminarayana, B., and Reynolds B., "Turbulence Characteristics in the Near-Wake of a Compressor Rotor Blade," AIAA Paper 79-0280, 1979.

5 Raj, R. and Lumley, J. L., "A Theoretical Investigation on the Structure of Fan Wakes," *J. Fluids Engineering*, Vol. 100, 1978, pp. 113–119.

6 Anand, A. K., and Lakshminarayana, B., "An Experimental Study of Three Dimensional Turbulent Boundary Layer in Turbulence Characteristics Inside a Turbomachinery Rotor Passage," ASME JOURNAL OF ENGINEERING FOR POWER, Vol. 100, No. 4, Oct. 1978, pp. 676–690.

7 Raj, R. and Lakshminarayana, B., "Three Dimensional Characteristics of Turbulent Wakes Behind Rotors of Axial Flow Turbomachinery," ASME JOURNAL OF ENGINEERING FOR POWER, Vol. 98, Apr. 1976, pp. 218–228.

8 Hah, C., "Numerical and Experimental Analysis of Turbulent Wakes of Airfoil, Cascade, and Turbomachinery Rotor Blade," Ph.D. Thesis, Department of Aerospace Engineering, The Pennsylvania State University, Mar. 1980.

9. Ermshaus, R., "Typical Features of Turbulent Wake Flows," *Mitteilungen aus dem Max-Planck Institut fuer Stromungsforschung der Aerodyn. Versuchsanstalt*, Gottingen, No. 46, 1976.

Downloaded 01 Jun 2010 to 171.66.16.59. Redistribution subject to ASME license or copyright; see http://www.asme.org/terms/Terms_Use.cfm

P. W. Schilke
General Electric Company

W. S. Blazek
TRW, Inc.

W. F. Schilling
General Electric Company

Water-Cooled Gas Turbine Monometallic Nozzle Development

This paper describes the materials and processes development required to fabricate the second stage monometallic water-cooled nozzle for the Department of Energy funded High Temperature Turbine Technology (HTTT) program. Materials engineering and development work including alloy selection, hot isostatic pressing (HIP), and heat treat optimization necessary to fabricate this component is described and the results of this work are reported. Specialized processes utilized to achieve tight design tolerances such as TRW's split mold investment casting and shaped tube electrode machining (STEM) are also described. The advantages of these processes are discussed in terms of the overall component design goals.

Introduction

The General Electric Company began working toward the design and construction of a water-cooled gas turbine in the early 1960s. In 1967 the first laboratory water-cooled turbine was tested successfully. Since 1974 the Electric Power Research Institute (EPRI) has funded preliminary design and development work necessary to define and resolve potential problems. In May of 1976 the United States Energy Research and Development Administration (ERDA) awarded a High Temperature Turbine Technology (HTTT) Phase I contract to the General Electric Company to conduct a preliminary design study aimed at utilizing a water-cooled turbine in a combined-cycle plant. The resultant design was based on a gas turbine firing temperature (gas temperature entering the first stage buckets) of 2600°F (1427°C), combusting a coal-derived low-Btu gas or coal-derived liquid fuel and had a growth capability to 3000°F (1649°C) firing temperature.

At the conclusion of the Phase I contract, the United States Department of Energy (DOE) awarded an HTTT Phase II contract to the General Electric Company's Gas Turbine Division directed toward component design and technology testing in critical areas of water-cooled gas turbine technology. This effort was directed principally at the hot gas path components and included the fabrication and testing of critical water-cooled components.

This paper focuses on the development of one of these critical components, the second stage water-cooled monometallic nozzle, and describes the fabrication processes required to build it. The status of the nozzle fabrication as of August 1, 1979, is also presented. Information regarding the combined cycle, gas turbine design, and program definition has been previously reported [1–6] and is summarized here only as necessary to establish the goals of the second stage nozzle design. The final results of the second stage nozzle fabrication and testing will be presented in a subsequent paper.

Second Stage Nozzle Process and Material Selection

The overall goal of the HTTT program is to develop the technology for a high temperature gas turbine which can be operated in a combined cycle, burning coal-derived fuel, at a firing temperature of 2600°F (1427°C) with a growth capability to 3000°F (1649°C). More specifically, in the Phase II Program one of the major objectives is to perform component design and technology testing in critical areas. The second stage water-cooled monometallic nozzle is one of the critical components which is to be designd, developed, fabricated, and tested during the Phase II Program.

Metal temperatures should be maintained at 1000°F (538°C) or lower [7] to minimize the impact of both corrosion and performance degradation due to reduction of nozzle throat area caused by ash buildup. A full flow closed loop, pressurized water-cooling circuit has been designed to achieve these low metal temperatures in the second stage nozzle, where the gas temperature is predicted to be 2460°F (1349°C) for a 2600°F (1427°C) firing temperature. Internal water cooling was selected in order to avoid completely the potential problems associated with cooling hole plugging due to ash deposition. The water will be pressurized to approximately 1250 psi (8.618 MPa) and will enter the nozzle at 225°F (107°C) and exit the nozzle at 393°F (201°C). Water chemistry will be closely maintained at pH 9.0–9.5 and less than 10 ppb O_2 in order to minimize water circuit plugging rates.

Cooling water at 225°F (107°C), rather than cold water, is supplied to the second stage nozzle. This allows enough cooling to achieve the 1000°F (538°C) metal temperature goals while reducing thermal strain.

The cooling circuit configuration in the nozzle airfoil section is a series of 47 holes parallel to, and running the length of, the airfoil. They are located along the periphery of the airfoil (Fig. 1). Most of these holes are 0.070 in. (1.78 mm) in diameter and are located approximately 0.060 in. (1.52 mm) below the gas path surface. The cooling circuit configuration in the nozzle endwalls is a series of straight holes extending from the edges of the endwalls to the airfoil extension through the endwalls. Most of these holes are 0.090 in. (2.29 mm) in diameter and are located approximately 0.080 in. (2.03 mm) below the endwall gas path surfaces (Fig. 1).

The water flows through the airfoil twice in a pattern designed to minimize thermal strains before exiting the nozzle. It flows into the outer endwall through a manifold near the trailing edge of the nozzle, through the rear portion of the outer endwall, into a manifold, through the rear section of the airfoil, into a manifold, through the rear section

Contributed by the Gas Turbine Division and presented at the Gas Turbine Conference and Products Show, New Orleans, La., March 10–13, 1980 of THE AMERICAN SOCIETY OF MECHANICAL ENGINEERS. Manuscript received at ASME Headquarters December 19, 1979. Paper No. 80-GT-97.

Copyright © 1981 by ASME

Downloaded 01 Jun 2010 to 171.66.16.59. Redistribution subject to ASME license or copyright; see http://www.asme.org/terms/Terms_Use.cfm

of the inner endwall, through jumper tubes to the front of the inner endwall, through the front of the inner endwall, into a manifold, through the front portion of the airfoil, into a manifold, through the front portion of the outer endwall, into a manifold in the front of the outer endwall and finally exits the nozzle.

Preliminary design calculations indicated the maximum strains (induced by thermal gradients) were on the order of 0.5 percent at 850°F (454°C) for the nominal design wall thickness between the cooling passage and gas path. It was also determined that a strong relationship existed between this wall thickness and the magnitude of thermal strain in the nozzle and thus, low cycle fatigue life (Fig. 2).

To meet the cycle life goal of 1675 cycles it is necessary to closely control the wall thickness between the cooling passage and the gas path. It is therefore necessary to produce a nozzle with as-cast nozzle dimensions to tolerances which are tighter than normally produced by investment casting (0.005 in./in. (0.005 mm/mm)). The HTTT program requirements are ±0.006 in. (0.152 mm) for the airfoil and ±0.005 in. (0.127 mm) for the endwall sections; whereas conventional superalloy nozzle casting contours are currently ±0.010 in. (0.254 mm) for airfoil and ±0.035 in. (0.889 mm) for the endwall sections. The TRW split mold casting process described in references [8] and [9] was selected to accomplish this goal. This technique has demonstrated the capability to hold investment cast tolerances of 0.001 in./in. (0.001 mm/mm) [10]. This casting technique will be described in detail in the following sections.

The cooling passage installation in the nozzle must also be kept within a narrow tolerance band to maintain control over the wall thickness between the cooling passage and gas path. The shaped tube electrode machining (STEM) technique was selected to drill these cooling passages into the nozzle because it provides the most accurate technique for creating holes of this size and length in a superalloy and because more than one hole can be drilled at the same time. The STEM drilling process can hold a centerline hole tolerance of 0.002 in./in. (0.002 mm/mm) over the length of the hole (approximately 8 in. (20 cm) maximum). A hot isostatic pressing (HIP) cycle will be used on the cast part prior to STEM drilling to further improve the accuracy of the STEM drilling process. This HIP cycle will eliminate any microporosity and chemical gradients present in the casting, thereby eliminating the possibility of drilling into a porous region or non-homogeneous material which could cause a local variation in STEM drilling rates and thereby increase centerline drift.

A number of cooling hole plugs and manifold covers must be installed on the nozzle to seal the entrance ways and manifolds of the cooling hole passage. The plugs and covers must contain the 1250 psi (8.618 MPa) water pressure and must be able to withstand significant thermal strains. The configuration of the manifold covers, their limited accessibility, and the large total joint length of these covers makes welding of these covers and plugs an unattractive option. Therefore brazing was selected as the preferred method of sealing the entrances and manifolds of the cooling circuits.

The gold-nickel-palladium alloy Palniro-7 was selected for this application to maximize the joint's strain tolerance and be compatible with the alloy 718 heat-treatment schedule.

Criteria for selection of an alloy for this second stage nozzle must include not only the design and fabrication considerations previously discussed but also the part life goal of 41,000 hr. This life goal translates into two additional requirements:

1 Long term alloy stability and
2 Long term corrosion resistance

at 1000°F (538°C) under "dirty" fuel conditions. Alloy 718 (19 w/o Cr, 53 w/o Ni, 3 w/o Mo, 5 w/o Cb + Ta, 0.9 w/o Ti, 0.5 w/o Al, Bal. Fe) satisfies both of these criteria as well as the fabricability and cycle life criteria discussed previously. Alloy 718 has been studied after exposures ranging from 1000°F (538°C) to 1300°F (704°C) for up to 33,000 hours by Barker, et al. [11]. Their study concluded that on the basis of these exposure temperatures and times, there were no detrimental structural instabilities except for the expected overaging at 1300°F (704°C). Alloy 718 has also been the subject of numerous investigations to define the time-temperature phase relationships [12–15].

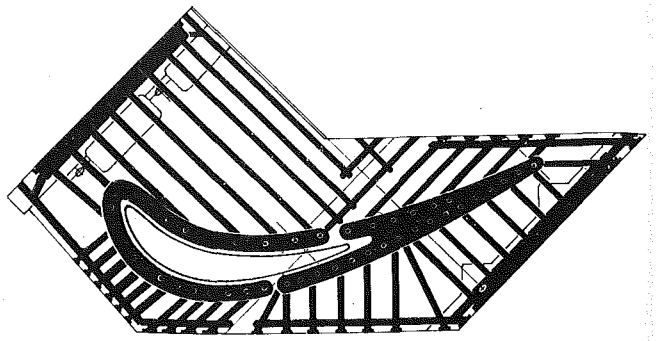

Fig. 1 Cooling circuit of the second stage nozzle outer endwall and airfoil

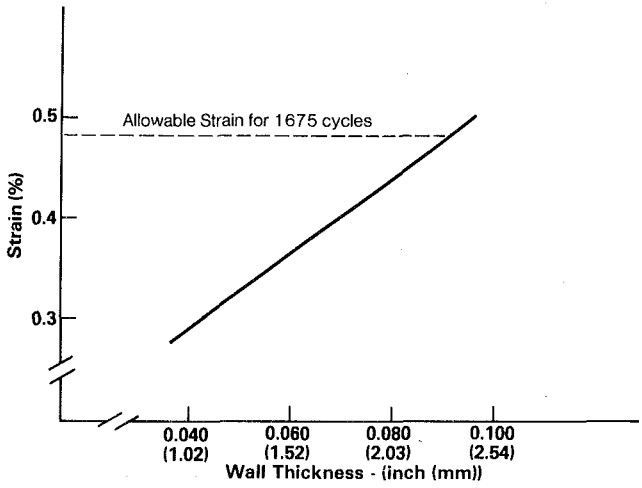

Fig. 2 Percent strain as a function of wall thickness between cooling passage and gas path and low cycle fatigue life

These relationships have now been established for well-homogenized alloy 718 and form the basis for predicting and optimizing phases present in alloy 718.

The corrosion resistance of alloy 718 in a dirty fuel environment at metal temperatures of 1000°F (538°C) maximum has also been investigated [16]. It was found that alloy 718 has a relatively low corrosion rate under these conditions compared with other superalloys and is projected to meet the very high lifetime design goals.

Preliminary design calculations indicated that the maximum strains due to thermal gradients in this second stage nozzle are on the order of 0.5% at 850°F (454°C). Cast and HIP'ed alloy 718 was found to satisfy this strain range cycle life requirement. Therefore alloy 718 was selected as the second stage nozzle material.

Fabrication Process

Split-Mold Investment Casting. The TRW split-mold investment casting process provides a unique method for fabrication of very accurate investment casting molds. This process eliminates the major sources of wax pattern dimensional discrepancies—nonuniform wax shrinkage and wax pattern distortion (during mold build-up)—by incorporating aluminum chills into the wax injection mold prior to wax injection. In addition, provisions are made during the design of the mold to allow for the later removal of these chills by adding parting flanges in the mold which effectively "split" the mold along predetermined locations. The locations of these flanges are shown schematically in Fig. 3. The thickness of the flanges is added to the thickness of the endwalls of the nozzle during pattern die fabrication. During the wax dipping operation (mold build-up) the flanges are wiped clean of ceramic material so that upon dewaxing, the mold splits along the flanges into three separate pieces allowing removal of the aluminum chills.

The aluminum chills incorporated into the wax injection mold are fabricated by sand casting to be approximately 0.100 in. (2.54 mm)

Downloaded 01 Jun 2010 to 171.66.16.59. Redistribution subject to ASME license or copyright; see http://www.asme.org/terms/Terms_Use.cfm

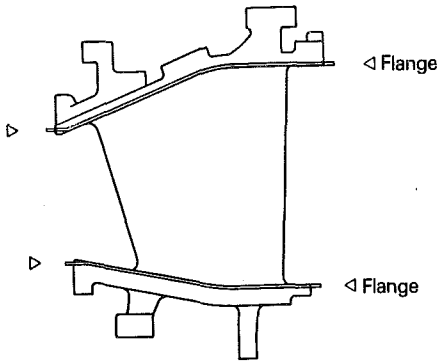

Fig. 3 Schematic of second stage nozzle showing location of flanges incorporated into the mold design

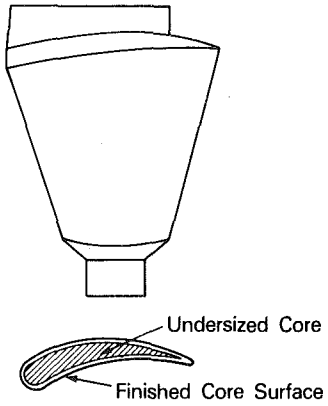

Fig. 4 Ceramic core construction used for the second stage nozzle

below the surface of the endwalls and approximately 0.200 in. (5.08 mm) below the surface of the airfoil. The chill in each of the endwalls also has two drilled and tapped holes in the leading edge face in which bolts are screwed to grip the wax pattern during mold build-up. Thus the aluminum chills provide both a uniform chill for the hot wax and a skeleton of support during the mold build-up thereby minimizing wax distortion.

Once the mold is dewaxed all the internal ceramic mold surfaces are available for inspection and local repair if necessary. The ceramic mold is then assembled with the ceramic core, cemented together, and leak checked. It is then ready for the normal investment casting processing.

The ceramic core used in this second stage nozzle is also a high precision core. It is constructed by fabricating an undersized (by approximately 0.150 in. (3.81-mm)) core which is fully fired. This undersized core is then used in the core die and additional ceramic material is poured around this undersized core. The full core is then fired and the resultant ceramic shrink due to sintering is thereby held constant throughout the core regardless of section thickness (Fig. 4).

Hot Isostatic Pressing And Heat Treatment. Cast alloy 718 has been shown to respond to hot isostatic pressing with significant improvements in tensile strength and tensile ductility [10, 17]. However, additional work was required to optimize the HIP cycle for the large section size present in the second stage nozzle component. This work resulted in the selection of the following HIP parameters: 2175°F ± 20°F (1191°C ± 11°C), 15 ksi (103 MPa), 4 hr. Metallographic investigations showed that the use of this HIP cycle resulted in complete elimination of Laves phases present in large section size, as-cast alloy 718 and complete homogenizing of the alloy. Figure 5, (*a*) and (*b*), shows the microstructure of as-cast versus HIP'ed alloy 718, and Table 1 shows the tensile test results for the as-cast and HIP'ed conditions.

The post HIP heat-treatment cycle for alloy 718 was also evaluated. Aging cycles of: (*a*) 1400°F (760°C) for 10 hr furnace cool at 100°F/hr (56°C/hr) to 1200°F (649°C) and hold for a total of 18 hr and (*b*) 1325°F (718°C) for 8 hr furnace cool at 100°F/hr (56°C/hr) to 1150°F (621°C) and hold to 1150°F (621°C) for 8 hr were evaluated on samples of cast and HIP'ed alloy 718. It was found that ductility, as measured by reduction in area, was maximized by the (*b*) aging cycle. Since the low cycle fatigue life of this component in the high strain range is maximized by maximizing the reduction in area of the alloy, the aging cycle (*b*) was selected for use in this component.

Shaped Tube Electrode Machining (STEM). The STEM process was developed by General Electric Aircraft Engine Business Group in 1958 to drill holes from 0.025 in. (0.635 mm) to 0.150 in. (3.81 mm) in diameter to depths of 12 in. [18]. The process is similar to ECM except that multiple small diameter dielectric-coated metal tubes are used as electrodes for gang-drilling holes (Fig. 6). The work piece is the anode as in ECM, however, the d-c polarity is reversed intermittently in STEM to prevent the deposition of dissolution products on the cathode surfaces, which are the uninsulated top ends of the electrodes.

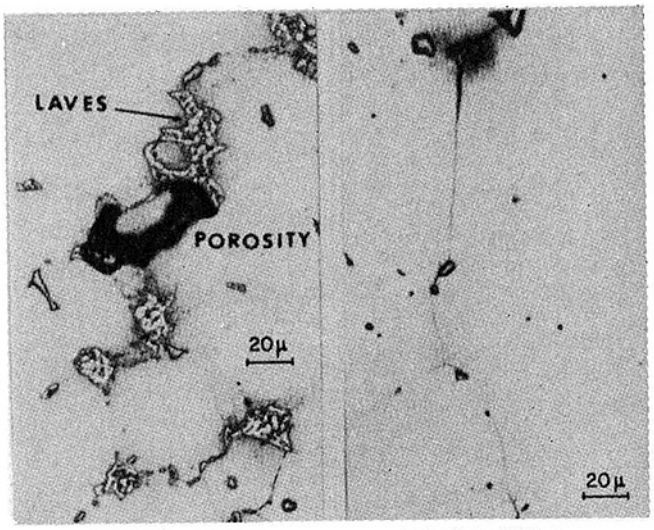

Fig. 5(*a*) As-cast Fig. 5(*b*) HIP'ed

Fig. 5 Microstructure of alloy 718

Table 1 Tensile test results (average) of alloy 718 as-cast and aged versus HIP'ED and aged

	Temperature (°F (°C))	Ultimate (ksi)	0.2% Yield (ksi)	% Elon.	% R.A.
As-Cast	70 (22)	167	138	12	17
and	600 (316)	146	129	7	21
Aged*	1000 (538)	136	118	5	17
HIP'ed	70 (22)	175	153	12	25
and	600 (316)	152	135	10	28
Aged†	1000 (538)	140	125	9	27

* As-cast and aged: 2000°F (1093°C)/2 hr
1750°F (954°C)/1 hr
1325°F (718°C)/8 hr
1150°F (621°C)/8 hr
†HIP'ed and aged: 2175°F (1191°C)/15 ksi (108 MPa)/4 hr
1325°F (718°C)/8 hr
1150°F (621°C)/8 hr
Conversion factor: (ksi) = (1.45 × 10^{-1} MPa)

This electrochemical drilling technique produces relatively smooth internal surfaces as opposed to the EDM process which leaves a "recast" surface layer on the internal surface of the hole. This internal surface is important since some of the highest thermal strains in the second stage nozzle are located on these surfaces. The presence of a recast layer is often associated with microcracks which can dramatically reduce the fatigue life of the part. Therefore the STEM drilling process provides for maximum low cycle fatigue life by producing smooth, residual stress free surfaces.

Downloaded 01 Jun 2010 to 171.66.16.59. Redistribution subject to ASME license or copyright; see http://www.asme.org/terms/Terms_Use.cfm

The STEM drilling process achieves hole centerline accuracy by feeding the metal tube electrodes through two precision-machined templates which align the electrodes for the initial drilling of the component. As the electrodes drill into the component the holes serve as a further guide to keep the electrodes on the planned centerline of the holes. By this technique the STEM drilling process can hold tolerances of ±0.002 in./in. (±0.002 mm/mm) on centerline.

Brazing. The joining of the nozzle manifold covers and cooling passage plugs will be accomplished by a vacuum brazing operation. Brazing has the capability to join all the manifold covers and plugs to the nozzle in one step. It also allows for local repair, by TIG torch or by another furnace cycle, if necessary to achieve a leaktight nozzle. Selection of the brazing alloy for use on this component was governed by the following criteria: (1) compatability with the alloy 718 heat treating cycle (2) sufficient alloy strength to retain the 1250 psi (8.618 MPa) water, (3) maximum strain and hence low cycle fatigue capability, and (4) good corrosion resistance in aqueous environments.

Palniro-7, a gold-nickel-palladium braze alloy (22 w/o Ni, 8 w/o Pd, Bal. Au) was selected for this application. Single lap shear test specimens were nickel plated and brazed with Palniro-7 at 1950°F (1066°C) in vacuum. The samples were tested at 500°F (260°C) and 1000°F (538°C) and the results, shown in Table 2, confirmed the selection of this alloy for brazing the second stage nozzle. All nozzles will be hydrostatically checked after brazing to verify that the nozzles are leaktight.

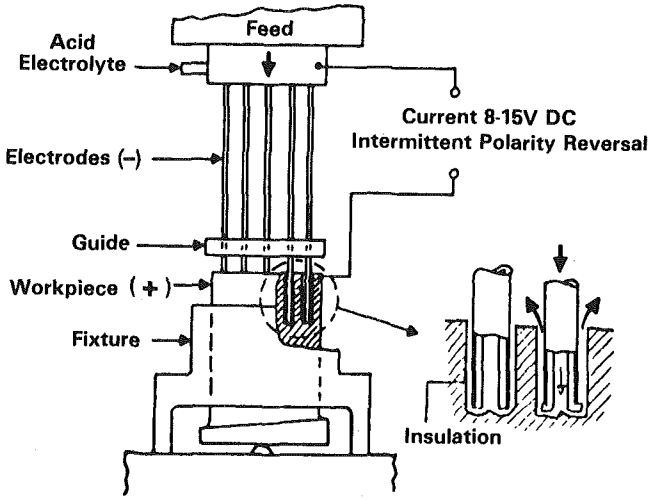

Fig. 6 Shaped tube electrode machining (STEM) process schematic

Table 2 Single lap shear sample results (average) of alloy 718 nickel-plated and brazed with palniro-7

Temperature (°F (°C))	Joint Clearance (in.)	Shear Strength (ksi)
500 (260)	0.002	46
500 (260)	0.009	37
1000 (538)	0.009	21

Brazed at: 1950°F (1066°C)/10 min
1325°F (718°C)/8 hr
1150°F (621°C)/8 hr
Conversion factors: (ksi) = $(1.45 \times 10^{-1}$ MPa)
(in.) = $(3.94 \times 10^{-1}$ m)

Fabrication Status

The second stage nozzle is in the initial stages of fabrication. Casting tooling has been built and trial castings have been made. The casting tooling with the aluminum chills in place is shown in Fig. 7. The chills are positioned in the die using 0.100-inch (2.54-mm) thick wax stand-off locating pads. The resulting wax pattern and chills incorporated into the wax are shown in Fig. 8. Both parting flanges in the wax pattern can also be seen in this figure.

Before attaching the gating to the pattern, threaded rods were inserted into threaded holes located in the two aluminum shroud chills. The gating was then attached (Fig. 9) the mold dipped, and the pour cup and riser attached to the gating system before pouring.

Between dips the ceramic was wiped off the shroud mold flanges which split the mold. After the finished mold was dried, it was dewaxed, which caused the mold components to separate and exposed the internal aluminum chills. The mold components were then inspected, cleaned, and assembled. Figure 10 shows the mold components. The small shroud segment was accurately positioned against the airfoil mold segment with the use of ceramic alignment pins and clamped. Figure 11 shows the fit-up of the mold component.

The cores were fabricated in a two-step process using the Shaw method. An undersized (by 0.150 in. (3.81 mm)) core was fabricated and fully fired to eliminate the major amount of ceramic shrink during the final core firing. This undersized core was then positioned in the ceramic core die and the die was filled with ceramic and fired. The resultant core is shown in Fig. 10.

The core was then carefully positioned in the airfoil cavity and its core print pocket. Go/no-go pins were used to position the core, and wax shims were then placed between the core and mold wall to lock the core in position.

The outer mold shroud was then lowered into position over the large core print and clamped in place. The mold was cemented together and allowed to dry and the separate pour cup was cemented in place. The finished mold was filled with water to check for potential leaks. The water was dumped out and weighed to determine the alloy charge weight needed.

The mold was then processed through the foundry unbacked and was preheated and vacuum cast in the conventional investment casting process. The resultant casting is shown in Fig. 12.

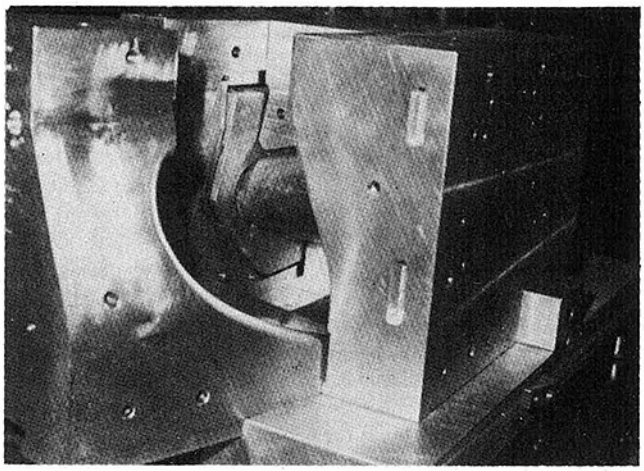

Fig. 7 Second stage nozzle casting tooling

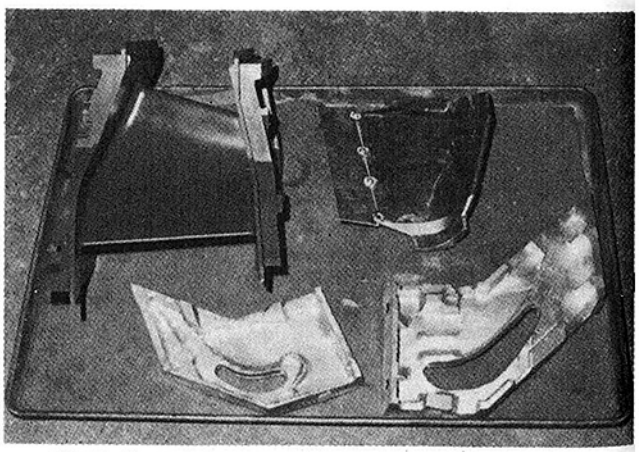

Fig. 8 Second stage wax pattern and internal aluminum chills

Downloaded 01 Jun 2010 to 171.66.16.59. Redistribution subject to ASME license or copyright; see http://www.asme.org/terms/Terms_Use.cfm

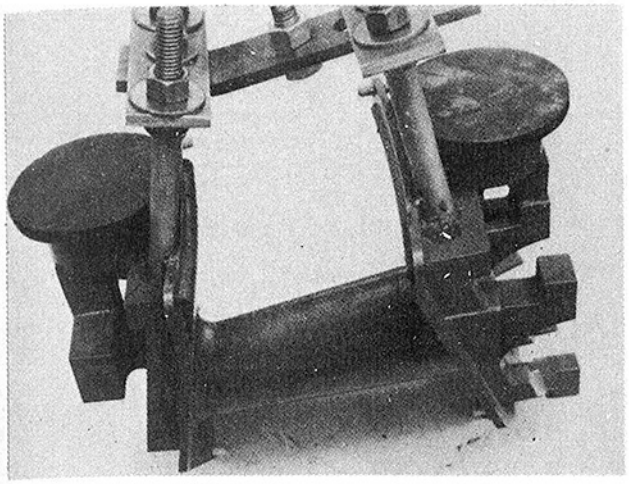

Fig. 9 Second stage wax pattern with gating attached

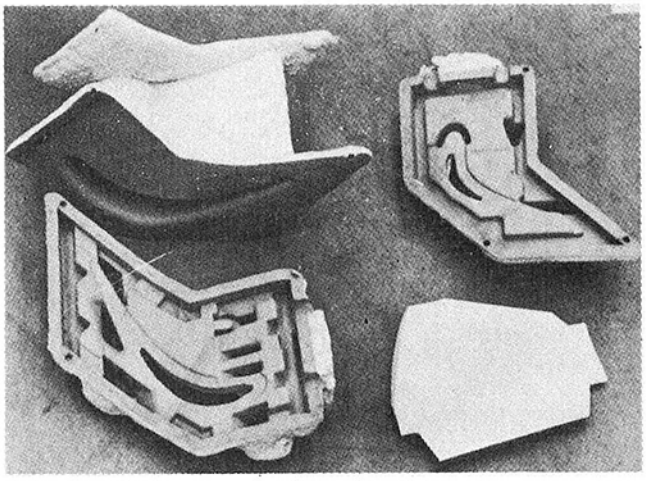

Fig. 10 Mold components prior to mold assembly

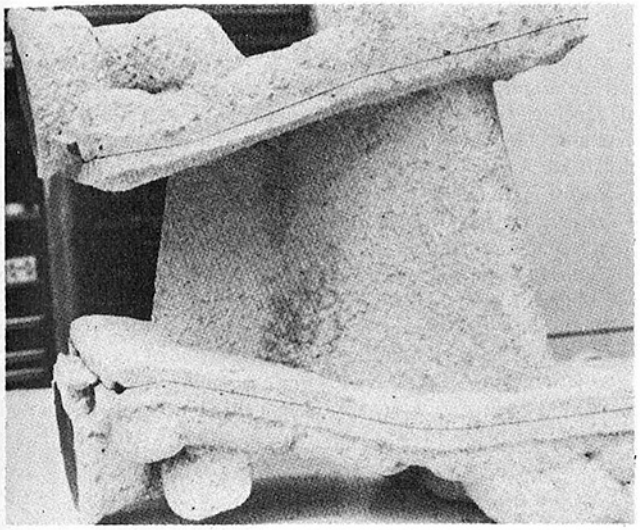

Fig. 11 Second stage nozzle mold component fit-up

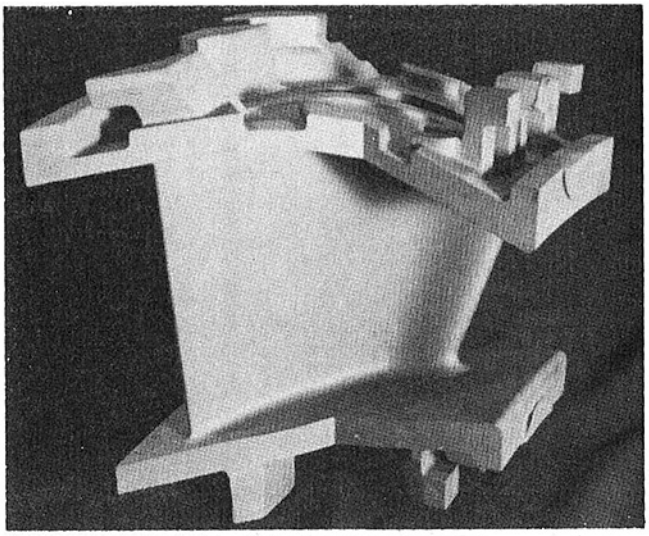

Fig. 12 Second stage nozzle casting

Summary

The HTTT water-cooled second stage nozzle design dictated the use of special materials processes to fabricate this component and achieve the long term design goals. This processing included development of the split-mold investment casting technology for nozzle application, development of hot isostatic pressing and heat treating cycles to maximize alloy 718 properties and machinability, and development of brazing procedures for joining nozzle manifold covers and plugs.

Initial castings have been made using the split-mold process and results are encouraging. Additional castings will be fabricated, HIP'ed, STEM drilled, brazed, final machined, and tested during the remainder of Phase II of the HTTT Program. These results will be used to verify the design goals and will serve to fine tune the design for future turbine engine testing in Phase III.

Acknowledgments

The authors would like to acknowledge C. DeGeorge, R. Montanye, K. L. Kettler, G. Bouse, and W. Ostergren of General Electric Company and T. Piwonka of TRW for their conscientious efforts on this program. The United States Department of Energy is recognized for sponsoring the HTTT Phase II program.

References

1 Caruvana, A., et al., "Evaluation of a Water-Cooled Gas Turbine Combined Cycle Plant," ASME Paper No. 78-GT-77, Apr. 1978.

2 Caruvana, A., et al., "System Status of the Water-Cooled Gas Turbine for the High Temperature Turbine Technology Program," ASME Paper No. 79-GT-39, Apr. 1979.

3 Horner, M. W., et al., "Development of a Water-Cooled Gas Turbine," ASME Paper No. 78-GT-72, Apr. 1978.

4 Horner, M. W., et al., "Water-Cooled Gas Turbine Technology Development," ASME Paper No. 79-GT-72, Mar. 1979.

5 Kydd, P. H., and Day, W. H., "An Ultra High Temperature Turbine for Maximum Performance and Fuels Flexibility," ASME Paper No. 75-GT-77, Mar. 1975.

6 Sims, C. T., "High Temperature Gas Turbine Engine Component Materials Testing Program, Task 1, Fireside I," Final Report, FE-1765-44, July 1978.

7 Caruvana, A., and Schilling, W. F., "High Temperature Technology Program for a Water-Cooled Gas Turbine," *Proceedings of the Conference On Advanced Materials For Alternate Fuel Capable Directly Fired Heat Engines,* Castine, Maine, Aug. 1979.

8 Blazek, W. S., Piwonka, T. S., Jackson, J. D., and Atanmo, P. N., U.S. Patent #4,066,116, Jan. 3, 1978.

9 Blazek, W. S., U.S. Patent #4,043,379, Aug. 23, 1977.

10 Schweikert, W. H., "Manufacturing Methods for Low Cost Turbine Engine Components of Cast Superalloys," AFML/LTM Contract F 33615-75-C-5084, Interim Progress Report II, March 31, 1976.

11 Barker, J. F., Ross, E. W., and Radavich, J. E., "Long Time Stability of INCONEL 718," *Journal of Metals,* Vol. 22, No. 1, 1970, pp. 31–41.

12 Eiselstein, H. L., "Advances in the Technology of Stainless Steels," ASTM STP 369, 1965, p. 62.

13 Boesch, W. J., and Canada, H. B., *Journal of Metals,* Vol. 21, 1969, p. 34.

14 Keiser, D. D., and Brown, H. L., "A Review of the Physical Metallurgy of Alloy 718," ERDA Report ANCR-1292 UC-25, Feb. 1976.

15 Cozar, R., and Pineau, A., *Metallurgical Transactions,* Vol. 4, 1973, p. 47.

16 Horner, M. W., "Water-Cooled Gas Turbine Development Program," Phase IA Topical Report, Contract RO 234-3, Aug. 1978.

17 Schweikert, W. H., "Manufacturing Methods for Production of Premium Quality Castings at a Lower Cost," AFML/LTM Contract F 33615-76C5076, Interim Progress Report I, Feb. 15, 1977.

18 Jollis, A. U., "Nonconventional Machining Practices in AEG Manufacturing," Report No. R76AEG382, July 1, 1976.

Downloaded 01 Jun 2010 to 171.66.16.59. Redistribution subject to ASME license or copyright; see http://www.asme.org/terms/Terms_Use.cfm

Low-Pressure Plasma-Spray Coatings for Hot-Corrosion Resistance

R. W. Smith
W. F. Schilling
H. M. Fox

General Electric Company, Schenectady, N.Y. 12345

The hot corrosion of low-pressure plasma-sprayed coating, GT-29 (Co-29Cr-6A1-1Y) on a γ'-strengthened nickel base superalloy, IN-738, was characterized at both 871 °C and 983 °C in a simulated gas turbine environment. The test results show that at 871 °C the dense, defect-free, low-pressure, plasma-sprayed GT-29 coatings provide good corrosion protection up to 8000 hr. The mechanism of protection was the formation of a dense, adherent Al_2O_3 scale underneath a mixed oxide scale; scale was maintained by a uniformly dispersed Al rich $\beta(CoAl)$ reservoir. At 982 °C, the coating corrosion protection exceeded 5000 hours and also utilized a protective Al_2O_3 scale. Due to the higher test temperature, interdiffusion of O, S, Al, Co, and Cr was higher and internal sulfidation/oxidation of the coating occurred; however, the rates were much lower than uncoated IN-738. Field tests were run (13 051 and 19 842 hr) to evaluate the low-pressure, plasma-sprayed GT-29 coatings' corrosion resistance on turbine buckets. Metallographic inspection of the field-tested coatings verified the simulated burner-rig test results and demonstrated that the low-pressure plasma process provides an attractive alternative to other coating processes for producing hot-corrosion resistant coatings.

Introduction

The gas turbine power plant is becoming the major baseload source of power for many developing countries. This application requires a highly reliable, long-term baseload machine which can operate using cheap, available fuels. One of the major roadblocks to designing this type of machine is hot corrosion. Hot corrosion is the rapid oxidation/sulfidation of the hot-gas path components due to the operating temperature and the impurities contained in today's fuels. The deterioration of these parts, if not protected from hot corrosion, is usually the life-limiting item of the gas turbine. Coatings, applied using various techniques, are being used to provide protection to critical hot-gas path components. These coatings contribute little to material strength but contain elements essential to provide hot-corrosion protection.

Over the past decade, considerable work has been done on developing coating alloys and processes for protection against sulfidation/hot-corrosion attack on nickel-base superalloys [1–6]. These studies show that the relatively oxide-free coatings applied via electron beam evaporative techniques, sputtering, or cladding produced the most corrosion resistant coatings. These coatings were based on the MCrAlY-type coatings which have been reported to be extremely hot-corrosion/sulfidation resistant and relied on extremely dense, defect/oxide-free structures to provide a reservoir of uniformly distributed Al and Y to be subsequently used in continuously forming a protective, adherent scale [7]. Field tests [6] have shown that defects such as unmelted particles and oxide inclusions in plasma coatings can lead to premature failure of these MCrAlY coatings.

Contributed by the Gas Turbine Division and presented at the Gas Turbine Conference and Products Show, New Orleans, La., March 10–13, 1980 of THE AMERICAN SOCIETY OF MECHANICAL ENGINEERS. Manuscript received at ASME Headquarters December 19, 1979. Paper No. 80-GT-98.

The recent developments in plasma-arc metallizing, utilizing controlled atmospheres that deposit a dense, defect/oxide-free coating, result in an extremely attractive alternative to the present group of gas turbine airfoil coating processes.

Low-pressure plasma spraying, the most recent development in controlled atmosphere plasma spraying, utilizes an evacuated water-cooled chamber [8]. The advantages of low-pressure plasma-arc metallizing have been demonstrated to be: (1) higher gas particulate velocities, (2) reduction/elimination of oxide inclusions especially with reactive metals, (3) high ascoated densities, (4) excellent bond strengths due to substrate heating inherent in the low-pressure plasma-coating process, and (5) large spray patterns/distances which simplify the coating of large parts. Given these advantages, the low-pressure, plasma-arc metallizing process was selected to evaluate the potential of using plasma-applied MCrAlY-type coatings on gas turbine airfoils. This report describes a program which was designed to evaluate the corrosion resistance of these low-pressure plasma-deposited coatings under both simulated and field test hot-corrosion conditions, using a reference alloy for comparison.

Experimental Procedures

Process and Alloy Selection. The selected high-velocity low-pressure process uses an 80 kW Ar/He plasma system which has been designed for Mach 3 conditions at a reduced pressure. The system (Fig. 1) consists of a water-cooled vacuum chamber which is ported for the plasma gun connections, substrate fixturing, and remote manipulation of the plasma-spray head. An exhaust system has been designed to cool the plasma gas and remove the particulates before they reach the vacuum pump.

GT-29, a Co-base containing 29 percent Cr, 6 percent Al, and 1 percent Y (wt %), was selected as the baseline composition because

Copyright © 1981 by ASME

Downloaded 01 Jun 2010 to 171.66.16.59. Redistribution subject to ASME license or copyright; see http://www.asme.org/terms/Terms_Use.cfm

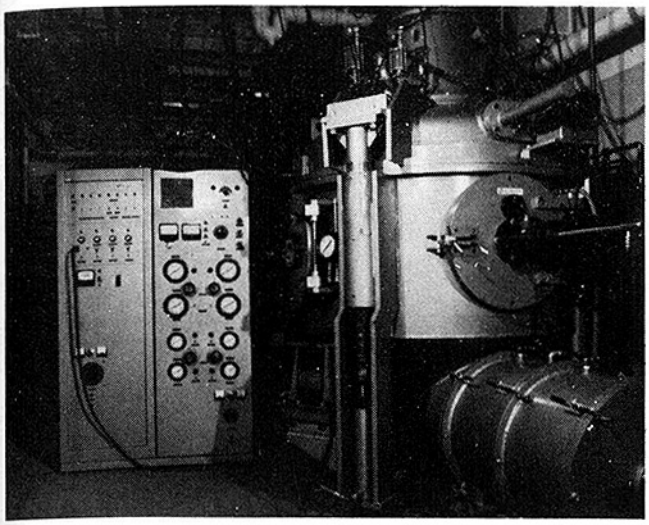

Fig. 1 Low-pressure plasma-spray system

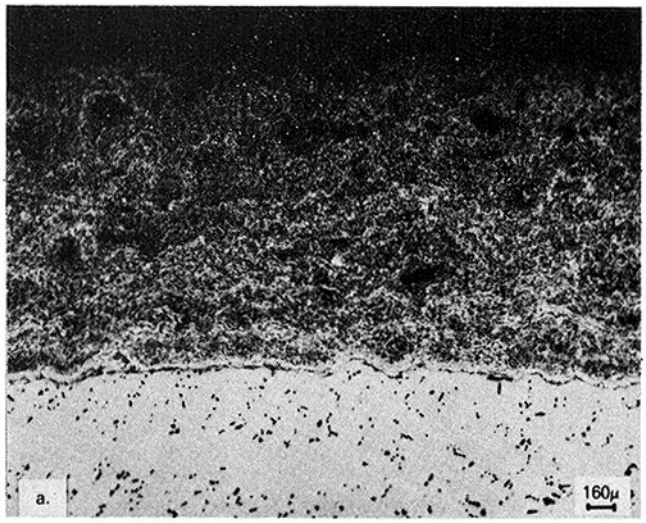

Fig. 3(*a*) Photomicrograph (2 percent chromic)

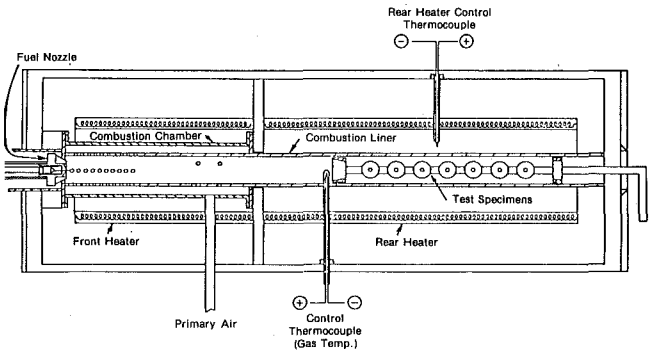

Fig. 2 Schematic cross section of small burner-rig test stand

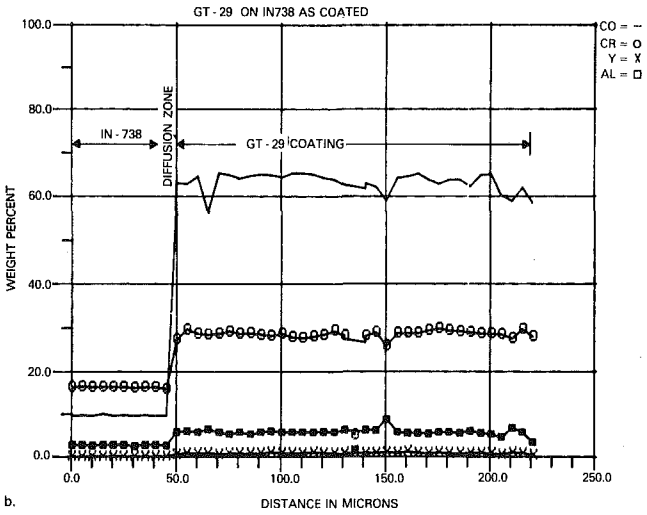

Fig. 3(*b*) Microprobe step scan

Fig. 3 As-coated, low-pressure, plasma-sprayed GT-29 coating

of its high intrinsic corrosion resistance which was demonstrated by laboratory burner-rig testing [5]. The material was argon atomized powder sieved to a −400 mesh.

Investment cast IN-738[1] pins were centerless ground to 4.32 mm, degreased, grit blasted, ultrasonically cleaned, and mounted on special fixtures for coating inside of the plasma spray chamber. The pins were coated for a 0.127 to 0.178 mm nominal thickness, cut to a 24 mm length, and then coated on each end. The pins were then diffusion heat treated at the IN-738 solution temperature (1121 °C for 2 hours in vacuum) and subsequently aged (843 °C for 24 hours in argon). Pins were submitted for burner-rig testing in the as-coated surface condition (0.008 mm A.A. (Arithmetic Average)) and a mechanically polished condition (0.001 mm A.A.).

Testing and Evaluation

Simulated Burner-Rig Test. The plasma-coated pins were tested in simulated gas turbine environments using small burner rigs [9] (Fig. 2). Tests were conducted in a hot-corrosion environment at 871 °C and at 982 °C produced by burning diesel oil containing 1 percent S and doped with synthetic sea salt (ASTM D665-135) to yield approximately 8 ppm sea salt in the combustion products. The burner rigs operate at atmospheric pressure, 20 mps gas velocity, and an approximate air-fuel ratio of 50:1 at 871 °C. The specimens, which are stationary during test, are cycled to room temperature by air blasting approximately once every 24 hr.

Following tests, the specimens were sectioned at the pin center (transverse) and metallographically examined for: (1) maximum depth of penetration, (2) average surface loss of coating, and (3) depth of internal sulfidation beyond the coating/substrate interface. Data were obtained on the basis of the original pin diameter and the final coated diameter, using the outside diameter as the reference point. Selected specimens from both the 871 °C and 982 °C tests were examined on a Cameca M546 electron microprobe analyzer to determine the extent of the coating/substrate interdiffusion, the coating composition gradients, and the composition of the precipitate phases. A JEOL JXA5A electron microanalyzer was used to obtain x-ray images for locating the concentrations of Ni, Co, Cr, Al, Y, and S before and after burner rig exposures.

Field Testing. Field testing of low-pressure plasma-sprayed GT-29 coatings has been described and reported previously [6, 10].

Results

As-coated/Diffused Condition. Plasma-sprayed GT-29 is a two-phase coating alloy containing a fine uniform dispersion of β(CoAl) and Y containing Co precipitates in an α(CoCr) matrix (Fig. 3(a)). This fine dispersion of the phase is a natural consequence of the rapid cooling rates during gas atomization of the raw material powder and the plasma-spray process. Microprobe scans of these coatings (Fig. 3(b)) show that after plasma spraying, all of the coating constituent elements remain uniformly distributed and at the starting powder concentrations (Table 1). Figure 4b is a microprobe trace of a diffused coating whose microstructure is seen in Fig. 4a. These figures show that the β(CoAl) phase coalesces and the substrate/coating diffusion zone increases from 0.010 mm (as coated) to almost 0.050

[1] *IN-738:

Ni	Co	Cr	Al	Ti	Mo	W	Cb	Ta	B	Zr	C
Bal	8.5	16	3.4	3.4	1.75	2.6	0.9	1.75	0.010	0.04	0.11

Downloaded 01 Jun 2010 to 171.66.16.59. Redistribution subject to ASME license or copyright; see http://www.asme.org/terms/Terms_Use.cfm

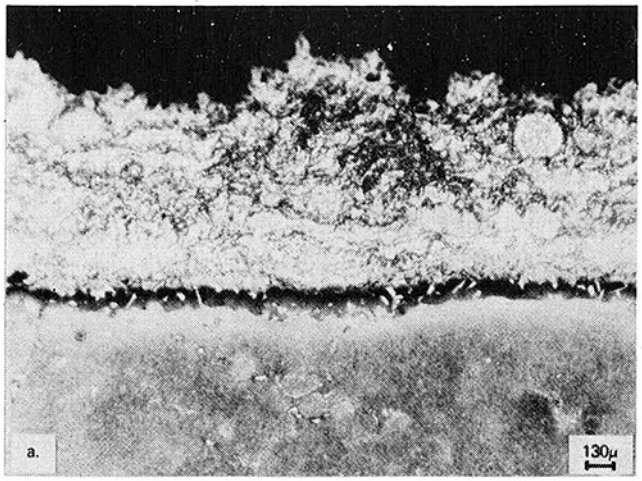

Fig. 4(*a*) Photomicrograph (2 percent chromic)

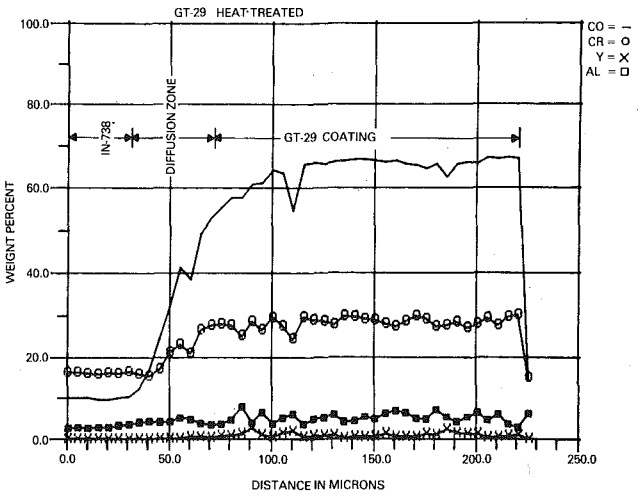

Fig. 4(*b*) Microprobe step scan

Fig. 4 Heat-treated (1129 °C for 2 hr), low-pressure, plasma-sprayed GT-29 coating

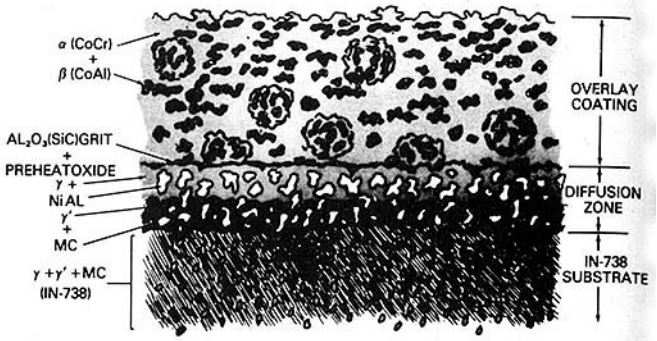

Fig. 5 Schematic illustration of low-pressure plasma-sprayed GT-29 coatings

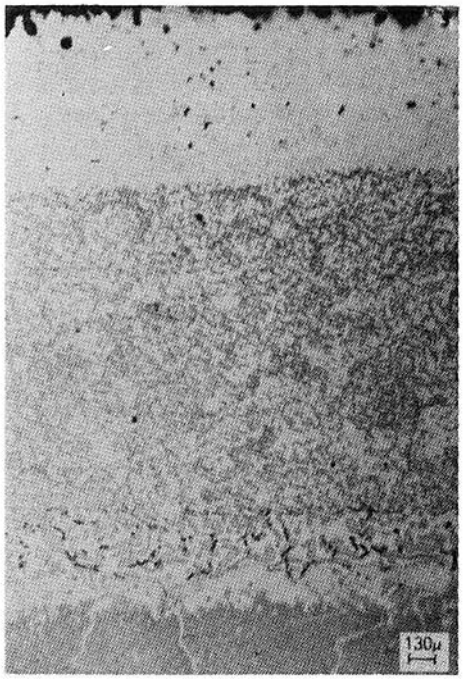

Fig. 6 Photomicrograph of 871 °C corrosion specimen after 2000 hr burner-rig exposure (2 percent chromic)

Table 1 Composition of GT-29 (wt %)

	Co	Cr	Al	Y
Design	Bal	29	6	1
As-received powder	Bal	29.1	6.0	0.98
As coated	Bal	28.7	5.7	0.7–0.9

mm during the diffusion heat treatment (1120 °C for 2 hr).

During heat treatment, the aluminum diffuses from the coating (6 percent Al) into the substrate IN-738 (3.5 percent Al) causing denudation of the coating β phase (near the interface), formation of a $\gamma'(Ni_3Al)$ band in the substrate, and precipitation of a finger-like high Al phase β(NiAl) in the diffusion zone. Cobalt and chrome also diffuse from the coating into the substrate and transform some of the γ' region to γ(light phase between the original interface and the γ' zone). The β denuded zone at the coating surface is attributed to the preferential oxidation of aluminum to form an Al_2O_3 scale. Figure 5 is a schematic which illustrates the microstructural aspects of the diffusion heat-treated, plasma-sprayed GT-29 coating.

Burner Rig Tests at 871 °C. Table 2 lists the penetration measurements of GT-29 high energy, low-pressure, plasma-coated IN-738 specimens after hot-corrosion burner-rig testing. After 1000 hours of exposure at 871 °C, penetrations vary between one-third and one-half the coating thickness; mechanically polished pins had lower penetrations mainly due to more accurate measurements made possible by the smooth surface. After 2000 hr, the average penetration of all of the samples increased slightly and after 4000 hr most of the specimens still had at least 25 percent of the coating remaining. These specimens were coated using various plasma-spray parameters; however, these data show that very few coatings had been completely penetrated even after 4000 hours of testing (t_0 = 0.127 mm to 0.178 mm).

The protective mechanism for the plasma-sprayed GT-29 coatings at 871 °C involves the formation of a dense adherent Al_2O_3 scale which is formed beneath an outer mixed oxide scale. The corrosion front was planar with little or no internal sulfidation/oxidation (Fig. 6). Scanning electron microprobe analysis shows this oxide scale to consist of the Co $(CrAl)_2O_4$ spinel, Cr_2O_3, and Al_2O_3. Figures 7(*a*)–7(*f*) are x-ray images for the elements Al, Co, Cr, S, and Ni taken on a specimen exposed in the burner rigs for 2000 hr. These figures show the distribution of these elements in the coating and especially in the scale. Depending on the time of exposure in the burner rig, the exact oxide scale morphology changes; however, there is always an inner layer of Al_2O_3.

Figures 8(*a*)–8(*c*) are the microprobe step scan traces and microphotographs of the corrosion specimens qg-1, qg-2, and qg-3 which have been tested for 1000, 2000, and 4000 hr, respectively. Figure 8(*a*) illustrates that after 1000 hr the outer mixed oxide scale is approximately 0.015 mm thick below which a 0.010 mm Al_2O_3 scale has formed. The aluminum-rich phase in the coating has been depleted by about 0.035 mm due to the formation of the protective Al_2O_3 scale. It can also be seen that Ni from the substrate is diffusing into the

Downloaded 01 Jun 2010 to 171.66.16.59. Redistribution subject to ASME license or copyright; see http://www.asme.org/terms/Terms_Use.cfm

Table 2 Corrosion Penetration Measurements

	Specimen ID No.	Test Temperature (°C)	Exposure Time (hrs)	Maximum Penetration (mm x 10²)	Average Surface Loss (mm x 10²)	Internal Sulfidation/ Oxidation Beyond Coating Interface (mm x 10²)
GT-29	qe-1	871	1014	8.1	3.9	--
	qf-1			10.5	3.1	--
	qg-1			9.5	6.1	--
	qh-1			7.9	4.2	--
	qi-1			7.5	4.2	--
	qj-1			9.4	4.1	--
	qk-1			9.5	5.5	--
	ql-1			10.8	5.2	--
	*rl-1		1005	7.5	4.3	--
	*rm-1			6.5	3.4	--
	*rn-1			5.5	2.9	--
	*rn-1			6.9	4.3	--
	rp-1			5.2	3.2	--
	*rq-1			5.5	3.2	--
	*rr-1			10.5	5.6	--
	*rs-1			10.2	4.8	--
	*rt-1			13.2	4.9	--
	ru-1			10.0	5.6	--
	rv-1			7.2	3.8	--
	rv-2			6.9	3.3	--
	qe-2		2009	9.3	4.6	--
	qf-2			8.5	4.6	--
	qg-2			7.0	3.8	--
	qh-2			9.3	4.6	--
	qi-2			7.9	4.9	--
	qj-2			10.3	4.9	--
	qk-2			8.9	4.9	--
	ql-2			11.7	6.0	--
	*rl-2		2012	10.8	5.5	--
	*rm-2			8.1	4.4	--
	*rn-2			7.4	3.8	--
	*ro-2			9.1	4.2	--
	*rp-2			6.5	4.1	--
	*rq-2			7.7	3.8	--
	*rr-2			8.5	4.4	--
	*rs-2			11.4	5.7	--
	*rt-2			10.5	5.3	--
	ru-2			11.0	4.7	--
	*sv-2		2014	4.8	1.1	--
	qe-3		4028	10.4	5.2	--
	qf-3			9.5	5.6	--
	qg-3			7.5	4.4	--
	qh-3			10.0	4.8	--
	qi-3			8.5	4.8	--
	qj-3			11.4	4.8	--
	qk-3			10.0	6.6	--
	ql-3			11.9	6.5	--
	rj-3		4038	11.3	6.5	--
	rj-9			18.5	10.4	3.3
	*rl-3		4002	9.9	4.7	--
	*rm-3			9.9	5.2	--
	*rn-3			7.7	4.8	--
	*ro-3			9.0	4.7	--
	*rp-3			21.2	13.4	6.0
	*rq-3			7.2	1.0	--
	*rr-3			11.7	5.3	--
	*rs-3			14.1	7.0	--
	*rt-3			20.5	8.0	5.3
	ru-3			18.9	6.2	3.7
	*sn-3			5.2	1.3	--
	*sp-3			13.6	2.4	--
	sv-3			5.3	0.8	--
	sn-4	982	2014	5.1	7.1	--
	so-4		2062	8.7	4.6	--
	ss-4			14.7	6.3	--
	sv-5			14.0	6.3	--
	sx-2		2014	13.6	7.0	--
	sy-2			23.1	10.5	6.1
	sq-2		4000	31.5	9.3	12.5
	st-6			24.8	8.3	5.8
	su-5			27.6	11.3	9.6
	sx-3		3916	34.5	18.2	15.5

			Average Maximum Penetration (mm x 10²)
IN-738**	871	1000	12.7
		2000	25.4
		4000	50.8
	982	2000	25.4
		4000	50.8

*Mechanically polished (0.001 mm A.A.)
**Ref: Sims, C.T., High Temperature Gas Turbine Component Materials Testing Program - Fireside I, Final Report, United States Department of Energy Contract No. EX76-01-1765, Gas Turbine Division, General Electric Co., Schenectady, N.Y., July 1978.

coating and substituting in both the matrix and the Al-rich phases. Correspondingly, a small amount of coating diffusion into the substrate has occurred, as can be seen by the coarsening of the β islands (Al diffusion from the original diffusion zone) and a small increase in the γ-rich zone due to diffusion of Co and Cr into the original diffusion zone.

Figures 8(*b*) and 8(*c*) are microprobe step scans of the plasma-sprayed GT-29 coating after 2000 and 4000 hr, respectively. These scans show the continuing depletion of β(~0.110 mm after 4000 hr) caused by diffusion of Al to the surface to form the protective Al_2O_3 scale. Figure 8(*b*) shows that a mixed oxide scale of Co (Cr, Al)$_2O_4$, Cr_2O_3, and Al_2O_3 still exists after 2000 hr of burner-rig exposure. However, after 4000 hr only an Al_2O_3 scale can be seen; this could be due to either spallation of the mixed oxide (spinel) just before or during preparation or establishment of the thermodynamically, more stable oxide scale of Al_2O_3. Table 3 is a summary of oxide scale formation. Coating/substrate interdiffusion can also be seen in Figs. 8(*a*)–8(*c*) and shows an increasing Ni diffusion to the coating surface while coating diffusion toward (Co, Cr, Al) remains negligible.

Burner Rig Tests at 982 °C. Table 2 lists the corrosion penetration measurements on the GT-29 plasma coatings after 2000 and 4000 hr exposures at 982 °C in the previously described burner-rig tests. The penetrations are much higher than the penetrations at 871 °C because of the more severe oxidation and higher interdiffusion rates that occur at 982 °C. The data show that the coatings vary in total penetrations from 0.051 mm to 0.231 mm after 2000 hr and from 0.241 mm to 0.345 mm after 4000 hr. These rates can be compared to the uncoated IN-738 penetrations at 871 °C and 982 °C also listed in Table 2. The variability in the 982 °C burner-rig test data show that this test temperature was more sensitive to process changes than the tests at 871 °C; however, only a few of the specimens tested over 4000 hr have been severely attacked beyond the coating.

Table 3 Hot corrosion specimen oxide scale

Test Temperature (°C)	Exposure Time (hr)	Scale of Type
871	1000	Co (Cr,Al)$_2O_4$ spinel, Cr_2O_3, Al_2O_3
871	2000	Co (Cr,Al)$_2O_4$ spinel, Cr_2O_3, Al_2O_3
871	4000	Al_2O_3 only
982	2000	Cr_2O_3, Al_2O_3, internal oxides/sulfides
982	4000	Al_2O_3, Cr_2O_3, internal oxides/sulfides

The protective mechanism of the GT-29 coating at 982 °C is also the formation of an Al_2O_3 scale at the surface of the coating. However, the attack is not frontal, showing internal sulfidation and oxidation instead. At 982 °C, the diffusion rates for both Al and O are much higher than those at 871 °C; therefore, the GT-29 plasma coatings become depleted in Al at a faster rate. In addition, the Al reservoir is consumed more rapidly via internal oxidation. Figure 9 is a photomicrograph of the coating after a 2000-hour exposure at 982 °C. Notice the heavily scaled, exfoliated appearance of the outer one-third of the coating. Microprobe and x-ray images, Figs. 9 and 10, show these areas to be high in Al, Y, and S. The Al and Y are found together due to the nature of the protective scale that has been formed near the surface. Sulfur is found within the coating in the form of internal sulfides which will subsequently oxidize and release more sulfur which can penetrate further into the coating. Oxygen and sulfur have both

Downloaded 01 Jun 2010 to 171.66.16.59. Redistribution subject to ASME license or copyright; see http://www.asme.org/terms/Terms_Use.cfm

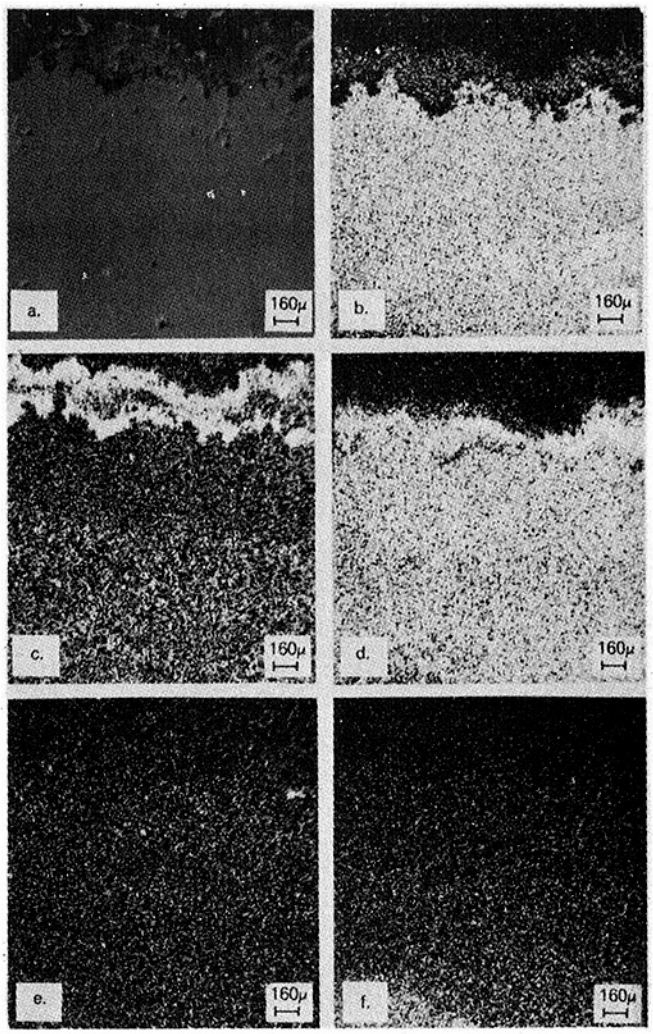

Fig. 7 Energy dispersive x-ray images on 871 °C corrosion specimen after 2000-hour exposure: (*a*) SEM, (*b*) cobalt, (*c*) aluminum, (*d*) chromium, (*e*) sulfur, (*f*) nickel

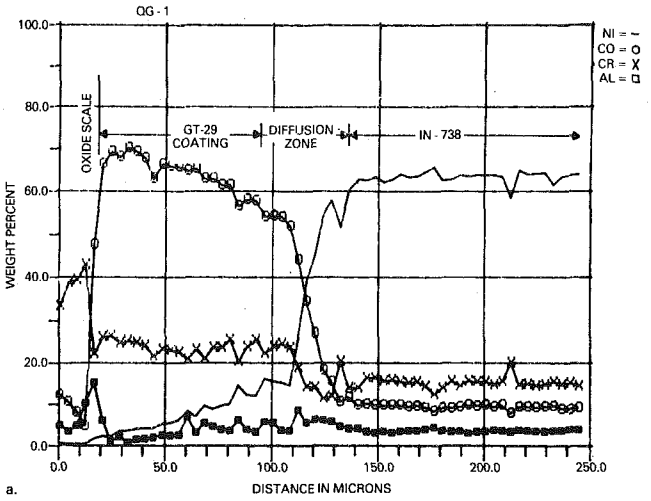

Fig. 8(*a*) 1000 hr exposure

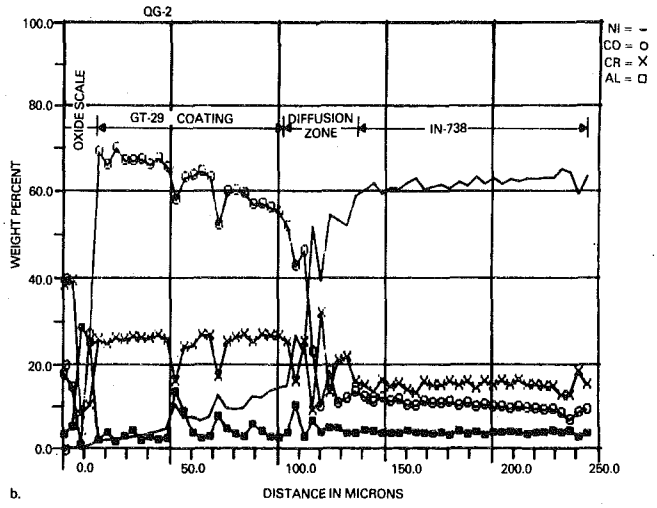

Fig. 8(*b*) 2000 hr exposure

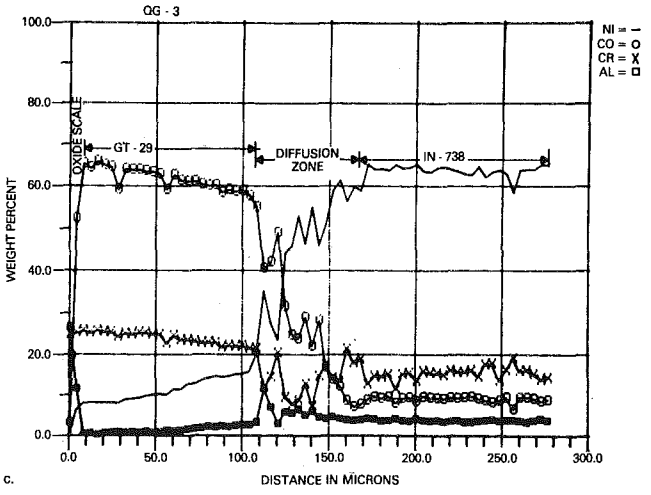

Fig. 8(*c*) 4000 hr exposure

Fig. 8 Microprobe quantitative step scans of 871 °C corrosion specimens

penetrated beyond the outer oxide scale to form internal Al_2O_3 (0.125 mm) particles in the coating and internal sulfides at the coating substrate interface (0.190 mm). The Co and Cr levels have generally decreased 6 to 10 wt percent from as-coated levels, while Ni has diffused to the coating surface (10 to 13 wt percent). A 0.090 mm wide diffusion zone has formed between the coating and the substrate.

Figure 11(*a*) is a photomicrograph of the GT-29 plasma coating after an exposure of 4000 hours at 982 °C. Corresponding microprobe and x-ray image data (Figs. 11(b) and 12) show that oxide penetration depths have increased to 0.170 mm while the sulfur penetration (0.180 mm) has remained fairly constant from 2000 hours to 4000 hr.

The x-ray images show that the Al_2O_3 scale has proceeded two-thirds of the way through the coating following the internal sulfidation particles which had been formed beyond the protective Al_2O_3 scale. Oxygen is now diffusing almost through the diffusion zone. The absence of any high Al (β) phases demonstrate that Al has diffused rapidly at 982 °C. Similar to the specimen after a 2000 hr exposure, the Co and Cr levels of the 4000 hr specimen have generally decreased by 9 to 12 wt percent while Ni has diffused outwards and still remains 12 percent at the coating surface. This suggests that the Co, Cr, and Ni elements diffuse to the surface where they become oxidized and either spall (NiO, CoO) or volatilize (Cr_2O_3).

Evaluation after Field Exposure. Figures 13(*a*) and 13(*b*), which show the GT-29 plasma coating after 13 051 and 19 842 fired hours, respectively, demonstrate that this coating exhibited excellent resistance to hot-corrosion attack. The metallographic analysis revealed that the coating successfully precluded base alloy attack providing, of course, that coverage of the IN-738 substrate by the coating had been achieved. The GT-29 coating is judged to exhibit a high intrinsic corrosion resistance; i.e., a 0.063 mm frontal attack was measured in almost 20 000 service hours.

It was observed that the plasma-sprayed coatings contained structural defects such as porosity, semicontinuous oxide layer or

Downloaded 01 Jun 2010 to 171.66.16.59. Redistribution subject to ASME license or copyright; see http://www.asme.org/terms/Terms_Use.cfm

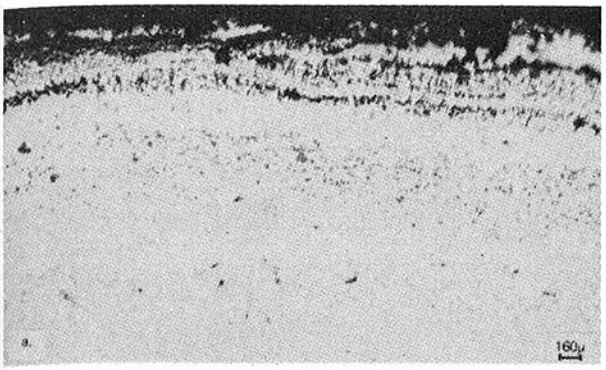

Fig. 9(*a*) Photomicrographic (as polished)

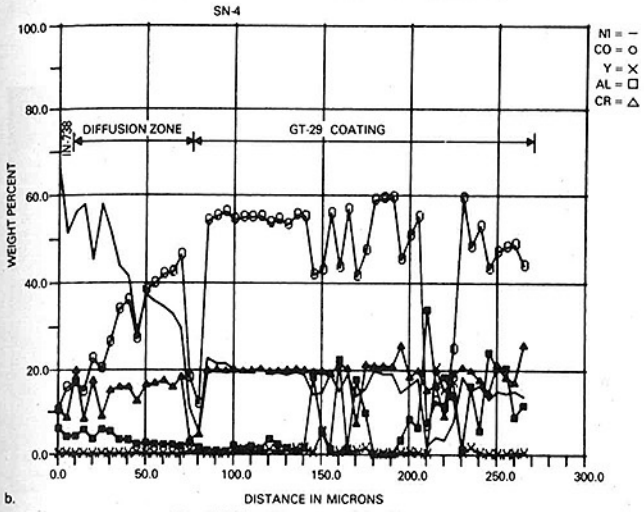

Fig. 9(*b*) Micrographic step scan

Fig. 9 982 °C burner-rig corrosion specimen after 2000-hour exposure

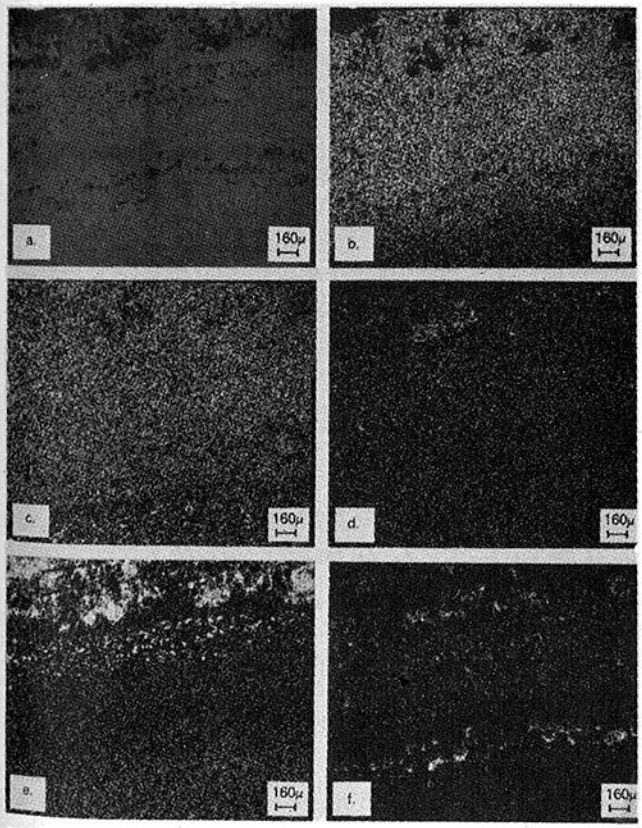

Fig. 10 Energy dispersive x-ray image of 982 °C corrosion specimen after 2000 hr burner-rig exposure: (*a*) SEM, (*b*) cobalt, (*c*) chromium, (*d*) yttrium, (*e*) aluminum, (*f*) sulfur

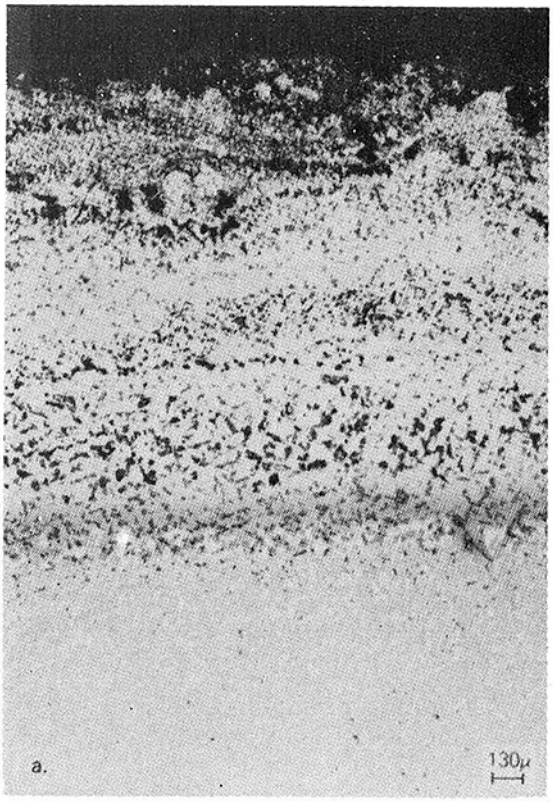

Fig. 11(*a*) Photomicrographic (as polished)

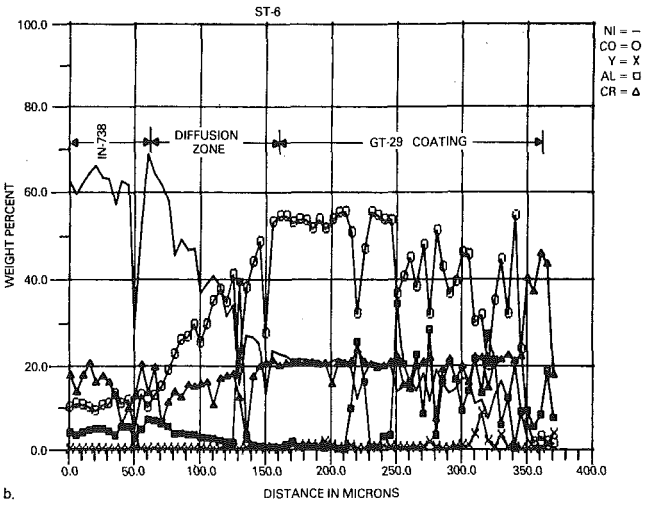

Fig. 11(*b*) Microprobe step scan

Fig. 11 982 °C burner-rig corrosion specimen after 4000-hour exposure

other contaminant at the coating/substrate interface, and oxide stringers within the coating. There appeared to be some corrosion associated with the porosity at the coating surface and along the internal oxide stringers. The coating was adherent despite the coating/substrate contamination. However, it should be noted that since these coatings were applied several years ago the processing has greatly improved to where coating defects are eliminated or minimized.

Field testing is continuing with the Arabian American Oil Company (ARAMCO) on the MS7001 first-stage bucket. The improved coatings (Figs. 14(*a*) through 14(*d*) are a result of an extensive development program which was designed to produce the best possible low-pressure plasma coatings. These figures show that the coating defects (porosity, interface oxides and oxide stringers) have been largely eliminated and will result in improved corrosion protection during field service.

Downloaded 01 Jun 2010 to 171.66.16.59. Redistribution subject to ASME license or copyright; see http://www.asme.org/terms/Terms_Use.cfm

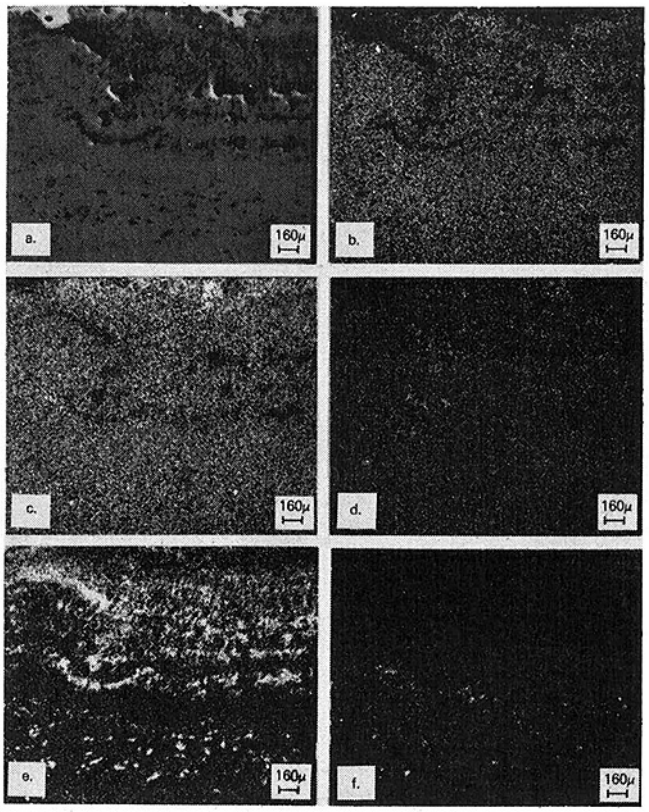

Fig. 12 Energy dispersive x-ray images of 982 °C corrosion specimen after 4000 hr exposure: (*a*) SEM, (*b*) cobalt, (*c*) chromium, (*d*) yttrium, (*e*) aluminum, (*f*) sulfur

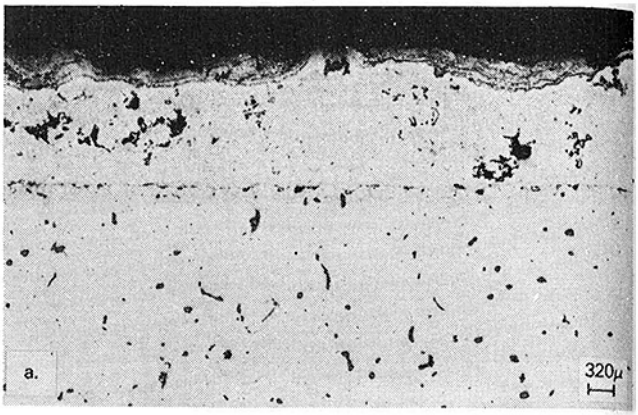

Fig. 13(*a*) 13,051 hr

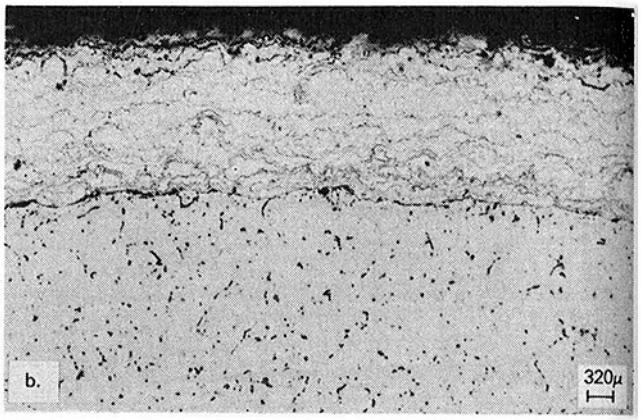

Fig. 13(*b*) 19,842 hr

Fig. 13 Photomicrographs of field-tested, low-pressure, plasma-sprayed GT-29 coatings after service

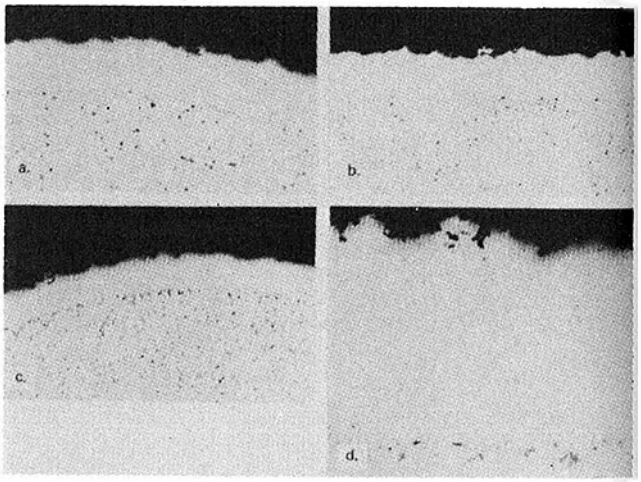

Fig. 14 Photomicrographs of GT-29 plasma-coated, MS7001 first-stage buckets: (*a*) pitchline, leading edge; (*b*) lower airfoil, midpressure face; (*c*) pitchline, trailing edge; (*d*) pitchline, midpressure face

Discussion

Hot Corrosion at 871 °C. Results show that the plasma-sprayed GT-29 coatings provide excellent corrosion protection in 871 °C burner-rig testing, based on the formation of a protective, dense, adherent layer of Al_2O_3. This layer of Al_2O_3 has been maintained by the diffusion of Al from the fine, dispersed β(CoAl) phase in the plasma-sprayed coating structure. The scale has been made more adherent by the uniformly distributed Y, most probably by a mechanism described by Allan, et al. [11]. Coating/substrate interdiffusion has been minimal and has also contributed to the corrosion behavior of this coating by not using up the Al reservoir.

Eventual failure of the coating will occur after the reservoir of Al (β) has been depleted and the Al_2O_3 protective scale cannot be formed. At 871 °C, the β(CoAl) depleted α(CoCr) matrix will still provide some corrosion protection through the formation of a Cr_2O_3 scale. Final failure will occur due to the diffusion of Ni to the surface in high enough concentrations to interrupt the Cr_2O_3 scale with the less protective scales of NiO or (Ni,Co) Cr_2O_4. Testing is continuing, and preliminary results indicate that 0.152-mm-thick coatings will provide corrosion protection, in the burner rig, for approximately 8000 hours at 871 °C.

Hot Corrosion at 982 °C. The burner-rig tests at 982 °C show that the GT-29 plasma coatings provide extremely good protection to IN-738, based on the formation of the dense Al_2O_3 scale. However, the higher test temperature (982 °C) allows elements such as Al, O, and S to interdiffuse more readily than at the lower test temperatures, hence the corrosion mechanisms change. An initial Al_2O_3 scale is rapidly formed with Cr oxides providing little or no effect on the formation of this scale due to their volatilization. Sulfur than diffuses through the oxide scale to form internal sulfides in the coating immediately beneath the outer scale (Fig. 9) and at the coating/substrate diffusion zone. As the scale ruptures, oxygen diffuses into the coating and the internal sulfides are oxidized to form part of the new outer scale.

Additional inward oxygen diffusion forms internal Al_2O_3 particles which subsequently used up the internal Al reservoir originally built into the coating. This mechanism proceeds until the Al levels are reduced to a level where the outer Al_2O_3 scale cannot be replenished and massive sulfidation/oxidation of the substrate proceeds. For a 0.200-mm-coated specimen, the internal oxidation proceeds into the substrate for about 4000 hr; however, continuing tests show that the final catastrophic sulfidation/oxidation occurs after 6000 hr.

Downloaded 01 Jun 2010 to 171.66.16.59. Redistribution subject to ASME license or copyright; see http://www.asme.org/terms/Terms_Use.cfm

The uncoated IN-738 penetration measurements listed in Table 2 show that without the plasma-sprayed GT-29 coating penetrations are approximately two to five times higher at 871 °C and at 982 °C. These results demonstrate that the dense, oxide/defect-free structure of the low-pressure plasma coatings provides a uniformly distributed reservoir of Al, Cr, and Y to be subsequently used in forming oxide scales that retard the progression of hot sulfidation/oxidation of the IN-738 base material.

Summary and Conclusions

This study has demonstrated and characterized the hot-corrosion protection of a low-pressure, plasma-deposited MCrAlY (GT-29) coating on IN-738, a γ'-strengthened nickel-base superalloy, and has compared burner-rig test experience to actual field test experience. These coatings provide excellent hot-corrosion protection for IN-738 at 871 °C and at 982 °C in simulated gas turbine environments and in service.

The low-pressure plasma-spray process has been demonstrated to produce dense (>98 percent) oxide-free coatings which were well bonded to the substrate. The rapid cooling rates of the plasma deposit, the complete melting of particles, and the absence of oxide inclusions inherent to the low-pressure plasma-coating process have produced an extremely fine uniform distribution of Al, Cr, and Y. These elements are essential in forming and maintaining the protective scale during high-temperature exposure.

GT-29 low-pressure plasma-coated IN-738 has been shown to be up to five times more resistant to hot-corrosion/sulfidation attack at 871 °C than uncoated IN-738. At 982 °C, the hot-corrosion protection is reduced to levels two to three times better than uncoated IN-738. The coating corrosion penetrations were found to have uniform general frontal attack, indicating that the low-pressure plasma coatings are free of accelerated attack which can be attributed to process related defects. MS5002 first-stage buckets coated for field testing were coated early in the development of low-pressure plasma coatings; therefore, processing-related defects were found in buckets coated for this part of the program. Results showed that the corrosion resistance of the low-pressure, plasma-coated, field-tested buckets correlated well with burner-rig evaluations. Therefore, it is concluded that the low-pressure plasma process is an attractive alternative for providing hot-corrosion resistant coatings on critical rotating gas turbine hardware.

Acknowledgments

The authors are grateful to the General Electric Company for their support and permission to publish the results of this study. We are also grateful to A. Glock for this metallography; M. McConnel for his work on microanalysis; and K. Kettler for her help in assembling this report.

References

1 Goward, G. W., "Coating and Coating Processing for Gas Turbine Airfoils Operating in the Marine Environment," *Proceedings of the Conferences on Gas Turbine Materials in the Marine Environment,* Castine, Maine, 1974, Metals and Ceramics Information Center Report No. MCIC-75-27.

2 *Proceedings of the Third Conference on Gas Turbine Materials in the Marine Environment,* Bath, England, Sept. 1976.

3 Stringer, J., "Hot Corrosion in Gas Turbines," Metals and Ceramics Information Center Report No. MCIC-72-08, July 1972.

4 Talboom, E. P., et al., "Evaluation of Advanced Superalloy Protection Systems," NASA Contract CR-72813 PWA-4055, Pratt and Whitney Aircraft Company, Dec. 1970.

5 Kaplan, S. M., "Heavy Duty Marine Gas Turbine Development Project, Task 1/6: Volume B," Final Report Prepared for U.S. Department of Commerce Maritime Administration, Contract No. 0-35510, Gas Turbine Division, General Electric Company, Schenectady, NY, Nov. 1974.

6 Lindblad, N. R., Schilling, W. F., Aeschbacher, H. J., and Knoll, W. H., "Gas Turbine Bucket Corrosion Protection Developments," ASME Paper No. 79-GT-47, Mar. 1979.

7 Goward, G. W., "Materials and Coatings for Gas Turbine Hot Section Components," *Gas Turbine Materials Proceedings,* NAVSEC/NASC, Washington, D.C., Oct. 1972.

8 Muehlberger, E., "A High Energy Plasma Coating Process," *Proceedings of the 7th International Thermal Spray Conference,* London, England, 1973.

9 Sims, C. T., *High Temperature Gas Turbine Components Materials Testing Program—Fireside I* Final Report Prepared for U.S. Department of Energy, Contract No. EX 76-01-1765, Gas Turbine Division, General Electric Company, Schenectady, NY, July 1978.

10 Schilling, W. F., Fox, H. M., and Beltram, A. M., "Field Testing and Evaluation of Next Generation Industrial Gas Turbine Coatings," *Proceedings of the Conference on Advanced Materials for Alternate Fuel Capable Directly Fired Heat Engines,* Castine, Maine, August 1979, sponsored by U.S. Department of Energy and Electric Power Research Institute, Inc.

11 Allan, I. M., Whittle, D. P., and Stringer, J., "Oxidation Behavior of CoCrAl Systems Containing Active Element Additions," *Oxidation of Metals,* Vol. 12, 1978, p. 35.

Downloaded 01 Jun 2010 to 171.66.16.59. Redistribution subject to ASME license or copyright; see http://www.asme.org/terms/Terms_Use.cfm

Y. Kemper

President,
Vadetec Corporation,
Troy, Mich.
Mem. ASME

The Nutating Traction Drive

The unique torque speed characteristic of the single-shaft gas turbine requires that it have a continuously variable-ratio transmission for successful application to automotive use. This paper discusses the development of a novel mechanical transmission which has the power density required for highway vehicles. Cost and efficiency are competitive with conventional automatic transmissions.

Introduction

The torque curve of the single-shaft gas turbine decreases sharply from its maximum value at maximum engine speed to zero net output at about 50 percent of maximum engine speed. Because of this unique torque-speed curve, the single-shaft gas turbine engine will have to operate over a much narrower speed range than all other types of engines currently used for highway vehicles. Therefore, the transmission used with this engine will require a wider speed-ratio range than currently available from conventional transmissions. For this and other reasons [1, 2], the single-shaft gas turbine engine will require a continuously variable-ratio transmission (CVT) for application to automotive use.

A study of Vadetec's continuously variable, mechanical transmission applied to highway trucks is presented in this paper to provide the technical information required to evaluate the concept. It is intended to demonstrate the practical feasibility of the concept.

The design presented is based on an evaluation of industry standards, competitive specifications and requirements as related to a typical diesel-powered highway truck with an output rating in the 200–250 hp range. The design can be optimized to meet the specific requirements of a single-shaft gas turbine application; for example, the speed ratio range can be increased for operation from 0 to 1/1.

Concept

The Vadetec continuously variable-ratio transmission (CVT) concept is based on the proprietary development of a compact, variable speed traction drive unit that operates with a unique nutating motion.

The key element of the Vadetec Nutating Traction Drive (NTD) [3] is the variator portion which utilizes smooth rolling conical members that are inherently silent in operation, have high torque transmitting capacity and deliver power at high efficiency. Output from the variator is directed through a double input planetary unit coupled to a set of range gears. The output gears provide high and low speed range steps between which the ratio is infinitely variable. Shifting between ranges is accomplished at synchronous speed without any interruption of power.

Traction drives are not new, having been successfully used in the machine tool industry for years, but until now they have not had the power density required for use in vehicular applications. Recent advances in traction fluid properties, however, have provided a significant breakthrough in areas of increased heat resistance, shear strength, lubricating characteristics and compatibility with ordinary metals and seals. Now, a completely new design approach could make the use of traction drives in vehicles practical for the first time.

As in all other types of traction drives, torque is transmitted through the viscous shear of a thin film of oil between loaded rolling contact surfaces which act like large roller bearings. High coefficients of traction are possible due to the rheological behavior of the oil at high pressure. The viscosity of oils, and particularly synthetic "traction fluids", increases greatly under pressure, becoming almost glass-like under the stresses prevailing between the rolling contact surfaces [4].

In the Vadetec NTD, the rolling contact motion is provided by the nutation of a roller member within a stationary reaction member (the kinematic principle of nutation describes the wobbling motion of a body during rotation about a skewed axis), hence the term, "Nutating Traction Drive."

Description

Traction Drive. The Vadetec NTD is made up of five basic components as shown in Fig. 1:

- transmission case or reaction member,
- input or driving member,
- nutating cone assembly or rolling member,
- reaction rings or control member,
- output gear or driven member.

For reference purposes, the input torque to the driving member is in a clockwise direction when viewed from the front of this unit.

The driving member has a cylindrical central section that has been hollowed out diagonally to accommodate the rolling member, which consists of two hollow cones—one piloted on the other to form a tapered shaft arrangement. The cone assembly, which is mounted on bearings in the input member, is skewed at an angle (approximately 20 deg as shown) so that its axis intersects the axis of the input member at the center. As the input member rotates, the cone assembly nutates, i.e., its axis describes two cones of revolution with their apexes at the point of intersection of its axis with the axis of the input member.

The rear cone has a thin wall extension which acts as a stabilizer in piloting the front cone so that it has axial freedom of movement in adjusting for system compliance. The cones are keyed together through a drive cam splined to the small end of the front cone which mates with the rear cone extension. Initial adjustment of the cam locking nut preloads the system.

The two cones are in contact respectively with two control rings through openings in the sidewall of the input member. The nutation of the cone assembly causes the cones to roll on the inside periphery of the rings in an epicyclic or planetary motion, but in a direction opposite to input rotation.

When a loading is applied, the drive cam transfers the torque of one cone into the other. The tangential force developed at each of the two

Contributed by the Gas Turbine Division and presented at the Gas Turbine Conference and Products Show, New Orleans, La., March 10–13, 1980 of THE AMERICAN SOCIETY OF MECHANICAL ENGINEERS. Manuscript received at ASME Headquarters, December 19, 1979. Paper No. 80-GT-99.

Copyright © 1981 by ASME

Downloaded 01 Jun 2010 to 171.66.16.59. Redistribution subject to ASME license or copyright; see http://www.asme.org/terms/Terms_Use.cfm

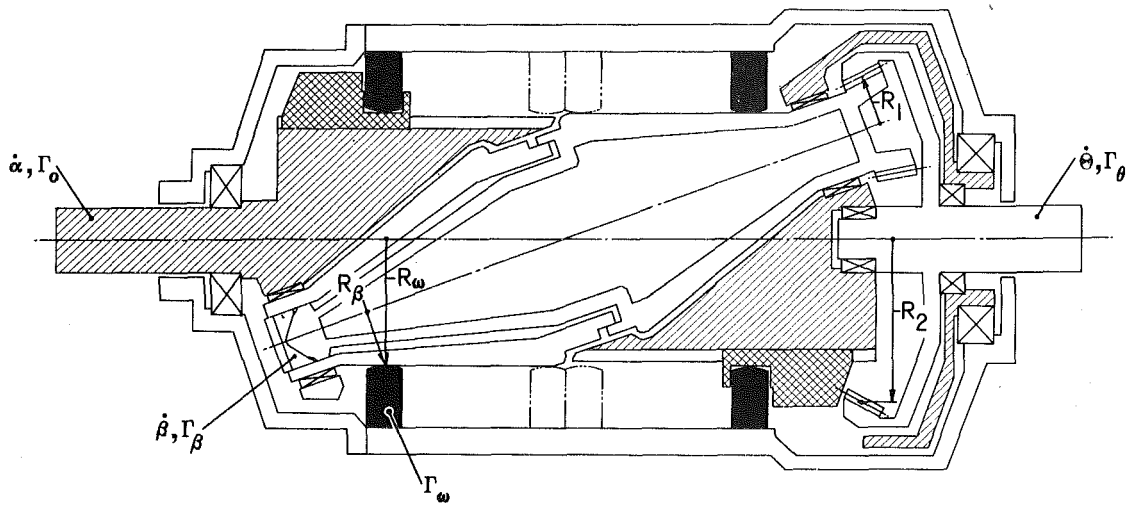

Fig. 1 Schematic of the nutating traction drive

contact points tends to twist one cone relative to the other, thereby causing the mating cam surfaces to slide and force the cones outward, which wedges them into the control rings. Thus, the contact pressure is a function of the torque transmitted and, by appropriate design of the cam angle, is always maintained at the level necessary to provide the required traction.

The output planetary motion of the nutating cone assembly can be viewed as orbiting about the main axis, at constant input speed and direction, while rotating about its own axis, or spinning, at speeds greater than input and in the opposite direction.

The rotational speed of the cone assembly about its own axis is a function of the geometric ratio represented by the perpendicular distance from the axis of the nutating cones to the contact point and the perpendicular distance from the axis of the input member to the contact point. The control rings are keyed to the transmission case, which is the reaction member, and can slide axially toward either the center or the ends of the case. Thus, by varying the position of the rings, the points of contact are shifted so that the rotational speed, and hence "speed ratio," change in accordance with the geometric ratio.

The output drive from the nutating cone assembly is delivered through a straight tooth pinion gear, an integral part of the rear cone, which meshes directly with a constant-spaced, tapered-tooth, reverse bevel, internal ring gear. Ring gear speed is determined from the motion of the nutating pinion gear, where the rotating effect at variable speed subtracts from the orbiting effect at direct engine speed. As the control rings move toward the center of the case, ring gear output speed is slowing down and subtracting less and less from its orbital speed.

This drive arrangement has the inherent advantage of providing a very high efficiency because there is a significant split power path. Part of the power passes directly through the input member to the output shaft and part through the rolling contacts of the nutating assembly. The basic formulas for calculating the speed and torque ratios of the Vadetec NTD are given for reference in the Appendix; the symbols are graphically defined in Fig. 1.

Output Gearing. The CVT design as proposed for use in a highway truck equipped with a diesel engine rated in the 200–250 hp range is shown in Fig. 2.

When operating in low range, the input member at engine speed and the internal tapered gear at variable speed both drive a planetary set through ring and carrier inputs respectively. Output from the planetary set is through the sun. For both high range and reverse, the output from the variator portion of the CVT is taken directly from the internal tapered gear. This system provides two different speed outputs from the variator to a final set of "range gears."

Low range is obtained by the sun gear output of the planetary set driving the front gear set and output shaft. High range is obtained by the internal tapered gear driving the rear gear set and output shaft through a disk clutch. For reverse, the internal tapered gear drives the output shaft through the jaw clutch and front gear set. As the selector is shifted to reverse, the control system simultaneously moves the rings out to their extreme end position to reach maximum reduction ratio. Neutral is obtained when the range section clutches are disengaged.

As the vehicle begins its acceleration from rest in low range, the control rings within the variator move continuously toward their extreme end position, then progress back toward their center position as acceleration continues uninterrupted in high range. Shifting between ranges is controlled by the hydraulically actuated cone clutch and occurs at synchronous speed. Operation of the main clutch is not required to change ranges. Engine braking is maintained throughout all ranges.

A parking brake can be provided as well as various power-take-off arrangements.

Installation. The CVT unit can be designed for mounting entirely within the space envelope of existing transmissions. Refer to the transmission package drawing of Fig. 3 for representative outline dimensions.

Controls. The CVT concept provides the driver with precise control of an infinite selection of speed ratios to obtain maximum acceleration and hill climbing ability without clutch actuation. Also, engine performance can be optimized to obtain more power and less fuel consumption if tuned to operate over a much narrower speed range, as allowed by the continuously variable-ratio transmission.

Automation of the transmission is easily accomplished through addition of a hydraulically-controlled centrifugal clutch and a hydraulic range selection actuator. A microprocessor programmer can

Nomenclature

$\rho = \dfrac{R_\beta}{R_\omega}$ = cone/ring geometric ratio

$k = \dfrac{R_1}{R_2}$ = cone shaft terminal gear output ratio

Γ_0 = input torque applied by power generating system

$\dot{\alpha}$ = speed of input member

Γ_θ = output torque resisted by the load (negative)

$\dot{\theta}$ = speed of output member

Γ_ω = torque reaction of the casing on the two control rings

Γ_β = torque applied by the cone shaft on its terminal gear

$\dot{\beta}$ = speed of cone shaft relative to main axis of drive

R_β = radius of cone

R_ω = radius of control ring

R_1 = pitch radius of cone shaft terminal gear

R_2 = pitch radius of output gear (sun gear if driven through idler, or ring gear)

Downloaded 01 Jun 2010 to 171.66.16.59. Redistribution subject to ASME license or copyright; see http://www.asme.org/terms/Terms_Use.cfm

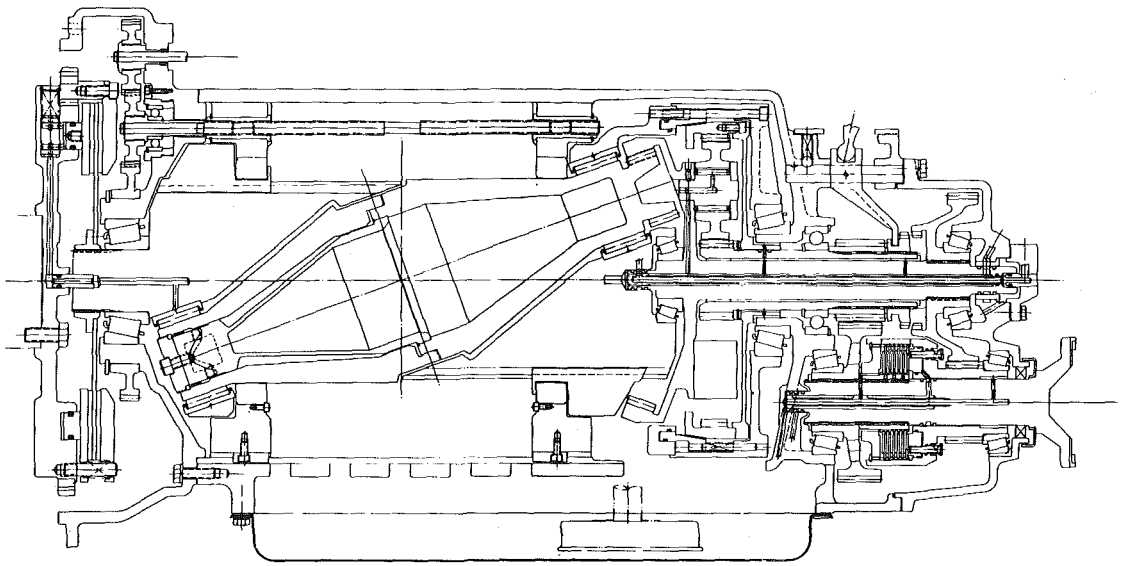

Fig. 2 Layout of truck transmission

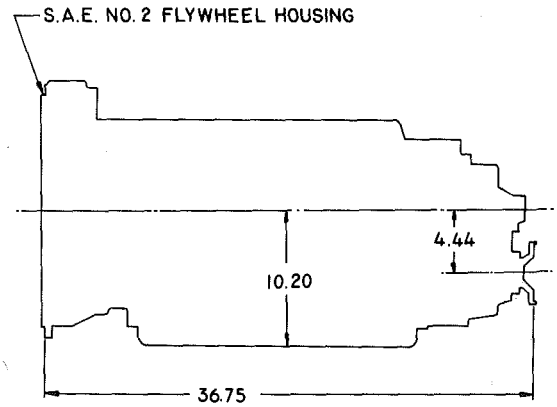

Fig. 3 Transmission package outline

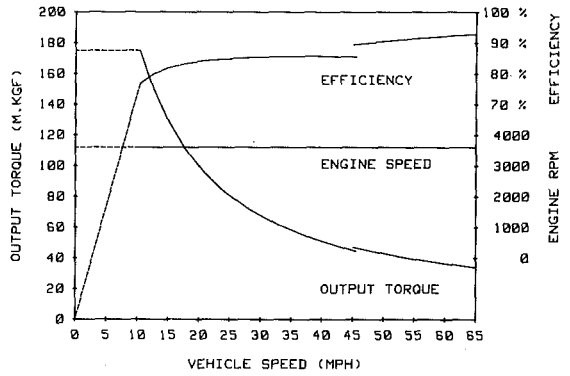

Fig. 4 Transmission performance for maximum power operation

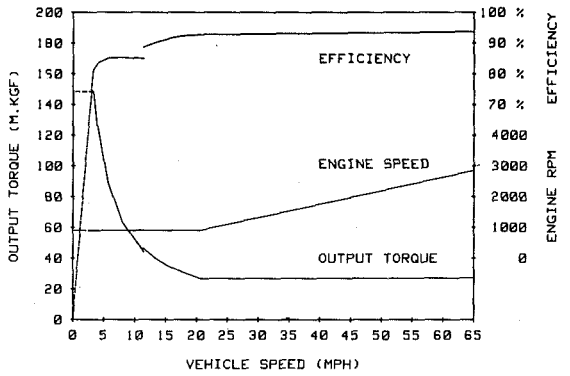

Fig. 5 Transmission performance for minimum fuel consumption operation

be added to fully optimize the vehicle as to the best compromise between performance, noise, and consumption.

The variator speed control consists of a 12-volt, electric motor drive, through a screw-type linear actuator which positions the cone rings in response to demand. Two magnetic speed sensors provide the required inputs for the microprocessor programmer; one for engine speed, the other for transmission speed.

Lubrication and Cooling. The transmission has a dry sump and requires an oil cooler. A traction oil is used in the CVT cone-members which is circulated throughout the entire system. The flow of this pump is also used to cool the centrifugally-operated main clutch as well as to actuate the high and low range clutches. A total theoretical flow rate of 6 gpm is required assuming a temperature drop in the heat exchanger of 30° F (−1°C); the maximum power absorbed by the pump is 0.6 hp.

Balancing. The nutating motion of the cone-shaft assembly creates an inertial torque which varies as the ring position is changed. This variation of inertial torque is balanced by a mass designed into the input member and a small moveable mass which slides with the rings and rotates at input speed.

Performance

The predicted transmission performance at maximum power operation is shown in Fig. 4. The calculations are based on an assumed actual 225 hp input at 3600 rpm constant speed and represent net output as all losses have been included. (The transmission efficiency accounts for the losses in the contacts, in the bearings, in the gears, and 1 percent pumping and splashing losses.)

For minimum fuel consumption operation, the engine must be operated close to maximum torque and at the transmission maximum overdrive ratio. The predicted transmission performance for this mode of operation is shown in Fig. 5.

The indicated level of performance is maintained nearly constant regardless of variations in the size of cones and rings (traction surfaces) because after assembly the ball bearings supporting the ring actuating screws are adjusted until the two sides of the transmission are perfectly symmetrical.

The rolling surface finish of the cones and rings is 10 micro-in. (.25 μm). This finish could probably be somewhat coarser if the transmission were allowed to run for a few hours at low torque because the cones tend to polish themselves while running.

Any failure of the contact surface will be progressive, like a ball bearing failure. Also, it is probable that damage would occur to only

Downloaded 01 Jun 2010 to 171.66.16.59. Redistribution subject to ASME license or copyright; see http://www.asme.org/terms/Terms_Use.cfm

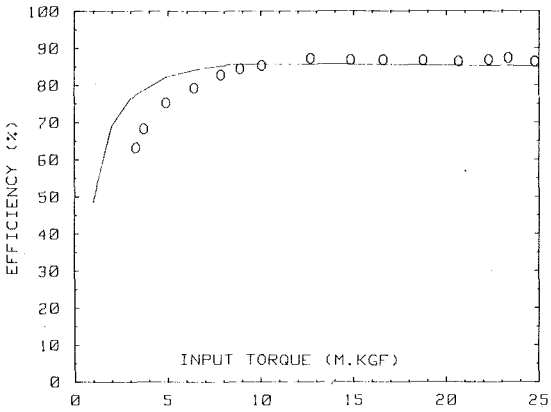

Fig. 6 Correlation of predicted efficiency and experimental results

one cone and the remaining good surface would carry more torque automatically.

The only critical manufacturing factor is to insure that the parts are round and concentric within .0004 in. (10 μm). Otherwise, cyclic overloads will occur at the bearings and the contact surfaces with a loss of performance and life.

Correlation of Theoretical and Experimental Performance

The design of the traction drive, shown in Fig. 2, is based on the same stress levels in the contact and the same traction fluid as were used in our last prototype. It is interesting to compare the results of our theoretical model (of the last prototype) with actual test results; this comparison is shown in Fig. 6 and represents low range operation of the CVT.

The correlation is excellent for moderate to high levels of input torque. The poorer correlation at very low input torques is due to the theoretical model assuming a constant efficiency for the output gears where the actual situation has their efficiency falling off at torque levels significantly below the level for which they were designed.

Overall, the correlation is very good, especially at the torque levels of most interest. Therefore, the computer predictions of performance for the new design are expected to be very close to the actual performance of the transmission.

Durability

Contact stress in the traction drive is low for most of the operating cycle because of the split power path in high range; the peak Hertz stress is 200,000 psi at high speed ratio. A very high life is expected at these stress levels when using conventional bearing-quality steels for the cones and the control rings.

The radial loads on the bearings are relatively low since the gyroscopic couple applies a large part of the required load on the contact areas, thus reducing the load carried by the bearings. There are no thrust loads since the axial forces from the two contact areas cancel one another. The calculated life of the transmission is 5000 hr at maximum continuous power.

Manufacturing Cost

Manufacturing cost and the required investment in tooling are less than for a conventional automatic transmission. The primary components are simple in shape, circular in cross-section and easily mass-produced. When produced in large quantities, it is expected that the Vadetec NTD will be no more than 2/3 of the price of an equivalent conventional automatic transmission. The tooling investment will be 1/3 of the investment for the conventional automatic.

Conclusion

The concept as described provides a practical, cost-effective, mechanical CVT with the necessary power density for use in trucks. A 12 to 20 percent improvement in fuel economy is expected when applied to trucks with diesel engines, if properly matched.

With an extended range from 0 to 1:1, it opens up many possibilities, not only for new types of drive lines in vehicles powered by spark and compression ignition engines but also for power trains based on single-shaft gas turbines for which the lack of such a transmission has been a major obstacle.

References

1 *Should We Have a New Engine?: An Automobile Power Systems Evaluation,* Jet Propulsion Laboratory, California Institute of Technology, Vol. 2, Chapter 5, 1975.

2 Shih, S., Trachman, E. G., and Kemper, Y., "Improvement of Automotive Fuel Economy Using the Vadetec Inertial Driveline," First International Automotive Fuel Economy Research Conference, Arlington, Virginia, Oct., 1979.

3 Kemper, Y., "Continuously Variable Transmission Has High Power Density," *Automotive Engineering,* Society of Automotive Engineers, Vol. 87, No. 9, 1979, pp. 44–47.

4 Trachman, E. G., and Cheng, H. S., "Thermal and Non-Newtonian Effects on Traction in Elastohydrodynamic Contacts," *Elastohydrodynamic Lubrication: 1972 Symposium,* The Institute of Mechanical Engineers, 1972, pp. 142–148

APPENDIX

Basic Formulas for Calculating the Vadetec NTD. The following relationships exist for the ideal case where torque and speed losses are neglected.

Speed

$$\dot{\theta} = \dot{\alpha}\left(1 - \frac{k}{\rho}\right); \dot{\beta} = \dot{\alpha}\left(1 - \frac{1}{\rho}\right);$$

$$\text{Speed Ratio} = 1 - \frac{k}{\rho}$$

Torque

$$\frac{\Gamma_\omega}{(-1)} = \frac{\Gamma_\beta}{(-\rho)} = \frac{\Gamma_\theta}{(\rho/k)} = \frac{\Gamma_0}{(1-\rho/k)};$$

$$\text{Torque Ratio} = \frac{\rho}{\rho - k}$$

Downloaded 01 Jun 2010 to 171.66.16.59. Redistribution subject to ASME license or copyright; see http://www.asme.org/terms/Terms_Use.cfm

O. E. Balje
Engineering Consultant,
P.O. Box D,
Sherman Oaks, CA 91413

Aerodynamic and Geometric Design Criteria for the Performance of Low Powered Vehicular Gas Turbines

A study of the design criteria for the performance of small single and two-spool vehicular gas turbines using metallic rotors shows that the acceleration capability, i.e., component inertia and the net power output, determine to a large degree the obtainable cycle efficiency. Fluid viscosity effects and manufacturing limitations cause the cycle efficiency to decrease with decreasing net powers. When fast acceleration capability is desired, aerodynamically compromised component designs may have to be selected which causes an efficiency penalty. It is found that the blade height of the compressor turbine in two-spool designs is a significant parameter for this penalty. One interesting result of the calculations is that single spool designs using metallic radial inflow turbine rotors can be quite competitive with two-spool designs using ceramic rotors in regard to efficiency. They suffer, however, from a comparatively high rotor inertia, i.e., reduced acceleration capability. Areas of uncertainties remain for the loss relations so that the calculated performance values must be viewed as trend data. The prime performance parameter used in this study is the flow path efficiency. The thermal cycle efficiency is presented only for constant values of heat exchanger effectiveness and mechanical efficiency.

1 Introduction

The designers of small vehicular gas turbines have to consider a multitude of optimization parameters to obtain a viable design configuration. The results of a study on the influence of some of these parameters on the performance of small (less than 600 hp) single and two spool gas turbines is presented.

2 Investigated Systems

Two systems are analyzed, the two-spool gas turbine shown schematically in Fig. 1(*a*) and the single spool gas turbine, presented schematically in Fig. 1(*b*). The common element in both systems is a single stage centrifugal compressor. This component is driven in the two-spool system by a mechanically coupled single stage uncooled axial turbine, the compressor turbine. Both elements comprise the gasifier spool. The power turbine is a single stage axial turbine with variable nozzles running independently of the gasifier spool. A burner and heat exchanger complete the cycle. In the single spool gas turbine a single stage uncooled radial inflow turbine is directly coupled with the compressor. Its output serves to drive the compressor and to deliver the net power.

3 Specific Speed Coupling

The compressor and turbine components of a typical gas turbine cycle are aerodynamically coupled by the common weight flow rate W and are mechanically coupled by a common rotative speed of compressor and compressor-turbine for the two-spool arrangement or by the common rotative speed of compressor and turbine for the single spool arrangement. The nature of this coupling may be recognized by analyzing the specific speed interrelations of the two components. The specific speed n_s is a dimensionless similarity parameter which expresses the similarity of fluid conditions at rotor inlet and rotor exit in terms of angular velocity ω, head H_{ad} and volumetric flow rate V

$$n_s = \frac{\omega\sqrt{V}}{(gH_{ad})^{3/4}} \tag{1}$$

Introducing additional fluid dynamic criteria and boundary layer arguments, the efficiency potential of a compressor or turbine stage can be expressed as a function of specific speed and the additional dimensionless similarity parameter, specific diameter defined as

$$d_s = \frac{D(gH_{ad})^{1/4}}{\sqrt{V}} \tag{2}$$

D denotes the rotor tip diameter. Actually, as demonstrated in detail in reference [1], the parameters n_s and d_s (or in the frequently used dimensional form N_s and D_s) are in many cases (i.e., for constant machine Reynolds number Re* and Mach numbers, for finite values of the blade trailing edge thickness and tip clearance) sufficient to determine the efficiency potential and associated optimum geometry (hub ratio, blade number, degree of reaction, etc.) of a turbocomponent. A typical diagram for single stage turbines operating at a fixed Re* value with incompressible media is presented in Fig. 2 [1] which shows lines of constant (maximum) total to static efficiencies η and the optimum values for the degree of reaction ρ and optimum values of the hub ratio λ. Figure 2 shows that, in general, turbine designs with $\rho = 0.5$ give the highest efficiency for nearly all specific speeds, that the optimum hub ratio decreases with increasing specific speeds and

Contributed by the Gas Turbine Division and presented at the Gas Turbine Conference and Products Show, New Orleans, La., March 10–13, 1980 of THE AMERICAN SOCIETY OF MECHANICAL ENGINEERS. Manuscript received at ASME Headquarters December 21, 1979. Paper No. 80-GT-117.

Copyright © 1981 by ASME

Downloaded 01 Jun 2010 to 171.66.16.59. Redistribution subject to ASME license or copyright; see http://www.asme.org/terms/Terms_Use.cfm

that maximum efficiencies can be expected for specific speeds between $n_s = 0.54$ and $n_s = 1.16$. It may be added that any deviation from the "optimum" ρ and λ values causes the efficiency potential to drop, but not catastrophically as shown in reference [1]; and that the trends shown in Fig. 2 do not change when compressible media are considered. The efficiency level, however changes due to Mach number effects.

Similar diagrams can and have been calculated for centrifugal compressors and radial turbines. Due to the specific speed coupling, however, only a comparatively narrow range of specific speeds is of interest for the different components. This can be recognized when single stage compressors are considered exclusively for the gas turbine cycle. Similar to the trends shown in Fig. 2, maximum efficiencies can only be expected for a narrow range of specific speeds—usually between $n_s = 0.62$ and $n_s = 0.93$ [2].

Considering first a typical single spool gas turbine cycle (Fig. 1(b)) where the driving element is a radial inflow turbine, the specific speed of the turbine n_{s-T} is interrelated to the specific speed of the compressor n_{s-C} by

$$\frac{n_{s-T}}{n_{s-C}} = \left(\frac{Y_C}{Y_T}\right)^{3/4}\left(\frac{(\kappa/(\kappa-1))_C}{(\kappa/(\kappa-1))_T}\right)^{3/4}\left(\frac{T_1}{T_4}\right)^{1/4}\sqrt{(1-\eta_T Y_T)\frac{p_1}{p_5}} \quad (3)$$

Figure 3 plots this relation and shows that the ratio n_{s-T}/n_{s-C} varies from 1 to about 0.75. This variation is small enough and the optimum specific speed regime of radial inflow turbines is wide enough that near maximum component efficiencies can nearly always be expected.

For a two-spool arrangement (Fig. 1(a)) the specific speed of the compressor turbine is again interrelated with the specific speed of the compressor by

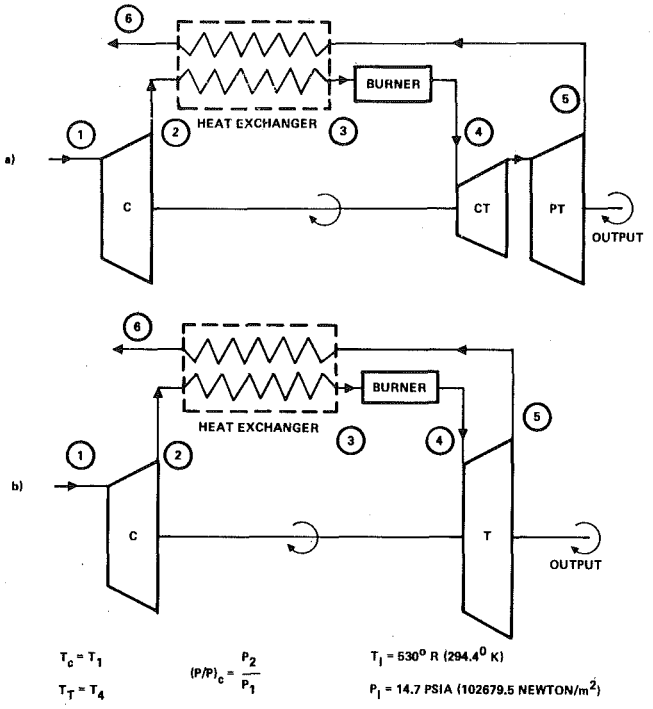

Fig. 1 Cycle notations

$$\frac{n_{s-T}}{n_{s-C}} = \sqrt{\frac{T_4 p_1}{T_1 p_4}}\sqrt{\frac{1-\eta_T Y_T^*}{\{1-(T_1/T_4)[(\kappa/(\kappa-1))_C/(\kappa/(\kappa-1))_T](Y_C/(\eta_C\eta_T))\}^{(\kappa/(\kappa-1))_T}}}(\eta_C\eta_T)^{3/4} \quad (4)$$

where the term Y^* is defined as

$$Y^*_T = 1-\left(\frac{p_5}{p_4}\right)^{((\kappa-1)/\kappa)_T} = \frac{Y_C T_1}{\eta_C\eta_T T_4}\frac{(\kappa/(\kappa-1))_C}{(\kappa/(\kappa-1))_T} \quad (5)$$

Here a somewhat wider ratio of specific speeds is typical as shown in Fig. 4, which indicates that the ratio n_{s-T}/n_{s-C} varies between 0.85 and 1.25 meaning that the specific speed of the compressor turbine can be lower or higher than the compressor specific speed. Selecting now the degree of reaction, the desired rotor pitch speed, and hence the rotor diameter is calculated. The additionally free variable left is the turbine hub ratio, i.e., the flow factor ϕ_{CT}.

Although not immediately obvious, the specific diameter of the power turbine is interrelated with the specific diameter of the compressor turbine. This result is obtained when a typical flow path of a two-spool arrangement. Figure 1(a) is examined. The hub diameter of the power turbine rotor d_{PT} will tend to be somewhat larger than the hub diameter of the compressor turbine rotor d_{CT} when typical automotive gas turbines are considered. This requirement is caused by the necessity to place the power turbine nozzle vanes between two

Conversion data

Symbol	Value	Multiply by	To obtain
D,s	in.	25.4	mm
p	psi	6985	newton/m^2
T_T	°R	0.55556	K

Nomenclature

A_i = interstage diffuser area ratio
c = velocity
c_f = resistance coefficient
D = rotor tip diameter
d_s = specific diameter
d_h = rotor hub diameter
g = gravitational constant
H_{ad} = adiabatic head
h = rotor blade height
h_i = rotor blade height of compressor turbine
h_{i-s} = specific initial blade height of turbine flow path
k_s = equivalent sand roughness (micro-in.)
N = rotative speed
n_s = specific speed
n = exponent
p = pressure
q_{ad} = head coefficient
Re = chord Reynolds number
s_{b1} = blade trailing and/or leading edge thickness
s_{tip} = rotor tip clearance for axial turbines, rotor axial clearance for centrifugal compressors and radial inflow turbines (in.)
T = temperature
V = volumetric flow rate at turbine exit and/or compressor inlet
Y = pressure function $Y_C = (p_{ex}/p_{in})^{((\kappa-1)/\kappa)} - 1$ and $Y_T = 1 - (p_{ex}/p_{in})^{((\kappa-1)/\kappa)}$
W = weight flow rate
β = relative blade angle
ϵ = heat exchanger effectiveness
δ = boundary layer displacement thickness
ζ = loss coefficient
η = efficiency
η_D = diffuser efficiency
η_{fl} = flowpath efficiency
η_{th} = thermal efficiency
η_m = mechanical efficiency
ν = kinematic viscosity
κ = ratio of specific heats
λ = hub ratio
ϕ = flow factor
ρ = degree of reaction
ω = angular velocity

Subscripts

C = compressor
CT = compressor turbine
D = diffuser
N = nozzle
R = rotor
PT = power turbine
T = turbine
pol = polytropic

Downloaded 01 Jun 2010 to 171.66.16.59. Redistribution subject to ASME license or copyright; see http://www.asme.org/terms/Terms_Use.cfm

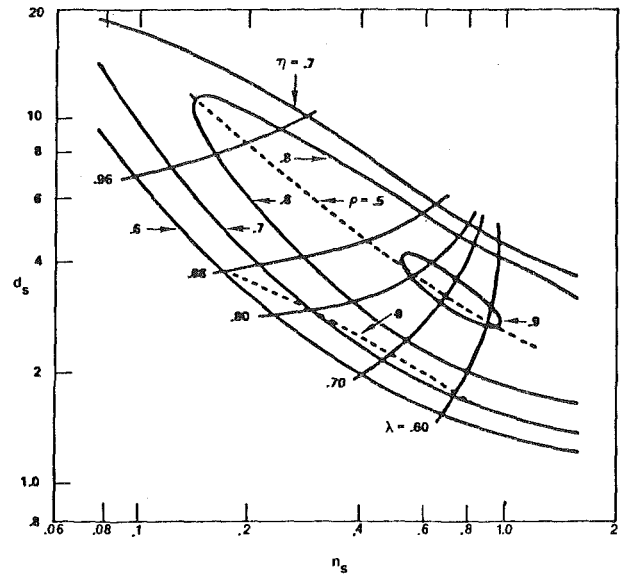

Fig. 2 $n_s d_s$ diagram for axial turbines [1]

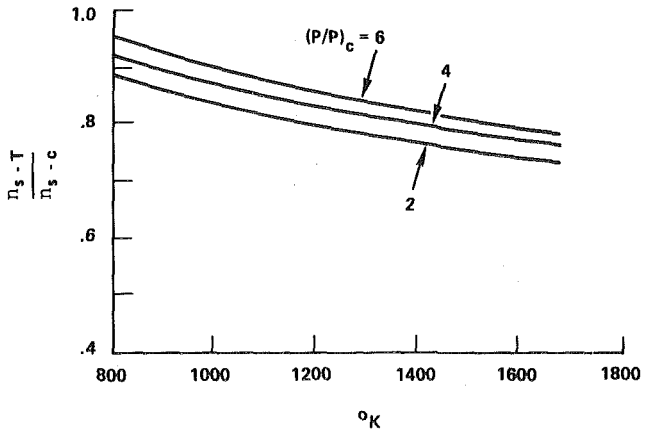

Fig. 3 Specific speed interrelation between turbine and compressor for single spool gas turbine

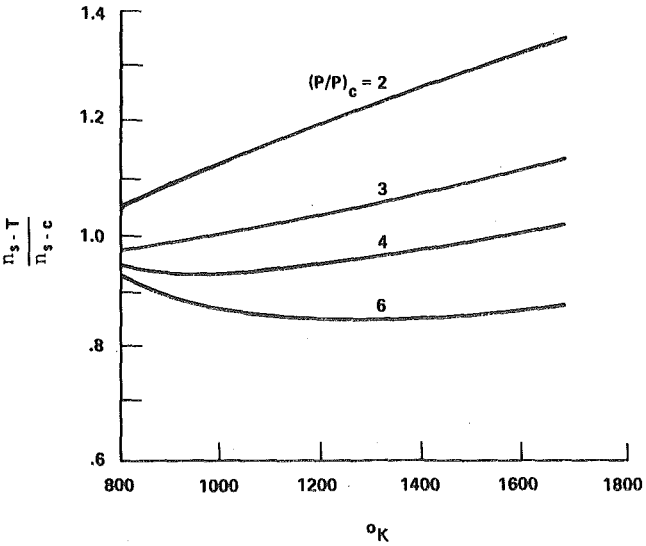

Fig. 4 Specific speed interrelation between compressor and compressor-turbine for two-spool gas turbines

spherical surfaces. Thus the hub diameter of the power turbine rotor is interrelated with the hub diameter of the compressor turbine rotor and the tip diameter of the power turbine rotor is interrelated with its hub diameter by the hub ratio, which in turn is interrelated with hub ratio of the compressor turbine rotor by the diffuser area ratio of the interstage duct, $A_i = (A_{ex}/A_{in})_i$, i.e.,

$$\lambda_{PT} = \frac{1}{\sqrt{1 + (1/\lambda_{CT}^2 - 1)A_i(d_{CT}/d_{PT})^2}} \tag{6}$$

Thus the throughflow area of the power turbine, and hence the meridional flow velocity, becomes related to the meridional flow velocity through the compressor turbine. Selecting now again the degree of reaction, the peripheral rotor pitch velocity is determined; i.e., the head coefficient q_{ad} of the stage since the available head is known from the cycle pressure ratio and gas inlet temperature after accounting for the pressure and temperature drop in the compressor turbine. Thus ϕ_{PT} and q_{ad-PT} are fixed and hence n_s and d_s of the power turbine.

These considerations show that all turbo components are closely coupled leaving only six variables: the compressor specific speed, the hub ratio of the compressor turbine (or ϕ_{CT}), the degrees of reaction for both turbines, the hub diameter ratio d_{PT}/d_{CT} and the interstage duct area ratio A_i.

Before presenting the results of the cycle calculations, the essential aspects of the component performance are discussed.

4 Component Performance

a Turbines and Diffusers. Several loss sources have to be distinguished in a turbine flow path: the profile losses and the endwall losses at nozzle and rotor blades, the tip clearance losses (for unshrouded rotors) and the rotor windage losses.

The relations for the profile losses are fairly well explored and can be obtained from boundary layer arguments. The boundary layer growth is found to depend primarily on the acceleration or deceleration of the flow in the cascade, the ratio of flow path length to passage inlet width and the chord Reynolds number. The acceleration or deceleration within the rotor channel depends essentially on the degree of reaction; a high degree of reaction indicates an accelerated velocity within the rotor channel whereas the impulse turbine rotor usually has a nearly constant flow velocity from inlet to exit. The ratio of flow path length to inlet width is commonly expressed by the cascade solidity. Its optimum value is represented by a blade loading coefficient defined originally by Zweifel [3] and having optimum values of about 0.9. The chord Reynolds number Re is a function of the exit velocity, the chord length, and the kinematic viscosity at passage exit; i.e., it depends on geometry as well as operating conditions, such as pressure and temperature. For chord Reynolds numbers in excess of Re = 2×10^5, the boundary layer is usually considered to be turbulent, with the exception of the initial (laminar) portion. For extremely low Reynolds numbers (Re < 10^4) the boundary layer may be laminar; whereas at intermediate Reynolds numbers (i.e., Re <2×10^5 but >10^4) the flow can be predominantly laminar or predominantly turbulent, depending on the degree of turbulence. In this flow regime the interrelation between loss coefficient and Reynolds number become somewhat complex. The loss coefficient for purely laminar flow is lower than for purely turbulent flow (Fig. 5 [4]). For low degrees of turbulence the transition from turbulent to laminar flow occurs at high Reynolds numbers. High degrees of turbulence reduce the transition Reynolds number to values where the difference between laminar and turbulent loss coefficients is small. Thus for typical rotors, where the degree of turbulence will tend to be high, the profile loss coefficient can be expected to follow essentially the turbulent loss coefficient until fully laminar flow conditions are reached (Re < 10^4). In contrast, the flow in the nozzle may be essentially turbulent or laminar so that the profile loss coefficient may be lower than calculated for turbulent flows; but its increase with decreasing Reynolds numbers may be more pronounced than expected from turbulent loss relations. Test data (Fig. 6) reflect turbulent and laminar Reynolds number trends as well as intermediate trends for chord Reynolds numbers Re < 2×10^5. Thus a certain amount of uncertainty exists

Downloaded 01 Jun 2010 to 171.66.16.59. Redistribution subject to ASME license or copyright; see http://www.asme.org/terms/Terms_Use.cfm

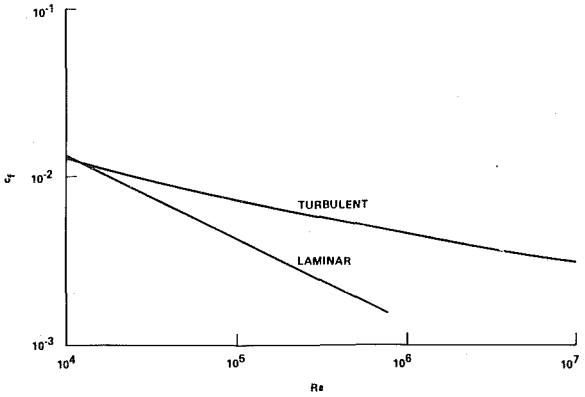

Fig. 5 Trend data for loss coefficients in the "intermediate" Reynolds number regime for flat plates

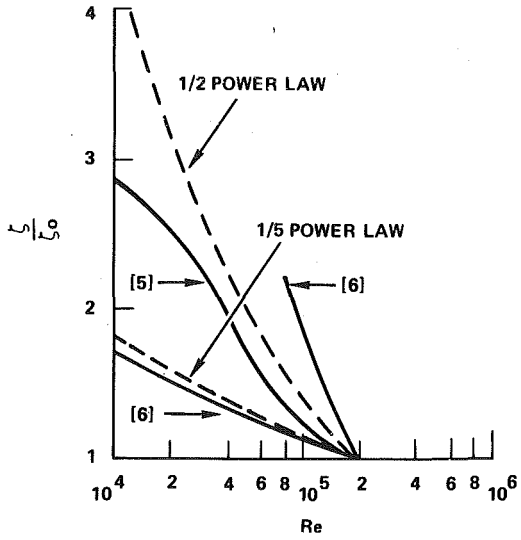

Fig. 6 Test data on profile loss coefficients

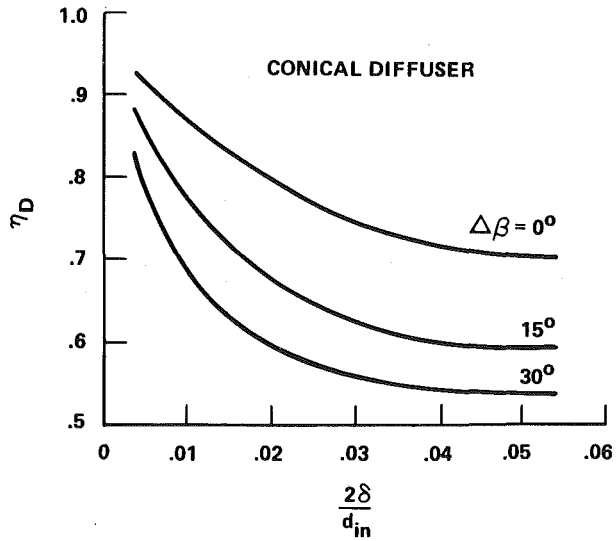

Fig. 7 Diffuser efficiency data [9]

for the magnitude of the profile losses in the transitory Reynolds number regime.

In addition to the losses caused by the boundary layer growth, the effect of the finite trailing edge thickness on the wake mixing losses will have to be considered. These losses increase with increasing ratios of projected trailing edge thickness to pitch [1].

A considerable amount of uncertainty also exists for the magnitude of the endwall losses. The information provided in [7] indicates that these losses are essentially a function of the flow deflection, ratio of blade height to chord length and initial boundary layer thickness (generated in the preceeding flow path) but independent of the chord Reynolds number. The endwall losses can increase up to three times the minimal values for a comparatively high ratio of initial boundary layer thickness to passage height.

Actually this trend is well confirmed by the results from diffuser tests. Reference [8] shows that the diffuser losses are not very dependent on Reynolds number but are a strong function of the initial boundary layer thickness. Unfortunately the variation of the Reynolds number in the diffuser test data is insufficient to rule out a Reynolds number effect entirely.

In addition, the diffuser losses depend on the flow path shape (Fig. 7 [9]). Minimum losses can be expected for straight surfaces. Higher losses are shown for curved diffuser passages, the losses increasing with increasing deflection angles and decreasing turning radii.

The dependency of the clearance losses have been investigated in reference [10] which shows that they are independent of Reynolds number and a function of the blade loading and ratio of tip clearance to chord length. Again an uncertainty exists in the numerical data. Reference [11] indicates substantially higher values than reference [10]. The rotor windage losses have been fairly well explored [12] and are a function of the Reynolds number.

A more detailed discussion of the loss and geometry interrelations is presented in references [1] and [13].

With these data, the losses and thus the efficiency potential of axial turbines is expressed as function of suitable similarity parameters (e.g., n_s and d_s or flow factor ϕ and head coefficient) which reflect the effect of the flow path geometry and operating conditions on the efficiency. For the subsequent calculations a constant blade height from cascade inlet to exit is assumed for axial turbines; i.e., the effect of the density change on the pertinent flow vectors was observed by modifying the relations used in references [1] and [13].

The efficiency potential of radial inflow turbines is calculated from similar arguments [14]. Only rotor geometries with a rotor inlet blade angle of $\beta_2 = 90$ deg and a "deep scalloped" disk are considered to favor a high gas inlet temperature potential.

b Centrifugal Compressor. Detailed studies on the flow and loss mechanism of the centrifugal compressor show that backward curved rotor blades with an angle of $\beta_2 = 40$ to 50 deg give the highest efficiency, and that specific speeds between $n_s = 0.62$ and $n_s = 0.78$ are near optimum values for pressure ratios up to about 4:1. Higher specific speed compressors can still give high efficiencies at higher pressure ratios when efficient transonic inducers can be designed. This trend follows from the interrelation between relative inducer inlet Mach number, specific speed and rotor tip Mach number, i.e., pressure ratio. The relative Mach number at the mean streamline of the inducer increases with increasing specific speeds and increasing stage pressure ratios and reaches values of unity at specific speeds of about $n_s = 0.78$ for pressure ratios of 6:1. This would imply inducer choking at this operating condition and supersonic relative Mach numbers at inducer tip so that lower specific speeds would be desired to obtain sufficient performance range.

Since the density change through the rotor increases with increasing pressure ratios, the rotor blade exit width decreases and thus the ratio of flow path lengths to channel height in the diffuser becomes less favorable causing higher diffuser losses. Thus a decrease in efficiency level with increasing pressure ratios becomes inevitable. Additionally the influence of the finite blade leading and trailing edge thickness has to be considered. A generalization of the data in reference [15] is used to account for the rotor blade leading edge thickness penalty as function of relative inlet Mach number for centrifugal compressors.

5 Cycle Performance Data Presentation

From an aerodynamic point of view the flow path efficiency η_{fl} is

Downloaded 01 Jun 2010 to 171.66.16.59. Redistribution subject to ASME license or copyright; see http://www.asme.org/terms/Terms_Use.cfm

a desirable parameter to express the aerodynamic quality of the design [16]. This term is defined as the product of the polytropic efficiencies of the turbocomponents and a factor which expresses the losses, i.e., referred pressure drop $\Delta p/p$ through the heat exchanger, compressor inlet ducting, turbine exhaust pipe and combuster polytropically. This term is defined by

$$\eta_{fl} = \eta_{C-pol}\eta_{T-pol}(1 - n) \tag{7}$$

when n is calculated from

$$1 - \frac{\Delta p}{p} = \left(\frac{p}{p}\right)_C^{-n} \tag{8}$$

To identify the cycle performance, however, the influence of the cycle inlet temperature T_{1-t} and heat exchanger effectiveness ϵ has to be expressed. This is conventionally done by calculating the thermal efficiency η_{th}. To be realistic, an assessment has to be made for the gear, bearing and accessory power losses (η_m). Thus additional parameters enter which do not depend on fluid dynamic criteria and are not a subject of the study. For the convenience of the calculations, the numerical values for these additional parameters were assumed constant, $\eta_m = 0.9$ and $\epsilon = 0.86$, although in reality these values vary with mechanical design features, the amount of accessory power needed and envelope dimensions of the units. In addition, the referred pressure drop of $\Delta p/p = 0.06$ = constant is assumed. This value is not a unique constant but a function of design features especially heat exchanger and burner design. Modifications of the numerical values for these parameter can be used to improve the thermal cycle efficiency, often at the expense of size and cost. By keeping the numerical values for these parameters constant the number of investigated parameters is reduced to a more managable amount.

For the convenience of the discussion certain fixed values for important geometrical dimensions are used as reference values. They are: a turbine rotor and nozzle blade trailing edge thickness of 0.02 in. (0.51 mm), an unshrouded rotor design with a tip clearance of .02 in. (0.51 mm), a compressor rotor blade leading edge thickness of .02 in. (0.51 mm). The turbine flow path efficiency accounts for the exit diffuser loss (up to the heat exchanger inlet). For the two stage axial turbine the losses in the interstage duct as accounted for additionally, together with the "reheat effect".

Since the turbine size depends primarily on the power output of the unit all pertient data are presented as function of net power output.

6 Cycle Performance Data

a Two-Spool Designs. A parameter which was found to be of critical significance for the efficiency of the turbine flow path in a two-spool unit is the blade height of the compressur turbine, i.e., the initial height of the turbine flow path, h_i. In cases where this height is comparatively small (as it might be desired for an early introduction of ceramic rotors) the throughflow velocity becomes high and thus the losses in the initial portion of the flow path. It would then be desirable to reduce this velocity as quickly as possible by demanding a large area ratio for the interstage duct. This element, however, will be working at a handicap due to the comparatively high initial boundary layer thickness generated by the preceding turbine stage and by the double curvature of the walls. When a high initial height of the turbine flow path can be selected, significantly reduced throughflow velocities result and the area ratio requirements for the interstage diffuser are reduced. Thus the losses are kept low. For fixed aerodynamic parameters of the turbine flow path the ratio of compressor turbine blade height (h_i) to the square root of net horsepower is nearly constant. Thus the ratio becomes important for the turbine flow path efficiency and may be expressed in a more general way in terms of operating conditions by defining a dimensionless specific initial blade height h_{i-s} in analogy with the specific diameter. This is done by replacing the diameter in equation (2) by the blade height (h_i) and by expanding equation (2) with the square root of the product of the mean density in the turbine flow path and the expanded head. This yields the relation

$$h_{i-s} = \frac{h_i g^{1/4} H_{ad}{}^{3/4}\sqrt{\gamma_m}}{\sqrt{WH_{ad}}} = \frac{h_i}{\sqrt{p^*}} g^{1/4} H_{ad}{}^{3/4}\sqrt{\gamma_m} \tag{9}$$

where the term $WH_{ad} = P^*$ represents the net output in ft-lb/s (or m-kg/s). Figure 8 shows the flow path efficiency as function of the specific initial blade height for a fixed value of the net output and for various values of the gas inlet temperature, pressure ratio and interstage duct area ratios. A rather significant decrease in flow path efficiency with decreasing specific initial blade heights is shown. As it was to be expected, 50 percent reaction compressor turbines yield a higher efficiency level but the flow path efficiency still decreases with decreasing h_{i-s} values.

The effect of ρ_{CT} is significant when metallic rotors are considered. The maximum allowable gas inlet temperature for 50 percent reaction uncooled axial turbines is nearly independent of pressure ratio and limited to values of about 2240° R (1244 K). In contrast the maximum allowable gas temperature for uncooled axial impulse stages increases with increasing pressure ratios and can be as high as 2560° R (1422 K) for a pressure ratio of 3, Fig. 9 [17]. It has to be considered that the gas stream approaching the first stage is very seldom of uniform temperature and that overtemperatures will have to be expected in transient operation. Thus a certain temperature margin, i.e., difference between the nominal maximum cycle inlet temperature and maximum allowable turbine inlet temperature, will have to be allowed for. This margin is assumed with 200° F (111° C) in the subsequent calculations so that a nominal turbine inlet temperature of 2240° R (1244 K) results for a cycle pressure ratio of 4:1 and a somewhat higher value of 2290° R (1272 K) for a cycle pressure ratio of 6:1 when the compressor turbine is designed as an axial impulse stage.

The temperature drop in the compressor turbine is sufficiently large to make a 50 percent reaction design acceptable for the axial power turbine. Selecting a 50 percent reaction axial compressor turbine design reduces the allowable maximum cycle temperature considerably.

Single stage radial inflow turbines allow a significantly higher maximum cycle temperature, as indicated by the dashed lines in Fig. 9. It thus appears that for metallic turbine rotors only "near impulse" designs should be considered for the compressor turbine.

An appreciation of the predominant trends is obtained when the operating points of the different designs are spotted on the $n_s d_s$ diagram for axial stages (Fig. 10). For a cycle inlet temperature of T_{1-T} = 2210° R (1228 K), a cycle pressure ratio of 4:1 and a compressor specific speed of 0.58 all turbine stages operate at specific speeds where high stage efficiencies can be expected. The specific diameters of the compressor turbines designed as impulse stages for low and high $h_i - s$ values or designed as high reaction stages are near the optimum

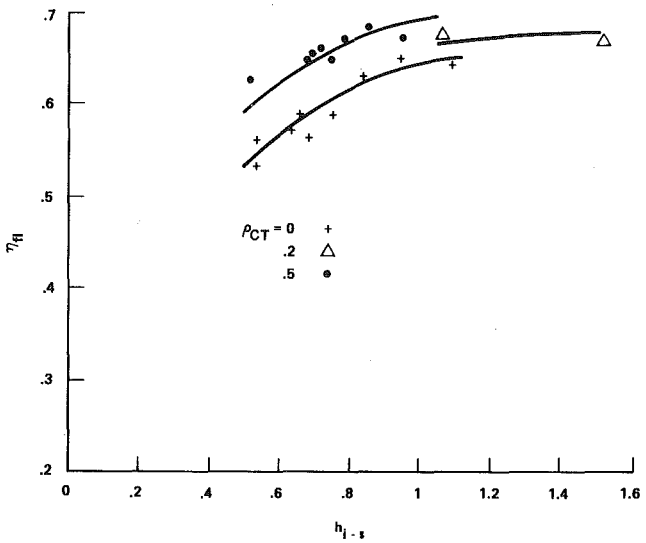

Fig. 8 Influence of initial blade height on flow path efficiency

Downloaded 01 Jun 2010 to 171.66.16.59. Redistribution subject to ASME license or copyright; see http://www.asme.org/terms/Terms_Use.cfm

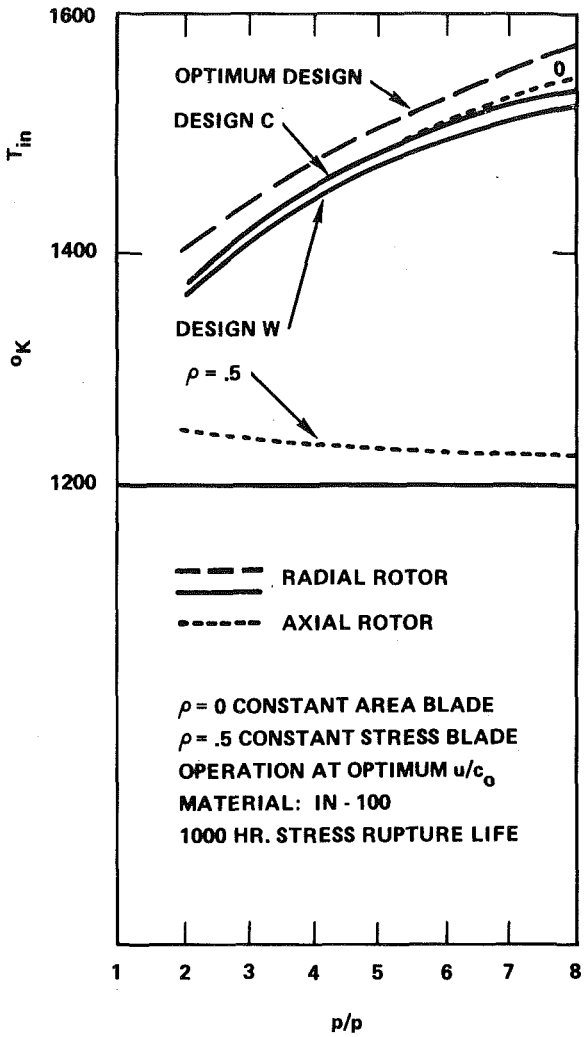

Fig. 9 Allowable gas inlet temperatures for metallic turbine rotors [16]

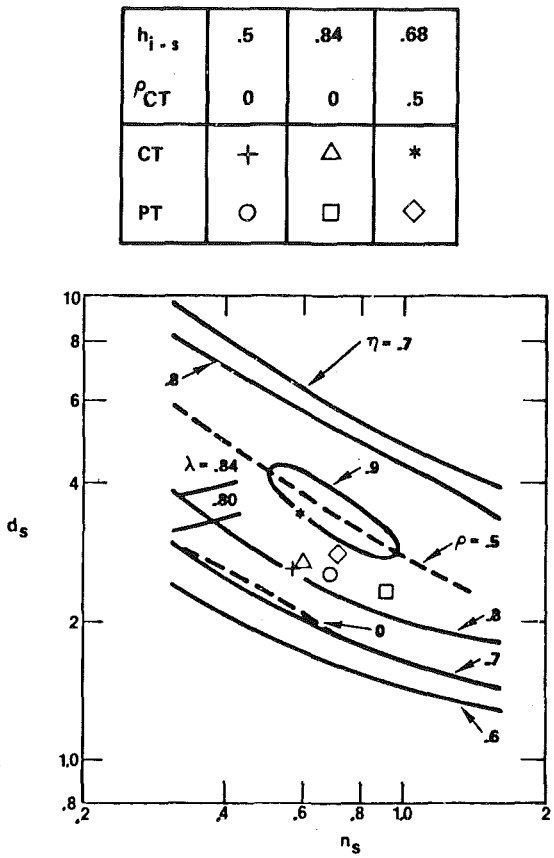

Fig. 10 Specific speed and specific diameter coupling between power turbine and compressor turbine in two-spool gas turbines (p/p = 4, n_{s-C} = 0.58, T_{1-T} = 2210° R (1288 K))

values. The specific diameters of the power turbines, designed for 50 percent reaction is lower than desired. The associated penalty, however, is comparatively small as indicated in reference [1]. Thus, in general, all stages are fairly well matched although somewhat larger power turbine diameters, i.e., large d_{PT}/d_{CT} or A_i values than actually selected (d_{PT}/d_{CT} = 1.15 to 1.35 and A_i = 1.3 to 2.0), would appear to be preferable. This may, however, be of dubious benefit since interstage diffuser losses could become excessive.

Increasing the compressor specific speed to 0.74 will increase all turbine stage specific speeds by about 27 percent and decrease the specific diameters by $\sqrt[3]{1.27}$, i.e., about 8 percent (since the flow factors stay about constant). Thus the quality of the stage match hardly changes.

The cycle performance data are presented by plotting the flow path efficiency η_{fl} and the thermal efficiency η_{th} as function of the net output for various values of the cycle inlet temperature T_t. Two parameters are singled out for a more detailed study, the trailing edge thickness t_{b1} (or leading edge thickness for centrifugal compressors) and the tip clearance t_{tip} (radial gap in axial turbines and axial gap at rotor tip for radial turbines and compressors). These values usually are controlled by fabrication limitations, e.g., cost and by the realities of the mechanical design, e.g., housing distortions due to peripheral temperature gradients and do not respond well to aerodynamic arguments. The calculated data are presented in Figs. 11 to 20 and show the same basic trends: a reduction in efficiency with decreasing net outputs and increasing blade trailing edge thickness and clearance values. A more detailed discussion follows.

Selecting low h_{i-s} values, a cycle pressure ratio of 4:1 and a compressor specific speed of 0.58 (Fig. 11) the efficiency penalty is higher for high temperature operations and low net outputs than for low temperature operation and high net outputs. The reason is that low net output and high temperature cycles have significantly smaller rotor diameters, so that the blade displacement effect becomes more pronounced. When the compressor specific speed is increased to 0.74, the performance improves mainly due to an improved compressor efficiency and a slightly higher h_{i-s} value (Fig. 12). The rotors are smaller due to the increased specific speed. This causes a higher blade trailing edge and tip clearance sensitivity. When the cycle pressure ratio is increased to 6:1 the flow path efficiency and thermal efficiency decrease (Fig. 13) since the rotor diameters are reduced further thus increasing the sensitivity to clearance and trailing edge thickness.

Considerably higher flow path and thermal efficiencies result for designs with an increased specific blade height (Fig. 14). It is interesting to note that for this design the thermal efficiency calculated for a net power of 75 hp and a maximum cycle temperature of 2460° R (1367 K) is lower than calculated for a maximum cycle temperature of 2210° R (1228 K) when the higher temperature design requires a heavier turbine blade trailing edge thickness and larger tip clearances than the lower temperature design. Thus a heavy trailing edge requirement can well negate the performance improvements usually associated with high cycle temperatures.

Another point of interest is the variation in chord Reynolds number for power turbine and compressor turbine for the different operating conditions. Highest Reynolds numbers are calculated for the compressor turbine nozzle and lowest Reynolds numbers for the power turbine rotor, as shown in Fig. 15. All Reynolds numbers decrease with decreasing net outputs inversely proportional to the square root of the net output. By increasing the turbine inlet temperature the Reynolds numbers decrease reaching extremely low values for small net outputs. Actually, most of the Reynolds numbers are in the transitory Reynolds number regime where precise interrelation be-

Downloaded 01 Jun 2010 to 171.66.16.59. Redistribution subject to ASME license or copyright; see http://www.asme.org/terms/Terms_Use.cfm

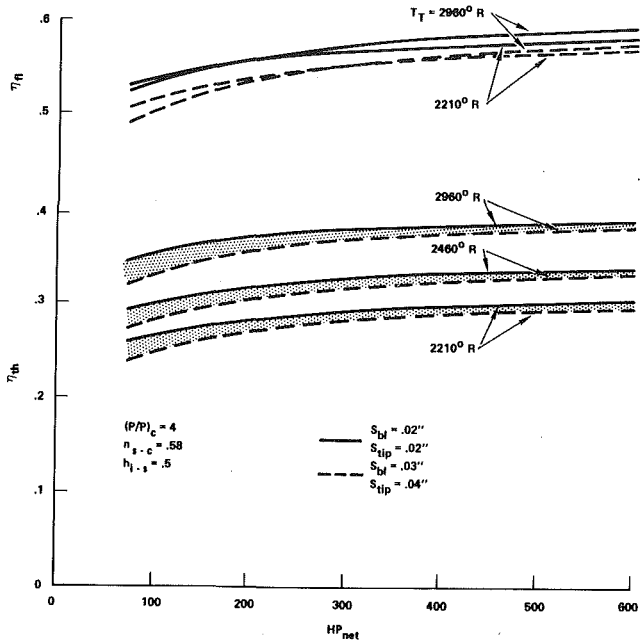

Fig. 11 Cycle performance data for two-spool design with low h_{i-s} value $n_{s-c} = 0.58$, $p/p = 4$

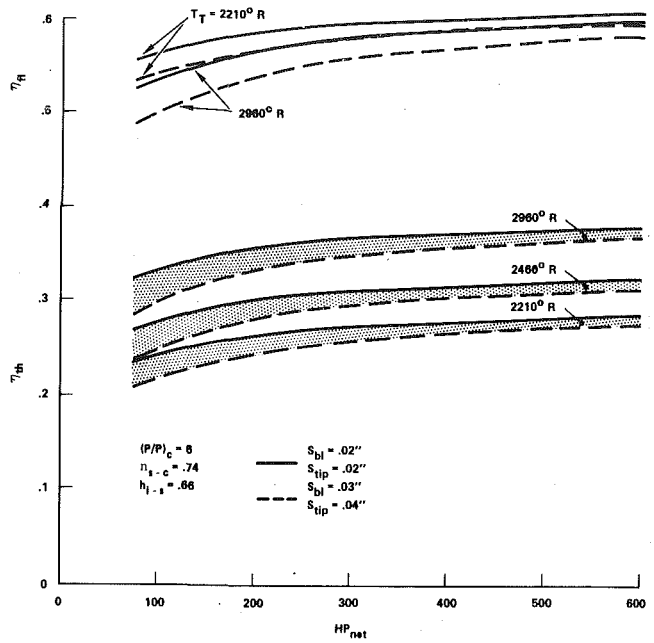

Fig. 13 Cycle performance data for two-spool design with low h_{i-s} value $n_{s-c} = 0.74$, $p/p = 6$

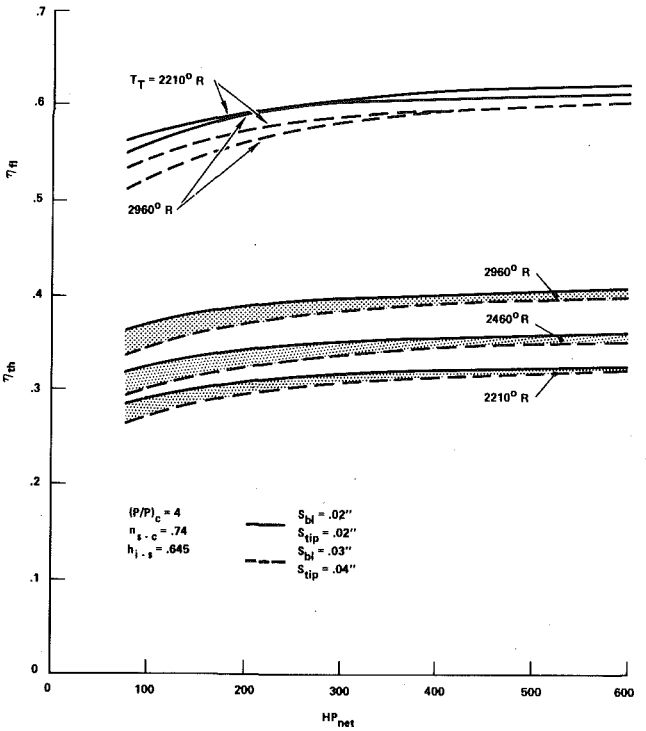

Fig. 12 Cycle performance data for two-spool design with low h_{i-s} value $n_{s-c} = 0.74$, $p/p = 4$

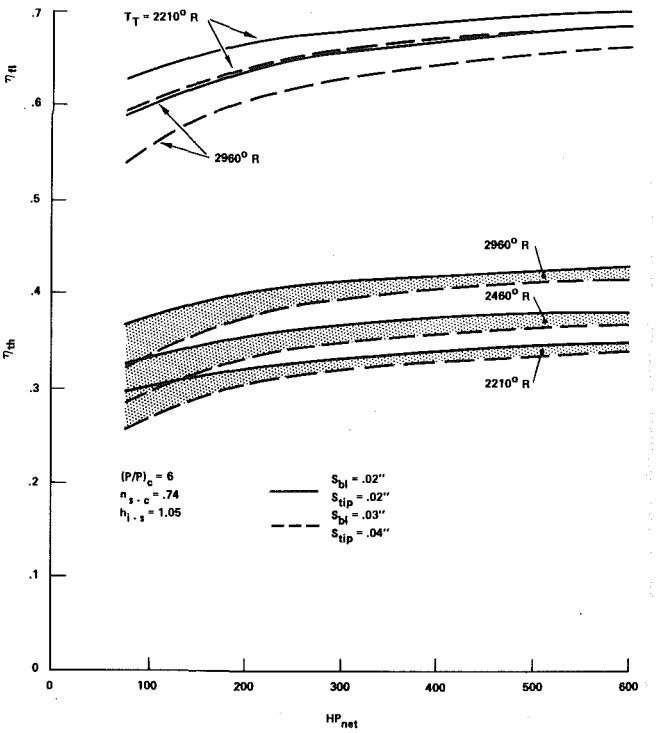

Fig. 14 Cycle performance data for two-spool design with high h_{i-s} value $n_{s-c} = 0.74$, $p/p = 6$

tween loss coefficient and Reynolds number are not well established. The presented data are calculated with the assumption of a turbulent boundary layer. This gives pessimistic results when the boundary layers, for example in the compressor or power turbine nozzles, are predominantly laminar.

Inspection of the component efficiency data shows that the turbine flow path efficiency (which includes the diffuser losses) is lower than the compressor efficiency for low h_{i-s} designs and is relatively unaffected by the net power. This was to be expected since most of the losses (endwall losses and diffuser losses) are Reynolds number independent. The low level of the turbine flow path efficiency is caused by the proponderance of the diffuser losses. In contrast, the turbine flow path efficiency of high h_{i-s} designs is higher than the compressor efficiency and shows a higher dependency on the net power. The compressor efficiency reflects the highest influence of the unit size due to the sensitivity of the losses to the rotor and diffuser leading edge thickness. This influence is particularly strong at high pressure ratios since the flow Mach numbers are high.

Another observation is important: It is not necessarily a forgone conclusion that turbine stages have to be designed for zero exit swirl; in some cases designs with exit swirl can offer advantages. Thus the sensitivity of the diffuser efficiency to inlet swirl has to be considered in the design studies. Reference [18] reports that inlet swirl in general tends to reduce the diffuser efficiency. Reference [19] shows that the

Downloaded 01 Jun 2010 to 171.66.16.59. Redistribution subject to ASME license or copyright; see http://www.asme.org/terms/Terms_Use.cfm

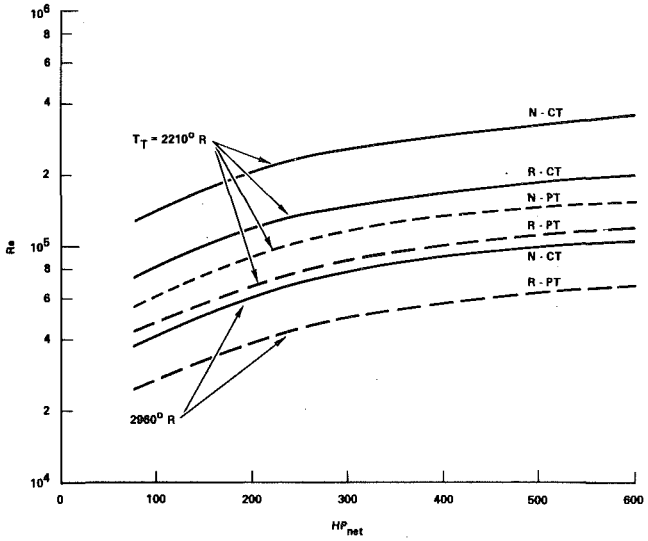

Fig. 15 Chord Reynolds number data for two-spool axial turbines

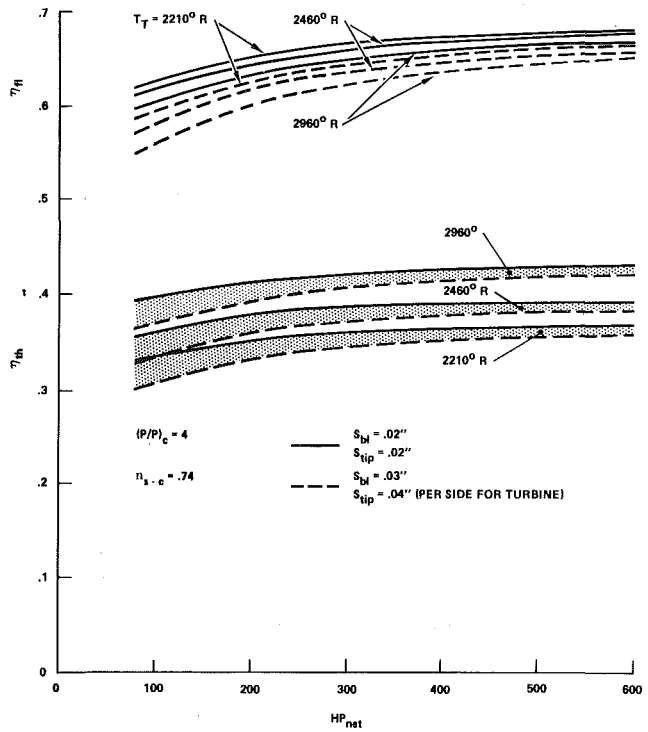

Fig. 16 Cycle performance data for single spool design $n_{s-c} = 0.74$, $p/p = 4$

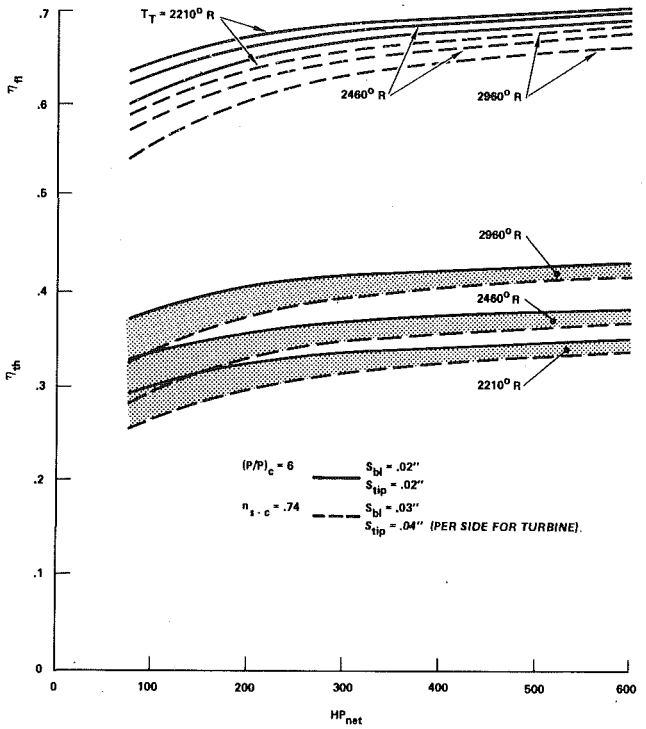

Fig. 17 Cycle performance data for single spool design $n_{s-c} = 0.74$, $p/p = 6$

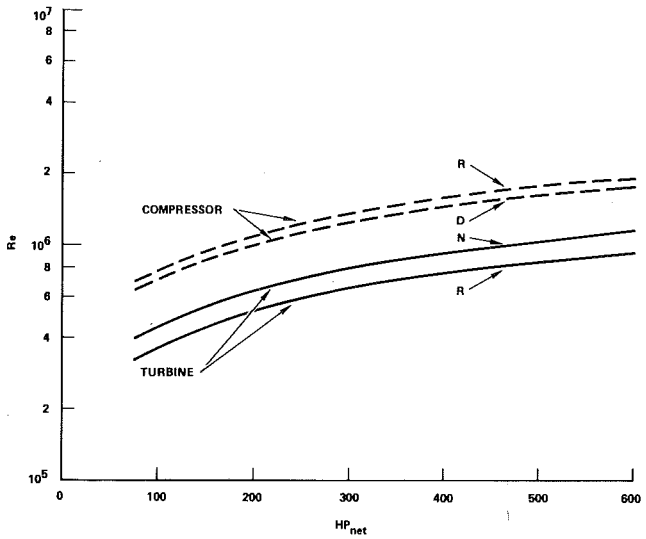

Fig. 18 Chord Reynolds number data for radial inflow turbine and centrifugal compressor

efficiency of straight conical diffusers increases with increasing amounts of swirl (up to swirl angles of 50 deg) for divergence angles larger than 8 deg, as long as the meridional flow component at the inner radius is larger than the meridional flow component at the outer radius, but decreases for swirl angles larger than 20 deg when the meridional component at the inner radius is smaller than at the outer radius. Thus the flow distribution at the preceding rotor exit becomes a design criterion, i.e., the design mode (free vortex or forced vortex) of the preceding turbine stage. It would appear, however, that this issue needs further clarification.

It is noteworthy that smooth surfaces will be required, even for low powered units. This follows from the relations which govern the allowable surface roughness (equivalent sand roughness k_s)

$$k_s \leqq \frac{100\, l}{R_e} \leqq \frac{100\, \nu}{c_{ex}} \qquad (10)$$

Equation (10) shows that k_s depends only on the kinematic viscosity and on the velocity c_{ex} at cascade exit and thus does not depend on the component size, i.e., net power. The variation of ν and c_{ex} in the analyzed cycles is comparatively small. The calculated k_s values vary between 50 and 120 micro-in., the lower values pertaining to the compressor-turbine nozzle and rotor. Thus polished steel surfaces would be desired here whereas "machined steel surfaces with flow direction parallel to tool marks" [20] should be sufficient for the power turbine.

b Single Spool Units. The performance of single spool gas turbines employing a single stage radial inflow turbine exhibits similar trends as discussed before. The main difference is that the flow path efficiency and thermal efficiency are significantly higher and that the trailing edge thickness effect is less pronounced. The axial rotor clearance, however, has to be carefully controlled since this value is

Downloaded 01 Jun 2010 to 171.66.16.59. Redistribution subject to ASME license or copyright; see http://www.asme.org/terms/Terms_Use.cfm

critical. This is shown in Figs. 16 and 17 for a compressor specific speed of 0.74 and for cycle pressure ratios of 4:1 and 6:1. The performance decrease with decreasing outputs is also less pronounced partly due to the comparatively high chord Reynolds numbers, Fig. 18. Even at 75 net hp the Re values are above the transitory Reynolds number regime. It is interesting to note that this holds also for the compressor as indicated by the dashed lines in Fig. 18. Again the allowable surface roughness is independent of net output and has values similar to the axial components.

Another reason for the improved performance becomes apparent from a comparison of the turbine flow path designs (Fig. 19). The turbine flow path for the single spool design (lower diagram) is comparatively short and can readily be expected to be efficient when blade overloading is avoided, i.e., when a sufficient number of nozzle and turbine blades is provided. In contrast, the flow path of a two-spool design (upper diagram) is comparatively long and has large frictional surfaces, some of them exposed to high velocities when h_{i-s} is small. Additionally the number of blade rows is doubled so that the total wake mixing losses are increased particularly for low net outputs.

c Cycle Temperature Limitations Due to Uncooled Metallic Rotors. Calculating the cycle performance for single spool and two-spool designs assuming uncooled metallic rotors and a temperature margin of 200° F the data in Fig. 20 result when a cycle pressure of 6:1, a compressor specific speed of 0.74 and a high value of the initial blade height h_{i-s} is selected for the two-spool design. These data show that the single spool design has a performance which is 10 percent better than the two-spool design for high net powers and about 11 percent better for low net powers. Considering that a single spool design will need an infinitely variable transmission for vehicular application, even with a comparatively low transmission efficiency, the performance of the single spooler will be equal to that of a two-spool design.

The disadvantage of the single spool version is the comparatively large turbine rotor diameter, i.e., turbine inertia which will impair the acceleration capability, without the provision of special and possibly cumbersome devices in the transmission. The penalty can be reduced by selecting a high compressor specific speed thus reducing the rotor diameters. This will require transonic inducers for the compressor rotor when high cycle pressure ratios are used.

The dotted lines in Fig. 20 represent the calculated thermal efficiency for two-spool designs assuming a maximum cycle temperature of 2960° R (1644 K) (the apparent goal of the ceramic rotor development) and a comparatively low initial blade height as it is likely to be desired for ceramic rotors. Comparing these data with the solid lines, the result is that only in cases where the compressor-turbine is designed as a 50 percent reaction stage will the thermal efficiency of the high temperature (ceramic) two-spool design be superior to the single spool unit with uncooled metallic rotors. The difference is comparatively small, about 3 percent for low net powers and up to about 4 percent for high net powers.

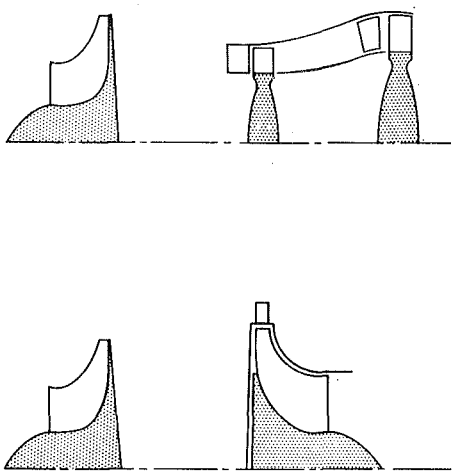

Fig. 19 Flow path comparison

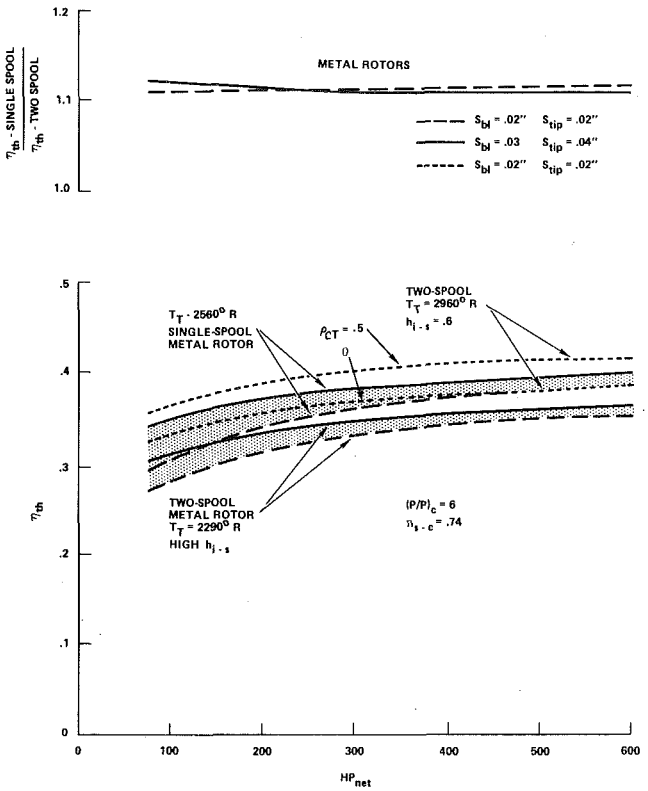

Fig. 20 Cycle performance data for metallic rotors

7 Summary

The predominant trends which emerge from the study is that the efficiency potential of the cycle is dominated by the turbine flow path. A significant criterion for the two-spool design is the throughflow velocity in the initial portion of the turbine flow path. In cases where a high value is selected, i.e., a low initial blade height to favor early introduction of ceramic rotors, the turbine flow path efficiency becomes comparatively low and suffers severely from a large trailing edge thickness for low powered units. The turbine flow path efficiency improves and is less sensitive to a large trailing edge thickness when a high value of the initial blade height is selected. Another influential parameter is the degree of reaction of the turbine stages. When impulse designs are selected for the compressor-turbine to favor high maximum cycle temperatures for uncooled metallic rotors, the turbine rotor diameter and thus the inertia is kept low, the cycle efficiency, however, is impaired. Selection of a 50 percent reaction compressor turbine improves the cycle efficiency but reduces the acceleration capability due to the increased rotor diameter.

Single spool designs with an uncooled metallic rotor show a higher efficiency potential than two-spool designs with uncooled metallic rotors. The rotor inertia, however, is higher than the inertia of an impulse metallic rotor.

Thus it appears that a comparatively high performance penalty will have to be paid to obtain metallic rotor equipped gas turbines with fast acceleration capability.

High temperature ceramic rotors will alleviate the acceleration impairment providing that the ceramic design technology can progress to the point where the rather stringent fabrication requirements can be met.

Due to the Reynolds number, trailing edge thickness and clearance effects, the performance potential decreases with decreasing net outputs. Severe performance penalties are calculated for a large trailing edge thickness in axial turbines and for a large axial clearance in deep scalloped radial inflow turbines.

It is to be emphasized that the presented data are calculated on the basis of commonly used aerodynamic arguments. The assumption is made that the boundary layer is essentially turbulent. The experi-

Downloaded 01 Jun 2010 to 171.66.16.59. Redistribution subject to ASME license or copyright; see http://www.asme.org/terms/Terms_Use.cfm

mental evidence is insufficient to postulate this behavior for the Reynolds number regime encountered in low powered axial turbines. Additionally it has to be acknowledged that some of the aerodynamic criteria, e.g., swirl influence and curvature effects on diffuser efficiency are insufficiently quantified and may cloud the calculations, particularly for multispool axial designs.

The prime emphasis of this study was to determine the effect of some of the significant design criteria on the flow path efficiency. No effort is made to evaluate the influence of the heat exchanger effectiveness on cycle performance.

References

1 Binsley, R., and Balje, O. E., "Axial Turbine Performance Evaluation," ASME JOURNAL OF ENGINEERING FOR POWER, Oct. 1968.

2 Baumeister and Marks, Ed., *Standard Handbook for Mechanical Engineers,* Seventh Edition, Section 14, Compressors, McGraw Hill, New York, 1966.

3 Zweifel, O., "The Spacing of Turbomachine Blading, Especially with Large Angular Deflection," *The Brown Boveri Review,* Dec. 1945.

4 Bullock, R. O., "Analysis of Reynolds Number and Scale Effects on Performance of Turbomachinery," ASME JOURNAL OF ENGINEERING FOR POWER, July 1964.

5 Newstein, J., "Low Reynolds Number Experiments in an Axial Flow Turbomachine," ASME JOURNAL OF ENGINEERING FOR POWER, July 1964.

6 Gersten, K., "The Influence of the Reynolds Number on the Flow Losses in Cascades," (in German), Institute ufer Stroemungsmechanik, Technische Hochschule Braunschwig, 1958.

7 Wolf, H., "Endwall Losses in Straight Cascades," (in German), *Wissenshaftliche Zeitschrift der Technischen Hochschule,* 1961.

8 Cockrell, D. J., and Markland, E., "A Review of Incompressible Diffuser Flow," *Diffuser Design,* Aircraft Engineering, Oct. 1963.

9 Schlichting, H., "Three-Dimensional Boundary Layer Flow," Report No. 62/64, Institute of Aerodynamic, DFL Braunschweig, 1962.

10 Hubert, G., "Problems in Secondary Flows of Axial Turbomachines," (in German), *VDI Forschungsheft,* 496.

11 Traupel, W., *Thermische Turbomaschinen,* Springer Verlag, Berlin, 3rd Ed., 1978.

12 Daily, J. W., and Nece, R. E., "Chamber Dimension Effects on Induced Flow and Frictional Resistance of Enclosed Rotating Discs," ASME *Journal of Basic Engineering,* Vol. 82, No. 1, Mar. 1960.

13 Balje, O. E., "Axial Cascade Technology and Application to Flow Path Design," ASME JOURNAL OF ENGINEERING FOR POWER, Oct. 1968.

14 Binsley, R., and Balje, O. E., "Turbine Performance Prediction: Optimization Using Fluid-Dynamic Criteria," Final Report, Contract No. NONR 4507(00), Rocketdyne Report R-6805, Dec. 1966.

15 Stiefel, W., "Experiences in the Development of Radial Compressors," Lecture Series 50, von Karman Institute for Fluid Dynamics, Belgium, 1972.

16 Wood, H. J., "A Polytropic Technique for Gas Turbine Performance Evaluation," SAE Paper No. 660161, Jan. 1966.

17 Arnold, D., and Balje, O. E., "High Temperature Potential of Uncooled Radial Turbines," ASME JOURNAL OF ENGINEERING FOR POWER, Apr. 1978.

18 Japikse, D., and Pampreen, R., "Annular Diffuser Performance for an Automotive Gas Turbine," ASME Paper No. 78-GT-147.

19 Albring, W., *Applied Fluid Dynamics,* (in German), Fourth Edition, Theodor Steinkopff Verlag, Dresdon, 1970.

20 Scholz, N., *Cascade Aerodynamics,* (in German), G. Braun, Karlsruhe, 1965.

Downloaded 01 Jun 2010 to 171.66.16.59. Redistribution subject to ASME license or copyright; see http://www.asme.org/terms/Terms_Use.cfm

Hydrostatic Power Splitting Transmissions Design and Application Examples

J. Pichard
B. Besson

Societe Le Moteur Moderne,
Boulogne, France

After recalling the inventive methods used in the design analysis procedure of hydrostatic power splitting transmissions, theoretical and experimental application examples are presented. More particulars are detailed: (1) determining elements and tests results of a 230-kw experimental transmission that can be applied to road and off-road propulsion. (2) design analysis procedure and prediction of a large ratio coverage transmission appropriate to light vehicles such as automotive cars. Conclusions are drawn as regards the future prospects of these transmissions.

Introduction

In the field of continuous variable transmission, the hydrostatic power splitting transmissions (H.P.S.T) combined with a mechanical assembly composed of epicyclic and gear trains with a dual-element hydrostatic converter, constitute a family of systems presenting interesting qualities for the application to land vehicle propulsion:

1 possibility of achieving large ratio coverage,

2 high efficiency, higher than variator systems and variator + in line mechanism,

3 reduced overall dimensions of the converter.

The multiplicity of possible designs point out the importance of a theoretical and experimental approach to get the necessary elements for defining and designing these transmissions according to their applications.

The present paper treats:

1 the theoretical methods for a rational determination and characterization of the possible solutions,

2 the achievement and test works of an experimental H.P.S.T. which is representative of this technique,

3 application of this type of transmission to the automotive car.

Power Splitting Transmissions Design Analysis Procedure [1]

Basic Transmission Graphical Model. Basically, a power splitting transmission can be represented by:

1 a rigid mechanical assembly composed of epicyclic and gear trains interconnected in a relatively complex way,

2 utilization shafts (input and output),

3 control shafts.

Methods Used. The analysis mainly concerns the mechanical assembly. The characteristics of utilization and control shafts give the system data and conditions to comply with.

The study of the mechanical system shows that we have to deal with systems of linear equations for speeds and torques. The methods applied are, therefore, the conventional methods of linear algebra using matrical calculations.

The easy application of these methods requires the implementation of an adequate graphic representation of the systems. We come to a certain number of fundamental physical laws connecting the components of the mechanical group to the conditions dictated or desired, relative to utilization and control shafts.

The knowledge of these fundamental laws and the use of the graphic representation allows in a rapid and defined way:

1 the complete analysis of the proper working of known systems,

2 the design of systems satisfying the conditions required for the transmission (input and output conditions) and the definition of working conditions of the control shafts.

Example 1 Power Splitting Transmissions Basic Systems Analysis. The power splitting transmissions basic systems are well known [2]. Table 1 shows for the three systems: (1) coupled output, (2) coupled input, (3) two zero hydraulic power points ("2 ZHPP"):

1 on the left, the technological diagram,

2 at the center, the graphic representation based on the method where the epicyclic trains are represented by 0 and the gear trains by ● (the latter can be reduced in the technological diagram to simple shaft connections),

3 on the right, the characteristic curve of power ratio transmitted by the converter (Wh) versus the transmission ratio (r = output speed/input speed) with conventionally, a positive value when the system works in a nonrecirculative mode and a negative value when it works in a recirculative mode.

The methods allow the direct determination (based on the graphical representation) of the input, output and control shafts speeds and torques relations. For example, the relations for the "2 ZHPP" systems are as follows:

speeds relations	torques relations
$N_1 = a_{1E} \cdot N_E + a_{1S} \cdot N_S$	$C_E = -a_{1E} \cdot C_1 - a_{2E} C_2$
$N_2 = a_{2E} \cdot N_E + a_{2S} N_S$	$C_S = -a_{1S} \cdot C_1 - a_{2S} C_2$

with N = rotation speed, C = torque, a_{ij} = coefficients computed from the mechanism characteristics, subscripts E = input, S = output, 1 = control shaft No. 1, 2 = control shaft No. 2.

Example 2 Characterization of a H.P.S.T. Family. Table 2 shows the characterization of the H.P.S.T. family first systems obtained through the use of above stated methods.

Contributed by the Gas Turbine Division of THE AMERICAN SOCIETY OF MECHANICAL ENGINEERS for presentation at the Gas Turbine Conference and Products Show, New Orleans, La., March 10–13, 1980. Manuscript received at ASME Headquarters December 17, 1979. Paper No. 80-GT-123.

Copyright © 1981 by ASME

Downloaded 01 Jun 2010 to 171.66.16.59. Redistribution subject to ASME license or copyright; see http://www.asme.org/terms/Terms_Use.cfm

Table 1 Characterization of the three H.P.S.T. basic systems (E = input shaft, S = output shaft, 1 and 2 = no control shaft, Wh = hydraulic power, r = transmission ratio = output speed/input speed)

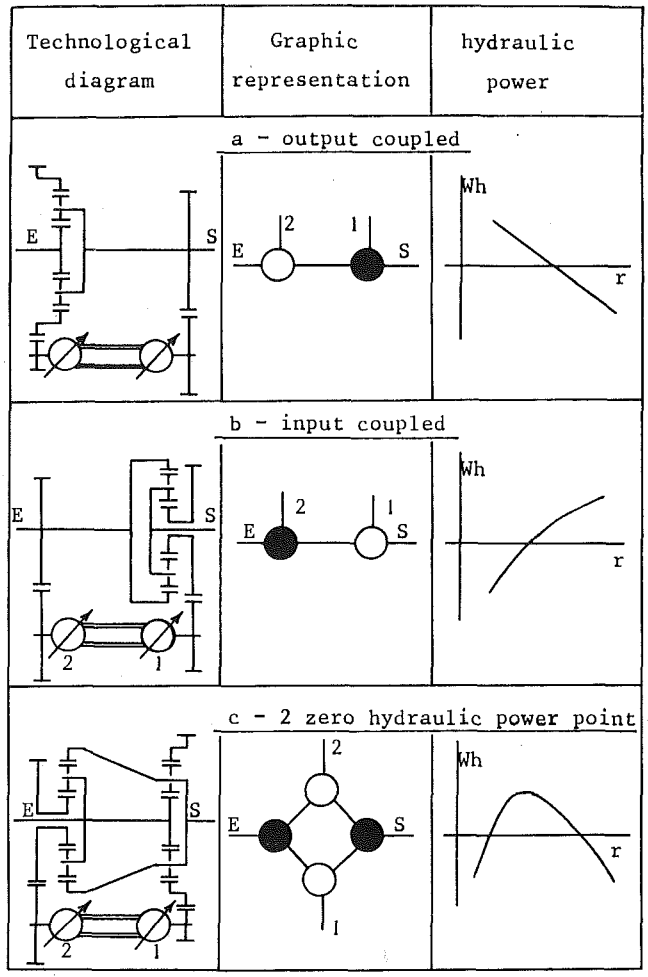

The definition general parameters of this family are:

1 transmissions with one input shaft and one output shaft with independent torques and speeds (continuous variable transmissions),

2 successive hydromechanical modes associated in one common zero hydraulic power point,

3 mode change between control shafts at zero torque,

4 identical maximum derived hydraulic power in each mode,

5 global transmission ratio coverage equal to 5.

Table 2 shows the following elements:

in column 1: the transmission graphic representation,

in column 2: the derived hydraulic power characteristic with the mode change points marked by ⊕,

in columns 3, 4 and 5: the mechanism technological characteristics, with m = number of gear trains (which can be reduced during the design of the technological diagram), p = number of epicyclic trains, CM = number of mode changes,

in column 6: the hydrostatic converter dimensioning power for an imput power equal to 1 (the dimensioning power is the product of maximum torque by maximum speed rate required from the element in order to ensure control of the transmission in the whole range; the value indicated in the table corresponds to the sum of the both elements dimensioning powers),

in column 7: the maximum hydraulic power effectively derived in the hydrostatic converter for an input power equal to 1.

Conclusion. As seen from the examples stated above, the applied method allows the proper characterization of transmission systems. We have studied much more complex systems such as steering transmission systems applied to tracked vehicles with this method.

Table 2 Characteristics of the 12 first systems of the H.P.S.T. family

1 graph	2 Wh	3 m	4 p	5 CM	6 Wapp	7 Wh max
SR		1	1	0	4	.67
RE		1	1	0	4	.67
SE		2	1	1	2.47	.55
R2R		2	2	0	4.92	.28
S2R		3	2	1	3.33	.27
R2E		3	2	1	3.33	.27
S2E		4	2	2	2.44	.25
R3R		4	3	1	2.47	.17
S3R		5	3	2	2.10	.16
R3E		5	3	2	2.10	.16
S3E		6	3	3	1.77	.16
R4R		6	4	2	2.16	.12

Experimental Hydrostatic Power Splitting Transmission [3]

Table 2 shows that the H.P.S.T. constitute a family allowing numerous designs based on the same elementary mode. An experimental study of a transmission representative of this family is therefore undertaken in order

1 to check the feasibility of these systems, in particular to analyze the losses, to evaluate the efficiency in the running field and to study the system behavior in transient conditions,

2 to define the actions needed for development prospects.

Downloaded 01 Jun 2010 to 171.66.16.59. Redistribution subject to ASME license or copyright; see http://www.asme.org/terms/Terms_Use.cfm

Choice of Transmission Type. We have chosen the R3R system (line 8 of Table 2) because it includes functional aspects which are representative of these transmissions (elementary modes, mode change). This system can also prefigure an actual application should the occasion arise.

As we can see, this system includes two modes "2 ZHPP" connected at one point of zero hydraulic power.

The cinematic chain consists of three epicyclic trains connected respectively to the input shaft, the output shaft, and to one of the three control shafts. In each mode, two of the three control shafts are connected to the two hydrostatic elements of the converter. The third control shaft is set free. The mode change is achieved by permuting this last shaft with one of the two shafts connected to the converter.

Required Specifications. The power source selected is a diesel engine fitting road or off-road heavy vehicles with the following performances:

1 maximum power .....230 kW at 2200 rev/mn
2 maximum torque .....1000 Nm from 1000 to 2200 rev/mn
3 speed range .....600 to 2400 rev/mn

Concerning the transmission of approximately 5 ratio coverage (extreme output speeds ratio for the same input speed) at maximum power has been selected for the following reasons:

1 This value is consistent with the R3R system (space occupied, technological organization).

2 Moreover, it can easily be raised and fitted to a vehicle propulsion of a chosen type by associating a third mode.

Characteristics of the Achieved Transmission. Figure 1 represents the technological diagram of the experimental transmission. The general characteristics are the following:

1 transmission ratio (output speed/input speed ratio).
(*a*) minimum full power 0.16
(*b*) 1st zero hydraulic power point 0.18
(*c*) 2nd zero hydraulic power point 0.36
(*d*) 3rd zero hydraulic power point 0.76
(*e*) maximum full power 0.82
2 global ratio coverage, full power 5.1
3 dimensioning power
(*a*) of each hydrostatic element .....290 kW
(*b*) of the converter .....580 kW
4 derived hydraulic power
(*a*) maximum .....0.18 times the input power
(*b*) average .....0.11 times the input power

Mechanism Characteristics. It consists of three epicyclic trains on the same shaft line as the input and output shafts.

The mode changing system is arranged along an axis parallel to the main shaft line. It is composed of a low capacity double clutch ensuring shafts synchronism during mode change, and of two gearwheels insuring a connection with no slip between the control shaft and the hydrostatic element in the normal operational zones.

The servitudes pumps ensuring pressure greasing of the mechanism, the housing draining, the hydrostatic system feeding, and the controls are driven by the input shaft.

Hydrostatic Converter Characteristics. It is composed of two identical hydrostatic elements of variable displacement axial pistons type. Their characteristics are:

1 maximum speed .....4200 rev/mn
2 maximum displacement .....107 cm^3/rev
3 maximum pressure .....40 MPa

The hydraulic circuit is nearly the same as that of a conventional hydrostatic transmission.

Experimental Transmission Design. Figure 2 is a profile view of the transmission. It has been conceived as an experimental tool and not as a prototype, consequently, it offers poor comparity. But it does allow good accessibility to the different components and the easy setting of measuring instruments.

The input shaft is on the left and the output shaft on the right. The servitudes pumps are fixed on the front cover. The hydrostatic elements and the hydraulic circuit are added to the transmission and not integrated as it would be in actual application.

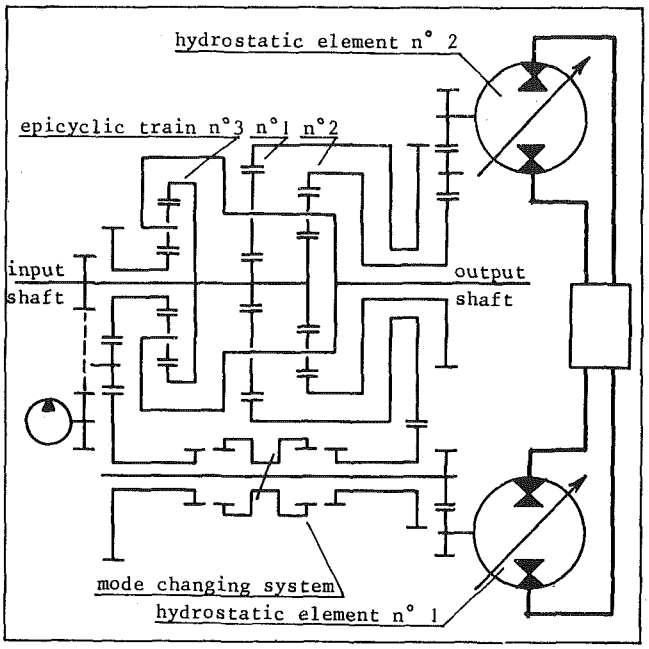

Fig. 1 Experimental transmission technological diagram

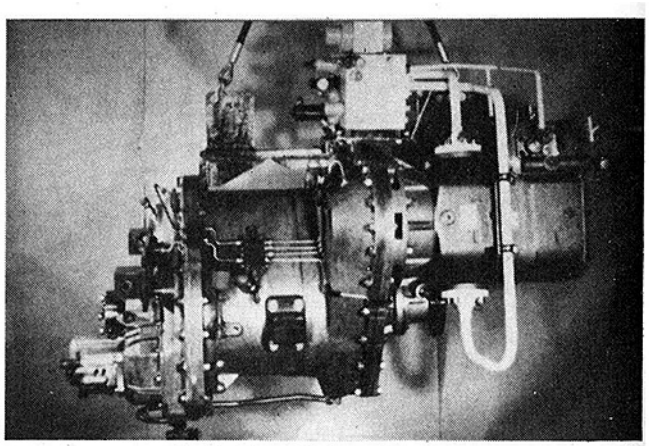

Fig. 2 Transmission profile view

Tests Carried Out. The tests are conducted on a testing stand equipped with a diesel engine. Technical characteristics are nearly the same as those described above with a brake by way of outlet and an inertia flywheel for tests in transient conditions.

The input and output speeds and torques, pressures and temperatures and hydraulic massflows are measured. Some of these measures were done in time for the tests in transient conditions.

Results Obtained. After some improvements, particularly on the epicyclic trains 1 and 2, the transmission has run for about 300 hr at variable ratio, speed load, allowing achievement of our program.

Steady State. The transmission operates properly with excellent stability in every part of the range.

A reduction in output speed with regard to the theoretical value is stated. It corresponds to the adjustments of hydrostatic elements. (See Fig. 3.) This sliding, due to internal leakage increases with load, but does not exceed 8 percent in extreme cases and does not involve instability.

Efficiency. Figure 4 represents the evolution of the global efficiency (all losses included, even servitudes) versus transmission ratio for different values of the input conditions.

Figure 5 represents the evolution of the average global efficiency versus input torque for different input speeds.

Downloaded 01 Jun 2010 to 171.66.16.59. Redistribution subject to ASME license or copyright; see http://www.asme.org/terms/Terms_Use.cfm

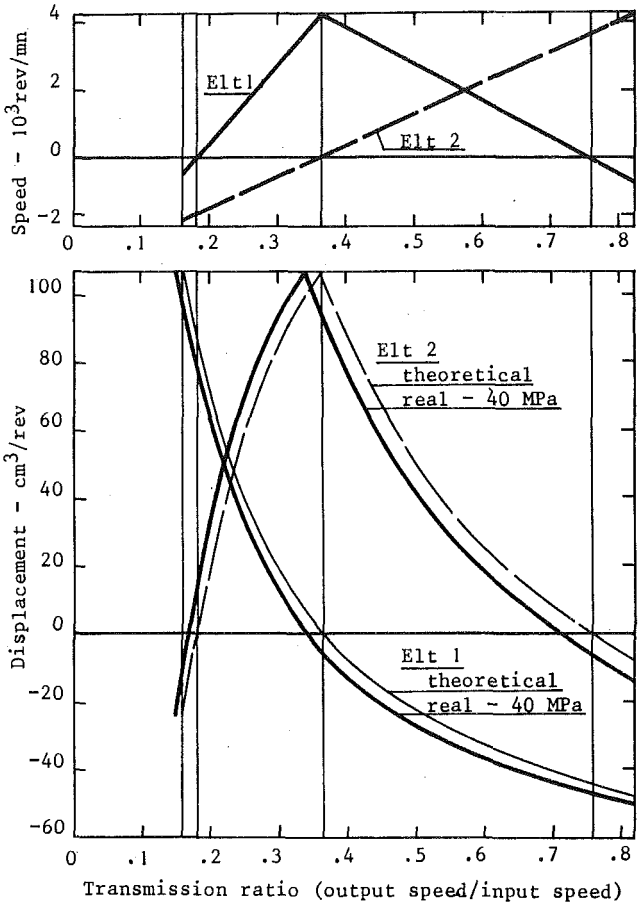

Fig. 3 Real and theoretical laws of hydrostatic elements operation

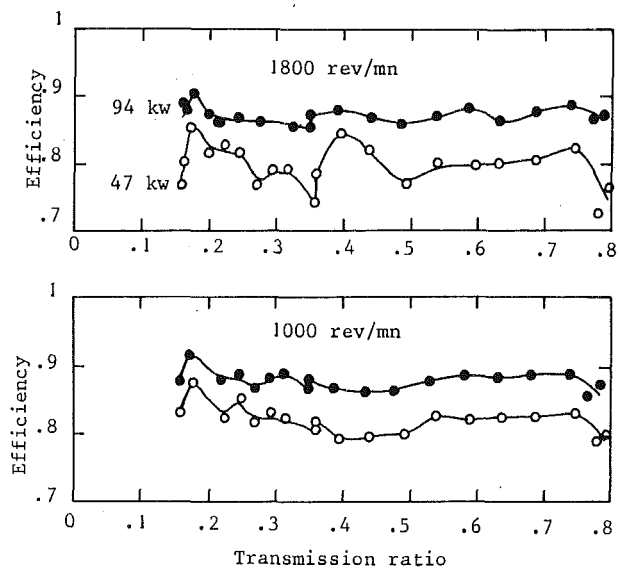

Fig. 4 Global efficiency versus transmission ratio

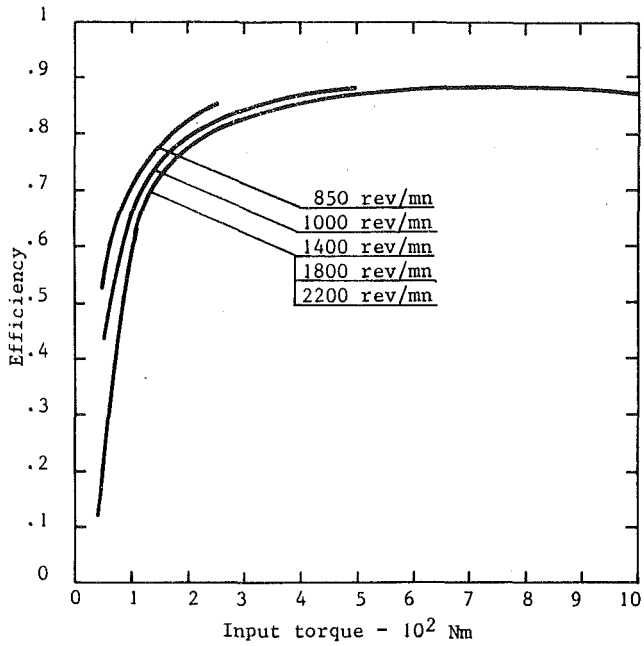

Fig. 5 Average global efficiency versus transmission input conditions

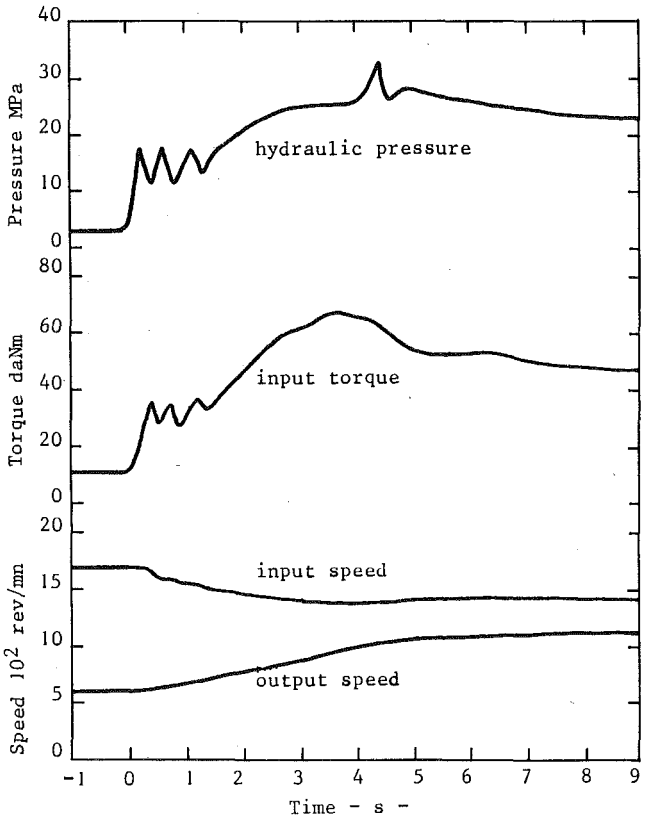

Fig. 6 Transmission ratio increase for speed regulated thermal engine

These results show an average global efficiency between 87 and 88 percent in a power range of 50 to 230 kW (20–100 percent of maximum power). The global efficiency is in fact not very sensitive to transmission variable operation. This is justified by an excellent exploitation of hydrostatic elements by this kind of transmission: reduced derived power at low hydraulic efficiency points and good hydraulic efficiency in high derived power conditions.

Transient Operation. The study was limited by the design of the testing stand, especially since no automatism system has been provided. The test's purpose is to underline specific characteristics of the transmission with regard to its ability to naturally satisfy speed variations.

Numerous transient tests were conducted, particularly the transmission ratio variation while maintaining the engine at constant speed through its regulation. This was the same operation as for a simple shaft gas turbine. Output conditions were dictated by the brake curve. Figure 6 shows a recording of the main operational parameters during such a test.

An interesting result of these tests is that the transmission operates as a simple hydrostatic chain. Maintaining pressure in one of the

Downloaded 01 Jun 2010 to 171.66.16.59. Redistribution subject to ASME license or copyright; see http://www.asme.org/terms/Terms_Use.cfm

circuits insures mass flows compatibility. This characteristic permits simplification of the required automatism.

Works in Progress. A study of transmission matching to a test vehicle is in progress at the present time. Test works under different load condition, i.e., with different power weight ratios are provided on road and off-road.

Design Analysis Procedure and Prediction of a Power Splitting Transmission for Automotive Applications

In view of the results obtained from the conducted test works, we have raised the question of possible applications in the low power field of motor propulsion such as the automotive car.

We know that works have been carried out in this field, even with differently organized systems, and that they can meet both specifications of comfort and fuel economy in the future.

The study presented below is a preliminary to the design of a test vehicle.

To achieve the best transmission-engine matching regarding economy, transmission specifications are

1 a sufficiently large ratio coverage to take advantage of the thermal engine minimum specific consumption curve,

2 a sufficiently high efficiency to keep the former advantage.

Engine adjustments could be modified to take better advantage of the freedom offered by transmission continuity, but this has not been done.

Data System Choice. A Renault R20 TS, which is representative of a high or average range European vehicle, was selected for this study because of the following points:

1 Expected consumption gains are greater on a higher powered vehicle.

2 Cost increases introduced by more complex technology is not as important as on a low range vehicle.

The main characteristics of the reference vehicle are:

1 vehicle weight ..... 1250 kg
2 engine displacement ..... 1995 cm^3
3 maximum power ..... 77 kW at 5500 rev/mn
4 maximum torque ..... 165 Nm at 3000 rev/mn
5 four speed mechanical gearbox

Study Objectives. The design purpose is a H.P.S.T. insuring the following vehicle performance:

1 maximum speed at least equal to 95 percent of the reference vehicle's maximum speed,

2 similar performances,

3 maximum rim tractive effort at least equal to 90 percent of the reference vehicle's.

In addition, the transmission has to provide the following features:

1 overall dimensions satisfying the available space,

2 reasonable technological complexity,

3 significant consumption gains.

Systems Study. To satisfy performance conditions, the full power ratio coverage must be nearly equal to that of the mechanical gearbox (3.5 at 5500 rev/mn). To meet significant consumption gains, the transmission should present a very large ratio coverage at the thermal engine low speeds (7 to 8 at 1500 rev/mn).

The five systems defined in Table 3 are compared from the following points of view: vehicle performance, fuel consumption economy, and technological complexity.

The single-mode system (r2), technologically the simplest, provides too low efficiency to insure reasonable vehicle performance and requires very bulky hydrostatic elements.

The three-mode systems (s3, S3) met poor additional gains compared with the two-mode systems and needs higher technological complexity.

The two-mode "coupled output + 2 ZHPP" system (S2) was more advantageous than the two-mode "2 × 2 ZHPP" system (r3). For similar performances and consumption gains, it was technologically simpler (two epicyclic trains instead of three). It behaved properly in starting and reverse operations because of the coupled output zone.

Table 3 Definition of the systems for automotive applications with: *Wh* = derived hydraulic power - - - - starting —— full power, Wapp = dimensioning power, *p* = number of epicyclic trains, *CM* = number of mode changes

	1 mode	2 modes		3 modes	
	r2	S2	r3	s3	S3
Wh	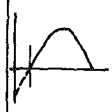	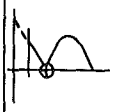		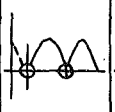	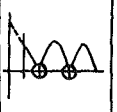
Wapp	254 kw + 88 kw 342 kw	88 kw + 88 kw 176 kw	88 kw + 88 kw 176 kw	88 kw + 88 kw 176 kw	70 kw + 70 kw 140 kw
p	2	2	3	3	3
CM	0	1	1	2	2

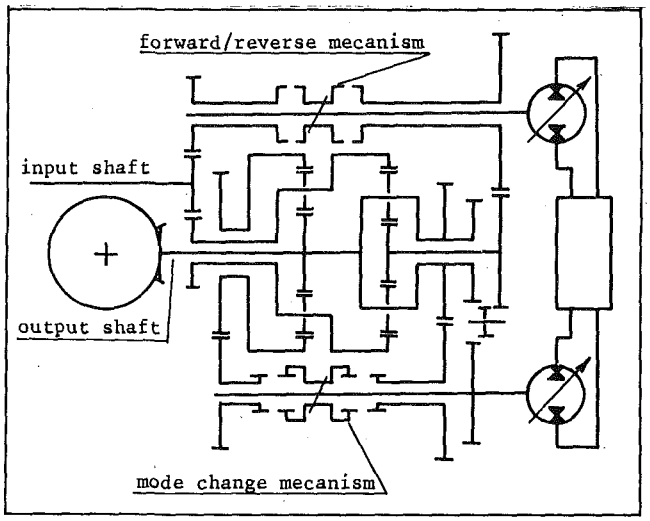

Fig. 7 H.P.S.T. technological graphic line for automotive application

Transmission Choice. Considering the previous analysis, the two-mode S2 system is retained as offering the best compromise. Figure 7 shows the transmission technological graphic line.

This transmission is designed to take the place of the mechanical gearbox. The mechanism is achieved with two epicyclic trains and one mode change. Starting occurs in coupled output mode, and the reverse drive is hydrostatic.

Both axial piston type, hydrostatic elements have the following characteristics:

1 maximum speed ..... 6000 rev/mn
2 maximum displacement ..... 22 cm^3/rev
3 maximum pressure ..... 36 MPa

Figure 8 shows the speed evolution of hydrostatic elements, and the evolution of derived power versus the transmission ratio for the two input conditions 1500 rev/mn − 18 kW and 5500 rev/mn − 77 kW.

We note that the second mode special design limits the maximum transmission ratio in relation to the input speed (engine speed) while respecting the required specifications. This allows the reduction of the converter overall dimensions through a better utilization of hydrostatic elements capacities.

Prediction Study Results.

Performances Prediction. The performance of the vehicle matched either with the four-speed gearbox or the H.P.S.T. are calculated by considering the real efficiencies of the two systems. The results are given in Table 4.

The following points are to be noted:

1 The maximum speed obtained with the H.P.S.T is lower be-

Downloaded 01 Jun 2010 to 171.66.16.59. Redistribution subject to ASME license or copyright; see http://www.asme.org/terms/Terms_Use.cfm

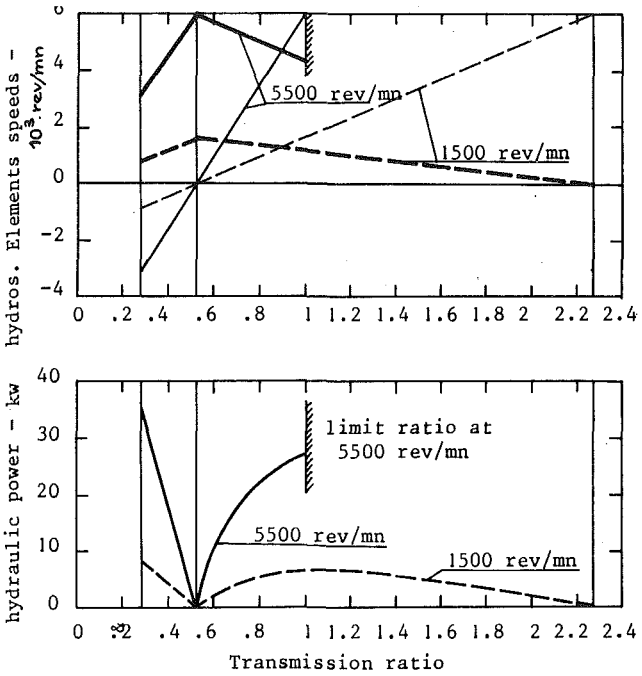

Fig. 8 Hydrostatic elements operation versus transmission ratio

cause of its lower efficiency in relation to the mechanical gearbox.

2 In spite of this lower efficiency, accelerations are similar, efficiency loss being balanced by tractive effort continuity.

Consumption Predictions. Consumption was computed according to the same method for both systems at stabilized speed on flat road, with ECE and EPA cycle. The results are given in Table 5.

A significant gain of 15 to 20 percent is obtained at average speeds and in urban traffic with the H.P.S.T.

Cost Prediction. A first analysis shows that the mechanical assembly has a level of complexity and price equivalent to the present automatic gearbox fitting the vehicle. The cost total increase, primarily due to the introduction of hydrostatic and automatism, represents 4 to 5 percent of the total vehicle price.

Prospects. The above results lead to a positive balance for all the studied points. We would like to undertake, with the agreement and assistance of our partners, an experimental realization allowing an accurate estimation of the industrial applications of these transmissions to motor vehicles.

Conclusion

The power splitting transmissions combining a cinematic chain and a converter, are most likely to give both continuity and high efficiency in a wide field of application.

The hydrostatic converters are those which can, presently, be best integrated with these transmissions, even if industrialized components are not really fitted to this type of operation. Progress can be expected in this field.

These transmissions constitute a nearly infinite generation of possible systems. This offers the advantage of satisfying numerous present or future needs; but it also introduces a difficulty for the definition of the best matched designs to a precise need. Therefore, before having any concrete results, we tried to use an efficient and simple analysis procedure, avoiding the above difficulty.

The definition of the experimental transmission that has been achieved, and the motor vehicle transmission that we have presented, are examples of the possibilities of this method.

From this foundation, we have developed an experimental transmission representative of the most complex systems. The results obtained have shown no impediment to their development at that level of knowledge. It is important to have stated high efficiencies even at low powers and a behavior satisfying the various conditions of a vehicle propulsion almost naturally.

Table 4 Performances predictions with the 4-speed manual gearbox and the H.P.S.T. Computer simulation results

PERFORMANCES		4 SPEEDS MANUEL	H.P.S.T.
Maximal speed (km/h)		169	162
Standing 400 m	(s)	17	17
Standing 1000 m	(s)	30.9	31.1
0 to 100 km/h	(s)	10.2	10
80 to 120 km/h	(s)	7	7.2
Max. tractive effort	(N)	7090	6535

Table 5 Characteristic consumptions of both transmission systems. Computer simulation results

CONSUMPTIONS	4 SPEEDS MANUAL	H.P.S.T	GAINS
Stabilized speed			
30 km/h	8.7 in 2nd gear 6.55 3rd gear	5.8	33% 11%
60 km/h	8.2 3rd gear 6.2 4th gear	4.9	40% 21%
90 km/h	8.2 4th gear	6.45	21%
120 km/h	10.8 4th gear	10.25	5%
ECE cycle	12.3	10.6	14%
EPA cycle	10.2	8.6	16%

For the time being, we have not studied application fields other than those combining alternative engines with these transmissions. More complex power chains may be achieved. Some components can advantageously take part in both mechanical energy production and transformation. For example, in gas turbine applications, we could use power chains combined with compressor and turbine components, the hydrostatic elements and the cinematic chain. Another example could concern the turbocompound engines.

Acknowledgments

We particularly wish to acknowledge the Direction des Recherches Etudes et Techniques (D.R.E.T.) of the Délégation Ministérielle pour l'Armement, which financed the theoretical study of analysis and determination methods, the Direction Technique des Armements Terrestres (D.T.A.T.), which financed the experimental achievement, the Etablissement Technique d'Angers (E.T.A.S.) where the tests were performed, the Société d'Etude et de Développement de Materiels Speciaux (SEDEMS) of RENAULT group which helped us carry out this experimental study, the Institut de Recherche des Transports (IRT) for its financial contribution to the study of automotive application, and the Direction des Affaires Scientifiques et Techniques (D.A.S.T.) of RENAULT group for its collaboration in this study.

References

1 Pichard, J., Besson, B., "Proposition d'un Modele General Representatif des Transmissions de Puissance. Exemples d'Applications," *Ingénieurs de l'Automobile*, No. 4, Apr. 1977, pp. 183–191.

2 Kress, J. H., "Hydrostatic Power Splitting Transmissions for Wheeled Vehicles," SAE preprint, No. 680549.

3 Besson, B., Blanquet, J. M., "Transmission a Derivation de Puissance Hydrastatique. Conception et Essais d'une Maquette Experimentale, Resultats Acquis et Perspectives," *Ingeniéur de l'Automobile*, No. 1, Jan. 1979, pp. 36–42.

Downloaded 01 Jun 2010 to 171.66.16.59. Redistribution subject to ASME license or copyright; see http://www.asme.org/terms/Terms_Use.cfm

Experiments on the Vibration Characteristics of a Rotor With Flexible, Damped Support

Yan Li-Tang
Li Qi-Han

Beijing Aeronautical Institute, Beijing
Peoples Republic of China

Experiments were performed on a model rotor test rig with a disk located at the mide-span and a squeeze film damper and/or flexible support at one end and a rigid support at the other end. The damping effects of the flexible support and stress variation of the support itself have been tested. Emphasis was placed on the steadystate characteristics and the damping effects of the flexible supports and dampers with different radial clearances under various level of rotor unbalance. The dampers are without end seals and oil grooves. Comparative tests of the damping effects of the flexible, damped support were done during passing through the first and second critical speeds. Simulating tests of the vibration of the bearing housing excited by nonrotor exciting sources have been carried out and the damping effects of the oil film dampers on this type of vibrations were examined.

Introduction

Vibration of aircraft engines is still an important problem for today. In order to damp vibration of the engine so as to increase its service life and limit excessive deformation of the rotor caused by rotor unbalance or maneuver flight, squeeze film dampers and/or flexible supports have been used in a number of types of the aircraft engines. Though several methods of theoretical computation for damped supports have been presented, relevant information is not yet sufficient to meet the requirements for designing the optimal supports for damping vibration. Thus, at present, it is still quite important to make some regularities available to design dampers by means of research tests.

This paper deals with research work using experimental methods on the effects of varying support stiffness on deflection of the rotor and transmitted loads and also on stress variations of the flexible support itself, while the flexible support is used on the model rotor.

Emphasis is placed on observing the steady-state vibration characteristics of the rotor with flexible supports and dampers, including effects of different damper clearances and rotor unbalances on the nondimensional amplitude and transmissibility by using experimental methods.

Vibration damping effects for different clearances of squeeze film damper under different rotor unbalance levels are also examined by means of tests in slowly increasing rpm.

In order to understand the damping effect of the type of support on vibrations resulting from some nonrotor sources, simulating tests are performed to examine the vibration damping effects of dampers with different clearances upon this kind of vibration.

Contributed by the Gas Turbine Division of THE AMERICAN SOCIETY OF MECHANICAL ENGINEERS for presentation at the Gas Turbine Conference and Products Show, New Orleans, La., March 10–13, 1980. Manuscript received at ASME Headquarters December 27, 1979. Paper No. 80-G7-124.

Test Equipment

The model rotor test rig with a disk placed at the mid-span and squeeze film damper and/or flexible support at one end and a rigid support at the other end is adopted. The schematic of the test rig and the cross section of the flexible support and the squeeze film damper are shown in Fig. 1 and Fig. 2, respectively.

The test rig's rotor can attain a maximum speed of 16,000 rpm. Operating within this limit, the test can be performed at constant or slowly increasing speeds.

The damper possesses its own oil supply system and the oil pressure can be adjusted within a wide range.

The flexible support is of the squirrel-cage type. By varying the length and number of cage ribs, different values of support stiffness are obtained, and all of them are far lower than that of the rotor at the disk connection.

When the rotor passes the first critical speed, the bending deflection of the rotor itself is quite small as compared with the deformation of the flexible support; thus, the rotor can be considered a "rigid rotor."

The squeeze film dampers are simple ring structures without end seals and oil grooves. Four 2mm dia oil inlet holes are distributed uniformly along the circumference of the ring which has a length of 20 mm and an inner diameter varied in the range of 80.04–80.70 mm. Six rings with different inner diameters combine with the cylindrical face—which is used for a journal—on the right end of the flexible support, forming six clearance diameter ratios ($\Delta D/D$ given in percent).

The varying stiffness of the flexible supports, its corresponding rotor critical speeds, the various clearance/diameter ratios of the dampers, etc. are listed in Table 1 and Table 2, respectively.

Instrumentation

A strain gage is used to measure the shaft stress. It is attached to the surface of the shaft near the disk in the eccentric direction of the rotor. The output signal from the strain gage is carried from the mercury type collector ring to the amplifier and is finally recorded.

Copyright © 1981 by ASME

Downloaded 01 Jun 2010 to 171.66.16.59. Redistribution subject to ASME license or copyright; see http://www.asme.org/terms/Terms_Use.cfm

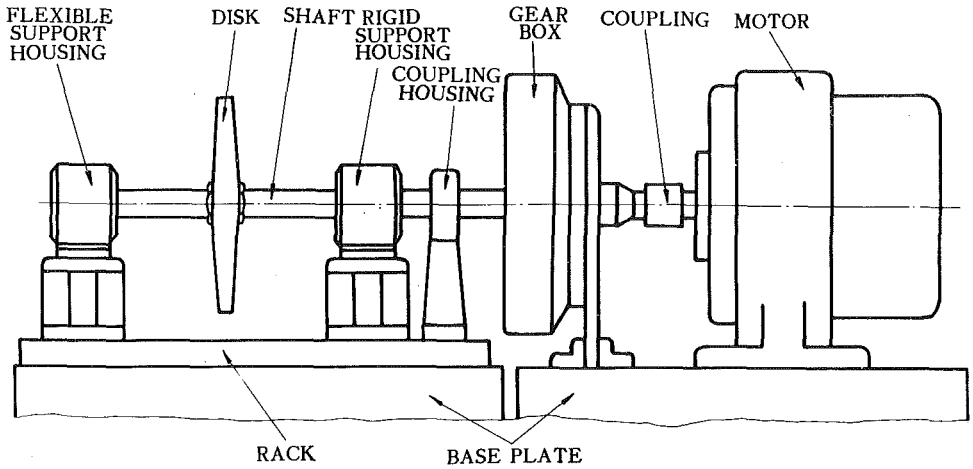

Fig. 1 Schematic of the experimental equipment

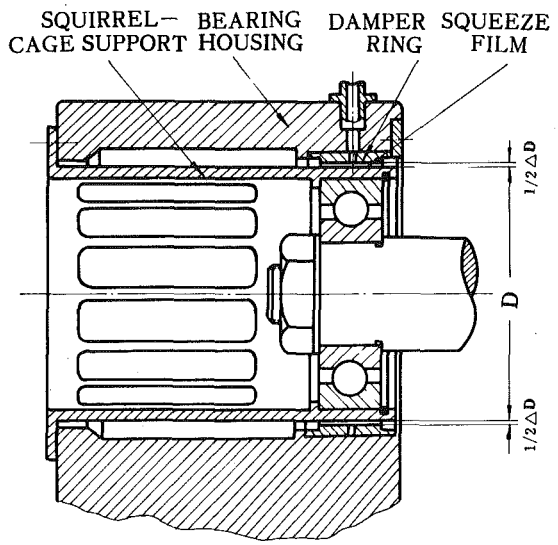

Fig. 2 Cross-sectional view of damper and flexible support assembly

Table 1 Related parameters of the flexible supports

Flexible Support No.	Stiffness Ks kg/cm	Stiffness Ratio Ks/Kr*	First Critical n_{c1} rpm	Second Critical n_{c2} rpm
1	2480	0.62	3900	13,200
2	1824	0.46	3700	12,400
3	1376	0.34	3600	12,000
4	820	0.21	3000	10,800
5	518	0.13	2500	10,600
6	275	0.07	1980	10,200

*Kr = 4,000 kg/cm, rotor stiffness

Table 2 Related parameters of the dampers

Damper Ring No.	Length mm	Inner Diameter D mm	Diametral Clearance ΔD mm	Clearance Ratio $\Delta D/D$ percent
1	20	80.04	0.04	0.05
2	20	80.08	0.08	0.1
3	20	80.16	0.16	0.2
4	20	80.30	0.30	0.375
5	20	80.40	0.40	0.5
6	20	80.70	0.70	0.875

Strain at some point on the shaft surface in the eccentric direction of the rotor will be changed into opposite sign when the rotor passes the critical speeds. Using this phenomenon, the exact value of the critical speeds of the rotor can be identified.

A strain gage is attached to the end of one of the ribs of the squirrel-cage support to measure the vibrating stress of the flexible support.

In order to measure the vibration amplitude of the damper journal, an inductance-type sensor is placed on the end of the shaft near the flexible support.

An accelerometor is mounted perpendicularly or horizontally on the bearing housing to measure vibration acceleration of the bearing housing.

A strain gage is placed at some position on the bearing housing to

Nomenclature

A_r = amplitude of rotor with flexible support at mid span

A_{rh} = amplitude of rotor with flexible support of higher stiffness ratio (K_s/K_r = 1.7) at mid span

a_s = vibrating acceleration of the bearing housing with flexible support

a_{sh} = vibrating acceleration of the bearing housing with flexible support of higher stiffness ratio (K_s/K_r = 1.7)

a_{sd} = vibrating acceleration of the bearing housing with flexible, damped support

a_d = vibrating acceleration of the bearing housing with squeeze film damper

a_{dmin} = minimum vibrating acceleration of the bearing housing with a certain squeeze film damper

C = radial clearance of the damper, $(D - D_i)/2$

D = inner diameter of the oil film ring

D_i = diameter of the damper journal

ΔD = diametral clearance of the damper, $(D - D_i)$

e_{sd} = damper amplitude of the flexible, damped support

e_s = amplitude of the flexible support without damper

f_1, f_2 = natural frequencies of bearing housing system

K_s = stiffness of the flexible support

K_r = stiffness of the rotor at mid span

L = length of the damper

n = rotor speed

n_{c1}, n_{c2} = the first, second critical speed of the rotor-support system

P = oil supply pressure of the damper

T = transmissibility, i.e., the ratio of load transmitted to the housing to the unbalance force acting on the damper journal

u = rotor unbalance distributed to the damper journal

UC = eccentricity of the mass of the rotor

U = eccentricity ratio of the mass of the rotor, (UC/C)

ϵ = nondimensional amplitude, (e/C)

δ = nondimensional rotor speed, (n/n_{c1})

σ_s = stress of the flexible support without damper

σ_{sh} = stress of the flexible support with higher stiffness ratio (K_S/K_r = 1.7)

σ_{sd} = stress of the flexible support with damper

Downloaded 01 Jun 2010 to 171.66.16.59. Redistribution subject to ASME license or copyright; see http://www.asme.org/terms/Terms_Use.cfm

obtain vibrating stress values; then, the transmitted load can be calculated.

All the aforementioned signals from the sensors are amplified and recorded by a recording oscillograph.

A magnetic sensor is used to measure and monitor the speed of the rotor.

Contents of Tests

After some research tests were done, it was seen that the chief factors which had significant effects and could be easily controlled were stiffness of the flexible support and diametral clearance of the damper, when flexible supports and squeeze film dampers were applied to an engine. Other factors, such as oil supply pressure, oil viscosity, length of damper, etc. were not changed in a wide range. Thus, for the tests, the oil supply pressure was taken as $p = 1$ kg/cm^2, the length of the damper ring as $L = 20$ mm, and the rotor unbalances acting on the journal of the damper were taken as 10, 20, and 40 gm.cm, respectively. In order to investigate the superior limit of unbalance of the rotor below which the damper would efficaciously take effect, the tests in which the unbalance acting on the damper journal was up to 140 gm.cm were performed.

According to different assigned conditions, several tests under different conditions of various stiffness of flexible support, damper clearance and rotor unbalance were performed.

1 *Tests of damping effects and stress variations of the flexible support.* Because maximum vibration amplitude and stress occur near the critical speed and strong vibrations for a long time should be avoided, the tests were performed under the condition of slow accelerations which were kept as constant as possible during each test.

2 *Tests for steady-state vibration characteristics of the rotor-support system.* Nondimensional deformation of the damper journal and load transmissibility were checked and computed under the conditions of constant rotor speeds and changing support stiffness, damper clearance and rotor unbalance.

3 *Tests for damping effects of flexible, damped supports during the transition of critical speeds.* The rotor vibrates violently and should be damped during the transition of critical speed. For this purpose, the film damper was most effective. Vibration characteristics of rotor passing through the critical speeds were tested under various combinations of support stiffness, damper clearance and rotor unbalances.

4 *Tests for damping effects of the flexible, damped support during passing through the second critical speed of the rotor.* For the sake of investigating the damping effect of flexible support with a damper during transition from the second critical speed, comparative tests were performed for the damping effects of the damper during transition from the first and second critical speeds.

5 *Tests for superior limit of unbalance below which the damper could take effect to damp rotor vibrations.* In order to determine the superior limit of rotor unbalance below which the damper was valid and the factors effecting the limit, damping tests of the damped support were performed under gradually increasing rotor unbalance until the vibration swiftly increased and the damper was no longer valid.

6 *Tests for damping effects of the flexible, damped support upon bearing housing vibration from nonrotor sources.* Resonant vibration of the bearing housing was excited by electromotive exciter. The damping effects of different dampers upon this type of vibration were tested and measured.

Typical Test Results

The vibration characteristics passing through the first critical speed under slow acceleration of the rotor without squeeze film damper and only with flexible support is shown in Fig. 3. The vibration amplitude of the flexible support (i.e., the deformation at the left end of the rotor) and the vibration acceleration of the bearing housing decreased with the decrease of the flexible support stiffness. On the other hand, stress of flexible support itself increases with the decrease of stiffness. The increase amount is much greater at lower stiffness values. Thus, there

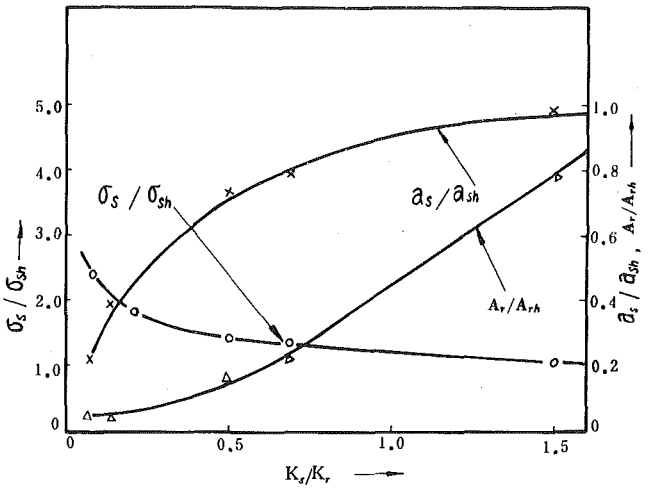

Fig. 3 Vibration characteristics of the rotor with flexible support

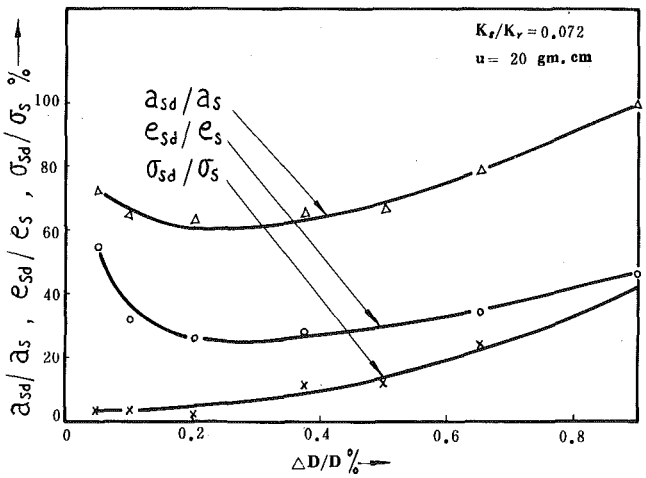

Fig. 4 Vibration characteristics of the rotor with flexible, damped support

is a contradiction between optimal damping characteristics and the lesser support stress. In order to acquire better damping characteristics, structure design, material selection or arts of technology must be determined so as to increase the strength of the flexible support; otherwise, support stiffness cannot be made much lower and in consequence, the optimal damping effect will also not be obtained easily.

Conditions are quite different when flexible support is added in squeeze film damper. This can be seen from Fig. 4, which shows the vibration characteristics of a rotor with low stiffness flexible support and squeeze film damper. Stress of flexible support with a damper is very small during transition from the critical speed; thus, both good damping effects and small support stress can be obtained within a rather wide range of damper clearances (0.2–0.6 percent D). This condition makes the strength problem of the flexible support easy to solve.

The nondimensional deformation (ϵ/U) of the damper versus speed ratio under the steady-state condition is shown in Fig. 5.

Fig. 5(a) indicates that, for a determinate rotor unbalance (20 gm.cm) and several damper clearances within the range in which the damper takes effect to damp vibration, the larger the damper clearance, the greater the nondimensional deformation. Figure 5(b) indicates the variation of nondimensional deformation (ϵ/U) of the damper versus the speed ratio under steady-state conditions when the better clearance is selected. It can be seen that the ϵ/U is large when rotor unbalance is small and it is clear there is a nonlinear relationship between the vibration of the rotor with damper and rotor unbalance here.

Transmissibilities versus different damper clearances for a determinate rotor unbalance (20 gm.cm) are shown in Fig. 6(a). In com-

Downloaded 01 Jun 2010 to 171.66.16.59. Redistribution subject to ASME license or copyright; see http://www.asme.org/terms/Terms_Use.cfm

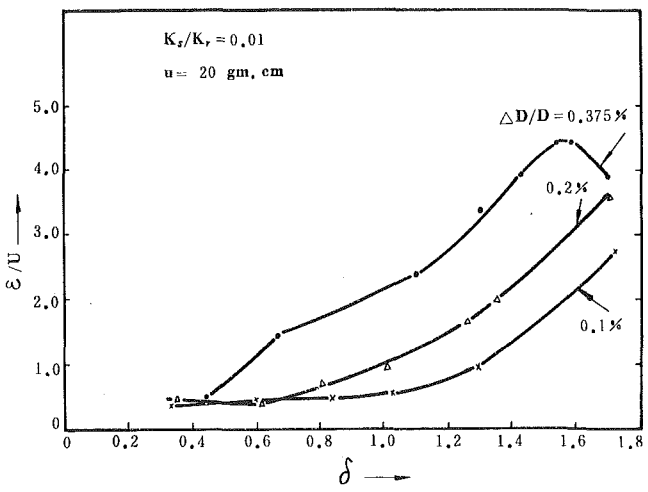

Fig. 5(*a*) ϵ/U for various damper clearances

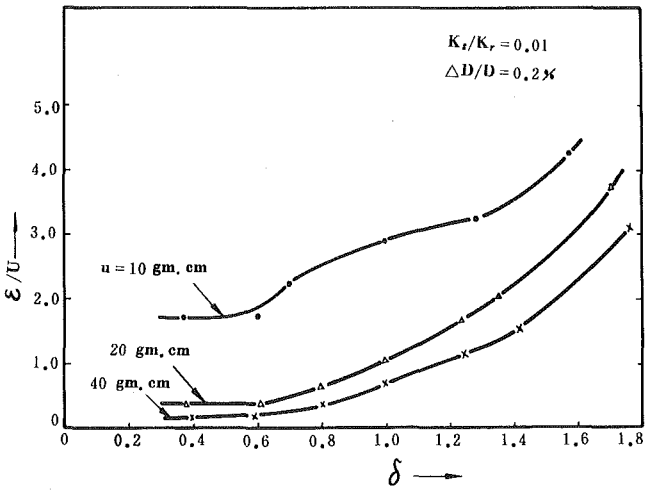

Fig. 5(*b*) ϵ/U for various rotor unbalances

Fig. 5 Steady-state vibration characteristics of the dampers

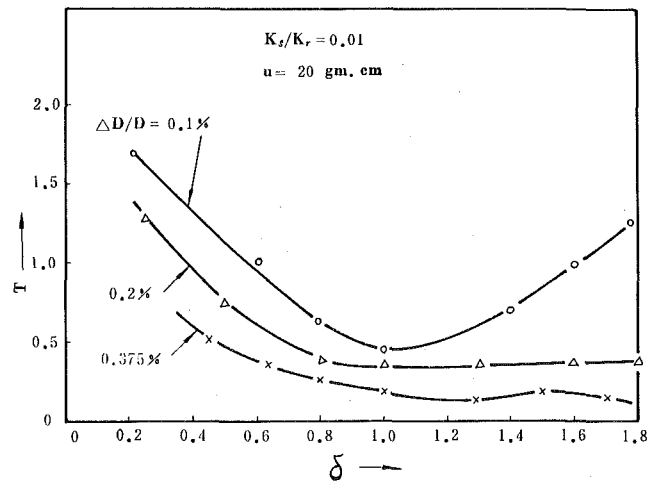

Fig. 6(*a*) *T* for various damper clearances

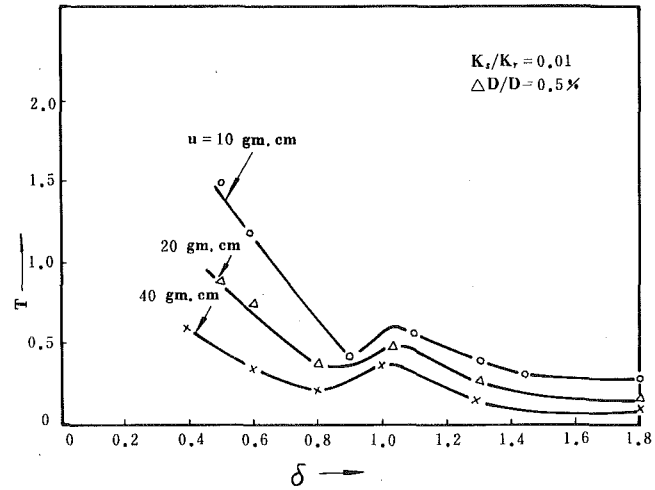

Fig. 6 (*b*) *T* for various rotor unbalances

Fig. 6 Steady-state vibration characteristics of the dampers

parison with the case of flexibly supported rotor without damper, it is known that all of the transmissibilities are reduced on a large scale when the rotor passes through the first critical speed, and the damper clearances are taken as $\Delta D = 0.1$–0.375 percent D. Within the range of clearance where the damper gives better damping effects, the transmissibility is large for small clearance.

Transmissibilities for determinate damper clearance and different rotor unbalances are shown in Fig. 6(b). It indicates that the transmissibility is larger while rotor unbalance become smaller.

In order to show the damping effects of the damper more visually, an alternative type of variations of nondimensional vibration parameters σ_{sd}/σ_s versus speed ratios is presented in Fig. 7 as an example. For the sake of comparison, the curve of the variations of stress σ_s for a flexible support without damper is also shown in the same figure. All dampers with different clearances in the figure can damp vibration. In the vicinity of the first cirtical speed, the damping effects behave extraordinarily well and stress can be reduced to less than 10 percent. Damping effects also exist at other speeds, but they are not as good as those in the vicinity of the first critical speed. Thus, a squeeze film damper is specially effective for damping vibrations near the nonbending critical speed of the rotor. The reason for the upward bend of the curve after a speed ratio of about $n/n_{c1} = 2.8$ is that the rotor is approaching its second critical speed.

Curves for variations of nondimensional amplitudes e_{sd}/e_s of the damper journal, and nondimensional vibration accelerations a_{sd}/a_s of the bearing housing versus the rotor speed ratios are similar to that in Fig. 7, but are greater in value. This means the effects of damper on the damping of the damper deformation and transmitted vibration are rather inferior to that on the reduction of support stresses.

In case of different support stiffness ratios, three nondimensional parameters versus different damper clearances while the rotor passes through the first critical speed are shown in Fig. 8(a) and Fig. 8(b).

The stress ratio diminishes with the decrease of $\Delta D/D$, but the ratio of damper deformations and the ratio of transmitted vibrations each have their own minimum values, and in their vicinity ($\Delta D/D$ is about 0.1–0.4 percent, and the range is still wider for low flexible support stiffness) the curves are rather flat.

Ratios of deformations and ratios of transmitted vibrations increase while clearance is too large or too small, but it is more violent for the latter case.

Especially for the transmitted vibration, sometimes the condition is even worse than without a damper if the selected damper clearance is too small. The optimum damper clearance is about 0.2 percent D.

Damping effects of the squeeze film damper while rotor passes through the second critical speed (i.e., the bending critical speed of the rotor) is shown in Fig. 9.

During transition from the bending critical speed, the damper gives the same good effects to reduce stress of the flexible support as that mentioned above, but the damping effects on rotor deformations and transmitted vibrations are rather inferior. The reason is that, under this condition, besides the deformation of the flexible support, the

Downloaded 01 Jun 2010 to 171.66.16.59. Redistribution subject to ASME license or copyright; see http://www.asme.org/terms/Terms_Use.cfm

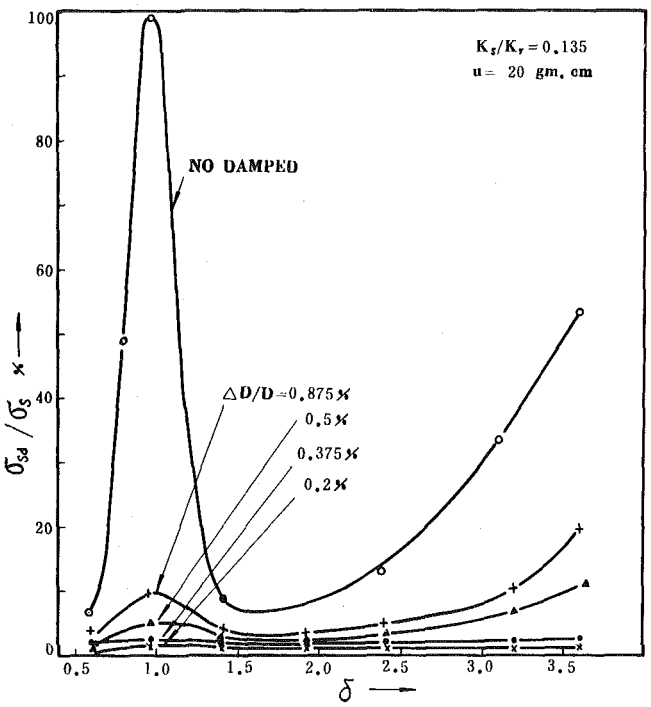

Fig. 7 Nondimensional vibration stress of the flexible, damped support

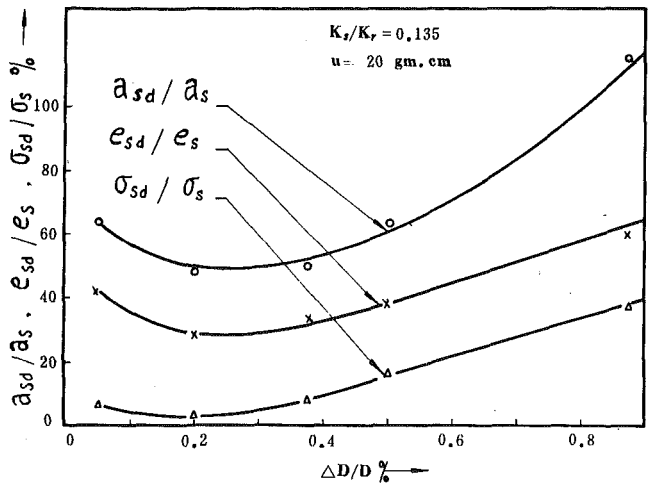

Fig. 8(*a*) Nondimensional vibration characteristics of the flexible, damped supports for *Ks/Kr* = 0.135

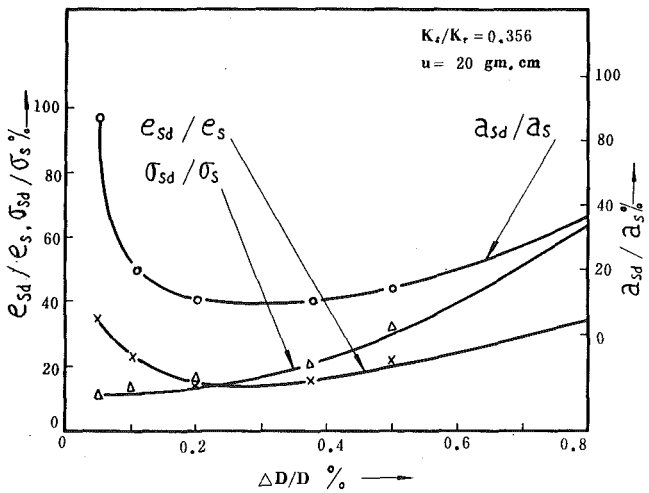

Fig. 8(*b*) Nondimensional vibration characteristics of the flexible, damped supports for *Ks/Kr* = 0.356

deflection of the shaft is also rather large; thus, obviously, the damping effect of the damper attached to the support on the bending vibration of the shaft will be inferior.

Test results for the investigations of damping effects of the damper without flexible support under large rotor unbalance are shown in Fig. 10. It can be seen that vibration is not increased very much while rotor unbalance increases; but when rotor unbalance increases to a certain value, the damping effect of the damper will be worse and, in consequence, the vibration will be greatly increased. A determinate damper only gives its good damping effect within a determinate range of rotor unbalance. If this limited range is exceeded, the vibration will swiftly increase. Within the range of damper clearances under which the damper can take effect, the larger the clearance, the greater the corresponding superior limit of rotor unbalance. Thus, in the course of designing, the selection of damper clearance must be considered also in accordance with the value of unbalance the rotor will reach. It is notable that the corresponding superior limit of rotor unbalance will increase when the damper is used in combination with flexible support.

Simulated test results to make out the damping effect of the damper attached to the support upon the bearing housing vibrations excited by nonrotor vibrating sources are shown in Fig. 11. The ordinate indicates the ratio of vibration acceleration under resonant condition of the bearing housing system with a damper or without one. It can be seen that the damper on the support has the same good damping effect on the vibrations excited by nonrotor vibrating sources. The

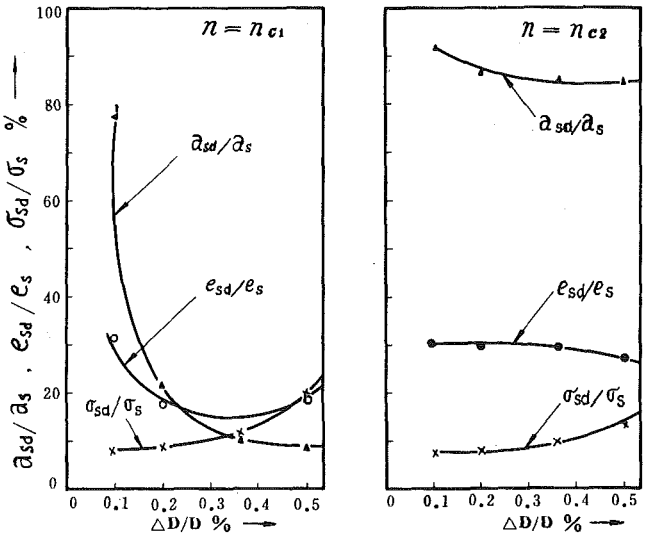

Fig. 9 Comparison of vibration characteristics passing through 1st and 2nd critical speeds

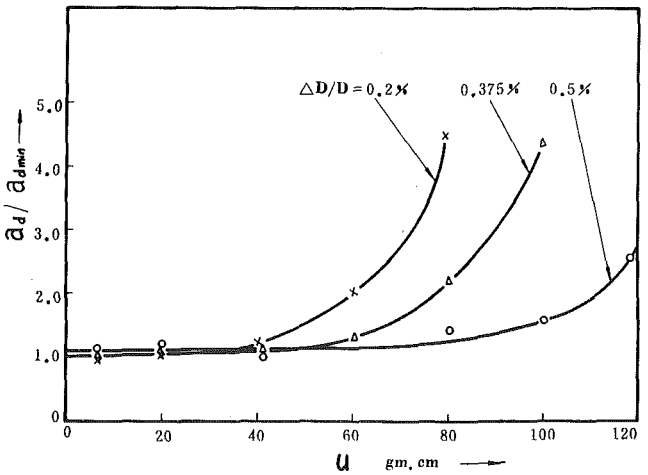

Fig. 10 Vibration of bearing housing of the rotor with squeeze film damper versus rotor unbalance

Downloaded 01 Jun 2010 to 171.66.16.59. Redistribution subject to ASME license or copyright; see http://www.asme.org/terms/Terms_Use.cfm

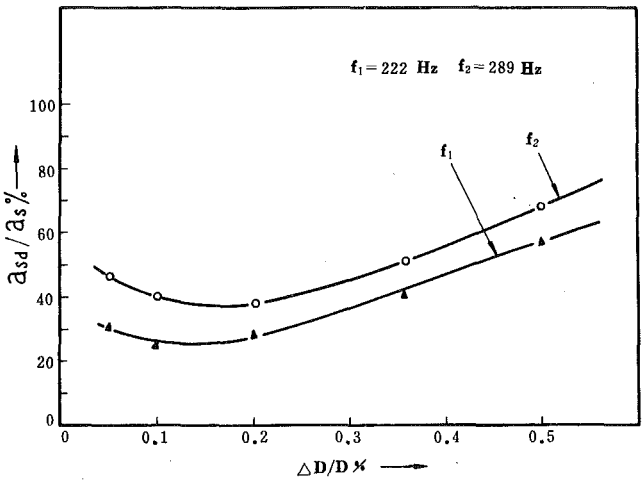

Fig. 11 Nondimensional vibration of bearing housing excited by electromotive exciter

shape of the curves for vibration characteristics are similar to that of the bearing housing vibration excited by the rotor itself, and they also possess the corresponding minimum values. The optimum damper clearances are about 0.1–0.2 percent D, which is quite near the optimum clearance of about 0.2 percent D for damping the vibration excited by the rotor. Thus, the squeeze film damper attached to the support can be used not only for damping the vibration excited by rotor unbalance to make the rotor pass through its critical speed smoothly, but also for damping the housing vibration excited by other vibrating sources. For either kind of application, the selection of the main parameters of the damper made in the same way.

Conclusion

When flexible support is adopted solely for lowering the critical speed of rotor and damping the rotor vibration, the support stiffness should not be too low because it is limited by the strength of the flexible support itself; therefore, the damping effect is not prominently featured. If a squeeze film damper is adoped additionally, then, not only the rotor vibration can be further damped, but also the stress of flexible support itself can be reduced considerably.

Flexible, damped support possesses proper damping effects under various rotor speeds and its damping effect is exceptionally prominent for transition from the first critical speed (nonbending critical speed). Under the definite rotor-support and working conditions there exists an optimum damper clearance. The optimum diametral clearance obtained from tests stated in this paper is about 0.2 percent D. The range of useful damper clearance is wider for lower support stiffness. Definite damper clearance corresponds to definite superior limit of rotor unbalance. If the superior limit of unbalance is exceeded, the damping effect will be very inferior.

Flexible, damped support also has some damping effects on the bending critical speed of rotor, but it is worse than its damping effect upon the first critical speed.

This type of damper also possesses good damping effect upon the housing vibrations excited by nonrotor vibrating sources. If parameters of flexible, damped support are selected properly so that the vibration excited by rotor unbalance is damped, then, generally, the bearing housing vibrations excited by nonrotor vibrating sources will be damped also.

Acknowledgment

The authors wish to thank the Engine Structure-Strength section of the Bejing Institute of Aeronautics and Astronautics for their help in preparing this paper.

References

1 Cooper, S., "Preliminary Investigation of Oil Film for the Control of Vibration," Institution of Mechanical Engineers (England), Lubrication and Wear Convention, Paper 28, 1963.

2 White, D. C., "The Dynamics of a Rigid Rotor Supported on Squeeze Film Bearings," Conference on Vibrations in Rotating Systems, London, *Proceedings, Institution of Mechanical Engineers,* Feb. 14–15, 1972, pp. 213–229.

3 Barrett, L. E., and Gunter, E. J., "Steady-State and Transient Analysis of a Squeeze Film Damper Bearing for Rotor Stability," NASA CR-2548, May 1975.

4 Sharma, R. K., and Botman, M., "An Experimental Study of the Steady-State Response of Oil Film Dampers," ASME *Journal of Mechanical Design, Trans.* Vol. 100, Apr 1978, pp. 216–221.

5 Kirk, R. G., and Gunter, E. J., "The Effect of Support Flexibility and Damping on the Synchronous Response of a Single Mass Rotor," ASME, *Journal of Engineering for Industry, Trans.* Feb. 1972.

Downloaded 01 Jun 2010 to 171.66.16.59. Redistribution subject to ASME license or copyright; see http://www.asme.org/terms/Terms_Use.cfm

D. A. Wilson
Senior Materials Engineer,
Pratt & Whitney Aircraft Group,
Government Products Division,
West Palm Beach, Fla.
Mem. ASME

D. W. Hoeppner
Cockburn Professor,
University of Toronto,
Toronto, Canada
Mem. ASME

A Statistical Investigation of Microstructure and Crack Growth in Titanium Alloys

Crack growth rates in various microstructures of Ti-6Al-4V and commercially pure titanium were studied using modified wedge opening load (WOL) specimens. Data were modeled using a Weibull four parameter survivorship function, selected because it meets the physical boundary conditions. The resulting models were exercised to determine the statistical significance of microstructure on the fatigue crack growth properties of these materials. Finally, inferences concerning gas turbine engine component design are considered.

Introduction

In recent years it has become obvious that the empirical approach to fatigue design is not always adequate to prevent structural failure. As mission and performance demands of modern aircraft gas turbines increase, the engineering community must improve structural design to prevent failure.

One area needing much greater emphasis is the relationship between microstructure and material application to fatigue crack growth design.

There are many examples of mismatched microstructure and application, not only in the aircraft industry, but also in the bridge industry, nuclear industry and others. Clearly, the material employed may appear to be superior to all other candidate alloys in classical and traditional materials evaluation procedures, such as tensile and yield strength, but the microstructure is inappropriate. This is because standard practices for microstructural characterization, evaluation, and application, as they relate to structure and loading, do not exist. In addition, procedures to relate material behavior to design parameters have not been fully developed.

Some information on the influence of microstructure on fatigue behavior is available in the literature, but there are differences in the conclusions presented. These conclusions range from no significant correlation, to a strong correlation between microstructure and fatigue crack growth properties.

This study was accomplished by developing several microstructures of the alloys selected. Each microstructure is tested by the fracture mechanics fatigue method of crack growth versus number of cycles (a-N). The data were then reduced to crack growth rate versus stress intensity range ($\Delta/a/\Delta N - \Delta K$). These results were then statistically compared to determine the significance of any microstructural effect.

Microstructural effects have generally been considered to be one of the least important of the variables involved in fatigue crack growth [1–3]. Attempts to investigate the influence of microstructural parameters on fatigue lives have usually concluded that any improvements in fatigue occur through an improvement in initiation behavior, rather than in increased resistance to fatigue crack growth [4, 5].

In fatigue, which is basically a manifestation of plasticity at the microscopic level, it is possible that microstructural parameters do significantly influence fatigue life including the propagation of cracks, as well as their initiation. These microstructural parameters will undoubtedly prove important as more concern develops for safe-life structural components as well as for crack propagation at low levels of stress intensity.

Many research programs have been performed to study the fatigue mechanism in titanium and titanium alloys. However, some conflicts exist when comparing results from different programs. Some results that may seem to conflict can be better understood by separate consideration of total fatigue life (S-N), fracture toughness, time for crack nucleation, crack growth rates, and fractographic analysis.

Robinson [6] performed fatigue crack propagation tests on commercially pure alpha-titanium alloys, and two distinct modes of crack growth were identified. At low-growth rates the crack path was highly dependent on the orientation of the grain the crack was traversing. Robinson suggested that the extent of crack path dependence on grain orientation was greatest when crack tip plasticity was less than the grain size. This would indicate that the major influence of microstructure on fatigue-crack growth would be most pronounced at low ΔK or near threshold area.

Irving [7] concluded that microstructural changes in Ti-6Aℓ-4V can produce changes in fatigue crack growth rate of up to a factor of three. The crack growth differences occur at low values of ΔK. The transition from microstructure sensitive to microstructure insensitive crack growth can again be correlated with the plastic zone size becoming equal to or exceeding the alpha grain size. However, further studies appear necessary in this important area.

Yoder [8] investigated microstructure sensitive fatigue-crack growth in Ti-6Aℓ-4V, and observed that fatigue-crack growth rates for mill annealed, alpha plus beta rolled Ti-6Aℓ-4V can be reduced by as much as an order of magnitude with a beta anneal. This occurs to the point at which the plastic zone attains the average Widmanstätten packets. The multiple cracks are not along alpha plus beta interfaces primarily, but rather, closer to normal to the axes of the alpha platelets.

Amateau [9] showed a significant dependence of fatigue-crack growth rates on the microstructure of Ti-6Aℓ-6V-2Sn. Mill annealed

Contributed by the Gas Turbine Division of THE AMERICAN SOCIETY OF MECHANICAL ENGINEERS and presented at the Gas Turbine Conference and Products Show, New Orleans, La., March 10–13, 1980. Manuscript received at ASME Headquarters December 27, 1979. Paper No. 80-GT-125.

Copyright © 1981 by ASME
Downloaded 01 Jun 2010 to 171.66.16.59. Redistribution subject to ASME license or copyright; see http://www.asme.org/terms/Terms_Use.cfm

material containing equiaxed primary alpha had the lowest crack propagation resistance of the microstructures tested. The acicular alpha (Widmanstätten) structure resulting from beta annealing showed the highest fatigue crack growth resistance by a factor of four. The solution treated and aged microstructure also displayed high fatigue crack growth resistance due to crack branching and deviation around primary alpha particles.

Hall [10] found that extension of a crack in Ti-6Al-2Sn-4Zr-6Mo involves propagation along the aged alpha-beta interfaces. When the alpha particles are irregular in shape and somewhat elongated, a crack propagating in any plane not parallel to the axial face will find the path offered to be more tortuous than that of the equiaxed alpha microstructure. The net result is the absorption of less energy in the fracture toughness testing of the latter microstructure.

Therefore, Hall concluded that the optimum microstructure for Ti-6Al-2Sn-4Zr-6Mo was a combination of both acceptable fracture toughness and tensile ductility. This microstructure contained about ten volume percent equiaxed alpha, along with a relatively coarse acicular alpha and aged beta.

Very few fractographic studies have been made on fatigue crack growth in titanium alloys with respect to microstructure, but the few that exist report some very interesting results.

Irving [7] observed that fracture surfaces revealed great differences between microstructure sensitive and microstructure insensitive fracture paths in Ti-6Al-4V. The microstructure sensitive fracture paths were characterized by a very irregular, angular appearance, and by the presence of facets with alpha grains. Microstructure insensitive growth regions were similar in all microstructures, being relatively smooth and rather amorphous in appearance.

Greenfield [11] also studied the fracture surfaces with a scanning electron microscope. The fracture surfaces show that a greater number of crack path deviations occurred in the acicular microstructure leading to a lower da/dN for beta-processed material, compared to alpha plus beta processed material.

Hoeppner [12], making a fractographic analysis of fatigue crack growth in IMI 685, an alpha-beta structured titanium alloy, found a complex relationship between environment, loading mode and microstructure. These relationships must be considered when assessing the role of microstructure in fatigue behavior.

From Griffith's [13] work and other literature, it now appears possible to state in energy terms the physical process of fatigue crack growth. It is possible to cross an energy threshold that will produce fatigue crack propagation. After this energy threshold is crossed, the crack propagates under continued loading. Clearly, the rate of crack extension is related to the resistance it encounters from the surrounding material. This resistance can be presented as surface energy requirements for crack extension, plastic work terms, heat dissipation and other factors. Since microstructure affects surface energy requirements and plastic work terms, microstructure becomes one of the principal factors that determines the energy requirement for crack extension [14].

Experimental Details

Experimental Plan. It has been established that microstructure does have an effect on the fatigue crack growth properties of titanium. However, in the literature reviewed, no experiments were planned to show this effect statistically and provide evidence that the variation of fatigue crack growth properties with microstructure is statistically significant. Instead, conclusions have usually been stated in generalities. Therefore, the experiments reported here have been formulated so that the results can be statistically analyzed to evaluate them using tests of significance.

The materials tested in this work were Ti-6Al-4V and commercially pure titanium. The Ti-6Al-4V was supplied from three different heats by Ladish Co., Cudahy, Wisc. Therefore, it was decided to treat all three heats as different alloys. This was done to prevent any bias due to variations in composition. Also, it allows one to determine if small variations in composition can have a statistically significant effect on fatigue of this titanium alloy. For these reasons it was decided to test four alloys—three variations in Ti-6Al-4V and one of commercially pure titanium. The composition of each will be presented later.

Many different microstructures can be developed from these materials by changing the quench rate, the time and temperature of the heat treatment or the working cycle, or combinations of these factors. After carefully studying the various microstructures developed, three were selected for study. These particular microstructures were selected because it was believed that they would yield the widest variation in results. The process used for each heat treatment is presented later.

From the above discussion, a 4 by 3 factorial crack growth test matrix was developed. The next step was to determine the number of replications needed for each block. In any randomized block experiment at least two replications are necessary for an estimate of the experimental error variance. Kempthorne [15] has developed an estimation for the number of replications needed for various percentage chances of discovering an effect of a specified size (Δ). From this estimation, it was found that five replications for each block of the matrix would be needed.

A complete factorial experiment of this size would be beyond the reach of this experimental effort due to the limited amount of material available, the cost of machining the needed specimens, the time required to test all the specimens, and the availability of a test machine to do the testing. So it was decided to do a fractional factorial replication [16] of this test matrix. Only a small amount of information on interaction effects is sacrificed to reduce the size of the experiment.

From the fractional factorial replication method a final test matrix was formulated as shown:

	Alloy			
	Al	*A2*	*A3*	*A4*
Microstructure M1	5	2	2	2
Microstructure M2	2	5	2	2
Microstructure M3	2	2	5	2

The testing order of the entire test matrix was then randomized to prevent any bias from changes in the test machine, change in operators or other factors that could introduce random error.

All other variables, such as the test machine used, the stress ratio, wave form and environment, were held constant. A chamber for an inert argon environment was built to maintain a constant environment.

By following this procedure of statistically planning the experiment, the maximum amount of information may be obtained with minimum specimens and minimum bias.

Materials and Heat Treatment. The heat compositions of the titanium alloys appear in Table 1.

The three microstructures that were selected were obtained by vacuum heat treating in the following manner:[1]

1 Heated to 1065°C (1950°F) for 4 hr, water quenched and tempered at 540°C (1000°F) for 4 hr, argon cooled. (Will be referred to subsequently as M1.)
2 Heated to 955°C (1750°F) for 4 hr, argon cooled and tempered at 540°C (1000°F) for 4 hr, argon cooled. (Will be referred to subsequently as M2.)
3 Heated to 845°C (1550°F) for 4 hr, furnace cooled and tempered at 540°C (1000°F) for 4 hr, argon cooled. (Will be referred to subsequently as M3.)

All specimens were vacuum heat treated and cooled by argon rather than air. This was done to prevent formation of the alpha case (titanium oxide) on the surface. The alpha case is brittle and could introduce long deviations in the fatigue crack growth results.

Photomicrographs of typical microstructures obtained by heat treating the Ti-6Al-4V and the commercially pure titanium are shown in Figs. 1 and 2.

[1] The heat treatment was performed by Lockheed Calif. Co., Physical Metallurgy Group. Mr. Sid Bocarsly of Lockheed coordinated the heat treatment for this effort.

Downloaded 01 Jun 2010 to 171.66.16.59. Redistribution subject to ASME license or copyright; see http://www.asme.org/terms/Terms_Use.cfm

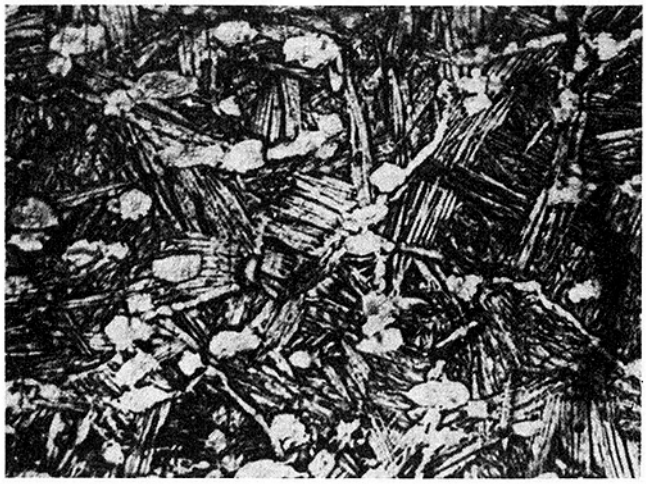

Center 500x

Fig. 1 M2A2 microstructure

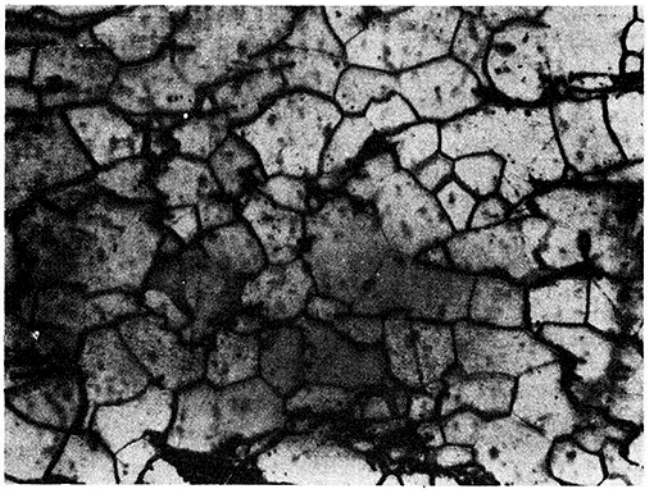

200x

Fig. 2 M3A4 microstructure

Table 1 Chemical composition (weight percent)

Element	*Alloy A1 Ti-6Al-4V Heat Number N3776Z*	*Alloy A2 Ti-6Al-4V Heat Number N0950Z*	*Alloy A3 Ti-6Al-4V Heat Number N2791Z*	*Alloy A4 Commercially Pure Heat Number D4236D*
Carbon	0.01	0.02	0.01	0.037
Nitrogen	0.014	0.010	0.02	0.013
Oxygen	0.018	0.19	0.17	0.413
Aluminum	6.65	6.65	6.60	—
Iron	0.22	0.20	0.25	0.18
Hydrogen	0.0066	0.0063	0.0015	0.0026
Vanadium	4.10	4.08	4.23	—
Titanium	Remainder	Remainder	Remainder	Remainder

Table 2 Metallographic values for the α phase of each microstructure

	V_v^{α}	$S_V^{\alpha\beta}$	$\bar{\lambda}^{\alpha}$
M3A3	0.620	1.85 mm²/mm³	1.34 mm
M2A2	0.616	1.74 mm²/mm³	1.42 mm
M1A1	0.612	2.00 mm²/mm³	1.22 mm

Table 3 Metallographic values for the equiaxed α phase of each microstructure

	V_v^{α}	$S_V^{\alpha\beta}$	$\bar{\lambda}^{\alpha}$
M3A3	0.244	0.277 mm²/mm³	3.52 mm
M2A2	0.240	0.291 mm²/mm³	3.30 mm
M1A1	0.204	0.206 mm²/mm³	3.96 mm

Table 4 Tensile data for three microstructures of Ti-6Aℓ-4V

	M1	*M2*	*M3*
Ultimate Strength	1019.1 MPa (147.8 ksi)	999.1 MPa (144.9 ksi)	1034.9 MPa (150.1 ksi)
Standard Deviation	5.3 MPa (0.77 ksi)	7.5 MPa (1.09 ksi)	15.2 MPa (2.21 ksi)
Yield Strength	940.5 MPa (136.4 ksi)	935.7 MPa (135.7 ksi)	971.5 MPa (140.9 ksi)
Standard Deviation	18.3 MPa (2.65 ksi)	22.2 MPa (3.22 ksi)	11.7 MPa (1.70 ksi)
Modulus of Elasticity	12.9×10^{11} dyne/cm² (18.75×10^{6} lb/in.²)	13.1×10^{11} dyne/cm² (18.99×10^{6} lb/in.²)	13.1×10^{11} dyne/cm² (19.00×10^{6} lb/in.²)
Standard Deviation	0.33×10^{11} dyne/cm² (0.48×10^{6} lb/in.²)	0.19×10^{11} dyne/cm² (0.28×10^{6} lb/in.²)	0.37×10^{11} dyne/cm² (0.54×10^{6} lb/in.²)

Since the Widmanstätten microstructures are extremely complex and thus difficult to compare, the metallurgical characteristics were quantified.

Photomicrographs from the center and near the edge of each specimen were used for the quantitative metallography. Two specimens of each microstructure were used for this analysis.

Each photomicrograph at 500X was divided into nine areas. Each of these areas had a grid of 400 rows with 400 points in each row. Therefore, 1.44×10^6 points were measured on each photomicrograph. A gray level threshold was set to correspond to the alpha and beta phases. Due to high contrast film and paper, a good classification of the gray levels would be expected.

The percents of α phase and mean phase size were calculated as follows [17, 18]:

$$V_V^{\alpha} = \frac{\text{average point count of } \alpha}{\text{number of points}}$$

$$S_V^{\alpha\beta} = \frac{4 \times \text{average intercept count}}{\text{number of points} \times \text{point size}}$$

$$\bar{\lambda}\alpha = \frac{4\, V_V^{\alpha}}{S_V^{\alpha\beta}}$$

where V_V^{α} = volume fraction of α (dimensionless); $S_V^{\alpha\beta}$ = surface area per unit volume (mm^2/mm^3); and $\bar{\lambda}^{\alpha}$ = mean α phase size (mm); the average point count of α = number of points within the α phase; and the average intercept count = the number of intersections a line per unit length crosses grain boundaries in a sample.

Since an automated system cannot differentiate between the equiaxed alpha and the acicular alpha, a manual test was done to determine this difference. The results of both the automated and manual tests are shown in Tables 2 and 3. These results show that there is little difference in the quantity of the alpha and beta phases in the three microstructures. However, there are differences in the size and shape of the alpha phase. The M1 microstructure has the largest mean phase size of equiaxed alpha but the acicular alpha platelets are very narrow and fragmented. The M2 microstructure has the smallest mean phase size of equiaxed alpha but acicular alpha platelets are wider and more defined. The M3 microstructure is an intermediate structure.

The tensile properties of the three microstructures of the three different Ti-6Aℓ-4V heats were determined by using ASTM standard round specimens [19]. The results obtained are given in Table 4.

Downloaded 01 Jun 2010 to 171.66.16.59. Redistribution subject to ASME license or copyright; see http://www.asme.org/terms/Terms_Use.cfm

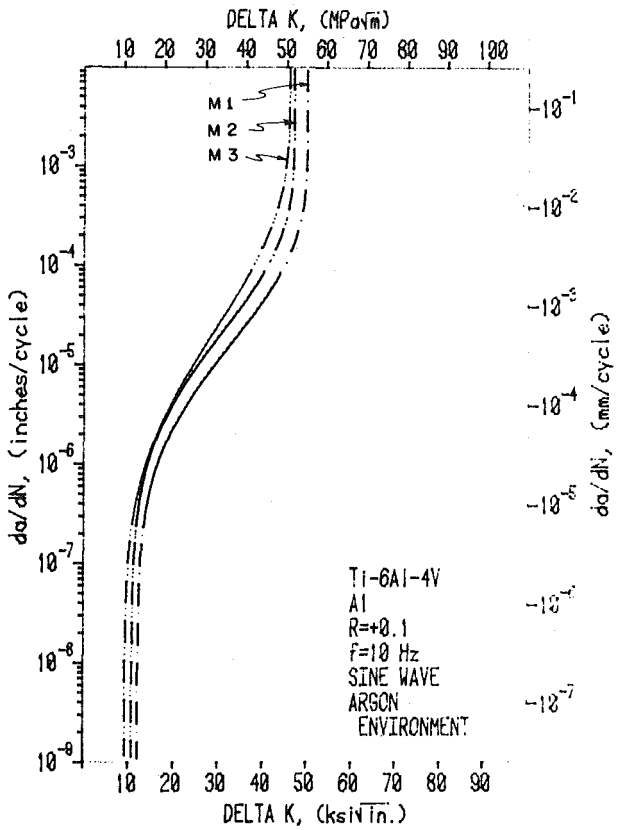

Fig. 3 Mean curve comparison for A1

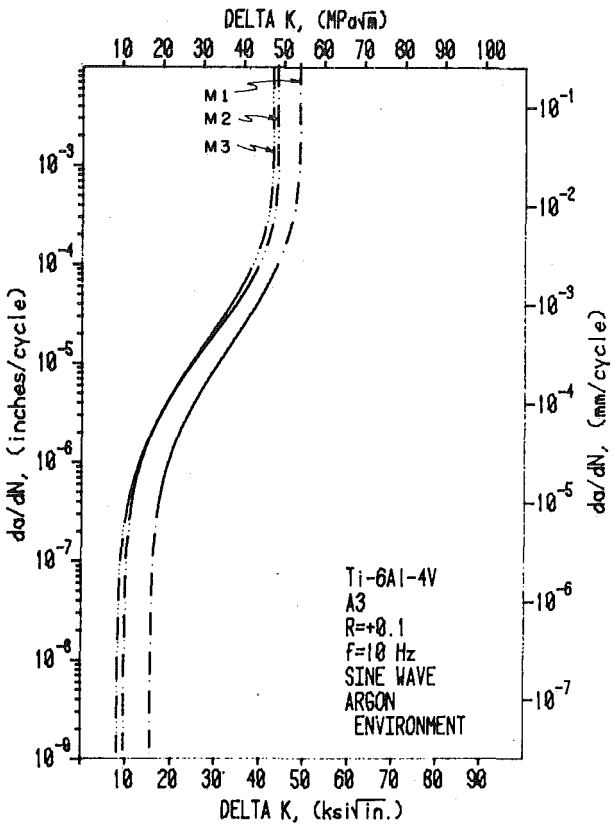

Fig. 5 Mean curve comparison for A3

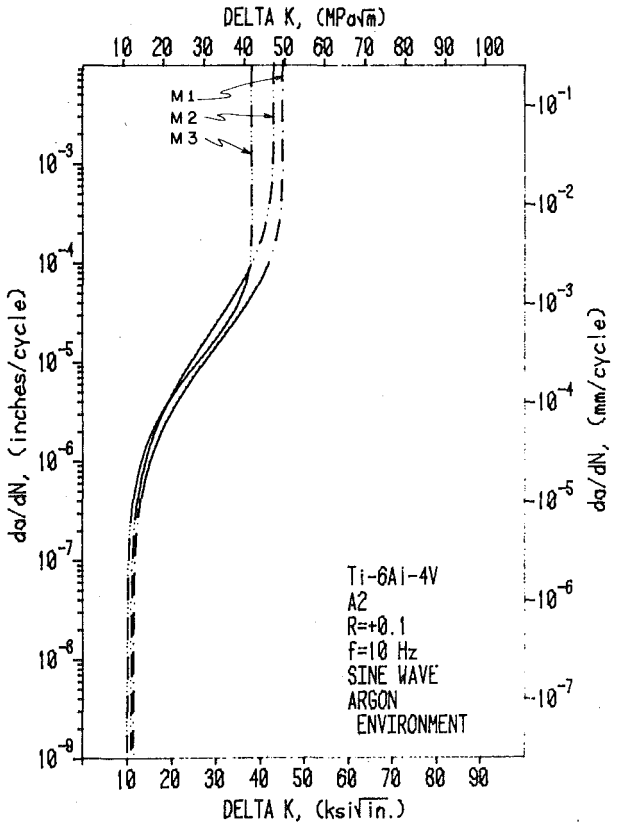

Fig. 4 Mean curve comparison for A2

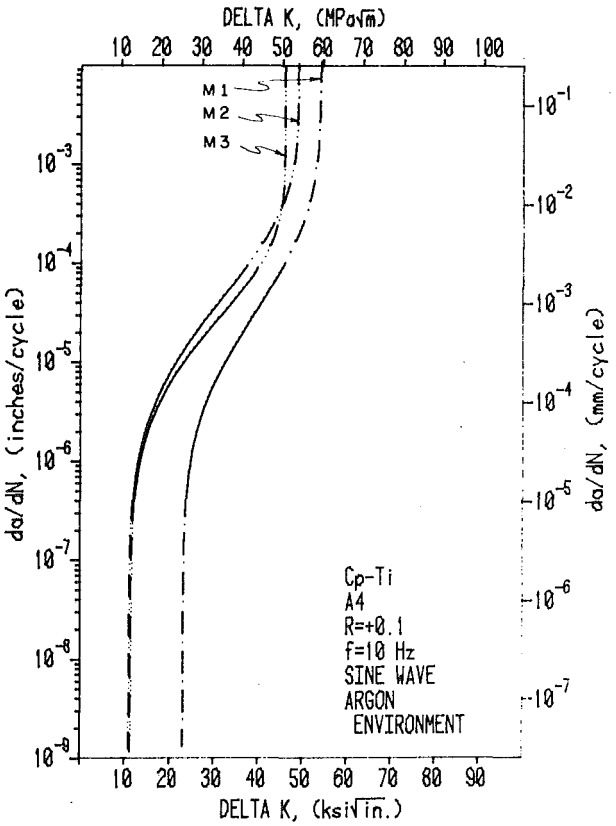

Fig. 6 Mean curve comparison for A4

Downloaded 01 Jun 2010 to 171.66.16.59. Redistribution subject to ASME license or copyright; see http://www.asme.org/terms/Terms_Use.cfm

Presentation and Discussion of Results

The crack length versus number of cycles (a-N) data were accumulated. The data were then reduced to crack growth rate data ($da/dN - \Delta K$) by the direct secant method. These crack growth rate data for all specimens of the same alloy and microstructure were combined. The plots of these data are shown in the Appendix. The Weibull four parameter survivorship function, as follows, was used to model each test condition.

$$\Delta K = K_b \left\{1 - \exp\left[-\left(\frac{da/dN - e}{\upsilon - e}\right)^k\right]\right\}$$

The threshold stress intensity (K_0), which is the stress intensity for a crack growth rate of zero, is also listed with the parameters.

The results in each of the sets were very similar for the replicated tests except M1A3. This set had the largest variance, but microstructure M1 in all alloys has a larger variance than microstructures M2 and M3. Crack initiation in this microstructure was also very difficult.

The mean curves for each microstructure have been plotted in Figs. 3–6 for each alloy. These plots show that the mean curve for M1 is shifted to the right in all cases. The threshold stress intensity is highest for M1 in all four alloys. This partially explains why the M1 microstructures were more difficult to precrack.

The curves for microstructures M2 and M3 overlap or coincide in all four alloys. This could be expected from the quantitative metallography, which showed relatively small microstructural differences.

Even though the change to the M1 microstructure has shifted the mean curves, the significance of that shift on fatigue crack growth properties remains to be determined. This significance is difficult to deduce from Weibull curves, since they may cross, start at different points and converge, or exhibit other types of behavior. Therefore, it was decided to linearize the equation and determine whether two regression lines are identical.

The Weibull four parameter survivorship function is

$$\Delta K = K_b \left\{1 - \exp\left[-\left(\frac{da/dN - e}{\upsilon - e}\right)^k\right]\right\}$$

By algebraically manipulating this equation it can be arranged into a linear form,

$$\ln\left(\frac{da}{dN} - e\right) = \ln(\upsilon - e) + 1/k \ln\left[-\ln\left(\left(1 - \frac{\Delta K_i}{\Delta K_b}\right)\right]\right.$$

$$yi = b_0 + b_1 x_1$$

where b_0 and b_1 are sample estimators from the Weibull parameters; b_0 = y intercept = $\ln(\upsilon - e)$; b_1 = slope = $1/K$.

Therefore, the hypotheses are [20]: H_0: $\beta_{01} = \beta_{02}$ and $\beta_{11} = \beta_{12}$ or the regression lines are identical; H_A: either $\beta_{01} \neq \beta_{02}$ or $\beta_{11} \neq \beta_{12}$ or both where β = sample estimator of B.

If the null hypothesis, H_0, is true, then both the intercept and slope terms must be equal. Then under the null hypothesis, the two regression lines must have a common slope and intercept.

The F statistic [21] is used to determine whether these lines are common. For comparing M1 with M2 or M3 in all alloys, it could be concluded with a 95 percent confidence that H_A is true or that a significant difference exists.

A fractographic analysis was also performed at both the macroscopic and microscopic level. In both cases, the different microstructures appeared to have varying fracture modes.

Concluding Remarks

The following conclusions are made based on the experimental and analytical results of this research effort [22].

1 The effects of microstructure are:
   (a) Statistically significant on the fatigue crack growth properties of titanium and titanium alloys to a 95 percent confidence level;
   (b) important in the crack initiation and near threshold region.
   (c) important in the instability region, but sufficient data are difficult to obtain;
2 Experiments must be statistically planned to evaluate experimental results fully.
3 Quantitative metallography with fractographic studies can improve understanding of the effects of microstructure on fatigue crack growth properties.
4 The bulk properties do not order the same as the fatigue crack growth properties in these titanium alloys.

Since Ti-6Aℓ-4V and other high strength titanium alloys are used to produce advanced, high thrust-to-weight gas turbine engines, microstructural development can greatly increase the damage tolerance of these materials.

As a result, component critical flaw sizes will increase and our present nondestructive evaluation will be more reliable. Also component lives will be extended.

Acknowledgments

The authors wish to acknowledge Lockheed California Company and the University of Missouri—Columbia, College of Engineering, for the support given this study. A special thanks to William Krupp.

The technical assistance of Larry Mueller, Art Braun, Larry Clark and Sathish Das is also greatly appreciated.

References

1 Plumbridge W. J., *Journal of Material Science*, Vol. 7, 1972, p. 939.
2 Clark, W. G. Jr., *Metals Engineering Quarterly*, Aug. 1974, p. 16.
3 Laird, C., "The Influence of Metallurgical Structure on the Mechanisms of Fatigue Crack Propagation," ASTM STP 415, American Society for Testing and Materials, Philadelphia, PA, 1967, p. 131.
4 Thompson, A. W., and Backofen, W. A., *Acta Metallurgica*, Vol. 19, 1971, p. 597.
5 Turner, N. G., and Roberts, W. T., "Fatigue Behavior of Titanium," *Transactions of the Metallurgical Society of AIME*, Vol. 242, July 1968, p. 1223.
6 Robinson, J. L., and Beevers, C. J., "Some Observations on Fatigue Crack Growth in Alpha-Titanium," *Titanium Science and Technology*, Plenum, London, 1973, p. 1245.
7 Irving, P. E., and Beevers, C. J., *Materials Science and Engineering*, Vol. 14, 1974, p. 229.
8 Yoder, G. R., Cooley, L. A., and Crooker, T. W., "Observations on Microstructurally Sensitive Fatigue Crack Growth in a Widmanstätten Ti-6Aℓ-4V Alloy," *Metallurgical Transactions A*, Vol. 8A, Nov. 1977, p. 1737.
9 Amateau, M. F., Hanna, W. D., and Kendall, E. G., "The Effect of Microstructure on Fatigue Crack Propagation in Ti-6Aℓ-6V-2Sn Alloy," *Mechanical Behavior of Materials*, Vol. 2, The Society of Material Science, Japan, 1972, p. 77.
10 Hall, J. A., Pierce, C. M., Ruckle, D. L., and Sprague, R. A., *Materials Science and Engineering*, Vol. 9, 1972, p. 197.
11 Greenfield, M. A., Pierce, C. M., and Hall, J. A., "Mechanism of Void Formation, Void Growth, and Tensile Fracture in an Alloy Consisting of Two Ductile Phases," *Transactions of the Metallurgical Society of AIME*, Vol. 3, Oct. 1972, p. 2649.
12 Hoeppner, D. W., "A Fractographic Analysis of Flaw Growth in a High Strength Titanium Alloy," UMC Report, Aug. 1975.
13 Griffith, A., "The Phenomena of Rupture and Flow in Solids," *Philosophical Transactions of the Royal Society*, Vol. 221A 1920, p. 163.
14 Hoeppner, D. W., "Effect of Microstructure on Fatigue Crack Growth Behavior in Forged Materials," presented at Joint Conference: Forging and Properties of Aerospace Materials, University of Leeds, Jan. 1977.
15 Kempthorne, O. *The Design and Analysis of Experiments*, John Wiley & Sons, New York, 1952.
16 Johnson, N. L., and Leone, F. C., *Statistics and Experimental Design in Engineering and the Physical Sciences*, Vol. II, John Wiley & Sons, New York, 1977.
17 DeHoff, R. T., and Rhine, F. N., *Quantitative Microscopy*, McGraw-Hill, New York, 1968.
18 Underwood, E., *Quantitative Stereography*, Addison-Wesley, Reading, Mass., 1970.
19 American Society for Testing and Materials, 1978 ASTM Standards, Part 10 E-8, Philadelphia, Penn.
20 Neter, J., and Wasserman, W., *Applied Linear Statistical Models*, Richard D. Irwin, 1974.
21 Walpole, R. E., and Meyers, R. H., *Probability and Statistics for Engineers and Scientists*, Macmillan, New York, 1972.
22 Wilson, D. A., "A Statistically Based Investigation of Microstructural Effects on the Fatigue Properties of Titanium and Titanium Alloys," a PhD dissertation presented to the Faculty of the Graduate School, University of Missouri-Columbia, Dec. 1978.

Downloaded 01 Jun 2010 to 171.66.16.59. Redistribution subject to ASME license or copyright; see http://www.asme.org/terms/Terms_Use.cfm

APPENDIX

Crack Propagation Data

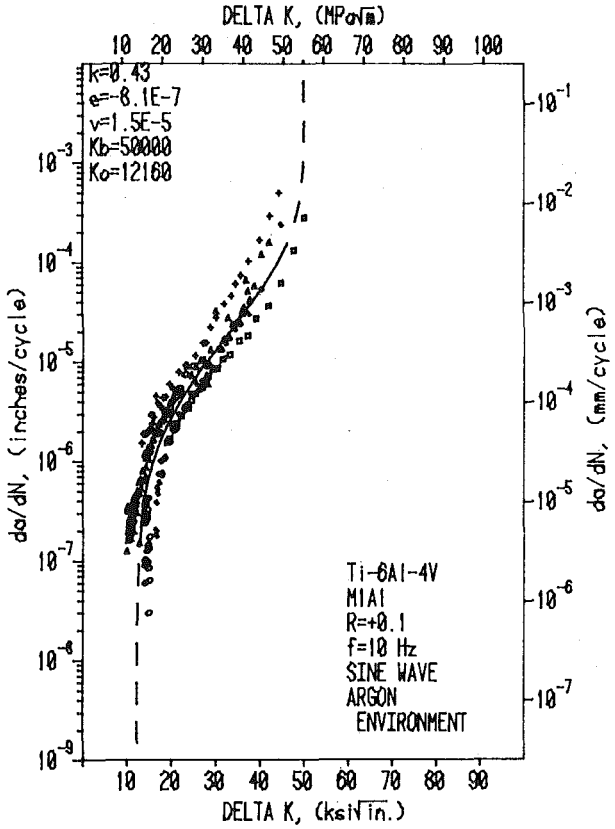

Fig. A1 Crack growth rate data for M1A1

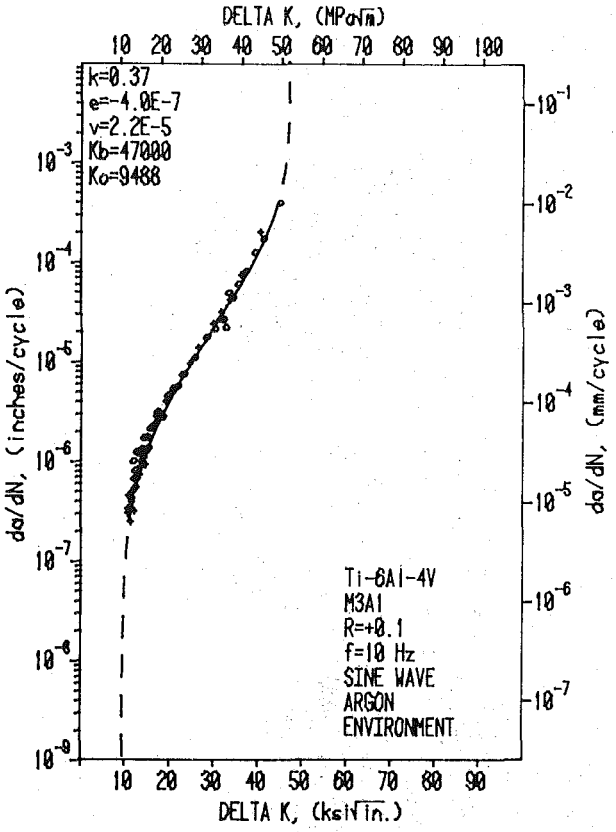

Fig. A3 Crack growth rate data for M3A1

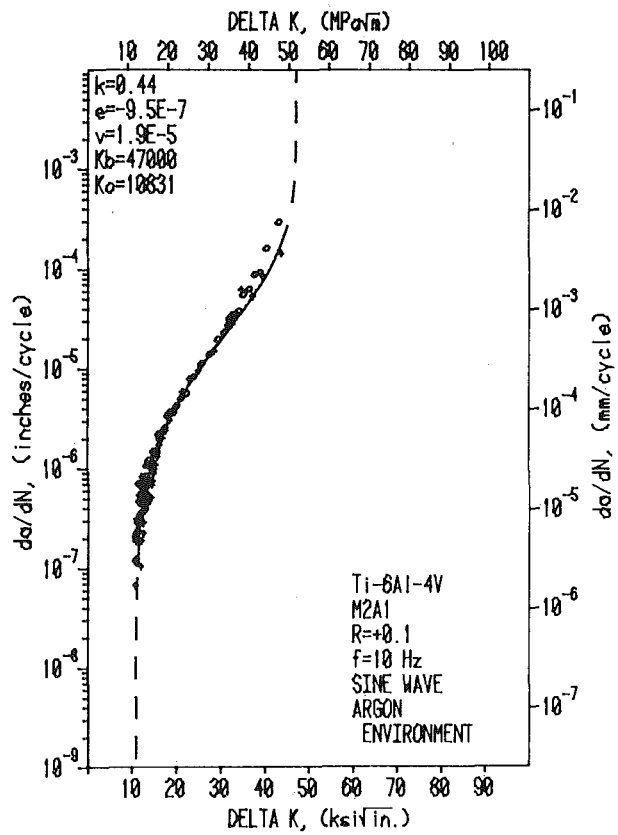

Fig. A2 Crack growth rate data for M2A1

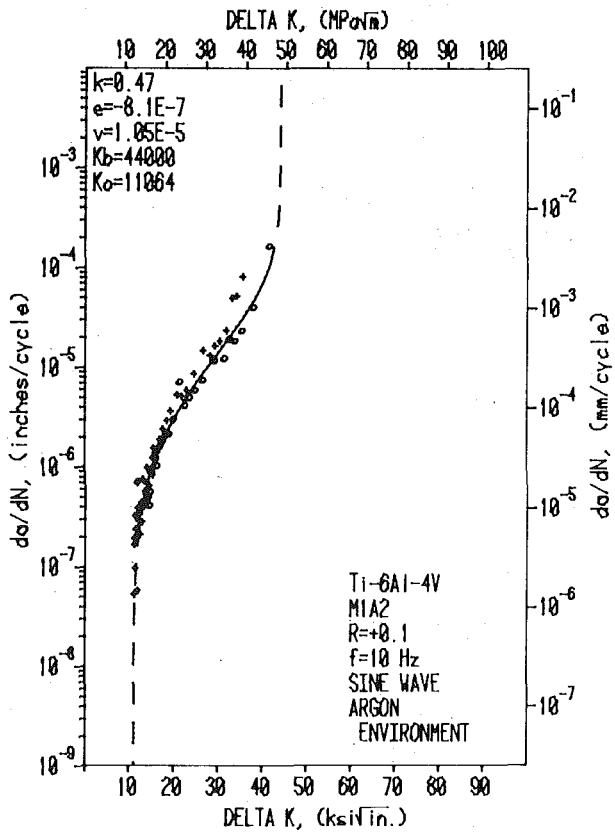

Fig. A4 Crack growth rate data for M1A2

Downloaded 01 Jun 2010 to 171.66.16.59. Redistribution subject to ASME license or copyright; see http://www.asme.org/terms/Terms_Use.cfm

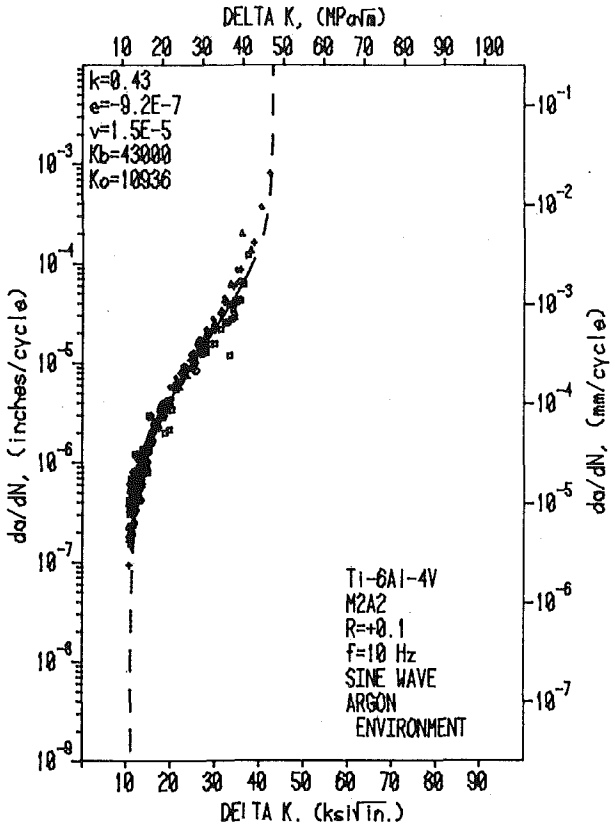

Fig. A5 Crack growth rate data for M2A2

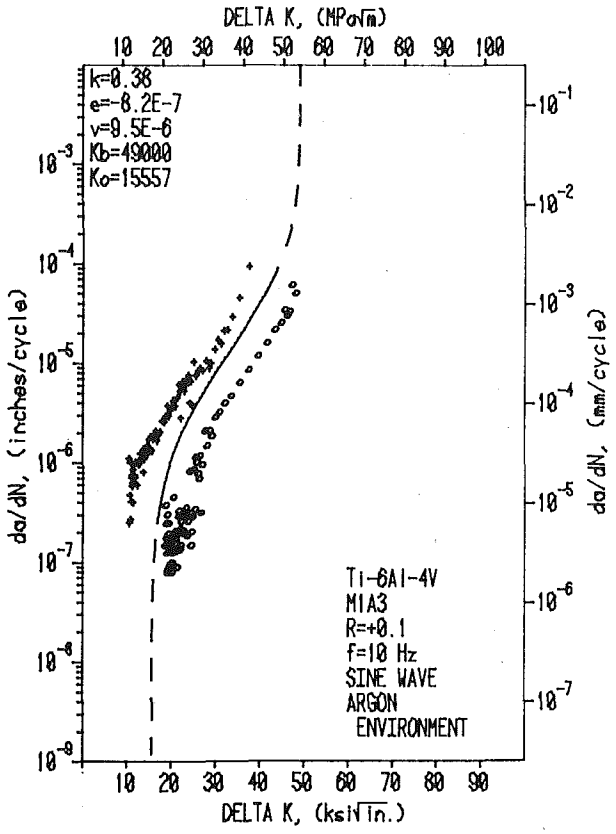

Fig. A7 Crack growth rate data for M1A3

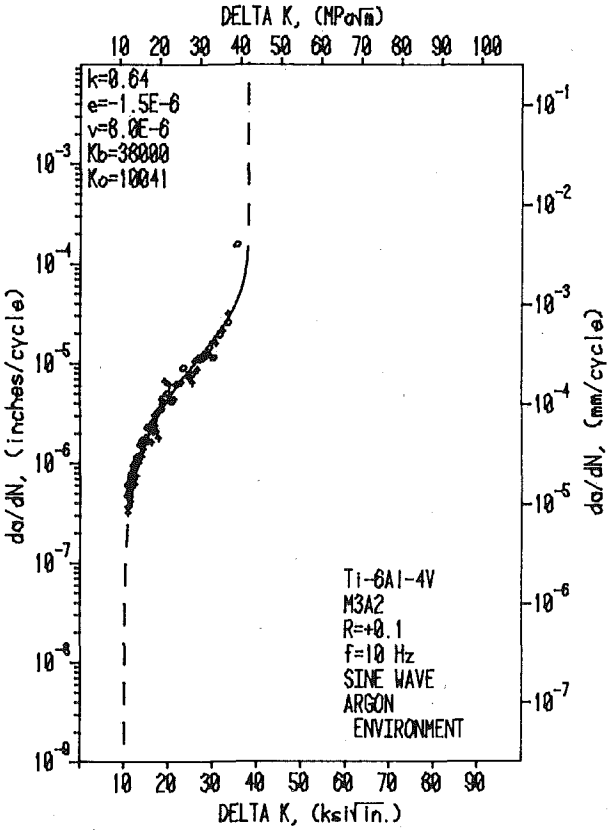

Fig. A6 Crack growth rate data for M3A2

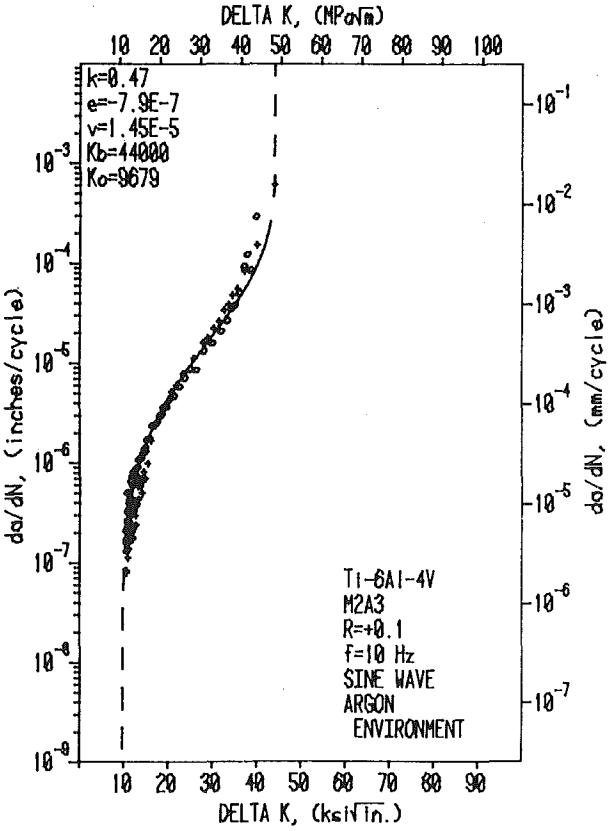

Fig. A8 Crack growth rate data for M2A3

Downloaded 01 Jun 2010 to 171.66.16.59. Redistribution subject to ASME license or copyright; see http://www.asme.org/terms/Terms_Use.cfm

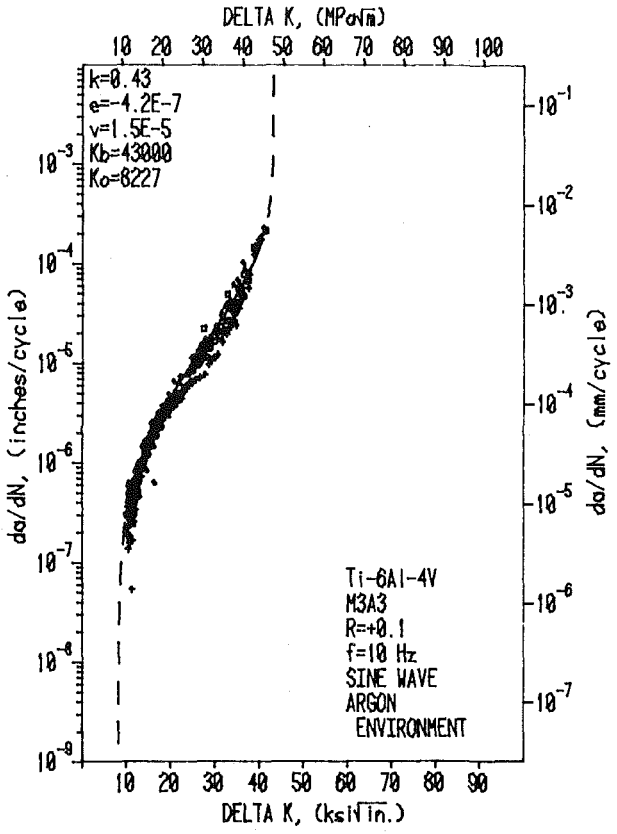

Fig. A9 Crack growth rate data for M3A3

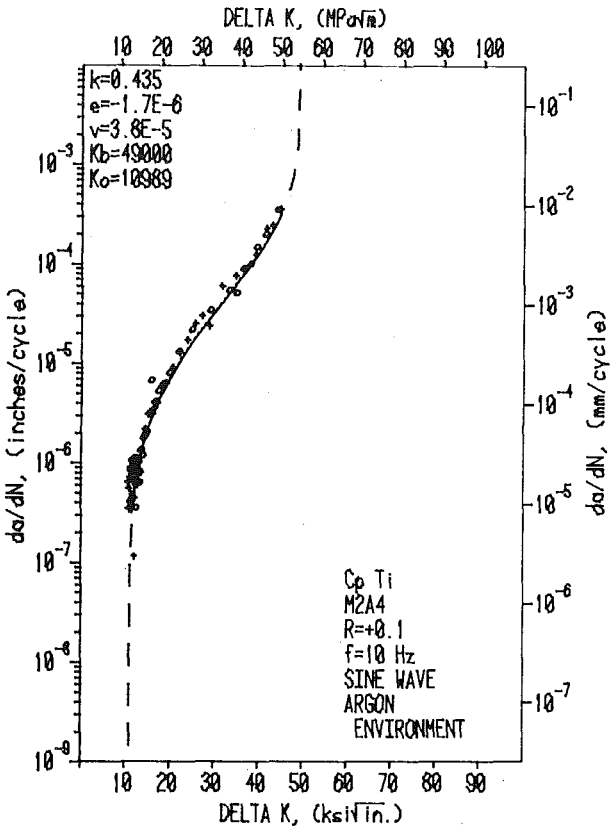

Fig. A11 Crack growth rate data for M2A4

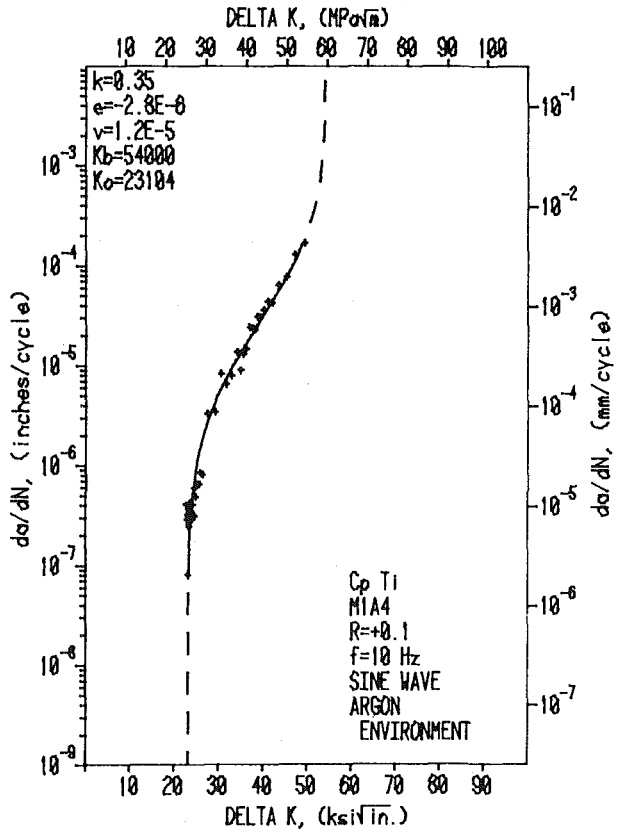

Fig. A10 Crack growth rate data for M1A4

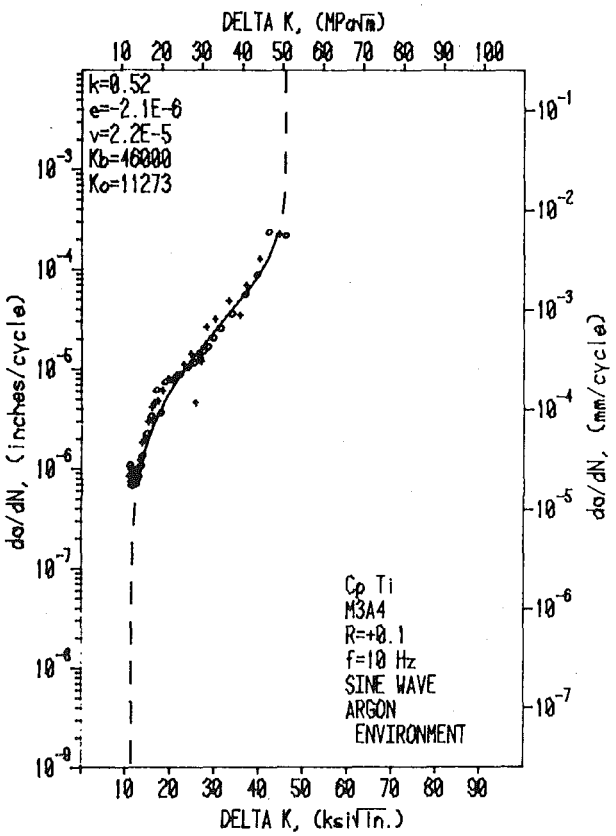

Fig. A12 Crack growth rate data for M3A4

Downloaded 01 Jun 2010 to 171.66.16.59. Redistribution subject to ASME license or copyright; see http://www.asme.org/terms/Terms_Use.cfm

J. F. G. Condé
Procurement Executive,
Ministry of Defence,
AMTE(HH), Holton Heath Poole,
Dorset, U. K.

C. G. McCreath
University of Sheffield,
Sheffield, U. K.

The Control of Hot Corrosion in Marine Gas Turbines

Ingestion of sea salt and sulphur from fuel can lead to aggressive environments in gas turbines operating in marine conditions resulting in corrosion damage to hot end components, even in well-filtered engines. The nature of the environment in the engine and the factors which influence this are indicated. The chemistry of salt contaminant particles in the engine and combustion environments and temperature levels prevailing in naval engines are described in relation to the normal operating profile and the incidence of corrosion effects in relation to temperature. Results of rig evaluation of materials and coatings are given. Erosion resistance, the combined effects of erosion/corrosion and the mechanisms of hot corrosion are discussed together with the effects of material composition and the use of inhibition as a control procedure. The effects of a salt environment on the creep and stress-rupture behavior of superalloys are covered briefly.

Introduction

The high temperature components of gas turbines employed for the propulsive machinery and auxiliaries in ships may, under certain conditions, be subject to hot corrosion due to sea salt contamination. The characteristic effects of hot corrosion (Fig. 1) have been recognized since about 1950 and essentially comprise sulphidation of the surface layers of the superalloy material accompanied by accelerated or, in some instances, catastrophic oxidation. In general the attack is fairly localized in the engine and is normally confined to the turbine entry guide vanes and first or second stage turbine blades. The sheet metal combustion chamber liners may also be affected but such instances are rare.

Naval gas turbines are normally fuelled with diesel fuel or gas oil with a maximum sulphur content of about 1.0 percent and the air and fuel are filtered to reduce the maximum sea salt burden to 0.01 ppm NaCl equivalent in the air and 0.3 ppm Na equivalent in the fuel. Seawater in the fuel arises from the practice of ballasting fuel tanks with seawater and in some instances water displacement may be employed. In practice fuel filtration, employing coelescers and, in some instances, centrifugal separation is highly effective and reduces the salt content of fuel to below the limits of accurate chemical analysis. Air filtration efficiency is related to a variety of factors such as sea state, humidity, wind speed, ship's speed, etc. but the system of three stage filtration consisting of spray eliminators, knitted mesh filters and inertial vane separators is designed to maintain the salt level at below 0.01 ppm NaCl.

This paper seeks to identify the nature of the aggressive environment which can exist in the marine gas turbine and to indicate how this may result in degradation of hot end components by corrosion and/or erosion processes.

Definition of the Engine Environment

Initially a literature survey was made on the mechanisms of salt deposition processes in marine gas turbines. Measurements were then made on the compressor section of a G6 industrial type marine gas turbine under realistic marine operating intake conditions. These sought to define the quantity and particle size of sea salt emerging from the compressor. It was demonstrated that a clean compressor acted as an efficient salt collector and suggested that large salt particles might result from re-entrainment of fragments from friable deposits, certainly if compressors were not washed regularly but probably also before fouling of the compressor had reached noticeable levels as indicated by engine efficiency.

In parallel with these studies on sea salt behavior, research was initiated on the short residence chemistry of sea salt in the combustion environment [1]. This was to establish the kinetics of sulphation of sodium chloride (i.e., conversion to sodium sulphate by SO_2/SO_3 present in the gas phase) and to test the hypothesis that kinetics and thermodynamic factors might not favor the immediate and complete conversion to sulphate which had often been assumed by other workers. In particular it was necessary to determine whether conversion was significant in the short residence times characteristic of gas turbine combustion systems (5 to 7 ms) to establish whether sodium chloride could credibly reach the turbine. The results of this work are summarized in Fig. 2 which demonstrates that conversion of chloride to sulphate is not instantaneous. Supporting theoretical studies of the chemical equilibria suggested that in the instance of sea salt, which has the composition shown in Table 1, the sulphate already present in the salt would represent a super equilibrium level at high temperatures and make the conversion reaction unfavorable.

Subsequent studies at the University of Sheffield and at the Admiralty Marine Technology Establishment have been based on the philosophy that corrosion in real engines is related to the nature, form and behavior of the sea salt contaminant in its transit through the engine. It is the end product of a chain of events which begin with environmental conditions near the compressor intake duct and extend through the filters, transfer ducting, compressor and flame tube to finally give rise to corrosion of blades in the turbine of the engine. Each of the stages through which the salt-contaminated air flow passes can exert some influence on the nature and form of the salt contaminant. The environment which the turbine finally sees and to which the corrosion mechanism responds is a function of the design and operating environment of all stages upstream the turbine. Hence, it can

Contributed by the Gas Turbine Division of The American Society of Mechanical Engineers and presented at the Gas Turbine Conference and Products Show, New Orleans, La., March 10–13, 1980. Manuscript received at ASME Headquarters December 27, 1979. Paper No. 80-GT-126.

Copyright © 1981 by ASME
Downloaded 01 Jun 2010 to 171.66.16.59. Redistribution subject to ASME license or copyright; see http://www.asme.org/terms/Terms_Use.cfm

be envisaged that corrosion can possibly exhibit different degrees even within identical engines (having been operated under different sea conditions).

In order to examine this basic philosophy in more detail a series of experimental and theoretical attacks have been made on various engine "elements." These elements are: (1) the transfer ducting upstream the compressor, (2) the compressor, (3) the flame tube, and (4) the hp turbine nozzle guide vanes.

Intake Transfer Ducting Effects. Liquid drops escaping from the filters have some time available to evaporate before arriving at the compressor intake plane. The extent to which such droplets do evaporate is clearly a function of ducting size, engine power, temperature, and relative humidity of the environment within the duct.

It is noteworthy that intake ducting frequently contains 90 deg bends and that turning vanes in these bends have been shown [2] to be capable of small droplet (~4 μm) capture by inertial means. The wet film so formed on the vane could then generate larger drops by shedding from the trailing edge.

In order to evaluate the state in which "drops" arrive at the compressor a theoretical evaluation [3] of the evaporation history of various initial drop sizes has been carried out for a variety of environmental conditions. This theoretical evaluation has shown that drops arriving at the compressor entrance plane are likely to be in a wet state unless conditions of very low relative humidity (<10 percent) and high temperature (>25°C) are found in conjunction with small drop sizes (~5 μm).

The arrival of wet drops at the compressor intake plane is felt to be relevant since a wet drop by definition has a larger mass and hence a larger inertia/drag ratio than a particle. It will also tend to impact, shatter, stick and run to form a wet film rather than bounce and shatter as would a dry particle. The temperature gradient in the compressor is significant even at low power conditions and it is unlikely that droplets in a wet state survive transit of the compressor.

Compressor Effects. In order to evaluate more fully the role of the compressor a number of particulate sampling trials on a real OLYMPUS compressor have been carried out at NGTE. These trials [3] have shown that particle shedding from the compressor can occur under conditions of accelerating power. This effect is particularly marked when prolonged idle conditions have been experienced by the compressor immediately prior to the increase in load. Particle sizes up to 15 μm have been measured at compressor exit after a 3 hr idle duration and the shedding effect is still pronounced after idle durations of only 30 min.

It has thus been shown again and more positively that the compressor can act as a filter or as a concentrator and a large particle generator. Its preference for a particular role is a function of its power condition and immediate power condition history.

The Flame Tube. Particle matter shed by the compressor can traverse the flame tube by a variety of routes. The number of particles which take a particular route is a function of the air distribution design of the flame tube. The major routes available are: (1) the swirler va-

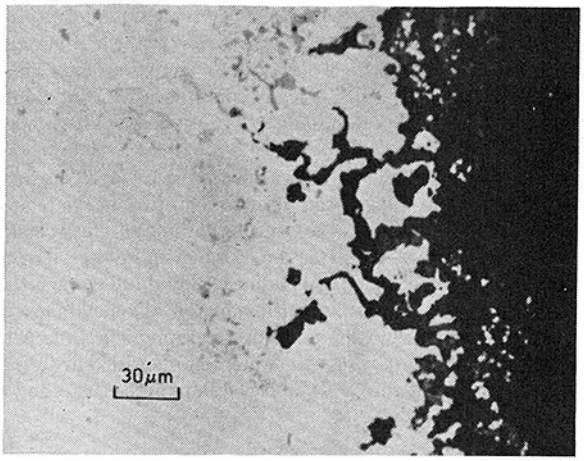

Fig. 1(*a*) Wrought Alloy: Pack-Aluminized Nimonic 115 first stage turbine blade run for 951 hr with last 409 hr 0.01 ppm salt in air and 0.6 ppm sodium in fuel. Peak temperature 870°C

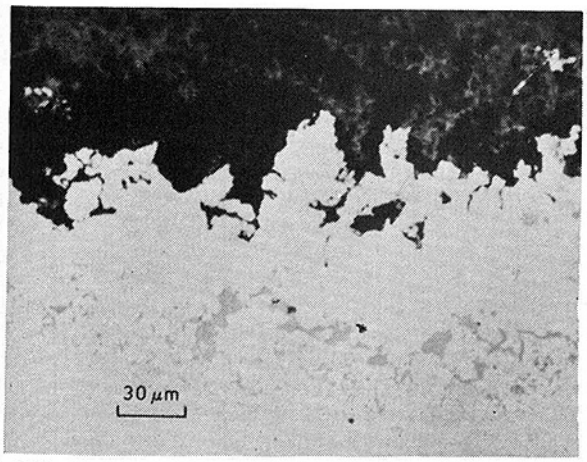

Fig. 1(*b*) Cast Alloy: Pack-Aluminized IN 738 test specimen after 200 hr, 750°C, 1.0 ppm sea salt, in AMTE Low Pressure Combustion test rig

Fig. 1 Typical hot corrosion effects

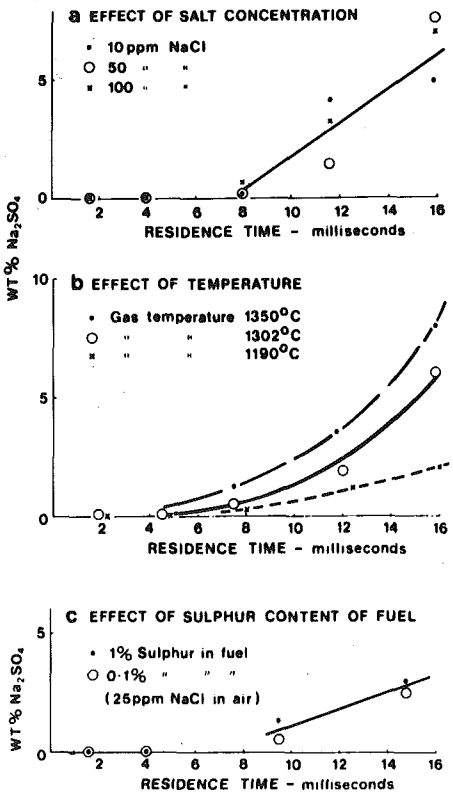

Fig. 2 Gas phase sulphation of sodium chloride

Table 1 Composition of Sea Water

Element/Radical	Cl^-	$SO_4^=$	HCO_3^-	Br^-	F^-	H_3BO_3
Concentration ppm	18980	2649	140	65	1	26
Element/Radical	Na^+	Mg^{++}	Ca^{++}	K^+	Sr^{++}	
Concentration ppm	10556	1272	400	380	13	

Downloaded 01 Jun 2010 to 171.66.16.59. Redistribution subject to ASME license or copyright; see http://www.asme.org/terms/Terms_Use.cfm

porizer route, (2) the secondary port route, and (3) the dilution port route.

As a result of a combined theoretical and experimental attack on the rates of evaporation of sea salt and sodium chloride it has been shown [3, 4] that particulate salt, even up to 10 μm, entering into the primary zone probably undergoes significant evaporation but that particulate material entering the dilution zone has neither the residence time nor a high enough temperature available to evaporate to any significant extent before entering the hp turbine nozzle guide vanes. In order to carry out the evaporation studies it was necessary to establish the vapor pressure of sodium chloride over sea salt since no data were available in the literature. This was accomplished by workers at Imperial College of Science and Technology employing a mass spectrometer effusion technique [13]: Log PNaCl (bar) = 10720/T + 6.71 (over the temperature range 770 to 920°C).

The role of salt in fuel is also worthy of mention at this stage. Salt in fuel probably exists in the form of very small brine droplets finely distributed in the fuel. The size of fuel droplets generated in typical combustion chambers is in the range 5–200 μm and it is likely that the brine is so finely distributed that it will constitute only a small part of each individual fuel droplet. Under such conditions it has been shown [5] that the fuel droplets undergo premature disintegration prior to burning due to their aqueous content. The resulting fuel droplets are extremely small and burn quickly. Any salt content of such a droplet would not generate a particle of sufficient size to survive transit of the primary zone and thus could only add to the salt vapor content of the combustion products at flame tube exit.

HP Nozzle Guide Vane Effects. It has been shown that both vapor and particles are likely to survive long enough to enter the turbine. The salt vapor content of the combustion products arriving at the turbine could include sodium chloride and sodium sulphate, the former having insufficient time available in the gas phase to sulphate before arrival at the turbine blade surfaces [6].

Further work on vapor deposition which has been carried out at Sheffield [3] has shown that sodium chloride vapor is unlikely to deposit on nozzle guide vane surfaces exhibiting temperature profiles typical of those found under operational conditions, but that sodium sulphate is likely to deposit in preferred areas of the nozzle guide vanes—the preferred areas being a function of the NGV surface temperature.

The role of particles which form part of the turbine environment has been shown to be important from a deposition viewpoint. So far, a combined theoretical and experimental investigation [3] into particle trajectories over static nozzle guide vanes has illustrated that the NGV pressure surface can be hit even by small particles (~5 μm) which then sulphate in situ [6]. Inertial impaction of particles on static and moving aerofoils may also contribute to an erosive effect [7]. If it is assumed that particles containing chloride are capable of inertial impaction and can also exhibit an erosive influence, a route for chloride directly to metal substrates is available without the need to postulate oxide scale cracking or diffusional effects.

A summary of those factors contributing towards the final environment which the turbine experiences is illustrated in Fig. 3.

Chemistry of Sea Salt Particles. To study the short residence chemistry of sodium chloride and sea salt particles two approaches have been adopted: sampling of a high temperature, high velocity, low pressure (1 bar) corrosion rig which employs seawater injection and injection of sodium chloride into a combuster at the University of Sheffield with examination of catch samples after various residence times. Samples, together with EDS analysis, are shown in Fig. 4 after various maximum residence times in the AMTE low pressure rig. The chloride content reduces and the sulphur content increases with residence time, the rig being fired by dieso fuel containing about 1.0 percent sulphur. Samples were taken on alumina targets from the Sheffield combustor after 10, 30, 60, and 120 s in a burned fuel atmosphere containing 0.2 percent SO_2 at temperatures of 650, 750, and 850°C. Samples were also taken after 180 s at 750°C. X-ray diffraction analysis confirmed that conversion to sodium sulphate was essentially complete in 60 s at 650 and 750°C and in 30 s at 850°C. The extent to which apparent conversion is increased by evaporation of chloride is not established. Thus it would be anticipated that under the conditions in a marine gas turbine, sea salt surviving the transit through the combustion, dilution and cooling gas flow paths and impacting onto hot turbine blades would survive for a similar order of time. In practice with sea salt, which already contains significant sulphate (Table 1), the conversion reaction might be expected to be somewhat slower.

Temperature Levels in Naval Engines. Naval engines in warships may spend a high proportion of their time at low temperatures since they will normally be operating at some part load condition and will spend only a small fraction of life at full power. The temperature profile through a typical marine engine at full power is shown in Fig. 5. In practice first stage turbine blades will spend most time at lower temperatures in the range up to around 750°C. Low temperature hot corrosion phenomena were first identified in early generation gas turbine engines in Royal Naval ships in the 1960's and were

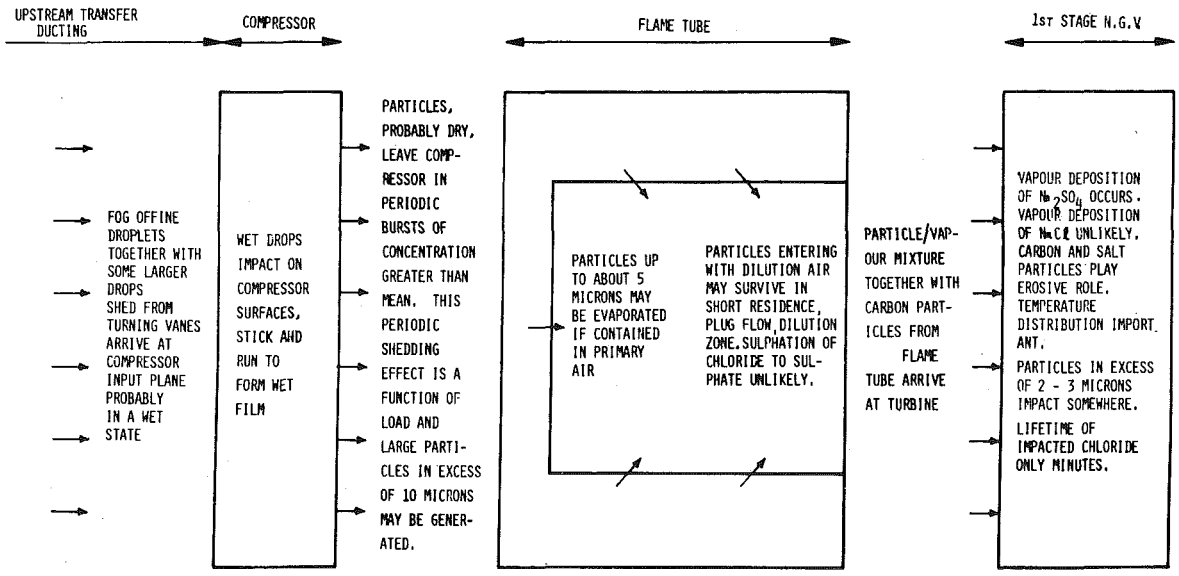

Fig. 3 Factors contributing to the turbine environment

Downloaded 01 Jun 2010 to 171.66.16.59. Redistribution subject to ASME license or copyright; see http://www.asme.org/terms/Terms_Use.cfm

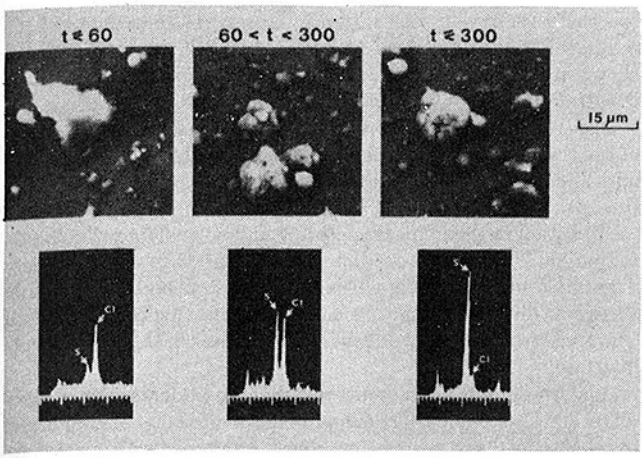

Fig. 4 Typical salt particles collected in the AMTE LP rig in times ranging from 60 to 300 s together with their analysis

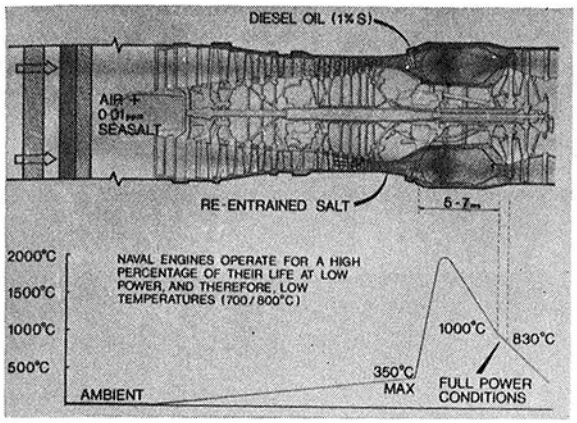

Fig. 5 Temperature profile through a typical marine gas turbine at full power

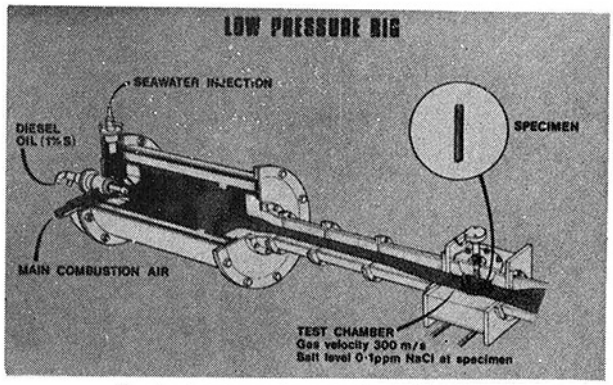

Fig. 6 Low pressure corrosion test facility

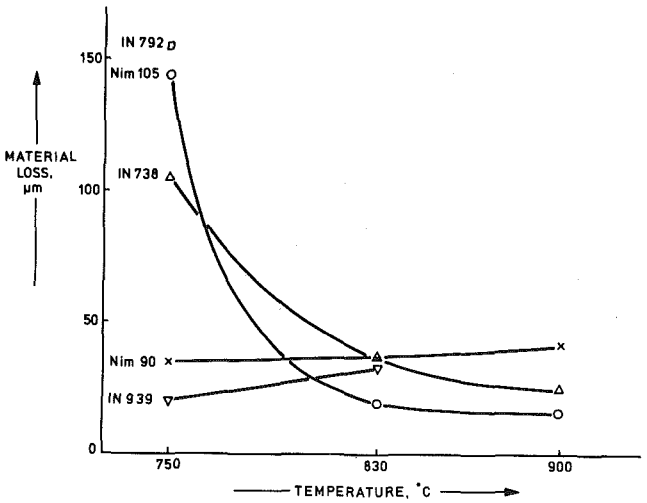

Fig. 7 Corrosion/temperature relationships—200 hr exposure AMTE LP corrosion test facility

associated with temperatures substantially below 800°C. These low temperature corrosion phenomena, believed to occur mainly in the range of 650 to 750°C, have now become recognized as of more common occurrence in marine gas turbines. Even where engines operate at full power or the maximum blade temperatures are higher, corrosion is apparently more severe on the cooler parts of the blade.

Rig Evaluation of Materials and Coatings

The use of engines to carry out corrosion evaluation of materials is expensive and time consuming; hence simulation of engine conditions is employed for this purpose, using low and high pressure test facilities.

Low Pressure Rig. The AMTE low pressure test facility shown in Fig. 6 uses dieso fuel, and 1 ppm of seawater is injected into the combustion air. Measurements indicate that a high proportion of the sea salt is held up on the walls of the system and that approximately 0.1 ppm is present at the test section. Pin specimens 6.25 mm dia by 43.5 mm long are held vertically in a rotating carousel exposed to the hot combustion gases flowing at a velocity of approximately 330 m/s. The air/fuel ratio is in the range 40/1 to 50/1. Tests may be made at temperatures in the range of 650 to 1000°C. A cooling cycle is applied every 25 hr and fuel-rich conditions occur on restarting. In the main, tests have been at 750, 830, 900 and 1000°C, temperatures which are relevant to operating conditions in engines in service or under development. Pin specimens are machined from rod for tests on wrought alloys and cast nearly to size with surface grain refinement for cast alloys. Both types of material are finally centerless ground to facilitate accurate measurement.

Interest in corrosion at relatively low temperature has been in order to simulate the low temperature effects found in engines in service and the rig has been able to faithfully reproduce this type and morphology of corrosion. Test times have been extended to 1200 hr in some instances but in general the standard test time is 200 hr with up to 600/1200 hr for promising materials or coatings. Test results after 200 hr exposure on a range of commercial superalloys at 750, 830 and 900°C are shown in Fig. 7 and indicate that the lower chromium alloys IN 792 (12.5 percent Cr) Nimonic 105 (14 percent Cr) and IN 738 (16 percent Cr) suffer far greater loss of material at 750°C than at the two higher temperatures. The differing forms of attack at 750 and 830°C are illustrated in Fig. 8 which relates to IN 738. The two higher chromium alloys Nimonic 90 (20 percent Cr) and IN 939 (23 percent Cr) (now called Nimocast Alloy 739) show little change in the 200 hr corrosion rate with temperature over the range examined.

Pack aluminized coatings produced by diffusion treatment have been employed in marine engines for many years and a wide variety of proprietary aluminide and other more complex diffusion coatings have been evaluated in the LP corrosion rig. Coatings have been found to fail most rapidly at round 750°C in the rig test and in engine experience and hence this condition of test is normally employed. Specimens are removed at intervals up to 200 hr to enable the time to coating penetration to be estimated with reasonable accuracy. In general the more complex diffusion coatings show little advantage over the simple aluminide varieties although there are indications that the platinum modified aluminides may show some limited improvement in life under certain conditions which are as yet ill defined.

Overlay coatings applied by PVD (physical vapor deposition), ion-plating, sputtering, high velocity, low pressure plasma arc, etc. have also been evaluated, initially on IN 738 and/or IN 792 substrates. As an example of this work complex M-Cr-Al-Y coatings were applied to IN 738 and IN 792 substrates by PVD and tested in the LP rig

Downloaded 01 Jun 2010 to 171.66.16.59. Redistribution subject to ASME license or copyright; see http://www.asme.org/terms/Terms_Use.cfm

under the standard conditions for 200 hr at 750 and 830°C. The nominal compositions and chemical analyses of these coatings are presented in Table 2. Chemical analyses were made on turnings taken from the outer 75 μm of the "as-received" coatings. Although the analyses indicated variations from the nominal compositions the deviations were not marked except for No. 1 on IN 792 where the aluminium content was 4.2 percent compared with a nominal 11 percent.

Metallographic examination of the pins after exposure at 750°C revealed that in nearly all instances corrosion had penetrated the coating and in some places had extended into the substrate alloy as shown in Fig. 9. The No. 1 coating on IN 792 suffered least attack, penetration being only half way through the 130 μm thickness.

Dispersive energy X-ray analysis was made to establish the nature of the scale and the presence of sulphur. No sulphides were visible optically but there was evidence of sulphur at the scale/metal interface. Ahead of the corrosion front there was no apparent structural modification in the remaining coating and no evidence of sulphide formation. The original position of the coating surface was clearly discernible and the scale products above this were porous and loosely adherent. The scale within the nodules penetrating the coating had a layered structure which followed the contours of the coating/scale interface.

Analysis of these nodules revealed that the oxide was rich in chromium and also contained aluminium. The porous outer oxide was rich in cobalt (CoO) and magnesium, chloride and calcium were also detected in the outer layer, and iron at the extreme outer edge. Clearly this outer scale was a mixture of corrosion products and material deposited from the environment.

The iron was believed to have originated from rust arising from steel and cast iron components in the test rig. Iron is a corrosion contaminant found in a similar position in the outer scale on blades from service in industrial and marine engines and is believed to originate from rust in fuel tanks, on the intake ducting or from its presence in the air environment and ingested into the engine.

The test at 750°C was repeated to check these somewhat unexpected results, some specimens being removed after 25 hr exposure.

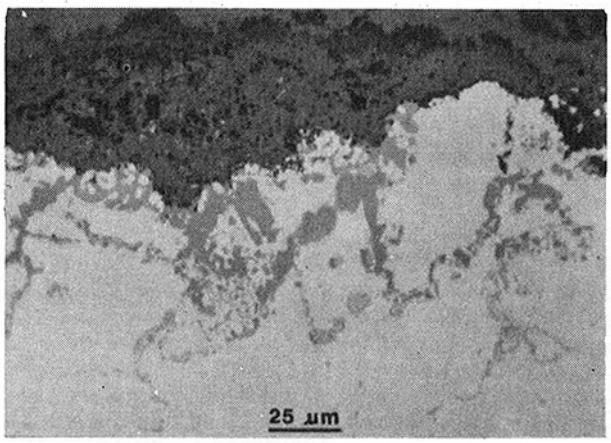

Fig. 8(*a*)

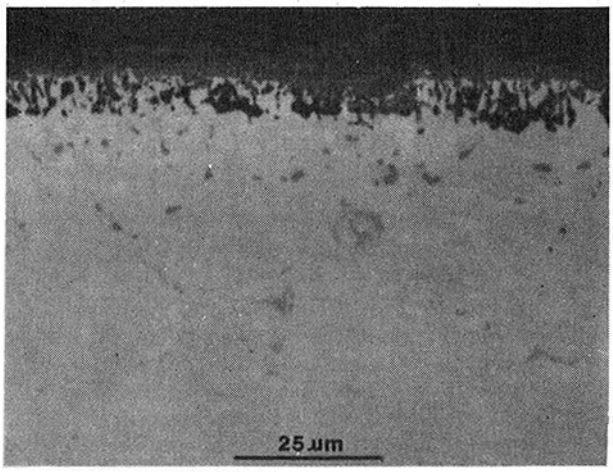

Fig. 8(*b*)

Fig. 8 Form of attack on IN 738 after 600 hr exposure at (*a*) 750°C and (*b*) 830°C in the AMTE LP corrosion test facility

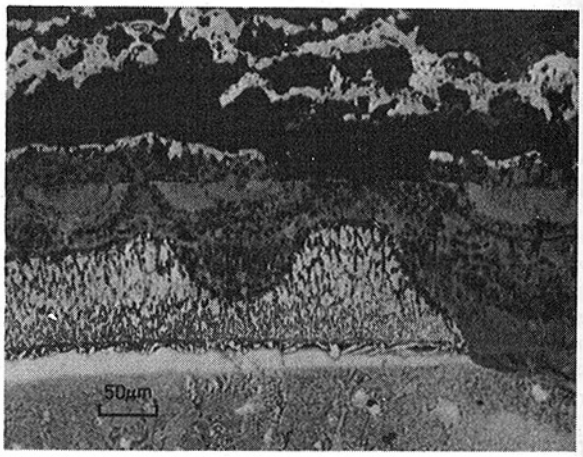

Fig. 9 Typical corrosion of M-Cr-Al-Y coating after 200 hr test at 750°C

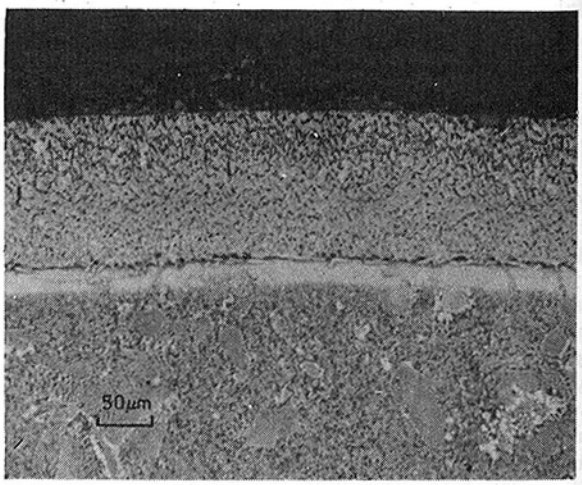

Fig. 10 M-Cr-Al-Y coating after 200 hr test at 830°C

Table 2 Nominal compositions and chemical analyses of M-Cr-Al-Y coatings

Coating-Substrate	Wt percent Al		Wt percent Cr	
	Spec	Analysis	Spec	Analysis
1*—IN738	11	13.6	38	30.3 32.3
2 —IN738	12.5	15.4	25	21.0 23.5
4 —IN738	13.5	16.0	22	17.0 18.1
6 —IN738	9.25	9.8	18	18.4 21.1
1 —IN792	11.0	4.2	38	38.8 40.5
2 —IN792	12.5	13.8	25	21.7 23.3
4 —IN792	13.5	13.9	22	17.6 18.3

* Coating No. 1 was nickel base, the others cobalt base

Downloaded 01 Jun 2010 to 171.66.16.59. Redistribution subject to ASME license or copyright; see http://www.asme.org/terms/Terms_Use.cfm

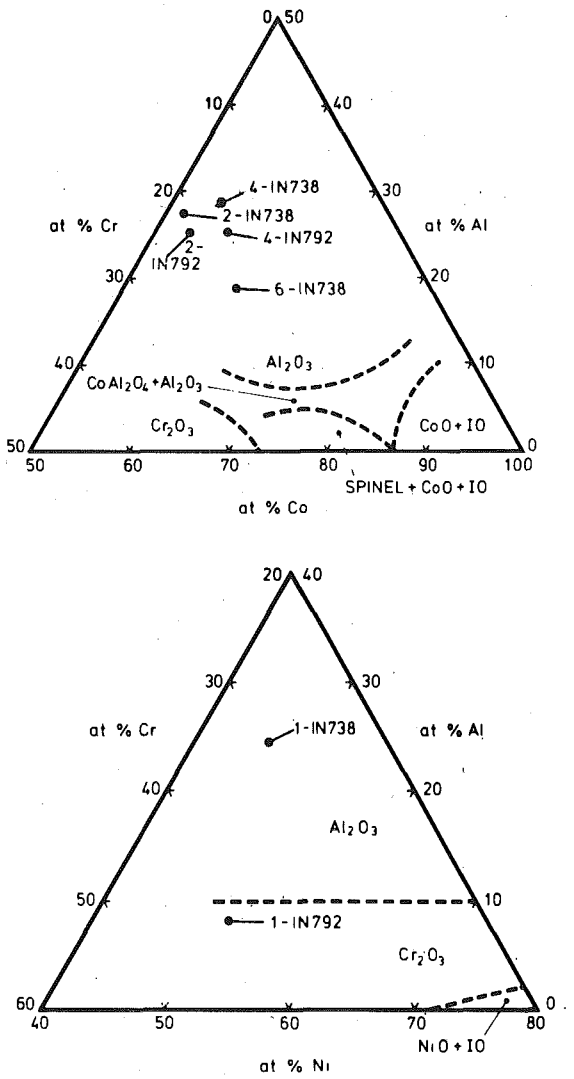

Fig. 11 Ternary diagrams showing oxide compositions for the Co-Cr-Al system (at 1100°C) and the Ni-Cr-Al system (at 1000°C) (see text)—compositions of M-Cr-Al-Y coatings tested superimposed

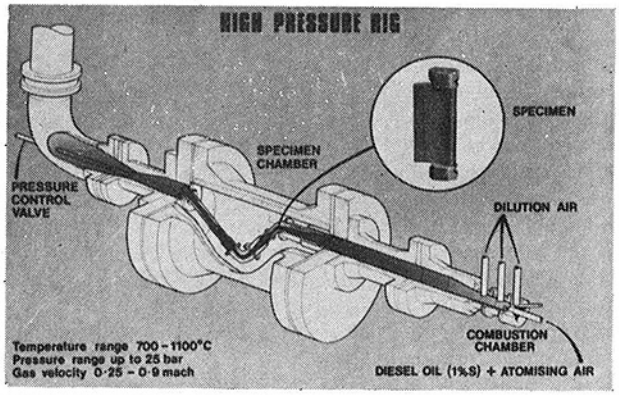

Fig. 12 High pressure corrosion test facility

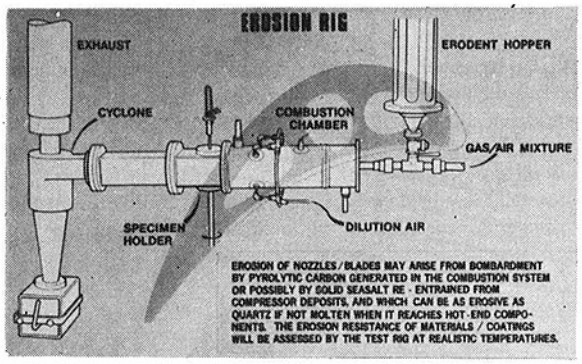

Fig. 13 High velocity, high temperature erosion test rig

A further test run was made at 830°C and the specimens examined after 25, 75, and 200 hr. Specimens tested at 830°C showed less than 30 μm penetration of the coatings as illustrated in Fig. 10.

From the results of the two tests at 750°C and the one at 830°C it was estimated that the approximately 130 μm thick Co-Cr-Al-Y coatings and also Ni-Cr-Al-Y on IN 738 were penetrated after 120 hr at 750°C whereas the Ni-Cr-Al-Y on IN 792 suffered only 50 percent penetration in 200 hr.

The M-Cr-Al-Y coating analyses are shown plotted on the appropriate Co-Cr-Al and Ni-Cr-Al diagrams in Fig. 11, together with the nature of the oxides formed on simple ternary alloys. The oxide regions relate to results at respectively 1000 and 1100°C but the boundaries are unlikely to change much with temperature [8]. This indicates that all of the coatings were alumina formers except for No. 1 on IN 792 which had low aluminium content and hence would be a chromia former. This provides further evidence that chromia formers (cf. high chromium alloys) are most resistant to the low temperature (750°C) form of corrosion and that there is probably a transition in mechanisms somewhere in the range 750 and 800°C since at 830°C alloys forming alumina scales behave well.

Subsequent studies of coating composition have been directed to higher chromium levels and the resistance to corrosion at 750°C appears to improve with increasing chromium level. In practice because of diffusion from very high chromium coatings into the substrate material it is possible that there may be practical limitations on chromium level where coatings are applied to thin wall cooled blades since formation of sigma phase or other topologically close-packed phases could affect creep and other mechanical properties adversely. Plain binary nickel-chromium or cobalt-chromium alloys suffer from spalling of the oxide scale when thermally cycled; and hence to insure surface stability, an addition of some aluminium is advantageous plus an element such as yttrium or zirconium to enhance scale adhesion [9]. The aluminium should be less than required to promote formation of an alumina scale at low temperatures (i.e., below 800°C).

High Pressure Rig. A high pressure rig to permit studies at pressures up to 25 bar has recently been commissioned. This is to enable realistic study of temperature and pressure effects, fluid dynamics, thermal shock and the influence of engine operating mode on corrosion behavior. An impression of the rig is shown in Fig. 12. Specimens are modelled on the nozzle guide vanes of the engine of interest, the walls of the specimen duct being formed to the stream lines. Seawater is injected with the fuel (dieso with up to 1 percent sulphur) but provision is made for ingestion of salt in air if required. Pin specimens can also be exposed in place of the model blade forms and initial studies have been made in this mode. A blank run without added salt on IN 738 pins at 10 bar gave only an oxide scale which was substantially TiO_2. Test runs at 750 and 830°C with 0.2 ppm seawater in the fuel gave similar results to those found with the LP rig at 1 bar pressure, i.e., greater attack at the lower temperature. Additional tests are currently in progress at other pressures and on a range of superalloy materials. It is also the intention to employ the HP rig to study the effect of blade cooling on corrosion behavior and provision has been made to provide adequate cooling air at the correct temperature to simulate the condition of a cooled blade in a real engine.

Erosion

Erosion can occur in gas turbine engines with high energy density

Downloaded 01 Jun 2010 to 171.66.16.59. Redistribution subject to ASME license or copyright; see http://www.asme.org/terms/Terms_Use.cfm

combustion systems due to formation of pyrolytic carbon on burners and flares, etc., the deposits subsequently breaking off and impacting on to the nozzles and turbine blades [10]. Such carbon can lead to erosion of leading edges of first stage turbine blades and may also enhance corrosion due to salt contaminants. There is also some suspicion that sea salt, if unmelted, can also be erosive as well as inducing corrosion and some simple experiments [10] suggested that it may well be as erosive as silica sand. While formation of pyrolytic carbon can be minimized by attention to the combustion conditions, it is not feasible to optimize these for all power levels. Thus even with carbon formation greatly reduced there could still be a problem of erosion after long times of several thousand hours operation.

To anticipate the need for development of erosion-resistant coatings an erosion rig has been installed at AMTE and this is shown in Fig. 13. This is a natural gas-fired burner producing hot, high velocity combustion products to which erosive particles (e.g., alumina) and/or fuel-and-air salt contaminants can be added. Pin specimens identical with those for the LP corrosion rig will be used. It is the intention initially to study erosion of alloys and coatings without salt and sulphur contaminants or carbon. Subsequently erosion by pyrolytic carbon and combined erosion/corrosion by carbon plus sea salt will be investigated. It has been noted that the maximum metal loss on hot corroded components does not necessarily coincide with maximum internal sulphidation. It is hoped to establish if this is due to removal of deposits and corrosion products (and hence the necessary conditions appropriate to sulphidation) or if the sulphidized metal is more easily removed by erosion. The effect could also simply be indicative of a cyclic sulphidation/oxidation mechanism.

Mechanisms

Hot corrosion is a complex process and there is now substantial evidence that it is dependent not only on the nature of the contaminant species and their particular physical form but also temperature and alloy/coating composition. Different mechanisms may be operative depending on alloy composition and temperature range. Many investigators have argued that hot corrosion is due solely to a condensed deposit of sodium sulphate and have proposed that sulphidation occurs due to low oxygen partial pressure under the sulphate deposit at the scale metal interface. It has been demonstrated [11] that once sulphides have formed in the metal then they will persist and migrate inwards under oxidizing conditions. Accelerated or catastrophic oxidation as sometimes occurs has been attributed [12] to acid or basic fluxing in the presence of sodium sulphate.

The investigations at AMTE and the University of Sheffield described earlier in the present paper have established that sodium chloride is not converted instantaneously to sulphate in hot combustion gas containing SO_2 and that salt particles may not evaporate completely or lose their high vapor pressure chloride content in transit through the combustion system. Such substantially unchanged sea salt particles may impact onto hot blades and sulphate in situ or lose chloride by evaporation. Related studies [13] have demonstrated that when sea salt is heated, SO_3 is generated from the sulphate which it contains. This has been related to large negative deviations from ideality for Na_2O in the presence of small amounts of NaCl. In addition, time of flight mass spectrometry has been employed to assess the formation of volatile species when superalloys were heated in the presence of sea salt powder, Na_2SO_4 or Na_2SO_4 + NaCl, at temperatures in the range 700 to 1000°C [6]. It was demonstrated that $CrCl^+$ species formed over alloy and sea salt systems at temperatures as low as 750°C, and that TiS^+ was formed with titanium containing superalloys and sea salt or Na_2SO_4 + NaCl at as low as 705°C. TiS^+ was detected with titanium heated in contact with sea salt, sulphate or sulphate/chloride mixture at 800°C. When TiS_2 powder was heated, the TiS^+ peak was very large at only 494°C indicating the great volatility of titanium sulphide.

Low temperature corrosion of Co-Cr-Al-Y type coatings is believed to be related to formation of eutectic salt mixtures [14] at temperatures around 700°C in the presence of SO_2/SO_3.

It has been shown previously that the presence of chloride even in the vapor phase can produce cracking of scales on superalloys with

Fig. 14(*a*) NaCl 750°C

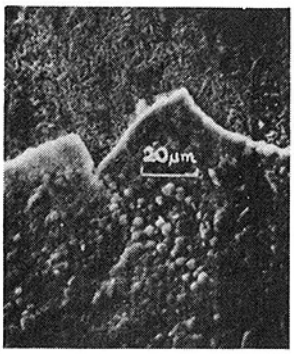

Fig. 14(*c*) Sea salt 850°C

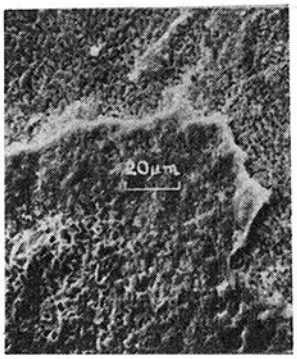

Fig. 14(*b*) NaCl 850°C

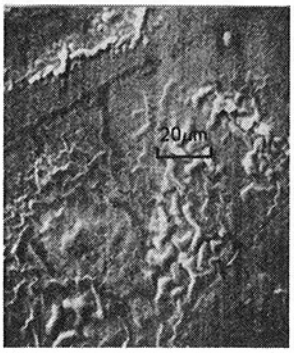

Fig. 14(*d*) Na_2SO_4 850°C

Fig. 14 Surfaces of Nimonic 90 heated for 6.5 hr in contact with NaCl, sea salt and Na_2SO_4 in air

Downloaded 01 Jun 2010 to 171.66.16.59. Redistribution subject to ASME license or copyright; see http://www.asme.org/terms/Terms_Use.cfm

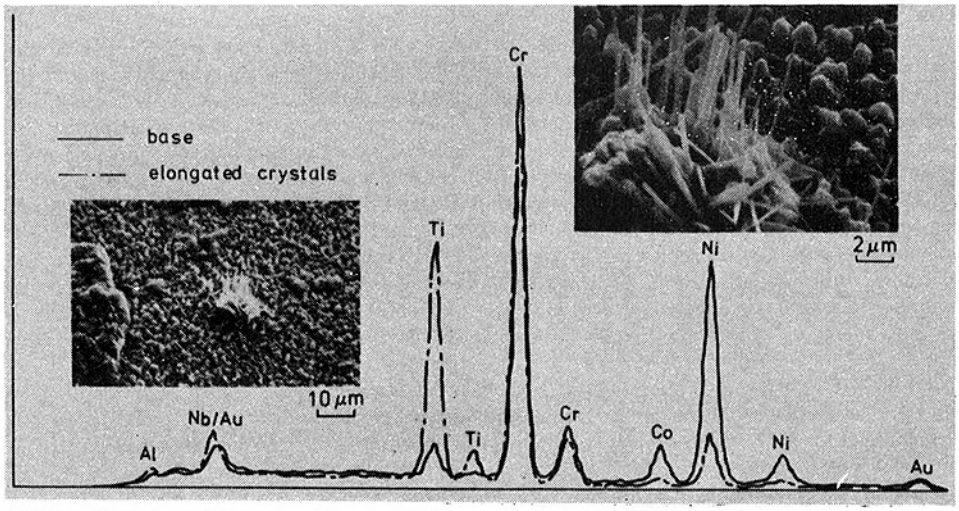

Fig. 15 Crystals of TiO_2 and Cr_2O_3 formed on scale surface on IN 738 preoxidized at 850°C and exposed for 5 min to sea salt vapor in air at 750°C

spalling on cooling. The effects of sodium chloride and sea salt are contrasted with those of sulphate in Fig. 14 which shows Nimonic 90 surfaces heated in contact with these reagents at 750 or 850°C. Other researchers in another related program [15] have demonstrated the significant effect of chloride on the mechanical properties of oxide films.

Recent joint studies by AMTE and Imperial College [6] employing specimens exposed to sea salt vapor in air or $SO_2 + O_2$ which were examined by scanning electron microscopy and EDS analysis have confirmed the formation of crystals of TiO and Cr_2O_3 (Fig. 15) by what are almost certainly vapor deposition mechanisms. The identification by X-ray diffraction of TiO_2 and Cr_2O_3 as separate crystalline species and not a spinel in the scale surface lends support to formation by different routes. Formation of such crystals is accompanied by a reduction in the chromium and titanium levels in the surface of the substrate alloy as shown by EDS analysis. The evidence of volatile species such as TiS^+ and $CrCl^+$ obtained by mass spectrometry at temperatures in the range of 700 to 800°C suggests that reactions such as $Cr + 2HCl = CrCl + H_2$ and $Ti + S_2 = TiS_2$ may be responsible. Since the products are volatile (and escape) quite low K values may still cause appreciable reaction. On reaching an oxidizing environment both the chloride and sulphide species will form oxide, i.e., Cr_2O_3 and TiO_2, thus providing a credible vapor phase transport process leading to enhanced formation of Cr_2O_3 in the presence of chloride and TiO_2 in $SO_2 + O_2$. Titanium sulphides have been detected [16] in hot corroded superalloy specimens from both rig and engine exposures and it has recently been demonstrated that protective oxide scales can be penetrated by SO_2 molecules resulting in the formation of sulphides at the metal/scale interface. If the sulphur activity in the scale is too low to stabilize TiS_2 during its transport through cracks in the scale, then TiO_2 may form at the scale/metal interface underneath the scale and, similarly, apparently vapor-deposited crystals have been observed on the underside of spalled scale.

It has been suggested recently [17] by studies of NiAl oxidized in the presence of traces of NaCl, that aluminium may also be subject to a vapor phase transport process via chloride or some other volatile species. However in mass spectrometer studies [13] on alloys of lower aluminium content no known volatile aluminium species have yet been detected.

The presence of iron in deposits on low pressure rig specimens after exposure taken together with iron detected in deposits on blades from a variety of engines operated in ships, shore trials and power stations [16] lead to interest in the possible effects of iron contamination on hot corrosion. From chemical data and the results of a range of laboratory experiments it was concluded that for temperatures of 750°C and above, iron could exist on surfaces only in the form of oxides. Iron oxides were found to be unreactive with other oxides likely to be

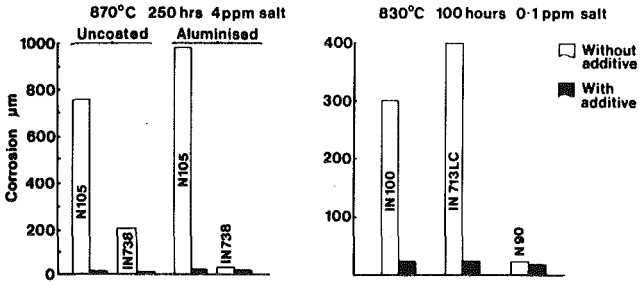

Fig. 16 Results of tests on hot corrosion inhibitor

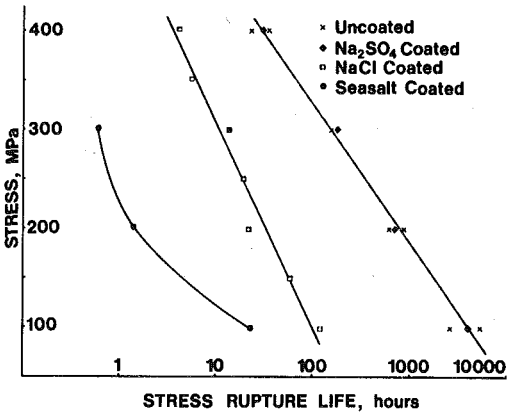

Fig. 17 Stress rupture data on salt-coated Nimonic alloy 90 specimens at 750°C

present at such surfaces. $FeCl_3$ and $FeSO_4/Na_2SO_4$ were found to react with Nimonic 90; but as the iron chloride and sulphate, respectively, volatilize and decompose at temperatures below those occurring in the engine, it is unlikely that they will be able to influence the corrosion mechanism significantly except if they impact on particulate matter on the hot surfaces or if $FeCl_3$ reacts in the vapor phase. The optimum temperature range for iron and chromium oxides to catalyze the reaction $2SO_2 + O_2$ $2SO_3$ is 450 to 500°C. Thus idling and low power operation might favor such catalytic increase in SO_3 levels.

It is known from studies of the effect of alloy composition on hot corrosion behavior that increasing the chromium level and raising the Ti/Al ratio both have beneficial effects in improving overall resistance.

Downloaded 01 Jun 2010 to 171.66.16.59. Redistribution subject to ASME license or copyright; see http://www.asme.org/terms/Terms_Use.cfm

The effect of chromium has been related [18] to its influence on "oxide ion" activity in the instance of Na_2SO_4 since Cr_2O_3 has the effect of decreasing the Na_2O activity. Contemporary studies at AMTE showed that Cr_2O_3 was effective in suppressing the effect of not only Na_2SO_4 but also NaCl and sea salt. Additions of expendable Cr_2O_3 using plasma spray deposits, decomposition of ammonium dichromate or preoxidation showed that sacrificial Cr_2O_3 provided protection from NaCl. Rig tests were carried out to establish whether chromium containing organic additives in fuel could inhibit hot corrosion due to sea salt ingestion. Results are shown in Fig. 16 and demonstrate that such additions can be effective in reducing corrosion. The additions are not so completely effective if corrosion has already started.

Environmental Effects on Creep

Conventional creep and stress-rupture data are derived from tests carried out under conditions of simple oxidation in air. Thus it was considered essential to establish whether the presence of salt contaminants in the hot combustion environment in the marine gas turbine might lead to deterioration of creep or stress-rupture properties over and above that due to purely loss of section due to corrosion. Initially tests were made [19] on a 20 percent chromium alloy Nimonic 90 which has fairly good corrosion resistance since it was considered that should such a material show a significant effect than the stronger, lower chromium, alloys might be expected to show the effect in greater degree. Specimens were coated with Na_2SO_4, NaCl and sea salt employing coatings of about 1 mg/mm^2. The results of tests at 750°C are shown in Fig. 17. Na_2SO_4 had no effect but NaCl led to a significant reduction in rupture life and sea salt produced an even greater effect. Further studies are in progress to investigate the effect on current superalloys such as IN 738, IN 792, IN 939 etc., and in addition to identify whether it is likely to be significant at the deposit composition levels likely to apply in real engines. Deposits from specimens exposed to corrosion test rig conditions [16] indicated sulphate to be present with cations Na:Mg:Ca in the ratio 4:2:1 (seawater ratio 35:4:1) and chloride:sulphur 1:1000, i.e., enrichment in Mg and Ca compared with sea salt and loss of Na and chloride. This general trend may be characteristic of the bulk composition of long residence deposits sustained by the dynamic equilibrium and competing processes of impaction, condensation, sulphation, decomposition, evaporation and reaction with the oxide/metal surface. Data given earlier on the persistance of chloride in deposits at high temperatures also suggest that the equilibrium chloride level may be higher than revealed by historic deposits which may have lost chloride during cooling.

To date, no dramatic short-life failures due to accelerated creep or stress-rupture have been identified in engines in service. However, it is still necessary to obtain a realistic assessment of possible effects in the longer term.

Discussion and Concluding Remarks

While gas turbines have been employed in the Royal Navy at sea since the early 1950's it is only since 1973 that new major surface vessels have been dependent on the gas turbine as the sole means of propulsion. Earlier uses of the gas turbine for propulsion had been mainly the employment of the marinized PROTEUS aero-type gas turbine for fast petrol boats and the industrial G6 engine for boost propulsion in combined steam and gas turbine (COSAG) plants of some 15 destroyers and frigates [20]. Since 1973, gas turbines installed for propulsion have been of the marinized aero-type.

Based on accrued experience at sea it has been possible to foresee the potentially damaging effects of hot corrosion in the marine environment and to take steps such as the use of air and fuel filtration, compressor washing, more corrosion resistant nozzle and blading alloys and coatings to ensure that corrosion is not a factor which controls time between overhauls (TBO). The need to enhance efficiency and to further increase TBO requires that research on improving corrosion control must continue.

Progress to an understanding of the factors which control the environment in the engine is continuing along the lines detailed in the initial sections of this paper. To date, significant progress has been achieved in understanding the short residence chemistry of contaminants and deposits and this has led to a better appreciation of the factors which influence the corrosion behavior of alloys and coatings and the mechanisms which may be operating. Mechanistic studies have cast light on the significance of alloying elements and the balance of composition in relation to corrosion morphology and the extent of corrosion as a function of temperature. Corrosion at low temperatures in the range up to about 750°/800°C differs in form of attack and probably in mechanisms from the apparently less aggressive attack found with certain alloys at above 800°C. The data on persistence of chloride and generation and survival of particulate salt suggest that these differences may be related, at least in part, to the level of chloride which is present since chlorides may be short-lived at higher temperatures due to high volatility. Undoubtedly chlorides (either as volatile NaCl or HCl) will be present in the gas phase at all temperatures and will modify behavior in the presence of condensed sulphate. Low temperatures may also favor the formation and stability of sulphides and hence this may be a further factor in enhancing corrosion effects at around 700°/750°C. Low temperature attack on Co-Cr-Al-Y coatings has been attributed [14] to low melting eutectic salt mixtures associated with $CoSO_4$, decomposition of which may occur in the range 700 to 720°C in a pressurized combustion environment with up to about 1 w/o sulphur. The decomposition temperature can vary depending on the SO_2 and SO_3 partial pressures. However, this does not account entirely for the apparent effect of aluminium level on corrosion behavior.

Studies at AMTE(HH) employing the high pressure corrosion test facility at 750 and 850°C and 10 bar pressure when compared with results from the AMTE low pressure rig and other low pressure high and low velocity test rigs in the UK have focused attention on the importance of the sulphur content of the fuel in relation to low temperature corrosion. Differences in behavior of materials and coatings in different test rigs and engines have been suggested [21] as being in part related to various sulphur levels in the fuels employed. AMTE rigs employ dieso fuel with around 1.0 percent sulphur whereas many other rigs use fuel with around 0.3 percent sulphur and are not able to reproduce the low temperature corrosion morphology often found in marine engines in service and apparently faithfully simulated in the AMTE test rigs. Re-examination of results obtained by Schirmer and Quigg [22] suggests that higher sulphur levels (e.g., 0.4 percent) result in enhanced corrosion at low temperatures in the presence or absence of sea salt. In analyzing their own data Schirmer and Quigg only considered the effect of reducing sulphur level and did not point out that at higher sulphur levels low temperature corrosion was more aggressive than that at higher temperatures. It is apparent that the relationships between sea salt and sulphur effects are complex. In view of this, as close modelling as possible of the realistic engine conditions in terms of salt ingestion level (or flux rate) and sulphur in the fuel is essential if test rigs are to produce valid data.

Certain directions for alloy and coating modification to improve corrosion behavior are now apparent: e.g., the use of higher chromium levels and intermediate aluminium levels plus high Ti/Al ratio in superalloys. However there remains the need to investigate erosion and combined corrosion/erosion behavior in greater detail and to investigate the potential effects of salt contaminated combustion environments on creep behavior. Progress achieved to date provides confidence that adequate control of corrosion in marine gas turbines can continue to be achieved in the future.

Acknowledgments

The contributions of colleagues and contractors who have contributed information and assistance are acknowledged gratefully.

References

1 Hanby, V. I., "Sodium Sulphate Formation and Deposition in Marine Gas Turbines," Paper No. 73-WA-CO-2, *ASME Winter Annual Meeting*, Detroit, Nov. 11, 1973.

2 Hunt, A., and Randle, N. C., "The Trajectories of Spherical Particles in Flow Through Cascades of Vanes," Rept. No. 220, Dept. of Aeronautical

Downloaded 01 Jun 2010 to 171.66.16.59. Redistribution subject to ASME license or copyright; see http://www.asme.org/terms/Terms_Use.cfm

Engineering, University of Bristol, June 1978.
3 McCreath, C. G., unpublished work under MOD Contract, University of Sheffield, 1972–1979.
4 McCreath, C. G., "The Role of Evaporation of Ingested Salts in Hot Corrosion Mechanisms of Gas Turbines," *Transactions Institute of Marine Engineers,* Vol. 88, 1976, p. 145.
5 Jacques, M. T., Jordan, J. B., and Williams, A., *Deuxieme Symposium European sur la Combustion,* Orleans, France, Paper No. N 68, Sept. 1, 1975.
6 Condé, J. F. G., Birks, N., Hocking, M. G., and Vasantasree, V., unpublished work MOD 1979.
7 Grant, G., and Tabakoff, W., "Erosion Prediction in Turbomachinery Resulting from Environmental Solid Particles," *Journal of Aircraft,* Vol. 12, No. 5, May 1975, p. 471.
8 Whittle, D. P., Private Communication.
9 Whittle, D. P., and Strafford, K. N., unpublished work under MOD Contract at University of Liverpool and Newcastle-Upon-Tyne Polytechnic.
10 Restall, J. E., *Proceedings of 1974 Gas Turbine Materials in a Marine Environment Conference,* Castine, Maine, MCIC-75-27, pp. 195–218.
11 Spengler, C. J., and Viswanathan, R., "Effect of Sequential Sulphidation and Oxidation on the Propagation of Sulphur in an 85 Ni-15 Cr Alloy," *Mettalurgic Transactions,* Vol. 3, Jan. 1972, pp. 161–166.
12 Goebel, J. A., and Pettit, F. S., *Metal Slag Gas Reactions and Processes,* Toronto 1975, Ed. Foroulis, Z. A., and Smeltzer, W. W., Electrochemical Society, p. 693.
13 Hocking, M. G., and Vasantasree, V., unpublished work under MOD Contract.
14 Aprigliano, L. F., Private Communication D T NSRDC, Annapolis, Md.
15 Hancock, P., *Proceedings of 1974 Gas Turbine Materials in a Marine Environment Conference,* Castine, Maine, MCIC-75-27, pp. 225–236.
16 Taylor, A. F., unpublished work MOD, AMTE,
17 Smeggil, J. G., and Bornstein, N. S., The Effect of NaCl(g) on the Oxidation of NiAl. *Journal of Electrochemical Society,* Aug. 1978, Vol. 125, No. 8, pp. 1283–1290.
18 Bornstein, N. S., and De Cresente, M. A., "The Role of Sodium in the Accelerated Oxidation Phenomenon Termed Sulphidation," *Mettalurgic Transactions,* Vol. 2, October 1971, pp. 2873–2883.
19 Galsworthy, J. C., unpublished work MOD, AMTE.
20 Shaw, T. R., and Jefferis, T., Gas Turbines in the Royal Navy 1974 to 1976. *ASME 21st Annual Gas Turbine Conference,* New Orleans, Mar. 23, 1976.
21 Booth, G. C., unpublished work MOD, AMTE.
22 Schirmer, R. M., and Quigg, H. T., ASTM STP421, 1967, pp.270–296.

Downloaded 01 Jun 2010 to 171.66.16.59. Redistribution subject to ASME license or copyright; see http://www.asme.org/terms/Terms_Use.cfm

C. G. Annis, Jr.
Mem. ASME

M. C. VanWanderham
J. A. Harris, Jr.
D. L. Sims
Mem. ASME

Materials and Mechanics Technology Lab.,
Pratt & Whitney Aircraft,
Government Products Division,
West Palm Beach, Fla

Gas Turbine Engine Disk Retirement-for-Cause: An Application of Fracture Mechanics and NDE

Historically, gas turbine engine disks are retired when they accrue an analytically determined lifetime where the first fatigue crack per 1000 disks could be expected. By definition then, 99.9 percent of these components are being retired prematurely. Retirement-for-cause (RFC) is a procedure, based on fracture mechanics, which would allow safe utilization of the full life capacities of each individual disk. Since gas turbine disks are among the most costly of engine components, adopting a RFC philosophy could result in substantial systems life cycle cost savings. These would accrue from reduced replacement costs, conservation of strategic materials such as cobalt, and energy savings.

Introduction

Historically, methods used for predicting the life of gas turbine engine rotor components have resulted in conservative underestimation of useful life. Most rotor disks are limited by low cycle fatigue, generally expressed in terms of mission equivalency cycles. When some predetermined cyclic life limit is reached, disks are retired from service. These cyclic life limits are established by a statistical analysis of data indicating the cyclic life at which 1 in 1000 disks will have a fatigue-induced crack of approximately 0.03 in. length. It has been documented that many of the 999 remaining disks, which are also retired at the same time, have considerable useful residual life. Retirement-for-Cause provides a Fracture Mechanics based procedure for screening the one bad part and certifying the remaining 99.9 percent for additional safe engine service.

Methodology

Retirement-for-Cause Philosophy. The fatigue process can be visualized as illustrated in Fig. 1. Total fatigue life consists of a crack initiation phase followed by growth and linkup of microcracks. The resulting macrocrack(s) would then propagate subcritically until the combination of service load (stress) and crack size exceeded the material fracture toughness. Catastrophic failure would result had not the component been retired from service. To preclude such cataclysmic disk (and possibly engine) failures, disks are typically retired at the time where 1 in 1000 could be expected to have actually initiated a short (0.03 in.) fatigue crack. By definition, then, 99.9 percent of the retired disks still have useful life remaining therein at the time they are removed from service. Under the "retirement-for-cause" philosophy, each of these disks could be inspected and returned to service. The return-to-service (RTS) interval is determined by a fracture mechanics calculation of remaining *propagation* life from a crack just small enough to have been missed during inspection. This procedure could be repeated until the disk has incurred measurable damage, at which time it is retired for that reason (cause). Retirement-for-cause is, then, a methodology under which an engine disk would be retired from service when it had incurred quantifiable damage, rather than because an analytically determined minimum design life had been exceeded. Its purpose is *not* to extend the life of a rotor disk, but to utilize safely the full life capacity inherent in each component.

Disks Have Residual Life. For simplicity, this paper will consider component fatigue life limits to be determined from the crack initiation characteristics of the specific disk material, and will not address the problem of intrinsic crack-life defects.

Current low-cycle fatigue (LCF) life prediction methods for gas turbine rotor disks have proven satisfactory from the safety and reliability standpoints. These methods, however, have resulted in conservative underestimations of disk life.

All fatigue data have inherent scatter. The data base used for design life prediction purposes must be applicable to all disks of a given material, and therefore includes test results from many heats and sources. Data are treated statistically as shown schematically in Fig. 2. The distribution of life, defined as the number of cycles necessary to produce a crack approximately 0.03 in. long, is obtained for a given set of loading conditions (stress/strain, time, temperature). As can be seen the $\pm 2\sigma$ bounds, which contain 95 percent of the data, may span two orders of magnitude in fatigue initiation life.

When considered with other uncertainties in any design system (e.g., stress analysis error, field mission definition, fabrication deviations, temperature profile uncertainty) the final disk life prediction is made for disk crack initiation life for an occurrence rate of 1 in 1000 disks. It is at this life that all LCF-limited disks are removed from service. This procedure has been very successful in preventing the occurrence of catastrophic failure of disks in the field. However, in retiring 1000 disks because one may fail, the remaining life of the 999 unfailed disks is not utilized. The amount of usable life remaining can be significant, as shown in Fig. 3, where over 80 percent of the disks have at least ten lifetimes remaining.

Contributed by the Gas Turbine Division of The American Society of Mechanical Engineers and presented at the Gas Turbine Conference and Products Show, New Orleans, La., March 10–13, 1980. Manuscript received at ASME Headquarters December 27, 1979. Paper No. 80-GT-127.

Copyright © 1981 by ASME

Downloaded 01 Jun 2010 to 171.66.16.59. Redistribution subject to ASME license or copyright; see http://www.asme.org/terms/Terms_Use.cfm

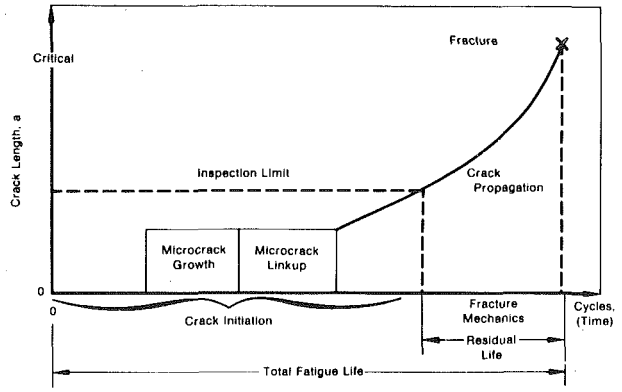

Fig. 1 Total fatigue life segmented into stages of crack development, subcritical growth, and final fracture

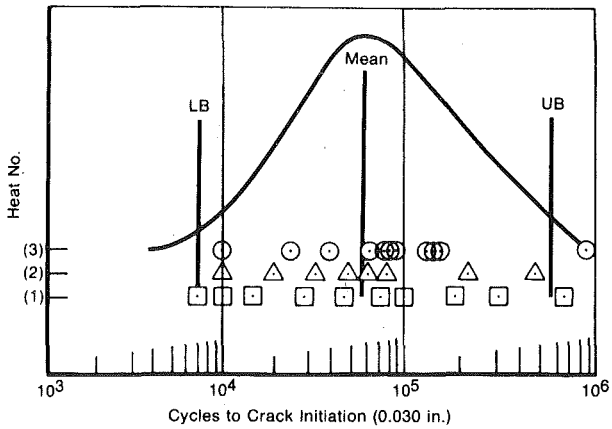

Fig. 2 Material data scatter results in conservative life prediction

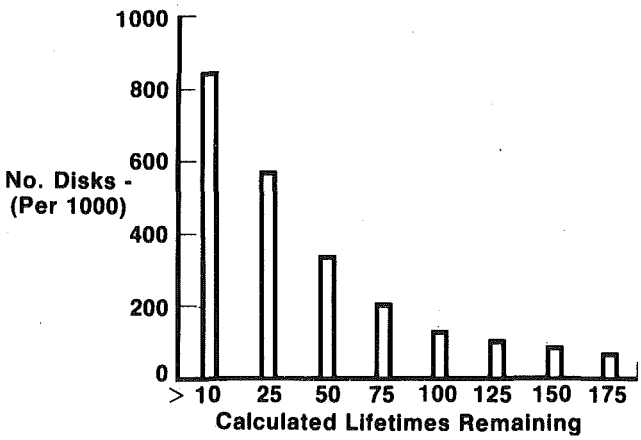

Fig. 3 The majority of disks have useful life after retirement

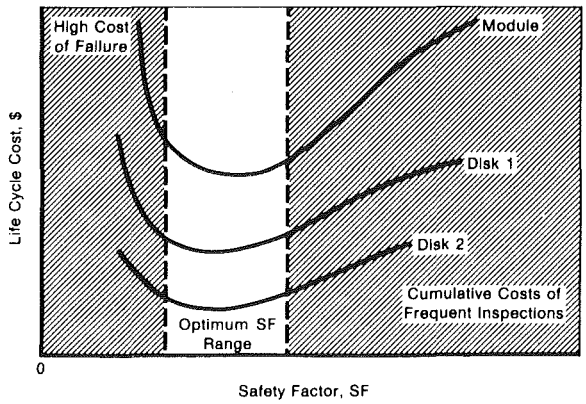

Fig. 4 'Safety factor is determined from an economic balance between high cost of failure versus cumulative costs of frequent inspections

The means of extracting the remaining useful life from each disk must be safe to avoid catastrophic failure. This is done by determining the disk crack propagation life (N_p) (at every critical location) from a defect barely small enough to be missed during inspection. The return-to-service (RTS) interval is then calculated by conducting a life cycle cost (LCC) analysis to determine the most economical safety factor (SF) to apply to N_p (RTS interval = N_p/SF). Cost versus SF is plotted for each individual disk and combined to determine the most economical interval to return a module and/or engine for inspection. An example is shown in Fig. 4.

The first required disk inspection is near the end of the analytically determined crack initiation life. Only one disk in 1000 inspected should have a crack and be retired. The other 999 will be returned to service for the calculated RTS interval. This inspection is repeated at the end of each RTS interval with the cracked disks being retired and all others returned to service. Figure 5 illustrates how the residual life is extracted from each disk after the crack initiation life has been used.

Required Technology

As Fig. 5 illustrates, return to service intervals are based on two broad technologies: nondestructive evaluation (NDE) and applied fracture mechanics.

Fracture mechanics must provide an assessment of the behavior of a cracked part should it pass NDE with a defect just below the inspection limit. To assure safe return to service of a part which *may* contain a small crack, an accurate crack propagation prediction is imperative. Recent strides in applied elevated temperature fracture mechanics [1–4] have provided the necessary mathematical description (models) of basic propagation, i.e., crack growth under conditions of varying loading frequency (ν), stress ratio (R), and temperature (T). Further work [5, 6] has expanded this capability to include loading spectra synergism, i.e., crack growth subjected to (frequent) periodic major load excursions separated by a small number (10–50) of varying subcycles. It is important to note that a typical mission loading spectrum to which gas turbine engines are subjected bears little resemblance to that experienced by air frames, and therefore different predictive tools are required for each [7].

Referring again to Fig. 5, it is seen that accurate propagation predictions constitute a necessary, but not sufficient, condition for the implementation of retirement for cause. The other requisite technology is high reliability nondestructive evaluation (NDE).

NDE must provide the means of screening disks with flaws that could cause component failure within an economically feasible RTS interval. A deterministic fracture mechanics method defines a maximum flaw size that can be missed without an in-service failure. An appropriate safety factor (SF) is applied to obtain the required NDE reliability (shorter RTS intervals and more frequent inspections). A probabilistic fracture mechanics life analysis [8, 9] uses a probability distribution of flaw sizes. This analysis shows failure probability as a function of time (includes NDE reliability). This allows selection of an RTS interval to obtain a sufficiently low failure probability (and sufficient NDE reliability).

Both the deterministic and probabilistic methods described above provide some of the NDE reliability through multiple inspections and partly through higher NDE limits due to shorter RTS intervals and higher SF. Since many NDE errors are the result of human frailty, the multiple inspections enhance detection reliability provided the same inspectors are not used in the repetitive inspections, the system is not automated, and the cause of the errors is not due to inspection techniques, flaw orientation, etc. If the system is automated or the flaw is missed due to orientation, a second inspection will miss the flaw for the same reasons and no increase in reliability is obtained.

Insufficient NDE reliability has been the major argument against implementation of a RFC maintenance program. NDE capability with acceptable flaw detection resolution has been available for some time

Downloaded 01 Jun 2010 to 171.66.16.59. Redistribution subject to ASME license or copyright; see http://www.asme.org/terms/Terms_Use.cfm

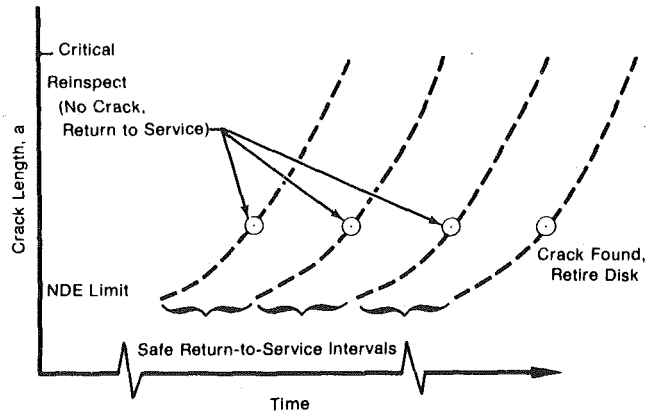

Fig. 5 Base retirement for cause concept

[10, 11], but adequate reliability of flaw detection has been lacking [12]. Complementary inspections and recent improvement in NDE single inspection reliability (by automation), can now provide the required reliability for many gas turbine engine components to economically utilize the RFC maintenance concept.

The retirement for cause (RFC) flow chart (Fig. 6) illustrates a simplified view of how this maintenance concept would be utilized. When an engine is returned for maintenance, an economic analysis is performed on the engine module (i.e., fan, compressor, high turbine, or low turbine) previously identified as a participant in the RFC maintenance program. If the module has already been in service for several inspection intervals, the probability of finding cracked parts may be great enough to make reinspection economically undesirable and the module is retired without being inspected. This is determined by the economic analysis at decision point one (Fig. 6) and is one of three possible decisions. An unscheduled engine return (UER) may being a module out of service that is more economical to return to service for the remainder of its inspection interval than to inspect and recertify it for a new full interval (the second possible decision at point one). The remaining choice at point one is to tear down the module and inspect the parts. During inspection there again are three possibilities (decision point two). If no crack is found, the part is returned to service. If the disk is found to be unsafe, it is retired. The third choice is to investigate modification or repair of a flawed part. An economically repairable part may be repaired and returned to inspection (decision point three).

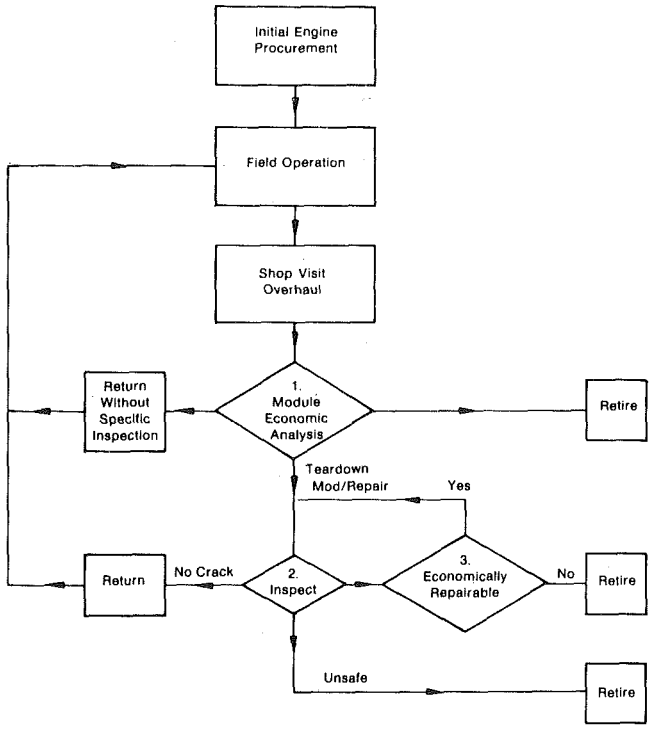

Fig. 6 Retirement for cause flowchart

Summary

Total fatigue life of a component consists of a crack initiation phase and a crack propagation phase. Engine rotor component initiation life limits are analytically determined using lower bound (1 occurrence in 1000) LCF characteristics. By definition, then, 99.9 percent of the disks are being retired prematurely. Retirement for cause would allow each component to be used to the full extent of its safe total fatigue life, retirement occurring when a quantifiable defect (as determined by nondestructive evaluation techniques-NDE) necessitates removal of the component from service. The defect size at which the component is no longer considered safe is determined through fracture mechanics analyses of the disk material and the disk fracture critical locations, the service cycle and the overhaul/inspection period. Realization and implementation of a retirement for cause methodology will result in system cost savings of two types: direct cost savings resulting from utilization of parts which would be retired and consequently require replacement by new parts; and indirect cost savings resulting from reduction in use of strategic materials, reduction in energy requirements to process new parts and mitigation of future inflationary pressures on cost of new parts.

References

1 Annis, C. G., Wallace R. M., and Sims, D. L., "An Interpolative Model for Elevated Temperature Fatigue Crack Propagation," AFML-TR-76-176, Part I, Nov. 1976, presented at 1977 SESA Spring Meeting, Dallas, TX, May 1977.

2 Wallace, R. M., Annis, C. G., and Sims, D. L., "Application of Fracture Mechanics at Elevated Temperatures," AFML-TR-76-176, Part II, Nov. 1976, presented to Air Force Materials Laboratory, WPAFB, OH, May 1977.

3 Sims, D. L., Annis, C. G., and Wallace, R. M., "Cumulative Damage Fracture Mechanics at Elevated Temperature," AFML-TR-76-176, Part III, Nov. 1976.

4 Sims, D. L., "Evaluation of Crack Growth in Advanced P/M Alloys," AFML-TR-79-4160, Sept. 1979.

5 Larsen, J. M., Annis, C. G., Jr., "Observation of Crack Retardation Resulting from Load Sequencing Characteristic of Military Gas Turbine Operation," presented at ASTM Symposium on Effects of Load Spectrum Variables on Fatigue Crack Initiation and Propagation, San Francisco, CA, May 1979.

6 Larsen, J. M., Schwartz, B. J., Annis, C. G., Jr., "Cumulative Damage Fracture Mechanics Under Engine Spectra," AFML-TR-79-4159, Sept. 1979.

7 Annis, C. G., Jr., "An Engineering Approach to Cumulative Damage Fracture Mechanics in Gas Turbine Disks," presented at ASME Gas Turbine Conference, San Diego, CA, Mar. 1979.

8 Annis, C. G., Jr., Haake, F. K., Sims, D. L., "Probabilistic Fracture Mechanics and Retirement-for-Cause," P&WA internal communication, to be submitted for external publication.

9 Rau, C. A., Jr., "The Impact of Inspection and Analysis Uncertainty on Reliability Prediction and Life Extension Strategy," presented at ARPA/AFML Quantitative Nondestructive Evaluation, San Diego, CA, July 1978.

10 Hyzak, J. M., Allison, J. E., Reimann, W. H., "Development of Quantitative NDI for Retirement-for-Cause," AFML-TR-78-198, Feb. 1979.

11 Cargill, J. S., Malpani, J. K., Cheng, Y. W., "Disk Residual Life Studies," AFML-TR-79-123, Sept. 1979.

12 Lewis, W. H., "Reliability of Nondestructive Inspections," SAALC/MME 76-6-38-1, Dec. 1978.

Downloaded 01 Jun 2010 to 171.66.16.59. Redistribution subject to ASME license or copyright; see http://www.asme.org/terms/Terms_Use.cfm

N. A. Mitchell[1]
Whittle Laboratory,
Cambridge University,
England

Nonaxisymmetric Blade Row Interaction in Axial Turbomachines

A three-dimensional nonaxisymmetric theory is presented to analyze the interaction effects due to wakes between two blade rows in an axial turbomachine. The relative importance of potential and wake interaction with varying row separations and the contribution to the flow of shed radial and shed streamwise vorticity from the first row are examined. Numerical calculations of turbine and compressor stages are presented to illustrate the theory.

Introduction

This analysis uses the following model to analyze a turbomachine stage (two blade rows) situated in an infinite annular duct (Fig. 1).

1 An upstream blade row represented by a set of radial lifting lines. Far upstream of this row the flow is axial and uniform.
2 A downstream row represented by an actuator disk. The circumferentially nonuniform flow from the upstream blade row is incident on this.

The use of an actuator disk to represent the downstream row effectively removes any problems associated with unsteady flow. A rotating coordinate system fixed to the first blade row is used, so that in this system the first row is always stationary. The following restrictions are placed on the flow: (1) incompressible, inviscid flow; (2) the primary flow is free vortex. Any perturbations from this state are small.

The object of the analysis is to find a complete three-dimensional solution to the nonaxisymmetric flow associated with this stage. It is intended to model the wakes due to the shedding of the upstream blade boundary layers by a redistribution of stagnation pressure imposed on the flow after each lifting line.

Background

The background of this wake theory can be described in terms of a combination of two established approaches: (1) lifting line theory [2, 6] and (2) nonaxisymmetric actuator disk theory [1, 4, 5].

Lifting line theories, which have been developed over the past few years, may be considered as an extension from well known axisymmetric actuator disk theory [8]. In actuator disk theory, the blade row is represented by a disk, which is in effect a distribution of bound (radial) vorticity over an annular disk, representing an infinite number of closely spaced blades. In lifting line theory the individual blades are each represented by a single "lifting line" of bound vorticity. In both theories the bound vorticity distribution can be non-uniform across a blade span, so that sheets of (streamwise) vorticity are shed into the flow from the blades. Lifting line theory enables the nonaxisymmetric nature of this flow to be investigated [7].

The general approach used is to consider that the nonaxisymmetric effects are small compared with the mean flow. This then allows heavily loaded blade row rows to be treated, an improvement over earlier analyzes limited to lightly loaded rows [10]. The nonaxisymmetric small perturbation flow can then be analyzed by use of the Clebsch transformation method [3]. This approach has been used in [2] for the case of a heavily loaded rectilinear cascade in incompressible flow, and extended to the annular case in [6] (although the solution to the differential equations given by Cheng in [6] is incorrect—the inhomogeneous solution given is a function only of r (radius), whereas it should be a function of r and z (axial distance), which leads to important three-dimensional effects [4]). It has been correctly applied to the wake flow from an isolated blade row by Tan [1]. Various extensions of the method to compressible flow have also been performed [9].

The development of nonaxisymmetric actuator disk theory has followed two different paths. In 1963 Dunham [5] developed a nonaxisymmetric three-dimensional theory of this form by linearizing the flow equations about a free vortex mean flow. However, the solution of the resulting flow equations using the appropriate boundary conditions across the disk proved too complex at that time, and the analysis was simplified to consider a rectilinear cascade. More recently Hawthorne, McCune, et al. [4] applied the Clebsch transformation already used for lifting line theory, to three-dimensional flow in actuator disks. The nonaxisymmetric flow was considered to be a small perturbation from the free vortex condition. Similar results to Dunham's were obtained, but in this case the equations proved solvable using modern computers.

Here this nonaxisymmetric actuator disk theory has been extended so that the nonaxisymmetric flow can be considered to be due to an upstream annular cascade of lifting lines, applying the Clebsch transformation method to both. Thus it will be shown how it becomes possible to calculate the interaction effects between two blade rows. This interaction is an example of a case where a simpler two-dimensional nonaxisymmetric theory (i.e., a strip theory) will totally fail to

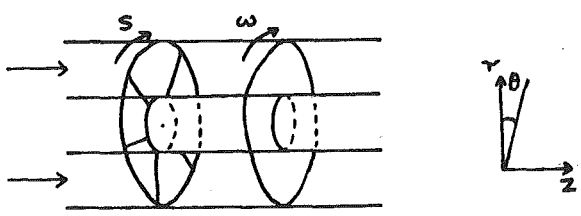

Fig. 1

[1] Now at Mechanical Engineering Laboratory, GEC, Whetstone, Leicester, England.

Contributed by the Gas Turbine Division of THE AMERICAN SOCIETY OF MECHANICAL ENGINEERS and presented at the Gas Turbine Conference and Products Show, New Orleans, La., March 10–13, 1980. Manuscript received at ASME Headquarters January 2, 1980. Paper No. 80-GT-133.

Copyright © 1981 by ASME
Downloaded 01 Jun 2010 to 171.66.16.59. Redistribution subject to ASME license or copyright; see http://www.asme.org/terms/Terms_Use.cfm

predict the more important features of the flow, due to its inability to calculate the correct pressure fields around the blade rows [1, 4].

Vorticity Modeling in the Flow

The interaction between the rows may be considered to be due to two effects: (1) The first row sheds vorticity into the flow. This vorticity is swept downstream and is incident on the second. (2) A potential flow interaction, due to the presence of the first row influencing the flow at the second, and the presence of the second row influencing the flow at the first.

These two effects are interconnected and cannot be analyzed separately. The method used in this analysis is to specify the behavior of the vorticity, and then find the resulting potential flow.

The first blade row is considered to shed two types of vorticity into the flow, from two independent effects: (1) At the blade trailing edge the blade boundary layers are shed into the flow. This results in a stagnation pressure defect in the flow behind each upstream blade (the wake behind each blade is actually a narrow region of intensely turbulent flow) which decays and spreads out behind the blades. This decay cannot be represented in this theory. The vorticity is considered to be initially purely radial. (2) There is the possibility of streamwise vorticity being shed into the flow due to nonuniform spanwise loading of the blades.

The initial vorticity is convected downstream by the flow and is incident on the downstream row. The downstream blades shed two types of additional vorticity into the flow. There is a streamwise component owing to the spanwise variations in lift along each blade and a radial component due to two effects. One component of the radial vorticity results from the unsteady lift experienced by each blade as it moves in a pitchwise direction, and the other from the blade boundary layers being shed into the flow.

In an annulus there is an additional complication due to the effects of swirl, as illustrated in Fig. 2. The initially radial vortex filament from an upstream blade is convected around the circumference at different rates according to the radius. This distorts the vortex filament and creates a tangential vorticity component. The vortex filament finally incident on the next row can stretch across several blade passages. This effect is also present downstream of the second row.

Theory

This theory assumes that the wake is a small three-dimensional perturbation from the free vortex condition. This allows the use of the small perturbation approximations as discussed in reference [3]. The vorticity in the flow is small (i.e., of 0 (ϵ)). The velocity can be divided into three components, a "primary" free vortex flow of 0(1), $\boldsymbol{V}_{FV}$, and two components of 0 (ϵ), $\mathbf{v}$, the nonaxisymmetric component with a circumferential average of zero, and $\mathbf{v}_{AX}$ the axisymmetric component.

Thus $\boldsymbol{W} = \boldsymbol{W}_{FV} + \mathbf{v} + \mathbf{v}_{AX}$, and $\boldsymbol{W}_{FV}$ is this free vortex primary flow relative to the upstream row. (γ represents the radius.)

$$\boldsymbol{W}_{FV} = \boldsymbol{V}_{FV} - \gamma s$$

It can be shown using small perturbation theory that the vorticity in the flow can be considered to be convected by the primary flow. The stagnation pressure relative to the upstream row is constant along a streamline of this primary flow.

It will be convenient later in the analysis to divide the annulus into three regions, denoting each by a subscript: u = upstream of the blade rows; d = between the blade rows; dd = downstream of the blade rows.

It is appropriate at this stage to define the losses occurring at each blade row. The stagnation pressure losses at the upstream blades may be divided into two components. (1) A total pressure loss ΔP_{OALS} which is the averaged loss over the annulus at the first row, relative to this first row. (2) A circumferential variation of stagnation pressure due to the presence of the individual blade wakes, expressed as a Fourier series, so that

$$\left(\frac{P_o{}^d - \overline{P}_o{}^d}{\rho V_2{}^2{}_{FV}}\right)_* = \sum_{n=1}^{\infty} P_n{}^d e^{in\beta\theta} \quad (\overline{P}_o{}^d = \overline{P}_o{}^u - \Delta P_{OALS})$$

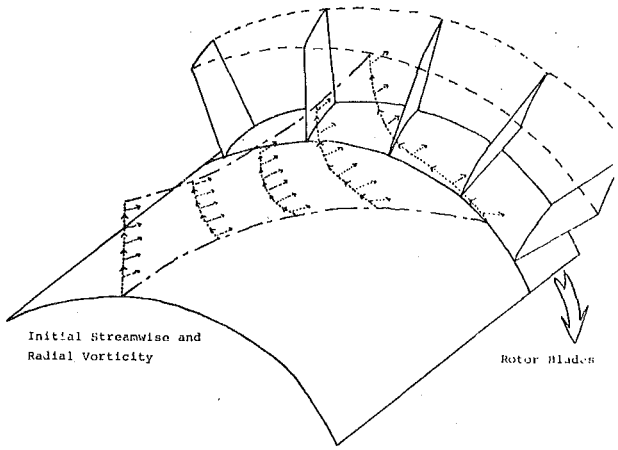

Fig. 2

The additional loss at the second row is represented by the annulus averaged total pressure loss $\Delta POALR$, again relative to the upstream blade row. The total pressure relative to the first row is denoted by subscript $_*$ (for example $(P_o/\rho)_*$).

Euler's equation of motion for the steady flow of an inviscid, incompressible fluid may be written relative to the upstream row

$$\boldsymbol{W} x (\nabla x \boldsymbol{V}) = \nabla (P_o/\rho) y \tag{1}$$

Using small perturbation theory equation (1) may be written as

$$\boldsymbol{W}_{FV} x (\nabla x (\mathbf{v} + \mathbf{v}_{ax})) = \nabla (P_o/\rho)_* \; to \; 0(\epsilon) \tag{2}$$

As in the case of the velocity, the absolute vorticity is separated into three components, each, however, of 0(ϵ), so

$$\nabla x (\mathbf{v} + \mathbf{v}_{AX}) = \Omega_\tau + \lambda \boldsymbol{W}_{FV} + \lambda_{AX} \boldsymbol{W}_{FV} \tag{3}$$

using the concept of the Beltrami vorticity to express the stream-wise vorticity as

$$\lambda \boldsymbol{W}_{FV} + \lambda_{AX} \boldsymbol{W}_{FV}$$

From the definition of $\lambda_{AX} \boldsymbol{W}_{FV}$

$$\nabla X \mathbf{v}_{AX} = \lambda_{AX} \boldsymbol{W}_{FV} \tag{4}$$

$$\nabla X \mathbf{v} = \boldsymbol{\Omega}_\tau + \lambda \boldsymbol{W}_{FV} \tag{5}$$

$\boldsymbol{\Omega}_\tau$ represents the component of the vorticity due to the stagnation pressure gradient.

From equation (4) $\boldsymbol{W}_{FV} \times (\nabla \times \mathbf{v}_{AX}) = 0$ so that, from (2)

$$\boldsymbol{W}_{FV} \times (\nabla x \mathbf{v}) = \nabla (P_o/\rho)_* \tag{6}$$

Using (5)

$$\boldsymbol{W}_{FV} \times \boldsymbol{\Omega}_\tau = \nabla (P_o/\rho)_* \tag{7}$$

It is required that $\nabla \cdot \boldsymbol{\Omega}_\tau = 0$ and so it follows from (4) and (5) that $\nabla \cdot (\lambda \boldsymbol{W}_{FV}) = 0$ and $\nabla \cdot (\lambda_{AX} \boldsymbol{W}_{FV}) = 0$. Since $\lambda \boldsymbol{W}_{FV}$ is solenoidal it may always be written

$$\lambda \boldsymbol{W}_{FV} = \nabla S \times \nabla \Gamma \tag{8}$$

which will be used later.

As shown in reference [3], $\boldsymbol{\Omega}_\tau$ may be written as

$$\boldsymbol{\Omega}_\tau = \nabla (P_o/\rho)_* \times \nabla \tau \tag{9a}$$

with

$$\boldsymbol{W}_{FV} \cdot \nabla \tau = 1 \tag{9b}$$

τ is the drift time, again discussed by Hawthorne [3]. The continuity equation $\nabla \cdot \boldsymbol{V} = \nabla \cdot \boldsymbol{W} = 0$ applies to each of the velocity components so

$$\boldsymbol{W}_{FV} + \mathbf{v}_{AX} + \mathbf{v} = \nabla \alpha_T \times \nabla \beta$$

and

Downloaded 01 Jun 2010 to 171.66.16.59. Redistribution subject to ASME license or copyright; see http://www.asme.org/terms/Terms_Use.cfm

$$\boldsymbol{W}_{FV} = \nabla\alpha \times \nabla\psi \tag{10}$$

where the streamlines of the primary flow are defined by the intersection of the two surfaces α = constant and ψ = constant.

It follows from $\nabla\cdot\lambda \boldsymbol{W}_{FV} = 0$ and $\nabla\cdot\lambda_{AX} \boldsymbol{W}_{FV} = 0$ that $\boldsymbol{W}_{FV}\cdot\nabla\lambda = 0$ and $\boldsymbol{W}_{FV}\cdot\nabla\lambda_{AX} = 0$. Thus it is possible to write

$$\lambda = \lambda(\alpha, \psi) \tag{11}$$

$$\lambda_{AX} = \lambda_{AX}(\alpha, \psi) \tag{12}$$

and from equation (2)

$$P_{o_*} = P_{o_*}(\alpha, \psi) \tag{13}$$

(noting that $\overline{P}_{o_*} = \overline{P}_{o_*}(\psi)$)

The choice of α and ψ is arbitrary. If ψ is the Stokes' stream for $\boldsymbol{W}_{FV}$, then α may be written $\alpha = \theta - f(\gamma, z)$ (as in reference [4]). $f(\gamma, z)$ is different for each of the regions u, d and dd and will be determined in the next part.

The nonaxisymmetric velocity component may be expressed as

$$\boldsymbol{v} = \nabla\phi + \boldsymbol{A} \tag{14}$$

and it follows from this using equations 5, 8 and 9 that

$$\boldsymbol{A} = \left(\frac{P_o - \overline{P}_o}{\rho}\right)_* \nabla\tau + S\nabla\Gamma \tag{15}$$

where it follows from (8) and (11) that $S\nabla\Gamma$ depends on ψ and α alone.

Thus it follows on integrating (9b)

$$\tau = z/V_{ZFV} \tag{16}$$

on dropping an unneeded constant of integration. V_{ZFV} is constant throughout the flow.

Upstream of the first row (region u) there is no stagnation pressure variation, so $(P_o{}^u - \overline{P}_o{}^u)_* = 0$. There is no swirl in the flow ($\boldsymbol{V}_{FV} = 0, 0, \overline{V}_{ZFV}$), so in this region $f(\gamma, z) = sz$. Thus $\alpha^u = \theta + sz$. Equation (14) reduces to

$$\mathbf{v}^u = \nabla\phi^u$$

Between the two blade rows (region d) the free vortex flow has the form

$$V_{FV} = (0, V_{\theta FV}, V_{ZFV}) = (0, K_d/\gamma\, V_{ZFV}, V_{ZFV})$$

where K_d/γ represents the strength of the swirl. Thus in this region $f(\gamma, z) = (K_d/\gamma^2 - s)z$ so that

$$\alpha^d = \theta - (K_d/\gamma^2 - S)Z \tag{18}$$

noting that the origin of the coordinate system will be placed at the first row, so that this row is at $z = 0$ and the next is at $z = z_0$. On using equations (16) and (15)

$$\left(\frac{P_o{}^d - \overline{P}_o{}^d}{\rho}\right)_* \nabla\tau = \left(\frac{P_o{}^d - \overline{P}_o{}^d}{\rho V_{ZFV}}\right)_* \hat{\boldsymbol{e}}_z = P_{o_*}{}^d(\alpha^d, \psi)\hat{\boldsymbol{e}}_z$$

On using equation (3) (ψ is the stream function of the primary flow, so $\psi = \psi(\gamma)$) and expressing the stagnation pressure variation as a Fourier series

$$P_{o_*}{}^d(\alpha^d, \psi) = \sum_{n=1}^{\infty} P_n{}^d(\psi) e^{in\beta\alpha^d} \tag{19}$$

This at $z = 0$ reduces to $\Sigma_{n=1}^{\infty} P_n{}^d e^{in\beta\theta}$ which is the Fourier series for the individual wakes. Using equations (11) and (12) it is possible to choose

$$\lambda^d + \lambda_{AX}{}^d = -F^d(\psi) \sum_{l=1}^{\beta} \delta(\alpha^d - \alpha_l) \tag{20}$$

where $\alpha_l = \pi/\beta, 3\pi/\beta, \ldots$ and $\delta(\ )$ is the Dirac impulse function. Effectively the trailing vorticity is in the form of sheets, each sheet originating at one of the β lifting lines representing the upstream row, situated at

$$\theta = \pi/\beta, 3\pi/\beta, \ldots$$

Using equations (10) and (20)

$$(\lambda^d + \lambda_{AX}{}^d)\boldsymbol{W}_{FV} = -F^d(\psi) \sum_{\iota=1}^{\beta} \delta(\alpha^d - \alpha_\iota)\nabla\alpha^d \times \nabla\psi \tag{21}$$

On taking the circumferential average of equation (21)

$$\lambda_{AX}{}^d \boldsymbol{W}_{FV} = \boldsymbol{\Omega}_{AX} = -\beta/2\pi F^d(\psi)\boldsymbol{W}_{FV} \tag{22}$$

The strength of the bound circulation representing each upstream blade is Γ_s, which it is assumed is known. $\Gamma_s = \overline{\Gamma}_s + \delta\Gamma_s(\gamma)$, where $\delta\Gamma_s$ (of 0 (ϵ)) is only present if the blades are running off the design condition.

Thus across the first row it can be shown that

$$\Delta(v_{\theta AX} + \mathrm{V}_{\theta FV}) = -\beta\Gamma_s/2\pi\gamma$$

However,

$$\Delta V_{\theta FV} = -\overline{\Gamma}_s\beta/2\pi\gamma$$

and as there is no swirl far upstream

$$v_{\theta AX}{}^d = \mathrm{V}_{\theta FV}{}^d\,(\Gamma_s/\overline{\Gamma}_s - 1) = V_{ZFV}\,K_d/\gamma\,(\Gamma_s/\overline{\Gamma}_s - 1) \tag{23}$$

The z component of $\nabla x\, \mathbf{v}_{AX}$ is $1/\gamma\partial(\gamma v_{\theta AX})/\partial\gamma$. Combining this with the z component of equation (22)

$$F^d(\psi) = \frac{-2\pi K_d}{\gamma\beta\overline{\Gamma}_s}\frac{\partial\Gamma_s}{\partial\gamma} \tag{24}$$

Using equations (21) and (22)

$$\lambda^d \boldsymbol{W}_{FV}{}^d = \nabla S^d \times \nabla\Gamma^d = -F^d(\psi)\nabla\left(H(\alpha^d) - \frac{\beta\alpha^d}{2\pi}\right) x\, \nabla\psi$$

$$= -F^d(\psi)\nabla\left(H(\alpha^d) - \left(\frac{\beta\alpha^d}{2\pi} - \frac{1}{2}\right)\right) x\, \nabla\psi \tag{25}$$

where the $\frac{1}{2}$ term is added to ensure that the circumferential average of $S^d\nabla\Gamma^d$ is zero, and $H(\alpha^d)$ is a Heaviside step function.

$$H(\alpha^d) - \left(\frac{\beta\alpha^d}{2\pi} - \frac{1}{2}\right)$$

is a sawtooth function which may be expressed as a Fourier series

$$H(\alpha^d) - \left(\frac{\beta\alpha^d}{2\pi} - \frac{1}{2}\right) = \mathrm{Real}\left[-\frac{1}{\pi}\sum_{n=1}^{\infty}\frac{(-1)^n i e^{in\beta\alpha^d}}{n}\right] \tag{26}$$

Thus, using equations (25) and (26)

$$S^d\nabla\Gamma^d = \hat{\boldsymbol{e}}_\gamma \sum_{n=1}^{\infty} \frac{-2k_d i(-1)^n}{n\beta\overline{\Gamma}_s}\frac{\partial\Gamma_s}{\partial\gamma} e^{in\beta\alpha^d}$$

$$= \hat{\boldsymbol{e}}_\gamma \sum_{n=1}^{\infty} G_n{}^d(\gamma) e^{in\beta\alpha^d} \tag{27}$$

Hence combining equations (14, 19) and (27)

$$v^d = \nabla\phi^d + \hat{e}_\gamma \sum_{n=1}^{\infty} G_n{}^d(\gamma) e^{in\beta\alpha^d} + \hat{\boldsymbol{e}}_z \sum_{n=1}^{\infty} P_n{}^d e^{in\beta\alpha^d} \tag{28}$$

Downstream of the two blade rows (region dd) the free vortex flow has the form

$$\boldsymbol{V}_{FV} = (0, K_{dd}/\gamma, V_{ZFV}, V_{ZFV})$$

Thus in this region

$$f(y, z) = (K_{dd}/\gamma^2 - s)(z - z_0)$$

so that

$$\alpha^{dd} = \theta - (K_{dd}/\gamma^2 - s)(z - z_0) \tag{29}$$

noting that the second row is placed at $z = z_0$. On using equations (13, 16) and (19) as with the upstream row

$$\left(\frac{P_o{}^{dd} - \overline{P}_o{}^{dd}}{\rho}\right)_* \nabla\tau = P_{o\gamma}{}^{dd}(\alpha^{dd}, \psi)\hat{\boldsymbol{e}}_z = \sum_{n=1}^{\infty} P_n{}^{dd}(\gamma) e^{in\beta\alpha^{dd}}\hat{\boldsymbol{e}}_z \tag{30}$$

In this case, however, the Fourier coefficients $P_n{}^{dd}(\gamma)$ are unknown

Downloaded 01 Jun 2010 to 171.66.16.59. Redistribution subject to ASME license or copyright; see http://www.asme.org/terms/Terms_Use.cfm

functions of γ. They are found by applying appropriate boundary conditions to the flow.

Using equations (11) and (12) it is possible to choose

$$\lambda^{dd} + \lambda_{AX}{}^{dd} = -F^{dd}(\psi) + \sum_{n=1}^{\infty} \lambda_n{}^{dd}(\gamma) e^{in\beta\alpha^{dd}} \tag{31}$$

On taking the circumferential average of equation (31)

$$\lambda_{AX}{}^{dd} \boldsymbol{W}_{FV} = -F^{dd}(\psi) \boldsymbol{W}_{FV} \tag{32}$$

Similar to the upstream row, the axisymmetric circulation distribution on the downstream is

$$(\beta_R \Gamma_R) = (\overline{\beta_R \Gamma_R}) + \delta(\beta_R \Gamma_R(\gamma))$$

with $\delta(\beta_R \Gamma_R(\gamma))$ only present for off-design running. However, there is a nonaxisymmetric additional circulation of 0 (ϵ) on this row due to the nonaxisymmetric upstream flow.

Thus across the second row

$$\Delta(v_{\theta AX} + V_{\theta FV}) = -(\beta_R \Gamma_R)/2\pi\gamma$$

and

$$\Delta V_{\theta FV} = -(\overline{\beta_R \Gamma_R})/2\pi\gamma$$

However, there is mean swirl upstream of the second row. Thus

$$v_{\theta AX}^{dd} = -V_{ZFV}\left(\left(\frac{K_{dd}}{\gamma} - \frac{K_d}{\gamma}\right)\frac{(\beta_R \Gamma_R)}{(\overline{\beta_R \Gamma_R})} - \frac{K_d}{\gamma}\frac{\Gamma_s}{\overline{\Gamma}_s} - \frac{K_{dd}}{\gamma}\right) \tag{33}$$

(Note that $\beta_R \to \infty$ for this row. However, $\beta_R \Gamma_R$ remains finite.) This has used the fact that $v_{\theta AX}$ in each region is independent of z. This is well known from actuator disk theory [8]. Thus

$$v_{\theta AX}{}^{d}|_{z=0} = v_{\theta AX}{}^{d}|_{z=z_0}$$

Comparing the z component of $\nabla X \mathbf{v}_{AX}$ using equations (33) and (32)

$$F^{dd}(\psi) = -\left((K_{dd}/\gamma - K_d/\gamma)\, 1/(\overline{\beta_R \Gamma_R})\frac{\partial(\beta_R \Gamma_R)}{\partial\gamma} - \frac{K_d}{\gamma}\frac{1}{\overline{\Gamma}_s}\frac{\partial \Gamma_s}{\partial\gamma}\right) \tag{34}$$

Using equations (31) and (32)

$$\lambda^{dd} \boldsymbol{W}_{FV}{}^{dd} = \nabla S^{dd} \times \nabla \Gamma^{dd}$$

$$= \sum_{n=1}^{\infty} \lambda_n{}^{dd}(\gamma) e^{in\beta\alpha^{dd}} \nabla \alpha^{dd} \times \nabla(\psi(\gamma))$$

$$= \sum_{n=1}^{\infty} \nabla e^{in\beta\alpha^{dd}} \times \nabla S_n(\gamma) \tag{35}$$

which leads directly to

$$S^{dd} \nabla \Gamma^{dd} = \sum_{n=1}^{\infty} e^{in\beta\alpha^{dd}} \nabla S_n(\gamma) = \hat{\boldsymbol{e}}_\gamma \sum_{n=1}^{\infty} G_n{}^{dd}(\gamma) e^{in\beta\alpha^{dd}} \tag{36}$$

combining equations (14, 30) and (36)

$$\mathbf{v}^{dd} = \nabla\phi^{dd} + \sum_{n=1}^{\infty} P_n{}^{dd}(\gamma) e^{in\beta\alpha^{dd}} \hat{\boldsymbol{e}}_z + \sum_{n=1}^{\infty} G_n{}^{dd}(\gamma) e^{in\beta\alpha^{dd}} \hat{\boldsymbol{e}}_\gamma \tag{37}$$

Thus the nonaxisymmetric component of the flow, $\mathbf{v}$, is given by equations (17, 28) and (37) in each of the flow regions. The axisymmetric component, $\mathbf{v}_{AX}$, could be determined from equations (32, 34) and (22, 24) by standard axisymmetric actuator disk theory [8]. It is not required for the determination of $\mathbf{v}$, so this will not be done in this analysis.

The expressions for $\mathbf{v}^d$ and $\mathbf{v}^{dd}$ are identical except for their superscripts. These will be dropped to simplify the next part of the analysis.

Applying continuity, $\nabla\cdot\mathbf{v} = 0$. Thus

$$\nabla^2 \phi^u = 0 \tag{38a}$$

$$\nabla^2 \phi = \sum_{n=1}^{\infty} \left(in\beta(K/\gamma^2 - s)P_n - 1/\gamma \frac{d(\gamma G_n)}{d\gamma}\right) e^{in\beta\alpha} - z\frac{2in\beta K G_n}{\gamma^3} e^{in\beta\alpha} \tag{38b}$$

which are to be solved with the boundary conditions of zero radial velocity at the hub and tip.

Equation (38a) has a simple exponentially decaying homogeneous solution

$$\phi^u = \sum_{n=1}^{\infty}\sum_{m=1}^{\infty} A_{mn}{}^{u} e^{\lambda_{mn} z} R_{n\beta}(\lambda_{mn}\gamma) e^{in\beta\theta} \tag{39}$$

Equation (38b) has a similar homogeneous solution plus an inhomogeneous solution.

$R_{n\beta}(\lambda_{mn}\gamma)$ is defined as a linear combination of Bessel functions of the first and second kinds such that

$$R_{n\beta}(\lambda_{mn}\gamma) = \frac{J_{n\beta}(\lambda_{mn}\gamma) + C_{mn} Y_{n\beta}(\lambda_{mn}\gamma)}{\sqrt{D_{mn}}}$$

where λ_{mn} and C_{mn} are given by the boundary conditions that

$$\left.\frac{\partial\phi}{\partial\gamma}\right|_{\gamma=\gamma_h,\gamma_t} = 0$$

so

$$C_{mn} = -\frac{J_{n\beta}'(\lambda_{mn}\gamma_h)}{Y_{n\beta}'(\lambda_{mn}\gamma_h)} = -\frac{J_{n\beta}'(\lambda_{mn}\gamma_t)}{Y_{n\beta}'(\lambda_{mn}\gamma_t)}$$

$$D_{mn} = \int_{\gamma_h}^{\gamma_t} y R_{n\beta}{}^2 d\gamma$$

The inhomogeneous solution to equation (38b) is chosen to be of the form

$$\phi_I = \sum_{n=1}^{\infty}\sum_{m=1}^{\infty} Z_{mn}(z) R_{n\beta} e^{in\beta\theta} \tag{40}$$

as is described in reference [4]. Noting that $G_n(\gamma)$, the radial velocity induced by the shed circulation, must be zero at the walls (as has been pointed out in (7) and (10)), this leads to

$$Z_{mn} = -\int_{\gamma_h}^{\gamma_t} \frac{\gamma G_n R_{n\beta}' + in\beta\gamma(K/\gamma^2 - s)R_{n\beta}P_n}{\lambda_{mn}{}^2 + n^2\beta^2(K/\gamma^2 - s)^2} e^{-in\beta(K/\gamma^2 - S)Z} d\gamma \tag{41}$$

The expressions for in each of the three flow regions may now be written as

$$\phi^u = \sum_{n=1}^{\infty}\sum_{m=1}^{\infty} A_{mn}{}^{u} e^{\lambda_{mn} Z} R_{n\beta} e^{in\beta\theta} \tag{42a}$$

$$\phi^d = \sum_{n=1}^{\infty}\sum_{m=1}^{\infty} R_{n\beta}(A_{mn}{}^{d} e^{-\lambda_{mn} Z} + B_{mn}{}^{d} e^{\lambda_{mn} Z} + Z_{mn}{}^{d}) e^{in\beta\theta} \tag{42b}$$

$$\phi^{dd} = \sum_{n=1}^{\infty}\sum_{m=1}^{\infty} R_{n\beta}(A_{mn}{}^{dd} e^{-\lambda_{mn}(Z - Z_0)} + Z_{mn}{}^{d}) e^{in\beta\theta} \tag{42c}$$

This leaves the constants $A_{mn}{}^{u}$, $A_{mn}{}^{d}$, $B_{mn}{}^{d}$, $A_{mn}{}^{dd}$, and the functions $G_n{}^{dd}(\gamma)$ and $P_n{}^{dd}(\gamma)$ to be found by the use of appropriate boundary conditions across each blade row.

Flow Matching Conditions at each Blade Row. There are two matching conditions to be applied at the first row and four at the second. (1) The axial velocity v_z is continuous across both blade rows. (2) The radial velocity v_γ is the same across each blade row. (3) The stagnation pressure change across the second row depends on the work done. Thus for a rotor at speed ω

$$(P_o{}^{dd} - \overline{P}_o{}^{dd})_* - (P_o{}^{d} - \overline{P}_o{}^{d})_* = \rho(w - s)\gamma(v_\theta{}^{dd} - v_\theta{}^{d})|_{z=z_0}$$

(4) It is assumed that the flow outlet angle relative to the second row is specified and is independent of the flow inlet angle,

$$\frac{V_{\theta FV}{}^{dd} + v_{\theta AX}{}^{dd} + v_\theta{}^{dd} - \omega\gamma}{V_{ZFV} + v_{ZAX}{}^{dd} + v_Z{}^{dd}} = \left.\frac{V_\theta{}^{dd} + v_{\theta AX}{}^{dd} - \omega\gamma}{V_{ZFV} + v_{ZAX}{}^{dd}}\right|_{Z=Z_0}$$

$$\Rightarrow 1/\gamma \frac{\partial\phi^{dd}}{\partial\theta}(V_{ZFV} + v_{ZAX}{}^{dd}) = (V_{\theta FV}{}^{dd} + v_{\theta AX}{}^{dd} - \omega\gamma) \times \left.\left(\frac{\partial\phi^{dd}}{\partial z} + \sum_{n=1}^{\infty} P_n{}^{dd}(\gamma) e^{in\beta\alpha^{dd}}\right)\right|_{Z=Z_0}$$

Downloaded 01 Jun 2010 to 171.66.16.59. Redistribution subject to ASME license or copyright; see http://www.asme.org/terms/Terms_Use.cfm

So, correct to 0 (ϵ)

$$1/\gamma \frac{\partial \phi^{dd}}{\partial \theta} = (K_{dd}/\gamma - \omega\gamma)\left(\sum_{n=1}^{\infty} P_n{}^{dd} e^{in\beta\alpha^{dd}} + \frac{\partial \phi^{dd}}{\partial z}\right)\Bigg|_{Z=Z_0} \quad (43)$$

Further details of the solution procedure are given in the Appendix.

So far no mention has been made of the axial positioning of the lifting lines and actuator disk models of the two blade rows.

It is assumed for simplicity that the lifting lines and actuator disk are placed at the trailing edge. It should be noted that the row separation z_0 is, therefore, the distance between blade row trailing edges, and that the axial gap between the rows is z_0—(axial blade chord of downstream row).

Implications of the Analysis

While the results produced by this analysis can only be found fully by numerical calculation, it is possible to expand and simplify some of the analytic expressions given in the previous section. This will enable qualitative deductions to be made about the flow behavior.

It was mentioned previously that the blade row interaction would be shown to be due to two components, potential and vortex. This can be illustrated using equations 42(b) and (c). The potential interaction is represented by two terms

$A_{mn}{}^d e^{-\lambda_{mn} Z}$ The influence of the upstream row downstream

$B_{mn}{}^d e^{\lambda_{mn} Z}$ The influence of the downstream row upstream

The vortex interaction is represented by the third term, written as

$$\int_{\gamma_h}^{\gamma_t} F_{nc}(\gamma) e^{-in\beta(K_d/\gamma^2 - S)Z} d\gamma$$

The fact that the unknowns in these equations are only given implicity (Appendix) illustrates the coupling between these interactions.

It can be seen that the vortex interaction term here contains two independent components, $G_n{}^d$ for the wake shed streamwise vorticity and $P_n{}^d$ for the shed radial vorticity. The vortex interaction term may usefully be explained in two ways, to examine (1) the behavior as z becomes large; (2) the relative importance of $P_n{}^d$ and $G_n{}^d$.

(1) Expanding the integral in powers of z by integrating by parts and neglecting terms in $1/z^2$, the vortex interaction term for large z becomes

$$\frac{in\beta\gamma\,(K_d/\gamma^2 - s) R_{n\beta} P_n{}^d e^{-in\beta(K^d/\gamma^2 - S)Z}}{(\lambda_{mn}{}^2 + n^2\beta^2\,(K^d/\gamma^2 - s))\, in\beta\,(K_d/\gamma^2 - s) Z}\Bigg|_{\gamma_h}^{\gamma_t}$$

(2) It is also possible to expand the integral as a series in ϵ where $\epsilon = 1 - \gamma_h/\gamma_t$ (the blade span in terms of the tip radius).

These equations suggest the following points about the interaction process.

i Potential interaction may be important at very small blade row separations. In this region, the interaction effects, controlled by $e^{-\lambda z}$, will change rapidly with z and z_0. The influence of the downstream row on the upstream will be significant due to the $B_{mn}{}^d e^{\lambda mz}$ term.

ii Vortex interaction will dominate for large blade row spacings. In this region the interaction effects are controlled by terms of the form $1/\beta z$ or $1/\beta z_0$ and hence change more slowly with z or z_0.

iii The streamwise vorticity term $G_n{}^d$ only appears in terms in ϵ^2 in the expansion of the interaction integral, and for large z does not appear at all. Thus the shed streamwise vorticity is a factor ϵ less significant than the shed radial vorticity in the vortex interaction terms.

It is also possible to estimate the relative importance of the viscous wake vorticity $P_n{}^d$ and the streamwise wake vorticity $G_n{}^d$ in the potential flow terms.

On referring to the Appendix, equation (A9) gives an expression for $A_{mn}{}^d$.

On expanding the expression for $A_{mn}{}^d$ in the terms of $\epsilon = 1 - \gamma_h/\gamma_t$

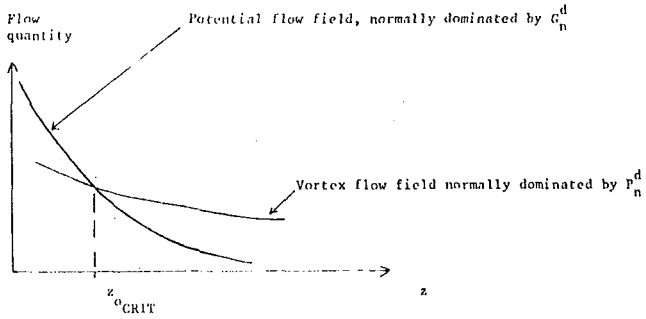

Fig. 3

(i) Γ_{mn} is of order $G_n{}^d(\gamma)$

(ii) $\int \gamma P_n{}^d R_{n\beta} d\gamma$ is of order $P_n{}^d$

(iii) $\int F_{mn}{}^d(\gamma)(\lambda_{mn} + in\beta\,(K_d/\gamma^2 - s))d\gamma$

is of order $P_n{}^d$ (and $\epsilon^2 G_n{}^d$)

Hence in the potential interaction both $G_n{}^d$ and $P_n{}^d$ are significant, in contrast to the vortex interaction when $P_n{}^d$ is dominant. A closer examination of the terms in the above equation for $G_n{}^d$ shows that for typical off free-vortex blade rows $G_n{}^d$ dominates $P_n{}^d$ for small n.

The flow downstream of the first blade row may therefore be considered to be in two regions for a typical off free-vortex blade row.

If the second row is placed upstream of $z_{0\,CRIT}$ then the interaction will be potential flow dominated and normally controlled by $G_n{}^d$. Interaction effects will vary as $e^{-\lambda z_0}$. Downstream of $z_{0\,CRIT}$ the interaction is vortex dominated and controlled by $P_n{}^d$. Here interaction effects vary as $1/n\beta z_0$. Evidently this analysis breaks down for $G_n{}^d$ zero or very small (Fig. 3).

Numerical Calculations

To illustrate the general behavior of a wake, the theory has been applied to the following free vortex machines (unless otherwise stated $G_n{}^d = 0$): (1) compressor, rotor-stator, low (0.4) hub:tip ratio $w = 0.$, $s = 2.2$, $K_d = .318$, $K_{dd} = 0.$, $z_0/\gamma_t = .3$. (2) turbine, stator-rotor, low (0.4) hub:tip ratio $w = 2.2$, $s = 0.$, $K_d = .318$, $K_{dd} = 0.$, $z_0/\gamma_t = .3$. (3) turbine, stator-rotor, high (0.8) hub:tip ratio $w = 1.4$, $s = 0.$, $K_d = 2.2$, $K_{dd} = -0.5$, $z_0/\gamma_t = .1$

In each case the upstream row has 23 blades, and the Fourier series used to represent the wake considers the first 5 terms. The peak to peak wake stagnation pressure defect is

$$\left(\frac{P_o{}^d - \overline{P}_o{}^d}{\rho V_{ZFV}{}^2}\right)_* = 0.06$$

Figure 4 shows the initial form of the wake immediately after the lifting lines for cases (1) and (2). In general it would be expected that the initial wake would be much larger than thus, but would rapidly decay to values close to those shown within a few trailing edge thicknesses.

Figure 5 shows the influence of the upstream wake ($G_n{}^d = 0$) on the work done by the downstream row for cases (1, 2) and (3). It is apparent that the presence of the downstream row considerably modifies the shape of the wake profile. The unsteady tangential force on the downstream blades is related to the change in stagnation pressure across the row, shown as a shaded area. In all these cases, therefore, the unsteady forces are large near the tip, and in case (1) are small at the hub. As case (1) represents the unsteady forces at a stator (with fixings at the tip) and cases (2) and (3) those on a rotor (with fixings at the root), this suggests that unsteady blade forces due to upstream wakes will be more important in the case of a rotor following a stator than vice versa. It is also apparent that the heavily loaded high hub:tip ratio turbine stage tends to smooth out the upstream wakes, whereas for the low hub tip ratio cases the peak to peak value of the stagnation pressure

Downloaded 01 Jun 2010 to 171.66.16.59. Redistribution subject to ASME license or copyright; see http://www.asme.org/terms/Terms_Use.cfm

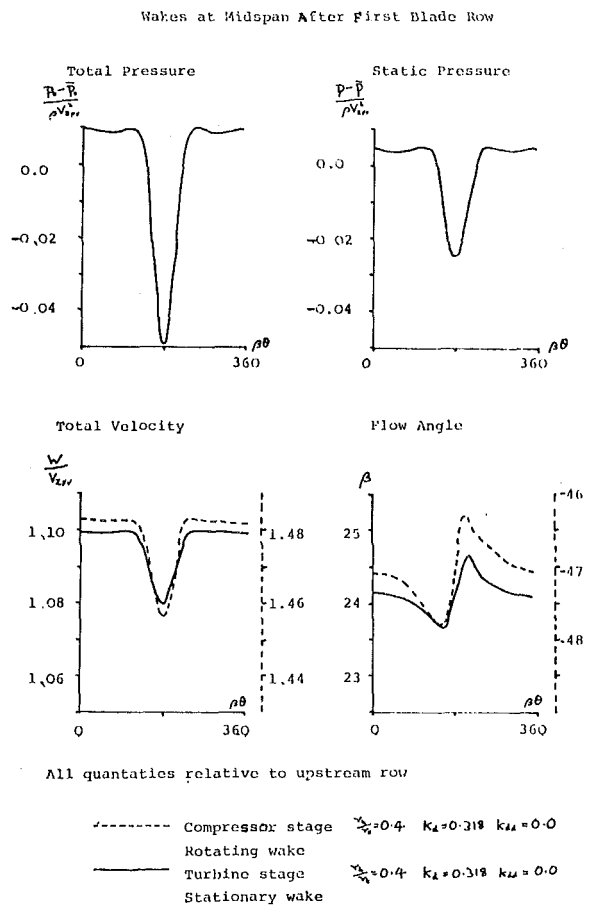

Fig. 4

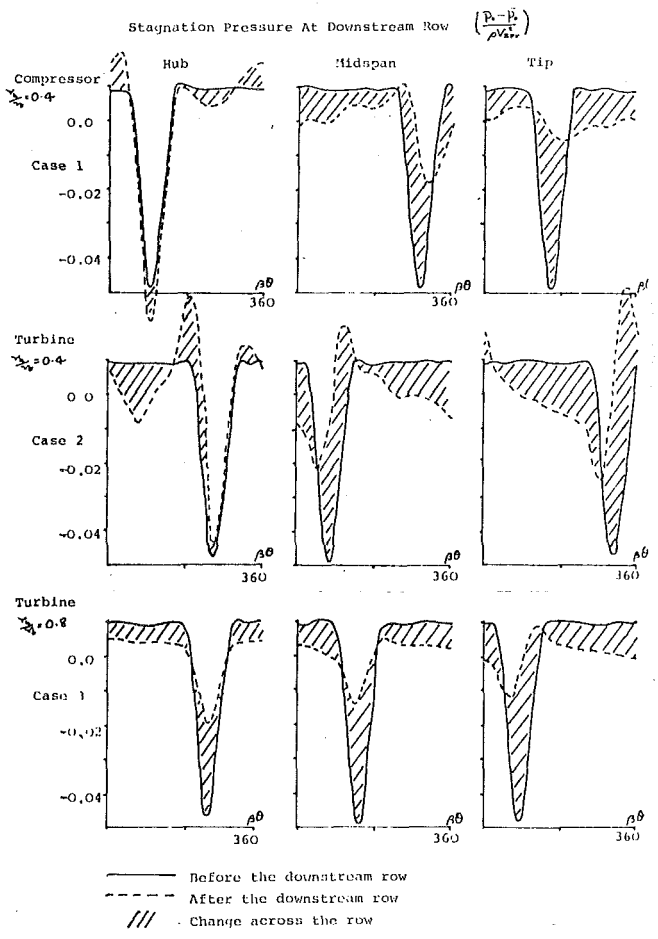

Fig. 5

$$P_o - \overline{P}_o/\rho V_{ZFV}^2$$

is actually increased at some radii.

Figure 6 considers a modified high hub:tip ratio turbine (case (3)). Here

$$P_n{}^d = 0$$

but

$$\tan \alpha = 2/\gamma \left(1 - 0.25 \cos \pi \left(\frac{\gamma - \gamma_h}{\gamma_t - \gamma_h}\right)\right)$$

or

$$\Gamma_s = \overline{\Gamma}_s \left(1 - 0.25 \cos \pi \left(\frac{\gamma - \gamma_h}{\gamma_t - \gamma_h}\right)\right)$$

there is nonuniform spanwise loading $-G_n{}^d \neq 0$

The free vortex flow angle is then defined by

$$K = \int_{\gamma_h}^{\gamma_t} \frac{\gamma \tan \alpha}{\gamma_t - \gamma_h}$$

The loading produces a closer approximation to constant outlet angle than the free vortex case. The potential flow field extending upstream and downstream of the first blade row reaches the downstream row. This nonuniform flow at the rotor then results in nonuniform rotor work and produces a stagnation pressure field downstream. The streamwise vorticity from the first row generates radial vorticity from the second.

Figure 10 shows the radial velocities downstream of the first blade row for the same off free-vortex turbine ($P_n{}^d = 0$). The development of large radial velocities in the form of a sawtooth function as predicted by equation (27) is evident. These velocities reach a peak-to-peak value of 10 percent of the primary axial velocity, and have correspondingly a very large radial velocity gradient in both γ and θ directions. Thus it is likely that in a real turbomachine viscous effects would prevent the radial velocities developing to this extent. Figures 7, 8 and 9 show the radial velocities downstream of the first blade row for cases (1, 2) and (3). The position of the wake centerline between the rows is denoted by * as it is convected by the swirling flow. Figures 8 and 9 show wakes from a stator and a rotor. In the case of the stator the existence of the wake velocity defect in the free vortex swirling flow produces an unbalanced radial pressure gradient, with pressure increasing with radius. Thus a radial flow develops towards the hub, as shown in Figure 9. This radial flow is almost entirely due to the nonhomogeneous component of the solution to the flow equations (equation (41)). In the case of a rotor the wakes are rotating and the absolute wake velocity is higher than the surrounding flow. Thus the radial flow develops towards the tip, as shown in Fig. 8. In Fig. 7, the high hub:tip ratio turbine, the radial flows develop similarly to those in Fig. 9. However, the radial velocities are of approximately the same size as those of the low hub:tip ratio machine, so very intense radial velocity gradients are occurring in a radial direction in the 0.8 hub:tip ratio turbine.

The magnitude of the radial velocities due to the viscous wake appears to be about 0.1 percent of V_{ZFV}—about 1/100 the magnitude which develops due to shed streamwise vorticity. Thus $G_n{}^d$ seems to be more significant than $P_n{}^d$ in the development of radial flows.

Conclusions

This three-dimensional theory has shown that the flow pattern is extremely complex, and the following generalizations must be used with caution.

1 An upstream wake is shown to contribute two separate components of vorticity to the downstream flow, $P_n{}^d$ due to shed radial vorticity and $G_n{}^d$ due to shed streamwise vorticity. Each of these components is shown to influence the flow in two ways: (i) through a potential flow field (close to the upstream blade row) (ii) through a vortex flow field (further downstream of the upstream blade row).

Downloaded 01 Jun 2010 to 171.66.16.59. Redistribution subject to ASME license or copyright; see http://www.asme.org/terms/Terms_Use.cfm

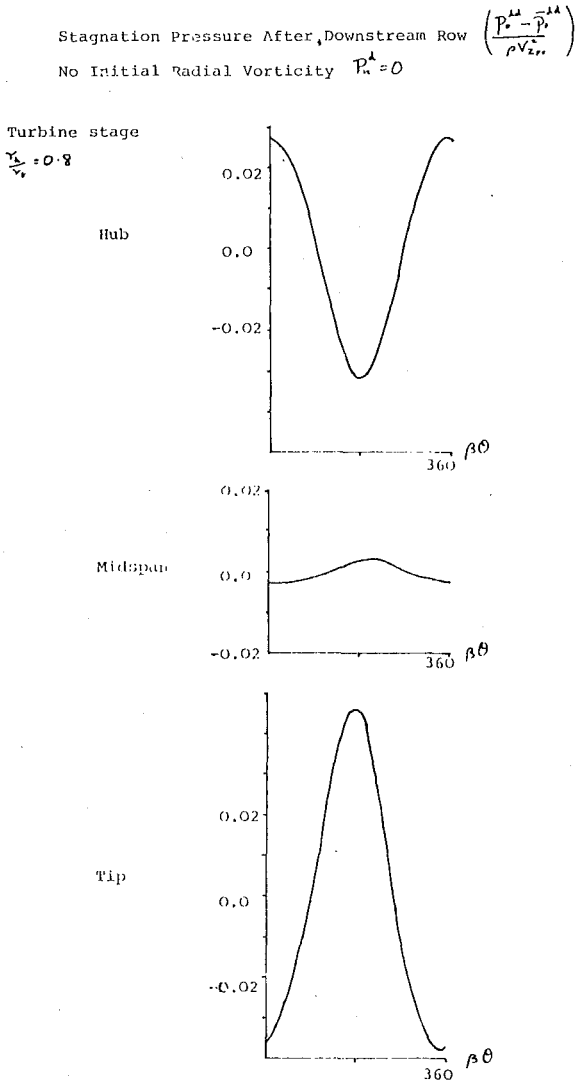

Fig. 6

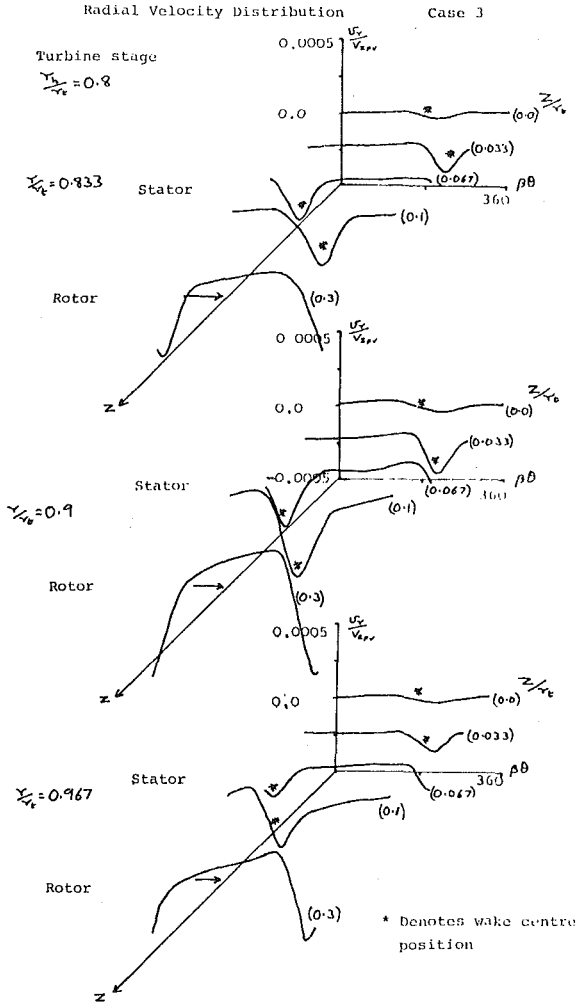

Fig. 7

If the downstream row is situated in the potential flow field, then the blade forces variations are extremely sensitive to row separation. If it is situated in the vortex flow field, then they are less so. Each component produces the following fields.

	$P_n{}^d$	$G_n{}^d$
Potential	Narrow region close behind upstream row. Perturbations of order	Region after upstream row. Perturbations of order
Vortex	Remainder of downstream flow. Perturbations of order	Remainder of downstream flow. Perturbations small.

Most practical blade rows have both a component $P_n{}^d$ and $G_n{}^d$ which is significant (only if they are close to free vortex is $G_n{}^d$ negligible). The theory enables the approximate boundary between the $G_n{}^d$ dominated potential flow field and the $P_n{}^d$ dominated vortex flow field to be found in terms of the stage parameters. From the point of view of blade vibration it is desirable for the downstream row to be just in the vortex flow field, since this position represents minimum unsteady potential effects and further increasing the row separation produces changes as only $1/\beta z$ rather than $e^{-\beta z}$.

2 It is shown that as a general rule in free vortex stages arranged either stator—rotor or rotor—stator the maximum forces on the downstream row occur at the tip. As a stator is fixed at the tip, but a rotor at the root, blade vibration may be expected to occur more readily in rotor rows. In high hub:tip ratio machines the peak to peak magnitude of the wake as it passes through a downstream row tends to be much reduced, but for a low hub:tip ratio it can be magnified.

References

1 Tan, C. S., "Three-dimensional Vorticity-Induced Flow Effects in High-Loaded Axial Compressors," Ph.D. Thesis, MIT, 1978.

2 McCune, J. E., Hawthorne, W. R., "The Effects of Trailing Vorticity on the Flow through Highly Loaded Cascades," *Journal of Fluid Mechanics*, Vol. 74, 1976, p. 721–741.

3 Hawthorne, W. R., "On the Theory of Shear Flow," MIT, GTL rep. No. 88, 1966.

4 Hawthorne, W. R., McCune, J. E., Mitchell, N. A., Tan, C. S., "Non-Axisymmetric Flow through Annular Actuator Discs: Inlet Distortion Problem," ASME JOURNAL OF ENGINEERING FOR POWER, 1978.

5 Dunham, J., "Non-Axisymmetric Flows in Axial Compressors," Ph.D. Thesis, Camb. Univ. Eng. Dept., 1963.

6 Cheng, W. K., "A Three-Dimensional Theory for the Velocity Induced by a Heavily Loaded Annular Cascade of Blades," SM Thesis, Aero and Astro, MIT, 1975.

7 De O. Falcao, A. F., "Three-Dimensional Flow Analysis in Axial Turbomachines," Ph.D. Thesis, Camb. Uni. Eng. Dept., 1970.

8 Hawthorne, W. R., Horlock, J. H., "Actuator Disc Theory of the Incompressible Flow in Axial Compressors," *Proceedings of the Institution of Mechanical Engineering*, Vol. 1976, No. 30, 1962.

9 Morton, K. B., "Three-Dimensional Compressible Flow through Highly Loaded Rectilinear Cascades," S.M. Thesis, Dept. of Aero and Astro, MIT, 1974.

10 McCune, J. E., Dharwadkar, S. P., "Lifting-Line Theory for Subsonic Axial Compressor Rotors," MIT, GTL, Rep. No. 110, 1972.

Downloaded 01 Jun 2010 to 171.66.16.59. Redistribution subject to ASME license or copyright; see http://www.asme.org/terms/Terms_Use.cfm

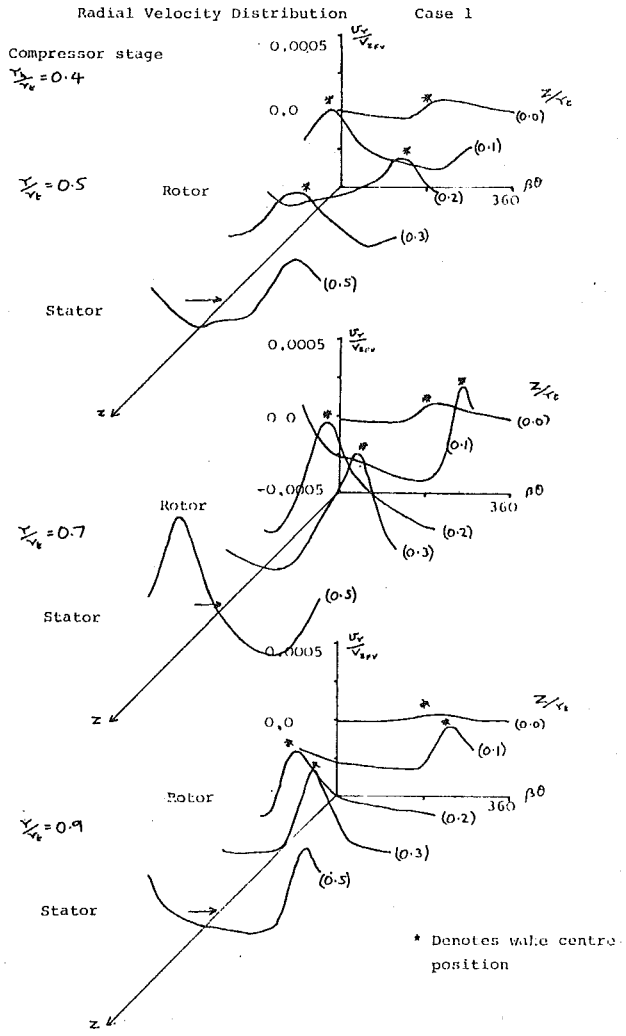

Fig. 8

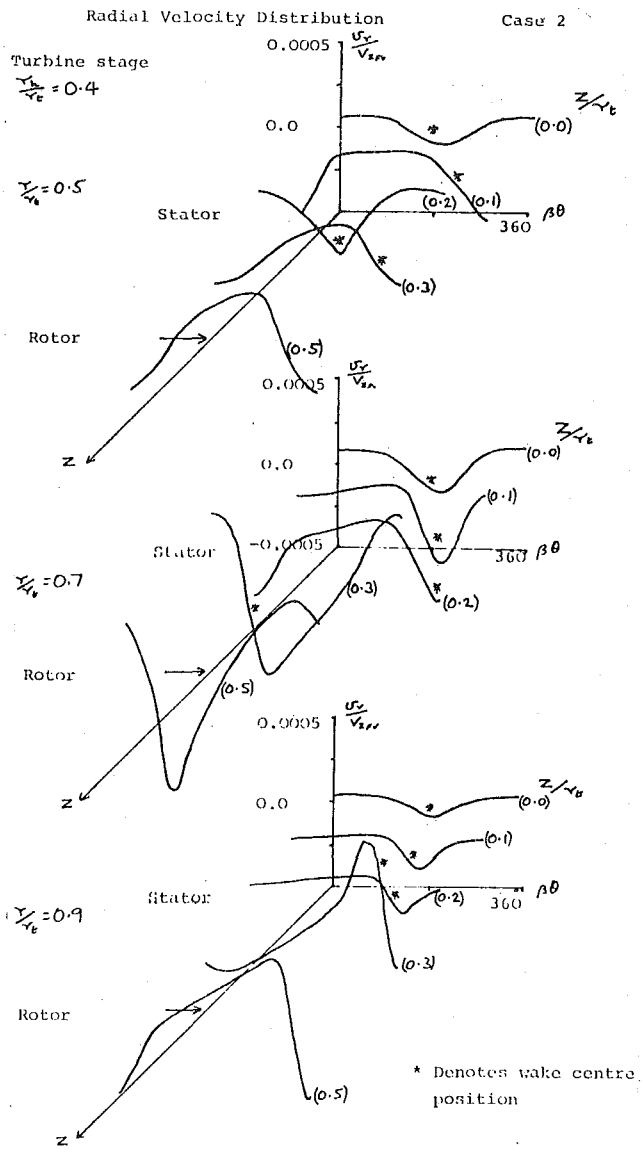

Fig. 9

APPENDIX

Solution of the Three-Dimensional Flow Equations

The equations giving the unknowns $A_{mn}{}^{u}$, $A_{mn}{}^{d}$, $B_{mn}{}^{d}$, $A_{mn}{}^{dd}$ and $G_n{}^{dd}$, $P_n{}^{dd}$ can be written

From condition (1)

$$\sum_{m=1}^{\infty} R_{n\beta}\left(\lambda_{mn}A_{mn}{}^{u} + \lambda_{mn}A_{mn}{}^{d} - \lambda_{mn}B_{mn}{}^{d} - \int_{\gamma_h}^{\gamma_t} in\beta\,(K_d/y^2 - s)\,F_{mn}{}^{d}(\gamma)d\gamma\right) = P_n{}^{d} \quad \text{(A1)}$$

$$\sum_{m=1}^{\infty} R_{n\beta}\left(-\lambda_{mn}A_{mn}{}^{d}e^{-\lambda_{mn}Z_0} + \lambda_{mn}B_{mn}{}^{d}e^{\lambda_{mn}Z_0} + \lambda_{mn}A_{mn}{}^{dd} + \int_{\gamma_h}^{\gamma_t} in\beta\,(K_d/\gamma^2 - s)\,F_{mn}{}^{d}(\gamma)e^{-in\beta(Kd/\gamma^2-S)Z_0}d\gamma - \int_{\gamma_h}^{\gamma_t} in\beta\,(K_{dd}/\gamma^2 - s)\,F_{mn}{}^{dd}(\gamma)d\gamma\right) = P_n{}^{dd} - P_n{}^{d}e^{-in\beta(Kd/\gamma^2-S)Z_0} \quad \text{(A2)}$$

From condition (2)

$$\sum_{m=1}^{\infty} R_{n\beta}{}'\left(A_{mn}{}^{u} - A_{mn}{}^{d} - B_{mn}{}^{d} + \int_{\gamma_h}^{\gamma_t} F_{mn}{}^{d}(\gamma)d\gamma\right) = G_n{}^{d}(\gamma) \quad \text{(A3)}$$

$$\sum_{m=1}^{\infty} R_{n\beta}{}'\left(A_{mn}{}^{d}e^{-\lambda_{mn}Z_0} + B_{mn}{}^{d}e^{\lambda_{mn}Z_0} - \int_{\gamma_h}^{\gamma_t} F_{mn}{}^{d}(\gamma)e^{-in\beta(Kd/\gamma^2-S)}d\gamma - A_{mn}{}^{dd} + \int_{\gamma_h}^{\gamma_t} F_{mn}{}^{dd}(\gamma)dy\right) = G_n{}^{dd}(\gamma) - G_n{}^{d}(\gamma)e^{-in\beta(Kd/\gamma^2-S)Z_0} \quad \text{(A4)}$$

From condition (3)

$$\sum_{m=1}^{\infty} R_{n\beta} in\beta(\omega - s)\left(A_{mn}{}^{dd} - A_{mn}{}^{d}e^{-\lambda_{mn}Z_0} - B_{mn}{}^{d}e^{\lambda_{mn}Z_0} + \int_{\gamma_h}^{\gamma_t} F_{mn}{}^{d}(\gamma)e^{-in\beta(Kd/\gamma^2-S)Z_0}d\gamma - \int_{\gamma_h}^{\gamma_t} F_{mn}{}^{dd}(\gamma)d\gamma\right) = P_n{}^{dd}(\gamma) - P_n{}^{d}(\gamma)e^{-in\beta(Kd/\gamma^2-S)Z_0} \quad \text{(A5)}$$

From condition (4)

$$\sum_{m=1}^{\infty} R_{n\beta}\left(in\beta A_{mn}{}^{dd} - in\beta\int_{\gamma_h}^{\gamma_t} F_{mn}{}^{dd}(\gamma)d\gamma - (K_{dd} - \omega\gamma^2)\left[-\lambda_{mn}A_{mn}{}^{d}e^{-\lambda_{mn}Z_0} + \lambda_{mn}B_{mn}{}^{d}e^{\lambda_{mn}Z_0} + \int_{\gamma_h}^{\gamma_t} in\beta\,(K_d/\gamma^2 - S)\,F_{mn}{}^{d}(\gamma)e^{-in\beta(Kd/\gamma^2-S)Z_0}d\gamma\right]\right) = (K_{dd} - \omega\gamma^2)P_n{}^{d}e^{-in\beta(Kd/\gamma^2-S)Z_0} \quad \text{(A6)}$$

where

Downloaded 01 Jun 2010 to 171.66.16.59. Redistribution subject to ASME license or copyright; see http://www.asme.org/terms/Terms_Use.cfm

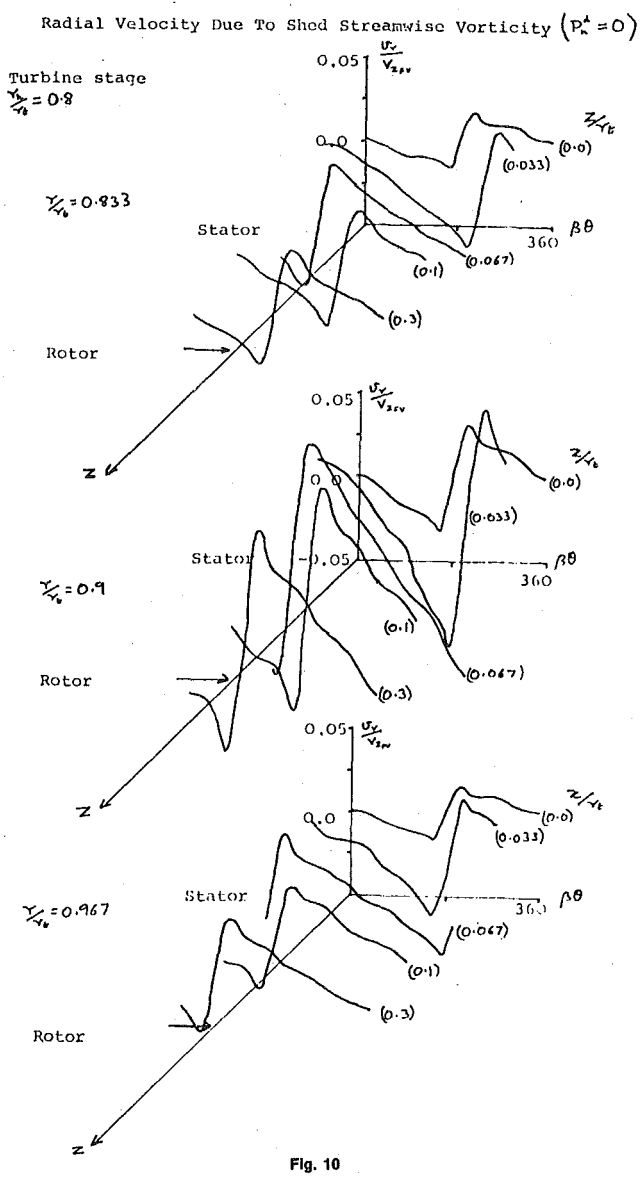

Fig. 10

$$\int_{\gamma_h}^{\gamma_t} F_{mn} e^{-in\beta(K/\gamma^2-S)Z} d\gamma = -Z_{mn}$$

Now

$$G_n{}^d(\gamma) = \frac{-2K_d i}{n\beta\bar{\Gamma}_s}\frac{\partial\Gamma_s}{\partial\gamma}(-1)^n$$

On expressing this as a series of Bessel functions such that

$$1/\bar{\Gamma}_s\ \partial\Gamma_s/\partial\gamma = \sum_{m=1}^{\infty}\Gamma_{mn}R_{n\beta'}$$

$$G_n{}^d(\gamma) = \sum_{m=1}^{\infty}\frac{-2\Gamma_{mn}K_d i(-1)^n}{n\beta}R_{n\beta'}$$

$$\Gamma_{mn} = \int_{\gamma_h}^{\gamma_t}(1-\Gamma_s(\gamma)/\bar{\Gamma}_s)\,\gamma R_{n\beta}d\gamma$$

From (A3),

$$A_{mn}{}^u - A_{mn}{}^d - B_{mn}{}^d = \frac{-2\Gamma_{mn}K_d i(-1)^n}{n\beta} - \int_{\gamma_h}^{\gamma_t} F_{mn}{}^d(\gamma)d\gamma \tag{A7}$$

From (A1), using the orthogonal properties of R,

$$\lambda_{mn}A_{mn}{}^u + \lambda_{mn}A_{mn}{}^d - \lambda_{mn}B_{mn}{}^d - \int_{\gamma_h}^{\gamma_t} in\beta\,(K_d/\gamma^2 - s)\,F_{mn}{}^d(\gamma)dy = \int_{\gamma_h}^{\gamma_t}\gamma P_n{}^d R_{n\beta}d\gamma \tag{A8}$$

Hence, from (A7) and (A8)

$$A_{mn}{}^d = 1/2\lambda_{mn}\left(\int_{\gamma_h}^{\gamma_t}\gamma P_n{}^d R_{n\beta}d\gamma + \frac{2\lambda_{mn}\Gamma_{mn}iK^d(-1)^n}{n\beta} + \int_{\gamma_h}^{\gamma_t} F_{mn}{}^d(\gamma)(\lambda_{mn} + in\beta\,(K_d/\gamma^2 - s))\right)dr \tag{A9}$$

On substituting (A9) into (A6) and rearranging

$$\begin{aligned}A_{mn}{}^{dd} = {} & \int_{\gamma_h}^{\gamma_t} F_{mn}{}^{dd}(\gamma)d\gamma - \frac{(\omega-s)}{in\beta} \\ & \times\left(\int_{\gamma_h}^{\gamma_t} y^3 R_{n\beta}\sum_{p=1}^{\infty} R_{n\beta}\lambda_{pn}B_{pn}{}^d e^{\lambda_{pn}Z_0}d\gamma\right) \\ & + \frac{K_{dd}\lambda_{mn}}{in\beta}B_{mn}{}^d e^{\lambda_{mn}Z_0} + \int_{\gamma_h}^{\gamma_t}\frac{\gamma R_{n\beta}}{in\beta}\left(\sum_{p=1}^{\infty} R_{n\beta}(K_{dd}-\omega\gamma^2)\right. \\ & \times\left[\int_{\gamma_h}^{\gamma_t} in\beta\,(K_d/\gamma^2 - s)\,F_{pn}{}^d(\gamma)e^{-in\beta(Kd/\gamma^2-S)Z_0}d\gamma\right. \\ & \left.\left. - \lambda_{pn}A_{pn}{}^d e^{-\lambda_{pn}Z_0}\right]\right)d\gamma + \frac{1}{in\beta}\int_{\gamma_h}^{\gamma_t}\gamma R_{n\beta}(K_{dd}-\omega\gamma^2) \\ & \times P_n{}^d e^{-in\beta(Kd/\gamma^2-S)Z_0}d\gamma\end{aligned} \tag{A10}$$

On subtracting (A5) from (A2) and rearranging

$$\begin{aligned}A_{mn}{}^{dd} = {} & 1/(\lambda_{mn} - in\beta\omega) \\ & \times\left[\int_{\gamma_h}^{\gamma_t} F_{mn}{}^{dd}\,(in\beta\,(K_{dd}/\gamma^2 - s) - in\beta\omega)\,d\gamma\right. \\ & - B_{mn}{}^d e^{\lambda_{mn}Z_0}(\lambda_{mn} + in\beta\omega) + A_{mn}{}^d e^{-\lambda_{mn}Z_0}(\lambda_{mn} - in\beta\omega) \\ & - \int_{\gamma_h}^{\gamma_t} F_{mn}{}^d\,(in\beta\,K_d/\gamma^2 - s) \\ & \left. - in\beta\omega)\,e^{-in\beta(Kd/\gamma^2-S)Z_0}d\gamma\right]\end{aligned} \tag{A11}$$

On substituting (A10) into (A4), and expression for $G_n{}^{dd}(\gamma)$ can be obtained, and an expression for $P_n{}^{dd}(\gamma)$ by substituting (A10) into (A6) in terms of $B_{mn}{}^d e^{\lambda_{mn}Z_0}$ alone. On equating equation (A10) and (A11) and using the expressions for $P_n{}^{dd}(\gamma)$ and $G_n{}^{dd}(\gamma)$, an implicit expression is obtained giving $B_{mn}{}^d e^{\lambda_{mn}Z_0}$ in terms of a double Bessel series.

This can then be solved by considering a finite number of terms and performing a matrix inversion. The remaining variables $A_{mn}{}^{dd}$, $P_n{}^{dd}(\gamma)$ and $G_n{}^{dd}(\gamma)$ can then be found which enables the flow velocities to be calculated. It is then possible to check the solution for accuracy by calculating the flow upstream and direction of the actuator disk. In general it was found sufficiently accurate to consider 15 terms of the Bessel (m, p) series. When used with five terms of the Fourier series representing the initial wakes, this gave a computing time of 90 s on an IBM 370/165 computer. The error in the final flow field was found to be less than 1 percent.

Downloaded 01 Jun 2010 to 171.66.16.59. Redistribution subject to ASME license or copyright; see http://www.asme.org/terms/Terms_Use.cfm

The Effect of the Axial Velocity Density Ratio on the Aerodynamic Coefficients of Compressor Cascades[1]

J. Starke

Institute of Fluid Mechanics,
Technical University of Braunschweig,
Braunschweig, Germany

The aerodynamic coefficients of compressor blade sections in two-dimensional flow can easily and very accurately be determined by use of the well-known Lieblein correlations. The flow across the compressor blade sections is often quasi-two-dimensional with the axial velocity density ratio (AVDR) differing from unity. To establish simple correlations for this type of flow as well, the AVDR effect on the aerodynamic coefficients of compressor cascades is theoretically and experimentally investigated. This results in simple but accurate formulae for the calculation of the AVDR effect on the turning angle, the reference minimum-loss inlet angle, and the losses in terms of the wake momentum thickness and the diffusion ratio.

Introduction

Commonly used design and performance calculation procedures for axial flow compressors demand reliable information on the turning angle, the reference minimum-loss inlet angle and the profile loss at each section of the blading.

If the flow is nearly two-dimensional at a blade section (the basic feature of such a flow is the constant axial velocity density product ρW_{ax} across the blading) this information can be taken from correlations described by Lieblein [1] for example. These correlations are based on numerous experiments on compressor cascades in subsonic flow.

For many reasons the value of ρW_{ax} is changed across the blading, i.e., the flow at the blade section cannot be regarded as two-dimensional

i if a compressor with cylindrical hub and casing is designed different from the free-vortex rule, Fig. 1(*a*) (to simplify matters, the meridional streamlines are plotted as straight lines);

ii if hub and casing are conical in order to compensate for the density change across the blading, Fig. 1(*b*);

iii if the growing boundary layers on hub and casing lead to a considerable contraction of the flow area.

The change of ρW_{ax} can be described by the so-called axial velocity density ratio (AVDR), Fig. 2(*a*)

$$\mu = \frac{\rho_2 W_2 \sin \beta_2}{\rho_1 W_1 \sin \beta_1} = \frac{\rho_2 W_{2ax}}{\rho_1 W_{1ax}}. \quad (1)$$

In case of a two-dimensional flow there holds $\mu = 1.0$; if the μ value deviates only little from 1.0, i.e., $0.8 \leq \mu \leq 1.2$, the flow is called quasi-two-dimensional. In axial flow compressors the μ values generally do not exceed these limits, thus such a type of flow is subject of the investigations described herein.

The AVDR effect on turning, reference inlet angle, and profile loss of an axial flow compressor blade section can roughly be characterized as an increase of these quantities if μ is increased, see for example Pollard and Gostelow [2]. It can easily be determined through investigations of the mid-span flow in plane compressor cascades with contracting sidewalls. As the above-mentioned flow parameters are almost independent of the (subcritical) Mach number for $\mu = 1.0$ as well as for $\mu \neq 1.0$ these investigations can be performed at incompressible flow [1, 3].

Much effort has been dedicated to this problem, only a few papers shall be mentioned: For potential flow calculations simple singularity methods are described by Pollard and Horlock [4], Mani and Acosta [5], Renken [6], complicated numerical methods by Katsanis [7], and Dodge [8]. Quasi-two-dimensional boundary layers are theoretically investigated by Dunham [9], Pierce [10], Mellor and Herring [11]. Mainly experimental investigations are performed by Pollard and Gostelow [2], Ikui, et al. [12], Masek and Norbury [13], and Hoheisel [3].

In spite of the great number and variety of investigations no methods are available which are as universal and reliable as the Lieblein correlations. To establish such methods systematic work has been done at the Institute of Fluid Mechanics, Technical University Braunschweig, for several years. Many results have been reported by Stark and Starke [14–17]. The most important results of these papers are summarized and new results from extensive experimental and theoretical investigations are presented in this paper. These investigations comprise potential flow calculations with well-known methods, see references [4] and [5], as well as a new modified Martensen method. Boundary layer calculations are performed with methods of Thwaites [18] and White [19], extended for the AVDR effect. Detailed experiments are carried out on several different

[1] This paper is a very abbreviated version of the author's Doctoral Thesis, which was submitted to the Technical University of Braunschweig, Germany in 1979. The thesis is entitled: "Der Einfluβdes axialen Stromdichteverhältnisses auf die aerodynamischen Beiwerte ebener Verdichtergitter" and is available as Report 79/2 of the Institute of Fluid Mechanics of the Technical University of Braunschweig (Director: Prof. Dr.-Ing. B. Laschka).

Contributed by the Gas Turbine Division of The American Society of Mechanical Engineers and presented at the Gas Turbine Conference and Products Show, New Orleans, La., March 10–13, 1980. Manuscript received at ASME Headquarters January 2, 1980. Paper No. 80-GT-134.

Copyright © 1981 by ASME

Downloaded 01 Jun 2010 to 171.66.16.59. Redistribution subject to ASME license or copyright; see http://www.asme.org/terms/Terms_Use.cfm

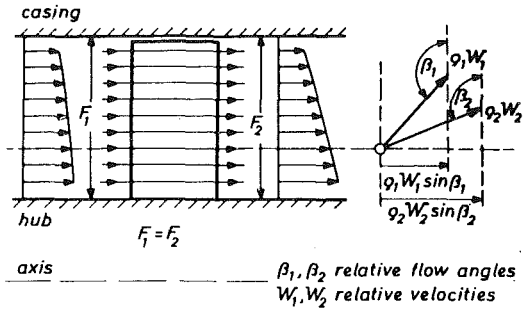

Fig. 1(*a*) Cylindrical hub and casing, non-free-vortex design

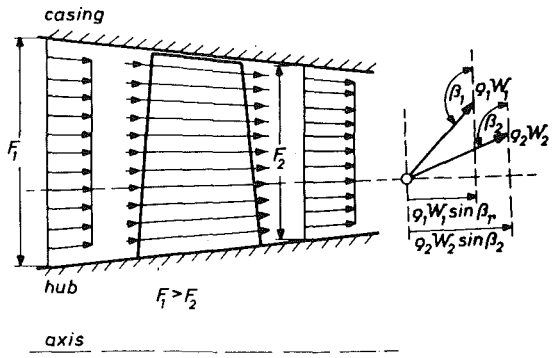

Fig. 1(*b*) Conical hub and casing, free-vortex design

Fig. 1 Meridional flow in axial compressors

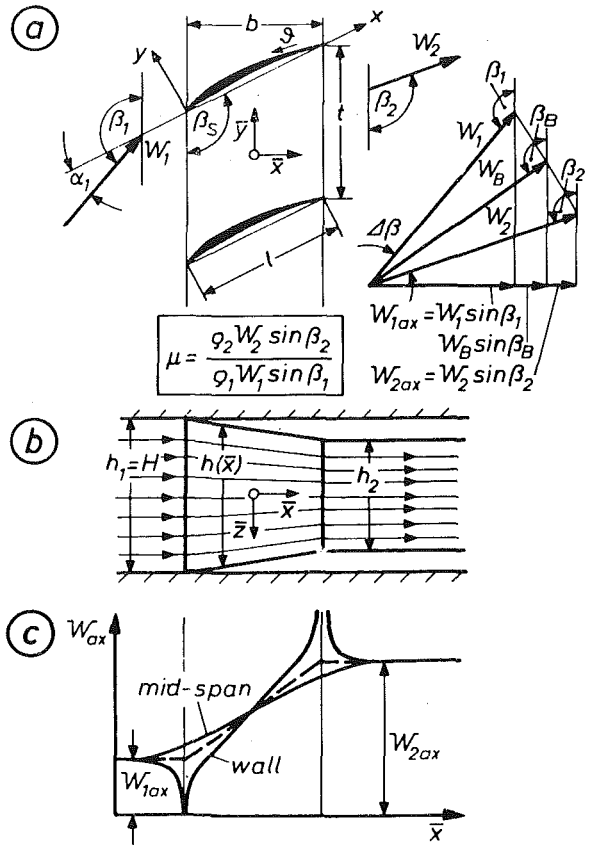

Fig. 2 Cascade notation, axial velocity distribution

compressor cascades consisting of 9C7/32.5C50 blades. From all these results simple correlations for the cascade turning, the minimum-loss inlet angle and the profile loss are established and checked against experiments and correlations by other authors. Sample calculations show the error in stage work and efficiency, if one neglects the AVDR effect on turning and losses.

Detailed information is given in reference [20].

Theoretical Investigations

Potential Flow Calculations. The quasi-two-dimensional, potential flow at the mid-span of compressor cascades is theoretically determined using the methods of Pollard-Horlock [4] (PH-method) and Mani-Acosta [5] (MA-method) for the calculation of the overall cascade parameters. A new modified Martensen method (MM-method) is used for the calculation of the pressure distribution. A detailed description is given in references [14] and [20].

Fundamental Equations of a Quasi-Two-Dimensional Inviscid and Incompressible Flow. The three-dimensional flow through a cascade with contracting sidewalls (Fig. 2(*b*)) can be regarded as quasi-two-dimensional, if $\mu = h_1/h_2$ does not differ too much from 1 ($0.8 \le \mu \le 1.2$). Then one can assume that $h(\bar{x})$ is a slowly varying function of $\bar{x}$ which allows to describe the flow approximately by spanwise averaged quantities. This results in fundamental equations for the potential function Φ and the stream function Ψ being formally two-dimensional:

Nomenclature

Only the most important quantities are given here, other quantities are explained in the text.

b = axial chord
c_p = specific heat at constant pressure
c_{p1} = static pressure coefficient, equation (17)
F = flow area
h = test section width
H = blade height
H = shape factor, δ^*/Θ
ℓ = blade chord
Ma = Mach number
p = static pressure
$\Delta p/q_1$ = static pressure rise, equation (15)
p_t = total pressure
q = dynamic pressure, $\rho W^2/2$
Re_1 = blade chord Reynolds number, $W_1\ell/\nu$
t = blade spacing
ΔT_t = total temperature rise across the rotor blading
x, y, z = rectangular coordinates
$\bar{x}, \bar{y}, \bar{z}$ = rectangular coordinates
u, v = boundary layer velocities, u tangential, v normal to the wall
U = free stream velocity
U_R = blade speed
v^* = friction velocity, $(\tau_W/\rho)^{1/2}$
W = air velocity
$W_{2'}$ = free-stream velocity, measuring plane
W_d = disturbance velocity due to sidewall
β = flow angle
β_S = blade angle
$\Delta\beta$ = flow turning, equation (15)
γ = vortex distribution
δ = boundary layer thickness
δ^* = displacement thickness
ζ_{V1} = total pressure loss coefficient, equation (15)
η = efficiency, equation (28)
ϑ = blade contour coordinate
Θ = momentum thickness
λ = skin friction parameter, equation (9) or work coefficient, equation (21)
μ = axial velocity density ratio, equation (1)
ν = kinematic viscosity
ρ = density
σ = solidity, ℓ/t
τ_W = wall shear stress
φ = flow coefficient, equation (21)
Φ = potential function
Ψ = stream function

Subscripts

1, 2 = for quantities in front of and behind the cascade
2′ = for quantities in the measuring plane
ax = axial ($\bar{x}$-direction)
P, S = blade pressure and suction side
B = basic flow
max = maximum
ref = reference
te = trailing-edge
$\bar{x}, \bar{y}$ = partial differentiation, $\bar{x}, \bar{y}$-direction

Superscripts

′ = x-derivative or inducing point
./.. = first/second ϑ-derivative

Downloaded 01 Jun 2010 to 171.66.16.59. Redistribution subject to ASME license or copyright; see http://www.asme.org/terms/Terms_Use.cfm

$$\Phi_{\bar{x}\bar{x}} + \Phi_{\bar{y}\bar{y}} = -\frac{h'(\bar{x})}{h(\bar{x})}\Phi_{\bar{x}} \tag{2}$$

$$\Psi_{\bar{x}\bar{x}} + \Psi_{\bar{y}\bar{y}} = \frac{h'(\bar{x})}{h(\bar{x})}\Psi_{\bar{x}}. \tag{3}$$

All flow quantities of these and the following equations are spanwise averaged quantities.

If h is finite (Fig. 2(b)) equations (2) and (3) apply approximately; they do, however, apply exactly in case of infinitesimal thin stream tubes with $h \to 0$, $h' \to 0$ but $h'/h \neq 0$ [5].

If h is constant, i.e., in case of a two-dimensional flow, equations (2) and (3) reduce to the Laplace equations.

The Calculation Methods of Pollard-Horlock and Mani-Acosta. As in the two-dimensional case, equations (2) and (3) for the quasi-two-dimensional case are linear. Hence the same solution procedures can be adopted: Φ and Ψ of a complicated flow can be determined from a superposition of simple fundamental solutions of equations (2) and (3).

The MA-method and the PH-method are based on the methods by Mellor [21] and Schlichting [22], respectively. They are restricted to typical compressor cascades because of the singularity distribution along the blade chord. In the MA-method the AVDR effect is introduced by determining the source- and vortex-type singularities as well as the basic flow from equations (2) and (3); in the PH-method, however, this is only done for the basic flow while sources and vortices of the common two-dimensional type are used. Thus these singularities are solutions of the Laplace equations.

In both methods a linear axial velocity variation across the cascade is incorporated, which again represents a spanwise averaged quantity, Fig. 2(c). It should be noticed, however, that the linear distribution differs from the local axial velocity distribution at mid-span, the consequence of which will be discussed later.

Theoretical results of both methods and experimental results from reference [14] for the turning angle $\Delta\beta$ as a function of μ are shown in Fig. 3 for different inlet angles β_1. At constant β_1 the turning increases almost linearly with increasing μ. The $\Delta\beta$ values of both theoretical methods agree very well. Only small differences occur at $\mu = 1.0$, these differences hardly change with μ. This indicates that the error in the PH-method because of the two-dimensional source and vortex-type singularities has no significant influence on the final results. Therefore the much simpler PH-method has been used for further calculations.

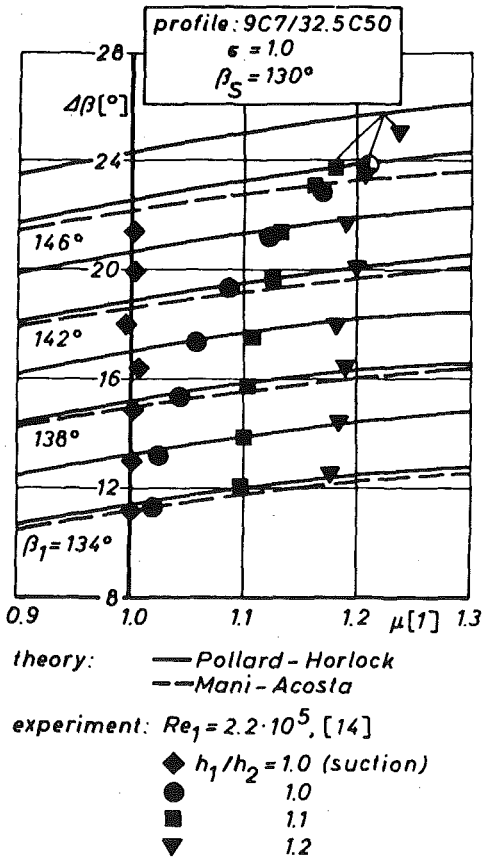

Fig. 3 Turning $\Delta\beta$ as a function of μ, comparison of theory and experiment

The theoretical results agree very well with the experimental results as long as no stronger viscous effects occur. Hence the linear axial velocity distribution seems to be accurate enough with respect to the calculation of the overall parameters.

The Modified Martensen Method. The pressure distributions from the PH-method on the other hand agree only fairly with experiments, see reference [23]. By use of a modified Martensen method the prediction of the pressure distributions is improved: (i) Any limitation with respect to the cascade geometry is avoided by distributing the singularities along the blade surfaces [24]. (ii) If one applies equations (2) and (3) to an infinitesimal thin stream tube at mid-span, thus the spanwise flow quantities being equal to the local ones, a better theoretical representation of the local flow properties than in the PH-method is achieved. This consequently requires to introduce the local axial velocity distribution at mid-span into the calculation procedure.

As in the PH-method only the basic flow satisfies the fundamental equations (2) and (3). This leads to the following main equation for the MM-method:

$$\hat{\gamma}(\vartheta) - \frac{1}{2\pi}\int_0^{2\pi}\left[K(\vartheta,\vartheta') + \frac{2\pi}{t}\dot{\bar{y}}(\vartheta)\right]\hat{\gamma}(\vartheta')d\vartheta' = 2W_1[\dot{\bar{x}}(\vartheta)\sin\beta_{1g}(\bar{x}(\vartheta)) - \dot{\bar{y}}(\vartheta)\cos\beta_1]. \tag{4}$$

Equation (4) is a Fredholm integral equation of second kind for the variable

$$\hat{\gamma}(\vartheta) = \gamma(\vartheta)\sqrt{\dot{\bar{x}}^2(\vartheta) + \dot{\bar{y}}^2(\vartheta)} \tag{5}$$

with $\gamma(\vartheta)$ as the vortex distribution (being identical with the surface velocity distribution) and $\bar{x}(\vartheta)$, $\bar{y}(\vartheta)$ as a parametric representation of the blade contour. The *l.h.s.* of equation (4) including the kernel $K(\vartheta, \vartheta')$ is the same as in the original equation [24]. In the r.h.s. the AVDR effect is incorporated into the axial component of the basic flow by

$$W_1\sin\beta_{1g}(\bar{x}(\vartheta)) = W_B\sin\beta_B + W_d(\bar{x}) = W_B\sin\beta_B\left\{1 - \frac{\mu-1}{\mu+1}\frac{h_1}{\pi b}\left[\ln\left(\cosh\frac{\pi b}{h_1} - \tanh\frac{\pi b}{h_1}\left(\frac{\bar{x}}{b}+\frac{1}{2}\right)\sinh\frac{\pi b}{h_1}\right)\right]\right\}. \tag{6}$$

Equation (6) describes the mid-span velocity distribution of blade free channels with (approximately) linearly shaped sidewalls [25]. At $\mu = 1.0$ there holds $g = 1.0$ and equation (4) reduces to the original Martensen equation [24]. In Fig. 4 the disturbance velocity $W_d(\bar{x})$ due to the sidewalls is plotted versus $\bar{x}$ for different aspect ratios revealing an increasing difference from the linear variation with increasing aspect ratio.

The fact that merely the basic flow satisfies equations (2) and (3) leads to very small normal velocities on the blade contour, i.e., the kinematic boundary condition is only approximately satisfied. In reference [20] it is shown, however, that the error in the final results is negligible compared to the difference between the results of the PH- and MA-method.

Experimental as well as theoretical pressure distributions from the three presented methods are compared in Fig. 5: The results of the PH- and MA-method again agree very well whereas there is only fair agreement with the experiments at $\mu > 1.0$. The results of the MM-method, however, agree perfectly with the experiments at any μ value.

Boundary Layer Calculations. Quasi-two-dimensional boundary layers are theoretically investigated with a modified Thwaites method [18] for laminar boundary layers and a new method

Downloaded 01 Jun 2010 to 171.66.16.59. Redistribution subject to ASME license or copyright; see http://www.asme.org/terms/Terms_Use.cfm

based on the inner variable method of White [19] for turbulent boundary layers.

Modified Thwaites Method. The boundary layer momentum thickness is calculated from the following simple integral relation [9]:

$$\left(\frac{\Theta(x^*)}{\ell}\right)^2 = \frac{0.45}{\mathrm{Re}_1}\frac{h^{*2}(x^*)}{U^{*6}(x^*)}\int_0^{x^*} U^{*5}(x^*)h^{*2}(x^*)dx^*, \qquad (7)$$

with the nondimensional quantities $U^* = U/W_1$, $h^* = h/h_1$, $x^* = x/\ell$. The remaining boundary layer parameters can be taken from (almost) universal graphs or tables [18].

At $\mu = 1.0$, $h^* = 1.0$ holds and equation (7) is reduced to the original Thwaites formula [18].

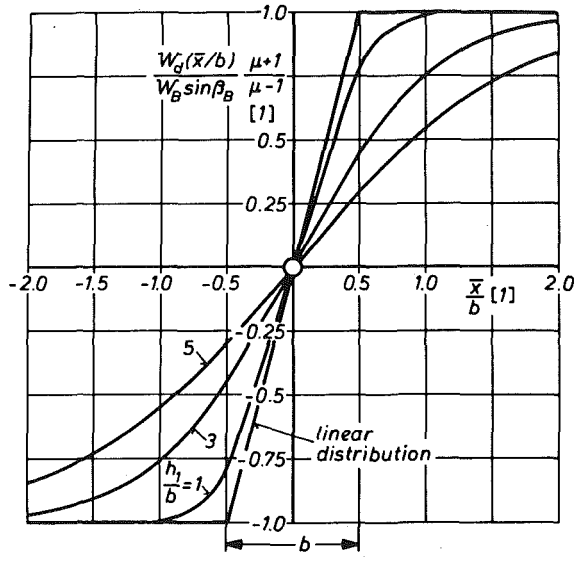

Fig. 4 Normalized axial velocity distribution at the mid-span of blade-free channels with (approximately) linearly converging sidewalls [25]

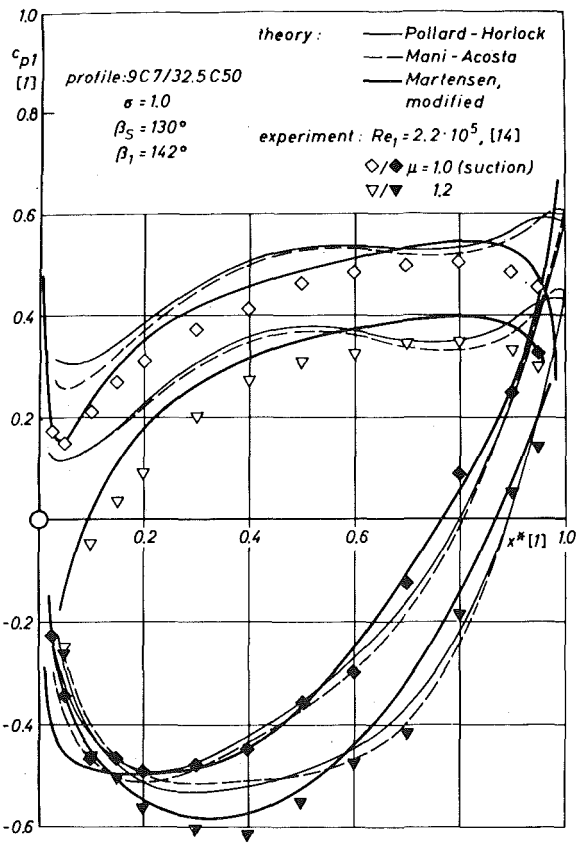

Fig. 5 Blade pressure distribution, comparison of theory and experiment

Modified White Method. White's method [19] belongs to the class of integral methods, though the Kármán integral relation is not used. It is based on the assumption that the turbulent velocity profile can be described with sufficient accuracy by the Coles law of the wall and a simplified linear term for the wake function. Using the inner variables $u^+ = u/v^*$ and $y^+ = yv^*/\nu$ leads to the following equation:

$$u^+ = \frac{1}{\varkappa}\ln y^+ + B + b\alpha y^+, \qquad (8)$$

the constants are $\varkappa = 0.4$ and $B = 5.5$. The simplified wake term contains the constant $b = 0.6$ from White's approximation and the pressure gradient parameter $\alpha = \nu\lambda^3 d(1/U)/dx$, [19]. The factor λ is defined as $\lambda = U^*/v^* = (\rho U^{*2}/\tau_W)^{1/2}$, it can be calculated from equation (8) setting $y^+ = \delta^+$

$$\lambda = \frac{U^*}{v^*} = \frac{1}{\varkappa}\ln\delta^+ + B + b\alpha\delta^+. \qquad (9)$$

The extension of the White method is based on the additional assumption that equation (8) also applies to a quasi-two-dimensional velocity profile. Then the corresponding v-component of the velocity profile can be determined from the u-component $u = u^+v^*$ and the continuity equation for a quasi-two-dimensional flow [5],

$$\frac{\partial(uh)}{\partial x} + \frac{\partial(vh)}{\partial y} = 0. \qquad (10)$$

Both velocity components substituted into the boundary layer equation for the blade symmetry plane (being identical with the two-dimensional boundary layer equation, [10]) finally yields after integration along y

$$\frac{d\lambda}{dx^*} = \frac{\dfrac{(1/U^*)'}{(1/U^*)}(1 + 7.8\hat{g}^*\mathrm{Re}^{*0.079})}{0.119\hat{f}^*\mathrm{Re}^{*0.018}} - \frac{\dfrac{\lambda}{h^*}\dfrac{dh^*}{dx^*}2.244\hat{i}^*\mathrm{Re}^{*0.092}}{0.119\hat{f}^*\mathrm{Re}^{*0.018}} + \frac{\dfrac{(1/U^*)''}{(1/U^*)'}1.85\hat{h}^*\mathrm{Re}^{*0.0099}}{0.119\hat{f}^*\mathrm{Re}^{*0.018}}. \qquad (11)$$

Equation (11) is a simple differential equation for the single variable λ with the second term of the numerator being new because of the AVDR effect. At $\mu = 1.0$ we have $dh^*/dx^* = 0$, then equation (11) is reduced to the original White formula [19].

Equation (11) contains a so-called stretched Reynolds number defined by

$$\mathrm{Re}^* = \frac{\mathrm{Re}_1}{(1/U^*)'}. \qquad (12)$$

The quantities $\hat{f}^*$, $\hat{g}^*$, $\hat{h}^*$, $\hat{i}^*$ are universal functions only depending on $\lambda^* = \lambda/\lambda_{\max}$ with

$$\lambda_{\max} = 4.215(\log \mathrm{Re}^*)^{1.353}, \qquad (13)$$

see Fig. 6. Compared to the functions $\hat{f}^*$, $\hat{g}^*$, $\hat{h}^*$ of the original White method the new function $\hat{i}^*$ fits in reasonably indicating that the modification of the method has been properly done.

An important feature of equation (11) is the fact that there is no need of a special separation criterion, because separation is predicted, if λ is infinite or $\tau_W = 0$. This occurs at $\lambda = \lambda_{\max}$, i.e., the denominator function $\hat{f}^*$ of equation (11) becomes zero, Fig. 6.

With the prescribed quantities $U^*(x^*)$, $h^*(x^*)$, Re_1 and an initial value λ_0 the boundary layer calculation can be performed: After Re^* and $\lambda_{\max}$ computed from equations (12) and (13) the functions $\hat{f}^*$, $\hat{g}^*$, $\hat{h}^*$ and $\hat{i}^*$ can be read from Fig. 6. With $d\lambda/dx^*$ from equation (11) the value of λ at the following point $x^* + \Delta x^*$ is obtained from $\lambda_0 + d\lambda/dx^*\,\Delta x^*$. Then the same procedure is repeated using the new λ value.

With λ substituted into equation (9) the boundary layer thickness

Downloaded 01 Jun 2010 to 171.66.16.59. Redistribution subject to ASME license or copyright; see http://www.asme.org/terms/Terms_Use.cfm

δ^+ can be calculated by iteration. If one defines an equivalent wake parameter

$$\Pi_{eq} = \frac{\varkappa}{2} b\omega\delta^+, \tag{14}$$

the original Coles formulae [19, 20], can be used to determine the displacement thickness δ^* and the momentum thickness Θ.

Figure 7 (taken from reference [26]) shows the blade trailing-edge momentum thickness $(\Theta/\ell)_{te}$ at $\mu = 1.0$ as a function of the suction surface diffusion ration $W_{max,S}/W_{te}$ based on the trailing-edge velocity. The curves are determined using the Mellor-Herring method (solid lines) and experimental data from reference [27] (dotted lines). For comparison, the results from the modified White method are also plotted in Fig. 7. The calculations are performed using simplified velocity distributions as shown in the upper part of Fig. 7. The initial value λ_0 for the White method is estimated at first trial from the Thwaites method assuming a very short laminar boundary layer behind the stagnation point, [20]. An artifical variation of λ_0 by ± 10 percent changes the final results only for smaller initial values than predicted by the Thwaites method.

Though the mathematical effort of both methods is remarkably different, the results agree perfectly, except for the fact that the White method predicts separation at smaller values $W_{max,S}/W_{te}$ than the Mellor-Herring method. In both methods, however, $W_{max,S}/W_{te}$ at separation is much smaller than 2.0 which is predicted from experiments.

Figure 8 shows that the momentum thickness varies linearly with μ, the influence of Re_1 and $W_{max,S}/W_{te}$ being negligible. Again both methods agree perfectly thus confirming the modification of the White method to be successful.

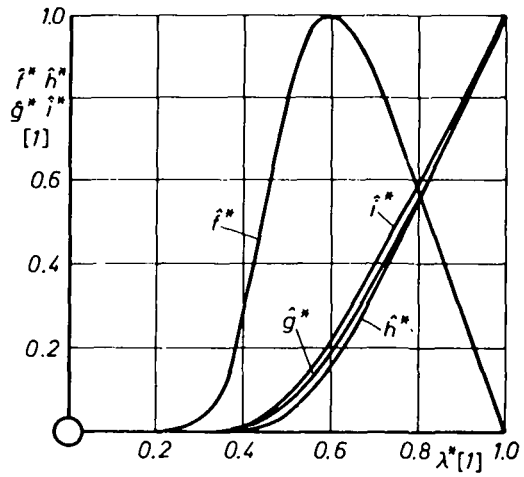

Fig. 6 The normalized functions $\hat{f}^*$, $\hat{g}^*$, $\hat{h}^*$ and $\hat{i}^*$ of the modified White method

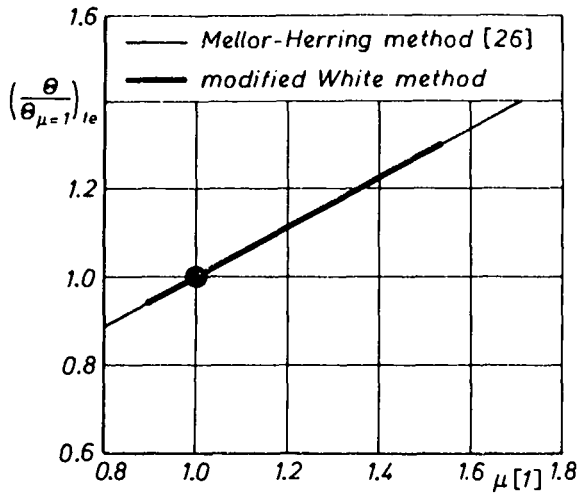

Fig. 8 The AVDR effect on the trailing-edge momentum thickness. Comparison of theories (Mellor-Herring method, modified White method)

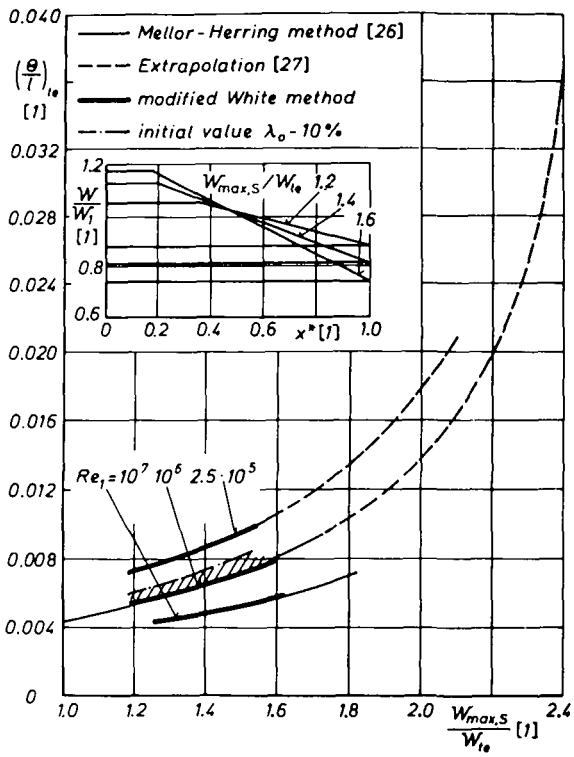

Fig. 7 Trailing-edge momentum thickness $(\Theta/\ell)_{te}$ as the function of the suction surface diffusion ratio $W_{max,S}/W_{te}$ at $\mu = 1.0$. Comparison of theories (Mellor-Herring method, modified White method)

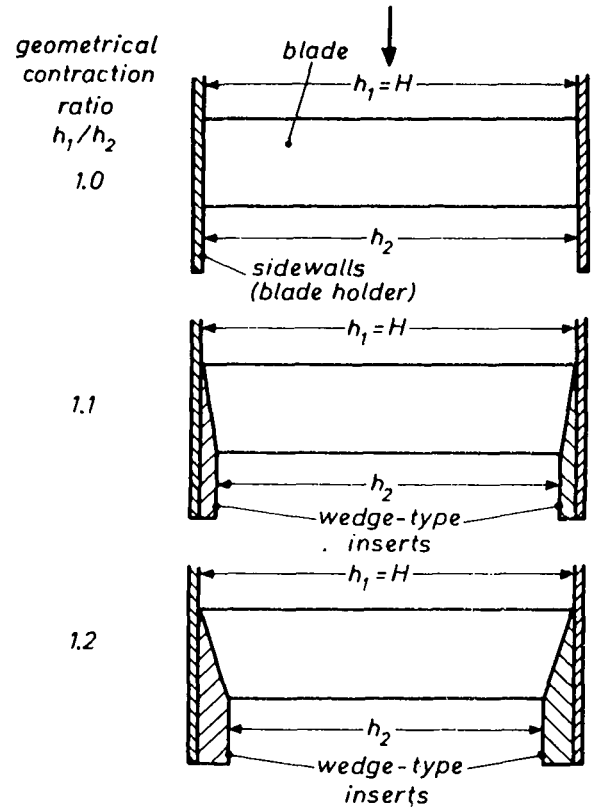

Fig. 9 Test section geometry, topview onto the cascade

Downloaded 01 Jun 2010 to 171.66.16.59. Redistribution subject to ASME license or copyright; see http://www.asme.org/terms/Terms_Use.cfm

Experimental Investigations

Experimental Apparatus. The experimental investigations were carried out in the Large Cascade Tunnel at the Institute of Fluid Mechanics. The nominal test section width is $h_1 = 600$ mm, its height varies from 340 to 900 mm depending on the inlet angle, solidity and blade number.

A periodic cascade flow was achieved by a boundary layer suction device installed at the horizontal test section walls just above and below the last blades of the cascades. The suction mass flow was controlled through the pressure distribution which is measured using pressure tappings in a plane located at about one chord in front of the cascade.

A μ variation is achieved by using the sidewall boundary layer displacement thickness in combination with a geometrical contraction (Fig. 9).

Wake measurements were performed with a wedge probe [20] located at about one chord behind the cascade outlet plane. Pressure distributions were measured using static pressure tappings on the suction and pressure side of two adjacent blades.

Cascade Geometry and Test Program. Eight different cascades were tested (Table 1). They consisted of 9C7/32.5C50 blades with a circular arc camber line (camber angle 32.5 deg) and a British C7-thickness distribution (9 percent relative thickness). The blade span was $H = 600$ mm, the chord length $\ell = 120$ mm, the aspect ratio $H/\ell = 5.0$. Blade geometry and aspect ratio were kept constant throughout the experiments. The test program mainly comprised wake and pressure distribution measurements at blade mid-span for the whole range of inlet angles β_1. Additional wake measurements along blade span and oil flow pictures ensured the flow properties to be sufficiently constant in the mid-span region.

The inlet velocity was $W_1 = 44$ m/s, the blade chord Reynolds number $\mathrm{Re}_1 = W_1\ell/\nu = 3.5 \cdot 10^5$ and the turbulence level was smaller than 0.3 percent.

Evaluation of the Experimental Data. The wake data were evaluated by transforming the nonhomogeneous flow at the measuring station into an equivalent homogeneous flow using continuity equation and momentum theorem [28]. This results in simple relations for the total pressure loss coefficient ζ_{V1}, the static pressure rise $\Delta p/q_1$ and the turning angle $\Delta\beta$ which are defined as

$$\zeta_{V1} = \frac{p_{t1} - p_{t2}}{q_1}, \qquad \frac{\Delta p}{q_1} = \frac{p_2 - p_1}{q_1}, \qquad \Delta\beta = \beta_1 - \beta_2. \tag{15}$$

Using the Bernoulli equation μ is obtained from

$$\mu = \frac{\sin\beta_2}{\sin\beta_1}\sqrt{1 - \left(\frac{\Delta p}{q_1} + \zeta_{V1}\right)}. \tag{16}$$

For the pressure distribution a nondimensional coefficient is defined as

$$c_{p1}(x^*) = \frac{p(x^*) - p_1}{q_1}. \tag{17}$$

The momentum theorem applied to a blade together with the flow parameters of equations (15) and (16) yields the blade force coefficients, [12, 14]. According to suggestions made by Emery, et al. [29], the quality of the measurements was checked by comparison of the normal force coefficients (with respect to the blade chord) from the wake data and the pressure distributions; both coefficients should agree to within ±5 percent.

Analysis of the Data

Turning Angle. The turning angle $\Delta\beta$ at $\mu = 1.0$ as well as $\mu \neq 1.0$ cannot be predicted precisely by the use of potential flow theories because viscous effects are not included. As the almost linear *change* of $\Delta\beta$ with μ, however, is very well predicted by the PH-method, a simple correlation formula was established [14, 16]. It contains $\Delta\beta$ at $\mu = 1.0$ to be taken from any reliable source and the slope factor

Table 1 Geometry of the tested cascades

profile: 9C7/32.5C50				
β_S [°]	110	120	130	140
$\sigma = \frac{l}{t}$ [1]	1.25	1.0 1.25	0.67 1.0 1.25 2.0	1.0

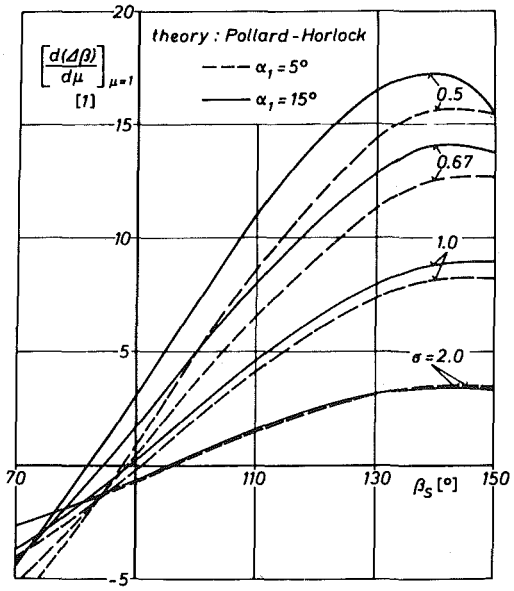

Fig. 10 Slope factor $d(\Delta\beta)/d\mu$ at $\mu = 1.0$ as a function of the cascade geometry and the angle of attack

$d(\Delta\beta)/d\mu$ at $\mu = 1.0$ calculated from the PH-method:

$$[\Delta\beta]_{\mu\neq1} = [\Delta\beta]_{\mu=1} + \left[\frac{d(\Delta\beta)}{d\mu}\right]_{\mu=1}(\mu - 1). \tag{18}$$

The slope factor depends on the cascade geometry as shown in Fig. 10, it depends linearly on the angle of attack whereas the influence of the blade geometry is negligible [16]. In Fig. 11 the turning angle $\Delta\beta$ from equation (18) (with $[\Delta\beta]_{\mu=1}$ from the Schlichting method) is compared with the measured $\Delta\beta$ of one of the tested cascades. The experimental data at $\mu > 1.0$ are supplemented by $\Delta\beta$ at $\mu = 1.0$ from the Lieblein correlation [1], slightly modified for C-profiles (design point, flagged symbol), and from the Schlichting method (slope $d(\Delta\beta)/d(\beta_1)$).

Correlation and experiment predict an increase of $\Delta\beta$ with μ at constant β_1. Both results agree very well; great differences with respect to the absolute values and the slopes occur at greater β_1, at which, depending on the loading, strong viscous effects become predominant. The loading itself is distinctly related to μ as will be discussed.

In Fig. 12 $\Delta\beta$ values from equation (18), from a similar correlation formula [4]

$$[\Delta\beta]_{\mu\neq1} = [\Delta\beta]_{\mu=1} + 10(\mu - 1) \tag{19}$$

and from experiments [13] are compared. Equation (18) yields much better agreement with the experiment than equation (19). This is due to the constant slope factor in equation (19), as it applies only for a few cascade configurations (Fig. 10).

Finally $\Delta\beta$ values from equation (18), from a calculation method based on the assumption that the blade circulation is not influenced by μ [30], and from experiments [31], are shown in Fig. 13. Again the

Downloaded 01 Jun 2010 to 171.66.16.59. Redistribution subject to ASME license or copyright; see http://www.asme.org/terms/Terms_Use.cfm

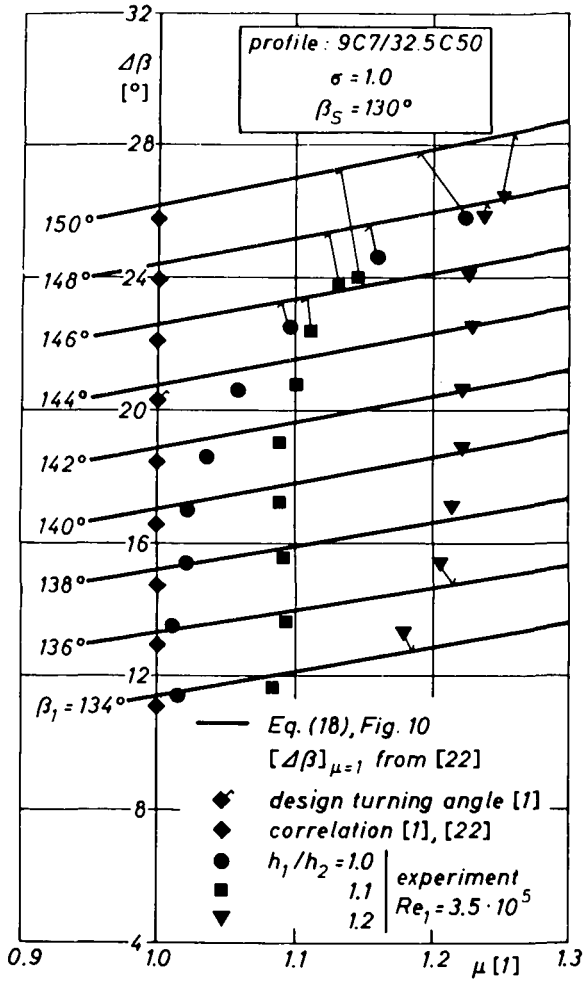

Fig. 11 Turning $\Delta\beta$ as a function of μ, comparison of correlation, equation (18) and experiment

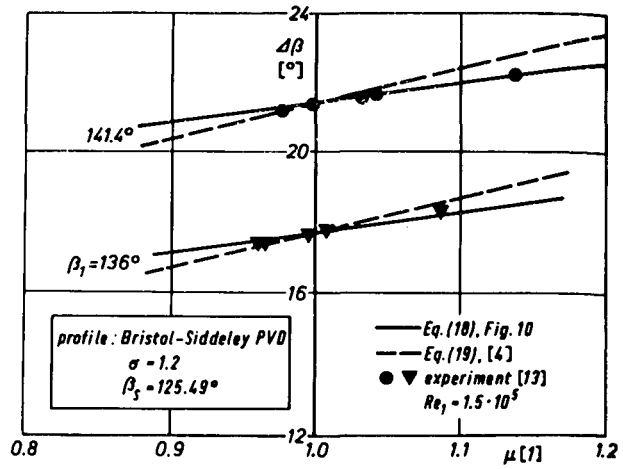

Fig. 12 Turning $\Delta\beta$ as a function of μ, comparison of correlations, equation (18) and equation (19), and experiment, [13]

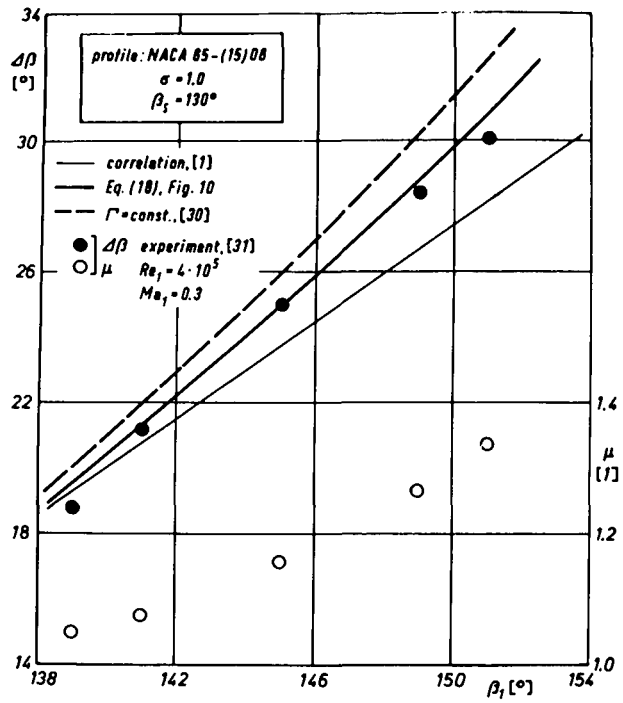

Fig. 13 Turning $\Delta\beta$ and AVDR as a function of β_1, comparison of correlation, equation (18), theory [30] and experiment [31]

best agreement with the experiments is obtained from equation (18), thus revealing a remarkable AVDR effect on the blade circulation (see reference [5]).

Sample calculations for the rotor work coefficient demonstrate the importance of a correct turning angle estimation including the AVDR effect: Different compressor rotors are considered at different Mach numbers with the axial *velocity* ratio $W_2 \sin\beta_2/W_1 \sin\beta_1$ kept constant at 1.0. Hence the μ value is only determined by the density ratio

$$\mu = \frac{\rho_2}{\rho_1} = \left\{\frac{\varkappa - 1}{2} \mathrm{Ma}_1^2 \left[1 - \left(\frac{\sin\beta_1}{\sin\beta_2}\right)^2\right] + 1\right\}^{1/\varkappa - 1} \tag{20}$$

which at the same time determines the area ratio F_1/F_2 necessary to compensate the increasing density at increasing Mach number. The work coefficient λ and the flow coefficient φ are defined as

$$\lambda = \frac{c_p \Delta T_t}{U_R^2} = \varphi(\cot\beta_2 - \cot\beta_1),$$
$$\varphi = \frac{W_{1ax}}{U_R} = \frac{W_1 \sin\beta_1}{U_R}. \tag{21}$$

In equations (20) and (21) only the outlet angle $\beta_2 = \Delta\beta - \beta_1$ has to be calculated with regard to the AVDR effect. Figure 14 shows a distinct variation of λ with μ, the slope of which depends on the cascade geometry. This indicates that considerable errors can occur (up to 6 percent for this example), if the AVDR effect on $\Delta\beta$ is neglected.

Reference Minimum-Loss Inlet Angle. The reference minimum-loss inlet angle $\beta_{1\mathrm{ref}}$ is commonly predicted by the loss coefficients plotted versus β_1, [1] (Fig. 15). The loss curves at constant μ, presented in Fig. 15, are generated by crossplotting the experimental ζ_{V1} data at varying μ. The AVDR effect on the loss curves leads to a shift of these curves toward higher β_1, thus influencing $\beta_{1\mathrm{ref}}$ in the same way (arrows from above).

For cascades in two-dimensional flow tested at fixed β_1-operation, $\beta_{1\mathrm{ref}}$ can easily be predicted from Lieblein's correlations [1]. For cascades tested at fixed β_S-operation as in the present investigations, a correction can be added.

Another method is proposed by Dodge [8]: The boundary layer development, and consequently the blade losses, are primarily determined by the blade surface diffusion ratio $W_{\max}/W_{2'}$. An overall diffusion ratio for both blade surfaces is defined as

$$\Sigma \frac{W_{\max}}{W_{2'}} = \left[\frac{W_{\max}}{W_{2'}}\right]_S + \left[\frac{W_{\max}}{W_{2'}}\right]_P. \tag{22}$$

This quantity plotted versus β_1 shows a distinct minimum [8, 20]. The losses are expected to have their minimum at the same β_1 value which is interpreted as the reference minimum-loss inlet angle β_{ref}.

Equation (22) is evaluated using the MM-method with the turning angle calculated by the PH-method ($W_{2'}/W_1 = W_2/W_1$ in inviscid flow), thus the AVDR effect on $\beta_{1\mathrm{ref}}$ can be incorporated. The resulting $\beta_{1\mathrm{ref}}$ values (arrows from below) are about 2 deg greater than the experimental values, Fig. 15. This is due to the fact that the ex-

Downloaded 01 Jun 2010 to 171.66.16.59. Redistribution subject to ASME license or copyright; see http://www.asme.org/terms/Terms_Use.cfm

perimental β_{1ref} value is not necessarily identical with β_1 at the actual minimum-loss [1]. Furthermore, the right branch of the loss curve cannot be reliably predicted from experiments because of three-dimensional effects [20]. It should be mentioned that the theoretically predicted β_{1ref} values at $\mu = 1.0$ are identical with β_{1ref} from the Lieblein correlation corrected with regard to the constant β_S operation [20].

Contrary to this, the almost linear β_{1ref} variation with μ from theory and experiment agree very well. Thus in analogy to equation (18) a very simple formula can be defined as

$$[\beta_{1ref}]_{\mu\neq 1} = [\beta_{1ref}]_{\mu=1} + \left[\frac{d(\beta_{1ref})}{d\mu}\right]_{\mu=1} (\mu - 1). \tag{23}$$

The slope factor is given in Fig. 16 but only for cascades with 9C7/32.5C50 profiles because of the extraordinary computational effort needed to establish these curves. With $[\beta_{1ref}]_{\mu=1}$ from any reliable source, equation (23) represents a very simple but accurate means to predict β_{1ref} including the AVDR effect.

Losses. A commonly used method to calculate the profile losses is due to Lieblein [27]. It applies to $\beta_1 \geq \beta_{1ref}$ at $\mu = 1.0$ and is based on a universal relation between the suction surface diffusion ratio $W_{maxS}/W_{2'}$ and the wake momentum thickness $(\Theta/\ell)_{2'}$ being a measure of loading and losses, respectively. To extend the method for $\mu \neq 1.0$, the AVDR effect on both quantities has to be examined.

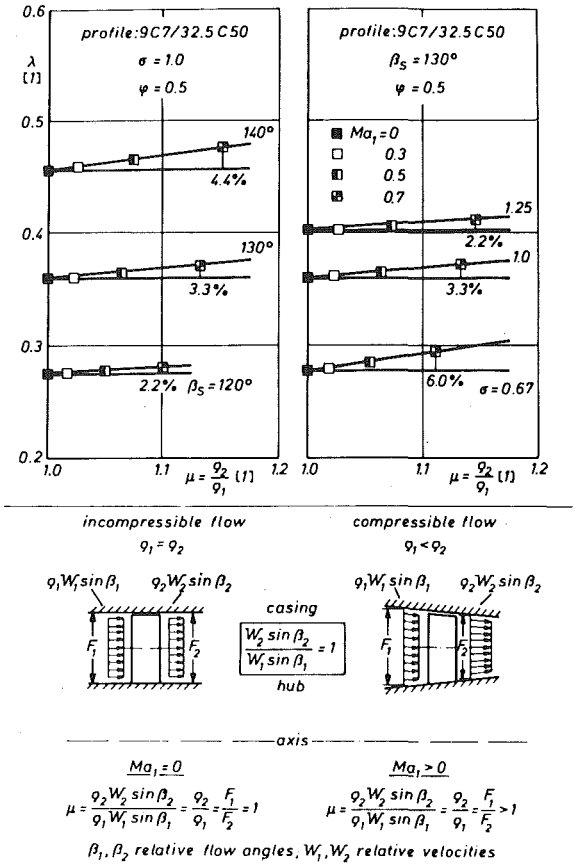

Fig. 14 The AVDR effect on the work coefficient λ of different compressor rotor bladings, compressible flow

Suction Surface Diffusion Ratio. $W_{maxS}/W_{2'}$ can be computed from experimental data by

$$\frac{W_{maxS}}{W_{2'}} = \frac{W_{maxS}}{W_1}\frac{1}{\mu}\frac{\sin\beta_2}{\sin\beta_1}\left[1 - \left(\frac{\Theta}{l}\right)_{2'}\frac{\sigma H_{2'}}{\sin\beta_2}\right] \tag{24}$$

with the wake momentum thickness

$$\left(\frac{\Theta}{\ell}\right)_{2'} = \frac{\frac{1}{\mu}\zeta_{V1}\frac{\sin\beta_1}{\sigma}\frac{\sin^2\beta_2}{\sin^2\beta_1}}{1 + b + \sqrt{1 + (2 + H_{2'})b}}, \qquad b = \frac{1}{\mu}\zeta_{V1}H_{2'}\frac{\sin^2\beta_2}{\sin^2\beta_1} \tag{25}$$

according to references [27] and [32]. These equations include the AVDR effect; at $\mu = 1.0$ they reduce to the original equations given in references [27] and [32]. For the evaluation of equations (24) and (25) $H_{2'} = 1.1$ was chosen [32].

As the pressure distributions from the MM-method and from the experiments agree almost perfectly at any μ (Fig. 17) the theoretical prediction of $W_{maxS}/W_{2'}$ is based on this method.

If no pressure distribution is available, a correlation formula for the equivalent diffusion ratio $D_{eq} \approx W_{maxS}/W_{2'}$ [27], can be used; it is modified for the AVDR effect according to a proposal by Klapproth [27]

$$D_{eq} = \frac{1}{\mu}\frac{\sin\beta_2}{\sin\beta_1}\left[1.12 + a(\beta_1 - \beta_{1ref})^{1.43} + 0.61\frac{\sin^2\beta_1}{\sigma}(\mu\cot\beta_2 - \cot\beta_1)\right]. \tag{26}$$

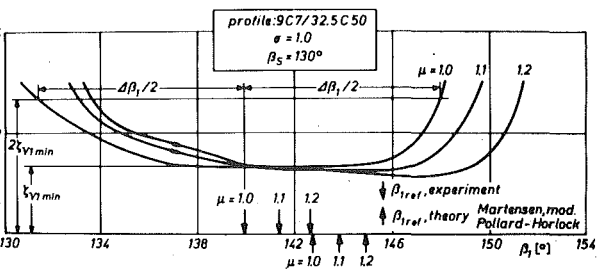

Fig. 15 Reference minimum-loss inlet angle β_{1ref} from total pressure loss coefficient ζ_{V1} as a function of β_1, comparison with theoretical results

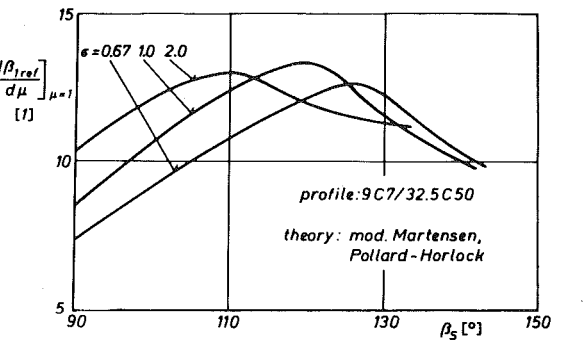

Fig. 16 Slope factor $d\beta_{1ref}/d\mu$ at $\mu = 1.0$ as a function of the cascade geometry for 9C7/32.5C50 profiles

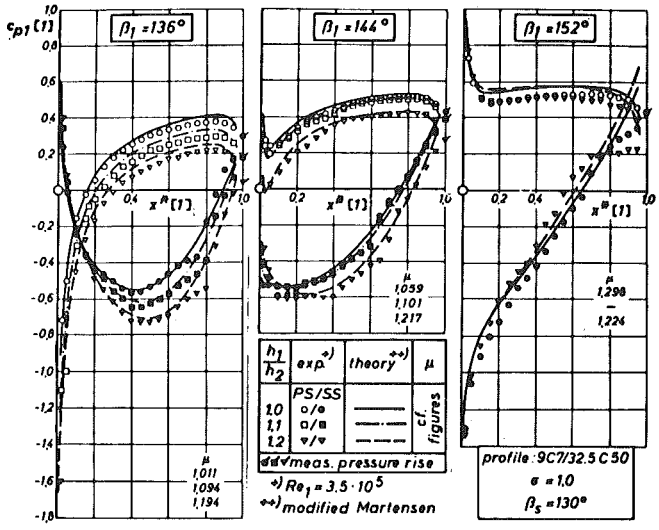

Fig. 17 Pressure distributions $c_{p1}(x^*)$ along the blade surfaces, comparison of theory and experiment

Downloaded 01 Jun 2010 to 171.66.16.59. Redistribution subject to ASME license or copyright; see http://www.asme.org/terms/Terms_Use.cfm

For C-profiles $a = 0.007$ is recommended in [27] whereas with $a = 0.013$ the results of equation (26) fit the experimental data much better.

The diffusion ratio values from experiment, theory and correlation are compared in Fig. 18 revealing a remarkable decrease of $W_{\max S}/W_{2'}$ with increasing μ. The agreement is very good as long as no stronger viscous effects occur. Even the simple correlation formula yields good results for the cascade under consideration, the agreement with experimental data, however, depends on the cascade geometry [20].

Wake Momentum Thickness. The computation of $(\Theta/\ell)_{2'}$ from experimental data is performed using equation (25). For the theoretical computations the modified methods of Thwaites and White are used assuming simplified velocity distributions (Fig. 7) with a laminar boundary layer and a turbulent boundary layer on the pressure and suction side respectively. These methods actually yield the trailing-edge momentum thickness, its value, however, is nearly equal to the wake momentum thickness, if $W_{\max S}/W_{2'}$ is not too great [26].

Results from theory and experiment are compared in Fig. 19. The experimental data points are arranged in a way similar to Lieblein's results [27]. No distinct AVDR effect on $(\Theta/\ell)_{2'}$ or the loading limit is visible. The theoretical results on the other hand show an increase of $(\Theta/\ell)_{2'}$ with μ, the slope of which is the same as in Fig. 8 for the turbulent boundary layer alone. As the theoretical loading limit, $W_{\max S}/W_{2'} \approx 1.5$, is hardly influenced by μ, it is concluded that the experimental loading limit for $\mu = 1.0$, $W_{\max S}/W_{2'} \approx 2.0$, also holds for $\mu \neq 1.0$. The theoretical results agree perfectly with the experimental results covering, however, only part of them, see also Fig. 7. To predict $(\Theta/\ell)_{2'}$ over the whole range of $W_{\max S}/W_{2'}$ a correlation formula has to be used which is based on experimental data. Such a formula is given by Lieblein [27] for $\mu = 1.0$, the modification for $\mu \neq 1.0$ is performed using theoretical results:

$$\left[\frac{\Theta_{2'}}{\ell}\right]_{\mu \neq 1} = \frac{\epsilon[1 + K(\mu - 1)]}{1 - K_S \ln (W_{\max S}/W_{2'})}. \tag{27}$$

At $\mu = 1.0$ equation (27) is identical with the original equation [27]. For better agreement with the experimental data the constants are chosen to be $\epsilon = 0.0045$ and $K_S = 0.95$; $K = 0.56$ can be read from Fig. 8. $(\Theta/\ell)_{2'}$ calculated from equation (27) at $\mu = 1.0$ and 1.2 is also shown in Fig. 19. Both curves slightly diverge with $W_{\max S}/W_{2'}$, they agree very well with the experimental data except for $W_{\max S}/W_{2'} > 2.0$ where stall is present.

The AVDR effect on the wake momentum thickness is so small that it cannot be recognized from the experimental data because of their scatter. Thus it may be possible to neglect the AVDR effect in order to simplify matters. To clarify this the efficiency of several rotor bladings in incompressible flow at $\mu \neq 1.0$ is computed by

$$\eta = \frac{\Delta h_{ts}}{\Delta h_t} = 1 - \frac{\zeta_{V1}}{\sin^2 \beta_1} \frac{\varphi^2}{2\lambda},$$

$$\lambda = \varphi \left[\frac{W_2 \sin \beta_2}{W_1 \sin \beta_1} \cot \beta_2 - \cot \beta_1\right]. \tag{28}$$

With σ, β_1, β_2 prescribed at $\mu = 1.0$, the corresponding cascade geometry is taken from [1] the AVDR effect on β_2 is computed by use of equation (18). The ζ_{V1} value is computed from equations (25–27); in this case, equation (27) was evaluated with and without taking the AVDR effect into account. This results in two corresponding efficiency values which are plotted versus μ in Fig. 20. Depending on the blading geometry, considerable differences between both curves can occur. This demonstrates that even the small AVDR effect on the wake momentum thickness should not be neglected to avoid distinct errors in the efficiency estimation of a rotor.

Experimental investigations [1, 3, 20], show the important flow parameters $\Delta\beta$, $\beta_{1\text{ref}}$ and ζ_{V1} to be almost independent of the inlet Mach number Ma_1 as long as Ma_1 remains subcritical. Hence, the foregoing analysis, though developed by use of incompressible flow data, is also valid for compressible cascade flows at subcritical inlet Mach numbers.

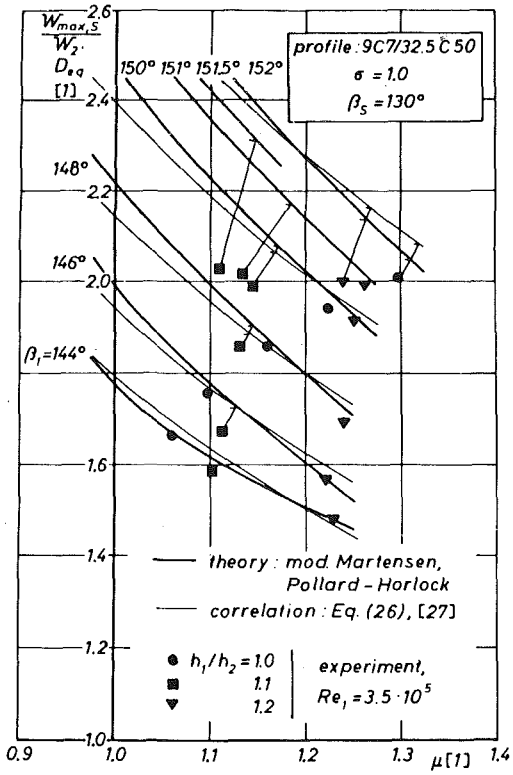

Fig. 18 Suction surface diffusion ratio $W_{\max S}/W_{2'}$ and equivalent diffusion ratio D_{eq} as a function of μ. Comparison of theory, correlation and experiment

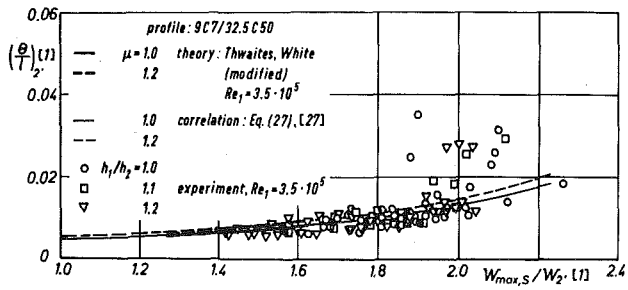

Fig. 19 Wake momentum thickness $(\Theta/\ell)_{2'}$ as a function of $W_{\max S}/W_{2'}$. Comparison of theory, correlation and experiment

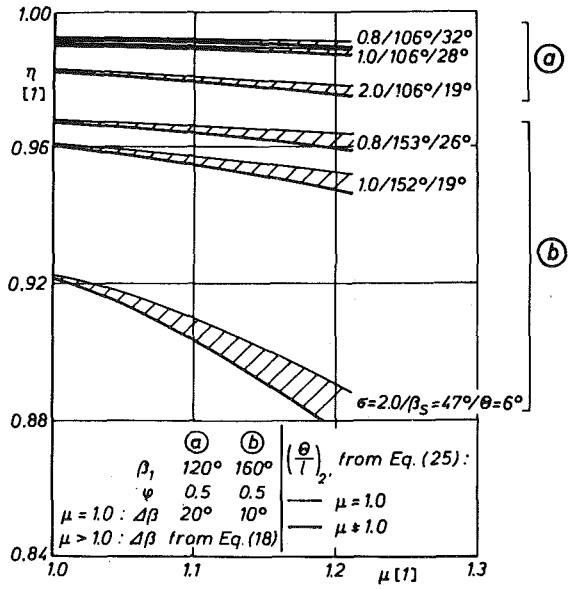

Fig. 20 The AVDR effect on the efficiency η of different rotor bladings, incompressible flow

Downloaded 01 Jun 2010 to 171.66.16.59. Redistribution subject to ASME license or copyright; see http://www.asme.org/terms/Terms_Use.cfm

Summary

The present paper deals with theoretical and experimental investigations on the effect of the axial velocity density ratio μ (AVDR) on the mid-span flow parameters of compressor cascades in incompressible flow.

The potential flow is calculated by the methods of Pollard-Horlock and Mani-Acosta (overall flow parameters) and a new modified Martensen method (pressure distributions) including the AVDR effect.

The laminar and turbulent boundary layers on the blades are calculated by a modified Thwaites method and a new modified inner variable method of White respectively, both methods include the AVDR effect.

Detailed wake and pressure distribution measurements are performed at 8 different compressor cascades with 9C7/32.5C50 blades, the μ value is varied using a geometrical sidewall contraction.

By examination of all these results, simple correlation formulae are developed for cascade turning, reference minimum-loss inlet angle, and profile loss in terms of wake momentum thickness and suction surface diffusion factor. Turning and reference inlet angle as functions of μ are described by linear equations which contain the corresponding quantities at $\mu = 1.0$ to be taken from any reliable source and the slopes to be read from theoretically established diagrams. The equations for the loss prediction are based on equations given by Lieblein, the influence of μ is incorporated by means of theoretical results.

Though developed using incompressible flow data, these correlations are also valid for compressible flow with subcritical Mach numbers.

The AVDR effect on the flow parameters is significant and has to be taken into account to avoid considerable errors in the work coefficients and efficiencies of axial flow compressors.

Acknowledgment

These investigations have been supported by the *Deutsche Forschungsgemeinschaft.*

The author is also indebted to Prof. Dr. H. Schlichting and to Dr. U. Stark for their help and encouragement in carrying out this work. The support of the whole staff at the Institute of Fluid Mechanics is gratefully acknowledged as well.

References

1 Lieblein, S., "Experimental Flow in Two-Dimensional Cascades," *Aerodynamic Design of Axial-Flow Compressors,* Johnson, J. A., and Bullock, R. O., (Editors) NASA SP-36, 1965.

2 Pollard, D., and Gostelow, J. P., "Some Experiments at Low Speed on Compressor Cascades," ASME JOURNAL OF ENGINEERING FOR POWER, Vol. 89, No. 3, 1967, pp. 427–436.

3 Hoheisel, H., "Ergebnisse von Untersuchungen an ebenen Verdichterschaufelgittern in kompressibler Unterschallströmung bei Variation der axialen Stromdichte," VDI-Bericht Nr. 264, 1976, pp. 71–80.

4 Pollard, D., and Horlock, J. H., "A Theoretical Investigation of the Effect on Change in Axial Velocity on the Potential Flow Through a Cascade of Aerofoils," ARC-Report, C.P. No. 619, 1962.

5 Mani, R., and Acosta, A. J., "Quasi Two-Dimensional Flows Through a Cascade," ASME, JOURNAL OF ENGINEERING FOR POWER, Vol. 90, No. 2, 1968, pp. 119–128.

6 Renken, J., "Potentialtheoretische und experimentelle Untersuchung der dreidimensionalen Unterschallströmung in geraden Verdichtergittern," DFVLR-FB 79-09, 1979.

7 Katsanis, Th., "Computer Program for Calculating Velocities and Streamlines on a Blade-to-Blade Stream Surface of a Turbomachine," NASA TN D-4525, 1968.

8 Dodge, P. R., "The Use of a Finite Difference Technique to Predict Cascade, Stator, and Rotor Deviation Angles and Optimum Angles of Attack," ASME JOURNAL OF ENGINEERING FOR POWER, Vol. 95, No. 3, 1973, pp. 185–190.

9 Dunham, J., "The Effect of Stream Surface Convergence on Turbomachine Blade Boundary Layers," *Aeronautical Journal,* Vol. 78, No. 758/759, 1974, pp. 90–92.

10 Pierce, F. J., "The Turbulent Flow at the Plane of Symmetry of a Collateral Three-Dimensional Boundary Layer," ASME *Journal of Basic Engineering,* Vol. 86, No. 2, 1964, pp. 227–233.

11 Albers, J. A., and Gregg, J. L., "Computer Program for Calculating Laminar, Transitional and Turbulent Boundary Layers for a Compressible Axisymmetric Flow," NASA TN D-7521, 1974.

12 Ikui, T., Inoue, M., and Kuromaru, M., "Researches on the Two-Dimensional Retarded Cascade," *Bulletin of the JSME,* Vol. 15, No. 84, 1972, pp. 705–712.

13 Masek, Z., and Norbury, J. F., "Low-Speed Performance of a Compressor Cascade Designed for Prescribed Velocity Distribution and Tested with Variable Axial Velocity Ratio," *The Institution of Mechanical Engineers,* Conference Publication No. 3, 1973, pp. 224–236.

14 Stark, U., and Starke, J., "Theoretische und experimentelle Untersuchungen über die quasizweidimensionale inkompressible Strömung durch vorgegebene ebene Verdichtergitter," Teil I: *Rechenverfahren und Nachlaufmessungen,* Bericht 73/6 des Instituts für Strömungsmechanik der TU Braunschweig, 1973; vgl. auch: *Forschung im Ingenieurwesen,* Band 40, 1974, Heft 6, pp. 172–186.

15 Starke, J., and Stark, U., "Theoretische und experimentelle Untersuchungen über die quasizweidimensionale inkompressible Strömung durch vorgegebene ebene Verdichtergitter," Teil II: *Druckverteilungsrechnungen und -messungen,* Bericht 74/8 des Instituts für Strömungsmechanik der TU Braunschweig, 1974.

16 Stark, U., and Starke, J., "Ueber die Umlenkeigenschaften ebener Verdichtergitter aus Profilen der NACA-Serie-65 in quasizweidimensionaler Strömung," Bericht 74/2 des Instituts für Strömungsmechanik der TU Braunschweig, 1974; vgl. auch: *Abhandlungen der Braunschweig, Wissenschaftlicn Gesellschaft,* 24, 1973/74, pp. 91–118.

17 Stark, U., and Starke, J., "Der Einfluß des axialen Stromdichteverhältnisses auf die aerodynamischen Beiwerte von Verdichtergittern," Bericht 76/4 des Instituts für Strömungsmechanik der TU Braunschweig 1976; vgl. auch: VDI-Bericht Nr. 264, 1976, pp. 59–70.

18 Thwaites, B., (Ed.), *Incompressible Aerodynamics,* Clarendon Press, Oxford, 1960.

19 White, F. M., "A new Integral Method for Analyzing the Turbulent Boundary Layer with Arbitrary Pressure Gradient," ASME *Journal of Basic Engineering,* Vol. 91, No. 3, 1969, pp. 371–378.

20 Starke, J., "Der Einfluß des axialen Stromdichteverhältnisses auf die aerodynamischen Beiwerte ebener Verdichtergitter," Dissertation 1979, Technische Universität Braunschweig; vgl. auch: Bericht 79/2 des Instituts für Strömungsmechanik der TU Braunschweig, 1979.

21 Mellor, G. L., "An Analysis of Axial Compressor Cascade Aerodynamics," ASME *Journal of Basic Engineering,* Vol. 81, No. 3, 1959, pp. 362–378.

22 Schlichting, H., "Berechnung der reibungslosen inkompressiblen Strömung für ein vorgegebenes Schaufelgitter," VDI-Forschungsheft 447, VDI-Verlage, Düsseldorf, 1955.

23 Starke, J., "Theoretische und experimentelle Untersuchungen über den Einfluß des axialen Stromdichteverhältnisses auf die aerodynamischen Beiwerte ebener Verdichtergitter," Bericht 77/4 des Instituts für Strömungsmechanik der TU Braunschweig, 1977.

24 Martensen, E., "Die Berechnung der Druckverteilung an dicken Gitterprofilen mit Hilfe von Fredholm'schen Integralgleichungen zweiter Art," Mitteilungen aus dem Max-Planck-Institut für Strömungsforschung und der Aerodynamischen Versuchsanstalt Nr. 23, 1959.

25 Stark, U., "Berechnung der reibungslosen, quasizweidimensionalen Strömung für vorgegebene ebene Verdichtergitter," in *Vorbereitung befindlicher Bericht des Instituts für Strömungsmechanik der* TU Braunschweig.

26 Koch, C. C., and Smith, L. H., "Loss Sources and Magnitudes in Axial-Flow Compressors," ASME JOURNAL OF ENGINEERING FOR POWER, Vol. 98, No. 3, 1976, pp. 411–424.

27 Lieblein, S., "Loss and Stall Analysis of Compressor Cascades," ASME *Journal of Basic Engineering,* Vol. 81, No. 3, 1959, pp. 389–400.

28 Scholz, N., "Ueber die Durchführung systematischer Messungen am ebenen Schaufelgitter," ZFW, Band 4, 1956, pp. 313–335.

29 Emery, J. C., Herring, W. J., Erwin, J. R., and Felix, A. R., "Systematic Two-Dimensional Cascade Tests of NACA 65-Series Compressor Blades at low Speeds," NACA-Report 1368, 1958.

30 Jansen, W., and Moffatt, W. C., "The Off-Design Analysis of Axial-Flow Compressors," ASME JOURNAL OF ENGINEERING FOR POWER, Vol. 89, No. 4, 1967, pp. 453–462.

31 Hebbel, H. H., "Untersuchungen über den Einfluß der Profilwölbung auf die Strömung durch ebene Verdichter-Schaufelgitter bei hohen Unterschallgeschwindigkeiten," Teil II: *Untersuchungen bei kompressibler Strömung,* Bericht 64/31 des Instituts für Aerodynamik der Deutschen Forschungsanstalt für Luft- und Raumfahrt (DFL) Braunschweig, 1964.

32 Lieblein, S., and Roudebush, W. H., "Theoretical Loss Relations for Low-Speed Two-Dimensional-Cascade Flow," NACA TN 3662, 1956.

Downloaded 01 Jun 2010 to 171.66.16.59. Redistribution subject to ASME license or copyright; see http://www.asme.org/terms/Terms_Use.cfm

J. C. Lee
J. Campbell, Jr.
D. E. Wright

Rockwell International/
Rocketdyne Division,
Canoga Park, Calif.

Closed-Cycle Gas Turbine Working Fluids

Characteristic requirements of a closed-cycle gas turbine (CCGT) working fluid were identified and the effects of their thermodynamic and transport properties on the CCGT cycle performance, required heat exchanger surface area and metal operating temperature, cycle operating pressure levels, and the turbomachinery design were investigated. Material compatibility, thermal and chemical stability, safety, cost, and availability of the working fluid were also considered in the study. This paper also discusses CCGT working fluids utilizing mixtures of two or more pure gases. Some mixtures of gases exhibit pronounced synergetic effects on their characteristic properties including viscosity, thermal conductivity and Prandtl number, resulting in desirable heat transfer properties and high molecular weights. Typical examples of such synergetic gas mixture are helium-xenon and helium-carbon dioxide.

Introduction

From the thermodynamic standpoint, all permanent gases can be candidate closed-cycle gas turbine (CCGT) working fluids, because the only requisite for the thermodynamics of the Brayton cycle is that the working fluid be operated in the gaseous region above its critical temperature throughout the entire cycle. Obviously, practical considerations such as thermal stability, chemical inertness, inflammability, and toxicity will eliminate almost all organic gases, and only a few of the inorganic fluids have been considered suitable for the CCGT applications. Among them, air has been the most common working fluid used in stationary CCGT powerplants [1, 2]. For CCGT space power systems [3], weight and size optimization has generally narrowed the selection of working fluids to monotomic gases with medium molecular weights including neon, argon, and mixtures of helium and xenon.

With the advent of gas-cooled nuclear reactors during the past decade, both carbon dioxide and helium gases have been used successfully as working media for reactor cooling and steam generation. Design studies have been carried out in the US [4], Germany [5], and France [6] on utilizing helium gas turbines for high-temperature, gas-cooled reactors (HTGR). A fossil-fueled pilot helium CCGT powerplant was completed in 1976 and has since been in operation in Germany [7] to test nonnuclear components and to acquire the necessary background experience leading to the eventual development of large-scale helium HTGR-CCGT powerplant.

The content of this paper is based principally upon the CCGT working fluids study conducted under the DOE sponsored program to evaluate advanced coal-fired heat exchanger design concepts for closed-cycle gas turbine power generation systems. The purpose of the working fluids study is to identify the characteristic requirements of a CCGT working fluid; to select candidate working fluids to be used in the coal-fired CCGT powerplant; and to investigate the effects of their thermodynamic and transport properties on the cycle performance and on the size, complexity and cost of the equipment. Material compatibility, thermal and chemical stability, safety, cost, and availability are also major factors of consideration in the study.

Effect on Cycle Performance

If there is no pressure loss in the heat exchangers and the lines, the CCGT cycle thermal efficiency should theoretically be independent of the working fluid and should remain the same with any perfect gas operating at the same temperature levels, although the pressure ratio will be different for gases having different specific heat ratios, γ.

With finite pressure loss in the circuit, the compressor will be required to deliver a higher pressure ratio than the turbine experiences. The pressure ratio factor defined as the ratio of the overall turbine pressure ratio to the overall compressor pressure ratio has a significant effect on the CCGT cycle efficiency, as shown by the plots of the optimum cycle efficiency and optimum pressure ratio versus pressure ratio factor for a recuperated CCGT cycle with reheating and intercooling in Fig. 1. The steep decline of the cycle efficiency with the decrease in pressure ratio factor indicates the importance of minimizing the pressure losses in the CCGT cycle circuit.

The adverse effect of pressure loss also depends upon the relative magnitude of the pressure loss to the overall operating pressure ratio. Thus, with a fixed pressure ratio factor, the performance degradation by the pressure loss will be less severe with gases requiring higher optimum operating pressure ratios even though the temperature ratio may be the same. In other words, diatomic gases such as air, N_2, etc., will give higher CCGT cycle efficiencies than monatomic gases (He, Ar, Xe, etc.) with higher γ values, because the optimum operating pressure ratios for diatomic gases are generally higher than those for monatomic gases.

Figure 2 shows the effect of the specific heat ratio, γ, of the working fluid on the efficiency of a recuperated, reheat, and intercooled CCGT cycle at a fixed pressure ratio factor of 83.3 percent. The dotted curve gives the optimum efficiency versus the optimum compressor pressure ratio with varying γ values. At fixed pressure ratio factor, an approximate difference to 1.6 percentage points is noted along the curve between the optimum efficiency value for diatomic gases of $\gamma = 1.4$ and the optimum efficiency value for monatomic gases of $\gamma = 1.67$, because of the higher optimum operating pressure ratio of the diatomic gases.

Contributed by the Gas Turbine Division of The American Society of Mechanical Engineers and presented at the Gas Turbine Conference and Products Show, New Orleans, La., March 10–13, 1980. Manuscript received at ASME Headquarters January 2, 1980. Paper No. 80-GT-135.

Copyright © 1981 by ASME

Downloaded 01 Jun 2010 to 171.66.16.59. Redistribution subject to ASME license or copyright; see http://www.asme.org/terms/Terms_Use.cfm

Effect on Turbomachinery Design

Specific heat, C_p, and molecular weight, M, are the two primary physical properties of the working fluid affecting the turbomachinery design and performance. With fixed gas temperature levels across the turbine or the compressor, the total enthalpy drop is proportional to the specific heat. The number of turbine or compressor stages, n, required is then given by

$$n = \frac{C_p \Delta T}{\Delta H} \tag{1}$$

where ΔT is the gas temperature difference across the turbine or compressor and ΔH is the design enthalpy change across each turbine or compressor stage. With low molecular weight gases such as helium and hydrogen having high sonic velocities, the maximum design stage enthalpy change in the turbine is usually limited by the blade centrifugal stress while with gases having low sonic velocities, the maximum stage enthalpy change is generally sonic velocity limited. Table 1 shows the comparison of the sonic velocities for the three working fluids, air, He/CO_2 (0.6/0.4 by mole) mixture, and He at various temperatures. The sonic velocity of the helium gas is almost three times that of the other two gases. For impulse turbines, the design blade tangential velocity is approximately half of the nozzle exit velocity. The helium gas turbines can be run up to its stress limited tip speed without exceeding its sonic velocity at the nozzle exit, while the turbine speed with working fluids such as air or He/CO_2 mixture would probably be limited by the sonic velocity at the nozzle exit before the limiting blade stress is exceeded. Hence, the maximum allowable tip speed and the design stage enthalpy change can be higher for helium turbine than for air or He/CO_2 turbine. Higher tip speed means higher rotative speed for helium turbine.

A larger number of turbine or compressor stages is also expected with helium working fluid than with air or He/CO_2 mixture from equation (1), although the ratio of the numbers of stages (helium relative to air or He/CO_2) will be less than their relative ratio of specific heats, due to the higher design stage enthalpy drop of helium.

Since the compressor is driven at the turbine shaft speed, the limiting tip speed criterion does not exist because its blade tip diameter is substantially smaller than those of the turbine. The limiting factor in the compressor design, however, usually lies in the blade annular flow area which is equal to the blade height times the pitch circle circumference. Because of large variations of gas density and volume flow, as the gas undergoes changes of its pressure and temperature along the compressor stages, the required annular flow area or blade height will often exceed the maximum limit at the compressor inlet stage or becomes exceedingly small at the last stage, particularly for working fluids operating at high pressure ratios.

It is to be noted that the optimum operating pressure ratios for air and He/CO_2 mixture are higher than that for helium gas. Therefore, with a fixed design turbine inlet pressure, the air or He/CO_2 compressor inlet stage will operate at significantly lower pressure and will be more likely to encounter the blade height limitation than the helium compressor inlet stage. This may result in even lower rotative speed than is allowed in the turbine design.

A design option such as splitting the turbine and the compressor into high-pressure and low-pressure units and operating them at different speeds is usually taken to circumvent this limitation. The complexity associated with this option must be weighed in a tradeoff against the reduced efficiency with lower operating pressure ratio for lower molecular weight gases. However, it appears that adequate turbomachinery can be designed for any of the common candidate CCGT gases.

Heat Transfer and Pressure Drop

A number of heat exchangers, including fired gas heaters, recuperators, coolers, unfired bottoming cycle econimizers and boilers, are employed in the CCGT cycle. The cost and sizes of these heat exchangers are dependent upon the heat transfer coefficients of the CCGT working fluid and the allowable pressure drops across these heat exchangers. Since the pressure drop is critical to the CCGT cycle thermal efficiency, it is desirable that working fluids with high heat transfer and low flow friction characteristics be selected.

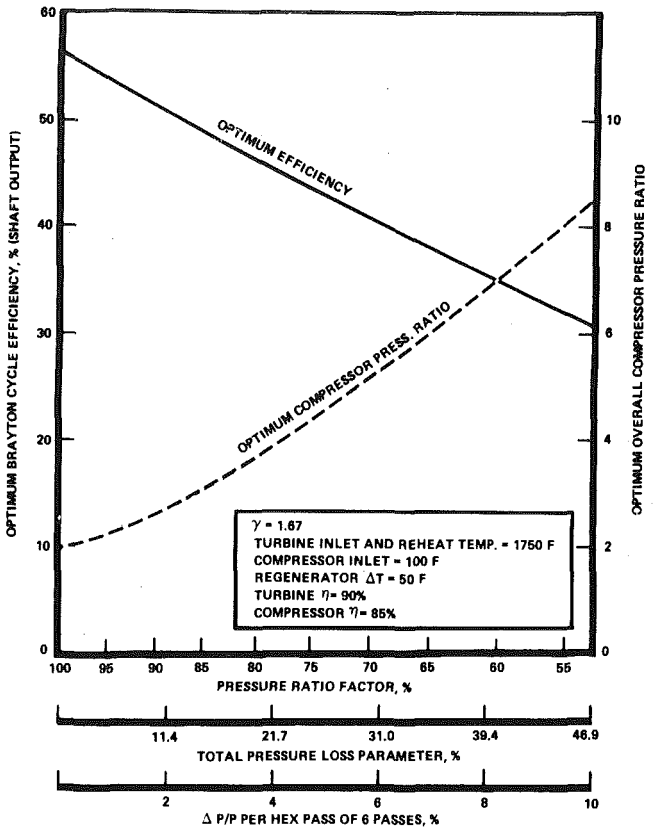

Fig. 1 Effect of CCGT pressure drop on optimum CCGT cycle efficiency (regenerative, reheating, and intercooling)

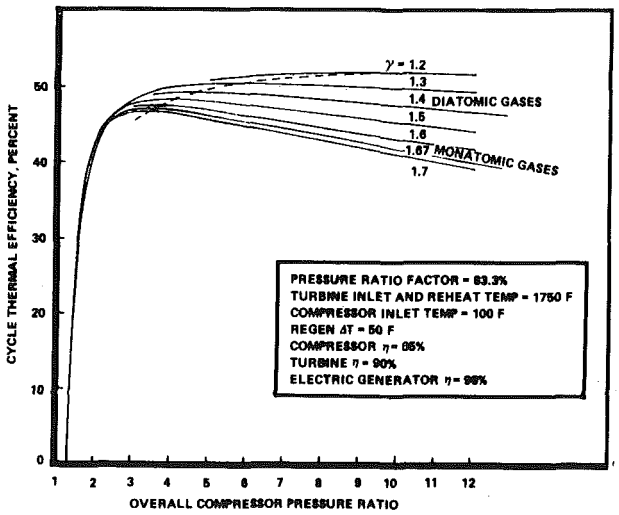

Fig. 2 Effect of γ on CCGT cycle performance (regenerative, reheat, and intercooling)

Table 1 Comparison of sonic velocities for air, He/CO_2, and He

	M = 28.96 AIR			M = 20.008 He/CO_2			M = 4.003 He		
T °F	C_p	γ	v^* fps	C_p	γ	v^* fps	C_p	γ	v^* fps
1500	.276	1.331	2116.4	.4155	1.314	2530.3	1.240	1.667	6371.5
1000	.2635	1.352	1841.1	.375	1.360	2221.8	1.240	1.667	5498.9
500	.2505	1.377	1506.6	.364	1.375	1811.4	1.240	1.667	4458.7
80	.238	1.405	1053.4	.33	1.430	1385.3	1.240	1.667	3343.5

M = MOLECULAR WEIGHT, C_p = SPECIFIC HEAT, BTU/LB-F, γ = SPECIFIC HEAT RATIO, v^* = SONIC VELOCITY, FPS

Downloaded 01 Jun 2010 to 171.66.16.59. Redistribution subject to ASME license or copyright; see http://www.asme.org/terms/Terms_Use.cfm

In general, the required surface area for the unfired heat exchangers including the recuperator, bottoming cycle heater or boiler, and the cooler is almost directly proportional to the working fluid heat transfer coefficient (mainly because the controlling thermal resistance is on the working fluid side). With fired heat exchangers, however, the combustion gas side usually exerts the controlling influence on the overall heat transfer coefficient. Hence, the required surface area for the fired heat exchanger is less strongly affected by the working fluid heat transfer coefficient than for the unfired heat exchanger. The effects of variation of CCGT working fluid side heat transfer coefficient with the composition of the gas are felt differently in various types and regions of the combustor/heat exchanger. In the radiant section of a pulverized coal furnace, the heat transfer rate and wall surface required is only slightly affected by variations in CCGT working fluid side heat transfer coefficient, but the temperature of the tube walls is very much affected. At the same $\Delta P/P$, helium cooling will result in significantly lower metal temperatures than air cooling. For the "in-bed" surface of a fluidized bed combustor/heat exchanger, however, a change from helium-to-air cooling may make less than 10 percent difference in the total surface required, but will not seriously affect metal temperatures.

The relationship between the working fluid heat transfer coefficient and the pressure drop can be derived as follows.

$$\frac{hD_e}{K} = 0.023\left(\frac{C_p\mu}{K}\right)^{1/3}\left(\frac{GD_e}{\mu}\right)^{0.8} \tag{2}$$

where h = heat transfer coefficient on the working fluid side; D_e = equivalent diameter = 4 × flow cross-sectional area/wetted perimeter; K = thermal conductivity of the working fluid; C_p = specific heat of the working fluid; μ = viscosity of the working fluid; and G = mass flow velocity of the working fluid.

The pressure drop across the tubes in the turbulent regime is given by

$$\Delta P = 0.3164\left(\frac{\mu}{GD_e}\right)^{0.25}\left(\frac{\Delta L}{2\rho D_e}\right)G^2 \tag{3}$$

where ΔP = frictional drop across the tubes; ΔL = length of the tubes; and ρ = mass density of the working fluid.

Combining equation (2) and (3) by eliminating G leads to

$$h = 0.0534\left(\frac{C_p\mu}{K}\right)^{-0.667}\cdot\left(\frac{\mu}{D_e}\right)^{0.086}\cdot\left(\rho\Delta P\cdot\frac{D_e}{\Delta L}\right)^{0.457}\cdot C_p \tag{4}$$

Substituting the perfect gas equation $\rho = (PM)/(RT)$ in equation (4) gives

$$h = 0.0543\left(\frac{C_p\mu}{K}\right)^{-0.667}\cdot\mu^{0.086}\cdot D_e{}^{0.371} \times\left(\frac{P^2}{RT}\cdot\frac{\Delta P}{P\cdot\Delta L}\right)^{0.457}\cdot(C_pM)^{0.457}\cdot C_p{}^{0.543} \tag{5}$$

where M = molecular weight of the working fluid; and R = universal gas constant per mole of working fluid.

Pure Gases. For pure perfect gases containing equal numbers of atoms, the molal specific heat (C_pM) and the Prandtl number ($C_p\mu/K$) are approximately constant. With constant values of tube diameter (D_e), operating pressure (P), temperature (T), and constant pressure drop parameter per unit tube length, $\Delta P/P\Delta L$, the heat transfer coefficient of the working fluid will vary with $C_p{}^{0.543}$. The term ($\mu^{0.088}$) in equation (5) has negligible effect due to its small power index. Figure 3 shows the log plots of comparative heat transfer coefficient versus C_p for various pure perfect gases using helium coefficient as the reference, and based on constant pressure, temperature, tube diameter and pressure drop parameter. The three lines having slopes equal to 0.543 represent families of monatomic, diatomic, and triatomic gases. Obviously from the standpoint of heat exchanger surface requirement, the low molecular weight gases such as hydrogen and helium are preferred. The heat transfer coefficient of helium is more than three times that of argon and more than twice that of air, oxygen, or nitrogen at constant pressure drop parameter and constant tube length.

The foregoing analysis is much simplified when compared against actual conditions, especially in the combustor/heat exchanger. The length of the circuits and the number of parallel circuits are not fixed but vary with the fluid and with design options (often in discrete steps). Also, the operating pressures are not necessarily the same from fluid to fluid. Thus, the comparative data presented serve as a guide. More rigorous comparisons would require consideration of the heat transfer coefficient of the fluid on the other side of the heat exchanger and will be discussed later in this paper.

Mixture of Gases. As shown in equation (5), the working fluid heat transfer coefficient varies inversely with ⅔ power of the Prandtl number. For all pure perfect gases containing equal numbers of atoms, the Prandtl numbers are approximately equal. This, however, does not hold true with mixtures of gases. It has been established that gas mixtures have a pronounced synergetic effect stemming mainly from

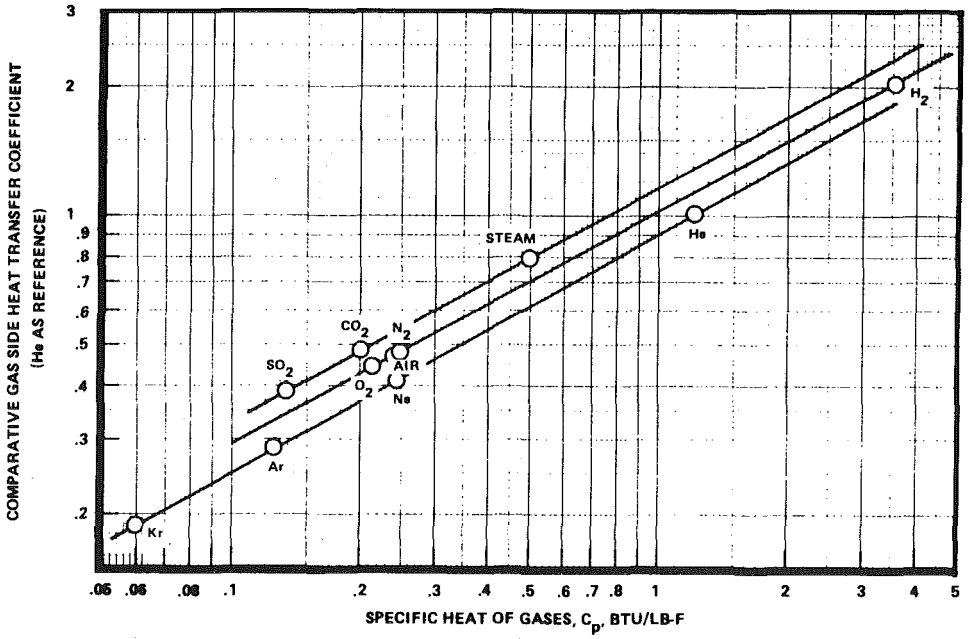

Fig. 3 Comparative heat transfer coefficients for various working gases (based on equal pressure, temperature, length, and pressure loss ratio in the heat exchanger)

Downloaded 01 Jun 2010 to 171.66.16.59. Redistribution subject to ASME license or copyright; see http://www.asme.org/terms/Terms_Use.cfm

the differences in variations of the three physical properties C_p, μ, and K and of the Prandtl number $C_p\mu/K$ with the mixture ratio of the component gases. This results in a lower value of the Prandtl number than either of the Prandtl numbers of component gases, as exemplified by the helium-xenon mixture which has a Prandtl number less than 1/3 of that of helium or xenon at a molal ratio of 1:1 or a mixture molecular weight of about 68. Figure 4 shows the plots of specific heat C_{pm}, viscosity μ_m, thermal conductivity K_m, and Prandtl number Pr_m of the mixture of helium and xenon versus the mixture molecular weight M_m.

The specific heat, C_p, density, ρ, and the molecular weight, M, of a mixture generally follow the relationship of the molal mean values of those of the constituent gases. As can be seen from the log-log plots, the viscosity (μ_m) curve is relatively flat and does not significantly vary with the molecular weight of the mixture, while the C_{pm} and K curves have rather steep slopes. The Prandtl number (Pr_m) is thus essentially determined from the ratio of C_{pm}/K_m which is represented by the vertical distance between the two curves on the logarithmic scale.

Thermodynamic properties of other gas mixtures including He/Ar, He/CO_2, N_2/CO_2 and H_2/CO_2 of various molecular weights (various mixture ratios) were investigated and heat transfer coefficients for these mixtures at various temperatures were computed using equation (5) in reference [8]. Figure 5 shows plots of the heat transfer coefficients versus molecular weight of the mixture for a temperature of 524 R. The curves were all based on a constant tube i.d. of 1 in., tube length of 30 ft, and an average pressure level of 1000 psia. The gas mass flow velocity (G) through the tube was varied so as to give a constant pressure loss factor, $\Delta P/P$, of 3 percent over the 30-ft tube length. As previously indicated, the data presented in Fig. 5 only serve as a guide because the actual heat exchanger designs would have varied length of the tube circuits and varied number of parallel circuits with different working fluids.

It is interesting to note, in Fig. 5, that at a given value of $\Delta P/P$, the heat transfer coefficients of pure He, Ar, and Xe all fall on a straight line with a negative slope of 0.543. This is consistent with the plots shown in Fig. 3 because the molecular weight is inversely proportional to the specific heat for the three monatomic gases. Same linear relationships can also be observed with the two pure diatomic gases H_2 and N_2 and with triatomic gases such as CO_2.

Each curve connecting the two end points of the straight line, which represent the two pure component gases of the mixture, illustrates the synergetic effect on the heat transfer characteristic of the gas mixture. It is apparent from the curves that the wider the difference between the molecular weights of the two gases, the greater is the synergetic effect. In the case of N_2/CO_2, there is hardly any benefit from the mixing in view of the small difference of molecular weights between the two component gases.

He/CO_2 mixtures appear to offer several attractive features as a candidate working fluid for CCGT application. First, both He and CO_2 have been used successfully as heat transfer media in nuclear reactor powerplants, and the cost of the mixture is substantially reduced by the addition of CO_2.

At a molal ratio of 0.6 He/0.4 CO_2 (molecular weight of 20.006), the heat transfer coefficient of the mixture remains at about 80 percent of that of pure He as compared to about 46 percent for the air or nitrogen. Figure 6 gives the plots of C_p and γ versus temperature for air, N_2, and two mixtures of 0.6 He/0.4 CO_2 (M = 20) and 0.65 He/0.35 CO_2 (M = 18). Lower C_p and γ values of the mixtures as compared to those of pure He offer the advantages of higher operating pressure ratio and higher CCGT cycle thermal efficiency, and fewer turbocompressor stages than those required with pure helium working fluid. Figure 7 shows the plots of the thermal transport properties, K, μ, and Pr versus temperature for the He/CO_2 mixtures, air, and N_2. The synergetic effect of the He/CO_2 mixture stems mainly from its low value of Prandtl number as compared to those of the pure gases.

Primary Combustor/Heat Exchanger Tube Wall Operating Temperature. In fired heat exchangers, the combustion gas side usually exerts the controlling influence on the overall heat transfer coefficient; so the required surface area for the fired heat exchanger is less affected by the working fluid heat transfer coefficient than for the unfired heat exchangers, which includes the recuperator, the cooler, and the bottoming cycle heater or boiler. The working fluid heat transfer coefficient (at the allowable design pressure drop), however, has a significant bearing on the fired heat exchanger tube wall operating temperature and its allowable design stress, especially in the high heat flux regions such as in the radiant furnace systems. In the high temperature creep range, the rupture stresses of the tube materials (on which the allowable design stresses for the tubes are based) become very sensitive to increment of temperature change. As shown in the plots of rupture stresses at 100,000 hr versus metal temperature for the materials Inconel 617, HS 188, and Incoloy 800 in Fig. 8, a reduction of rupture stress by a factor of 1.6 to 1.75 occurs for every 100°F temperature increase. The same factors apply to the increase in required tube wall thickness with increase in temperature. Increased temperature gradient across the tube wall and decreased fatigue life are also associated with increased tube wall thickness. Increase in wall thickness also raises the outside metal wall temperature and further reduces the allowable design stress. It is, therefore, important to strive for high working fluid side heat transfer coefficient so as to maintain the tube wall operating temperature as close to the working fluid temperature as possible. This is particularly significant in high heat flux regions of a radiant furnace, where the heat source (flame) temperature is well above the melting temperature of most metals.

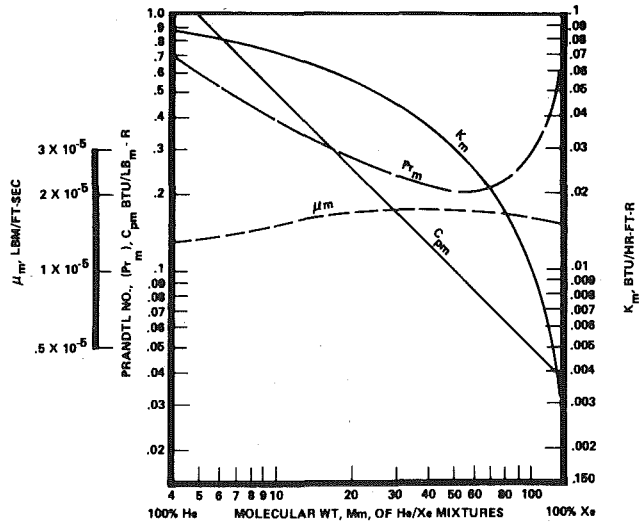

Fig. 4 Thermal and transport properties of He/Xe mixtures

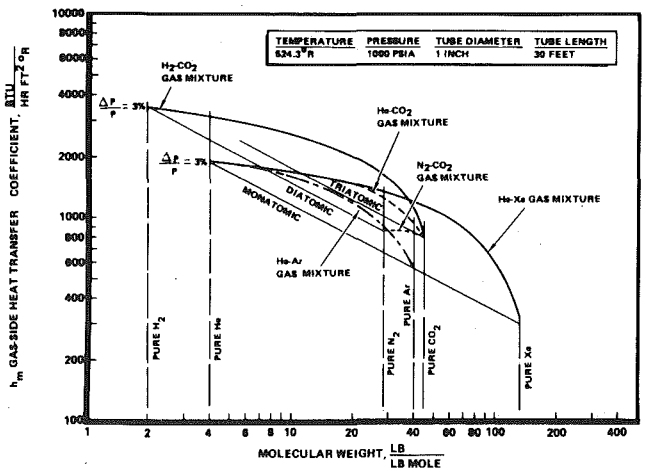

Fig. 5 Gas-side heat transfer characteristics for gas mixtures of varying composition (based on equal pressure, temperature, tube length, and pressure loss ratio in the heat exchanger)

Downloaded 01 Jun 2010 to 171.66.16.59. Redistribution subject to ASME license or copyright; see http://www.asme.org/terms/Terms_Use.cfm

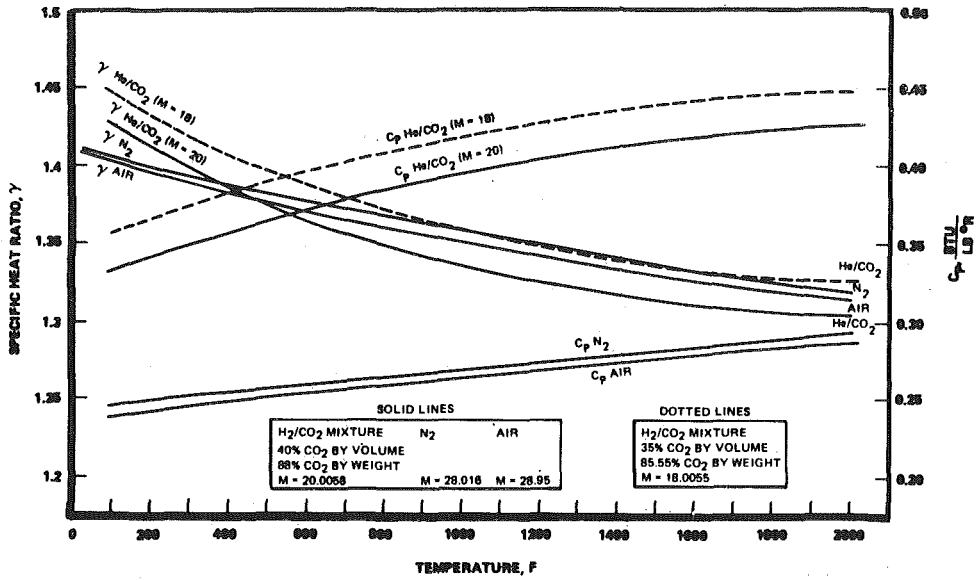

Fig. 6 Thermodynamic properties of various gas mixtures

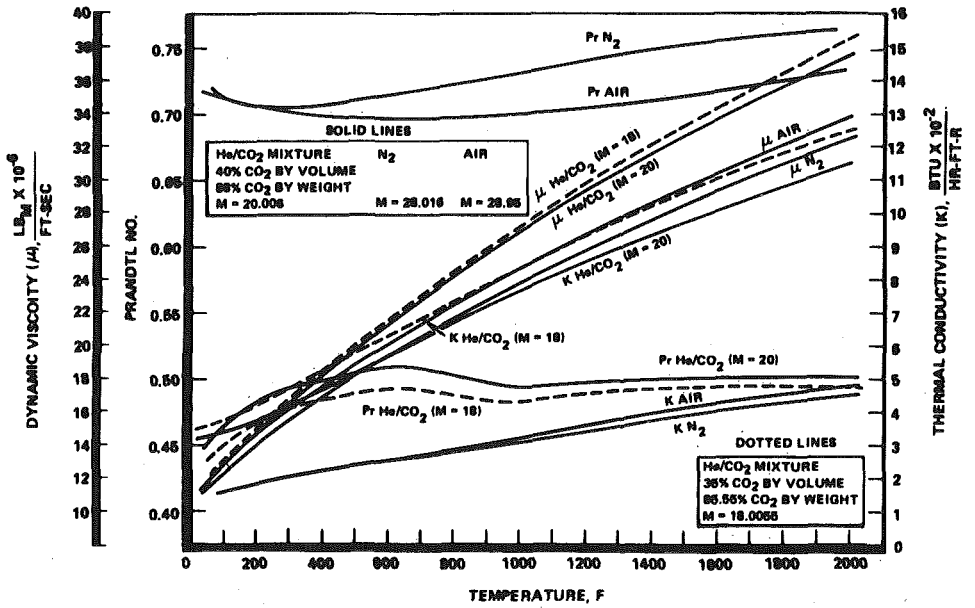

Fig. 7 Thermal and transport properties of various gas mixtures

Since the pressure drop in the working fluid circuit is limited by CCGT system performance considerations, increase in mass flow velocity is not deemed desirable. Other ways to achieve high working fluid side heat transfer coefficients will be to increase the operating pressure (or density) in the fired heat exchanger and to employ working fluids with better heat transfer characteristics such as Helium and He/CO_2 gas mixtures.

The comparative heat transfer coefficients of these working fluids shown in Fig. 3 and 5 are based on constant tube diameter and constant heat exchanger length (constant tube length) but with different numbers of tubes in parallel to give a constant pressure drop for a fixed total mass flowrate. In fired heat exchanger designs, the combustion gas side heat transfer coefficient is the controlling factor, and it would be more appropriate to evaluate the working fluid side heat transfer coefficient on the basis of constant average heat flux (constant total quantity of heat transferred divided by constant total heat transfer surface area) with both tube length and number of tubes varied to give a constant pressure drop. The derivation of the heat transfer equation based on this assumption is given in the following.

The heat exchanger is assumed to consist of a number of identical parallel circuits with equal equivalent diameter D_e and equal flow path length ΔL. The total free flow area, A_{ff}, and the total wetted surface area on the working fluid side (total heat transfer surface area) ΔA_h are related to the D_e and ΔL as follows

$$D_e = 4\,A_{ff} \cdot \frac{\Delta L}{\Delta A_h} \tag{6}$$

Substitution of equation (6) and the relationships $\rho = (PM)/(RT)$ and $G = \dot{m}/A_{ff}$, where $\dot{m}$ is the total working fluid mass flowrate, in equation (2) and (3) leads to

$$\frac{\Delta P}{P} = 0.1582 \left(\frac{\mu}{D_e}\right)^{0.25} \cdot \left(\frac{\Delta A_h}{4\,A_{ff}{}^{2.75}}\right) \left(\frac{RT}{P^2 M}\right) \dot{m}^{1.75} \tag{2a}$$

$$h = 0.023 \left(\frac{C_p}{K}\right)^{-0.667} \cdot \left(\frac{\mu}{D_e}\right)^{0.2} \cdot C_p \left(\frac{\dot{m}^{0.8}}{A_{ff}{}^{0.8}}\right) \tag{3a}$$

Combining equation (2a) and (3a) by eliminating A_{ff} gives

$$h = 0.0589 \left(\frac{C_p \mu}{K}\right)^{-0.667} \cdot \left(\frac{\mu}{D_e}\right)^{0.127} \cdot \left(\frac{\Delta P}{P\,\Delta A_h} \cdot \frac{P^2}{RT} \cdot C_p \dot{m}\right)^{0.291} \cdot (C_p M)^{0.291} \cdot C_p{}^{0.418} \tag{7}$$

Downloaded 01 Jun 2010 to 171.66.16.59. Redistribution subject to ASME license or copyright; see http://www.asme.org/terms/Terms_Use.cfm

Since the heat input to the working fluid $Q = C_p \dot{m}\ \Delta T$ where ΔT is the bulk working fluid temperature rise and average heat flux q (over the total heat transfer surface area, ΔA_h) = $Q/\Delta A_h$, equation (7) becomes

$$h = 0.0589 \left(\frac{C_p \mu}{K}\right)^{-0.667} \cdot \left(\frac{\mu}{D_e}\right)^{0.127} \cdot \left(\frac{\Delta P}{P \Delta T} \cdot q \cdot \frac{P^2}{RT}\right)^{0.291} \cdot (C_p M)^{0.291} \cdot C_p{}^{0.418} \quad (8)$$

In CCGT cycles using different working fluids, the bulk working fluid temperature rise, ΔT, is usually fixed, and the total heat input to the working fluid Q is also fixed by varying the mass flowrate $\dot{m}$. In this case, the heat transfer coefficients for different working fluids can be compared with equal heat transfer surface areas ΔA_h and hence equal average heat fluxes ($q = Q/\Delta A_h$). Comparison can also be made (from equation (7)) of the surface area required with each working fluid if the working fluid side heat transfer coefficient h is fixed. In either case, the heat flux obtained (through equation (7) and (8)) from the working fluid side must correspond to the heat flux obtained from the combustion gas side. In addition, the assigned $\Delta P/P$ value must also satisfy equation (2a).

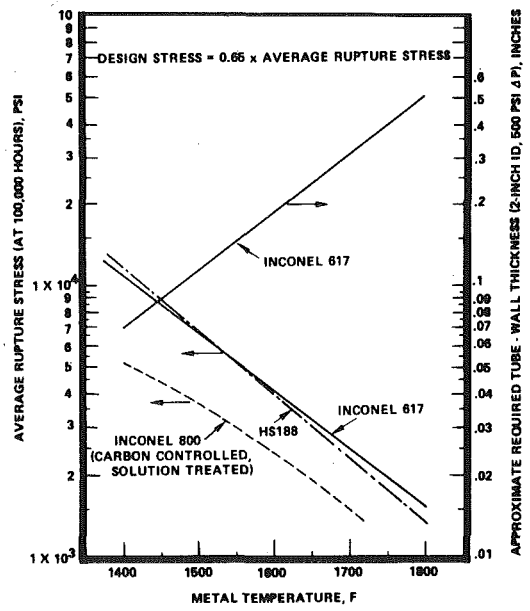

Fig. 8 Rupture stresses and required tube wall thickness versus temperature

Figure 9 shows plots of comparative heat transfer values for various gas mixtures at 524 R (using helium as the reference) based on constant heat input and heat flux, and constant $\Delta P/P$. The curves are similar to those in Fig. 5, except that the straight lines joining the points for pure gases have a slope of 0.418 (from equation (7) and (8)) as compared to a slope of 0.543 (equation (5)). The heat transfer coefficients for the three candidate working fluids, He, He/CO_2 (M = 20) gas mixture and air (close to N_2) are in the proportions of 1: 0.87:0.52, respectively, based on constant heat flux.

In fluidized bed combustor/heat exchanger, the operating bed temperature is usually limited to 1650°F, and the difference between the bed temperature and the maximum working fluid temperature is only 100 to 150°F. The ΔT across the working fluid film, therefore, amounts to only 20 to 30°F for air and 10 to 15°F for helium, because the combustion gas side heat transfer coefficient is only a fraction of the working fluid side heater transfer coefficient (about 1/4 for air and 1/8 for helium). Hence, the maximum tube wall temperature is less than 30°F above the maximum working fluid temperature.

On the radiant furnace wall heat transfer surfaces, however, the radiative heat flux is much higher (of the order of 20,000 to 50,000 Btu/ft^2-hr) and the ΔT across the working fluid film could be as high as 50 to 125°F with helium working fluid at a design film heat transfer coefficient of 400 Btu/ft^2-°F-hr. If air working fluid were used, the film coefficient with the same pressure drop would reduce to 208 Btu/ft^2°F-hr, and the ΔT across the film would become 96 to 240.4°F. The difference in operating tube wall temperatures between helium and air working fluid would be 46 to 115°F and the tube wall thickness and weight would have to be increased by a factor of 1.3 to 1.9 with air working fluid. In addition, increase in tube wall thickness can also result in higher temperature gradient across the tube wall and lower fatigue life.

Effect of Operating Pressure. As shown in equation (8), at a fixed pressure loss factor $\Delta P/P$, the heat transfer coefficient varies with the 0.6 power of the working fluid pressure. Therefore, increase in operating pressure will decrease the heat transfer surface area and the tube wall temperature. The advantage is, however, offset by the increase in tube stress and hence increase in required tube wall thickness. This is particularly significant in heaters with high design heat fluxes. As the tube wall thickness is increased, ΔT across the tube wall and the maximum tube wall temperature also increase for a given design heat flux and given design working fluid temperature. The increase in tube wall temperature, in turn, reduces the allowable design stress and requires further increase in wall thickness and wall

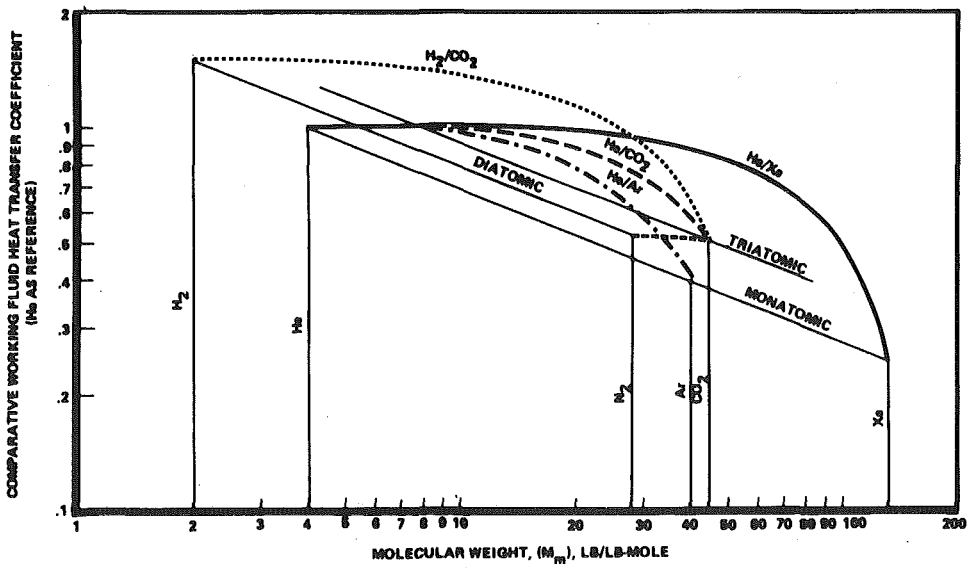

Fig. 9 Comparative heat transfer coefficients for various gas mixtures (based on equal pressure, temperature, equal average heat flux and pressure loss ratio in the heat exchanger)

Downloaded 01 Jun 2010 to 171.66.16.59. Redistribution subject to ASME license or copyright; see http://www.asme.org/terms/Terms_Use.cfm

temperature. Thus, at a certain critical point, further increase in operating pressure will be followed by excessive increase in tube wall thickness and tube wall temperature.

The operating pressure levels of the CCGT are also, to a large extent, dictated by the capacity and design of the turbocompressor. As discussed in the previous section on turbomachinery design, at a given shaft speed the maximum and minimum ratios of blade height to the hub radius determine the maximum and minimum limits of gas volume flow through the turbine or the compressor. Hence the pressure levels have to be changed to change the capacity or mass flow beyond that allowed within the limits of the design blade height. In general, lower operating pressures (< 500 psia) are required for small capacity turbomachines (< 50 MW) to maintain reasonably high turbocompressor efficiencies. Turbomachines with capacity ranges from 50 to 350 MW are best operated at pressures of 500 to 1000 psia.

Effect on Duct Size. The size of the duct carrying the gas flow is a function of the allowable pressure drop, mass flowrate, and thermal transport properties of the working fluid. The flow friction in a circular duct of diameter D and length ΔL is given by

$$\Delta P = 0.3164 \left(\frac{\mu}{GD}\right)^{0.25} \left(\frac{\Delta L}{2\rho D}\right) G^2 \tag{9}$$

Substituting

$$G = \frac{\dot{m}}{\frac{\pi D^2}{4}} \quad \text{and} \quad \rho = \frac{P}{\frac{RT}{M}}$$

equation (9) becomes

$$\frac{\Delta P}{\Delta L P} = 0.2414 \cdot \frac{RT}{P^2} \cdot \frac{\mu^{0.25}}{M} \cdot \frac{\dot{m}^{1.75}}{D^{4.75}} \tag{10}$$

where $\dot{m}$ = mass flowrate of working fluid and R = modal universal gas constant. Based on constant heat input and constant operating temperature levels, the mass flowrate of the working fluid $\dot{m}$ will be inversely proportional to specific heat of the working fluid C_p. Equation (10) then leads to

$$D^{4.75} \propto \frac{RT}{P^2 \left(\frac{\Delta P}{\Delta L P}\right)} \cdot \frac{\mu^{0.25}}{C_p M} \cdot \frac{1}{C_p{}^{0.75}} \tag{11}$$

Figure 10 gives the plots of comparative duct diameter versus C_p for various working fluids at constant pressure, temperature, and $\Delta P/(\Delta L P)$. Equation (11) shows that D is a relatively weak function of C_p and the required duct diameters for working fluids CO_2, O_2, N_2, air, and 0.6 He/0.4 CO_2 are within 8 percent of each other. Helium requires the smallest duct size, about 25 percent smaller than air requires, mainly because helium working fluid requires the lowest mass flowrate for constant heat input.

Material Compatibility

Compatibility of the working fluid with the materials of construction, particularly of the heater tubes, is an important consideration in the selection of candidate working fluids and candidate materials. Although it is somewhat obscured by the more critical problem of fireside corrosion, it is nevertheless important in view of the extreme temperature conditions intended.

Three candidate working fluids, He, He/CO_2 gas mixture, and air have been considered suitable for CCGT applications, with advantages and disadvantages in various aspects of considerations. In this section, the compatibility of these three working fluids with heater tube materials is discussed.

The corrosion effect of these working fluids on two candidate ceramic materials for heater tubes, SiC and SiN, is expected to be minimal for temperature levels at which the CCGT heaters will be operated. In metals and alloys, however, in addition to surface oxidation or corrosion occurring in oxidizing atmosphere such as air and H_2O, there can also be a grain or chemical structure change in the material to affect the mechanical properties in atmospheres such as CO_2 and He.

Air Working Fluid. The mechanism of corrosion resistance of most of the high-temperature alloys is the formation of a protective oxide layer on the surface which retards the diffusion of oxygen into the subsurface of the alloy. Chromium, for instance, forms a protective surface layer of chromium sesqui-oxide, Cr_2O_3, in oxidizing atmospheres. But, it can also be oxidized to be volatile oxide CrO_3 via $Cr_2O_3 + \frac{3}{2} O_2 \rightarrow 2CrO_3$. The surface corrosion in oxidizing atmosphere is a rate-controlled process of oxidative volatilization of Cr_2O_3 which is dependent on the mass transport of O_2 and gaseous CrO_3 through the gaseous boundary layer. It, therefore, increases with increase in oxygen partial pressure, flowrate, and with decreases in total pressure. Hence in air, surface alloy removal by oxidation volatilization is the main cause of the material degradation. Adequate protection against severe corrosion in a dry air environment is believed possible with the tube materials normally utilized for the operating temperature.

Helium Working Fluid. Helium is thermodynamically attractive choice of working fluid, and its alleged inert nature toward metallic components is often taken for granted. In nuclear practice, however, the low levels of impurities inevitably appearing in pure helium have led to problems through selective reaction with alloy constituents. In the gas-cooled nuclear reactor systems where the use of helium has been considered, the level of impurities (CO, CO_2, CH_4, H_2, H_2O) is

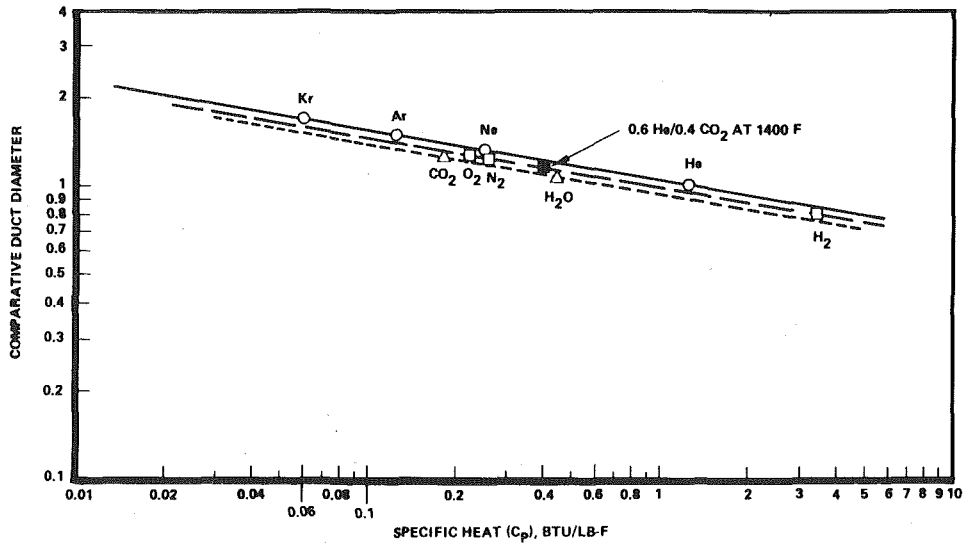

Fig. 10 Effect of working gas on required pipe size (based on constant $C_p\dot{m}$ and $\Delta P/\Delta L P$) helium = 1 (ref)

Downloaded 01 Jun 2010 to 171.66.16.59. Redistribution subject to ASME license or copyright; see http://www.asme.org/terms/Terms_Use.cfm

very low, and is controlled to some extent by equilibrium reactions between the impurities and the hot graphite core of the reactor. At these impurity levels there are insufficient oxygen-containing species to allow the formation of complete protective oxide films on alloys designed to do so. This apparently leads to the situation where the next most stable reaction products can form, which in this circumstance are usually carbides. These tend to be formed by carbon usually diffusing into the alloy to react with minor alloying additions such as titanium, niobium, tantalum, and zirconium.

Creep in impure He environments has been found to be accelerated at 1562°F for alloys which carbonized at this temperature, the degree of increase in creep correlating with the amount of carbon pickup [9]. Creep strains at 1472°F and below in air were not significantly different from those in impure He.

Differences in behavior have been observed for alloys exposed to laboratory helium-impurity mixtures, depending critically on the levels of impurities. For dry helium, for instance, the results from the DRAGON program [10] indicate localized carburization of a range of alloys, whereas for wet helium, many of the alloys formed almost complete protective films. Japanese workers [11, 12] on the other hand, using helium-oxygen at low oxygen partial pressures, reported decarburization of alloys. A fair amount of accessible data is available [13] on the effect of helium on some alloys (though not cobalt-base), which should only be considered as useful if the impurity levels under which the data were measured are representative of the intended application. As an example [13], after exposure in helium containing 500 μatm H_2, 1.5 H_2O, 53.1 CH_4, 32.9 CO, 0 CO_2, and 6.2 N_2 for 10,000 hr, Inconel 617 exhibited carbide precipitation to mean depths of 2500 μ (0.25 μ/hr), 180 and 52 μ at 1652, 1472, and 1202°F, respectively.

Unlike the helium gas-cooled reactor systems, the coal-fired heat exchanger system can tolerate a larger amount of oxygen-containing impurities without affecting the thermodynamic and transport properties of the impure helium. A practical solution to this problem is initially to run the working fluid with sufficient oxidant (oxygen, carbon dioxide, or water vapor) to allow the contacting metals to form protective scales, which will in most cases be chromia (Cr_2O_3)-rich. The helium can then be gettered of oxygen to a level of 1 mole percent which would represent a compromise between that required to repair damaged films and that necessary to reduce the danger of oxidative-volatilization of the Cr_2O_3-rich scales.

He/CO_2 Working Fluid. Since CO_2 is the active component in the He/CO_2 mixture, its effect on the alloys will be mainly governed by the concentration of CO_2. Carbon dioxide has been employed as a working fluid, particularly in the British Magnox reactors, so that research data are available on the effect of CO_2 on a range of alloys at temperatures up to 1700°F, on the effect of pressure, and for exposure times to 4000 hr [9, 14–21]. Because of the relatively low operational temperatures of the CO_2-cooled reactors, however, the range of alloys for which investigations are reported is mainly confirmed to the low-alloy and stainless steels and Inconel 600. In general, atmospheres rich in carbon dioxide are oxidizing toward Fe-Ni-Cr alloys and lead to minor amounts of carburization, whereas carbon monoxide-rich atmospheres are carburizing. Localized serious carburization has been observed in carbon dioxide, but this has generally occurred where carbon monoxide concentrations have accumulated in stagnant areas or in porous scales. The main scale-forming reaction in carbon dioxide oxidation is

$$M + CO_2 = MO + CO$$

Solid carbon deposits, from other scale-forming reactions

$$2M + CO_2 = 2\,MO + [C]$$

$$M + CO = MO + [C]$$

or from

$$2\,CO = C + O_2$$

can lead to some carburization attack but this is generally slow. Water vapor or hydrogen additions to the atmosphere tend to reduce its carburizing potential by reacting with carbon monoxide, and in some cases could lead to decarburization.

Antill and Warbutron [21] have characterized the behavior of stainless steels in CO_2-CO environments in the following way. For the 20/25/Nb-type stainless steels in pure CO_2, at temperatures up to 1560°F, there is a small pickup of carbon during the initial stages of exposure, followed by a slow, steady decarburization up to at least 700 hr exposure at 1560°F. Increased initial carbon pickup and long-term carburization are favored by large additions of CO. Similarly, carburization can occur in the long term if the protective oxide deteriorates, and CO accumulation can occur in any porous, nonprotective scale that forms. This carburization is favored by a low Cr and/or Ni content, repeated thermal cycling, extremely long exposure times, or temperatures appreciably above 1560°F. High chromium levels can apparently buy longer alloy lifetimes, as in air oxidation.

The detailed processing history can affect the susceptibility of stainless steels to carburization in CO_2, and the rate and morphology of attack. Annealing of AISI 316 in nitrogen instead of air, for instance, resulted in increased oxide scale thickness and greater depths of carbide penetration after exposure to CO_2 at 1202°F for 3000 hr [19].

Problems of variability in oxidation rates of 2¼ Cr-1 Mo and 1 Cr-½ Mo steels in CO_2 at 1022°F have been correlated with the shape, form, and distribution of MnS particles in the alloys [17]. Minor constituents in the CO_2, especially water vapor, also exert an effect. Differences in terminal rates of 0.0044 to 0.0857 mg/cm^2/hr have been observed in exposures ranging up to 7000 hr although acceleration to the rapid corrosion rates can occur after a few, or 2000 to 3000 hr exposure.

It is apparent, then, that the alloy degradation with He/CO_2 working fluid stems from essentially similar mechanisms as with the impure He gas. It is related to localized accumulations of CO for the protective scale-forming alloys, and to unpredictable corrosion behavior for the low-alloy steels. Since He/CO_2 mixture would eventually become a mixture of He/CO_2/CO through reaction with the metallic components, the ratio CO_2/CO would have to be controlled to maintain protective behavior. This could be accomplished by maintaining a small percentage of oxygen (1 mole percent) in the mixture to insure a high CO_2/CO ratio.

Cost and Availability

The cost and availability of a CCGT system working fluid naturally influences its desirability for application to real systems. Previous discussion has brought out that helium, air, and mixtures of He/CO_2 and He/Xe are strong contenders for application from the viewpoint of heat transfer capability and materials compatibility.

Xenon is a rare and expensive gas, with a cost/scf several thousand times that of helium and is not a practical candidate on that account.

Air, nitrogen, and CO_2 are all available in unlimited supply and at very modest cost. It should be understood that air will not be free in that it will need careful processing to remove moisture and particulate matter.

Helium is one of the noble gases and one might question the adequacy of its supply and price. An investigation of the helium supply situation with the U.S. Bureau of Mines at Amarillo, Texas, was conducted. Helium is controlled by the U.S. government. The present base price is 35 dollars per 1000 scf. This price is only remotely related to the cost of production and storage, has not changed in many years, and is not expected to escalate with inflation. Purchasers of helium now pay from about 45 to 65 dollars per 1000 scf depending upon the supplier. The difference from 35 dollars represents the cost of delivery and the cost of doing business for the commercial suppliers. These differential costs would be expected to escalate. If one assumes that the total volumetric capacity of a 350-MWe CCGT system is on the order of 60,000 actual cubic feet, the average pressure is 750 psia, and the average temperature is 1000°F, then the volume of helium in the system is on the order of 1,000,000 scf. Recent information on the Oberhausen II CCGT installation projects a yearly loss of one full

Downloaded 01 Jun 2010 to 171.66.16.59. Redistribution subject to ASME license or copyright; see http://www.asme.org/terms/Terms_Use.cfm

helium charge. At a cost of 50 dollars per 1000 scf, the cost of one system charge with helium would be 55,000 dollars. This compares with a yearly coal cost of 1 dollar per million Btu and 65 percent load factor of approximately 17 million dollars. One recharge with helium per year would thus cost about $^3/_{16}$ of 1 percent of the cost of the coal. As the CCGT systems provide about a 10 percent fuel savings over the standard steam stations, this helium cost would be only 3 percent of the coal savings relative to steam. If there were 350,000 MW of helium-cooled CCGT capacity in the United States, each requiring one yearly helium renewal, the helium consumption would be about 1.33×10^9 scf. This consumption rate is roughly equal to the yearly consumption that existed in the United States during the height of the missile and space program and would not constitute a serious drain upon the supply. These facts concerning the costs and availability of helium lead one to conclude that helium would be a viable CCGT system working fluid, provided that the system's helium integrity were such as to avoid excessive helium losses.

Safety

The choice of working fluid influences the CCGT system safety because of the possible hazardous effects of leakage, and possible explosions of pressure parts due to metals embrittlement.

The three leading working fluid contenders: 0.99 He/0.01 C_2; 0.6 He/0.39 CO_2/0.01 O_2; and air are safe in that they are nontoxic, nonflammable, and nonembrittling. Hydrogen has very attractive heat transfer and fluid transport properties, but was not seriously considered as a working fluid because it is so flammable, and embrittles many metals.

Conclusions

1 Helium, air, and helium/carbon dioxide (0.6 He/0.4 CO_2 by mole) gas mixtures were selected as possible candidate working fluids for coal-fired, closed-cycle gas turbine power generation and cogeneration systems. Both helium and He/CO_2 gas mixture may require the addition of small percentage (1 mole percent) of oxygen to safeguard against carburization of the alloy tube materials.

2 Air and He/CO_2 working fluids having higher optimum operating pressure ratios, give slightly higher thermal efficiencies than helium working fluid at equal design pressure loss factors ($\Delta P/P$).

3 Closed-cycle gas turbine using helium working fluid can be designed to operate at higher rotative speeds with smaller blade tip diameters than those using air and He/CO_2 mixture, because of the lower operating pressure ratio and higher sonic velocity of helium working fluid. But helium turbines and compressors will require many more stages than air or He/CO_2 turbines and compressors.

4 Mixtures of gases, particularly those with widely different molecular weights, have pronounced synergetic effect on heat transfer coefficients, mainly due to decreased Prandtl numbers of gas mixtures. 0.6 He/0.4 CO_2 mixture appears to offer attractive features of substantially higher molecular weight and fewer turbine compressor stages with only about 13 percent decrease in heat transfer coefficient as compared to the pure helium working fluid.

5 Based on equal heat fluxes and equal $\Delta P/P$, the film coefficients of heat transfer for the three candidate working fluids of He, He/CO_2 and air are in the proportions of 1:0.87:0.52. The heat transfer surface areas required for the unfired heat exchangers would also be approximately in this order with the three working fluids. The required heat transfer surface area for the fired heat exchanger is largely dependent upon the controlling combustion gas side heat transfer coefficient. But the tube wall operating temperature and its allowable design stress are significantly affected by the working fluid side heat transfer coefficient particularly in the high heat flux regions of a radiant furnace. An increase in tube wall thickness by a factor as much as 1.9 is required when air working fluid is used instead of helium in a radiant furnace system.

6 In this paper, only the characteristic requirements and the effects of the working fluids on the CCGT cycle performance and the various component designs were covered. These effects will vary in extent according to the selected cycle and component designs. Therefore, overall tradeoff between various working fluids will have to be based on the final criterion of either cost of electricity or return on investment which would require an extensive and detailed design study of each CCGT system.

Acknowledgment

The working fluids study was conducted under the DOE sponsored program "Advanced Coal-Fueled Combustor/Heat Exchanger Technology Study," Contract No. EF-77-C-01-2612, March 1977 through June 1978. The DOE program manager was Mr. C. Kinney, who provided the overall direction of the program and helpful suggestions in the preparation of the paper. Acknowledgment is also due to Dr. I. Wright of Battelle Columbus Laboratories for his contribution in the material compatibility study.

References

1 Bammert, K., and Groschup, "Status Report on Closed-Cycle Power Plants in the Federal Republic of Germany," JOURNAL OF ENGINEERING FOR POWER, Jan. 1977, pp. 37–46.

2 Bammert, K. and Bohm, E., "Nuclear Power Plants With High-Temperature Reactor and Helium Turbine," ASME Paper 69-GT-43.

3 Harrach, W. G. and Caldwell, R. T., "System Optimization of Brayton Cycle Space Power Plants," ASME Paper 63-WA-87, Nov. 1963.

4 McDonald, C. F., Fortescue, P., and Krase, J. M., "Primary Systems Preliminary Designs for Gas Turbine HTGR Power Plant," ASME Paper 76-GT-92, Mar. 1976.

5 Kramer, H. and Schlenker, H. V., "The Development of the HTR-Gas Turbine Cycle in Germany," presented at the 1976 ASME-ANS International Conference on Advanced Nuclear Energy Systems, Pittsburgh, PA, Mar. 1976.

6 Tilliette, Z. P., Pierre, B., and Jude, P., "Description, Output and Development Prospects of a 750 C Helium Direct Cycle Nuclear Power Plant With a Single Turbomachine and Intermediate Cooling," ASME Paper 77-GT-2, Mar. 1977.

7 Zenker, P., "The Oberhausen 50 MW Helium Turbine Plant," *Combustion*, Apr. 1976, pp. 21–25.

8 Anon, "Advanced Coal-Fueled Combustor/Heat Exchanger Technology Study," Final Report RI/RD78-212A, DOE Contract No. EF-77-C-01-2612, Mar. 1977–June 1978, Rockwell International/Rocketdyne Division, Canoga Park, California.

9 Noden, J. D., Knights, C. J., and Thomas, M. W., "Growth of Austenitic Stainless Steels Oxidizers in C- and O-Bearing Gases," *British Corrosion Journal*, Vol. 3, 1968, p. 47.

10 Gray, P. B. and Watts, C., "Operating Experience With the Dragon Reactor," *Proceedings of the Symposium on Advanced and HT Gas Cooled Reactors*, IAEA, 1969, p. 197.

11 Sekino, Shozo, "Studies of Heat Resistant Materials for High Temperature Gas Reactors," NASA TTF-15, 576, May 1974.

12 Yuzo, Hosoi and Abe Seizabuyo, "The Effect of Helium Environment on the Creep Rupture Properties of Inconel 617 at 1000 C," *Metallurgical Transactions A*, Vol. 6A, June 1975, pp. 1171–1178.

13 Rosenwasser, S. M. and Johnson, W. R., "Gas Turbine and Advanced HTGR Materials Screening Test Program, 10,000 Hour Results and Semiannual Progress Report," GA-A14407 UC-77 on Contract EY-76-C-03-0107, July 1977.

14 Martin, W. R. and Weir, J. R., "Influence of Chromium Content on Carburization of Cr-Ni-Fe Alloys in CO_2," *Journal of Nuclear Materials, 16*, 19 (1965).

15 Jepson, W. B., Antill, J. E., and Warburton, J. B., "The Oxidation and Carburization of a 20/25/Nb Steel in CO_2, in CO and in CO_2-CO Mixtures," *British Corrosion Journal*, Vol. 1, 1965, p. 15.

16 McCoy, H. E., "Type 304 Stainless Steel vs Flowing CO_2 at Atmospheric Pressure and 1100–1800°F," *Corrosion*, Vol. 21, 1965, p. 84.

17 Harris, R. J. and Menzies, J. A., "Variability in CO Oxidation Resistance of 2-1/4Cr-1Mo and OCr-1/2 Mo Steels," *British Corrosion Journal*, Vol. 3, 1968, p. 34.

18 Cribb, R. J. P., Summerling, R., and Dobing, E., "Corrosion of a Vented Stainless-Steel Tube Exposed to CO_2 Containing 1% CO in a Nuclear Reactor," *British Corrosion Journal*, Vol. 3, 1968, p. 1976.

19 Board, J. and Winterbourne, R., "Oxidation of Austenitic Stainless Steel Boiler Tubing in CO_2, *British Corrosion Journal*, Vol. 4, 1969, p. 86.

20 Stevens, C. G. and Board, J., "Effect of Moisture on the Oxidation of Mild Steel and Low Alloy Steel in CO_2," *British Corrosion Journal*, Vol. 4, 1969, p. 80.

21 Antill, J. E. and Warburton, J. B., "Behavior of Carbon During the Corrosion of Stainless Steel of CO," *Corrosion Science*, Vol. 7, 1967, p. 645.

Downloaded 01 Jun 2010 to 171.66.16.59. Redistribution subject to ASME license or copyright; see http://www.asme.org/terms/Terms_Use.cfm

R. C. Adkins
Principal Research Officer,
Thermal Power Group,
School of Mechanical Engineering,
Cranfield Institute of Technology,
Cranfield, Bedfordshire, England

D. S. Matharu
Development Engineer.

J. O. Yost
Chief Aerodynamicist,
(Turbomachinery)

Rolls-Royce Aero Division,
Filton, Bristol, England

The Hybrid Diffuser

A vortex controlled diffuser has recently been reported [1], which attained high levels of pressure recovery within a short length. This diffuser has, however, achieved only a limited application because of its bleed-off requirements. The present work indicates a means by which this disadvantage can be overcome by using a hybrid arrangement of conventional and vortex controlled diffusers. The outcome was an efficient diffuser, half the length of the equivalent conical diffuser, and which would operate satisfactorily without either bleed-off or vanes projecting into the flow.

Introduction

The modest angle of divergence between the walls of conventional diffusers is an acute embarrasment to the Gas Turbine designer. Several diffusers can be needed in the engine and their accumulative length contributes significantly to the overall engine length and weight. In addition, mechanical complications arise due to the distances imposed by the diffusers between the compressor spools and their driving turbines. It is common knowledge, however, that if the divergence angle in the diffusers is increased, then the flow will separate from the walls giving rise to a pressure loss, instability of flow, and a marked deterioration of any component which may be located immediately downstream.

A potential solution to the diffuser problem was reported in [1]. This described a diffuser which can achieve greater pressure recoveries than those obtainable from conventional diffusers, and in only one-third of the length. A tubular arrangement of such a diffuser is shown in Fig. 1, where a bound vortex is used to guide the flow smoothly over the sudden step expansion between two concentric tubes. Here, the frictional losses incurred by the vortex had to be offset in order to maintain stability. This was achieved by venting air directly from the vortex which then encouraged the entrainment of high energy air from the mainstream flow. The rate of extraction of this vented air, or bleed, was reduced to a reasonable quantity by use of the fence, as included in the sketch. Optimisation of the fence height and axial location to produce a configuration requiring the minimum rate of bleed-off was achieved by experiment.

Figure 2 shows the characteristic variation of diffuser effectiveness with bleed-off, which is of a step-like form. The bleed rate quantity coinciding with the top of the step was termed the minimum bleed requirement, B'. This is expressed as either a fraction or as a percentage of the mainstream flow and was found to be strongly dependent on the area ratio of the step A_2/A_1. A correlation based on experimental data taken from small scale models was given as follows.

$$B' = 0.393\,\eta(1 - AR^{-2})(AR/d_e)^{0.5} \qquad (1)$$

here d_e, the equivalent diameter at inlet (mm), was defined as

$$d_e = \frac{4\ (\text{cross-sectional area})}{\text{vortex controlled perimeter}} \qquad (2)$$

and the area ratio, AR, equals A_2/A_1.

This relationship was used as a basis for Fig. 3 which shows that the minimum bleed requirement increases quite rapidly with area ratio.

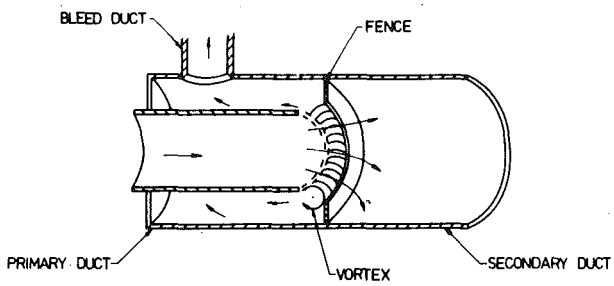

Fig. 1 A Typical tabular vortex flow controlled diffuser

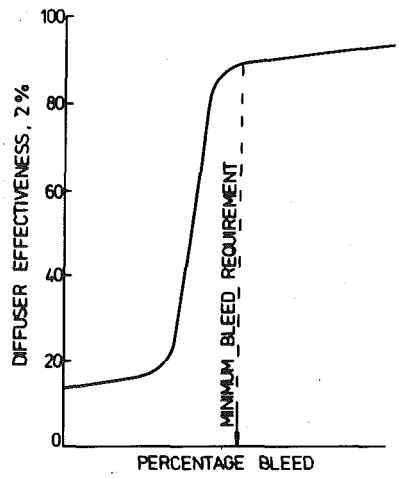

Fig. 2 Typical diffuser characteristic

Contributed by the Gas Turbine Division of The American Society of Mechanical Engineers and presented at the Gas Turbine Conference and Products Show, New Orleans, La., March 10–13, 1980. Manuscript received at ASME Headquarters January 2, 1980. Paper No. 80-GT-136.

Copyright © 1981 by ASME

Downloaded 01 Jun 2010 to 171.66.16.59. Redistribution subject to ASME license or copyright; see http://www.asme.org/terms/Terms_Use.cfm

Assuming that the relationship can be extrapolated up to the larger scale diffusers used in gas turbine engines, then a typical bleed requirement would be of the order of 5 percent. Such quantities may sometimes be acceptable as, for instance, when drawn from the precombustor diffuser and then used for turbine cooling, the drop in pressure between the two sections providing the necessary motivation. Similar convenient usage of the bleed air, taken from diffusers at other locations in the engine cannot always be envisaged, however, and the discriminate dumping of such quantities of air would significantly increase the engine's fuel consumption. The purpose of the present work was to investigate a means of reducing the quantity of bleed-off with the object of making the vortex controlled diffuser applicable to most locations in the gas turbine engine and installation.

In order to fully exploit the vortex controlled diffuser it is firstly necessary to consider the mechanism by which it operates. A completely satisfactory explanation has not yet been devised but a useful hypothesis was proposed in reference [1]. This used the model sketched here as Fig. 4. Due to the application of external suction, the static pressure inside the vortex chamber is below that in the mainstream. As a result, the stream '*a*' which is being drawn into the vortex, experiences a considerable acceleration. On the other hand, the stream '*b*', which flows down the diffuser is flowing to a region of greater static pressure and will therefore decelerate. A shearing action, produced by the velocity differential between the streams, then results in the creation of an extremely turbulent layer. This has been confirmed by Sutherland, [2], who measured turbulence intensities in the order of 50 percent near the aperture above the vortex chamber and also in a layer flowing beyond the fence and which eventually reattaches to the downstream wall. An indication that this turbulent layer can inhibit flow separation from a wide-angled conventional diffuser, located immediately behind the vortex diffuser, was first given in reference [3]. Here, a description is given of a highly efficient but relatively short length diffuser, located in the Rolls-Royce compressor test facility at Bristol.

The concept of hybrid diffuser being evaluated in the present study is illustrated in Fig. 5, where the vortex controlled step only accounts for a small increase in cross-sectional area and will therefore only require a minimal bleed-off. The turbulent layer generated by the step is then used to inhibit flow separation from a relatively wide angled conventional diffuser which contains a much greater part of the overall increase in area. Of particular interest was the level of anticipated compromise that would be involved between pressure recovery, overall length and bleed-off.

Experimental Program

1 Scope of Experiments. Due to their exploratory nature, the tests were confined to the tubular/conical configuration shown in Fig. 5. They were also limited to one inlet condition with a nominal inlet Mach number of 0.25, chosen so that the flow could be treated as incompressible and yet be at a sufficiently high Reynolds number as to be considered insensitive to any small variation in it.

The Reynolds number based on inlet diameter was 8.4×10^5 while that based on the approach distance between the contoured contraction piece and the vortex aperture was 14.5×10^5. This latter value ensured a turbulent boundary layer condition in the critical region near the vortex.

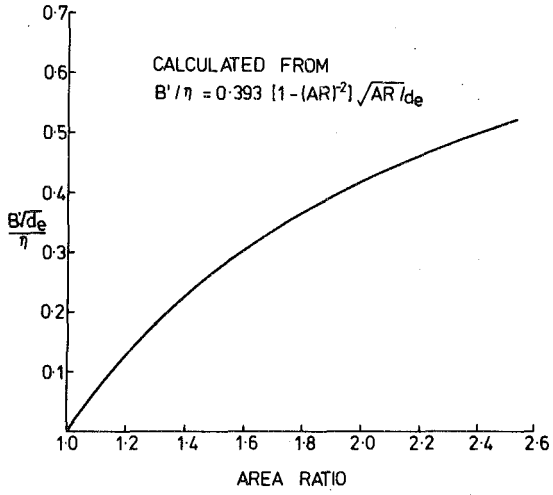

Fig. 3 Predicted minimum bleed requirement for vortex controlled diffusers

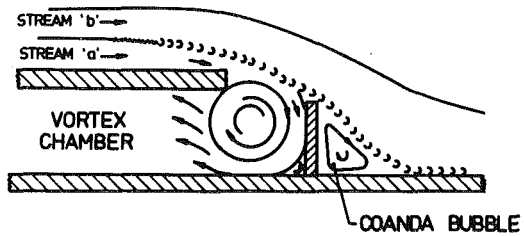

Fig. 4 Flow mechanism of vortex control

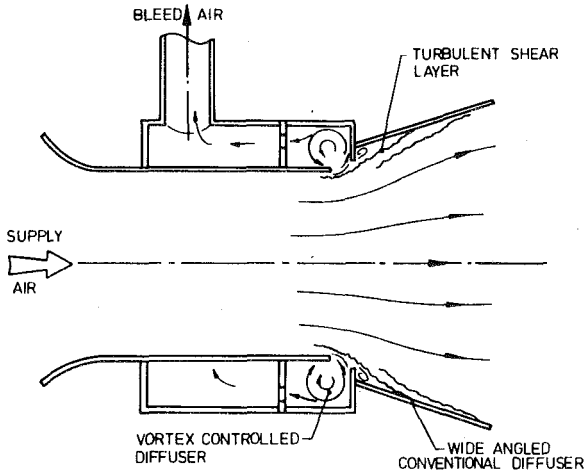

Fig. 5 A hybrid diffuser arrangement

Nomenclature

A_1 = cross-sectional area at diffuser inlet
A_2 = cross sectional area at base of vortex controlled step
A_3 = cross sectional area at diffuser exit
AR = area ratio, expressed as a ratio of inlet to exit area
B = percentage of mainstream flow which is bled out through the vortex
B' = minimum bleed requirement (defined in text)
C_p = coefficient of static pressure recovery
C_p^* = maximum static pressure recovered by a conventional diffuser within a specified length
D_1 = diameter of diffuser inlet duct
d_e = equivalent diameter (defined in text)
$\dot{m}_1$ = rate of mass flow into diffuser
p_a = ambient pressure
p_1 = static pressure at diffuser inlet
p_c = static pressure inside vortex chamber
$\bar{u}_1$ = mean velocity at diffuser inlet
V_c = coefficient of vortex chamber depression
x = axial gap between inlet duct and vortex retaining fence
y = radial gap between inlet duct and vortex retaining fence
η = diffuser effectiveness = measured C_p divided by $(1 - AR^{-2})$
ρ = density of air at test conditions
θ = total divergence angle of follow-on diffusing cone
ϕ = fence subtended angle = $\tan^{-1}(y/x)$

Downloaded 01 Jun 2010 to 171.66.16.59. Redistribution subject to ASME license or copyright; see http://www.asme.org/terms/Terms_Use.cfm

The diffuser inlet diameter was fixed at 152.4 mm but the other parameters illustrated in Fig. 6 were made variable.

Three sets of diffusing cones were manufactured from sheet metal, each covering a range of included divergence angle, θ, from 10 up to 30 deg. Details of these cones, together with their associated total diffusing length ratio, L/D_1 are given in Table 1. In addition, a simple parallel pipe was provided which could revert the diffuser back to a wholly vortex controlled arrangement similar to that shown in Fig. 1. This gave an overall area ratio, A_3/A_1, of 2.0:1 with a length ratio, L/D_1 of 1.025:1.

The radial gap, 'y', between the fence and inlet duct was varied by changing the fence, three values of 'y' were available, namely 2.41 mm, 3.81 mm and 5.46 mm. The axial gap 'x', was made infinitely variable between the limits of 'x' greater than 4.1 mm and less than 17.4 mm. During tests, pre-determined values of the subtended angle, ϕ, were obtained by adjustment of the gaps 'y' and 'x'.

2 Diffuser Model and Instrumentation. Constructional details of the model are shown in Fig. 7, air was supplied from a contoured transition piece having a contraction ratio of 4:1. Variation of the fence axial gap 'x' was obtained by relaxing the nip on the '0' ring seal and sliding the entire vortex chamber assembly along the major axis. The concentricity of the fence and follow-on conical diffuser was guaranteed by using fitted locating pins which penetrated into the vortex chamber assembly. In turn, the accurate concentricity of this assembly was controlled by the machined disks which could slide along the outer surface of the inlet duct. Numerous small holes were drilled uniformly around the machined disc located inside the assembly. These were to insure that the bleed-off was extracted evenly from around the circumference of the vortex.

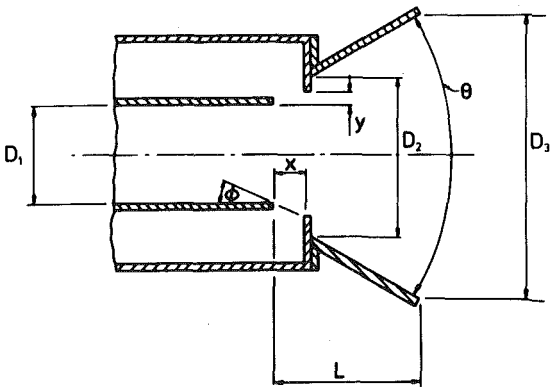

Fig. 6 Geometric parameters

Sharp edged orifice plates, installed according to British Standards 1042 were used to measure the airflow rate approaching the diffuser and also that flowing in the bleed-off duct. These measurements were made to an estimated accuracy of ± 1½ percent. Performance of the diffuser was assessed by the rise in static pressure between diffuser inlet and exit. The inlet pressure was measured using three static wall tappings, located at a distance of one duct diameter upstream of the vortex chamber aperture. This location was chosen so as to avoid the strong pressure gradients to be found nearer the commencement of diffusion. The pressure at diffuser exit was simply assumed equal to the test cell ambient pressure. Further static pressure measurements were taken from three tappings, located in the wall of the vortex chamber. Readings from these were used to assess the pressure loss experienced by the bleed air. The mean static pressures, both at diffuser inlet and in the vortex chamber, were estimated to have an error of less than ± 0.25 percent during steady flow conditions.

3 Performance Parameters. These were specifically chosen to permit a direct comparison with the more conventional type of diffuser. Diffuser length is nondimensionalised by dividing by inlet duct diameter, and static pressure recovery is presented as a static pressure coefficient, C_p defined as

$$C_p = \frac{p_a - p_1}{\frac{1}{2}\rho\bar{u}_1^2} \text{ where } \bar{u} = \frac{\dot{m}_1}{\rho A_1}$$

The quantity of bleed-off, B, like the minimum bleed requirement, B', is expressed as a percentage of the flow rate at diffuser inlet.

In many applications when a bled diffuser is used it is necessary to take full account of the losses entailed by bleeding air off. Unfortunately there is no universal term which can be used to satisfactorily

Table 1

Area Ratios		Length to diameter ratios, L/D_1 for nominal Cone Angles, θ of				
A_3/A_1	A_2/A_1	θ = 10	θ = 15	θ = 20	θ = 25	θ = 30
2.0	1.2	2.04	1.35	1.01	0.80	0.59
2.0	1.34	1.57	1.04	0.77	-	0.51
2.5	1.2	2.78	1.84	1.38	1.09	0.91

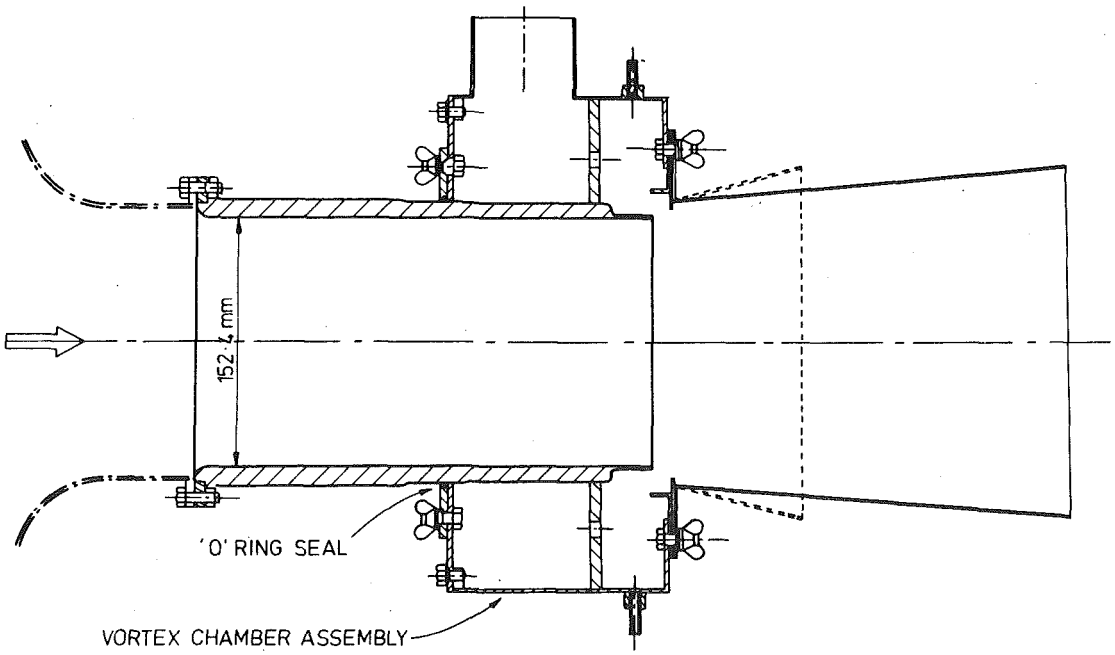

Fig. 7 Arrangement of the hybrid diffuser model

Downloaded 01 Jun 2010 to 171.66.16.59. Redistribution subject to ASME license or copyright; see http://www.asme.org/terms/Terms_Use.cfm

provide this assessment. It depends on whether the bled air is to be simply dumped overboard or whether it is to be re-introduced back into the flow stream. In this latter case, consideration must be made as to where the air is to be reintroduced, whether at diffuser inlet or exit, and to any losses that may be involved during the pumping process. Furthermore, consideration should also be given to the effects that poor diffusion might have on any component, such as a heat exchanger, combustor or compressor that may be located just downstream. To enable assessment to be aimed at a particular application the pressure loss experienced by the bled air is given by the coefficient of vortex chamber depression, defined as

$$v_c = \frac{p_1 - p_c}{\frac{1}{2}\rho \bar{u}_1^2}$$

4 Test Procedure. The supply air flow was adjusted to give a nominal Mach number of 0.25 at diffuser inlet. This was obtained before the introduction of suction to the vortex chamber; when suction was applied, however, there was a slight increase in Mach number produced by the improvement to diffusion but no attempts were made to readjust this.

Static pressure measurements were recorded at the zero bleed condition and at various bleed rates of up to about 5 percent of the total flow. From these the values of C_p were calculated and then plotted against percentage bleed to give control curves similar to that shown as Fig. 8. Most of the control curves derived from the tests can be obtained from reference [4]. Interpolated values of C_p, corresponding to bleed rates of 0, 1, 2 and 3 percent were transferred from the control curves to the results tables given here in the Appendix.

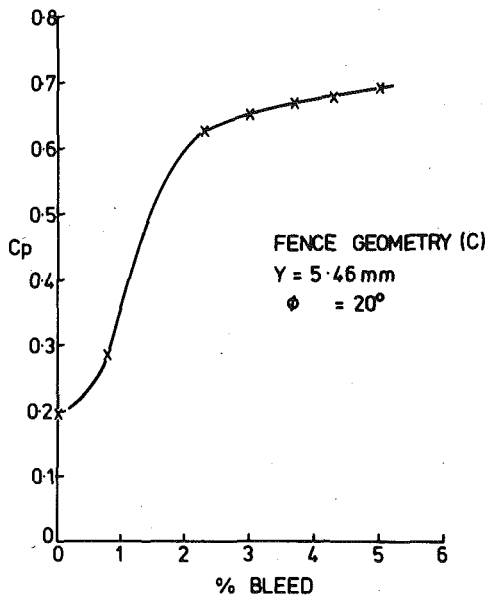

Fig. 8 Measured performance of a vortex controlled diffuser of area ratio = 2.0 and an inlet diameter of 152.4 mm ($L/D_1 = 1.025$)

Table 2 Details of the fence geometry

Fence Geometry	Values of fence subtended angle, ϕ, when		
	y = 2.41	y = 3.81	y = 5.46
(a)	10	12.5	/
(b)	15	15	17.5
(c)	20	20	20
(d)	25	25	25
(e)	30	30	30

During testing, it was attempted to use predetermined values of the fence subtended angle, ϕ, namely 10, 15, 20, 25 and 30 deg. Due to the limited movement of the vortex chamber assembly however, the smaller angles could not be achieved with the two larger fences. When this situation arose then the smallest angle obtainable was substituted. Details of the angles used are given in Table 2, together with an identity code which is also applicable to the tables giving the diffuser performance.

Results and Discussion

1 Wholly Vortex Controlled Diffuser. Tests were conducted on this arrangement to provide a comparison with the earlier work, reported in [1], and to establish a datum for assessing the hybrid diffuser arrangements.

The curve presented in Fig. 8 shows the step rise in static pressure recovery that was a characteristic feature of the earlier research. The value of C_p coinciding with the top of the step is subjective, but is clearly in the order of 0.63. The ideal value of C_p for a diffuser of this area ratio, given by $C_{p_{ideal}} = 1 - (AR)^{-2}$, is 0.75 and so the diffuser has achieved an effectiveness of 84 percent. Inserting this quantity into equation (1) leads to a value of minimum bleed requirement, B', of 2.84 percent which is compatable with the present data. It is therefore reasonable to accept that there is a good agreement between present work and the earlier series of tests reported in reference [1].

Additional data derived from using all 14 of the available fence configurations are presented in Table 3. A noteworthy feature shown by the table is that at a bleed rate of 3 percent the highest values of C_p were obtained by using both the widest available fence radial gap, $y = 5.46$ mm, and the largest fence subtended angle, $\phi = 30$ deg. This contrasts to the zero bleed case when both the smallest gap and the smallest angle ($y = 2.41$ mm and $\phi = 10$ deg) provided the most effective configuration. This feature suggests that the two conditions used different flow mechanisms for promoting the diffusion process.

2 Hybrid Diffusers. Data taken from the control curves in reference [4] are presented in Tables 4, 5 and 6, from which the maximum values of C_p, irrespective of fence configuration, have been used to plot Figs. 9–11. These figures show curves, derived for constant values of bleed flow rate, plotted against the non-dimensional length of the diffuser.

Hybrid Diffusers of Overall Area Ratio 2.0:1. A direct comparison between Figs. 9 and 10 clearly indicates that the arrangement using the smallest vortex controlled step ($A_2/A_1 = 1.2{:}1$), produces the highest pressure recovery. Both hybrid arrangements, however, outperform the wholly vortex controlled diffuser when constrained to the same length ($L/D_1 = 1.025$) and rate of bleed-off. For instance, at 3 percent bleed-off the hybrid diffuser produced a C_p of 0.75 compared to a corresponding value of 0.65 from the vortex controlled diffuser, and at lower bleed rates the improvement is even more evident.

Alternatively, the benefits to be obtained by the new diffuser can take the form either of a reduction in bleed rate or a reduction in length, or some compromise between the two. This statement can be substantiated by making reference to Fig. 9. This shows that in order to produce a C_p of 0.65, within a nondimensional length of 1.025, it

Table 3 Wholly vortex controlled diffuser, area ratio = 2.0:1; $L/D_1 = 1.025$

Fence Geometry	Values of C_p at the following bleed rates and fence radial gaps											
	0% B			1% B			2% B			3% B		
	y=2.41	y=3.81	y=5.46	y=2.41	y=3.81	y=5.46	y=2.41	y=3.81	y=5.46	y=2.41	y=3.81	y=5.46
(a)	0.380	0.335	/	0.425	0.520	/	0.450	0.580	/	0.480	0.610	/
(b)	0.365	0.280	0.258	0.438	0.515	0.420	0.488	0.590	0.610	0.523	0.630	0.650
(c)	0.330	0.210	0.195	0.435	0.430	0.300	0.500	0.610	0.561	0.540	0.650	0.650
(d)	0.288	0.145	0.175	0.460	0.270	0.235	0.540	0.580	0.610	0.590	0.660	0.675
(e)	0.235	0.160	0.160	0.460	0.210	0.210	0.550	0.620	0.355	0.595	0.675	0.680

Downloaded 01 Jun 2010 to 171.66.16.59. Redistribution subject to ASME license or copyright; see http://www.asme.org/terms/Terms_Use.cfm

Table 4 Overall area ratio = 2.0:1; area ratio of vortex controlled step = 1.2:1

Fence Geometry	Values of C_p at the following bleed rates and fence radial gaps											
	0% B			1% B			2% B			3% B		
	y=2.41	y=3.81	y=5.46	y=2.41	y=3.81	y=5.46	y=2.41	y=3.81	y=5.46	y=2.41	y=3.81	y=5.46
	θ = 9 degrees; L/D = 2.04											
(a)	0.590	0.635	/	0.668	0.690	/	0.702	0.715	/	0.719	0.730	/
(b)	0.640	0.635	0.625	0.686	0.688	0.680	0.705	0.720	0.715	0.720	0.740	0.732
(c)	0.620	0.615	0.615	0.682	0.680	0.670	0.715	0.718	0.720	0.730	0.740	0.740
(d)	0.590	0.602	0.610	0.690	0.645	0.655	0.715	0.707	0.715	0.729	0.739	0.740
(e)	0.605	0.600	0.595	0.675	0.650	0.650	0.720	0.712	0.700	0.730	0.736	0.735
	θ = 14 degrees; L/D = 1.35											
(a)	0.560	0.583	/	0.656	0.671	/	0.698	0.707	/	0.722	0.730	/
(b)	0.580	0.595	0.560	0.670	0.667	0.672	0.695	0.710	0.715	0.720	0.740	0.732
(c)	0.555	0.532	0.535	0.662	0.668	0.640	0.695	0.718	0.712	0.719	0.730	0.735
(d)	0.457	0.498	0.520	0.665	0.610	0.615	0.705	0.720	0.700	0.720	0.747	0.735
(e)	0.495	0.495	0.512	0.665	0.600	0.606	0.710	0.733	0.687	0.730	0.745	0.735
	θ = 18 degrees; L/D = 1.01											
(a)	0.495	0.515	/	0.588	0.645	/	0.640	0.691	/	0.670	0.720	/
(b)	0.500	0.500	0.450	0.625	0.655	0.640	0.685	0.695	0.707	0.708	0.720	0.737
(c)	0.455	0.400	0.380	0.638	0.640	0.610	0.675	0.705	0.705	0.705	0.728	0.735
(d)	0.420	0.360	0.375	0.650	0.550	0.555	0.695	0.720	0.700	0.718	0.747	0.735
(e)	0.390	0.365	0.365	0.632	0.490	0.530	0.698	0.720	0.675	0.718	0.750	0.735
	θ = 23 degrees; L/D = 0.80											
(a)	0.365	0.405	/	0.475	0.606	/	0.580	0.682	/	0.650	0.705	/
(b)	0.450	0.360	0.320	0.560	0.580	0.610	0.657	0.680	0.700	0.680	0.710	0.730
(c)	0.400	0.267	0.290	0.575	0.610	0.560	0.655	0.698	0.690	0.705	0.728	0.726
(d)	0.295	0.237	0.255	0.615	0.460	0.450	0.670	0.720	0.675	0.700	0.747	0.730
(e)	0.270	0.200	0.232	0.615	0.420	0.390	0.675	0.708	0.667	0.700	0.745	0.735
	θ = 27 degrees; L/D = 0.59											
(a)	0.240	0.328	/	0.326	0.570	/	0.480	0.650	/	0.565	0.695	/
(b)	0.280	0.275	0.245	0.450	0.565	0.560	0.560	0.660	0.675	0.630	0.700	0.712
(c)	0.280	0.200	0.230	0.495	0.560	0.500	0.608	0.675	0.672	0.665	0.717	0.712
(d)	0.230	0.135	0.150	0.555	0.330	0.320	0.635	0.690	0.660	0.685	0.730	0.730
(e)	0.180	0.120	0.140	0.550	0.250	0.265	0.643	0.690	0.650	0.680	0.730	0.725

Table 5 Overall area ratio = 2.0:1; area ratio of vortex controlled step = 1.34:1

Fence Geometry	Values of C_p at the following bleed rates and fence radial gaps											
	0% B			1% B			2% B			3% B		
	y=2.41	y=3.81	y=5.46	y=2.41	y=3.81	y=5.46	y=2.41	y=3.81	y=5.46	y=2.41	y=3.81	y=5.46
	θ = 10 degrees; L/D = 1.57											
(a)	0.540	0.540	/	0.620	0.670	/	0.665	0.710	/	0.690	0.730	/
(b)	0.545	0.525	0.500	0.623	0.670	0.610	0.680	0.710	0.710	0.695	0.730	0.735
(c)	0.515	0.485	0.490	0.650	0.620	0.620	0.690	0.715	0.715	0.715	0.735	0.735
(d)	0.480	0.463	0.475	0.670	0.560	0.540	0.705	0.710	0.710	0.720	0.750	0.740
(e)	0.465	0.430	0.460	0.650	0.540	0.530	0.700	0.725	0.630	0.715	0.750	0.745
	θ = 15 degrees; L/D = 1.04											
(a)	0.450	0.455	/	0.520	0.683	/	0.570	0.683	/	0.620	0.710	/
(b)	0.465	0.397	0.355	0.565	0.610	0.520	0.613	0.687	0.695	0.655	0.728	0.730
(c)	0.435	0.305	0.315	0.563	0.500	0.450	0.637	0.650	0.680	0.680	0.730	0.730
(d)	0.380	0.270	0.283	0.595	0.395	0.355	0.663	0.710	0.700	0.690	0.750	0.735
(e)	0.352	0.245	0.265	0.590	0.360	0.374	0.670	0.708	0.550	0.695	0.740	0.735
	θ = 20 degrees; L/D = 0.77											
(a)	0.330	0.320	/	0.395	0.550	/	0.450	0.630	/	0.520	0.680	/
(b)	0.325	0.280	0.230	0.455	0.565	0.355	0.515	0.655	0.590	0.568	0.700	0.720
(c)	0.270	0.210	0.218	0.480	0.540	0.300	0.560	0.690	0.675	0.620	0.720	0.720
(d)	0.225	0.145	0.160	0.520	0.270	0.260	0.590	0.705	0.680	0.643	0.745	0.730
(e)	0.195	0.110	0.130	0.520	0.250	0.195	0.603	0.690	0.660	0.650	0.740	0.745
	θ = 30 degrees; L/D = 0.508											
(a)	0.265	0.200	/	0.280	0.420	/	0.300	0.510	/	0.345	0.570	/
(b)	0.230	0.195	0.155	0.282	0.440	0.300	0.335	0.540	0.590	0.390	0.610	0.655
(c)	0.185	0.090	0.090	0.300	0.390	0.238	0.372	0.590	0.590	0.432	0.660	0.670
(d)	0.125	0.005	0.200	0.340	0.160	0.130	0.410	0.640	0.600	0.480	0.700	0.695
(e)	0.022	0.005	0.000	0.320	0.100	0.120	0.440	0.640	0.600	0.505	0.720	0.715

Downloaded 01 Jun 2010 to 171.66.16.59. Redistribution subject to ASME license or copyright; see http://www.asme.org/terms/Terms_Use.cfm

Table 6 Overall area ratio = 2.5:1; vortex controlled area ratio = 1.2:1

Secondary Diffuser Cone Angle, θ, = 10 degrees; Overall L/D=2.776												
Fence Geometry	Values of C_p at the following bleed rates and fence radial gaps											
	0% B			1% B			2% B			3% B		
	y=2.41	y=3.81	y=5.46	y=2.41	y=3.81	y=5.46	y=2.41	y=3.81	y=5.46	y=2.41	y=3.81	y=5.46
(a)	0.700	0.705	/	0.730	0.765	/	0.755	0.790	/	0.770	0.805	/
(b)	0.700	0.675	0.668	0.745	0.752	0.750	0.770	0.790	0.795	0.788	0.808	0.810
(c)	0.685	0.665	0.680	0.750	0.735	0.730	0.780	0.790	0.768	0.795	0.820	0.808
(d)	0.660	0.670	0.670	0.750	0.710	0.720	0.785	0.790	0.780	0.800	0.813	0.810
(e)	0.675	0.655	0.660	0.760	0.700	0.710	0.795	0.790	0.760	0.800	0.810	0.808
	θ=15 degrees; L/D= 1.84											
(a)	0.630	0.625	/	0.690	0.730	/	0.720	0.770	/	0.743	0.798	/
(b)	0.615	0.625	0.585	0.715	0.730	0.728	0.751	0.770	0.785	0.772	0.795	0.802
(c)	0.580	0.555	0.575	0.698	0.700	0.700	0.750	0.780	0.780	0.775	0.810	0.808
(d)	0.520	0.525	0.545	0.730	0.630	0.655	0.770	0.750	0.762	0.785	0.808	0.810
(e)	0.525	0.520	0.525	0.720	0.650	0.610	0.770	0.785	0.770	0.790	0.810	0.815
	θ=20 degrees; L/D = 1.377											
(a)	0.460	0.485	/	0.560	0.685	/	0.650	0.738	/	0.707	0.770	/
(b)	0.480	0.455	0.430	0.635	0.700	0.683	0.707	0.755	0.770	0.738	0.780	0.798
(c)	0.440	0.380	0.400	0.655	0.620	0.640	0.730	0.750	0.763	0.755	0.792	0.797
(d)	0.390	0.340	0.355	0.670	0.500	0.550	0.740	0.720	0.760	0.768	0.792	0.803
(e)	0.365	0.320	0.345	0.680	0.480	0.510	0.748	0.773	0.750	0.770	0.805	0.808
	θ=25 degrees; L/D= 1.095											
(a)	0.355	0.385	/	0.500	0.640	/	0.620	0.715	/	0.672	0.745	/
(b)	0.405	0.350	0.285	0.475	0.620	0.610	0.580	0.725	0.732	0.695	0.770	0.770
(c)	0.330	0.235	0.255	0.570	0.560	0.560	0.660	0.712	0.740	0.710	0.775	0.775
(d)	0.260	0.200	0.215	0.610	0.395	0.415	0.705	0.700	0.740	0.743	0.780	0.790
(e)	0.230	0.170	0.195	0.620	0.330	0.375	0.720	0.740	0.705	0.750	0.800	0.787
	θ=30 degrees; L/D= 0.906											
(a)	0.260	0.275	/	0.375	0.595	/	0.485	0.680	/	0.580	0.723	/
(b)	0.310	0.230	0.200	0.420	0.600	0.490	0.550	0.690	0.705	0.630	0.735	0.750
(c)	0.230	0.143	0.175	0.482	0.420	0.310	0.595	0.640	0.710	0.668	0.750	0.755
(d)	0.190	0.110	0.160	0.540	0.270	0.290	0.645	0.730	0.720	0.705	0.770	0.765
(e)	0.145	0.100	0.145	0.550	0.230	0.200	0.665	0.715	0.680	0.715	0.760	0.770

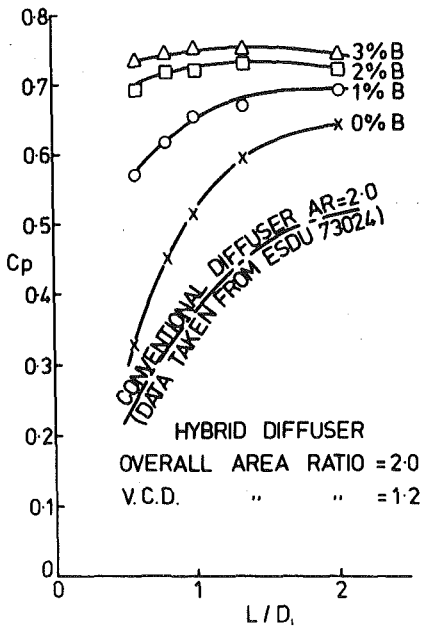

Fig. 9 Measured pressure recoveries

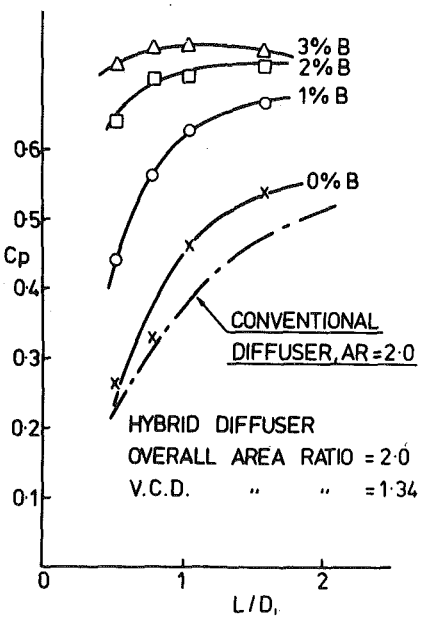

Fig. 10 Measured pressure recoveries

is only necessary to extract a bleed flow of 1 percent compared to the corresponding quantity of 3 percent required by the wholly vortex controlled arrangement. Furthermore, if the length of the hybrid diffuser is halved (i.e.) $L/D_1 = 0.5$), then at a bleed-off of only 2 percent it still produces a higher pressure recovery than the standard vortex controlled diffuser did when operating with 3 percent bleed-off.

Probably the most important discovery to be made during these tests was that the hybrid diffuser can produce a high level of pressure recovery even without the application of bleed. This important fact is most pronounced in Fig. 9 where at zero bleed, the hybrid diffuser is shown to produce pressure recoveries far greater than the equivalent conventional conical diffuser. Again the benefits of the new diffuser can be demonstrated either by an increase in pressure recovery, of at least 25 percent, over that of the conventional diffuser of the same length; or by the attainment of an identical pressure recovery over a

Downloaded 01 Jun 2010 to 171.66.16.59. Redistribution subject to ASME license or copyright; see http://www.asme.org/terms/Terms_Use.cfm

considerably reduced length. For instance, the attainment of a value of C_p of 0.52 required a non-dimensional length of 1.0 compared with the conventional diffuser which required a length of 2.0.

Hybrid Diffusers of Overall Area Ratio 2.5:1. As mentioned previously these were only tested with a vortex controlled step of area ratio 1.2:1. The data, as extracted from control curves, are presented in Table 6, and summarized in Fig. 11. A comparison with Fig. 9 indicates that the performance at this larger area ratio only generally exceeded that of the smaller hybrid diffuser for non-dimensional lengths of greater than 2.0. However, a superior performance could still be obtained below lengths of 2.0, but only at the higher rates of bleed-off. For instance, at a nondimensional length of 1.0 the larger arrangement gave greater pressure recoveries once the bleed rates had exceeded 2 percent. Another interesting comparison is that the new arrangement produced a C_p of nearly 0.8 within a nondimensional length of 1.0, albeit at a bleed rate of 3 percent; a similar pressure recovery from a diffusing cone would have required a nondimensional length of 9.5 and an area ratio of 4.2:1 [5].

At zero bleed-off, the new arrangement again outperformed the equivalent conventional conical diffuser (AR = 2.5:1), but only after their nondimensional lengths had exceeded 1.0. For lengths of greater than 1.5, the improvement in pressure recovery again was particularly significant.

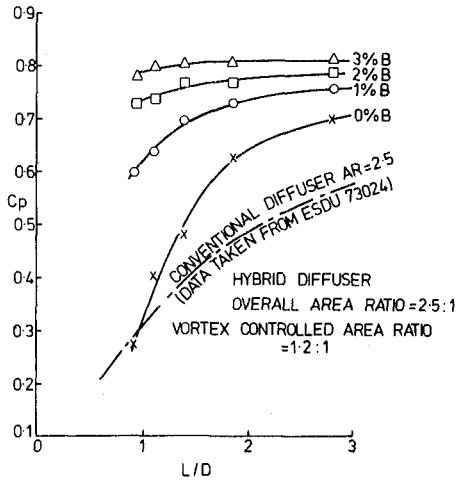

Fig. 11 Measured pressure recoveries

Comparison between Zero Bleed Hybrid Diffusers and Optimum Conical Diffusers. In most practical applications, and in the gas turbine in particular, the major constraint on diffusion is that imposed by length. Accordingly a diffuser is required with an area ratio which is optimised to produce the maximum pressure recovery within the specified length, such a device is referred to in the literature as a C_p* diffuser. Reference [5] was once again the source of standard data for the values of C_p* and corresponding area ratios that are used in Fig. 12. The evidence presented here clearly establishes the superiority of the hybrid diffuser, both in terms of pressure recovery and compactness. It is even pertinent to suppose that the limited range of tests so far conducted on the hybrid diffuser have not yet produced the optimum arrangement.

Pressure Loss Experienced by the Bleed Air. The value of vortex chamber depression, V_c, was found to be sensibly independent of geometric features downstream of the fence such as the cone angle, θ, the overall area ratio, and the size of the vortex controlled step. In general the value of V_c was found to increase with bleed flow rate and with increases in the radial fence gap, y, and the subtended angle, ϕ. Values of V_c, covering the whole range of bled diffuser experiments are presented in Fig. 13 where they are plotted against ϕ. These data, when combined with the rate of bleed-off, will enable the pumping losses associated with the secondary flow to be calculated for most specific applications when the hybrid diffuser is used with bleed-off.

Flow Mechanism. Evidence exists in the data which suggests that under certain circumstances the augmenting mechanism of the vortex controlled step changes from that described earlier in the paper. The change occurs as the bleed flow rate approaches zero. This is indicated in Fig. 13 by the curves giving values of V_c at a bleed flow rate of 1 percent. Here the curves for radial gaps of y = 3.81 and y = 5.46 mm exhibit different trends to any of the other curves. Similar variations in trend can also be observed in the tabulated values of C_p at the same operating conditions, here the values of C_p fall-off as the fence subtended angle is increased. A likely explanation for this phenominon is that at 1 percent bleed-off the suction is insufficient to retain the controlling vortex for all fence configurations.

On breakdown of the vortex, the bleed flow will originate from down-stream of the fence and will still produce a significant region of low pressure as it accelerates over the tip of the fence see Fig. 14. In addition to deflecting the main jet by the influence of the depression, the reverse flow will also generate a highly turbulent sheath

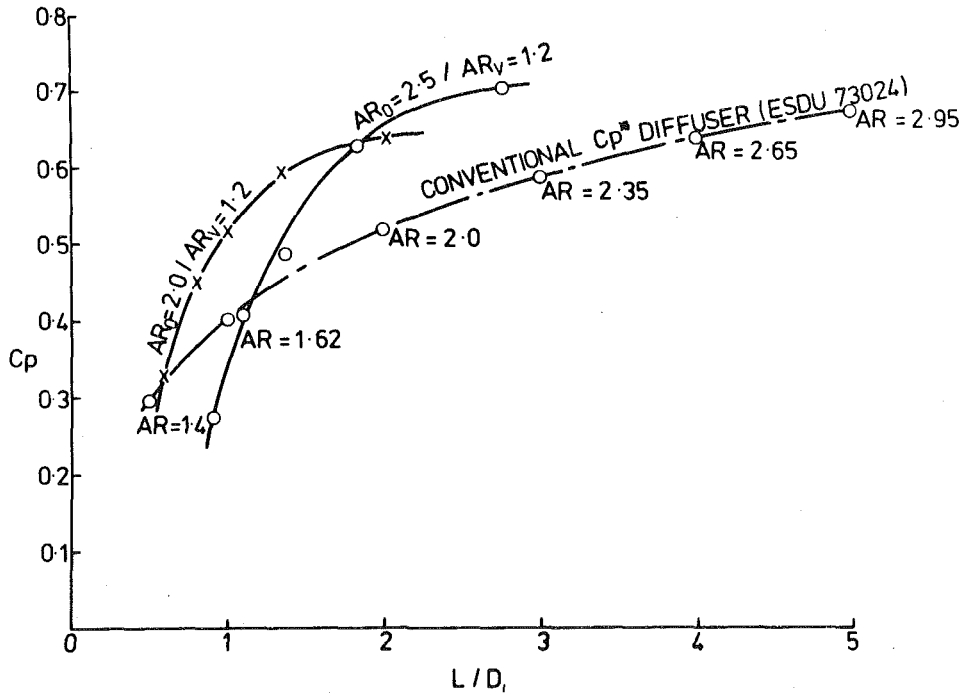

Fig. 12 Comparison between hybrid diffusers operating at zero bleed and optimum conventional diffusers

Downloaded 01 Jun 2010 to 171.66.16.59. Redistribution subject to ASME license or copyright; see http://www.asme.org/terms/Terms_Use.cfm

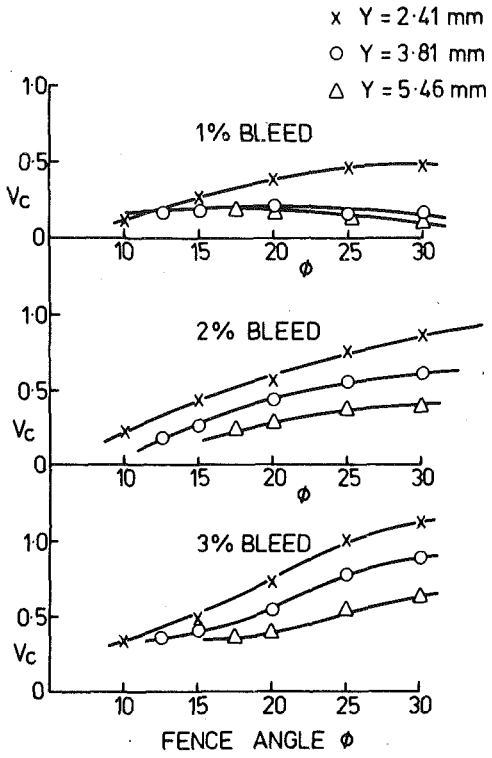

Fig. 13 Variation in coefficient of vortex chamber depression

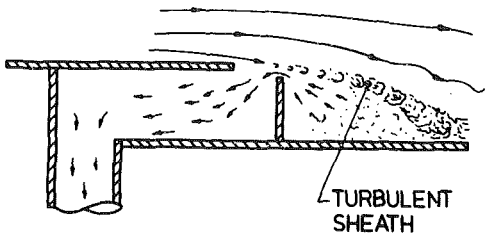

Fig. 14 Vortex controlled diffuser operating at low bleed

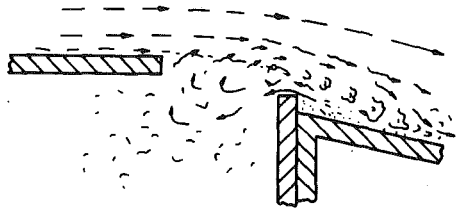

Fig. 15 Hybrid diffuser (zero bleed)

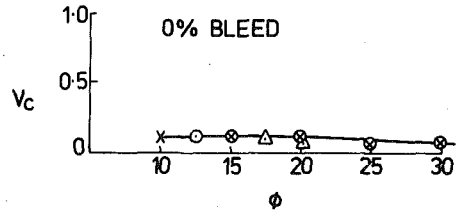

Fig. 16 Variation of vortex chamber depression with fence geometry

around the periphery of the jet which will promote its turbulent dissipation. The turbulent mixing process, in itself, is not aerodynamically efficient and relatively high pressure recoveries will not be achieved unless the flow reattaches to the diffuser wall. This occurs most readily when both the vortex controlled step is small and the angle of divergence of the follow-on diffuser is not too large. Both these suppositions are supported by the experimental data.

At zero bleed, it is likely that the above mechanism is maintained because of a 'jet pump action', produced by the mainstream flow in passing over the vortex chamber aperture, as sketched in Fig. 15. This pumping action produces a partial depression inside the vortex chamber which is controlled by the rate at which air is drawn into the driving jet and by the rate at which the incoming air can flow over the tip of the fence. The fence axial gap, x, will be dominant in controlling the rate of entrainment while the radial gap will be significant in controlling the rate at which air enters the vortex chamber. In addition the rate of divergence of the jet will be part controlled by the fence subtended angle, ϕ. Other factors, such as the volume and shape of the vortex chamber are also likely to be involved and more data will be needed before any useful analysis can be formulated. Figure 16 shows the values of V_c which were derived from measurements taken at zero bleed-off, these indicate that a depression exists and thereby support the supposition of the jet pump.

Conclusion

A limited series of tests have demonstrated that the hybrid diffuser has great potential. It is compact and can produce high levels of pressure recovery, both with and without external suction being applied.

With suction, it can match the pressure recovery of the extremely efficient vortex controlled diffuser when constrained to the same length. The hybrid diffuser, however was found to require only one-third the rate of bleed-off and so is more suitable for a wide range of applications. If a comparable rate of bleed-off is employed, then the new diffuser offers considerably higher pressure recoveries which are obtainable within a remarkably short length; for instance a value of C_p of near 0.80 was obtained within a nondimensional length, L/D_1 of 1.10 at a bleed-off rate of 3 percent of the mainstream flow.

Without suction being applied the diffuser is less efficient than the vortex controlled diffuser operating with suction. Even so, it produced pressure recoveries which were 25 percent higher than those obtainable from the optimum design of conventional divergent duct (C_p* diffusers) having the same length. Alternatively it can match the pressure recovery of the conventional diffuser but then only requires half of the diffusing length.

More data is required in order to optimise the design of the hybrid diffuser, to determine its performance over a wide range of operating conditions, and to establish a design procedure.

Acknowledgments

The authors are grateful to Cranfield Institute of Technology and to Rolls-Royce, Aero Division, Bristol for jointly sponsoring the research and for permission to publish.

References

1 Adkins, R. C., "A Short Diffuser With Low Pressure Loss," ASME *Journal of Fluids Engineering*, Sept. 1975

2 Adkins, R. C., and Yost, J. O., "A Combined Diffuser Arrangement," *Proceedings of the 1979 International Joint Gas Turbine Congress and Exhibition*, Technion, Haifa, Israel.

3 Sutherland, G., "An Investigation into the Flow of Vortex Diffusers," M. Sc. Thesis, Cranfield Institute of Technology, 1972.

4 Matharu, D. S., "An Investigation of a Hybrid Diffuser," M. Sc. Dissertation, Cranfield Institute of Technology, 1978.

5 E. S. D. U., "Performance of Conical Diffusers in Incompressible Flow," Engineering Science Data Unit, Item 73024, 1973.

Downloaded 01 Jun 2010 to 171.66.16.59. Redistribution subject to ASME license or copyright; see http://www.asme.org/terms/Terms_Use.cfm

M. L. G. Oldfield
Department of Engineering Science,
University of Oxford,
Parks Road,
Oxford OX1 3PJ,
England

R. Kiock
Deutsche Forschungs-und Versuchsanstalt
fur Luft-und Raumfahrt,
33 Braunschweig Flughafen,
West Germany

A. T. Holmes
C. G. Graham
Aero Division,
Rolls Royce Limited,
Bristol BS12 7QE,
England

Boundary Layer Studies on Highly Loaded Cascades using Heated Thin Films and a Traversing Probe

In the continuing quest for increased turbine efficiency, the part played by blade profile shape remains crucial. Three turbine vanes with successively increased aerodynamic loading were tested in the High Speed Cascade Wind Tunnel at DFVLR Braunschweig. In addition to wake traverses, measurements of the boundary layer behavior were made. These consisted of (1) use of a constant temperature anemometer to measure the fluctuating heat transfer rate on an array of thin film platinum thermometers deposited on the vanes and (2) a flattened, traversing pitot probe held against the vane surface. Transition measurement by these techniques is described.

Introduction

The question of optimum profile shape remains one of the most important aspects of turbine aerodynamic design.

The investigation presented here concerns a Rolls-Royce program to reduce the solidity of turbine blading in order to reduce engine weight and cost without detriment to performance (i.e., no increase in fuel consumption). Three cascades with pitch/chord ratios of datum, +13 and +20 percent were tested in the high speed cascade wind tunnel of DFVLR Braunschweig [1].

The datum blade T2 is a high pressure turbine stator with an aerofoil which is only just super-critical at the design operating condition of 0.955 exit Mach number. The significant aspect of this investigation is that increasing the suction surface velocities to give extra lift results in a locally supersonic region, raising the question of how the boundary layer will react to supersonic acceleration and diffusion on a highly curved surface.

Flow separation and laminar to turbulent transition influence the blade performance, and for cooled blades the heat transfer rate depends strongly on the state of the boundary layer. Although theoretical methods for predicting boundary layer behavior exist, e.g., [2], it was felt that an experimental investigation was necessary because of the complexity of the flow in a turbine cascade operating in the transonic regime.

Two techniques new to cascade testing were developed to study the boundary layers. One follows the work of Bellhouse and Schultz [3] and Owen [4, 5] which indicates that the condition of the boundary layer can be determined by observing the fluctuations in heat transfer from a heated thin film on the blade surface.

The other technique examines the velocity profile of the boundary layer by means of a flattened traversing pitot probe held against the surface, as reported by Schlichting [6].

Experimental Details

The experimental investigations were carried out in the high speed cascade wind tunnel of DFVLR Braunschweig (see Fig. 1). This facility operates continuously and allows the independent variation of Mach number and Reynolds number by changing the pressure level p_k of the tank. These parameters range from $Ma_{2th} = 0$ to 1 and $Re_2 = 10^5$ to 10^6. The large size of the test section yields an aspect ratio of $h/c = 3.75$ using a blade chord length of 80 mm. The cascade flow exhausts as a free jet into the tank. Upstream of the cascade a turbulence grid is installed in order to provide a turbulence level Tu_1 of 4 percent [7, 8]. Further details of this wind tunnel are described in [1].

Figure 2 shows the parameters of the investigated cascades. Each cascade consists of seven to nine blades. In the middle position, there is installed either a plain blade for boundary layer and wave traverses or a blade with an insert of machinable glass ceramic for heat transfer measurements. Both the neighboring blades are equipped with tappings for measuring the surface pressure distribution. The cascade exit flow conditions were measured by traversing a wedge probe across the central blade passages behind the cascade in the mid span plane. The local flow quantities are averaged using the laws of conservation of mass and momentum [9].

Cascade Blading

The cascades described form part of a continuing program to study the two-dimensional aerodynamics of turbine stator blades. The through-flow conditions are representative of a stator mid section for a turbine stage of 2.6 total pressure ratio and a loading ($\Delta H/U^2$) of 1.9. The design flow conditions are:

axial inlet flow, $\alpha_1 = 0$

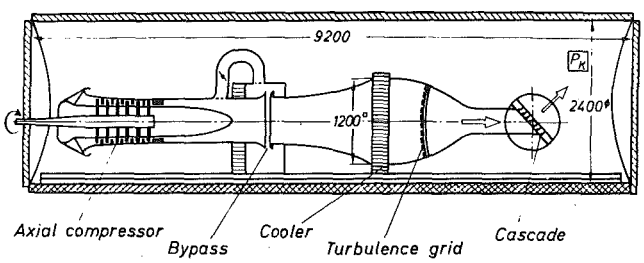

Fig. 1 The high speed cascade wind tunnel of DFVLR Braunschweig

Contributed by the Gas Turbine Division of THE AMERICAN SOCIETY OF MECHANICAL ENGINEERS and presented at the Gas Turbine Conference and Products Show, New Orleans, La., March 10–13, 1980. Manuscript received at ASME Headquarters January 2, 1980. Paper No. 80-GT-137.

Copyright © 1981 by ASME

Downloaded 01 Jun 2010 to 171.66.16.59. Redistribution subject to ASME license or copyright; see http://www.asme.org/terms/Terms_Use.cfm

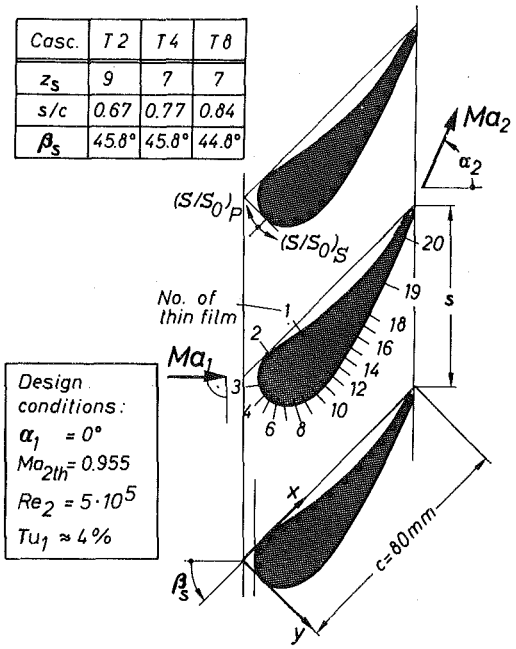

Fig. 2 Geometry of cascades

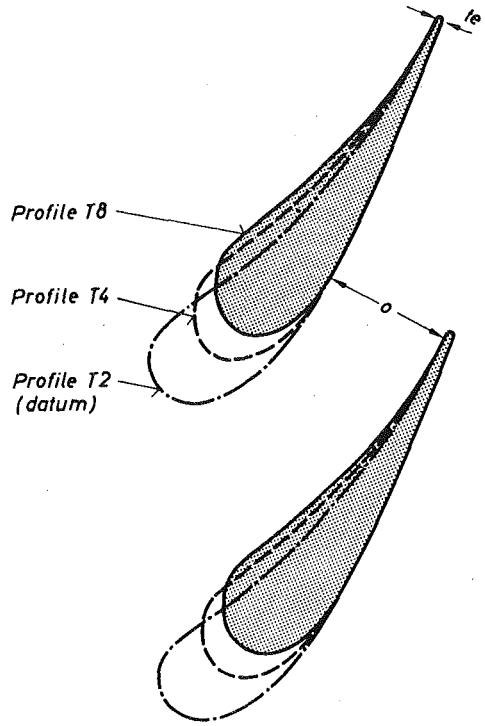

Fig. 3 Cascade profiles T2, T4, and T8

exit angle, $\alpha_2 = 65.2$ deg
isentropic exit Mach number, $Ma_{2th} = 0.955$
Reynolds number, $Re_2 = 5 \times 10^5$

The profiles, which are denoted T2, T4 and T8, are shown in Fig. 3 scaled to the same blade pitch. The coordinates are listed in the Appendix. The trailing edge geometry has been kept the same, i.e., a trailing edge blockage (te/o) = 5 percent and wedge angles of from 8 to 10 deg.

The datum cascade T2 was designed some years ago using a Prescribed Velocity Distribution (PVD) method developed at Rolls Royce, Ltd. from the original channel method of Stanitz [10]. Significant improvements in turbine performance have been achieved by replacing circular-arc profiles with blading designed using the PVD method. Cascade T4 was designed to exploit the method by increasing the suction surface loading to reduce blade solidity without any increase in loss. The major factor in this design concerns the flow behavior on the uncovered rear part of the suction surface. The effect of increasing the velocity levels in this region in the presence of a weak shock lying across the passage from the adjacent trailing edge was not known at the time. Unfortunately the PVD method is both (1) not fully compressible and (2) inviscid and could not provide reliable information concerning supersonic flow in the presence of shock waves. Hence, the increase in suction surface loading was confined to the covered portion, i.e., upstream of the throat position. The design surface Mach number distributions for cascades T2 and T4 are shown in Fig. 4. As far as the losses are concerned, it was expected that the increase in momentum thickness due to the increased diffusion on the suction surface would be offset by a reduction due to the shortened chord.

The surface Mach number distributions, derived from the measured values of surface static pressure and the inlet total pressure to the cascade, are shown in Fig. 5 for cascade T2 and T4. In passing, it is noted that, relative to the PVD design, suction surface velocities are lower upstream and higher downstream of the throat.

By the time that T4 was tested, the blade-to-blade time marching technique had been developed by Denton [11] into a usable design method, giving a fully compressible channel flow analysis with the ability to handle shock waves. At Rolls-Royce a program called TITAN was written, based on [11] and, although inviscid, it was felt that it could be used to design a blade with higher suction surface velocities than T4, allowing a further reduction in blade solidity from 13 to 20 percent to be achieved.

During the design of the new profile, T8, it was discovered that the time marching method predicted a local shock wave if the diffusion rate on the suction surface significantly exceeded the T4 diffusion rate. The increased loading was therefore achieved by raising the velocity levels mainly around the throat region of the suction surface giving increased surface curvature in this region.

Nomenclature

c = blade chord
e = a-c constant temperature anemometer (CTA) output voltage
e_{rms} = root mean square a-c CTA output voltage
E = mean CTA output voltage, with flow
E_0 = mean CTA output voltage, no flow
f = frequency
h = blade span
H = shape factor, ratio of displacement thickness δ to momentum thickness θ
$\Delta H/U^2$ = turbine stage work factor
Ma = Mach number
p = static pressure
p_0 = total pressure
q = dynamic head
$\dot{q}$ = fluctuating heat transfer rate
$\dot{q}_{rms}$ = r.m.s. fluctuating heat transfer rate
$\dot{Q}$ = mean heat transfer rate
$\dot{Q}_s$ = steady heat transfer rate to substrate
Re_2 = Reynolds number based on blade chord and exit gas conditions
s = blade pitch (spacing)
S = surface coordinate
S_0 = surface length from $x/c = 0$ to 1
te/o = ratio trailing edge diameter to blade throat width
Tu_1 = degree of upstream turbulence, $\sqrt{w_1'^2}/w_1$
w = flow velocity
x, y = bi-tangential blade coordinates
z_s = number of blades in cascade
α = gas angle relative to turbine axis
β_s = stagger angle relative to turbine axis
η = perpendicular distance from blade surface
ξ = energy loss coefficient = $1 - (w_2/w_{2th})^2$

Subscripts

1 = plane upstream of cascade
2 = plane downstream of cascade
∞ = edge of boundary layer
k = tank
S = suction surface
P = pressure surface
th = theoretical isentropic flow

Downloaded 01 Jun 2010 to 171.66.16.59. Redistribution subject to ASME license or copyright; see http://www.asme.org/terms/Terms_Use.cfm

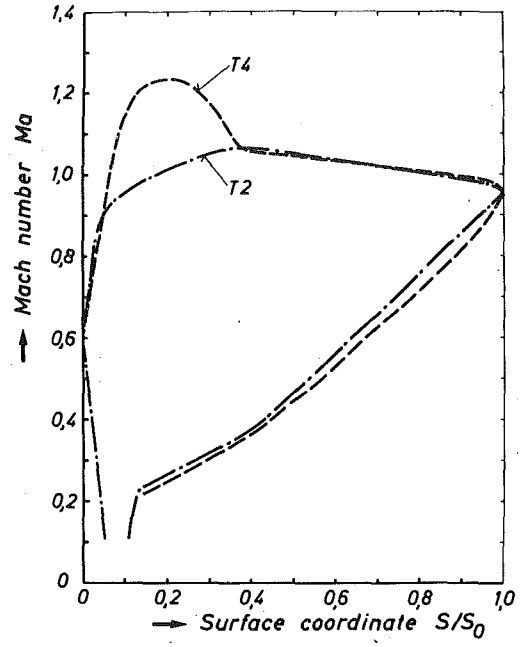

Fig. 4 Design point Mach number distributions, T2 and T4

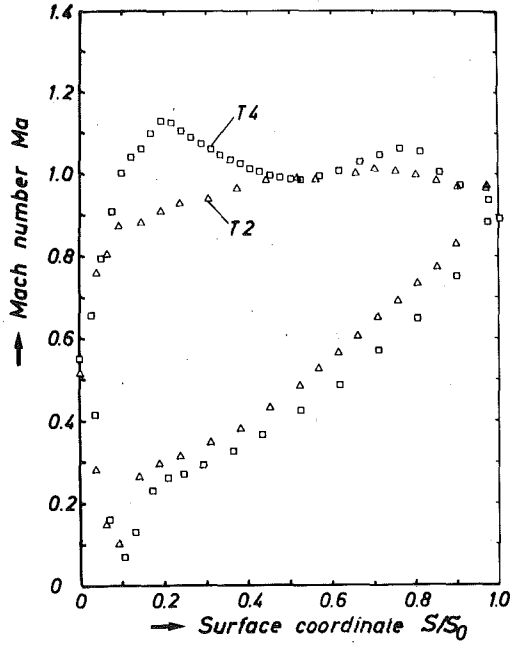

Fig. 5 Design point Mach number distributions deduced from tests, T2 and T4

A comparison between the calculated and measured surface velocity distributions, Fig. 6, shows quite good agreement. Fortuitously, the diffusion rate on the suction surface downstream of the throat is less than that predicted. Had this not been so, and a higher rate of pressure increase occurred, then a loss-producing shock boundary layer interaction of the kind described by Graham and Kost [12] may have resulted.

The tests reported here were carried out at design conditions plus a range of incidence angles from $\alpha_1 = -40$ deg to + 40 deg, exit Mach number Ma_{2th} from .3 to 1.0, and Reynolds number Re_2 from 1×10^5 to 7.5×10^5. No transition measurements were made on T2. A photograph of the cascade viewed on the exit side is shown on Fig. 7.

Cascade Performance

The exit angle characteristics at the design inlet angle are shown in Fig. 8(*a*). At the design point, $Ma_{2th} = 0.955$, the T8 cascade has the highest α_2, while, at lower values of exit Mach number, the T2 cascade has the highest value.

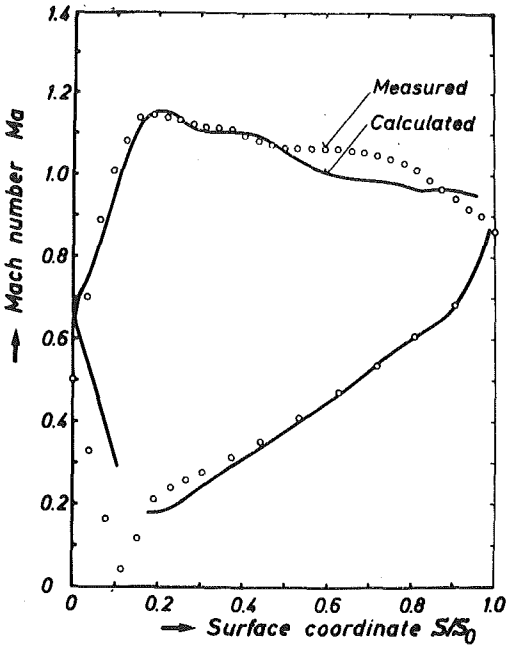

Fig. 6 Cascade T8, calculated and test Mach number distributions at design point

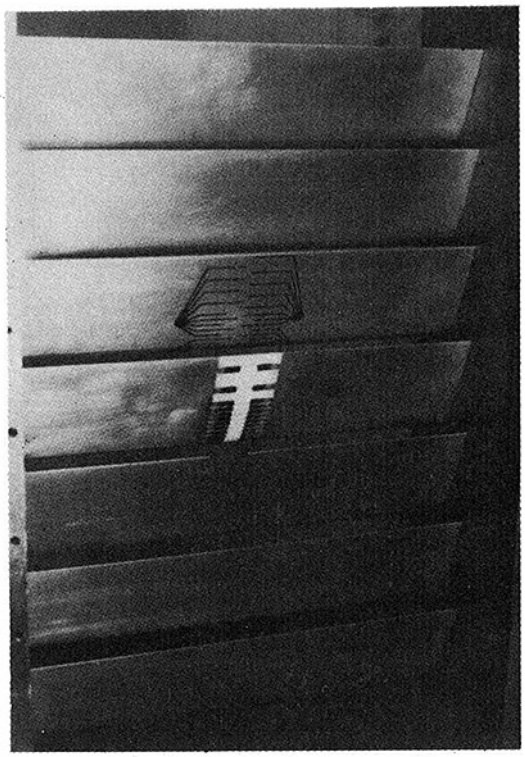

Fig. 7 View on exit plane of cascade T4

The loss coefficient characteristics (Fig. 8(*b*)) show that the objective of reducing blade solidity with no increase in profile loss has been achieved. In fact at the design point the loss coefficient cascade T8 is 22 percent lower than that of T2 even though the lift coefficient has been increased by over 20 percent. T4 shows a slight decrease in loss compared with the T2 datum. The shape of the loss curves in Fig. 8(*b*) indicates that the more highly loaded cascades are tuned to the design point flow condition which is now the minimum loss condition.

Considering the effect of incidence on the blade loss (Fig. 9) the trends are more or less as expected from general correlations such as that of Ainley and Mathieson [13]. The difference in loss levels between the cascades is fairly consistent with the exception of the T4

Downloaded 01 Jun 2010 to 171.66.16.59. Redistribution subject to ASME license or copyright; see http://www.asme.org/terms/Terms_Use.cfm

cascade which does not exhibit the sharp increase in loss of the other two cascades at a positive incidence of 40 deg (α_1 = 40 deg).

The Schlieren pictures of the flow, for example T4 and T8, Fig. 10, indicate that the flow behavior of the cascades is fairly similar. A series of weak shocks lie across the channel downstream of the throat plane. The Mach number distributions in Figs. 5 and 6, and the Schlieren picture in Fig. 10 show that T4 and T8 operate with supersonic patches on the suction surface which are free from strong shocks.

The enlarged Schlieren picture for the T4 cascade at Ma_{2th} = 0.7 (Fig. 11) shows the reason for the high loss at this condition for the T4 and T8 cascades. The laminar separation bubble clearly visible on the suction surface near the throat position confirms that suspected from the surface velocity distribution. This is discussed in more detail in the eighth section.

The analysis of the cascade performance cannot proceed further without information concerning the boundary layer behavior. The remaining major questions are:

1 Why does the highly loaded cascade, T8, have a significantly lower design point loss coefficient than the other two?
2 Why is there no sharp increase in loss when the T4 cascade is run at 40 deg of positive incidence?
3 Does the location of the transition region account for these effects?

An investigation into boundary layer transition was next carried out using heated thin films and a traversing pitot tube.

Heated Thin Film Technique

The state of a boundary layer, whether laminar, transitional or turbulent can be inferred by measuring changes in the mean and fluctuating heat transfer coefficients at the surface.

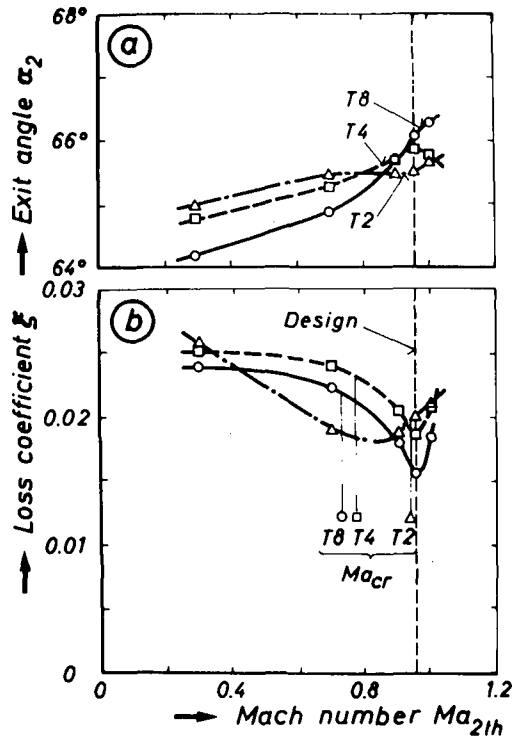

Fig. 8 Wake traverse data of T2, T4, and T8 at α_1 = 0

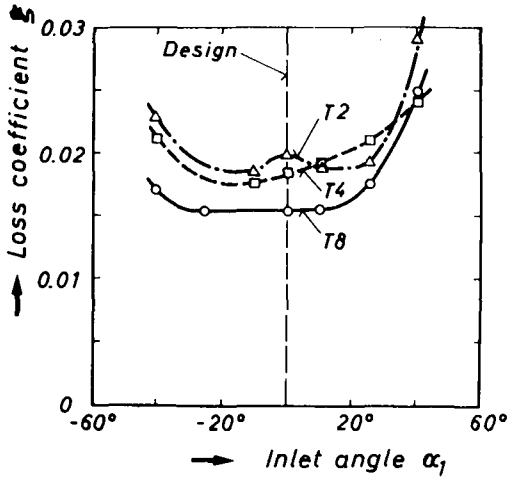

Fig. 9 Loss coefficient versus gas inlet angle for T2, T4, and T8 at Ma_{2th} = 0.955

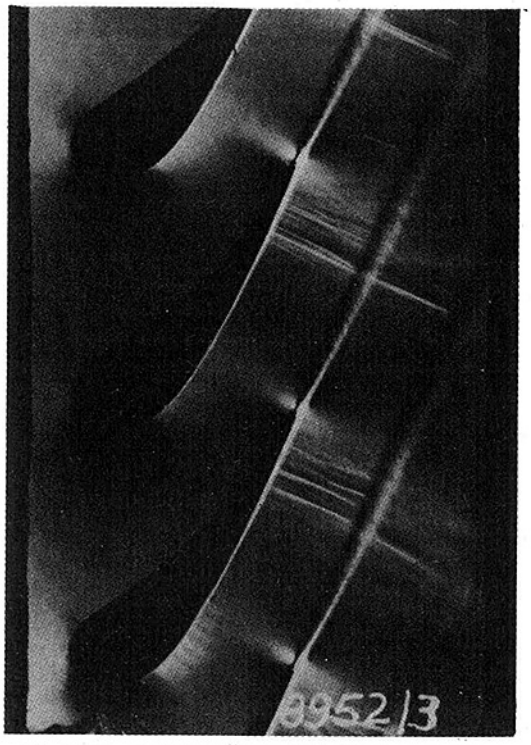

Fig. 10(a) Schlieren picture of T4 at design conditions

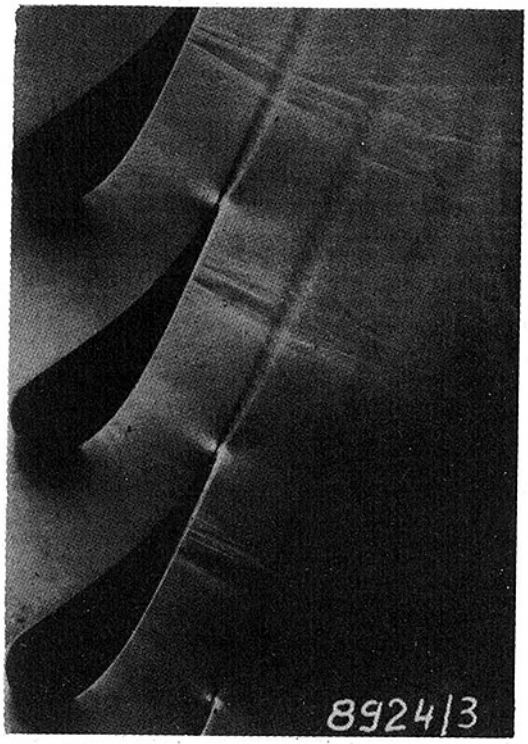

Fig. 10(b) Schlieren picture of T8 at design conditions

Downloaded 01 Jun 2010 to 171.66.16.59. Redistribution subject to ASME license or copyright; see http://www.asme.org/terms/Terms_Use.cfm

The transient measurement of heat transfer rates in short duration hypersonic flows by thin-film surface thermometers is well established [14], and this has been extended to hot cascade flows in the transient isentropic light piston tunnel at Oxford [15, 16].

The mean heat transfer rate increases with transition from laminar to turbulent boundary layer flow, but this is not the most sensitive indicator: Fig. 12, taken from tests in the Oxford tunnel on a rotor blade cascade having high subsonic exit Ma, shows the behavior of the fluctuating heat transfer signal $\dot{q}$ with increasing Reynolds number along a blade. Initially the signal is smooth in the laminar regime. Turbulent bursts give rise to large 100 Hz – 1 kHz fluctuations in $\dot{q}$ and give a peak in $\dot{q}_{\text{rms}}$. When the boundary layer becomes fully turbulent, the characteristic frequencies of $\dot{q}$ are far higher than the 2 kHz instrumentation bandwidth, and the measured $\dot{q}_{\text{rms}}$ falls to a lower value than the true turbulent level. Thus transition is clearly indicated by a peak in $\dot{q}_{\text{rms}}$.

In continuously running cascades, fluctuating heat transfer can be measured by using a constant temperature bridge anemometer to raise the temperature of a surface thin-film resistance thermometer above the recovery temperature of the flow. The fluctuations in the electrical heating power required to maintain a constant film temperature are proportional to $\dot{q}$ and can be used to study the boundary layer behavior. This technique is fully described in [3–5].

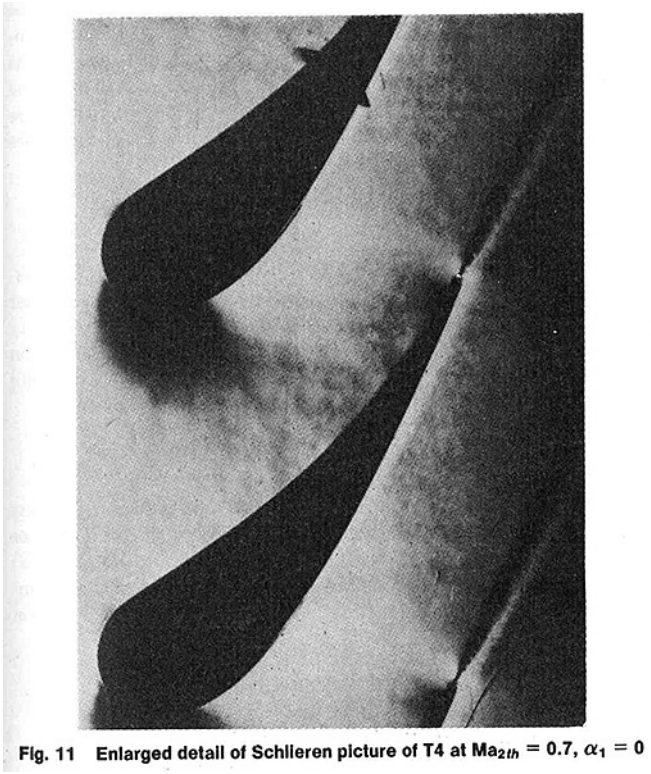

Fig. 11 Enlarged detail of Schlieren picture of T4 at $Ma_{2th} = 0.7$, $\alpha_1 = 0$

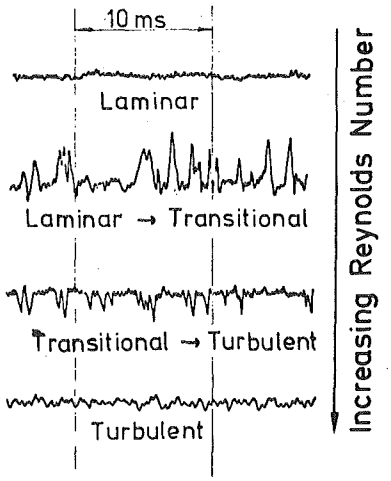

Fig. 12 Fluctuating heat transfer signals on a turbine blade in the Oxford transient cascade tunnel. Bandwidth = 0–2 kHz

In the work described here the thin film technique was extended to the more severe cascade tunnel environment where the fluctuating boundary layer signals can become masked by those arising from unsteadiness in the mainstream flow.

As is indicated in Fig. 13, the heat flow is from the thin film to the gas stream and to the substrate, and the total heat transfer rate measured is given by $(\dot{Q} + \dot{q} + \dot{Q}_s)$ where $\dot{Q}_s$ is the heat transfer rate to the substrate. Unfortunately, $\dot{Q}_s$ is usually larger than $\dot{Q}$, and is difficult to obtain independently; experiments with no flow do not give an accurate value. Consequently with this technique the fluctuating heat transfer rate $\dot{q}$ is used as the main indicator of boundary layer behavior. The difficulty in measuring $\dot{Q}$ makes detection of separation bubbles, where $\dot{Q}$ can be expected to fall, more difficult by the heated thin film technique than in the case of heat transfer measurements in a transient facility.

The instrumentation used in these cascade tests is shown in Fig. 13. Arrays of platinum thin films [14, 15] were painted and fired onto sections of the T4 and T8 profiles fabricated from Corning Macor machinable glass. These sections were then mounted on steel pins and set with epoxy resin between flanking aluminum alloy blade sections as shown in Fig. 7.

The films were then connected in turn to the constant temperature anemometer during the run. The anemometer output mean level, E, and fluctuating components e_{rms} were measured, and the a-c signal photographed on an oscilloscope screen.

The effects of small variations in film areas and resistances, and in the overheat used from film to film were eliminated by using the normalized voltage coefficient e_{rms}/E as the indicator of the fluctuating heat transfer rate $\dot{q}$.

The distribution of e_{rms}/E with surface distance from the leading edge, S/S_0, is shown in Fig. 14 for cascade T4 at 2 Mach numbers. For $Ma_{2th} = 0.3$, the curve shows transition clearly, commencing at film 11 with a peak at film 13. After film 14 the boundary layer is fully turbulent and the fluctuations are at higher frequency than the upper limit of the instrumentation (a bandwidth of 0.2 kHz–20 kHz was used). This is confirmed in the corresponding oscilloscope traces in Fig. 15. The flow over film 7 is laminar. The turbulent bursts in the transition region are clearly seen on film 12. By film 13 the flow has

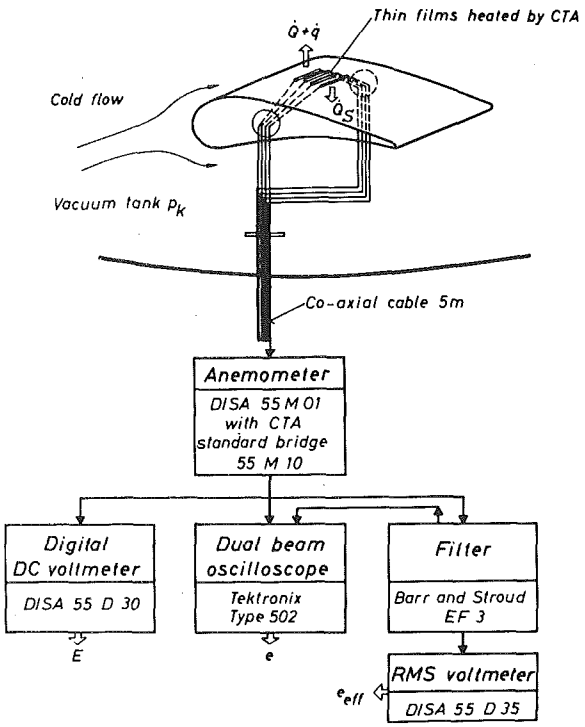

Fig. 13 Instrumentation for heated thin film technique

Downloaded 01 Jun 2010 to 171.66.16.59. Redistribution subject to ASME license or copyright; see http://www.asme.org/terms/Terms_Use.cfm

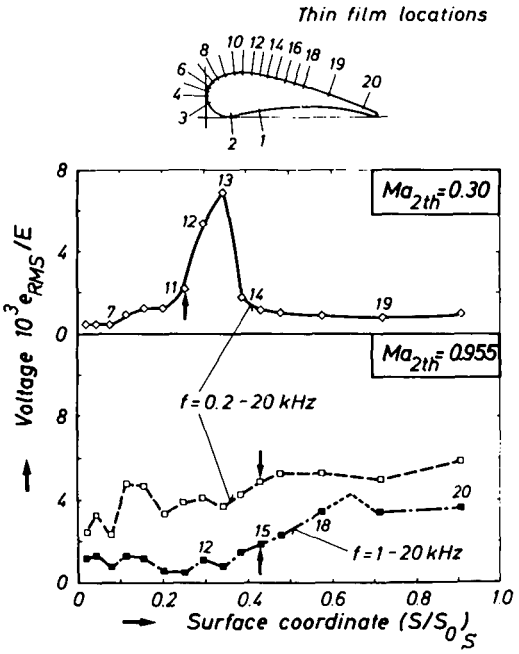

Fig. 14 Variation of heated thin film voltages $e_{rms/E}$ on T4 for various Mach numbers. Transistion onset indicated by arrows, $\alpha_1 = 0$

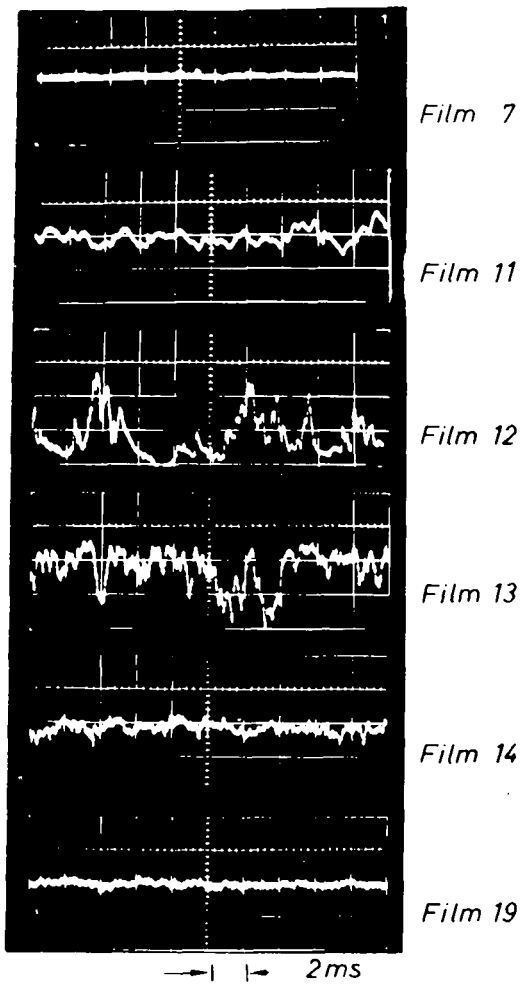

Fig. 15 Thin film oscilloscope traces for $Ma_{2th} = 0.3$ corresponding to the upper curve on Fig. 14, T4

only the occasional laminar periods, and the flow is fully turbulent by film 19.

At $Ma_{2th} = 0.955$ the e_{rms}/E curve with a 0.2 kHz–20 kHz bandwidth does not show a distinct peak and, at first glance, it is difficult to establish where transition occurs. However the corresponding oscilloscope traces in Fig. 16 show what is happening. In the laminar region, film 12, freestream fluctuations (and possibly blade vibrations) give rise to low frequency fluctuations in the trace. By film 15, small high frequency transition spikes are just beginning to appear superimposed on the low frequency signal, and by film 18 transition is well under way. The trace for film 20 shows clearly that the flow is still transitional even near the trailing edge of the blade. This is confirmed by the bottom curve in Fig. 14, where the low frequencies have been removed by restricting the bandwidth to 1 kHz–20 kHz. Transition is clearly indicated.

Clearly the thin film technique adds significantly to the range of boundary layer diagnostics, and will be shown to be very helpful to the understanding of the behavior of the T4 and T8 profiles.

Traversing Pitot Probe

Alternatively the transition was detected by a flattened pitot probe (Fig. 17 (*a*)). The head of this probe was held against the blade contour. Traversing the probe along the surface, the total pressure was measured at a constant distance from the surface, $\eta = 0.15$ mm. The local dynamic head was evaluated assuming constant static pressure normal to the surface and using the measured surface static pressure distribution.

$$\frac{q}{q_\infty}(S/S_0, \eta) = \frac{p_0(S/S_0, \eta) - p(S/S_0)}{p_{01} - p(S/S_0)}$$

q_∞ is the dynamic head at the edge of the boundary layer. p_0 is assumed equal to p_{01} since pressure losses at the level of Mach number used in these tests are negligible. The basic change in the velocity profile from the laminar to the turbulent state indicates the transition range (see Fig. 17(*b*)). This principle is mentioned by Schlichting [6] and it has been applied to flat plate measurements by Owen [4].

Results and Discussion of Boundary Layer Measurement

Suction Surface Data at Subsonic Flow Conditions. The first set of data describes the transition at an isentropic exit Mach number of $Ma_{2th} = 0.70$, i.e., when the flow is wholly subsonic. Figure 18(*a*) shows that the diffusion along the suction surface of cascade T4 untripped causes a local separation S at $(S/S_0)_S = 0.24$. The diffusion

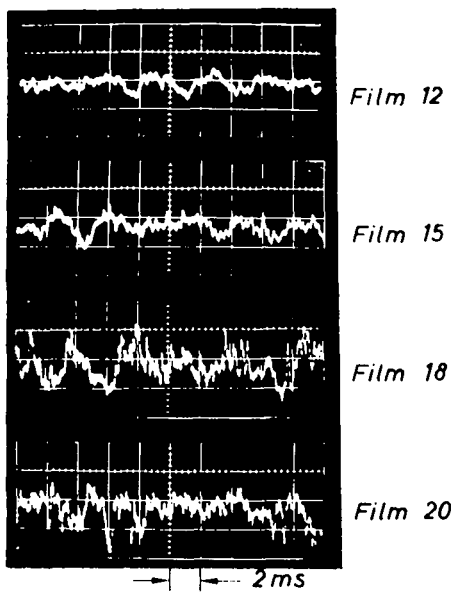

Fig. 16 Thin film oscilloscope traces for $Ma_{2th} = 0.955$ corresponding to the two lower curves of Fig. 14, T4

Downloaded 01 Jun 2010 to 171.66.16.59. Redistribution subject to ASME license or copyright; see http://www.asme.org/terms/Terms_Use.cfm

rate increases at $(S/S_0)_S = 0.35$; transition T occurs, and the turbulent boundary layer reattaches (R) at $(S/S_0)_S = 0.40$. This behavior is verified by the Schlieren picture (Fig. 11) and by the heat transfer measurements in Fig. 18(b). Transition onset $T.O.$ takes place at $(S/S_0)_S = 0.34$, and the peak, e_{rms}/E; i.e., the transition center follows 4 percent downstream. For comparison, the blade boundary layers were tripped at $(S/S_0)_S = 0.06$ with a 0.1 mm diameter wire. The Mach number distribution in Fig. 18(a) now shows a rapid perturbation in the vicinity of the wire. However, no bubble can be observed downstream. The thin film traces indicate transition onset close to the wire, and no peak in the e_{rms}/E appears in the region where the untripped blade showed transition.

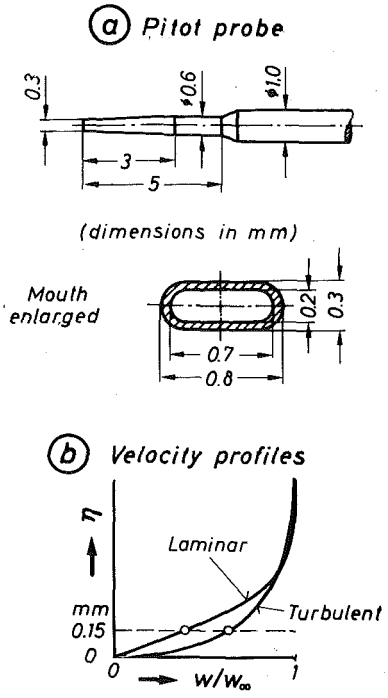

Fig. 17 Traversing pitot probe

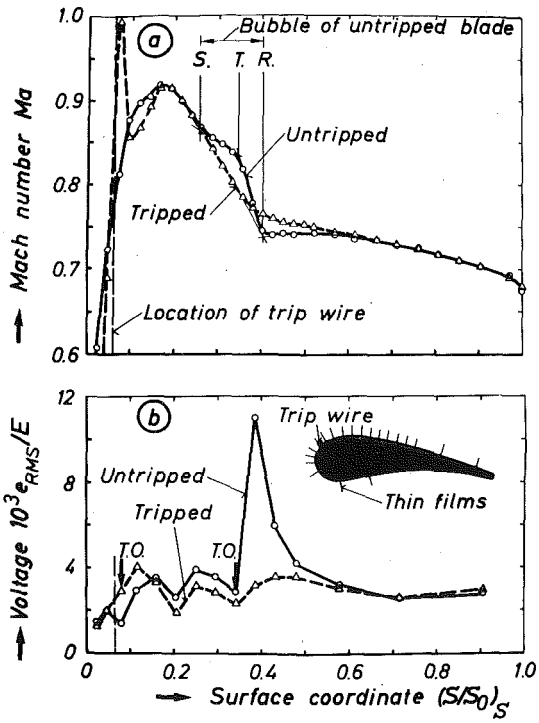

Fig. 18 Influence of trip wire on transistion, cascade T4 at $Ma_{2th} = 0.7$, $\alpha_1 = 0$

The corresponding Mach number distribution for the untripped cascade T8 is given in Fig. 19(a). Bubble transition is again observed and takes place roughly 5 percent downstream compared with T4. Nearly the same transition range is detected by boundary layer traverses giving the shape factor H of Fig. 19(b). It has to be noted that only in this case were complete boundary layer traverses taken. Here the transition range is indicated by the drop from $H = 3.1$ down to $H = 2.0$.

Figure 20 shows a direct comparison of T4 and T8 transition data. In Fig. 20(a) the heat transfer data shows clear peaks, with the T8 peak about 4 percent downstream of the corresponding T4 peak. This agrees with the Mach number curves.

Results from the traversing pitot probe are shown in Fig. 20(b). Both curves have a clear minimum indicating the start of transition as well as a clear maximum at the end of transition. The solid symbols for T8 signify that this measurement was started further downstream than for the open symbols. The small difference in dynamic head at the same position is due to slightly different inclinations of the probe axis to the blade surface.

Suction Surface Data at Transonic Flow Conditions. The next set of data, Fig. 21, is for the design Ma_{2th} of 0.955. The interpretation of the heat transfer results (Fig. 21(a)) is more difficult since there is no clear peak to indicate transition, and the oscilloscope traces show that this is due to the level of low frequency fluctuations. These occur in the range 300–350 Hz for both T4 and T8, and are believed to be due to blade vibrations. The traces show, however, that transitional spikes start to appear at the films indicated by arrows on Fig. 21(a). A repeat test of T4 using a 1–20 kHz filter (Fig. 14) showed an increase in voltage fluctuations over the range $(S/S_0)_S$ from 0.39 to 0.64, which corresponds reasonably well with the probe results on Fig. 21(b).

Transition starts later on T8 than T4, as would be expected from the weaker adverse pressure gradient in the middle of the suction surface.

It is known from boundary layer traverses that the profile corresponds to laminar flow at $(S/S_0)_S = 0.61$. In the thin film tests transition onset is observed just upstream of this position, and the fluctuation levels shown in Fig. 21(a) are still increasing near the trailing edge.

In Fig. 21(b), for T8, the traversing probe shows a kink at $(S/S_0)_S = 0.45$, but does not indicate the transitional rise in q/q_∞ until $(S/S_0)_S$

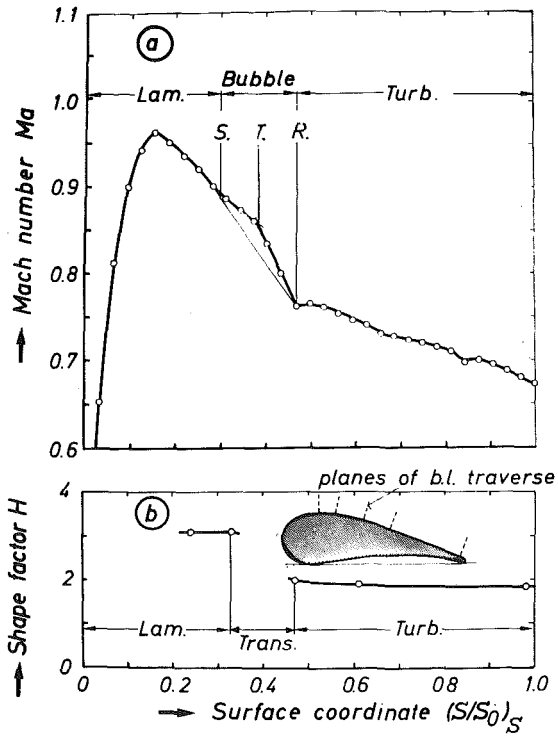

Fig. 19 Mach number distribution and boundary layer shape factor, T8, $Ma_{2th} = 0.7$, $\alpha_1 = 0$

Downloaded 01 Jun 2010 to 171.66.16.59. Redistribution subject to ASME license or copyright; see http://www.asme.org/terms/Terms_Use.cfm

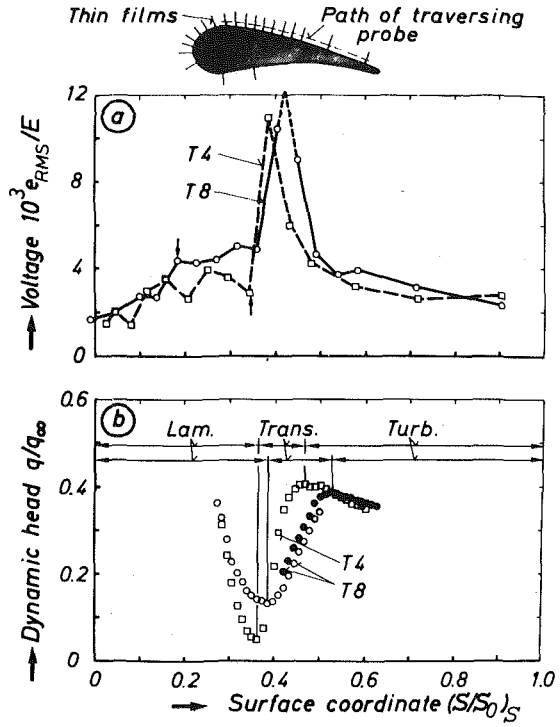

Fig. 20 Comparison of suction surface data, T4 and T8, $Ma_{2th} = 0.7 = \alpha_1 = 0$

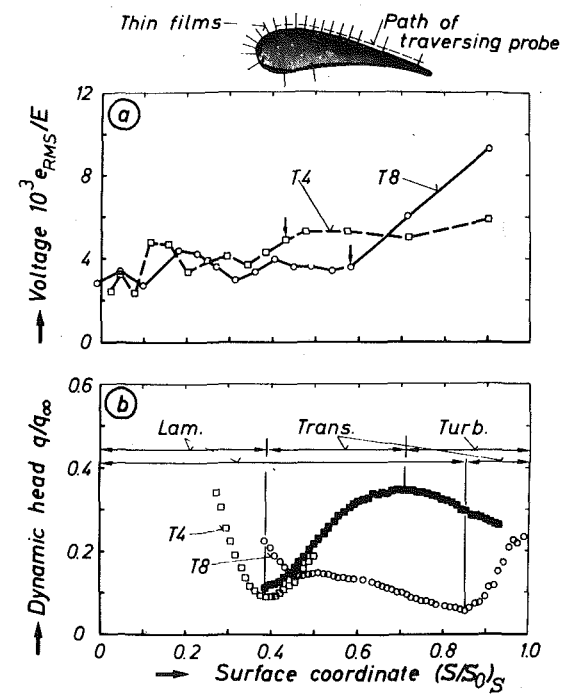

Fig. 21 Comparison of suction surface data, T4 and T8, $Ma_{2th} = 0955$, $\alpha_1 = 0$

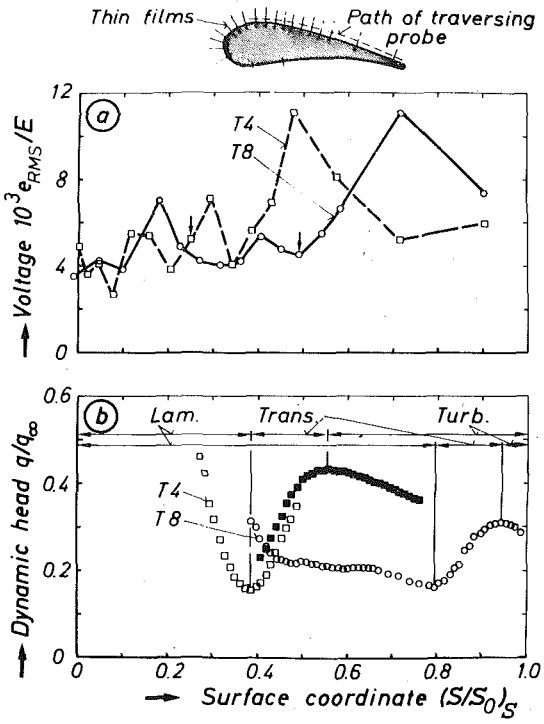

Fig. 22 Comparison of suction surface data, T4 and T8, at increased Reynolds number of 7.5×10^5

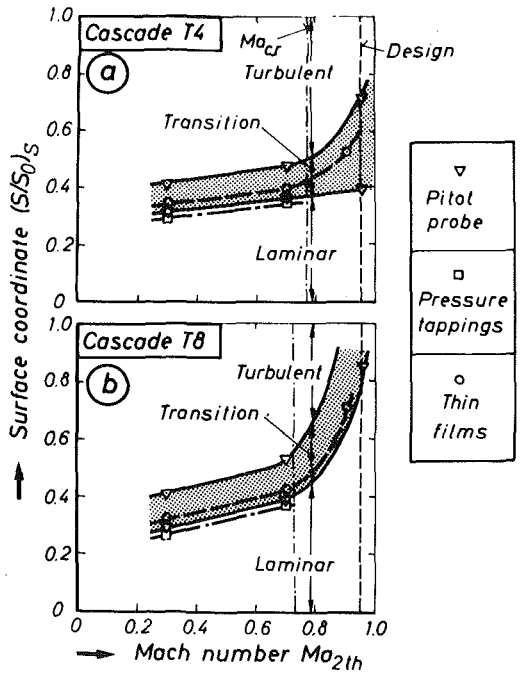

Fig. 23 Location of boundary layer transition, T4 and T8, $\alpha_1 = 0$

= .85. The difference between the two sets of results for T8 may indicate that the zone of transition extends over a large region of the blade, and the thin film technique is more sensitive to the initial stages of transition while the change in boundary layer profile registered by the probe becomes more apparent when transition is well established.

Furthermore, the shock pattern appearing in Schlieren photographs of the flow in the region $(S/S_0)_S = 0.7$ to 0.9 is certainly unsteady and will give rise to fluctuations in the thin film signals which may not be mirrored in the time averaged probe signals. This conclusion is supported by similar measurements conducted by Rubesin, et al. [17] using skin friction gauge wire elements on an airfoil at transonic speed. At the shock position, the ratio of rms to mean skin friction is ten times higher than that upstream. Investigations on the same airfoil with Kulite transducers were reported by McDevitt, et al. [18]. Fluctuations of $f = 188$ Hz were observed upstream and downstream of the mean shock position with strong pressure fluctuations of $\delta c_p = \pm 0.4$. The unsteady flow behavior of turbine cascades was investigated by Graham, et al. [12] using a high speed Schlieren film. The rapid motion of the shock pattern is demonstrated occurring at frequencies of $f = 400$ to 600 Hz.

Although the two techniques disagree as to the apparent commencement of transitions they both show that for T8 the flow is still transitional at the trailing edge.

Downloaded 01 Jun 2010 to 171.66.16.59. Redistribution subject to ASME license or copyright; see http://www.asme.org/terms/Terms_Use.cfm

Figure 22 shows the corresponding results at higher Reynolds number, $Re_2 = 7.5 \times 10^5$ at the same Ma_{2th} of 0.955. The thin film signal for T4 now shows a clear peak, and the transitional range agrees well with that indicated by the probe. For T8 there is again a difference in the indicated transition onset, but both techniques agree that the flow is fully turbulent by the trailing edge. Comparison between Figs. 21 and 22 shows that transition has moved upstream with increasing Reynolds number, as would have been expected.

Influence of Mach Number on Transition. Figure 23 summarizes all the data obtained in the measurement of transition on T4 and T8 suction surfaces at design α_1.

The band indicates the region where q/q_∞ measured by the traversing pitot probe is rising. The beginning of this band agrees well with the position of the end of the laminar part of the separation bubble as indicated by the measured Mach number distributions: at higher Mach numbers no clear bubble was observed. For the thin film results the peaks in rms voltage are indicated; these mostly appear within the traversing probe band. As the peak surface Ma rises above unity, indicated by $Ma_{2th} = Ma_{cr}$, the transition moves more rapidly to the rear part of the suction surface, and the sparse coverage of thin films in this region makes it difficult to determine the position of the peak. In Fig. 23, it can again be seen that T8 shows a later transition than T4, especially at the design Mach number.

APPENDIX

Profile Coordinates

T2			T4			T8		
x/c	$(y/c)_P$	$(y/c)_S$	x/c	$(y/c)_P$	$(y/c)_S$	x/c	$(y/c)_P$	$(y/c)_S$
.00000	.09604	.09604	.00000	.11865	.11865	.00000	.13585	.13585
.00016	.09172	.09922	.00182	.10123	.13619	.00150	.11255	.15379
.00178	.08467	.11201	.01077	.07507	.16299	.01084	.07897	.18390
.00466	.07303	.12176	.02931	.04578	.19034	.02751	.04997	.20996
.01238	.05725	.13696	.05666	.02154	.21392	.05061	.02730	.23130
.01944	.04458	.14693	.08497	.00771	.22914	.07696	.01122	.24716
.02410	.03765	.15203	.11494	.00098	.23962	.10896	.00194	.25960
.03434	.02600	.16261	.14570	.00122	.24615	.14621	.00070	.26790
.04146	.01968	.16818	.16357	.00414	.24842	.17278	.00345	.27081
.05039	.01349	.17516	.18562	.00802	.24991	.21858	.00941	.27149
.06291	.00686	.18289	.20589	.01170	.25013	.26426	.01561	.26785
.07071	.00390	.18735	.22425	.01504	.24950	.31050	.02204	.26078
.08373	.00081	.19382	.24699	.01917	.24773	.35982	.02866	.25022
.08876	.00039	.19604	.26702	.02278	.24534	.40526	.03419	.23840
.10493	.00074	.20250	.28665	.02630	.24237	.44991	.03887	.22525
.12919	.00409	.20973	.30906	.03022	.23828	.49764	.04322	.20992
.16890	.01294	.21795	.32685	.03322	.23466	.52793	.04546	.19967
.20463	.02126	.22203	.34553	.03625	.23064	.55022	.04674	.19189
.22837	.02667	.22275	.36842	.03973	.22552	.56788	.04750	.18559
.24821	.03107	.22315	.38533	.04221	.22135	.58727	.04810	.17856
.28609	.03902	.22168	.40745	.04479	.21624	.60867	.04852	.17067
.31798	.04516	.21866	.42848	.04711	.21095	.62713	.04866	.16377
.34302	.04946	.21552	.44737	.04903	.20603	.63977	.04862	.15901
.36815	.05321	.21192	.46996	.05116	.19993	.65372	.04847	.15373
.41717	.05859	.20284	.48917	.05279	.19456	.66856	.04817	.14808
.44661	.06101	.19627	.50751	.05415	.18928	.68338	.04774	.14241
.47282	.06267	.19024	.52982	.05552	.18264	.69608	.04727	.13751
.51635	.06440	.17924	.55061	.05649	.17626	.70771	.04676	.13300
.54105	.06492	.06492	.56939	.05708	.17036	.72037	.04608	.12807
.55683	.06500	.16799	.58911	.05741	.16403	.73515	.04513	.12228
.57522	.06485	.16267	.61127	.05745	.15677	.74845	.04412	.11704
.60412	.06418	.15393	.63107	.05719	.15017	.76006	.04311	.11245
.63035	.06302	.14569	.64893	.05669	.14413	.77206	.04196	.10768
.65655	.06135	.13722	.67050	.05576	.13674	.78682	.04037	.10180
.68270	.05917	.12854	.69068	.05460	.12972	.80050	.03876	.09634
.70233	.05721	.12190	.70890	.05330	.12331	.81199	.03729	.09173
.72192	.05495	.11519	.73045	.05140	.11564	.82349	.03573	.08710
.74959	.05125	.10550	.75131	.04922	.10812	.83810	.03360	.08121
.77842	.04688	.09523	.76942	.04703	.10153	.85239	.03136	.07541
.79984	.04326	.08747	.79022	.04417	.09390	.86430	.02935	.07056
.81920	.03973	.08036	.81190	.04081	.08588	.87619	.02721	.06571
.85496	.03256	.06715	.83002	.03769	.07912	.88915	.02473	.06038
.88987	.02496	.05394	.84912	.03412	.07194	.90372	.02175	.05438
.91543	.01901	.04416	.87108	.02964	.06361	.91758	.01871	.04863
.95011	.01055	.03072	.89011	.02548	.05632	.92952	.01587	.04365
.96643	.00649	.02428	.90802	.02134	.04941	.94162	.01281	.03857
.99374	.00000	.01343	.92950	.01609	.04102	.95521	.00924	.03280
.99753	.00140	.01125	.94945	.01095	.03313	.97093	.00508	.02606
.99973	.00464	.00824	.96709	.00631	.02601	.98381	.00174	.02051
1.00000	.00651	.00651	.98770	.00096	.01760	.99233	.00000	.01683
			.99713	.00160	.01300	.99844	.00341	.01295
			1.00000	.00751	.00751	1.00000	.00814	.00830

Downloaded 01 Jun 2010 to 171.66.16.59. Redistribution subject to ASME license or copyright; see http://www.asme.org/terms/Terms_Use.cfm

It is clear from Fig. 23 that the boundary layer on T8 is laminar over a much greater portion of the suction surface than on T4, and this contributes to the lower loss coefficient observed on T8.

Conclusions

Tests on three turbine cascades T2, T4 and T8 having successively increasing aerodynamic loading showed that:

1 The objective of reducing blade solidity with no increase in profile loss coefficient was achieved.
2 Transition of the boundary layer on the suction surface was detected by (i) heated thin films, (ii) a traversing pitot probe and (iii) static pressure tappings.
3 On T4 there was good agreement in determining the position of transition onset by these methods, but with T8 the agreement was less good, particularly at high Mach numbers. This was due to the lower diffusion rate and consequently longer region of transitional flow.
4 At high exit Mach numbers, it was necessary to choose the frequency cutoff carefully to reduce those voltage fluctuations in the thin film signals arising from unsteadiness in the main flow, and from blade vibrations.
5 With increasing exit Mach number, transition onset moved downstream, while the reverse effect occurred with increasing Reynolds number.
6 The change in the measured position of transition correlates with the observed loss coefficient characteristics.

Acknowledgment

The authors wish to thank Rolls-Royce Ltd., Oxford University Engineering Laboratory and DFVLR for permission to publish this paper, and for the help given by their colleagues, especially R. Lobel and T. Kotlarski. The work has been carried out with the support of the Procurement Executive, Ministry of Defence.

References

1 Hoheisel, H., and Kiock, R., "Zwanzig Jahre Hochgeschwindigkeits-Gitterwindkanal des Instituts für Aerodynamik der DFVLR in Braunschweig," *Zeitschrift fuer Flugwissenschaften und Weltraumforschung*, Vol. 1, 1977, No. 1, pp. 17–29.

2 Seyb, N. J., "The Role of Boundary Layers in Axial Flow Turbomachines and the Prediction of their Effects," in: AGARD-AG-164, 1972, pp. 241–259.

3 Bellhouse, B. J., and Schultz, D. L., "Determination of Mean and Dynamic Friction, Separation and Transition in a Low Speed Flow with a Thin Film Heated Element," *Journal of Fluid Mechanics*, Vol. 24, 1966, pp. 379–400.

4 Owen, F. K., "Transition Experiments on a Flat Plate at Subsonic and Supersonic Speeds," *AIAA Journal*, Vol. 8, No. 3, Mar. 1970, pp. 518–523.

5 Owen, F. K., Horstman, C. C., Stainback, P. C., and Wagner, R. D., "Comparison of Wind Tunnel Transition and Free Stream Disturbance Measurements," *AIAA Journal*, Vol. 13, Mar. 1975, pp. 266–269.

6 Schlichting, H., *Boundary-Layer Theory*, McGraw-Hill, New York, 1960, 4th edition, p. 381.

7 Kiock, R., "Turbulence downstream of Stationary and Rotating Cascades," ASME Paper No. 73-GT-80, 1973.

8 Kiock, R., "Einfluss des Turbulenzgrads auf die aerodynamischen Eigenschaften von ebenen Verzögerungs-gittern," *Forschung im Ingenieurwesen*, Vol. 39, 1973, No. 1, pp. 17–28.

9 Amecke, J., "Anwendung der transsonischen Ähnlichkeitsregel auf die Strömung durch ebene Schaufelgitter," *VDI Forschungsheft*, 540, 1970, pp. 16–28.

10 Stanitz, J. D., "Design of Two Dimensional Channels with Prescribed Velocity Distributions along the Channel Walls," NACA Report 1115, 1953.

11 Denton, J. D., "A Time Marching Method for 2 and 3 Dimensional Blade to Blade Flows," British ARC R & M 3775, 1974.

12 Graham, C. G., and Kost, F., "Shock Boundary Layer Interaction on High Turning Transonic Turbine Cascades," ASME Paper No. 79-GT-37, 1979.

13 Ainley, D. G., and Mathieson, G. C. R., "A Method of Performance Estimation for Axial Flow Turbines," British ARC R & M 2974, 1951.

14 Schultz, D. L., and Jones, V. T., "Heat Transfer Measurements in Short Duration Hypersonic Facilities," AGARD-AG-165, 1973.

15 Schultz, D. L., Jones, T. V., Oldfield, M. L. G., and Daniels, L. C., "A New Transient Cascade Facility for the Measurement of Heat Transfer Rates," AGARD-CP-229 High Temperature Problems in Gas Turbine Engines, Ankara, 1977.

16 Oldfield, M. L. G., Jones, T. V., and Schultz, D. L., "On Line Computer for Transient Turbine Cascade Instrumentation," IEEE Trans. AES-14, Sept. 1978, p. 738.

17 Rubesin, M. W., Okuno, A. F., Levy, L. L., McDevitt, J. B., and Seegmiller, H. L., "An Experimental and Computational Investigation of the Mean and Dynamic Flow Field about an Airfoil in Supercritical Flow with Turbulent Boundary Layer Separation," ICAS Paper No. 76-15, 1976.

18 McDevitt, J. B., Levy, L. L., and Deiwert, G. S., "Transonic Flow about a Thick Circular Arc Airfoil," *AIAA Journal*, Vol. 14, No. 5, 1976, pp. 606–613.

Downloaded 01 Jun 2010 to 171.66.16.59. Redistribution subject to ASME license or copyright; see http://www.asme.org/terms/Terms_Use.cfm

The Combined Effect of Axial Velocity Density Ratio and Aspect Ratio on Compressor Cascade Performance

U. Stark
Technische Universität Braunschweig,
Institut für Strömungsmechanik,
Braunschweig, West Germany

H. Hoheisel
Deutsche Forschungs—und Versuchsanstalt
für Luft—und Raumfahrt,
Institut für Entwurfsaerodynamik,
Braunschweig, Flughafen, West Germany

The paper describes theoretical and experimental investigations on the combined effect of axial velocity density ratio (AVDR) and aspect ratio (AR) on compressor cascade performance in incompressible and compressible flow. The results presented demonstrate that it is the aspect ratio that defines the axial velocity distribution through the cascade at a given wall shape and contraction ratio. It is further shown that it is, in turn, the axial velocity distribution that decisively determines the local values of pressure distributions as well as the cascade overall parameters like turning angles and loss coefficients.

Introduction

In general the design of axial flow compressor stages results in a change of the axial velocity density product through the stage at any given radius. Thus it would be useful for the designer to know the way in which cascade performance varies with the axial velocity density ratio across the blades.

The principal effects of the axial velocity density ratio (AVDR) in compressible flow and the axial velocity ratio (AVR) in incompressible flow on the performance of compressor cascades have been investigated experimentally by Pollard and Gostelow [1], Masek and Norbury [2], and Starken, et al. [3] and theoretically by Pollard and Horlock [4], Kubota [5], and Fottner [6]. A comparison between experimental and theoretical results has been described in reference [7] by Stark, in reference [8] by Stark and Starke, and in reference [9] by Hoheisel. These investigations indicated that an increase in AVDR or AVR is accompanied by an increase in turning angle and a decrease in static pressure rise across the cascade. The effect of an increase in AVDR or AVR on the blade pressure distribution was shown to consist in a fall in static pressure at all points of the blade surface, eventually with the exception of a small region near the leading edge on the suction side.

The references quoted constitute a selection only. There are much more publications in this field. But in spite of a large number of publications there is only a little information [1, 10, 11] available about the influence of the aspect ratio (AR) of the blades on the performance of compressor cascades.

In reference [1] and [10], the AR effect is regarded primarily as an effect of differently developed secondary flows while in reference [11] and in the present investigation the importance of the axial velocity distribution is stressed. It has been assumed and is theoretically and experimentally verified in this paper that it is the AR that defines the axial velocity distribution along the center line of the cascade at a given AVDR or AVR and wall shape. And it is in turn the axial velocity distribution that determines the blade pressure distribution as well as the cascade overall parameters like turning angle and loss coefficient. The results may of course be overshadowed by secondary flow effects under certain circumstances.

Theoretical Investigations

The inviscid flow in a cascade with contracting side walls (Fig. 1) is three-dimensional with spanwise gradients of the flow properties being small near the mid span section and large near the side walls. In an attempt to calculate the combined effect of AVR and AR on the performance of the center section of the cascade in inviscid and incompressible flow one may think of different approaches. The approach used in this investigation is two-dimensional with the exact axial velocity distribution of the test section center line incorporated. It consists of three steps:

i In the first step, the axial velocity distribution for the blade-free test section is calculated. A special result is the distribution for the center line of the test section.

ii In the second step, the axial velocity distribution of the center line is simulated as the sum of the induced velocities of a continuous distribution of strip sources and a constant velocity. The induced velocities are introduced in the Schlichting method [12] thus giving a method for the calculation of cascade exit angles and blade pressure distributions in axial accelerating or decelerating flow.

iii In the third step the induced velocities of the source distribution are incorporated in the Martensen method [13]. In this way a modified method for the calculation of blade pressure distributions in axial accelerating or decelerating flow is established. The blade pressure distributions calculated with this method are somewhat better than those of step ii). The outlet angle has to be prescribed.

Axial Velocity Function. The velocity field of the blade-free test section with contracting side walls was calculated by application of an image technique. The real test section was supplemented on both sides by an infinite number of image test sections (Fig. 2(*a*)) and a special nonstaggered cascade was arrived at. The blades of this cas-

Contributed by the Gas Turbine Division of THE AMERICAN SOCIETY OF MECHANICAL ENGINEERS and presented at the Gas Turbine Conference and Products Show, New Orleans, La., March 10–13, 1980. Manuscript received at ASME Headquarters January 2, 1980. Paper No. 80-GT-138.

Copyright © 1981 by ASME

Downloaded 01 Jun 2010 to 171.66.16.59. Redistribution subject to ASME license or copyright; see http://www.asme.org/terms/Terms_Use.cfm

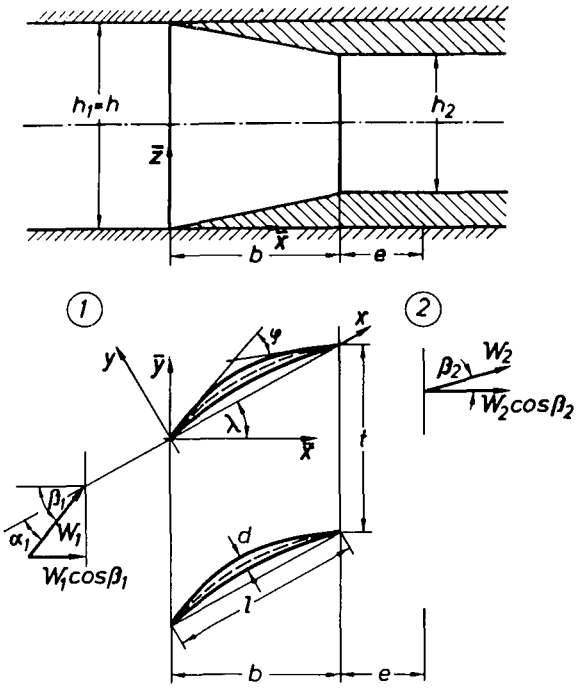

Fig. 1 Cascade geometry and nomenclature

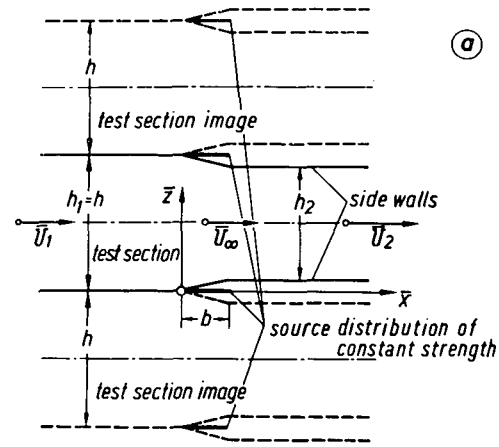

Fig. 2(*a*) Cascade model of the blade-free test section

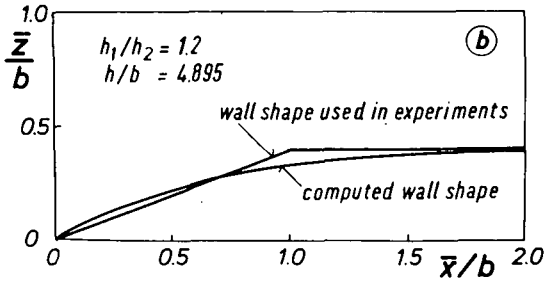

Fig. 2(*b*) Computed wall shape and linear contracting side wall

Fig. 2 Theoretical model of the test section and wall shapes

cade have a spacing which is equal to the test section width. The blade chord extends from the cascade leading-edge to downstream infinity. The simplest case of a calculation like this is given when the blades are represented by a source distribution of constant strength between cascade leading and trailing edge. Exactly this case was assumed. An associated wall shape was easily calculated and is shown in Fig. 2(*b*) as a curved line for the special case of an overall contraction ratio of $h_1/h_2 = 1.2$ and a ratio of $h/b = 4.895$.

The induced velocities of the infinite number of source distributions were calculated. For the test section center line the following expression was derived:

$$\frac{\bar{u}}{\bar{U}_\infty}\frac{\mu+1}{\mu-1} = -\frac{h}{\pi b}\ln\left[\cosh\frac{\pi b}{h} - \sinh\frac{\pi b}{h}\cdot\tanh\left(\frac{\pi b}{h}\frac{\bar{x}}{b}\right)\right]. \quad (1)$$

A numerical evaluation of this expression is shown in Fig. 3 for different values of AR using $l\cdot\cos\lambda$ with $\lambda = 40$ deg instead of b. As a result, an important effect of the AR on the axial velocity distribution, which is the sum of the induced velocities $\bar{u}$ and a constant velocity $\bar{U}_\infty$, can be seen.

A comparison of these curves with results of the actuator disk theory was thought to be useful. For this reason the perturbation velocities for a single blade row machine and a multistage machine both with an AR of 3.75 were calculated according to reference [14]. The results are also shown in Fig. 3. From this comparison the conclusion may be drawn that the axial velocity distribution of a machine can be approximated in cascade tests by choosing a proper AR.

Modified Schlichting Method. The Schlichting method [12] is a well-known method for calculating two-dimensional flows in lightly loaded compressor cascades. A modification of this method was developed by simulating the velocity distribution of equation (1) as the induced velocities of a continuous distribution of strip sources and introducing it into the conditions of flow tangency of the method. The source distribution extends from upstream to downstream infinity. Its strength is constant in cascade direction and varies in axial direction as the gradient of the desired axial velocity distribution. A detailed description of the modified Schlichting method is given in reference [15].

With the modified method the turning angles $\Delta\beta$ and the slope factors $d(\Delta\beta)/d\mu$ at $\mu = 1$ were calculated for a great number of compressor cascades with 9C7/32.5C50 profiles. The slope factors are shown in Figs. 4 and 5 for a space chord ratio of 1.0 and 0.5, respectively. Also shown in Figs. 4 and 5 are the slope factors which were obtained with the method of Pollard and Horlock [4] for the same cascades. The results presented demonstrate a remarkable influence

Nomenclature

b = axial chord and contraction length
c_{p1} = static pressure coefficient, equation (5)
D = diffusion factor, equation (6)
d = blade maximum thickness
e = standard location of traverse plane
F = abbreviation of right hand side of equation (1)
h = test section width
h/l = aspect ratio (AR)
l = chord length
Ma_1 = inlet Mach number
p = static pressure
$\Delta p/q_1$ = static pressure rise, equation (4*b*)
p_t = total pressure
q_1 = inlet dynamic pressure, $p_{t1} - p_1$
Re_1 = Reynolds number based on inlet velocity
Tu_1 = degree of turbulence at cascade inlet
t = blade spacing
U, V = components of W in x-/y-direction
$\bar{U}, \bar{V}$ = components of W in $\bar{x}$-/$\bar{y}$-direction
u, v = induced velocities in x-/y-direction
$\bar{u}, \bar{v}$ = induced velocities in $\bar{x}$-/$\bar{y}$-direction
W = air velocity
x, y, z = rectangular coordinates
$\bar{x}, \bar{y}, \bar{z}$ = rectangular coordinates
α = angle of attack, angle between inlet air direction and blade chord
β = air angle, angle between air velocity and axial direction
$\Delta\beta$ = turning angle, equation (4*c*)
δ = axial distance between two blade rows
ζ_{V1} = total pressure loss coefficient, equation (4*a*)
λ = stagger angle
μ = axial velocity density ratio (AVDR) in compressible flow, equation (4*d*) axial velocity ratio (AVR) in incompressible flow with $\rho_1 = \rho_2$
ρ = density
φ = blade camber angle

Subscripts

1,2 = for quantities in front and behind the cascade
∞ = for basic flow
cr = for critical values
l = for local values along $\bar{x}$

Downloaded 01 Jun 2010 to 171.66.16.59. Redistribution subject to ASME license or copyright; see http://www.asme.org/terms/Terms_Use.cfm

of the AR on the slope factor. This is not so with the results of the Pollard-Horlock method where a linear axial velocity distribution between cascade inlet and outlet is assumed for all values of AR. Even in the case of AR = 1 with an axial velocity distribution fairly close to the linear distribution of reference [4] considerable differences between the results of the new method and method [4] may be observed.

In quasi-two-dimensional flows with $\mu \neq 1$ there is always an axial velocity variation downstream of the cascade. Associated with this there is also an outlet angle variation which easily can be calculated when a constant velocity component in cascade direction is assumed. Final values of μ and β_2 are reached at downstream infinity.

With a prescribed μ-value the modified Schlichting method predicts the outlet angle β_2 at downstream infinity. Local values, μ_l and β_{2l}, at intermediate stations can be calculated from the following equations

$$\mu_l(\bar{x}/b) = \frac{1}{2}[\mu(1 + F_l(\bar{x}/b)) + (1 - F_l(\bar{x}/b))], \tag{2}$$

$$\beta_{2l}(\bar{x}/b) = \arctan\left[\frac{\mu}{\mu_l(\bar{x}/b)} \cdot \tan\beta_2\right], \tag{3}$$

with F_l as an abbreviation for the right hand side of equation (1). In experimental investigations only local values can be measured. Equations (2) and (3) may be used after having been solved for μ and β_2 to calculate final values at downstream infinity. Two illustrative examples of equations (2) and (3) may be found in the third section of this paper.

In addition to the sample calculations described before two flat plate cascades with linear contracting side walls and an AR of 3 and 6 were calculated. The results obtained for the deviation angles at mid span position were compared with those of a three-dimensional calculation [16]. For both values of AR exactly the same results as given in reference [16] were attained.

Modified Martensen Method. As mentioned before, the Martensen method calculates blade pressure distributions which are in better agreement with measured results than those calculated with the Schlichting method. For this reason a modified version of the Martensen method was also established utilizing the same ideas as were described before. The details of the modified Martensen method are given in reference [17]. No attempt was made to introduce a so-called trailing edge hypothesis in order to make calculation of the exit angle possible. As in the original version, an outlet angle, either calculated or measured and transformed to its final value far downstream, has to be prescribed in the modified method.

As an example Fig. 6 shows blade pressure distributions for two cascades having the same profile (9C7/32.5C50), inlet angle ($\beta_1 = 52$ deg), and AVR ($\mu = 1.2$) but different values of AR (1.0 and 3.75). Again a remarkable effect of the AR can be observed. Also shown in Fig. 6 is a pressure distribution which was computed with the Pollard-Horlock method.

The Krahn-Betz rule [18] was used to take account of compressibility effects. A comparison between theory and experiment is given in the next section.

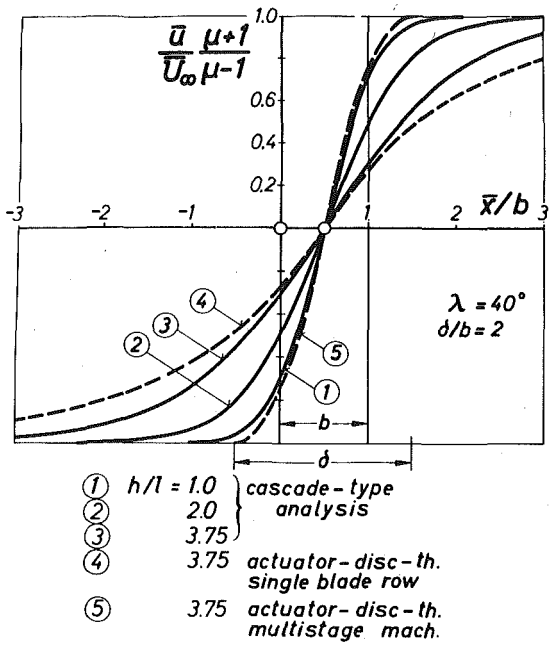

Fig. 3 Effect of test section dimensions on the axial velocity distribution in the blade-free test section

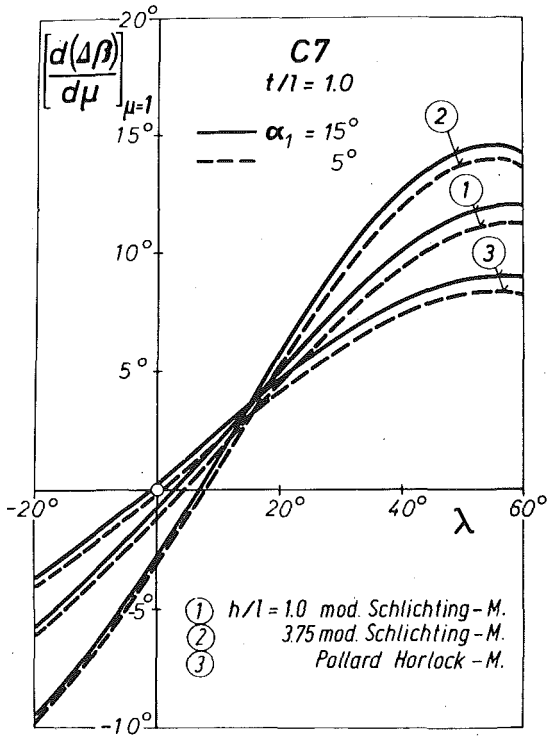

Fig. 4 Effect of stagger angle on turning angle slope $d(\Delta\beta)/d\mu$ at different values of AR and $t/l = 1.0$

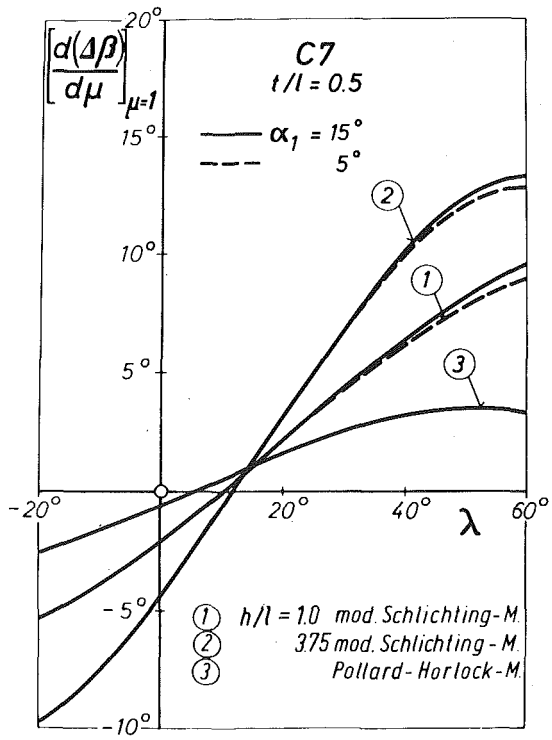

Fig. 5 Effect of stagger angle on turning angle slope $d(\Delta\beta)/d\mu$ at different values of AR and $t/l = 0.5$

Downloaded 01 Jun 2010 to 171.66.16.59. Redistribution subject to ASME license or copyright; see http://www.asme.org/terms/Terms_Use.cfm

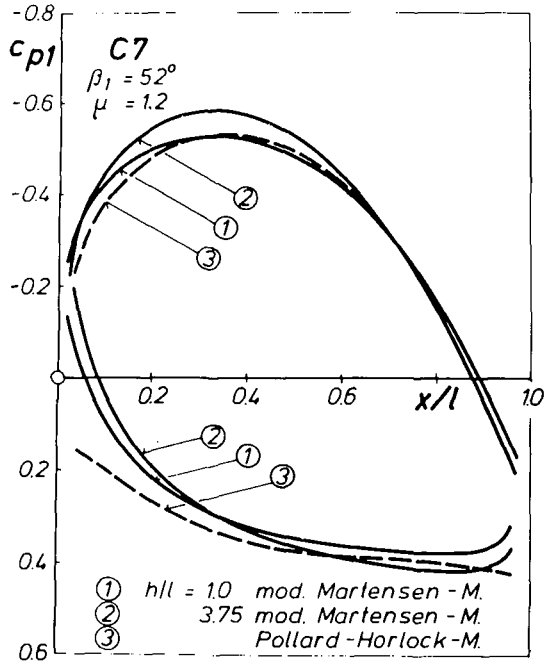

Fig. 6 Effect of AR on blade pressure distribution at an AVR of $\mu = 1.2$

Experimental Investigations

Experimental Apparatus. The experimental investigations were carried out in the High Speed Cascade Wind Tunnel of the DFVLR Braunschweig [19]. The tunnel is installed in a tank which can be evacuated from 1 to 0.05 bar. Therefore, the Mach number and Reynolds number can be varied independently. The normal turbulence level is about $Tu_1 = 1$ percent. It can be increased by using a tubulence grid in front of the test section.

The nominal test section width is $h = 300$ mm; its vertical height varies from a minimum value to a maximum value of 500 mm depending on inlet angle, space chord ratio, and blade number. A periodic cascade flow (constant static pressure along the test section height) can be adjusted with boundary layer suction devices installed at the end of the horizontal test section walls and positioned just above and below the last blades of the cascade.

Changes in AVDR through the cascade can be obtained by varying the amount of air removed through porous side walls (15 percent open area) or by using wedge type inserts of different size attached to solid side walls. Both possibilities were applied in the present investigation.

The AR can be changed either by varying the chord length of the profiles or by altering the test section width all along the test section length. Only the latter possibility was used.

Wake traverse measurements (total pressure, static pressure and outlet angle) are usually performed with a wedge type probe [20] located at a standard distance behind the cascade outlet plane. At inlet total pressure and static pressure (taken as an average of a number of pressure tappings on each side wall) are measured. Blade pressure distributions are measured using static pressure tappings on the suction and pressure side of two adjacent blades.

Cascade Geometry and Test Program. Two different cascades, one with 9C7/32.5C50 blades and the other with DCA 56.8-07 blades, were tested with only one AR (3.75) in the first case and two values of AR (3.75 and 2.0) in the latter case (Table 1). In both cases, the chord length was $l = 80$ mm. The number of blades used was different: seven in the first and 14 in the latter case. Three types of side wall conditions were applied: (i) parallel solid walls, (ii) parallel porous walls, and (iii) linear contracting walls with a contraction length of about the same as the axial chord length.

The test program mainly comprised wake and pressure distribution measurements at mid span position for a number of inlet angles and Mach numbers. The standard traversing plane was located $e = 60$ mm ($e/l = 0.75$) and $e = 24$ ($e/l = 0.3$) downstream of the cascade exit

Table 1 The tested cascades: (1) solid side walls (2) solid and porous side walls (3) linear contracting side walls

Parameter	C7-Cascade 9C7/32.5C50	DCA-Cascade DCA56.8-07	
φ	32.5°	56.8°	
d/l	0.09	0.07	
t/l	1.0	0.45	
λ	40°	19.2°	
Re_1	$4 \cdot 10^5$	$5 \cdot 10^5$	
Tu_1	1 %	3 %	
h/l	3.75	3.75	2.0
h_1/h_2	1.0[1]	1.0[2]	1.0[2]
	1.2[3]	1.07[3]	1.14[3]
		1.14[3]	
		1.17[3]	

plane for the C7- and the DCA-cascade respectively. For only a few configurations, the location of the traversing plane was changed several times in order to get insight into the flow development behind the cascade. Additional wake measurements along blade span were also performed in some cases (near design inlet angle).

Evaluation of the Experimental Data. The wake data were evaluated by transforming the non-homogeneous flow at the measuring station into an equivalent homogeneous flow assuming a constant-streamtube-height compressible-flow mixing process [21]. This results in simple relations for the total pressure loss coefficient ζ_{V1}, the static pressure rise $\Delta p/q_1$, the turning angle $\Delta\beta$, and the AVDR μ, which are defined as

$$\zeta_{V1} = \frac{p_{t1} - p_{t2}}{p_{t1} - p_1}, \tag{4a}$$

$$\frac{\Delta p}{q_1} = \frac{p_2 - p_1}{p_{t1} - p_1}, \tag{4b}$$

$$\Delta\beta = \beta_1 - \beta_2, \tag{4c}$$

$$\mu = \frac{\rho_2 W_2 \cos\beta_2}{\rho_1 W_1 \cos\beta_1} \tag{4d}$$

In quasi-two-dimensional flows with axial velocity variations like those shown in Fig. 3, the results obtained in this way depend on the location of the wake traverse plane. Therefore, they are regarded as local values (index l) with the exception of ζ_{V1} which shows no variation with the location of the measuring plane in to the experience of the authors. From the local values, final values at downstream infinity may be calculated. Neglecting compressibility effects downstream of the cascade, this can be done for μ and β_2 with formulas which are obtained when equations (2) and (3) are solved for μ and β_2.

For the pressure distribution a nondimensional coefficient is defined as

$$c_{p1} = \frac{p(x/l) - p_1}{p_{t1} - p_1}. \tag{5}$$

In some cases the diffusion factor

$$D = 1 - \frac{W_2}{W_1} + \frac{1}{2}\frac{t}{l}\left(\sin\beta_1 - \frac{W_2}{W_1}\sin\beta_2\right) + \frac{d}{l} \tag{6}$$

was calculated too.

C7-Cascade Test Results and Comparison with Theory. Figure 7(a) shows the measured and calculated variation of the turning angle and the AVDR downstream of the C7-cascade at an inlet angle of $\beta_1 = 52$ deg and with a geometrical contraction ratio of $h_1/h_2 = 1.2$. The measurements were actually performed in the low speed cascade wind tunnel which explains the relatively low Mach and Reynolds numbers. The low and high speed tunnels, however, have

Downloaded 01 Jun 2010 to 171.66.16.59. Redistribution subject to ASME license or copyright; see http://www.asme.org/terms/Terms_Use.cfm

identical test section dimensions so that the same cascade could be used. The evaluation of equations (2) and (3) was done in such a way that the theoretical curves pass through the measured points at $\bar{x}/b = 1.95$ which is very close to the standard location of the traverse plane in the high speed tests. The good agreement between the experimentally and theoretically obtained results gives some plausibility to the theoretical developments of the second section.

From the results discussed before, it may be concluded that similar flow angle variations might be present in front of the cascade. Flat plates as horizontal walls of the tunnel test section are somewhat questionable under these conditions.

In compressible flow measured turning angles, transformed to their final values at downstream infinity and plotted at final values of AVDR are shown in Fig. 8 along with calculated results for incompressible flow. The Pollard-Horlock method and the modified Schlichting method were used for the calculations. The results for both methods are rather different. However, this is in line with the results of Fig. 4 and with the results discussed in reference [16]. In comparing the measured turning angles with those calculated with the modified Schlichting method it is assumed in both cases, i.e., $h_1/h_2 = 1.0$ and 1.2, that the effective wall shape (that is the displacement thickness distribution of the side wall boundary layers alone or the combined displacement thickness distribution of the inserts and the side wall boundary layers) can theoretically be represented by a source distribution of constant strength. In other words, an effective wall shape similar to that shown in Fig. 2(*b*) is assumed in both cases. This implies the additional assumption of no variation of the effective wall shape in cascade direction.

As a result of the comparison between theory and experiment it is concluded that the variation of the turning angle with AVDR at prescribed AR (3.75) is more accurately predicted with the modified Schlichting method than with the Pollard-Horlock method. The effect of compressibility on measured turning angles turns out to be small as long as the critical Mach number is not reached.

Figure 9 shows measured and calculated blade pressure distributions for two inlet Mach numbers, $Ma_1 = 0.3$ and 0.7, and two values of AVDR ($h_1/h_2 = 1.0$ and 1.2) for each Mach number. The calculations were performed with the modified Martensen method coupled with the compressibility correction rule of Krahn and Betz [18]. Measured turning angles and values of AVDR, transformed to their final values at downstream infinity, were prescribed. The transformed μ-values are indicated in Fig. 9 and the $\Delta\beta$-values may be taken from Fig. 10. The agreement between theory and experiment is almost perfect in case of $Ma_1 = 0.3$ thus indicating that the combined effect of AVDR and AR is correctly incorporated in the theory. At $Ma_1 = 0.7$ certain discrepancies between theory and experiment can be observed on the suction side of the profile. This may be due to the compressibility correction rule used or due to the way the rule was applied.

For two cascade configurations ($h_1/h_2 = 1.0$ and 1.2) measured values of AVDR, turning angle, and loss coefficient are shown in Fig. 10 as a function of the inlet Mach number. Also shown are the transformed values of the AVDR and the turning angle. The differences between measured (local) and transformed values are an illustration of possible changes of flow properties downstream of the traverse plane in cascades with an AR of 3.75.

For the inlet angle under consideration, i.e., $\beta_1 = 52$ deg, the configuration with the highest μ-values ($h_1/h_2 = 1.2$) has the highest losses. This can be explained with Fig. 9 where the pressure distributions with the highest μ-values have the highest deceleration rates on the pressure side near the leading edge and on the suction side near the trailing-edge. This situation may change with an inlet angle variation.

DCA-Cascade: Test Results and Comparison with Theory. Experimental values of turning angle and loss coefficient as a function of inlet angle are shown in Fig. 11 for the DCA-cascade tested at two values of AR ($h/l = 3.75$ and 2.0) and two values of AVDR ($\mu = 1.0$ and 1.2) for each AR. The inlet Mach number was $Ma_1 = 0.3$. Nearly identical results were obtained at both aspect ratios and two-dimensional flow. At quasi-two-dimensional flow ($\mu = 1.2$), however, the results obtained at both aspect ratios were different from each other and also different from the results at $\mu = 1.0$.

The deflection curves exhibit the well-known AVDR effect, which consists in a shift of the curves towards higher deflections with increasing AVDR. The AR effect on the deflections at $\mu = 1.2$ is small in this case and more difficult to understand. It is known from theo-

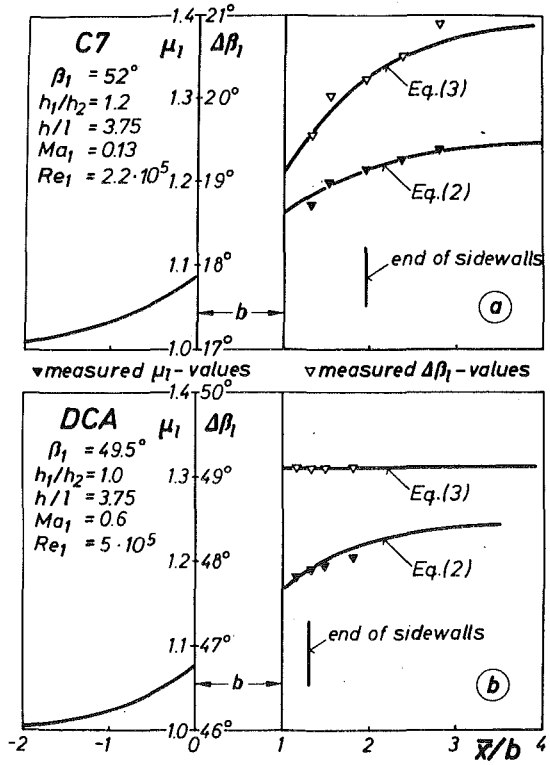

Fig. 7 Variation of local turning angle and local AVDR behind two different cascades. Comparison between theory and experiment (*a*) C7-cascade (*b*) DCA-cascade

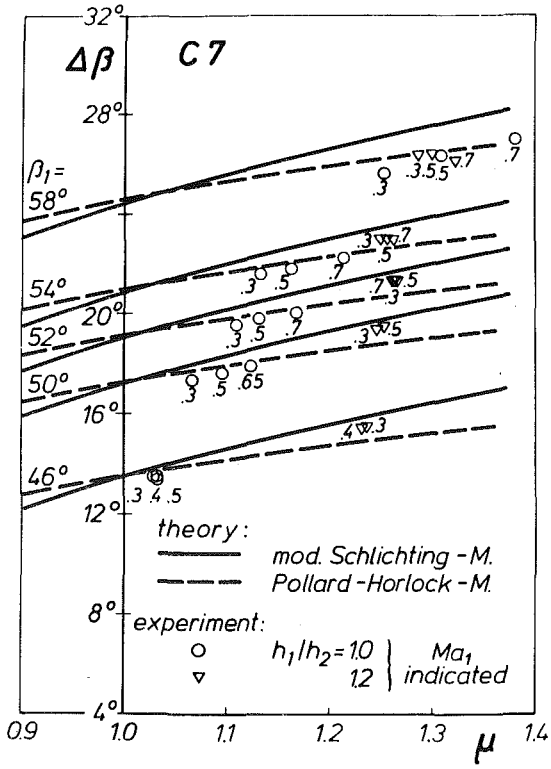

Fig. 8 Effect of AVDR on turning angle at different inlet angles. Comparison between theory and experiment

Downloaded 01 Jun 2010 to 171.66.16.59. Redistribution subject to ASME license or copyright; see http://www.asme.org/terms/Terms_Use.cfm

retical results, not included in this paper, that the slope factor $d(\Delta\beta)/d\mu$ is only a weak function of the profile camber angle in inviscid flow. Therefore, the influence of the AR on the turning angle at $\mu \neq 1$ may be estimated from Fig. 5. At $\lambda = 19.2$ deg and $t/l = 0.5$, which is close to the t/l-value of the DCA-cascade (0.45), Fig. 5 indicates only a small influence of the AR on the deflection. This result is in agreement with the experimental finding. For $\beta_1 = 49.5$ deg spanwise measurements were performed to insure that there was a sufficient large zone of constant flow properties for each AR demonstrating that the effect of secondary flow on the turning angles was negligible small.

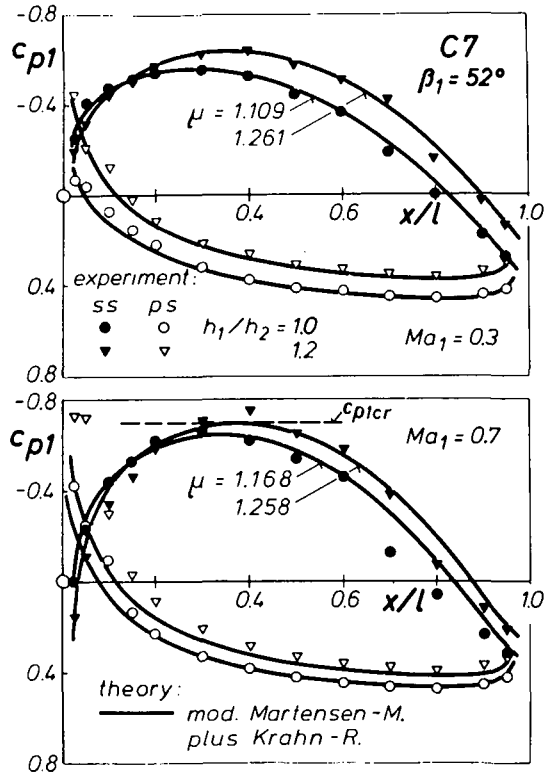

Fig. 9 Effect of AVDR on blade pressure distribution at different inlet Mach numbers. Comparison between theory and experiment

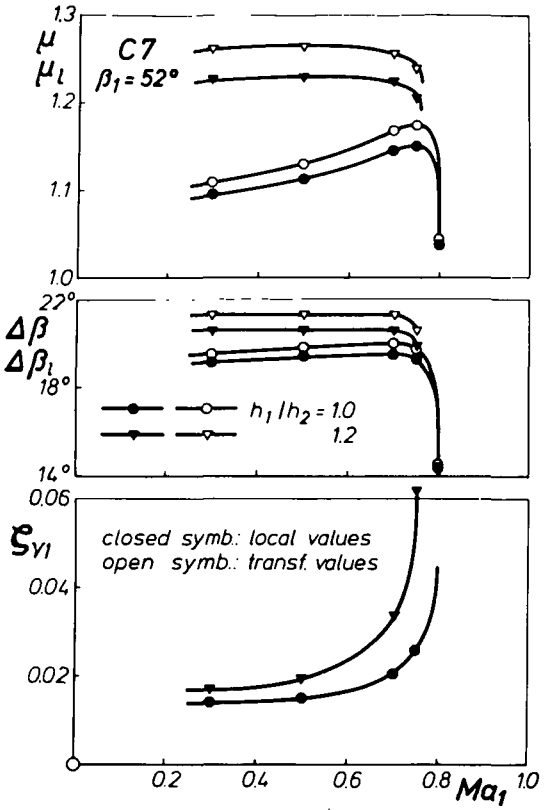

Fig. 10 Effect of inlet Mach number on cascade performance at two different contraction ratios of the test section

The AVDR effect on the loss curves consists in a well-known shift of these curves towards higher inlet angles thus influencing the reference minimum loss inlet angle in the same way. New is the fact, that the AR may also have an effect on the losses as shown in Fig. 11. This result can be explained with the pressure distributions, which are shown in Fig. 12 for $\beta_1 = 49.5$ deg, both aspect ratios, and two values of AVDR. The inlet Mach number is the same as in Fig. 11, i.e., $Ma_1 = 0.3$. The AVDR values are local values, which easily can be converted into final values with the aid of Fig. 13.

The loss coefficients at minimum loss and higher inlet angles are primarily determined by the pressure gradients on the suction side of the profiles. For the case at hand, the pressure gradient and the loss coefficient are obviously greatest for $\mu_l = \mu = 1.0$ and smallest for $\mu_l = 1.2$ and $h/l = 2.0$. For $\mu_l = 1.2$ and $h/l = 3.75$ the pressure gradient is somewhat higher as it is for $h/l = 2.0$ and so are the losses.

The theoretical curves in Fig. 12 were calculated with the modified Martensen method. Transformed experimental β_2- and μ-values were prescribed. The agreement between theory and experiment is very good with the exception of a small separation zone at the trailing-edge in the lower graph. The AR effect in the upper graph, neglecting the influence of slightly different μ-values, is accurately predicted. The lower graph is for two-dimensional flow and no AR effect can be seen, what of course was expected.

The good agreement between theory and experiment in the upper graph of Fig. 12 is an indication for the correctness of the assumption, that the effective wall shape (displacement thickness distribution of the wall boundary layers on porous side walls) can be approximated by that one, which is used in the modified Martensen method. Another hint for the correctness of the mentioned assumption is given by the results shown in Fig. 7(*b*). The development of the measured μ_l- and $\Delta\beta_l$-values behind the DCA-cascade with solid side walls and $h_1/h_2 = 1$ is correctly predicted by equations (2) and (3). The values of μ_l and $\Delta\beta_l$ at the standard traverse plane ($e/l = 0.3, \bar{x}/b = 1.32$) were

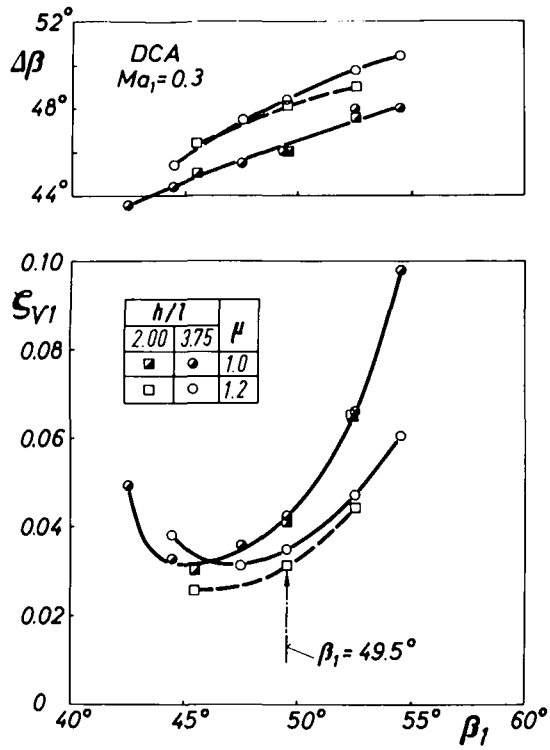

Fig. 11 Effect of inlet angle on cascade performance at different values of AR and AVDR. $Ma_1 = 0.3$

Downloaded 01 Jun 2010 to 171.66.16.59. Redistribution subject to ASME license or copyright; see http://www.asme.org/terms/Terms_Use.cfm

used in the calculations. Interesting is the fact, that there is no variation of $\Delta\beta_l$ when the direction of the outlet flow is nearly axial.

For $\beta_1 = 49.5$ deg it was checked, that there was for both aspect ratios a sufficient large zone of constant losses near the mid span position. This was not the case at high inlet angles. The results shown in the following figures are therefore for $\beta_1 = 49.5$ deg.

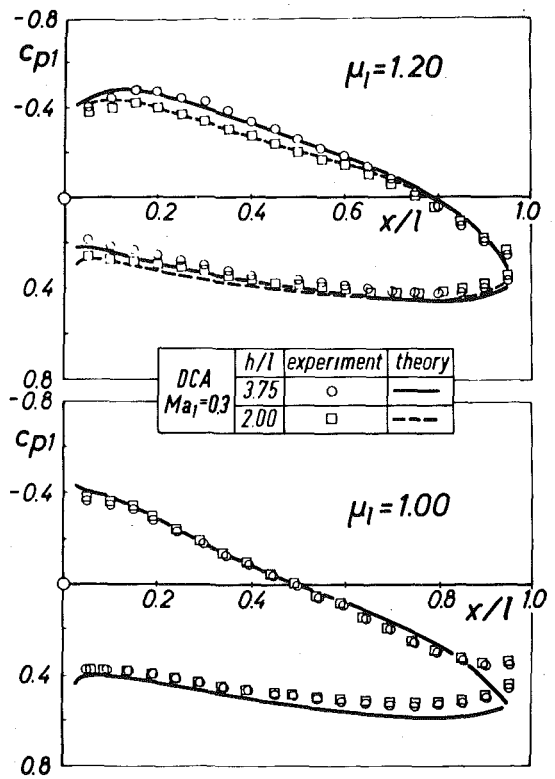

Fig. 12 Effect of AR on blade pressure distribution at different values of AVDR. Comparison between theory and experiment. $Ma_1 = 0.3$, $\beta_1 = 49.5$ deg

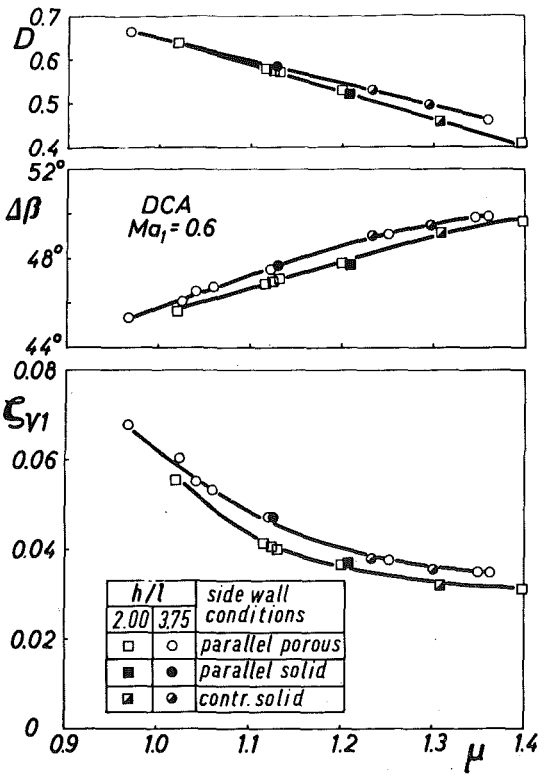

Fig. 14 Effect of AVDR on cascade performance at different values of AR. $Ma_1 = 0.6$, $\beta_1 = 49.5$ deg

The combined effect of AVDR and AR on diffusion factor, turning angle, and loss coefficient is shown in Fig. 14 for a subcritical Mach number (0.6). Pressure distributions for the same Mach number are given in Fig. 15. The AVDR variation was achieved with different side wall conditions, which are indicated in the figures. As may be seen, in most of the tests porous side walls were used. Test results from tests with other side wall conditions fit well into the results obtained with porous side walls. In some tests with identical values of AVDR but different side wall conditions exact the same results were measured.

For the inlet angle selected, that is $\beta_1 = 49.5$ deg equivalent to $i = +1.9$ deg, there is a continuous fall of the diffusion factor and loss

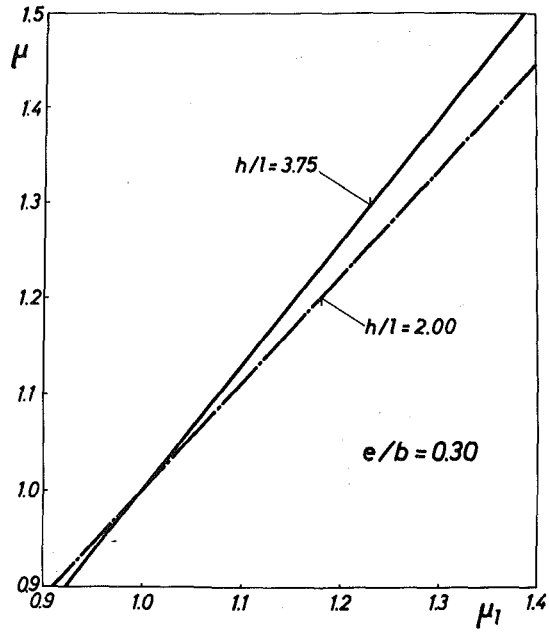

Fig. 13 The AVDR as a function of the local AVDR at $e/b = 0.3$ for different values of AR

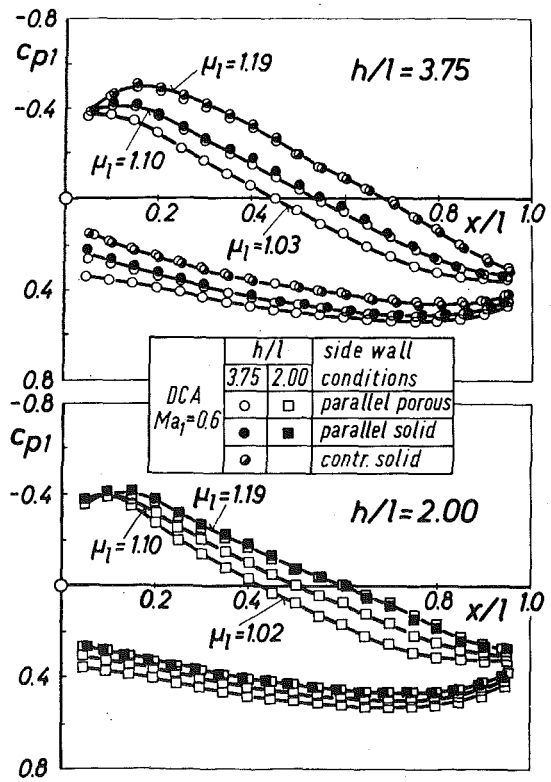

Fig. 15 Effect of AVDR and side wall condition on blade pressure distribution at different values of AR. $Ma_1 = 0.6$, $\beta_1 = 49.5$ deg

Downloaded 01 Jun 2010 to 171.66.16.59. Redistribution subject to ASME license or copyright; see http://www.asme.org/terms/Terms_Use.cfm

coefficient with increasing values of AVDR. This is true for both AR, the results for AR = 2.0 being, however, somewhat smaller than those for AR = 3.75. As it was done before, this behavior can be explained with the pressure distributions in Fig. 15.

According to theoretical considerations only a small slope factor $d(\Delta\beta)/d\mu$ was expected. Due to the increasing losses with decreasing values of AVDR a rather different behavior was measured. Nevertheless, the expected AR effect was obtained.

The supercritical performance of the DCA-cascade is shown in Figs. 16 and 17 for an inlet Mach number of $Ma_1 = 0.8$. This time rather substantial differences between the loss curves in Fig. 16 and between the pressure distributions in Fig. 17 were found as a consequence of different aspect ratios. With respect to Fig. 17 it should of course be kept in mind, that the pressure distributions shown are for the same μ_l-values but for different μ-values. This means, that beside the dominant AR effect there is also a small AVDR effect inherent in the pressure distribution curves.

Loss and deflection curves in Fig. 16 begin at an AVDR of about $\mu = 1.15$. Two-dimensional conditions with $\mu = 1.0$ were not achieved. With increasing values of AVDR nearly constant losses at an AR of 2.0 and rapidly increasing losses at an AR of 3.75 were measured. The pertinent pressure distributions in Fig. 17 show small supersonic pockets of extending size with changing AVDR at an AR of 3.75. This leads for all values of AVDR to suction side pressure gradients which are for the AR of 2.0 much smaller than those for the AR of 3.75. Therefore, different pressure gradients in both cases and, at an AR of 3.75, increasing shock losses and shock boundary layer interaction losses with increasing values of AVDR constitute the reason for the highly different loss curves in Fig. 16. The high losses at an AR of 3.75 are also the reason for vanishing differences in deflections.

The effect of inlet Mach number on diffusion factor, turning angle, and loss coefficient is shown in Fig. 18 for both aspect ratios and two values of AVDR for each AR. Figure 18 was derived from a number of plots like those shown in Figs. 14 and 16 by crossplotting the results at prescribed values of AVDR and AR. In two-dimensional flow ($\mu = 1.0$) a strong increase of the losses with increasing Mach number was obtained. Contrary to this a reduced loading of $\mu = 1.2$ resulted in a much lower effect of the Mach number on the losses. As it was expected the losses at AR = 3.75 are higher (especially at supercritical Mach numbers) than those at AR = 2.0. The critical Mach number is reached first with AR = 3.75.

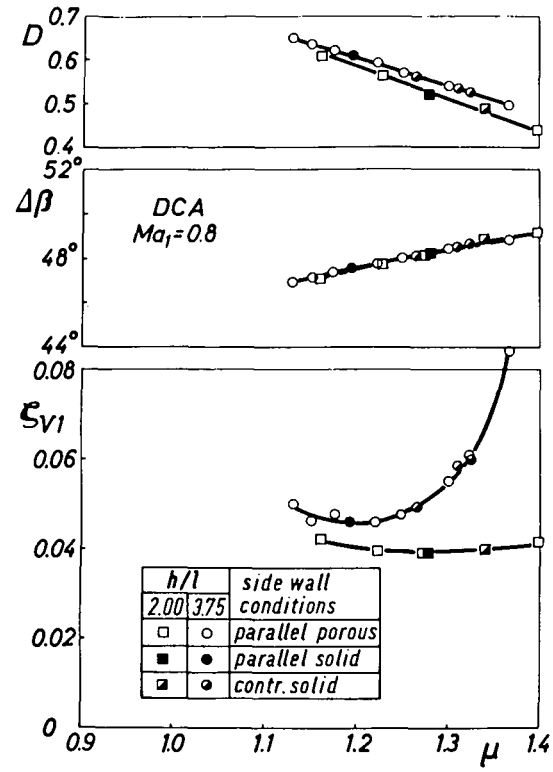

Fig. 16 Effect of AVDR on cascade performance at different values of AR. $Ma_1 = 0.8$, $\beta_1 = 49.5$ deg

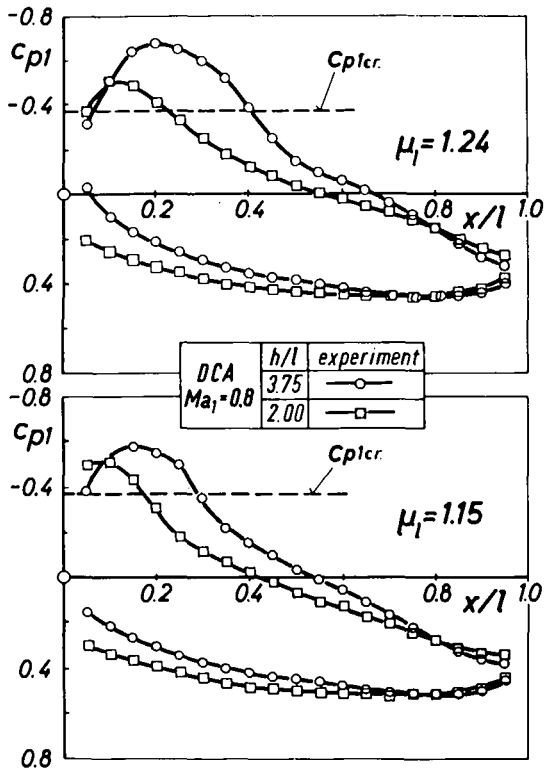

Fig. 17 Effect of AR on blade pressure distribution at different values of AVDR. $Ma_1 = 0.8$, $\beta_1 = 49.5$ deg

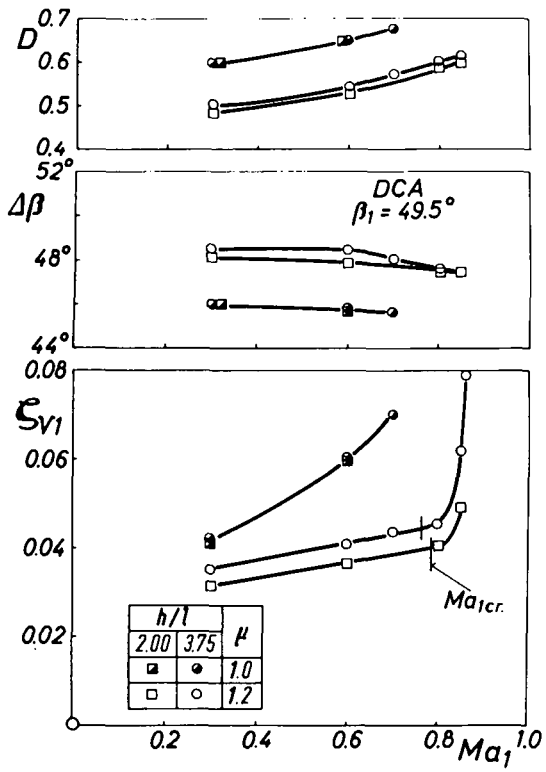

Fig. 18 Effect of inlet Mach number on cascade performance at different values of AR and AVDR. $\beta_1 = 49.5$ deg

Downloaded 01 Jun 2010 to 171.66.16.59. Redistribution subject to ASME license or copyright; see http://www.asme.org/terms/Terms_Use.cfm

Summary and Conclusions

The paper describes theoretical and experimental investigations on the combined effect of the axial velocity density ratio (AVDR) and the aspect ratio (AR) on compressor cascade performance in incompressible and compressible flow.

Using a special wall shape, approximating a linear contraction as well as the displacement thickness distribution of the wall boundary layers, a cascade-type analysis for the flow field of the blade-free test section has been developed. The analysis especially leads to an analytical expression for the axial velocity distribution at the center plane of the test section. The new expression has been

i evaluated for different aspect ratios and the results have been compared with solutions of the actuator disk theory for single blade row and multistage machines.

ii incorporated in the Schlichting and Martensen methods thus giving modified versions of these methods capable to account for both AVDR and AR effects. The Krahn-Betz rule has been used to take account for compressibility effects.

In comparing the results of the new axial velocity function with those of the actuator disk theory it has been found that high and low AR cascades approximate the axial velocity distributions in single blade row machines and multistage machines, respectively.

Sample calculations with the modified Schlichting and Martensen methods demonstrate at given values of AVDR $\neq 1$ a considerable effect of the AR on cascade turning angles and profile pressure distributions.

Experiments with two compressor cascades have been performed in the High Speed Cascade Tunnel of the DFVLR in Braunschweig. The first cascade was made up of conventional C7-blades. It has been investigated at geometrical contraction ratios of 1.0 and 1.2 at an AR of 3.75. The second cascade consisted of highly cambered double circular arc blades. It has been investigated at aspect ratios of 3.75 and 2.0 using plane solid, plane porous, and linear contracting side walls for both AR.

The experimental results have been compared with corresponding theoretical results and a good agreement has been found in cases where the theory is applicable. Thus it has been demonstrated that it is very important to account for both AVDR and AR effects. At supercritical Mach numbers, where no theory was available to the authors, a rather distinct influence of the AR on pressure distributions and losses has been measured.

Acknowledgment

This work was supported, in part, by the *Deutsche Forschungsgemeinschaft*. The help is gratefully acknowledged.

The authors wish to thank Rolls Royce Ltd. (Bristol Engine Division), in particular Mr. N. J. Seyb, for permission to publish in this paper some of the results which were achieved through a collaboration between Rolls Royce Ltd. and the DFVLR in Braunschweig.

The authors are also indebted to Mr. J. Starke who gave permission to use, prior to publication, the modified Martensen method which was developed by him in his Doctoral Thesis.

References

1 Pollard, D., and Gostelow, J. P., "Some Experiments at Low Speed on Compressor Cascades," ASME JOURNAL OF ENGINEERING FOR POWER, Vol. 89, July 1967, p. 427.

2 Masek, Z., and Norbury, J. F., "Low-Speed Performance of a Compressor Cascade Designed for Prescribed Velocity Distribution and Tested with Variable Axial Velocity Ratio," I. Mech. E. Thermodynamics and Fluid Mechanics Group, *Conference Publication 3*, 1973, p. 224.

3 Starken, H., Breugelmans, F. A. E., and Schimming, P., "Investigation of the Axial Velocity Density Ratio in a High Turning Cascade," ASME Paper No. 75-GT-25.

4 Pollard, D., and Horlock, J. H., "A Theoretical Investigation of the Effect of Change in Axial Velocity on the Potential Flow Through a Cascade of Aerofoils," ARC CP No. 619, 1962.

5 Kubota, S., "Cascade Performance with Accelerated or Decelerated Axial Velocity," *Bulletin of JSME*, Vol. 5, No. 19, 1962, p. 450.

6 Fottner, L., "Analytical Approach for the Loss and Deflection Behaviour of Cascades in Transonic Flow Including Axial Mass Flow Variation," AGARD-AG-164, Paper I-7, 1972, p. 119.

7 Stark, U., "The Effect of Axial Velocity Ratio on the Aerodynamic Coefficients of a Compressor Cascade in Viscous Flow," AGARD-AG-164, Paper I-12, 1972, p. 205.

8 Stark, U., und Starke, J., "Der Einfluß des axialen Stromdichteverhältnisses auf die aerodynamischen Beiwerte von Verdichtergittern," *VDI-Berichte*, No. 264, 1976, p. 59.

9 Hoheisel, H., "Ergebnisse von Untersuchungen an ebenen Verdichtergittern in kompressibler Unterschallströmung bei Variation der axialen Stromdichte," *VDI-Berichte*, No. 264, 1976, p. 71.

10 Shaalan, M. R. A., "The Stalling Performance of Compressor Cascades of Different Aspect Ratios," Ph. D. Thesis, Liverpool University, Oct. 1967.

11 Hoheisel, H., "The Effect of Aspect Ratio on Loss, Deflection, and Pressure Distribution Measurements of Two Compressor Cascades," Contribution to the *Symposium on Measuring Techniques in Transonic and Supersonic Cascade Flow*, Leatherhead, England, Mar. 22–23, 1979.

12 Schlichting, H., "Berechnung der reibungslosen inkompressiblen Strömung für ein vorgegebenes Schaufelgitter," *VDI-Forschungsheft*, 447, 1955.

13 Martensen, E., "Die Berechnung der Druckverteilung an dicken Gitterprofilen mit Hilfe von Fredholm'schen Integralgleichungen zweiter Art," Mitteilungen aus dem Max-Planck-Institut für Strömungsforschung und der Aerodynamischen Versuchsanstalt No. 23, 1959.

14 Marble, F. E., "Three-Dimensional Flow in Turbomachines," Aerodynamics of Turbines and Compressors, Vol. X of *High Speed Aerodynamics and Jet Propulsion*, Princeton University Press, 1964.

15 Stark, U., "Berechnung der reibungslosen, quasizweidimensionalen Strömung für vorgegebene ebene Verdichtergitter," in Vorbereitung befindlicher Bericht des Instituts für Strömungsmechanik der TU Braunschweig.

16 Galapatti, R., and Hawthorne, W. R., "Cascades with Arbitrary End Wall Contraction," ARC RM No. 3813, 1978.

17 Starke, J., "Der Einfluß des axialen Stromdichteverhältnisses auf die aerodynamischen Beiwerte ebener Verdichtergitter," Dissertation, Technische Universität Braunschweig, 1979, see also: Bericht 79/2, Institut für Strömungsmechanik der Techn. Universität Braunschweig, 1979.

18 Betz, A., und Krahn, E., "Berechnung von Unterschallströmungen Kompressibler Flüssigkeiten um Profile," *Ingenieur-Archiv*, Band XVII. Heft 6, 1949.

19 Hoheisel, H., und Kiock, R., "Zwanzig Jahre Hochgeschwindigkeits-Gitterwindkanal des Instituts für Aerodynamik der DFVLR in Braunschweig," *Zeitschrift Für Flugwissenschaften Weltraumforschaung*, Band 1, Heft, 1, 1977, p. 17.

20 Sieverding, C., Starken, H., Lichtfuss, H. J., and Schimming, P., "Aerodynamic Measurements In Cascades," *AGARD-AG-207*, Section I, 1975, p. 60.

21 Amecke, J., "Anwendung der transsonischen Aehnlichkeitsregel auf die Strömung durch ebene Schaufelgitter," *VDI-Forschungsheft*, 540, 1970, p. 26.

Downloaded 01 Jun 2010 to 171.66.16.59. Redistribution subject to ASME license or copyright; see http://www.asme.org/terms/Terms_Use.cfm